AD-A214 580

59th
Shock and Vibration
Symposium

Volume III

DTIC
ELEC
NOV 07 1989
S D
B

Proceedings of a conference sponsored by
The Department of Defense and
The Department of Energy
held in Albuquerque, New Mexico
October 18-20, 1988

89 11 06 038

59th
Shock and Vibration
Symposium

Volume III

**Proceedings of a conference sponsored by
The Department of Defense and
The Department of Energy
held in Albuquerque, New Mexico
October 18-20, 1988**

Sandia National Laboratories

SYMPOSIUM MANAGEMENT

Host Representatives:
Mr. David O. Smallwood - Sandia National Laboratories
Mr. Rodney G. Galloway - Air Force Weapons Laboratory

Contract Management:

Mr. David O. Smallwood - Sandia National Laboratories

SYMPOSIUM MANAGER

Henry C. Pusey
4193 Sudley Road
Haymarket, VA 22069

REGISTRATION MANAGER

Sallie C. Pusey

59TH SYMPOSIUM PROGRAM COMMITTEE

Lt. C-M Carlin, USN
Defense Nuclear Agency
SPWE
6801 Telegraph Road
Alexandria, VA 22310

Rodney G. Galloway
U.S. Air Force
AFWL/NTES
Kirtland AFB, NM 87117-6008

J. Scott Milne
NASA/GSFC
M/C 302
Greenbelt, MD 20771

Jerome Pearson
U.S. Air Force
AFWAL/FIBG
Wright-Patterson AFB, OH 45433

John A. Robinson
U.S. Army Combat Systems Test Act.
STECS-EN-EV
Aberdeen Proving Ground, MD 21005

Lt. Col. Al Schenker
Defense Nuclear Agency
TTST
Kirtland AFB, NM 87115-5000

David O. Smallwood
Sandia National Laboratories
Division 7544
P.O. Box 5800
Albuquerque, NM 87185

Rudolph H. Volin
Naval Research Laboratory
Code 6337
Washington, DC 20375

COMPILATION OF PROCEEDINGS

Henry C. Pusey
Sallie C. Pusey

PRODUCTION OF PROCEEDINGS

Vibration Institute

TABLE OF CONTENTS
Papers Appearing in Volume III

GUNS AND PROJECTILES

Papers Appearing in Volume I

DYNAMIC CRITERIA

MODAL APPLICATIONS

Papers Appearing in Volume II

DYNAMIC TESTING

SHOCK

DYNAMIC ANALYSIS

Papers Expected to Appear in Volume IV

FEATURED PAPERS

VIBROACOUSTIC PAYLOAD ENVIRONMENT PREDICTION SYSTEM (VAPEPS)

MACHINERY VIBRATION

SOME RECENT CONTRIBUTIONS TO
MECHANICAL SIGNATURE ANALYSIS

R. L. Eshleman
Vibration Institute
Clarendon Hills, IL 60514

Mechanical signature analysis is used to perform machine diagnostics, determine mechanical condition, verify performance, and identify system parameters through the use of measured vibration signals. Some of the significant recent contributions in the performance of mechanical signature analysis related to increased capabilities in machine diagnostics and parameter identification involve dual channel analyzers. Advances in expert systems involve increased machine knowledge and new computer hardware and software. These areas will be discussed along with their implications to the more efficient performance of mechanical signature analysis.

INTRODUCTION

Mechanical signature analysis requires a combination of data processing of measured vibration signals, knowledge of equipment, and cause and effect analysis. Signature analysis is used to perform diagnosis of machine faults, establish machine condition, verify performance, and identify system parameters. Today, mechanical signature analysis relies heavily on digitized data and the Fast Fourier Transform (FFT) spectrum analysis for data processing. Some significant contributions in mechanical signature analysis result from extension of the capabilities of microprocessors. Others result from increased knowledge and documentation of the cause and effect behavior of mechanical equipment -- in essence, what vibration signature or spectrum will result from a given machine fault or condition.

This paper will deal with the increased instrumentation and data processing capabilities available to engineers to do machine diagnostics, modal testing techniques for rotating machinery machines, and the development of expert systems to solve machine problems.

MACHINE DIAGNOSTICS

During the past five years, vast increases have been made in the capabilities of instrumentation used for mechanical signature analysis. This results from the continued development of microprocessors. For this reason, the drift to digital from analog instrumentation largely has been completed. Some analyzers, oscilloscopes, filters, and integrators remain analog. However, their numbers decrease every year. Analog display and processing hardware have less pitfalls yet digital processing has more versatility in storing and manipulating data.

Even though the Fast Fourier Transform (FFT) has been highly developed, the pitfalls of aliasing and windowing still remain. The limitation of sampling time in tracking rapid events often prevents the use of batch processing instruments like the FFT. Aliasing causes the identification of false frequency components of the signal due to too few samples per period of the event. The Nyquist sampling rate [1] defines the minimum sampling rate at more than twice the highest frequency of interest. Thus a low pass filter must be used that restricts the frequency content of the input signal. Perhaps the worst pitfall of the FFT process is windowing. By its very nature the FFT process works under the assumption that a periodic signal exists. While the signal may be periodic, the sampling cannot be synchronized with the basic signal; therefore, a window function is imposed on the block of digital data to force its values to zero on both ends. This process induces errors in frequency and amplitude. The final problem involves the very nature of the FFT process which is a block processing technique. This means that, depending on the frequency range selected, a fixed amount of time is required for data acquisition no matter how high the sampling rate. Even though the data processing may be very fast, the limitation of data acquisition time will always exist because the event must happen in its periodic form before data acquisition ends and data processing begins. Thus if one is trying to track a rapidly occurring event, data acquisition time limitations will not permit the acquisition of enough points for an acceptable Bodé plot (amplitude and phase versus frequency). Overlap processing (use of some data from the previous block) can reduce the problem to some extent.

The principal advances in FFT analyzers have been in their portability and sampling rate. The very small data collectors (less than 10 lbs.) have 400 line analysis which gives acceptable resolution for almost any application. Lab analyzers have up to 800 lines of resolution. However, the data collector analyzers do not yet have the full features of the larger dedicated analyzers, such as zoom for intricate resolution and time domain. Data collectors will always suffer a display problem in the field because of their size. It is interesting to note that full featured dual channel analyzers with adequate data displays that are in the 30-lb. range exist today. These analyzers are not as portable as the data collector yet offer full dual channel capabilities for modal testing and machine diagnosis. Full dual channel analysis and modal testing software can be used in a 386 type portable computer that weighs less than 20 lbs.

The dual channel analyzer has increased the power of machine diagnostics with the use of the basic FFT dual channel functions -- transfer function, phase, and coherence. In addition, events at two locations can be compared in time, Figure 1, and frequency, Figure 2, domains. The transfer function, which provides the relationship between two measured signals as a function of frequency, is obtained by dividing the signal of Channel B by the signal of Channel A. Similarly, the phase function yields the phase relationship between Channels B and A as a function of frequency. Figure 3 shows the transfer function (vibration velocity/force) and phase from an impact test on a calender. The coherence function, Figure 4, provides a measure of the cause and effect relationship between Channels B and A as a function of frequency. If the signal measured in Channel B is entirely caused by the stimulus (hammer) of Channel A, then the coherence is one. If a lesser percentage of the activity at Channel B is caused by the stimulus at Channel A, then a coherence relating to the percentage of the effect between 0 and 1 will be obtained. The transfer function, phase, and coherence can be used for more in-depth analysis of two simultaneously
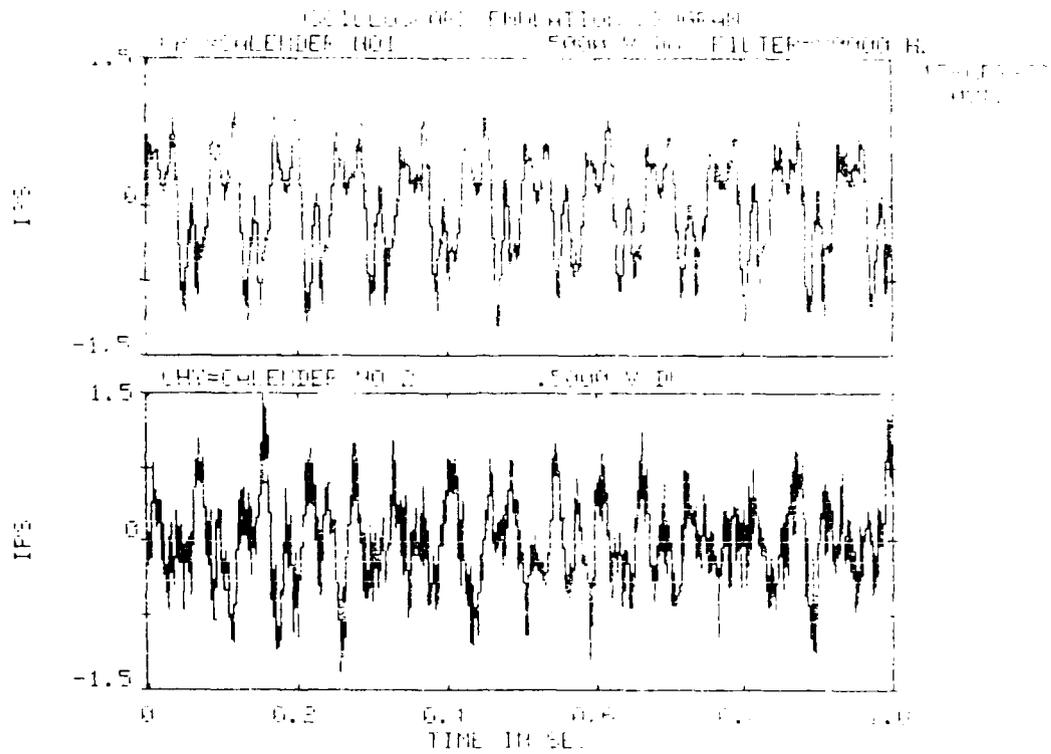
Figure 1. Time domain records from simultaneous vibration
measurements of two calender rolls
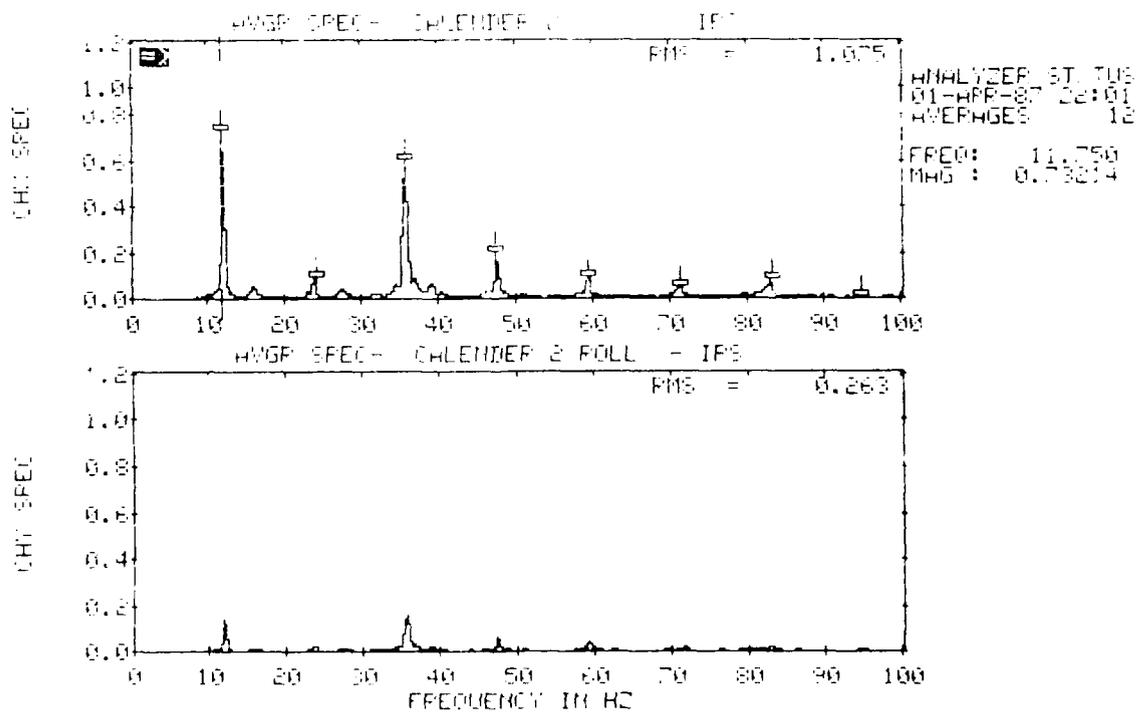
Figure 2. Spectral records from simultaneous vibration
measurements of two calender rolls
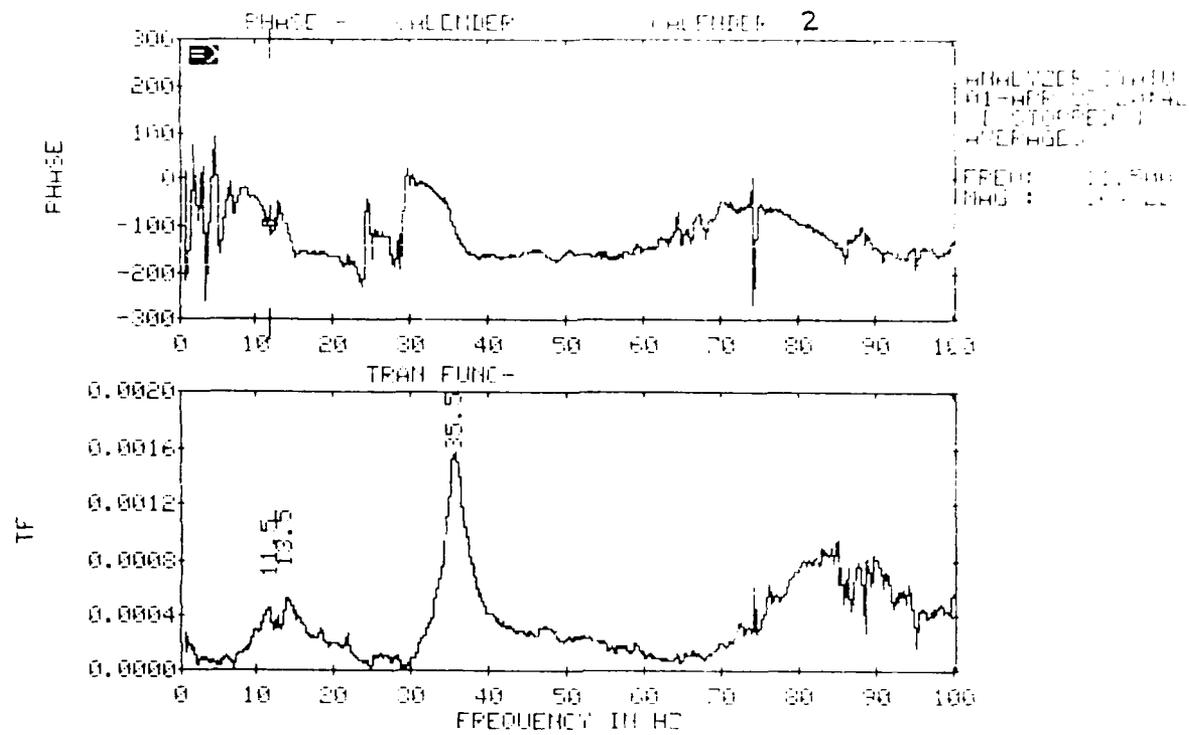
Figure 3. Transfer function (mobility) and phase
records for calender impact test
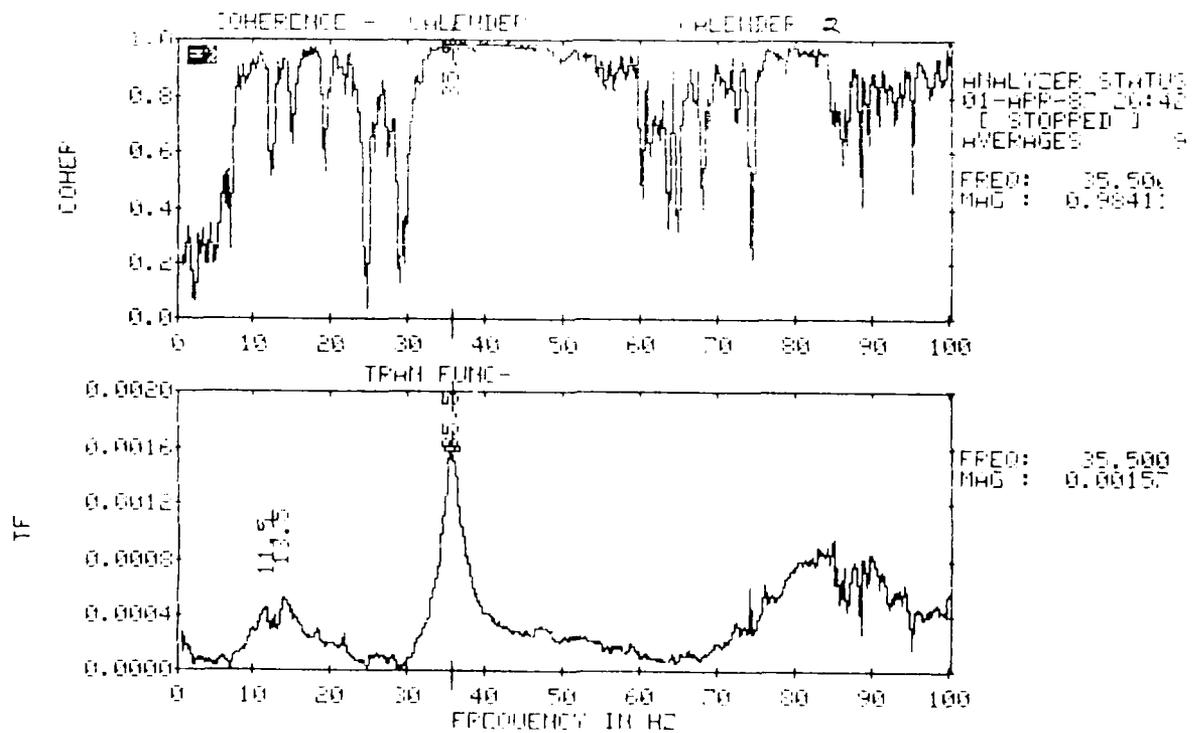
Figure 4. Transfer function (mobility) and coherence
records for calender impact test

occurring events in a machine. The coherence helps to determine sources of measured vibration when frequencies are similar. For example, if a frequency of 60 Hz were causing a problem at some location in a machine, and two possible origins were 2x from an 1800 RPM machine and 1X from a 3600 RPM machine, the coherence between each of the two machines and the problem machine would determine what portion of the vibration was originating at each source. The phase measurement permits establishment of phase relationships between measured points.

Real and imaginary values of the mode shape obtained from the transfer function and phase at selected positions on the machine provide the analysts more powerful tools. Damping can be obtained from the real plot and normalized imaginary values plotted at selected positions provide the mode shape of the rotor or structure. Thus, the dual channel analyzer provides data processing capability, when used along with machine or structural knowledge, that will yield much more complete machine diagnostics. The latter modal data can be used for design fault correction.

PARAMETER IDENTIFICATION

The dynamic characteristics of a machine or structure must be known before a vibration problem can be identified or corrected. These dynamic characteristics, or parameters, include natural frequencies, mode shapes, damping, and such modal properties as stiffness and mass. Parameters are quantified by exciting a machine using a hammer, shaker, or motion of the machine itself. (The magnitude of this stimulus may be known or unknown.) Response is measured with accelerometers, velocity transducers, or proximity probes. Oscilloscopes, tracking filters, swept-filter analyzers and FFT spectrum analyzers are then used to analyze the data.

Both forces and responses are measured to obtain cause and effect relationships with dual channel analysis. To date, the process of parameter identification which uses classical modal testing has been performed on stationary structures. Recent advances in modal testing of rotating machines have caused the generalization of modal testing techniques. However, this technology is not fully developed as in the case of modal testing of stationary structures. Significant advances in modal testing of rotating machines will be reviewed.

Natural Frequencies

Natural frequencies, which are unique to a machine or structural design, are important because they are excited by impact mechanisms and vibratory forces. The phenomenon is known as resonance. Natural frequencies are obtained experimentally from impact tests with hammers, variable-frequency shakers, or tests in which the speed of the machine is varied.

The natural frequencies of a machine can change with machine speed because they are influenced by stiffness and mass. In machines with self-acting fluid-film bearings, bearing stiffness is a function of machine speed. The natural frequencies of machines with large overhung disks and wheels are speed dependent because the gyroscopic moments vary with speed.

Natural frequencies of machines are typically determined by measuring vibration levels during start-up and coast down. However, these natural

7

frequencies must be associated with the speeds at which they occur. Less commonly used are impact and shaker tests. The hammer or shaker is applied to the housing of a bearing or to the machine to vibrate the rotor at various frequencies. In this case the natural frequency is excited at operating speed. If a nonoperating rotor is bumped, the natural frequency is that of the rotor resting in its bearings. The natural frequency of a rotor mounted in rolling element bearings is close to that obtained at the operating speed. But data obtained when the rotor is resting in its bearings as well as information obtained from rotors bumped in a sling in the free-free mode (horizontally) -- although not indicative of any parameter at operating speed -- are valuable for modeling the rotor and its support bearings.

Damping

Damping is important in assessing the sensitivity of system response to such forcing functions as mass unbalance, misalignment, and thermal distortion. Information about damping will reveal potential problems of a machine passing through or dwelling on a critical speed. Operating a machine with significant damping at a critical speed is not necessarily harmful; on the other hand, low damping can sometimes mean disaster. Evaluation of sensitive machines -- that is, those subject to mass unbalance from the process and those operating close to a critical speed -- requires data on damping. Damping of fluid film bearings varies with machine speed and thus must be obtained at the machine's operating speed or speeds.

Damping for a single mode can be measured in the domains of time, frequency, or phase [2]. Modal testing is used to evaluate multi-mode damping. Again, due to the variation of damping with machine speed, classical modal test techniques cannot be used.

Modal Testing Techniques

Modal testing techniques [3] are widely used for structural studies, but various problems must be overcome before they can be applied to rotating machinery. First, the rotor is not easily accessible for taking the many measurement points required to describe its mode shapes. In addition, the applied vibratory force, if obtained from the machine, is difficult to quantify. Measurements must be taken at speed because the dynamic properties of the rotor depend on speed. Responses from the excitation and dynamic properties are obtained and must be separated to effect a meaningful modal test. Extended and generalized testing techniques [4,5,6] are being developed to overcome these problems.

Modal testing of rotating machines and the foundations and piping associated with them has been motivated by several factors. Such test data as natural frequencies and mode shapes allow validation of computer models. Measured damping data are important because theoretical values are uncertain. In addition, modal test data are used experimentally to formulate models of components that can be incorporated into the machine assembly by substructuring processes. The data can also be used with a modal model to determine dynamic forces that cannot be measured directly. Finally, modal data are valuable for in-depth diagnosis of rotating machinery. The computer model, in combination with modal test data, allow the analyst to evaluate such components of design as critical speeds, resonances, damping, and modes as well as machine condition; e.g., excessive forces caused by mass unbalance, misalignment, bearing wear, and

looseness.

Frequency Response Function (FRF) Measurement. Modal parameters of rotating machinery are determined from a measured set of frequency response functions (FRFs) for which force, amplitude, and phase are required. The coherence function is examined to establish the validity of the data. However, more extensive testing is required because of the nonsymmetric properties of the machine.

Several experimental methods [4,5,6] have been developed for acquiring the data necessary to formulate FRFs. A force from a hammer or shaker can be applied or mass unbalance can be calibrated. In the latter case response on the rotor is measured with a proximity probe to obtain displacement; an accelerometer is mounted on the structure. When mass unbalance is used, a column of the matrix H, Table 1, is measured. The background response of the rotating machine must be eliminated. Unfortunately FRF's from both the columns and rows must be measured because they are different whereas in stationary structures, reciprocity applies and only a column or row must be measured depending solely on convenience. Usually columns are obtained with shakers (the shaker is fixed and the transducer moved) and rows with hammers (transducer fixed and hammer moved). Artificial excitation using swept sine forces from a shaker is time consuming but accurate because only one frequency is excited at a time. However, impact and random forces that simultaneously excite many modes are more often used today in structural modal testing. FRFs vary with rotor speed and are computed directly from the ratio of Fourier transforms of the measured output (response) and input (force) signals. In impact tests the frequency content and amplitude of the force signal are influenced by hammer mass, flexibility of the impact cap, and impact velocity. A long impulse yields low energy and a wide frequency range. A long impulse is required to excite low frequencies.

Table 1. Matrix of frequency response functions (after Nordmann [5])

$$H^{*}\{\Omega\} = \begin{bmatrix} H_{11} & H_{12} & \cdots & H_{1i} & \cdots & H_{1N} \\ H_{21} & & & & & \\ \vdots & & & & & \\ H_{k1} & H_{k2} & & H_{ki} & \cdots & \\ H_{N1} & & & & & H_{NN} \end{bmatrix}$$

$$Z_k^T = \sum_j \frac{\varphi_{ki}}{(i\Omega - \lambda_j)} \psi$$

$$S_i = \sum_j \frac{\psi_{ij}}{(i\Omega - \lambda_j)} \varphi_j$$

The six FRFs are given in Table 2. The standard FRF is typically response divided by force. Arguments have been made [6] for using the inverse FRFs. Dynamic stiffness, mechanical impedance, or apparent mass are used for such discrete parameter identification in rotating machines as bearing stiffness and damping.

Table 2.   Frequency Response Functions (FRFs)

Response Parameter	Frequency Response Functions	
	Response/Force	Force/Response
Displacement	Receptance Dynamic Flexibility	Dynamic Stiffness
Velocity	Mobility	Mechanical Impedance
Acceleration	Inertance Accelerance	Apparent Mass

Graphical displays of FRF data are complex; they are represented by three quantities that include frequency and two parts of a complex function.   The three common displays are the bode plot (FRF magnitude and phase vs frequency (Figure 3); real and imaginary parts of the FRF; and the Nyquist plot, Figure 5, (real vs imaginary plot), which does not explicitly contain frequency information.
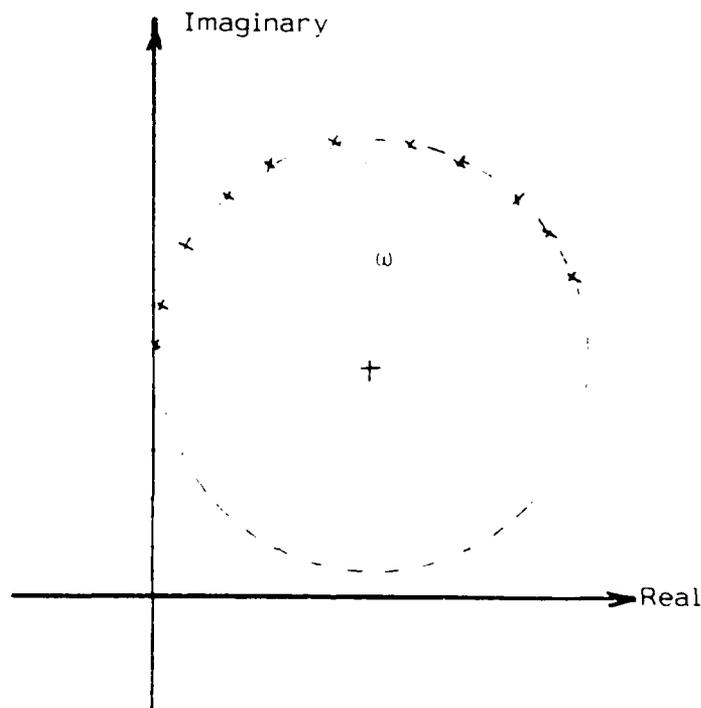
Figure 5.   Nyquist plot -- real vs imaginary FRF

Data Analysis.   The procedures of experimental modal analysis are applied to modal test data to identify the parameters of a theoretical model that will simulate the behavior of the machine.   The data must be matched or curve-fitted to a modal equation (single-degree-of-freedom) such as the modal response of a machine.

$$Y(\omega) = i\omega \sum_{2=1}^{N} \frac{Aj}{\lambda j^2 - \omega^2} \tag{1}$$

where: $Y(\omega)$ = measured modal values at various frequencies

Aj, λ_j = modal parameters that are related to the properties of the machine

The nature of the data dictates which of several procedures will be used to extract the modal parameters.   The most widely used approach is the single-degree-of-freedom curve-fit.   In systems with well-spaced modes, acceptable values for the parameters can be found by using test data around the natural frequency. The single-degree-of-freedom constants plus an offset term, which accounts for the contributions at other modes, can be used effectively.

The Nyquist plot generated from modal data for a single mode is given in Figure 5.   The process is repeated for each mode until the complete frequency range is covered.   A theoretical regeneration can then be performed to establish the entire mobility curve; circle-fit data are used.   Modes that are very close to other modes -- identifiable on the Nyquist plot by lack of a circular configuration -- indicate that more complex processes are occurring; a so-called multiple-degree-of-freedom curve-fit must then be used that simultaneously includes the effects of many modes.   The type of damping and slightly nonlinear behavior must be considered in the curve-fitting process.

Rotor Dynamic Considerations.   The dynamic response of a rotor/bearing system is calculated from the equations of motion:

$$M\ddot{q} + C\dot{q} + Kq = F(t) \tag{2}$$

where: M = mass or M matrix
C = damping or C matrix
K = stiffness or K matrix
q = displacement vector
F = force vector

The matrices C and K, which contain the stiffness and damping terms from the bearings as well as gyroscopic effects, are nonsymmetric and depend on the running speed of the rotor.   These properties account for the difficulties of carrying out modal testing on rotating machines.   In structural modal testing the C and K matrices are symmetrical and are not speed dependent.

The eigenvalues (natural frequencies and damping) and eigenvectors (mode shapes) are obtained from the homogeneous equations of motion, F = 0.   Rotors, unlike other structures, do not have a constant mode shape; rather, the constants and phases vary from point to point on the rotor.   The normal modes of nonconservative systems represent time-dependent curves in space; the plane motion of the rotor is an elliptical orbit.   In fact, two sets of eigenvectors are obtained for each eigenvalue -- the conventional right-hand eigenvector is obtained in modal analysis and the left-hand eigenvector is obtained from the transpose

11

of M, C, and K.

The frequency response function (FRF) Hkℓ(Ω) is speed (frequency) dependent whether calculated or measured. Complex FRF can be expressed in terms of the eigenvalues and the corresponding eigenvectors. For a rotor that is modeled or tested for N degrees of freedom, NxN FRF exist and can be assembled in a matrix H(Ω) shown in Table 1. Each row contains all left-hand eigenvectors, and each column contains all right-hand eigenvectors. One row and one column of the frequency response matrix H must be measured in order to identify the modal eigenvalues and right and left eigenvectors of a rotor, Figure 6.

FORCE   DISPLACEMENT   FORCE   DISPLACEMENT
TRANSDUCER   PICK UP   TRANSDUCER   PICK UP

| MEAUSUREMENT OF A COLUMN | | MEAUSUREMENT OF A ROW |

EXCITATION AT LOCATION ℓ,   EXCITATION AT ALL LOCATIONS,
MEASUREMENT OF DISPLACEMENT   MEASURENT OF DISPLACEMENT
AT ALL OTHER LOCATIONS   AT LOCATION k
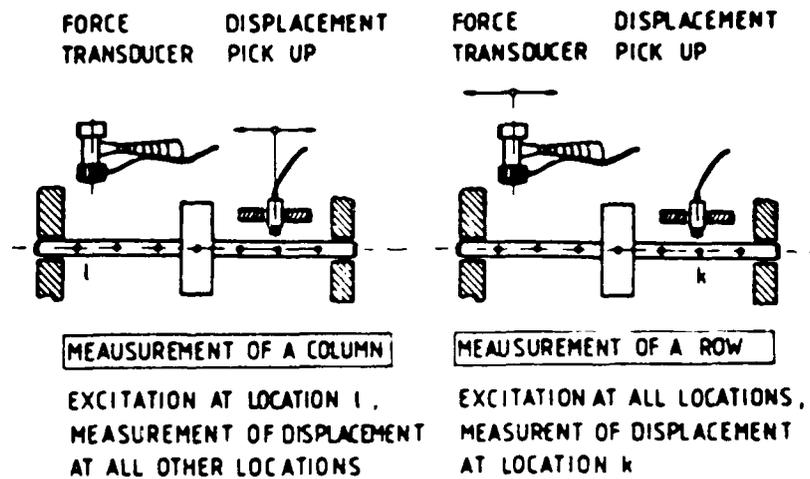
Figure 6.   Measurement of frequency response functions in
rotating machines (after Nordmann [5])

Modal Testing Procedures. Nordmann [5] has published a procedure for identifying modal parameters of rotors that utilizes analytical functions fitted to measured data. FRFs are measured at various speeds between excitation points, ℓ, and measurement points, k. Analytical FRFs, which depend on eigenvalues and right- and left-hand eigenvectors, are fitted to the measured data by varying modal parameters. The parameters that allow a fit of the measured data to the analytical functions represent the dynamic characteristics of the rotor/bearing system.

The modal parameter estimation procedure selected depends on the degree of modal coupling in the rotor system. According to the theory of modal analysis the total frequency response at a measurement point consists of the weighted sum of the contributions of all modes of the system. The contribution of a particular mode is usually greatest close to a natural frequency. When modal coupling is light and cross modal coupling is minimal, the single-degree-of-freedom model provides a good approximation of modal parameters of the system for that natural mode. Thus, if the modes of a system are well separated, data analysis -- bode, Nyquist, real, and imaginary plots -- can be used to determine modal parameters directly from natural frequencies and amplitudes at resonance. When heavy modal damping is present -- as is sometimes the case when journal bearings support a rotor -- a multi-degree-of-freedom curve-fitting technique must be

12

used based on an error function which contains real and imaginary components of the FRFs. Test data are curve-fit to the analytical expression to obtain modal parameters. A least squares procedure for minimizing the error function E is commonly used to extract modal parameters. The error function is differentiated with respect to each unknown and set equal to zero; the unknowns of the resulting set of equations are the modal parameters. The equations are nonlinear in the eigenvalue parts and must be solved by an iterative procedure. Analytical and experimental FRFs obtained by Nordmann [5] are shown in Figure 7.
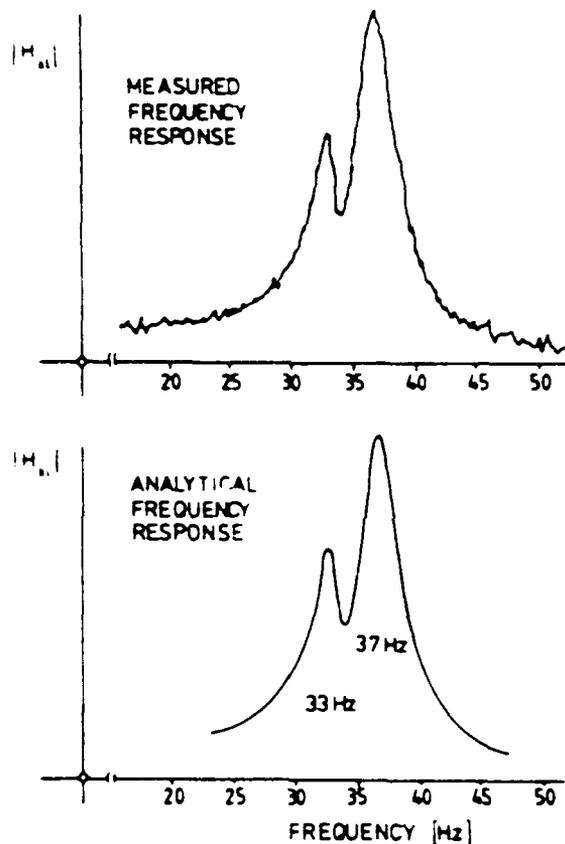
Figure 7. Comparison of measured and calculated frequency response for a rotating machine (after Nordmann [5])

The methods for extracting modal parameters from experimental data described above deal exclusively with compliance functions. Bently et al. [6] suggest that the dynamic stiffness functions (the inverse of compliance) are more useful in that direct numerical values of such specific physical properties of the systems as discrete mass, stiffness, or damping can be calculated. The method would be advantageous for direct experimental characterization of mechanical components; e.g., bearings, dampers, pedestals, rotors. This method can also be used to develop modal models.

The test setup for determining the dynamic stiffness of a rotor uses mass unbalance as the rotating excitation force. Flexural vibrations of the shaft are measured in two lateral directions with two noncontacting shaft displacement probes mounted orthogonally. A third displacement probe used as the key phasor

13

relates the phase angle between the rotating force (mass unbalance) and the vibration response. A known mass unbalance is used in this instance to identify parameters of the system. (The same setup is typically used to balance a rotor with unknown mass distribution.)

The parameters of a rotor that is straight and well balanced could be characterized by introducing a known mass unbalance at a known location on the rotor and then varying rotor speed from zero to the desired value. Unfortunately, the rotor also responds to forces other than the known mass unbalance. Therefore, calibration tests and subtraction of the residual response are necessary. It has been suggested that vectorial subtraction of start-up and coast-down test data over the speed range of the test will eliminate unwanted residual response. The known mass unbalance in the experimental setup is 180° out of phase for the two tests.

The data from the once-per-revolution excitation in the test setup are restricted to that frequency. For example, the properties of fluid-film bearings are frequency dependent. But data of the excitation from mass unbalance are within the frequency range of the highest test speed of the rotor. At a minimum the speed range of the rotor should include at least one critical speed.

Figure 8 shows plots of direct, K_D, and quadrature K_Q, dynamic stiffness vs speed squared and speed, respectively. The results were obtained from test data and the following relationships:

$$K_D = \text{force amplitude} \times \cos(\text{phase})/\text{response amplitude}$$

$$K_Q = \text{force amplitude} \times \sin(\text{phase})/\text{response amplitude}$$

SPEED, RPM x 1000
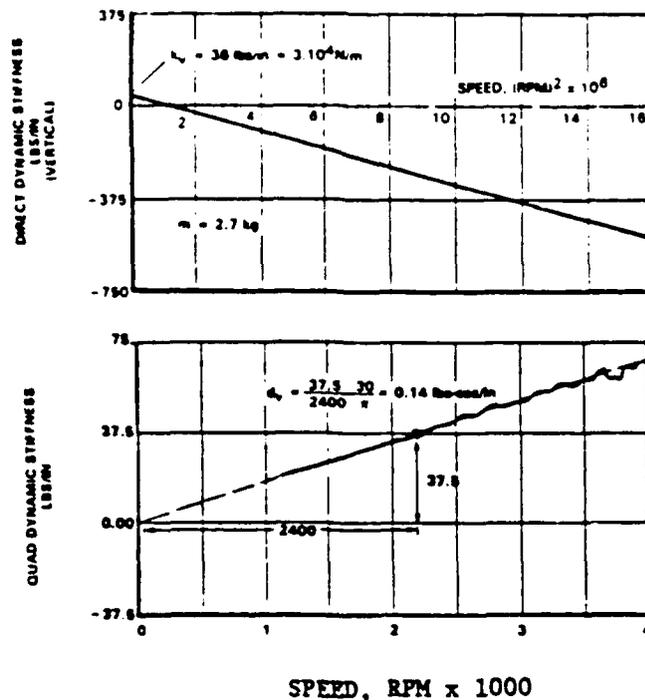
Figure 8.   Rotor dynamic stiffness versus rotational speed squared
             and quadrature dynamic stiffness versus rotational
             speed (after Bently et al. [6])

14

The mass in each direction is calculated from the slope of the K_D vs speed squared curve; stiffness K_V is derived from the intercept of the graph with the vertical axis. Damping is derived from the slope of the curve of K_Q vs speed. Results are excellent using this approach for near-symmetric rotors. Procedures are also given for excitation of rotors at nonsynchronous frequencies using free spinners on the rotor.

EXPERT SYSTEMS

The evolution of the digital computer has fostered the concept of artificial intelligence (AI). It is a technical area where millions of dollars are annually spent on research. The idea of emulating the function of the human brain for logic and reasoning is very attractive for machine diagnostics. AI follows the very successful application of the digital computer to numerical analysis of engineering problems where routine computation procedures are performed at a rapid rate.

Today there is considerable effort to apply AI to expert systems that will perform mechanical signature analysis. And, in fact, some limited success has been achieved on specific types of equipment. The motivation for the expert system is to use less skilled and experienced engineers and technicians to diagnose problems in rotating machinery. This diagnostic process requires residual knowledge and experience, an ability to perform deductive reasoning, and logical elimination and acceptance of facts. Even for a computer it is not an easy task because common sense is not easy to emulate.

Expert systems [7,8] for mechanical signature analysis use a knowledge base and inference procedures that would normally involve human expertise. The knowledge base is built up by an expert in the field in a narrow area such as motors or pumps and takes the form of heuristic rules and observed facts. Inference, performed by an AI shell, is the logical process that combines rules and facts to produce new facts. The idea is to emulate the process of problem solving on a computer -- a process common to detectives, mechanics, technicians, and engineers. It is fortunate that in mechanical signature analysis hard data involving narrow problem definition are encountered. This fact makes the application of the AI technology to these expert systems more feasible.

The two common approaches to expert systems, forward and backward chaining, both use a deductive form of inference. Forward chaining methods move through a rule base deducting all possible facts. This type of reasoning works from a given rule, "IF a THEN b" and the fact "a", it will conclude "b" and add it to a list of known facts. This type expert system is useful in real time control applications where all implications of each new piece of data must be investigated. The "backward chaining" inference method works best in this application because it is goal directed and therefore is directed at facts related to a single specific goal. It starts with a goal to be proven (the machine problem) and works backwards to resolve it. The backward chaining expert system directs the user session (technician interface with the computer) by asking very specific questions such as, "Does t. e frequency of the principal component of vibration vary with machine speed?" Facts not related to a current specific goal are not normally accepted. If a narrow focus is provided along with the goal-directed approach, expert systems that operate efficiently are easy to write and understand.

The key components and interfaces of a typical backward chaining expert system are given in Figure 9. It shows how the user interacts with the inference engine of the expert system. It is an active relationship where the expert system can ask the user questions related to the goal of solving a problem. A key part of the system is the knowledge base which contains the rules for solution of problems. Desirable expert system characteristics have been defined by Corley and Darby [7].

Good User Interface (menu driven)

Certainty Values for Rules

Ability to Handle "Unknown" and Uncertainties

Ability to Re-enter and Save Facts

Multiple Conclusions Ranked by Probability

Ability to Explore Reasoning

Graphics

User Written Functions

Inexpensive
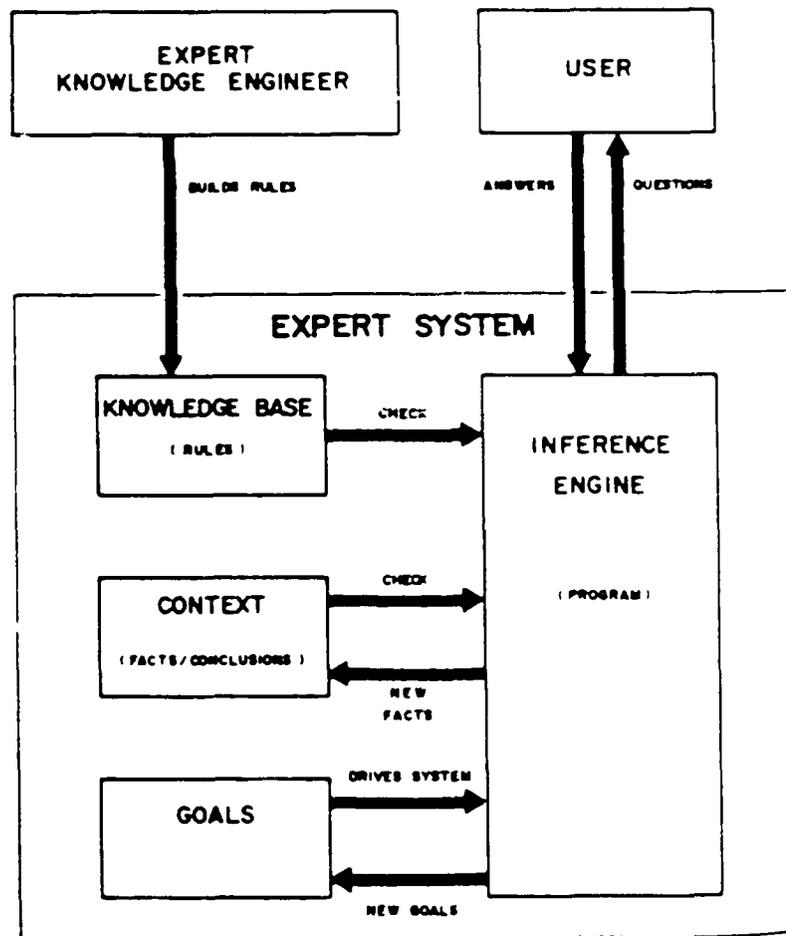
Figure 9. Schematic drawing of an expert system (after Corley and Darby [7])

It is obvious that the expert system is only as good as its knowledge base. In machines, like electric motors, substantial knowledge is available on the cause and effect nature of machine faults and related vibration signatures. The inference engine is a "canned" expert system program, several of which are available. Corley and Darby [7], who had a very broad knowledge base of over 100 rules on motors, report that their system is 90% effective. At this time, the system continues to be expanded to compressors, turbines, gears, and seals. Other expert systems have been reported by General Motors and Radian [8], a Hartford Insurance research group. The success of these expert systems has not been reported.

CONCLUSIONS

It can be concluded that the recent advances in mechanical signature analysis relate directly to the development of fast microprocessors that can deal with large volumes of digitized data in an efficient manner. The dual channel FFT which is based in a microprocessor provides support for more detailed machine diagnostics and modal testing with increased capabilities. In addition, the microprocessor coupled with large volume storage devices provide the hardware to implement the expert system software. While progress in mechanical signature analysis is strongly aided by computer oriented products, one must not forget the contributions being made by engineers who seek and find the basic cause and effect knowledge so necessary to make the computer systems work on real world problems.

REFERENCES

1. Brigham, E.O., The Fast Fourier Transform, Prentice-Hall, Inc., Englewood Cliffs, NJ, 1974.

2. Jackson, C., Mechanical Shop Testing, Rotor Dynamics Course, Vibration Institute, 1985.

3. Ewins, D., Modal Testing: Theory and Practice, John Wiley & Sons, New York, 1984.

4. Rodgers, P., "Genuine Modal Testing of Rotating Machinery," S/V Sound and Vibration, Vol. 22, No. 1, pp. 36-42, Jan. 1988.

5. Nordmann, R., "Identification of Modal Parameters of an Elastic Rotor with Oil Film Bearings," Trans. ASME (106), J. of Vib. Acoustics, Stress, and Rel. in Design, pp. 107-112, Jan. 1984.

6. Bently et al., "Some Aspects of the Application of Mechanical Impedance for Turbomachinery and Structural System Parameter Identification," 3rd International Modal Analysis Conference, Union College, Jan. 1985.

7. Corley, J.E. and Darby, G.D., "Development and Implementation of an Expert System to Diagnose Motor Vibration Problems," Proceedings of the Fifteenth Turbomachinery Symposium, Texas A&M University, pp. 111-117, 1986.

8. Pargé et al., "Application of TURBOMAC, An Expert Machinery Diagnostic System," Proceedings of the 10th Annual Meeting of the Vibration Institute, pp. 139-146, June 1986.

HIGH FREQUENCY VIBRATION ANALYSIS FOR
ROTATING EQUIPMENT AND PIPING SYSTEMS

Robert M. Jones
Nuclear Power Group
Sequoyah Nuclear Plant
Tennessee Valley Authority
Soddy-Daisy, TN 37379

The advent of portable computer controlled vibration data collectors and spectrum analyzers has moved the ability to do routine and special high frequency vibration analysis from the laboratory to the working environment of an operating power plant. This paper will describe some of the uses of these techniques in evaluating the mechanical condition of rotating equipment and piping systems.

Restarting the reactor after a long plant shutdown necessitates holding at an intermediate power level for an extended period of time and the secondary side of the steam generators are supplied by motor driven pumps. Plant operating temperature constraints dictate the pumps operate at a reduced flow. Operation of centrifugal pumps at reduced flow creates high "G" loading at both the inboard and outboard pump bearings. (Fig 1)
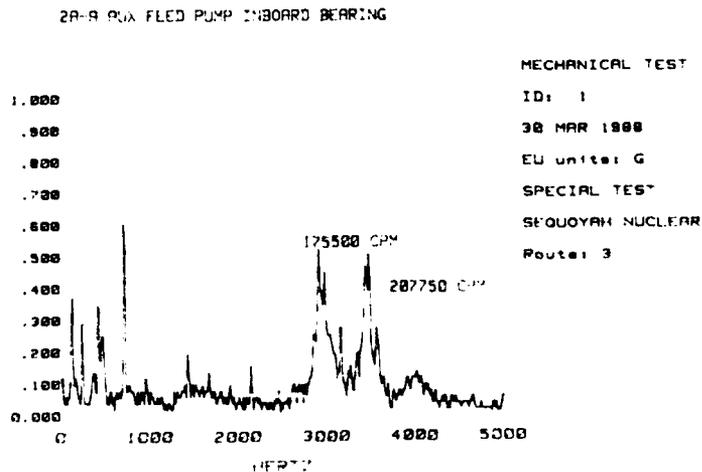
Fig. 1 2A-A Aux feed pump inboard bearing

By being able to provide daily monitoring of these high frequency vibrations the decision can be made to continue pump operation until it is determined that additional bearing degradation could cause damage to the pump. The economics of the situation are that if the bearings are changed too soon, then the plant startup would be delayed 12 to 15 hours, the time required for replacement. At $960,000 per day revenue, this would cost from $480,000 to $600,000. If the plant startup would be attained prior to a required bearing replacement then the turbine driven feedwater pumps would be in service and the motor driven auxiliary pump could be repaired while it is off line with no operational delay.

After two weeks of reduced flow operation, computer generated trends of critical frequency amplitudes, predicted that about two weeks of useful bearings life remained before the onset of possible pump shaft damage. (Fig. 2,3)
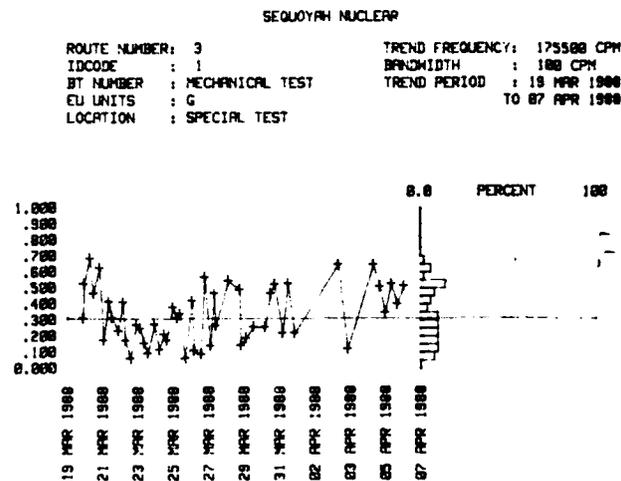
Fig. 2 Trend frequency: 175500 CPM
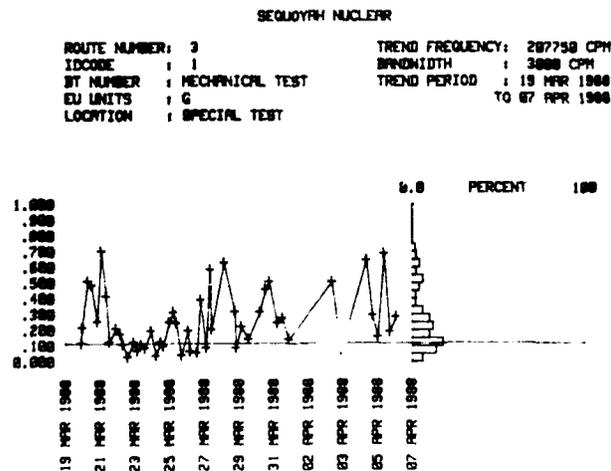
Fig. 3 Trend frequency: 207750 CPM

Shortly after this estimate was given the startup was aborted for other causes and the bearings were changed during the ensuing outage. Our spectrum analysis indicated no visible damage had occurred and bearing inspection verified the analysis. (Fig. 4)

2A-A AUX FEED PUMP OUTBOARD BEARING
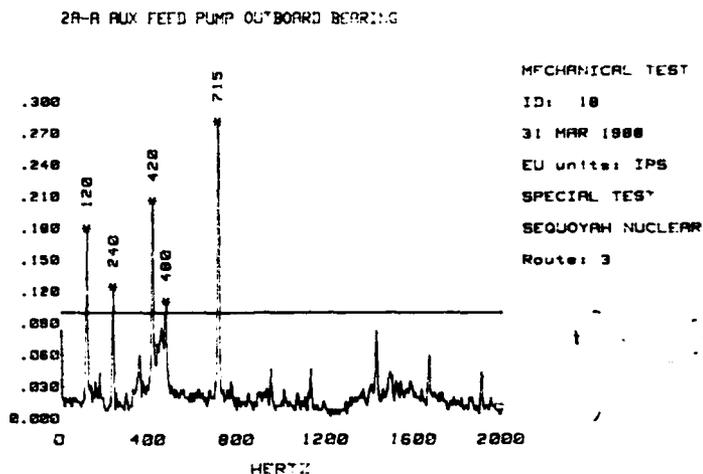
Fig. 4   2A-A Aux feed pump outboard bearing

However, as we pointed out to the maintenance personnel, our instruments were indicating that minute damage was occuring and the life of the bearing was limited if pump operation had continued under the imposed abnormal conditions.

When there are numerous pieces of equipment, all made by the same manufacturer, comparison analysis can make the job easier. With the portable analyzer, we did a frequency spectrum survey of each of the Chemical Lab Hood Fans motor and fan bearings. It quickly becomes apparent which bearing is bad when you look at a series of spectrums as in Fig. 5 a, b , and c.

CHEM LAB HOOD FAN "A"

Fig. 5a   Chem lab hood fan "A"

21

VIBRATION TEST
ID: 2
15 OCT 1987
EU units: G
OUTBD MTR HORIZ
SEQUOYAH NUCLEAR
Route: 1

1.000
.900
.800
.700
.600
.500
.400
.300
.200
.100
0.000

0   400   800   1200   1600   2000

HERTZ
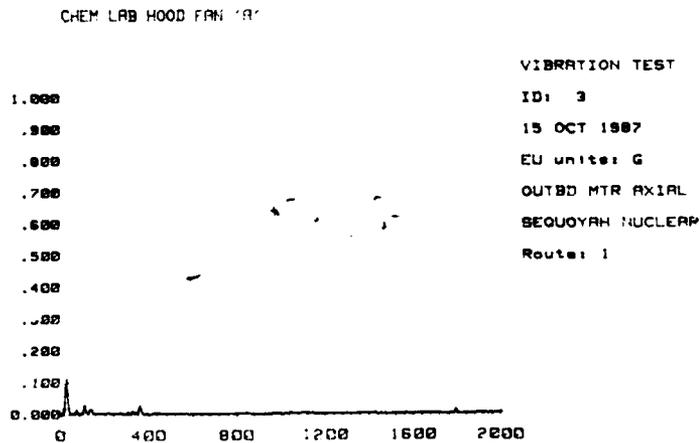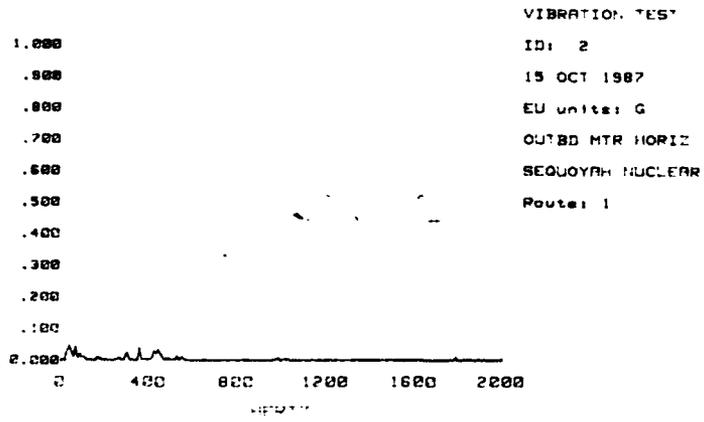
Fig. 5b   Chem lab hood fan "B"

CHEM LAB HOOD FAN "C"

VIBRATION TEST
ID: 1
14 OCT 1987
EU units: G
OUTBD MTR VERT
SEQUOYAH NUCLEAR
Route: 1

2.700
2.430
2.160
1.890
1.620
1.350
1.080
.810
.540
.270
0.000

0   400   800   1200   1600   2000

HERTZ
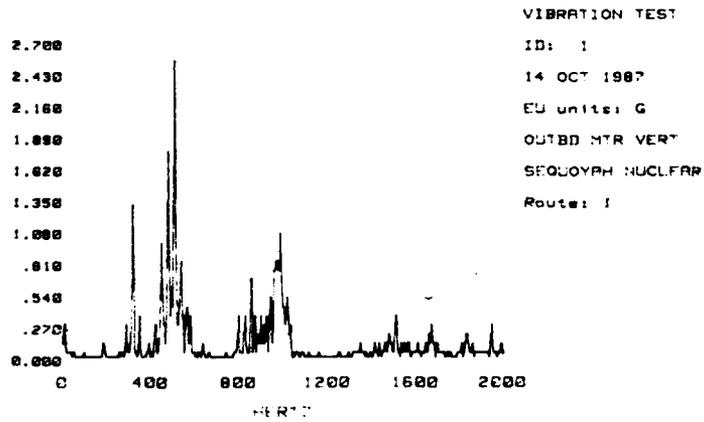
Fig. 5c   Chem lab hood fan "C"

22

When the pillow block bearing was disassembled, the inner race and balls were found to be pitted and cracked. By being able to do the repair on a routine basis, and before any fan or shaft damage occurred, the total maintenance cost was reduced. (Fig. 6)
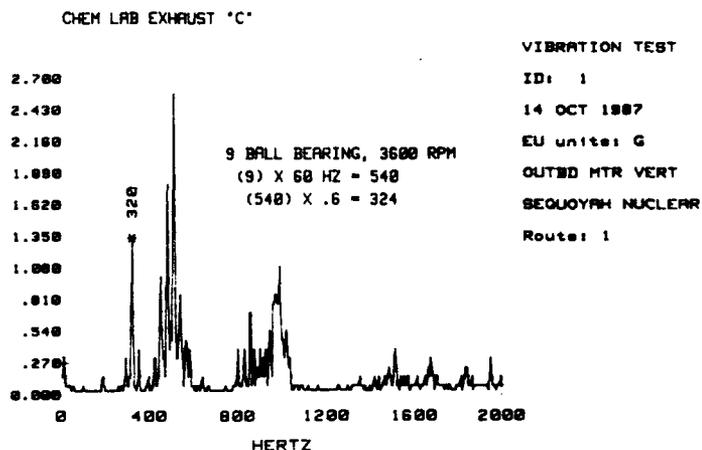
Fig. 6 Chem lab exhaust "C"

Another use of high frequency spectrum analysis occurred after the overhaul and rebuild of a pump speed increaser. The 1800 RPM motor input is increased to 4800 RPM to drive a charging pump required by safety regulations. This speed increase is obtained through a 2.66:1 ratio helical gear drive. The overhaul had been instigated when a low frequency spectrum analysis indicated a rub was occuring in the high speed shaft sleeve bearing. Disassembly revealed a worn and nicked babbit lining which was replaced.

On restart, an initial spectrum revealed high "G's" around 4,000 Hertz. (Fig. 7)
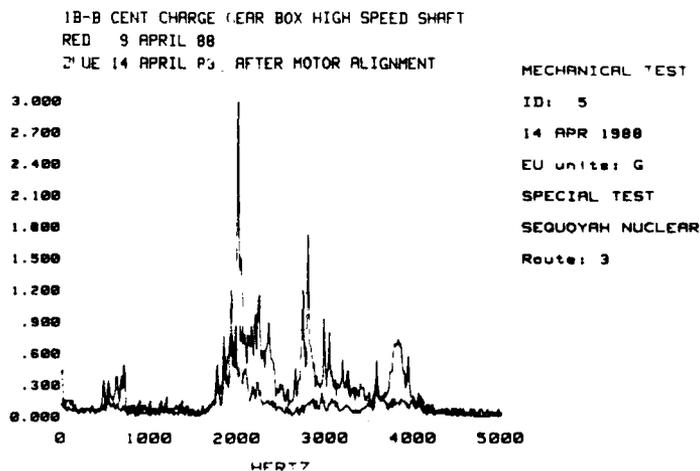
Fig. 7 1B-B Centrifugal charge gear box high speed shaft

23

Computation of the gear mesh frequency, (1800 RPM X 131 gear teeth = 235,800 CPM which is 3930 Hertz), showed we had another problem. After an inspection and review of the previous overhaul, it was found the motor had not been properly aligned. Motor realignment of .004" was accomplished and the subsequent spectrum showed no gear mesh problems. The significance of this example is that if the gear set had been operated and damaged, delivery time on a replacement set is 26 weeks and the other available spare set had just recently been installed on another pump. The accountants could probable come up with a dollar cost if the pump had to be fixed on an emergency order, and it certainly would be in the thousands of dollars.

Because of the ease of operation of the portable units, we check on a routine basis the bearing spectrums and gear mesh frequencies of all our safety related pumps and motors. Prior to the advent of the portable units, a bearing frequency spectrum could be collected but it was necessary to carry a "portable" 30 pound analyzer, a plotter, paper, and an extension cord into a controlled radiological zone which means everything was wrapped and taped. Not many spectrums were taken on a routine basis, usually only when some other indication showed there might be a problem Now we find problems much earlier which allows the solution to be accomplished on a scheduled basis rather than an emergency. Also, necessary repairs can be made before any extensive equipment damage has occurred which tends to lower the overall maintenance costs.

In addition to the high frequency spectrum analysis done on rotating equipment, piping system components are also examined with portable battery powered equipment. The Nuclear Regulatory Commission (NRC) requires that certain safety valves be stroked on a scheduled basis. On most valves this stroking can be observed by watching the movement of the valve stem. There are some cases however where the entire valve is encased in metal shielding and the valve stem is not visible. Our solution is to place a high frequency acoustical sensor on the valve body. With the valve in the closed position, a spectrum is taken. (Fig. 8)
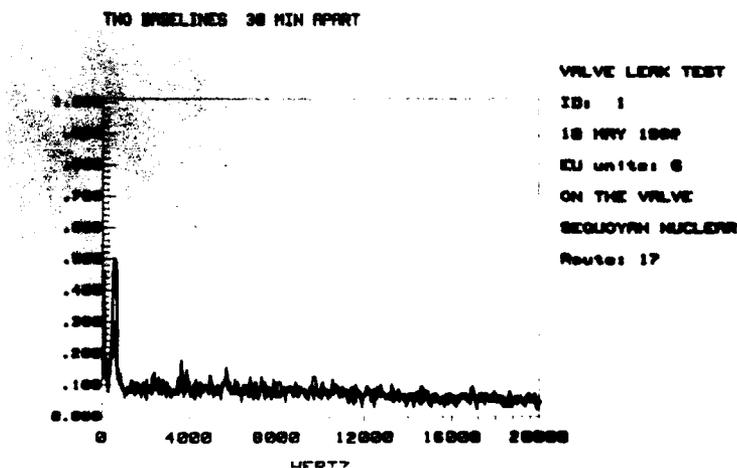
Fig. 8   Two baselines 30 minutes apart

The valve is then stroked to the open position and another spectrum taken, showing that there is flow in the valve. (Fig.9)
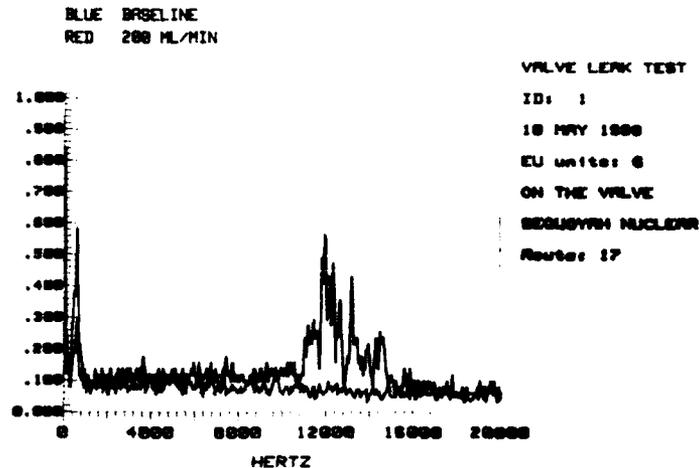
Fig. 9 Valve leak rate test

Then the final step is to take another spectrum after the valve is returned to the closed position showing the trace has returned to the orginal level. (Fig. 8)

The NRC has accepted this method of proving the valve stroke which changes a difficult problem to a very simple solution.

Valves in a power plant range in size from 1/4 inch to 36 inches and larger. And if any valves leak they can cause problems no matter what their size. A series of 24 one-inch test valves recently proved this point. An Engineered Safety Feature (ESF) system has accumulators which are kept filled with 10,000 gallons each of borated water at 400 psig. If there is a Loss of Coolant Accident (LOCA) these accumulator's contents would be dumped into the reactor vessel for cooling and to reduce reactivity of the reactor. However, during normal plant operations with the reactor pressure at 2235 psig, if these test valves leak, the borated water in the accumulators will be diluted with reactor system water. This is not an acceptable condition for operation and any leaking test valves must be corrected. Prior to the reactor being brought critical, the system was tested and found to be leaking into an accumulator. The question was, which of the 24 valves was leaking? The unit could not be brought critical until the leaking valves were found and fixed and each days delay was another $960,000 cost of lost revenue.

Using another portable high frequency analog analyzer each valve was examined and the leaking valves identified. The process is rather simple and straight forward. An accoustical accelerometer is placed on the valve and a reading taken with no pressure on the upstream side of the valve. Next, pressure is returned to the upstream side of the valve and another reading taken. The readings are in "dB" and if the reading has increased 5 dB after the pressure was returned, then the valve is probably leaking. In our case we identified 7 valves as possible leakers. When these 7 valves

were disassembled for repair all had physical evidence of leakage. The "proof of the pudding" was when the system was retested after valve repairs, the level in the accumulators did not increase. Although it is a simple application, the cost saving can be impressive. The processed water in each accumulator cost approximately $2 per gallon or $20,000 and there are 4 accumulators. If the dilution of the borated water is excessive, the tank must be drained and refilled within a time constraint of 2 hours. If 2 hours is exceeded, the unit has to be shut down and the $960,000 per day of lost revenue again is a factor. This does not even consider the lab cost of water testing and associated costs. Clearly the cost effectiveness of high frequency analysis of valves is apparent.

The final items that need to be covered are what is high frequency analysis and what does it cost? For purposes of reference, our portable spectrum analyzers function up to 10,000 Hz. This is adequate for bearing and gear analysis and we are currently working with the manufacture to develop the techniques for use of this equipment to identify flow. The portable valve leak testers operate to 100,000 Hz and are adequate for liquid or gas valve testing. The portable spectrum analyzers cost $7,000 plus software and computer. The valve leak testers cost $800 and accelerometers are $350. Finally, the beauty of high frequency analysis is that it is non-intrusive and can be conducted during normal operations without any disruption to the system process or any additional manpower for support.

DIAGNOSING PROBLEMS IN MODERN
2-POLE INDUCTION MOTORS

R. M. Kolodziej
Sr. Development Engineer
COOPER INDUSTRIES - TURBOCOMPRESSOR DIV.
3101 Broadway
Buffalo, NY 14225

With the advancements of CAD/CAM systems, better
materials and technology in general, motor manu-
facturers are able to pack more horsepower in a
smaller and lighter frame. From an economical point
of view, this philosophy may be rather attractive.
Unfortunately, action/reaction theory indicates
an amplification in vibration problems.

In the past, motor manufacturers and motor users
typically used velocity transducers to measure
structure vibration and C-T's to measure stator
currents. This basic method worked rather
well where the rotors were massive and the
structures were stiff. Currently, motor designs are
changing, the rotors are lighter and thinner and,
the structures are less stiff. I have found that
"the tail is wagging the dog", and identifying a pro-
blem may be very difficult. For this reason a collage of
vibration and electrical measurements have been
collected, to determine what data is the most relevant
and practical in evaluating a motor/base problem.

INTRODUCTION

The objective of this paper is to present electrical and structural
vibration readings on 2-pole induction motors, and display the data in
various conventions. The writer proves that if the same data is
reviewed in the time domain, frequency domain, Nyquist form and orbit
form, it will become apparent there is not one "best" method of
presentation. To get a good "gut" feeling of how the modern motor is
truly operating, you will not only have to select the most relevant
data acquisition method, but also the best method or methods for data
reduction.

Because of the two topics, structure and motor vibration, this paper
will be presented in two parts.
PART 1: Structural Resonance Change Due to Rotor Lift
PART 2: Comparison Of Electrical/Mechanical Vibration Readings On A
Motor With An Open Rotor Bar (bad motor) Vs. Brazed Repaired
Rotor Bar (good motor)

PART 1: Structural Resonance Change Due To Rotor Lift

It is totally accepted that all motors vibrate to some degree. The problem is, the same motor, will show a considerable vibration difference between the manufacturers test floor versus fully loaded on a fabricated base. Because of this, it is difficult to develop field operation vibration standards. But with the development of structural stiffness plots one will get a good idea of what to expect.

Initially point impedance transmissibility plots should be developed on the motor structure unit, fig 1. They should be created with the stimulus in the horizontal, vertical and axial direction at the motor centerline. Response data should be collected at the same points. A sledge hammer or ram instrumented with a load cell (mv/lb) should be used to supply the force. Simultaneously the response data should be collected with velocity (mv/in/sec) or acceleration transducers (mv/g). The data should be reduced and displayed in compliance (in/lb) form. At this point, knowing rotor balance tolerance and speed you can calculate how much bearing housing synchronous vibration will be created by rotor mass unbalance. Because the structural stiffness will probably be different in the horizontal and vertical direction the synchronous movement will also be different. This will create an elliptical orbit when running.
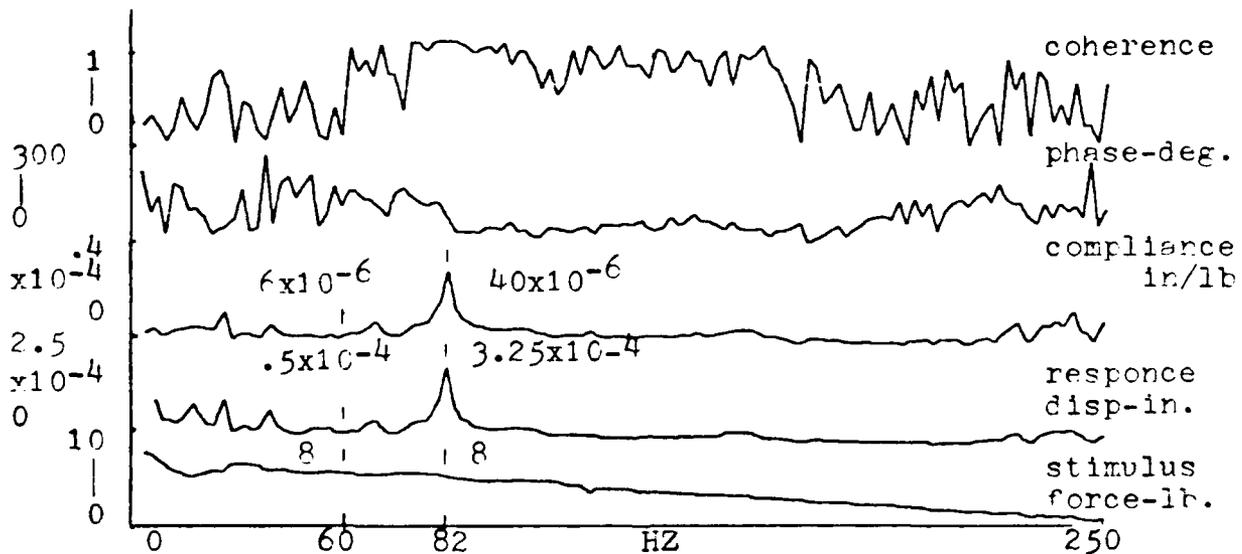
Fig 1: Point MZ Motor/Base Compliance Plots

Because all motors will generate a 1x and 2x synchronous speed excitor the relationship to resonant frequency should be known and avoided. A bearing housing vibration can go beyond 1. mil if motor/base structural resonances are sympathetic with rotor mass unbalance. This is true, even though the rotor is balanced within specification.

28

Example: Rotor Weight (W): 1000 lbs

Speed (N) : 3600 rpm

Permissible Unbalance U : oz.-in.

Balance Tolerance :

$$U = .25W \qquad N < 150 \text{ rpm}$$

$$U = \frac{5630\ W}{N^2} \qquad 150 < N < 1000 \text{ rpm}$$

$$U = \frac{4W}{N} \qquad N > 1000 \text{ rpm}$$

$$U = \frac{4.\ x\ 1000}{3600} = 1.11 \text{ oz-in}$$

$$F = mr\ w^2 = \left(\frac{1.11\ oz}{16.X\ 386}\right) x\ 1\ \text{in} \ x\ (2\pi60)^2 = 25.5\# \ (12.75\#/\text{brg.})$$

$$D = \left(\frac{1}{Kn}\right) x\ F = \text{Expected Synchronous Bearing Deflection Due to Mass Unbalance}$$

$$K60: \left(\frac{1}{160,000\ \#/\text{in.}}\right) \ x\ F\# = .16 \text{ mils Pk - Off Resonance}$$

$$K82: \left(\frac{1}{24,500\ \#/\text{in.}}\right) \ x\ F\# = 1.00 \text{ mils Pk - On Resonance}$$

NOTE: Stiffness Values (K60. K82) from fig. 1.

Once the structural resonances are determined the forcing functions are compared, looking for a possible match (and problem). Even though structural resonances are removed from running speed, other excitors such as misalignment (2x) could excite a structural mode.

Structural resonance can be excited by:

A) Unbalance - Synchronous speed
B) Misalignment - 2x synchronous speed
C) Rubs - Axially and with seals
D) Oil Whirl - 40-50% synchronous speed
F) Fan - Blade number x synchronous speed

29

It should be obvious at this time that a motor connected to a steel fabricated structure will have many resonant frequencies, along with many exciting frequencies. Consequently, matching up two or more of these frequencies is a good probability and practically unavoidable. This situation does not mean failure is eminent and, if the overall vibration is acceptable, you may not have a problem at all. However, it would be wise to collect trend data assuring a situation isn't turning into a problem.

A resonant condition can normally be identified by taking shutdown data. If the exponent is 5 or greater, and the phase changes between structure and rotor key, you are probably at or near resonance.

The bearing housing displacement in an off-resonance condition is proportional to force, fig. 2.
The bearing housing displacement in a resonance condition is proportional to force x amplification factor, fig 3.
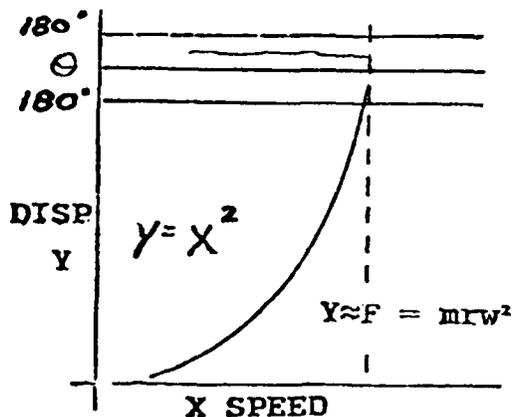
Fig. 2: Bearing Displacement -Off Resonance

$$Y = X^2$$

$$Y \approx F = mrw^2$$
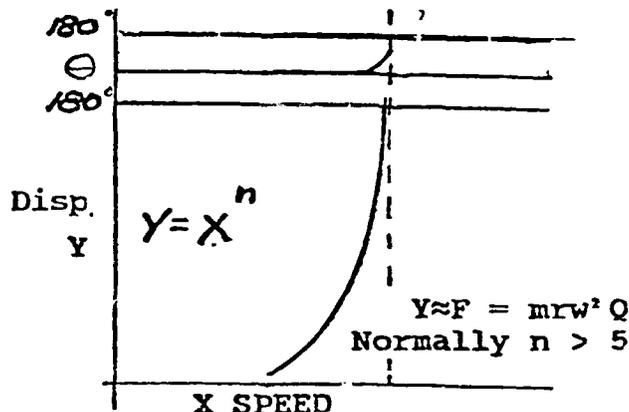
Fig. 3: Bearing Displacement -On Resonance

$$Y = X^n$$

$$Y \approx F = mrw^2 Q$$

Normally $n > 5$

If it is found that the motor/base structural resonance is a problem, the following "shoot from the hip" approach can be tried.
A)   Increase motor foot clamping area
B)   Gusset motor foot to pedestal
C)   Increase bearing stiffness

Don't be discouraged if the initial attempt does not help. Moving a low frequency structural mode is very difficult. A stiffening modification other than at a section of minimum stiffness will result in a minimal change in resonance frequency. If this is the case, a full structural modal analysis should be performed, determining modal shape and location of stiffening or weakening needed.

Theory and techniques of structural modal analysis tests is a topic all in itself and will not be discussed at this time.

Rotor Position Within Bearing (Lift) and its Effect on Resonance:

In the past motor-base structural resonances were usually handled as just mentioned. Unfortunately, with modern motors a new variable, rotor lift, (caused by radial magnetic pull and lighter loaded bearings), has to be addressed. Because the rotors are lighter and the length to diameter ratio is higher an unsymeterical magnetic field will reposition the rotor anywhere within the bearing journals. Consequently, when this happens the bearing stiffness and damping characteristics will change, moving the nonrunning resonance.

EXAMPLE: If the rotor is lifted (during running) bearing stiffness will decrease, lowering (at rest) structural resonance, fig 4.
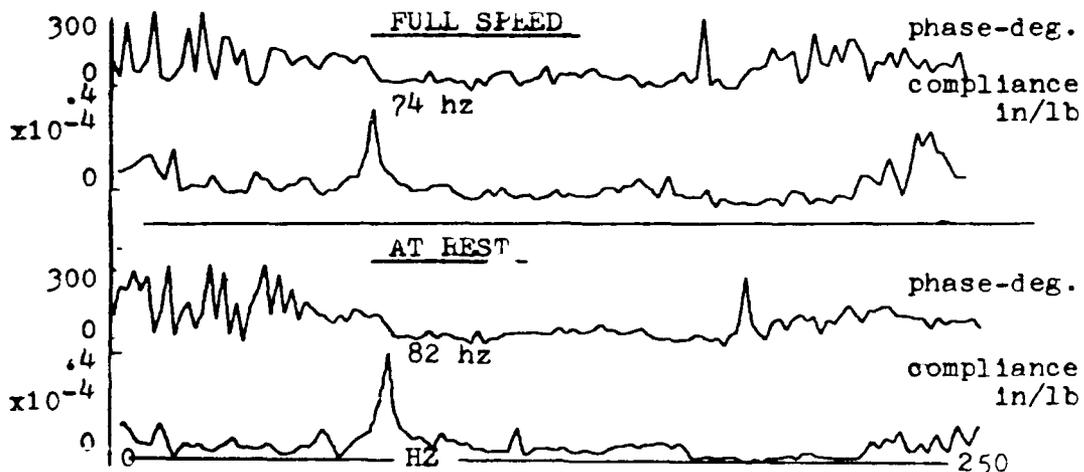
Fig. 4: Effect of Structural Resonance Change Due to Rotor Lift

Exactly, how much of an effective resonance change there will be between running and non-running condition depends upon two factors which are functions of each other:

1) How much and in what direction is the magnetic pulling force (action), equation 1.

$$P = \frac{Bg^2 \times L \times D \times e}{46. \ Ag} \tag{1}$$

> P = Radial Pull - lbs
> Bg = Flux Density - K-Lines/in^2
> L = Rotor Length - in.
> D = Rotor Diameter - in.
> Ag = Average Air Gap - in.
> e = Air Gap Eccentricity - in

NOTE: a) Direction of pull will be toward minimum air gap.
   b) Older motors had a flux density around 30.K-lines/in^2.

Some modern motors are now passing 40.K-lines/in^2.

31

EXAMPLE:

a) Radial Pull:

$$P = \left(Bg \cdot \frac{K\text{-}Lines}{in}\right)^2 \times \left(\frac{17 \text{ in} \times 10 \text{ in} \times .010 \text{ in}}{46. \times .100 \text{ in}}\right)$$

Bg = (30, 35, 40) Flux
         Density K-lines/in²
L = 17. in
D = 10. in.
Ag = .100 in
e = .010 in.

Bg	30.	35.	40.
P#	332.	452.	591

b) Rotor Weight: density of steel = .284 lb/in-cu.

$$W = \frac{\pi}{4} D^2 \times L \times .284 \text{ lb/in3}$$

$$= \frac{\pi}{4} 10.^2 \times 17. \times .283$$

W = 377. lbs

Thus, this rotor can be lifted if flux density goes higher than
30.K-lines/in² and minimum air gap is on top, fig 5.
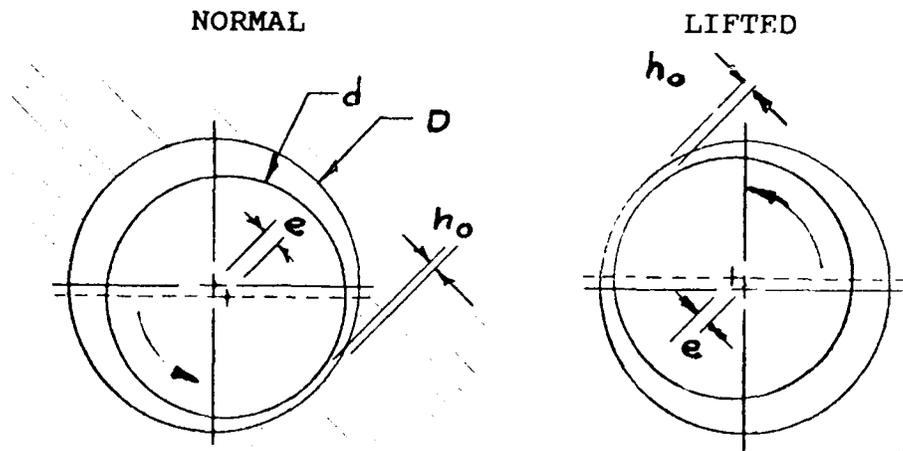
NORMAL   LIFTED

Fig. 5: Rotor Position Within Journal Bearing at Full Speed-
          Normal vs Lifted:

NOTE: There is as much of a chance for a rotor to be lifted
as pulled down.

2) Type of bearing used to counteract rotor action (reaction).

At one time the partial arc journal bearing was the motor industry standard. It was self lubricated, inexpensive and in general worked rather well. Unfortunately because of the lighter rotors the bearings are lighter loaded and run higher in the bearing. Normally journal bearings are designed around a dimentionless quantity called the eccentrically ratio e, equation 2. This value is a function of load number N_L, equation 3. The experimentally determined relationship between eccentricity ratio and load number is shown in fig. 6.

Eccentricity Ratio   (e)

$$e = 1 - \left(\frac{2ho}{D-d}\right) \tag{2}$$

Bearing Load Number (N_1)

$$N_1 = \left(\frac{60P}{un}\right)\cdot\left(\frac{Cd}{d}\right)^2\left(\frac{d}{L}\right)^2 \tag{3}$$

P=pressure on projected area, $P/l\ d$
ü=viscosity reyns,lb-sec/in^2
n=speed,rpm
Cd=diametral clearance,D-d
L=bearing length,in

(Journal/ Bearing Touching)
(In Center)

ECCENTRICITY RATIO (e)

LOAD NUMBER (N_1)

20   40   60   80   100   120   140
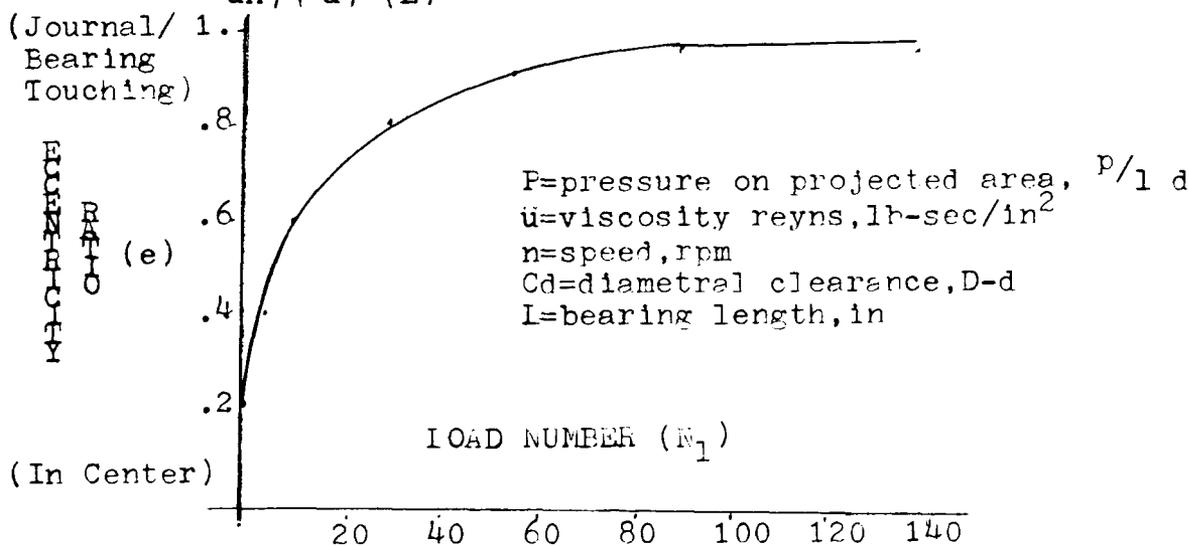
Fig 6: Journal Bearing Eccentricity Ratio vs Load Number

When this lifted condition happens with lightly loaded bearings and magnetic lift, a negative spring effect along with decrease in damping will be characteristic, fig 7. Consequently, the motor/base structural resonances will be constantly changing. In addition, the ability to dampen out normal mechanical or electrical vibrations would be greatly reduced.   In an attempt to handle the lift problem some users have direct coupled the motor to an offset load adding mass to the rotor holding it down. Another trick is to intentionally offset the air gap, 5% tight at the bottom, hoping that the rotor will be pulled into the bearing.   Both of these band aid solutions have made field units runable, but other problems such as high shaft currents and high modulating beat frequency will probably result.   Thus, be aware of possible consequences when forcing a motor rotor off its normal running position.

FULL VOLTAGE LIFTED   CUT POWER
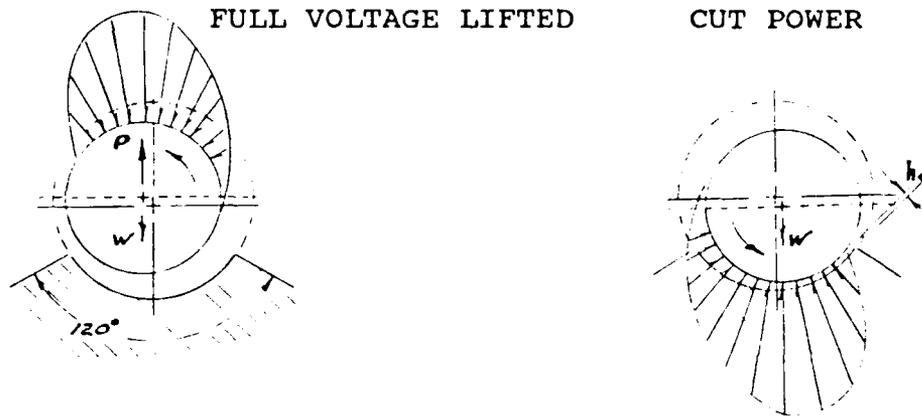
Fig. 7:   Rotor Position and Bearing Pressure Distribution of Partial
          Arc Bearing - Full Voltage (Lifted) vs Cut Power.

PART 2: Comparison Of Electrical/Mechanical Vibration Readings On a
         Motor With An Open Rotor Bar (bad motor) Vs. Brazed Repaired
         Rotor Bar (good motor)

The intent of this measurment comparison, fig.8, is to display the
effect, one open bar has on various vibration measurements.   In this
case the problem is specific and easy to fix.   The motor has an
unsymmetrical magnetic field created by one open rotor bar.   On a new
motor this condition of a clean cut rotor bar joint is unlikely.
However, you will find high resistant joints, blow holes, loose
laminations, and other forms of discontinuities. These discontinuities
will also create an unsymmetrical magnetic field causing vibrations
similar to that of the clean cut open bar.   As mentioned earlier all
motors are going to display all of the following characteristics to
some degree.   This example allows the motor user to compare vibration
data exhibited by a particular motor to one with a known open bar
defect.

Volts:	2300	Rotor Wgt :	560	Motor Bearings
Amps :	108	Rotor Slots :	45	Drive - 120° Partial Arc
				(Noninsulated)
Hp :	500	Stator Slots:	54	
Speed:	3600			Non-Drive - 120° Partial Arc (Insulated)
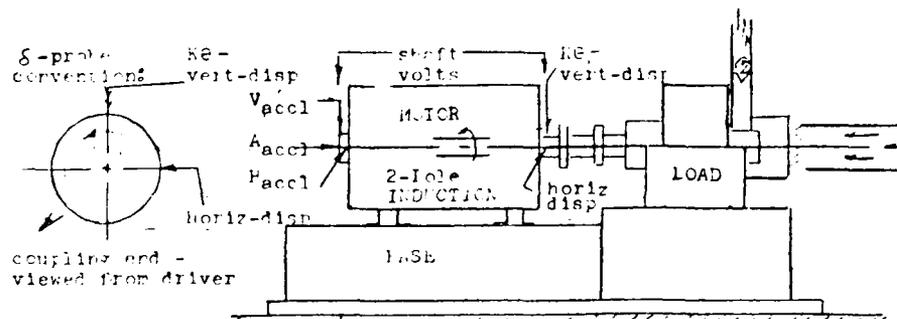
Fig. 8:   Vibration Measurement Locations and Cenral Parameters.

34

MOTOR SHAFT DISPLACMENT : unfiltered, coupling end, motor cold, from
rest to unloaded to loaded

Bad Rotor-A   Good Rotor-B
(1 rotor bar open)   (rotor bar brazed closed)
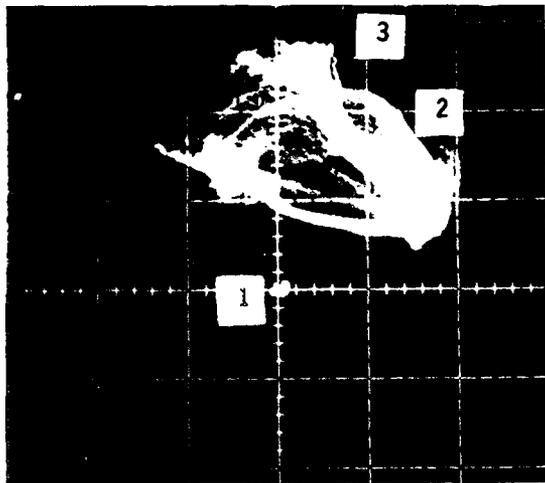
1=At Rest
2=Unloaded
3=Loaded

2.Mils/Div.
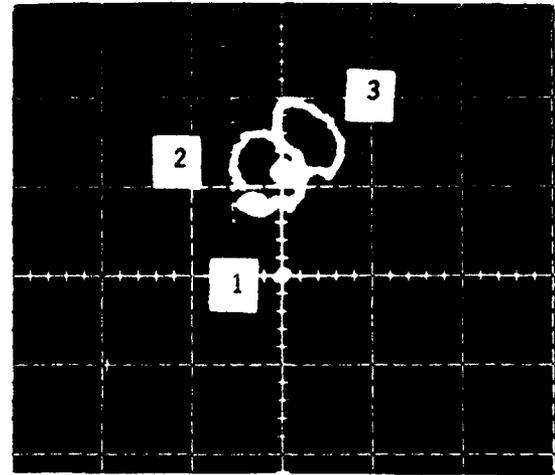
Fig.9a:Orbit-A   Fig.9b:Orbit-B
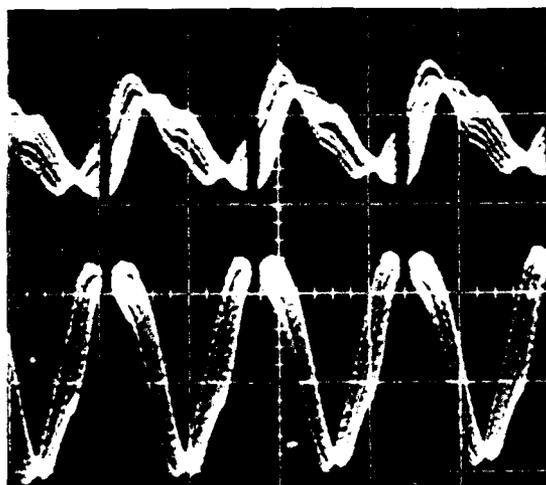
Vertical

(Unloaded)

Horizontal

Fig.10a:Time-A (10.ms/Div.)   Fig.10b:Time-B
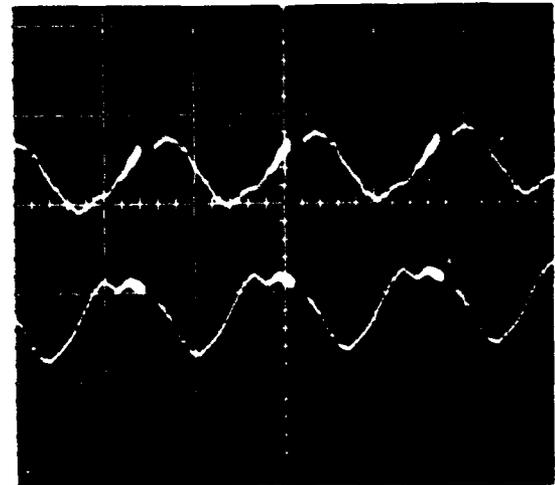
Observations:
9a – Rotor lifted 2.5 mils up and 1.5 mils to the right. When unloaded
(2), there is a modulating elliptical orbit, reversing direction at
slip frequency beat. When loaded (3), the orbit continues to modulate
but in linear form. This measured lift is more than three times that of
the calculated oil wedge.
9b – Unloaded (2), rotor lifted 2. mils from rest. When loaded (3), the
rotor lifted up an additional 1. mil and moved to the right .5 mils.
Regardless if loaded or unloaded the orbits are circular and c.c.w. in
direction (same as shaft rotation). The slip frequency beat was
minimal.
10a/b – Same unloaded signal viewed in the time domain.

In general unstable modulating orbits are caused by more than one
frequency (force) present within the bandwidth of data reduction.

35

MOTOR SHAFT DISPLACMENT : A.C. coupled, filtered 1/rev. (2. HZ. BW),
motor cold, unloaded to loaded

Bad Rotor-A
(1 rotor bar open)

Good Rotor-B
(rotor bar brazed closed)

Unloaded

2.Mils/Div.

Vertical
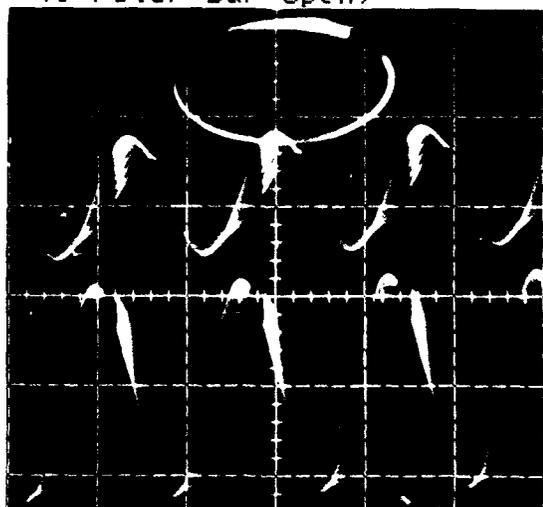
Horizontal

Fig.11a:Shaft-A Orbit/Time
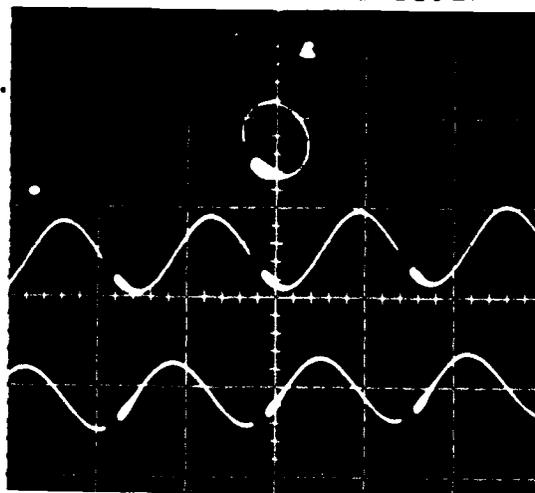
Fig.11b:Shaft-B Orbit/Time
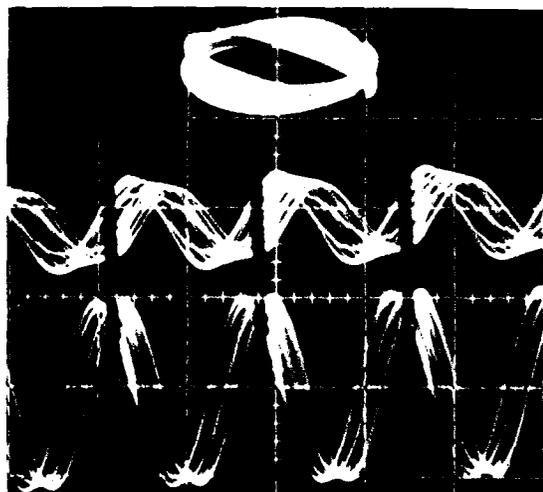
Loaded

2.Mils/Div.

Vertical

Horizontal

Fig.12a:Shaft-A Orbit/Time
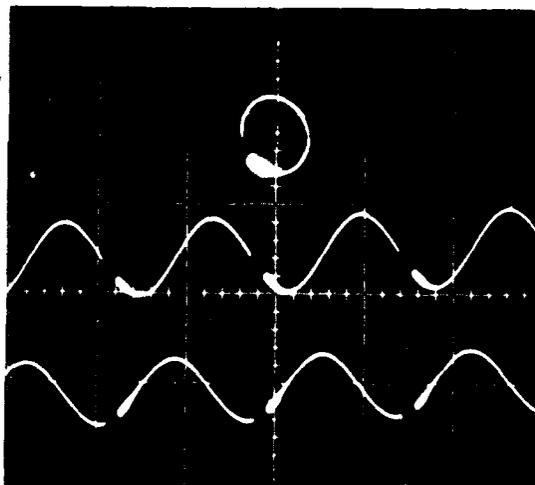
Fig.12b:Shaft-B Orbit/Time

Observations:
11a/12a - The modulating filtered signal indicates that there are
electrical and or mechanical forces within the 2. HZ. BW of the 1/rev.
frequency. Along with modulating amplitudes there is an aprox. 40 deg.
phase change between the loaded and unloaded condition, indicating
effective balancing will be very difficult.
11b/12b - Between the loaded and unloaded condition the orbits are
foward and circular with a stable phase. This indicates the major
excitation force is rotor mass unbalance, thus balancing would be
effective.

36

MOTOR SHAFT DISPLACMENT : unfiltered, coupling end, motor hot, from
loaded to unloaded to rest

Bad Rotor-A
(1 rotor bar open)

Good Rotor-B
(rotor bar brazed closed)
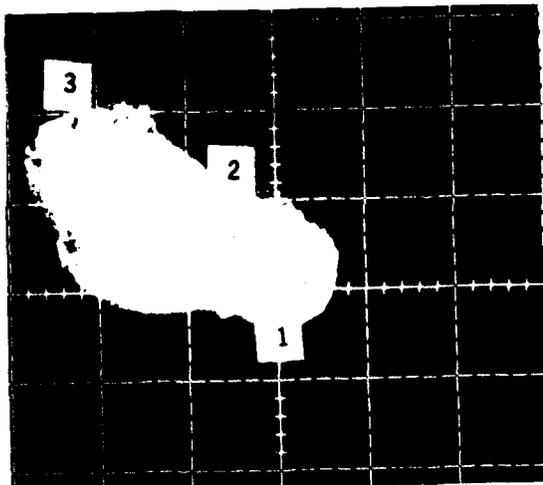
1=At Rest
2=Unloaded
3=Loaded

2.Mils/Div.

Fig.13a:Orbit-A

Fig.13b:Orbit-B

Vertical

(Unloaded)

Horizontal
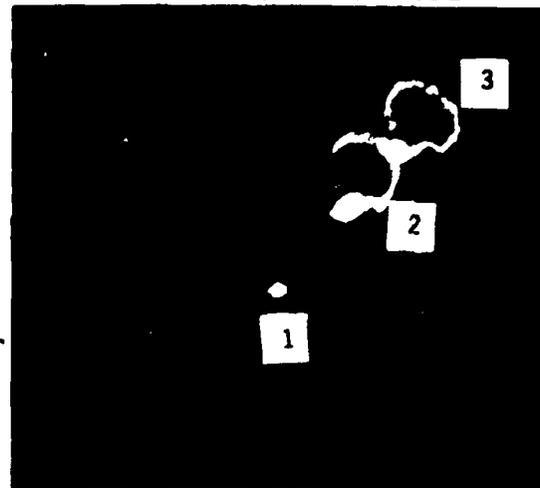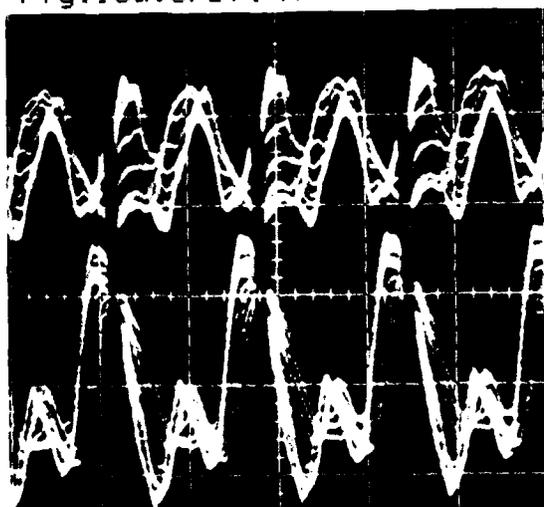
Fig.14a:Time-A (10.ms/Div.)
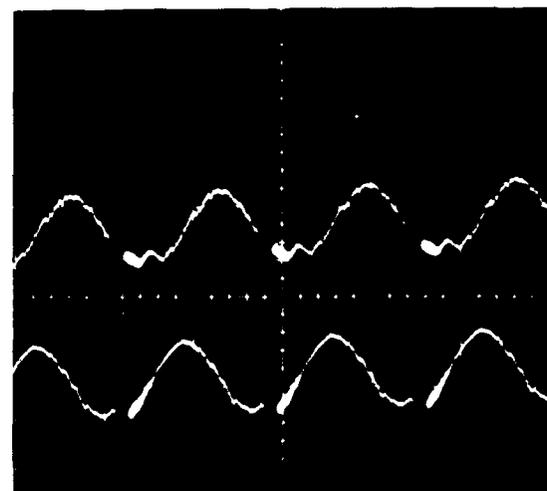
Fig.14b:Time-B

Observations:
13a - Once the rotor reached full temperature (hot), the rotor
repositioned itself toward the left side of the bearing. Both in the
loaded and unloaded condition the orbit modulated in a foward and
reverse pattern, varing only by rate. The bearing dosen't appear to
have a stable oil wedge.
14a - Compared to cold motor measurments (fig.10a) a 2x running speed
component is now present.
13b - Similar to cold motor measurments (fig. 9a and 10a) the orbit
direction, phase and load to unload position are comparable. The only
difference is that the shaft position lifted another .5 mils and moved
further to the right 2.mils.
There is probably not an exact cause for rotor reposition between load
and unload. It is probably a combination of thermal effects in the
rotor and structure along with a change in oil viscosity and megnetic
pull. The rotor is just as likly to be raised as lowered.

37

MOTOR SHAFT DISPLACMENT : A.C. coupled, filtered 1/rev. (2. HZ. BW), motor hot, unloaded to loaded

Bad Rotor-A
(1 rotor bar open)

Good Rotor-B
(rotor bar brazed closed)
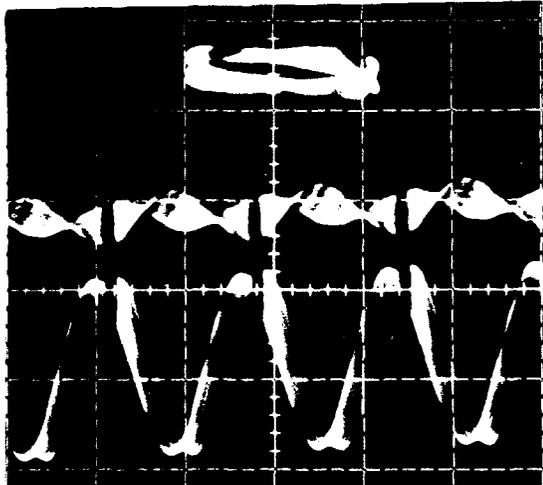
Unloaded

2.Mils/Div.

Vertical

Horizontal

Fig.15a:Shaft-A Orbit/Time
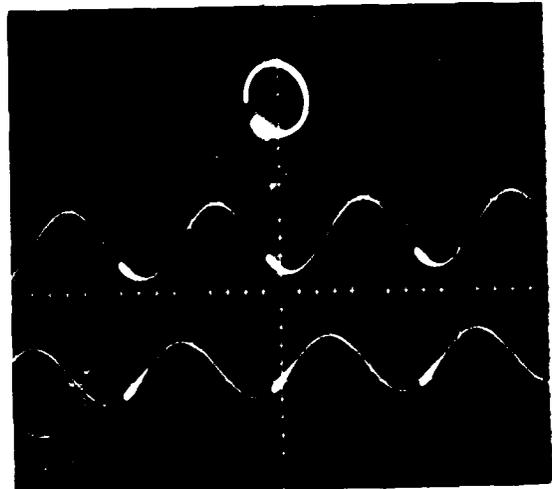
Fig.15b:Shaft-B Orbit/Time
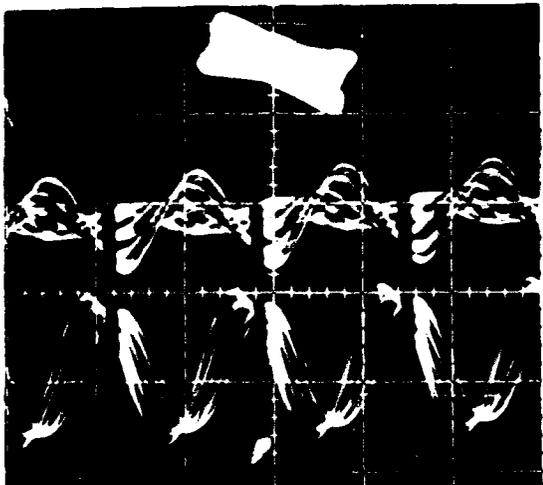
Loaded

2.Mils/Div.

Vertical

Horizontal

Fig.16a:Shaft-A Orbit/Time
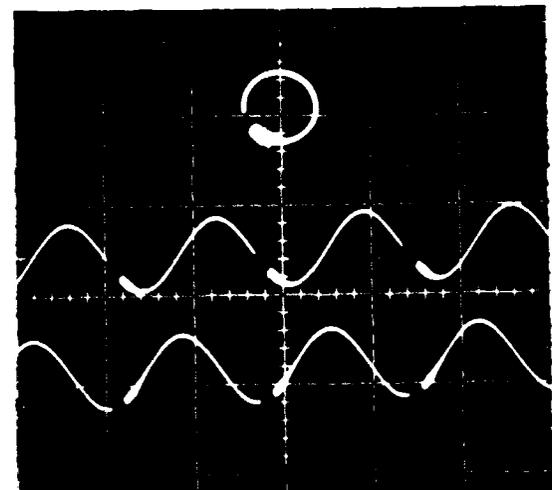
Fig.16b:Shaft-B Orbit/Time

Observations:
15a/16a - In addition to the beating at slip frequency the filtered 1/rev. orbit is now close to linear in the unloaded condition and reverses direction in the loaded condition at slip frequency rate.
15b/16b - The orbit and time domain signal is stable and similar regardless of being loaded, unloaded, hot or cold.

NYQUIST DIAGRAM: A.C. coupled, filtered 1/rev. (2.HZ. BW), horizontal
and vertical displacment coupling end, motor hot,
loaded to unloaded
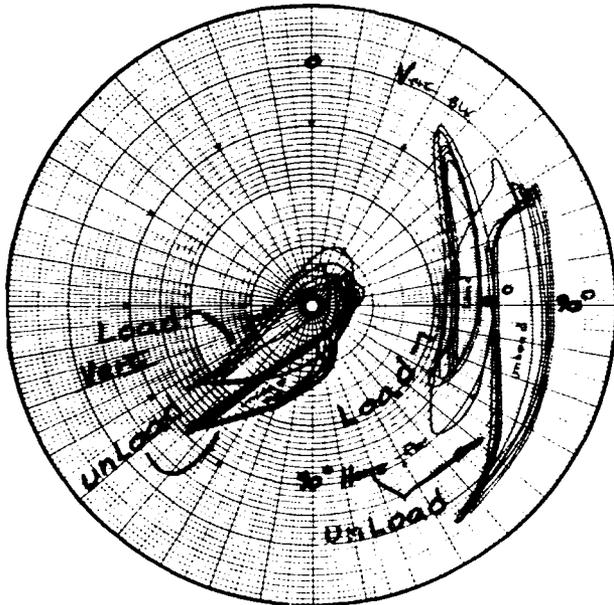
Bad Rotor-A   Good Rotor-B
(1 rotor bar open)   (rotor bar brazed closed)

5.Mils
Full
Scale
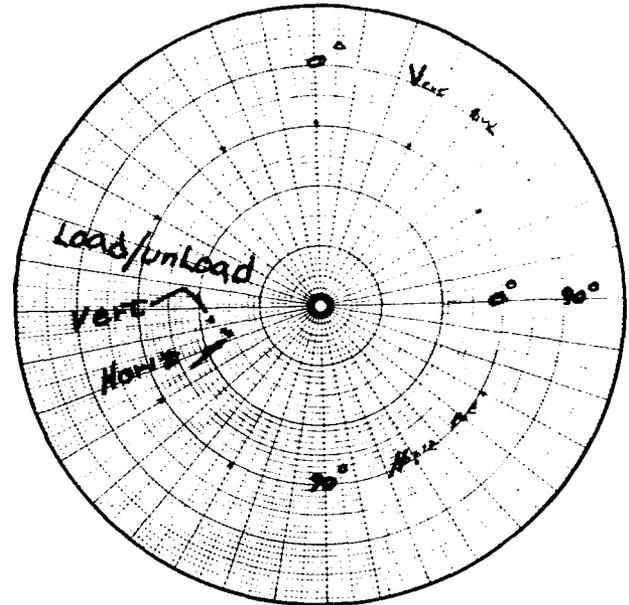
Fig.17a:Shaft-A Nyquist   Fig.17b:Shaft-B Nyquist

Observations:
17a - Horizontal displacment probe had phase excursions greater than 90
deg. and beating at slip frequency. Displacment amplitude remained
constant, 4. mils loaded and 2.5 mils unloaded. The vertical
displacment also beated at slip frequency with full 360 deg. phase
change. The amplitude changed from 0 to 3. mils.
17b - Both horizontal and vertical displacment remained constant in
phase and amplitude during load and unload. Because the horizontal and
vertical signals are in the same quadrant a circular orbit is
indicated.

39

MOTOR SHAFT VIBRATION — FFT: coupling end, horizontal and vertical,
loaded and unloaded, motor hot

Bad Rotor-A
(1 rotor bar open)
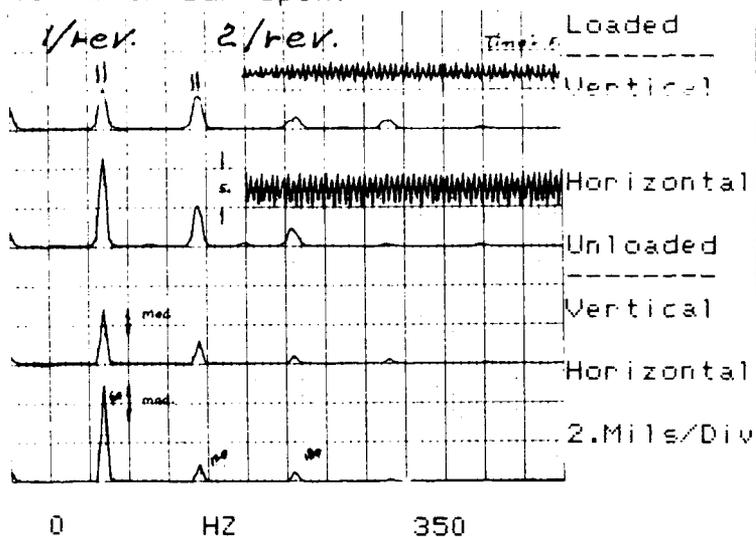
Good Rotor-B
(rotor bar brazed closed)
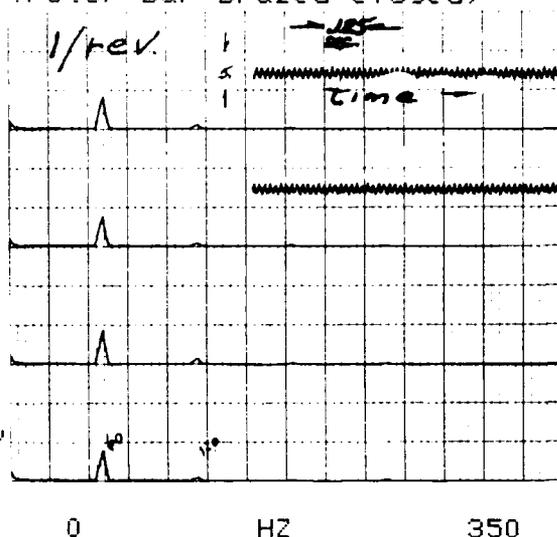
Fig.18a:Shaft-A FFT
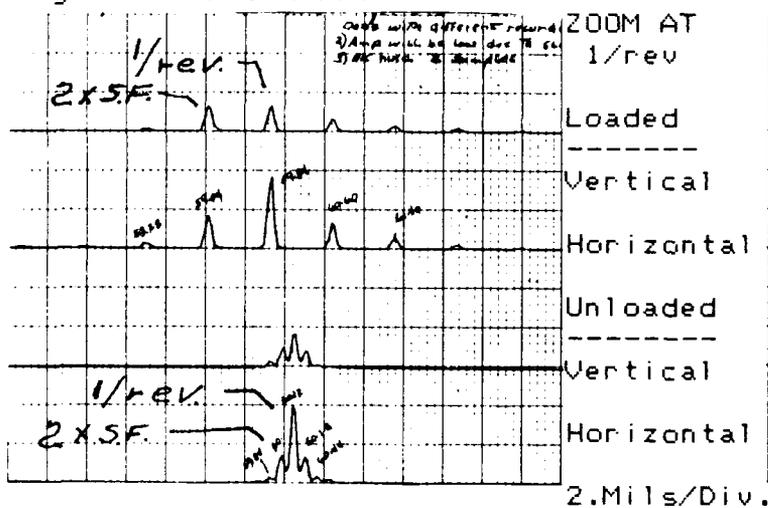
Fig.18b:Shaft-B FFT

60 +/- 2.HZ
fig.19a:Shaft-A FFT Zoom
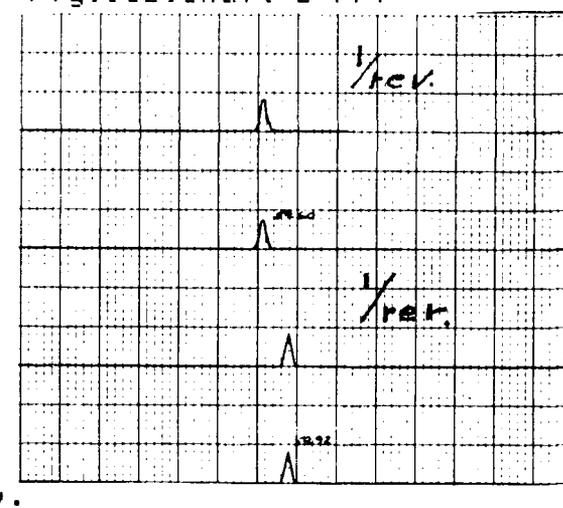
60 +/- 2.HZ
Fig.19b:Shaft-B FFT Zoom

Observations:
18a — Modulating 60 HZ and harmonic components with 2 HZ BW.
19a — Zoom FFT of 60 HZ shows 2x slip frequency components are creating
beat frequency.
18a — Stable 60 HZ component
19b — Zoom FFT of 60 HZ shows no side bands, thus no beating is
present.

40

MOTOR SHAFT CURRENT - TIME: shaft to shaft measurment, loaded to
                           unloaded, nondrive bearing insulated,
                           motor hot

Bad Rotor-A   Good Rotor-B
(1 rotor bar open)   (rotor bar brazed closed)
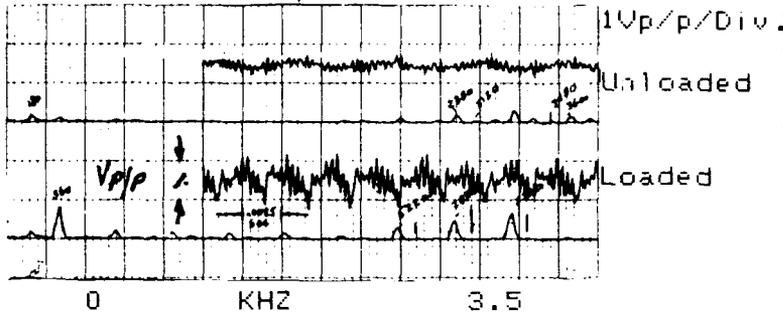
fig.20a:Shaft-A Shaft Current   fig.20b:Shaft-B Current
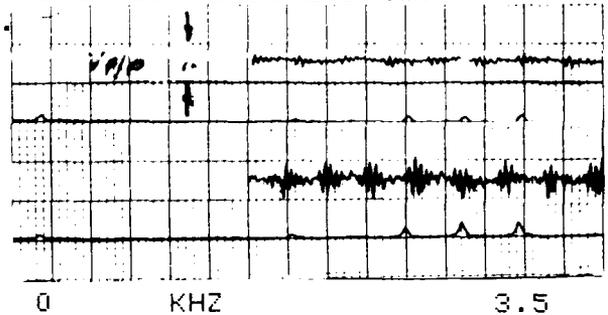
Observations:
20a - Overall pk to pk voltage increased with load. Components of slot
frequency and 360 HZ modulated at slip frequency.
20b - Slot frequency components are present but stable when loaded.
When unloaded voltage decreases at all frequencies.

        Because shaft currents are created by unsymetrical rotor flux the
data shows that the open rotor bar along with load will create this
discontinuity.

LINE CURRENT - 60 HZ ZOOM FFT: C.T. measurment, loaded, motor hot

Bad Rotor-A   Good Rotor-B
(1 rotor bar open)   ZOOM   (rotor bar brazed closed)
                            AT
                            60 HZ
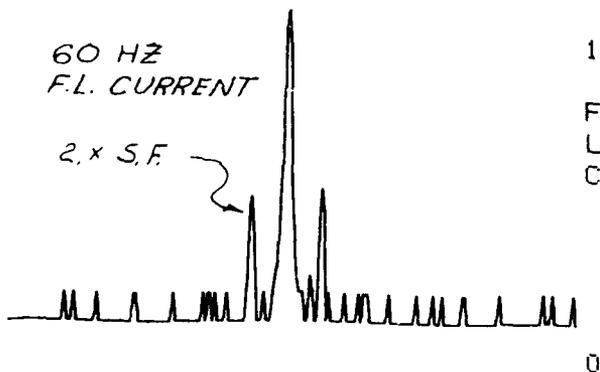
    60 HZ +/- 2. HZ   60 HZ +/- 2. HZ
Fig.21a;Shaft-A Line Current   Fig.21b:Shaft-B Line Current
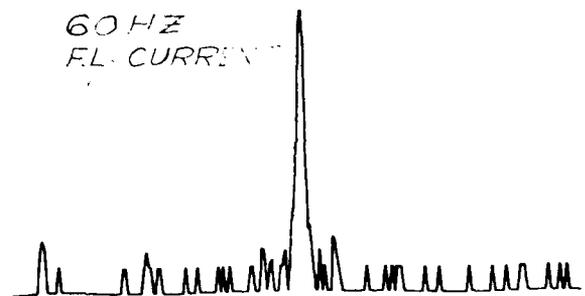
Observations:
21a - Direct CT. measurment of line current showed modulating side
bands at 2 x slip frequency. The amplitude of these sidebands decreased
with load.
21b - Minimal detection of 2 x sideband slip frequency.

41

BEARING HOUSING ACCELERATION - FFT: loaded, motor hot

Bad Rotor-A
(1 rotor bar open)
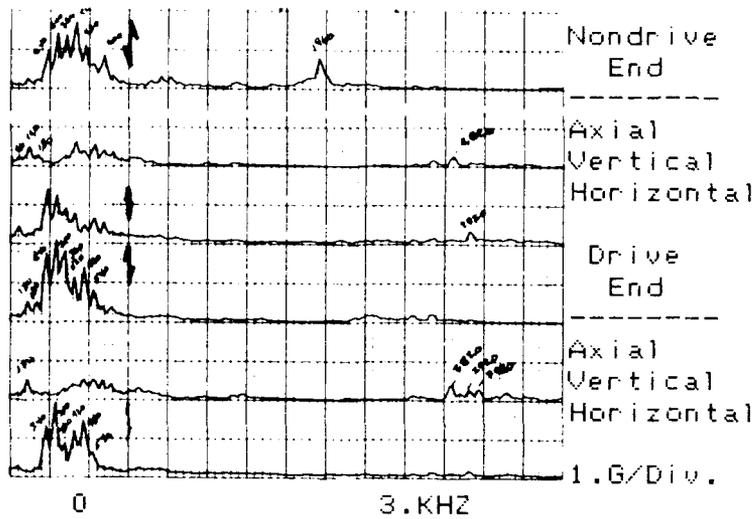
Good Rotor-C
(rotor bar brazed closed)

Fig.22a:Shaft-A
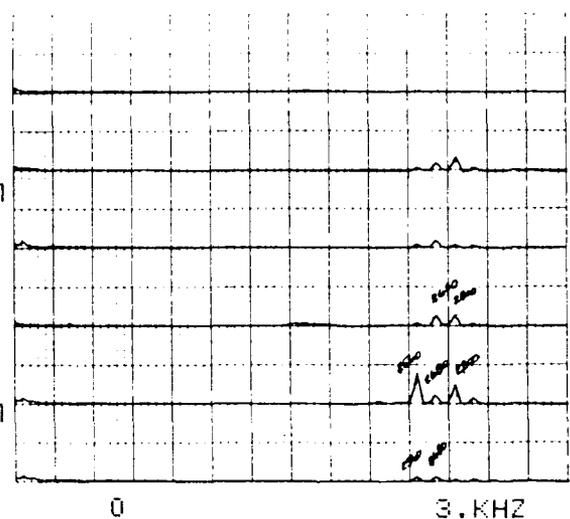
Fig.22b:Shaft-B

Observations:
22a - Large modulating harmonics of 60 Hz.
22b - Stable slot frequency 2680 HZ (45 x rps) with 120 Hz. sidebands

TABLE 1: Comparison of specific test vs. cost/time/relevency

Fig.	Title	Cost (relative)			Time			Relevent		
		Lo	Mod	Hi	Lo	Mod	Hi	Lo	Mod	Hi
9a/b	Motor Shaft Disp.-Orbit-unflt.	X			X			X		
10a/b	Motor Shaft Disp.-Time-unflt.	X			X			X		
11a/b	Motor Shaft Disp.-Orbit/Time-flt.		X			X			X	
17a/b	Motor Shaft Disp.-Nyquist			X			X			X
18a/b	Motor Shaft Disp.-FFT		X		X				X	
19a/b	Motor Shaft Disp.-FFT(ZOOM)		X		X					X
20a/b	Shaft Current -Time-unflt.	X			X			X		
21a/b	Line Current -FFT(ZOOM)		X		X				X	
22a/b	Bearing Accl. -FFT		X			X				X

42

CONCLUSION:

As mentioned earlier the intent of this paper is to give the motor user an idea of how his structure responds to rotor vibration at rest and at full speed. In addition measurements of the effective change in the rotors position and dynamics (forcing function) between hot, cold, loaded and unload conditions. This type data will give you a bench mark as to how the unit is currently operating and will give you a warning if future vibration data changes.

The broken rotor bar example created an unsymmetrical rotating flux which could have been caused by other mechanical discontinuities. In general, regardless which method of data collection or reduction is used an unsymmetrical magnetic field creates a 1/rev. and 2/rev. signal with 2x slip frequency side bands. It is also worth noting that an initial indication that you may have a problem with your 2-pole induction motor is that there will be a obvious audible growling beat at slip
frequency.

REFERENCES:

Reports:
1. W.T. Thomson - S.J. Chalmers - D. Rankin, "Current Monitoring System For Rotor Fault Diagnosis In 3-Phase Induction Motors", Turbomachinery International, Dec. 1987.

2. W.R. Camble, Diagnosing Alternating Current Electric Motor Problems", Arabian American Oil Company.

3. C. Hargis - B.G. Gaydon - K. Kamash, "The Detection of Rotor Defects In Induction Motors", Central Electric Generating Board, U.K.

Books:
4. Richard M. Phelan, "Fundamentals Of Mechanical Design", pp. 456-463, McGraw Hill, 1970.

5. Herbert W. Jackson, "Introduction To Electronic Circuits", pp. 238-251, Prentice Hall.

6. M. Liwschitz - Garik - Whipple, "A-C Machines", ch 1, D. VanNestrand Inc. 1961.

ABSOLUTE BALL BEARING WEAR MEASUREMENTS
FROM SSME TURBOPUMP DYNAMIC SIGNALS

M. J. Hine, Ph.D.

Rockwell International/Rocketdyne Division
6633 Canoga Avenue
Canoga Park, CA 91303

This paper describes how absolute bearing ball wear is measured in an operating turbopump from heavily loaded ball bearing vibration signatures. This technique was developed during testing of the high pressure oxidizer turbopump of the Space Shuttle Main Engine (SSME). A linear correlation was established between the cage frequency harmonic amplitudes on internal strain gages and the measured ball wear after pump disassembly. The dominant cage harmonics in the vibration spectra were shown to correspond to those of a Fourier series representation of the circumferential ball diameter variation or wear pattern. Strain gages and accelerometers on the external pump casing also show similar wear symptoms. These external measurements allow convenient wear monitoring for preflight testing of the SSME.

INTRODUCTION

The bearing wear measurements described herein resulted from the development testing of an uprated High Pressure Oxidizer Turbopump (HPOTP) for the Space Shuttle Main Engine (SSME). A cross section of this pump is shown in Fig. 1. The pump shaft rotates at up to 30,000 rpm and is carried by two sets of axially pre-loaded duplex ball bearings. Each of the original pump end bearings (1 and 2) had thirteen 11.1 mm diameter balls running on a 65 mm pitch diameter. Later designs had the number of balls reduced to 12 to accommodate oval-shaped ball cage pockets for increased relative ball motions. The turbine end bearings (3 and 4) also carry the transient axial shaft loads and have thirteen 12.7 mm balls running on an 80 mm pitch diameter. The bearings are run without lubrication and are cooled by a through flow of liquid oxygen.

For development testing, strain gages were attached to the pump end bearing carrier (isolator), to measure radial loads carried jointly by Bearings 1 and 2. Strain gages were also attached to the turbine bearing carrier (cartridge) for measuring axial loads at Bearings 3 and 4. The vibration signatures of these strain gages were found to contain dynamic behavior due to bearing ball wear. A typical isolator strain gage amplitude versus frequency spectrum is shown in
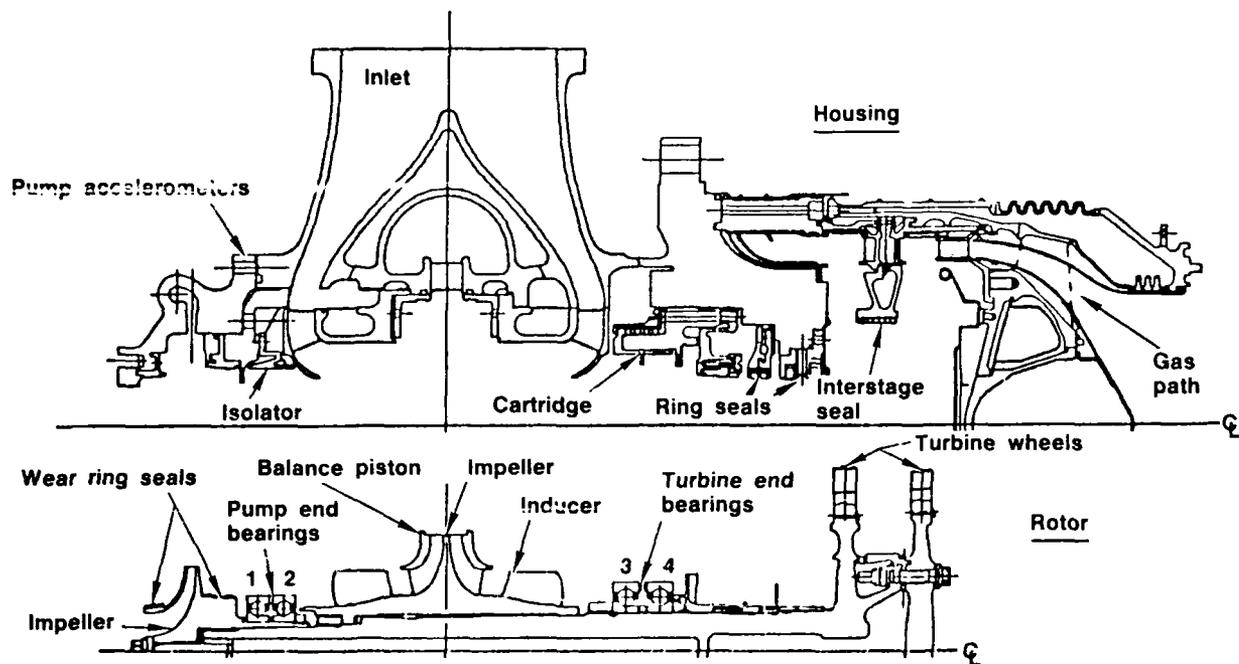
Fig. 1. Half Cross Section of High Pressure Oxidizer Turbopump

Fig. 2A. Some pumps would eventually show a spectrum as in Fig. 2B, where the harmonics of the ball cage frequency are apparent. The harmonics of ball cage frequency are generated by the different ball diameters within a bearing ball train as described by Sunnersjö [1].

Distinctive frequency modulation of the pump speed harmonics by the ball cage harmonics was also observed, as shown in Fig. 2C. This phenomenon has not been

Bandwidth = 4 Hz
S = synchronous
B_n = cage frequency harmonics
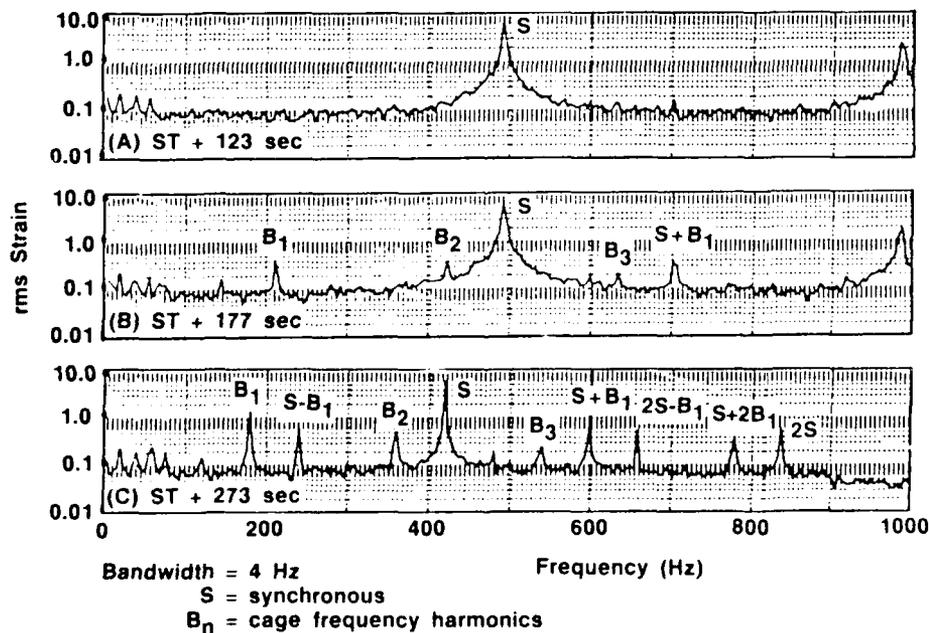
Fig. 2. Strain Gaged Isolator rms Amplitude Spectra

investigated but is thought to be due to inner raceway circumferential surface waviness interacting with the ball diameter variations.

VIBRATIONS DUE TO BALL WEAR VARIATIONS IN A BALL SET

The vibrations generated by geometric imperfections in lightly loaded roller bearings are well described by Sunnersjö [1] who demonstrated under laboratory conditions how the circumferential roller diameter variation in a roller set generates cage frequency harmonics. Similar arguments will be shown to describe the vibrations generated by heavily loaded and worn ball bearings in an extremely severe operating environment within a real turbopump.

The ball bearings of the HPOTP are heavily loaded radially with measured radial loads during flight simulated operations of 2 to 12 kN shared between Pump End Bearings 1 and 2. The results presented herein are therefore valid for a large load range.

Consider the crude representation of a radially loaded ball bearing in Fig. 3, where the only geometric error is the circumferential variation in ball diameter. The outer race is rolled into a straight line for clarity. The radial position of the inner race and supported shaft center, relative to the outer race center at the time when a ball is under the radial load action line, will be determined by the diameter of that ball. During one revolution of the 13 ball train set shown, the position of the shaft center will be known at 13 instants, if the ball diameters are known. Although the shaft position is not known between balls, it may reasonably be represented by a smooth line through the 13 known diameters. The amplitude of the shaft motion y, would then be due to the differences in ball diameters. Since the balls are manufactured to the same diameter, with a small tolerance, the ball diameter variation measured after a period of service will be due to wear. The shaft motion y is therefore proportional to the ball wear differences.
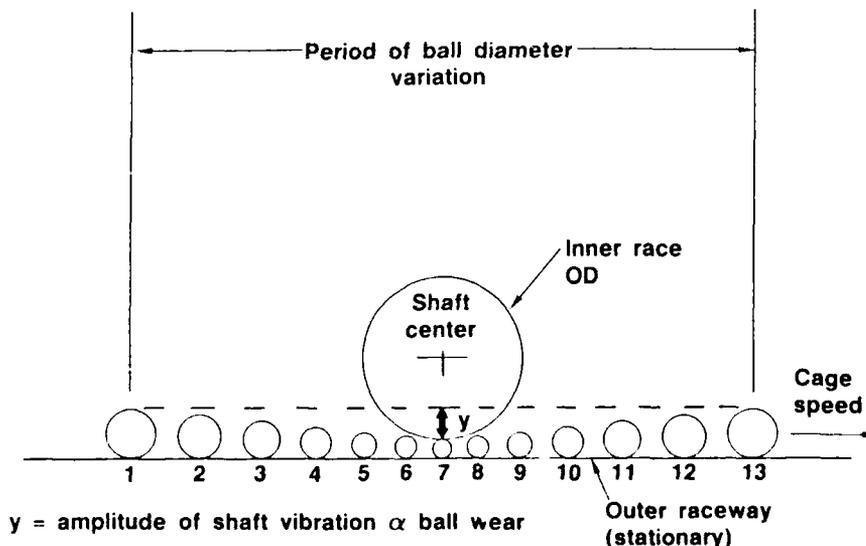
Fig. 3. Schematic of Ball Train Asymmetry

Consider the measured diametral ball wear variation versus ball sequence number shown in Fig. 4 for an HPOTP No. 2 bearing, after 1310 sec of operation. This ball wear variation may be represented by a Fourier series, since the ball wear variation is periodic over the ball train circumferential length.

The harmonic amplitudes of this series are shown in Fig. 5. Since the ball diameter sequence runs under the inner and outer race load line at the cage peripheral speed, the radial shaft center displacement will then be represented by the same Fourier series with the cage speed as the fundamental frequency.
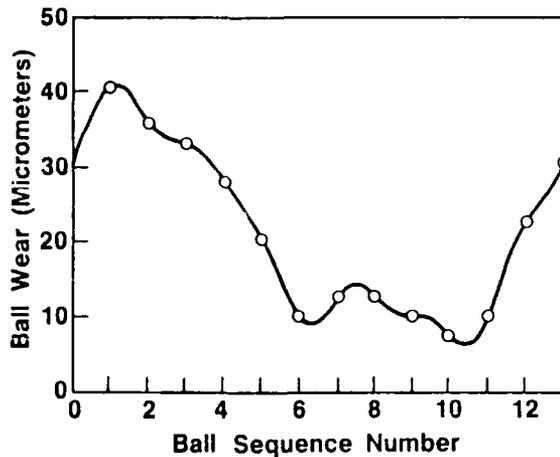
Fig. 4. Six-Term Fourier Fit
to Data (HPOTP 2606R1
Bearing 2)
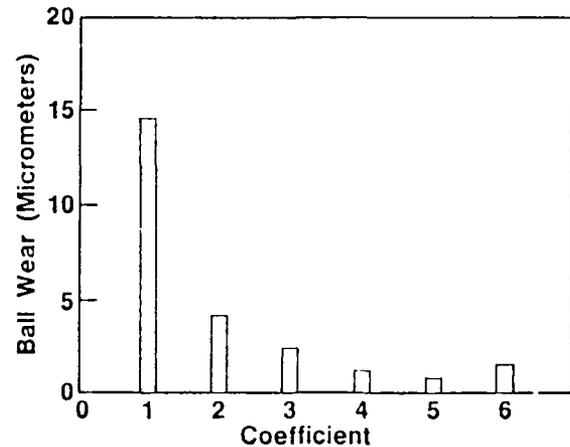
Fig. 5. Fourier Coefficient
Amplitudes (HPOTP
2606R1)

Neglecting phase, the radial shaft displacement may be written as:

$$y(t) = a_1 \cos (\omega_c t) + a_2 \cos (2\omega_c t) + \ldots \ldots = \Sigma a_n \cos (n\omega_c t)$$

where a_n = the nth Fourier coefficient, t = time, and ω_c = angular speed. The amplitude y is proportional to the amplitude of the circumferential ball diameter variation, or ball wear.

The individual Fourier coefficients, or displacement amplitudes, may be studied separately and superimposed since a linear model has been assumed. For a rigid shaft the force F(t) exerted on the outer race due to the shaft radial acceleration at a cage speed ω_c is approximated by:

$$F(t) \propto \omega_c^2 \sum_{n=1}^{\infty} a_n n^2 \cos (n\omega_c t)$$

This force produces vibrations of the bearing support at frequencies $n\omega_c$, where n = 1, 2, 3, ..., the amplitudes of which depend on the dynamic properties of the bearing support, and the harmonic amplitudes a_n caused by the ball wear variation. Thus the vibration signature of the bearing support contains information on the wear induced diameter differences and their relative phasing within a ball train.

Vibration amplitudes measured in the bearing support should be proportional to the dynamic force applied to the bearing by the ball diameter difference. This force is, in turn, proportional to the displacement amplitude of the ball diameter differences as shown in the above equation. Thus, measured vibration amplitudes in the bearing support should be directly proportional to the magnitude of the ball diameter differences or the sum of the components of the ball diameter differences.

The following are apparent from the above formulae:

1.   The relative amplitudes of the cage harmonics identify a particular ball wear pattern in the ball train. For example, if the second cage harmonic dominates the vibration spectrum, then the second Fourier coefficient amplitude should dominate the circumferential ball diameter or ball wear pattern.

2.   The sum of the cage harmonic amplitudes in the vibration signature are proportional to the magnitude of the ball diameter or wear differences within a ball set.

3.   If at least one ball remains close to its original size, then the sum of the cage harmonic amplitudes is proportional to the absolute ball wear differences.

HARMONIC CORRELATION

To verify the above theory, the isolator vibration strain spectra taken just before a pump was withdrawn from testing for disassembly were compared to the Fourier series curve fits to the measured ball wear sequences. For the pumps observed, the isolator strain gage signal spectrum is typified by that of Fig. 2C, for the pump whose wear pattern is shown in Fig. 4. Here it is noted that the first cage harmonic dominates the vibration spectrum as it does the wear pattern. For this pump, the relative cage harmonic amplitudes found in the vibration spectra and expected from the wear pattern agree well, as shown in Table 1.

Table 1. HPOTP 2606R1 Relative Cage Harmonic Amplitudes
(Normalized to First Harmonic)

Cage Harmonic	Spectrum Amplitude	Expected Amplitude from Wear Measurements
1	1.0	1.0
2	0.33	0.29
3	0.17	0.16
4	0.067	0.080

Good agreement was shown between the measured and expected dominant cage harmonics for 13 pumps as shown in Table 2. Some disagreement between theoretical and measured dominant cage harmonics must be expected as in Table 2 due to physical limitations. For instance, a major limitation in the vibration measurements is that the strain gages react the forces from two identical bearings in one common

Table 2. Correlation of Observed and Expected
Dominant Ball Cage Harmonic

| | Dominant Harmonic | | |
Pump	In Strain Gages at Test End	Expected from Wear Pattern	Gage Position
2606R3	1	No Wear	Isolator
9708	1	No Wear	Isolator
2409	1	2	Isolator
2409R1	1	1	Isolator
2606R1	1	1	Isolator
9605	1	1	Cartridge
0307R2	2	2	Isolator
9505	2	No Wear	Isolator
9505R2	1	1	Cartridge
9505R2	2	2	Isolator
9808R1	1	No Wear	Isolator
4204R1	1	3	Isolator
4104R1	1	1	Isolator
2116	2	1	Isolator
4204R2	1	1	Isolator

bearing carrier. Radial motion of the carrier expected from wear in one bearing could therefore be masked by the adjacent unworn bearing sharing an unknown portion of the radial load. This may account for no observations of cage frequencies higher than the fifth in vibration spectra. In all the pumps tested, only one bearing was worn, namely the No. 2 bearing. Fourier coefficients of a pump not showing agreement are shown in Fig. 6 and 7, with the corresponding vibration spectrum in Fig. 8.

Although the fourth cage harmonic was expected to dominate the vibration spectra, the second does. In this case, the first and second cage harmonics also appear equal from the wear measurements but differ considerably in the vibration spectra. Structural attentuation of the vibration signal is probable in this case. All the discrepant pumps showed dominant wear-expected harmonics greater than or equal to the fourth.

Fig. 6. Six-Term Fourier Fit to Data
(HPOTP 2116 Bearing 2)

It can be seen from Table 2 that one pump had ball wear at both a pump and turbine end bearing simultaneously. This was recognized from the bearing vibration spectra before pump disassembly, as shown in Fig. 9. This shows the vibration spectra of two strain gages on the isolator and cartridge. Figure 9A shows the Pump End Bearing No. 2 signature with two frequencies at the expected second

Fig. 7. Fourier Coefficient Amplitudes
(HPOTP 2116 Bearing 2)
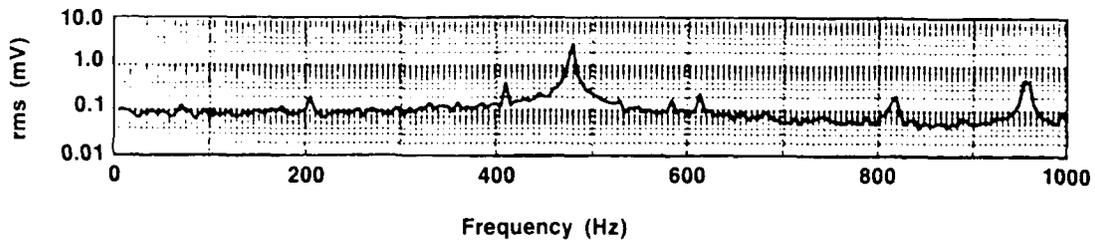
Fig. 8. Vibration Spectrum (HPOTP 2116)
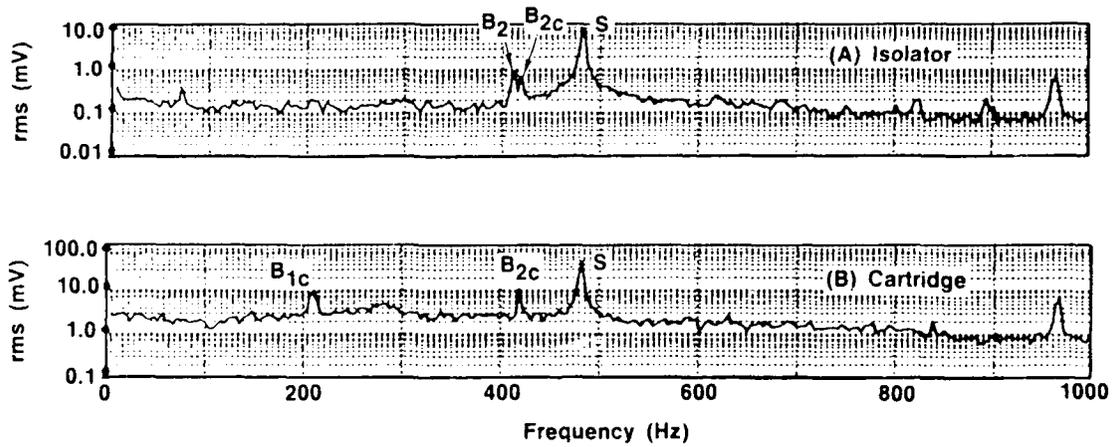
S = Synchronous pump speed
$B_{1c}B_{2c}$ = Ball cage harmonics from cartridge bearing
B_2 = Ball cage 2nd harmonic from isolator bearing

Fig. 9. Simultaneous Strain Gage Spectra

cage harmonic. This is due to the higher Bearing 4 cage harmonic feeding through the rotor structure to the isolator strain gages. This frequency difference is due to the different geometries of the pump and turbine end bearing sets. If they were similar, the source of the cage frequency would be difficult to establish. Figure 9B shows the higher Bearing 4 second cage harmonic from a turbine bearing cartridge strain gage.

Although the particular bearing having ball wear cannot be identified, the combination of pump isolator and bearing cartridge strain gages can identify the duplex set having wear symptoms.

WEAR CORRELATION

The measured ball wear for different pumps was compared with the cage harmonic amplitudes observed in the vibration spectra from a particular isolator strain gage location. Using regression techniques, a linear correlation was found to exist between the minimum, maximum, or average measured ball wear and the sum of the first three cage harmonics or either of the first three cage harmonics. This is shown in Fig. 10 for the average ball wear in a bearing set, together with the one and two standard deviation limits. Fifteen pumps are included in this analysis. The degrees of correlation found are shown in Table 3.

The correlation between average ball wear and cage harmonic sum is expected because, theoretically, the measured vibration amplitudes should be directly proportional to the magnitude of the ball diameter differences at the cage harmonic frequencies. Since the measured vibration amplitudes are time-averaged rms values, similar time-averaged values must be used for the magnitude of the
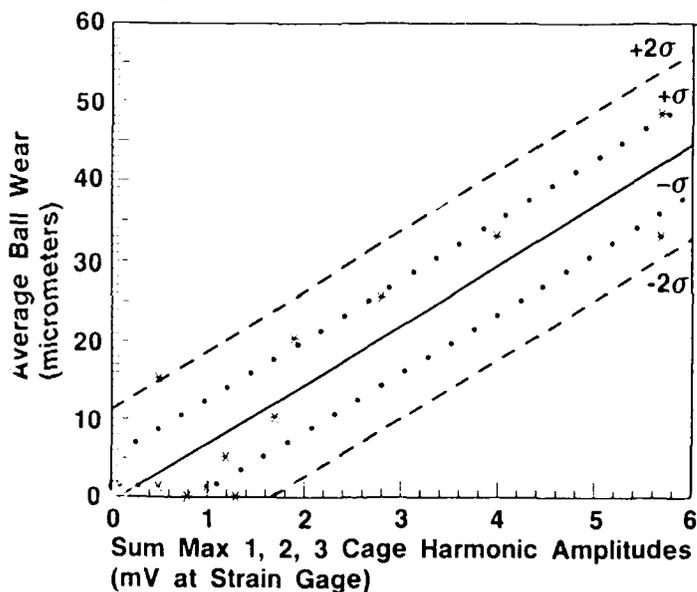
Fig. 10. HPOTP Average No. 2
Bearing Ball Wear

Table 3. Ball Wear vs Cage Harmonic Correlation Coefficients

Ball Cage Harmonic	Ball Wear Measurement		
	Average	Minimum	Maximum
1	0.90	0.92	0.79
2	0.89	0.86	0.87
3	0.82	0.83	0.78
Sum 1, 2, 3	0.92	0.91	0.86

ball diameter differences for the correlation. The average ball wear was thus used as a measure of ball wear since it approximates the rms value of ball wear within 10% for the pumps tested. If the rms ball wear is used, the correlation between the sum of the first three cage harmonics and ball wear is 0.91, little different from the 0.92 shown for the average ball wear correlation in Table 2. The strong correlation between the individual vibration harmonics and average ball wear probably implies that the ball wear initially grows in a set pattern, such that the average and each harmonic grow at relatively fixed proportions to one another. This may be observed later in the discussion of time variations in cage harmonics. A correlation should also be expected between the individual cage harmonics of wear and vibration. For the first and second cage harmonics, correlation coefficients of 0.70 and 0.69 were found. The third harmonic had a much lower correlation coefficient.

The correlation coefficients found are relatively high and verify the validity of the correlations found. All the correlations shown have a Student's t significance level of >0.1%, meaning that here is less than a 0.1% change of these correlations occurring by chance.

With ball wear charts, such as Fig. 10, actual ball wear can be determined during pump operation. The maximum strain gage amplitude observed during a test for the cage harmonic sum is used for wear predictions. The apparent zero wear data points occurring in Fig. 10 for small cage amplitudes, occur because ball wear was only measured within 0.00254 mm. They, in fact, represent small amounts of ball wear. The large standard deviations are expected since the theory assumes that at least one ball has no wear. Charts such as these continue to be used successfully to predict ball wear in development testing.

EXTERNAL CAGE FREQUENCY OBSERVATIONS

The cage frequency vibrations will increase as wear progresses to such a level that they are detectable on the external surfaces of the pump casing. This is shown in Fig. 11 for a strain gage and accelerometer. These spectra are for the

S = Synchronous pump speed
B_2 = 2nd ball cage harmonic from turbine bearing
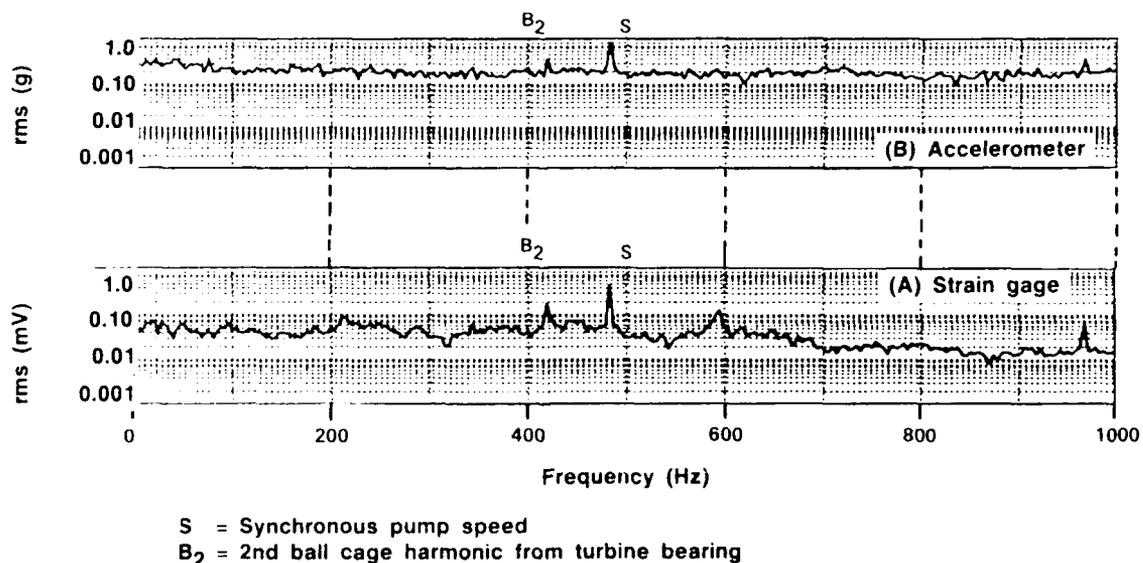
Fig. 11. Simultaneous External Spectra

same pump and time interval depicted in Fig. 9. On average, the internal strain gages precede the external strain gages by 1000 sec in indicating ball wear symptoms. The external strain gages precede the accelerometers by 2000 sec in indicating ball wear symptoms. These external strain gages are easier to apply than the internal ones with their cables penetrating the pump casing. Because of this, they are being used to screen pumps in preflight testing for ball wear symptoms. The current technology would also allow ball wear detection during SSME flights.

TIME VARIATIONS IN CAGE HARMONICS

The behavior of the different cage harmonics with time is of importance. Figure 12 shows time histories of the first three cage harmonics for a pump that had severe bearing wear. Figure 13 shows the corresponding sum of the cage harmonic amplitudes versus time. The amplitude drop after the first peak would suggest negative ball wear, which is obviously impossible. Since cage amplitudes are proportional to the relative ball wear, the amplitude drop is only indicative of a diminishing relative ball wear pattern. The absolute ball wear is, of course, continuing to increase with time. In other words, the amplitude peak suggests that the largest ball has started to wear more to catch up with the wear of the other balls, at the first amplitude peak, 0.076 mm of average ball wear was indicated from Fig. 10. Figure 12 clearly shows that the ball wear pattern is constantly changing in time. The pump depicted ended up with an average Bearing 2 ball wear of 0.79 mm with a maximum of 0.86 mm wear, on a bearing endurance test.
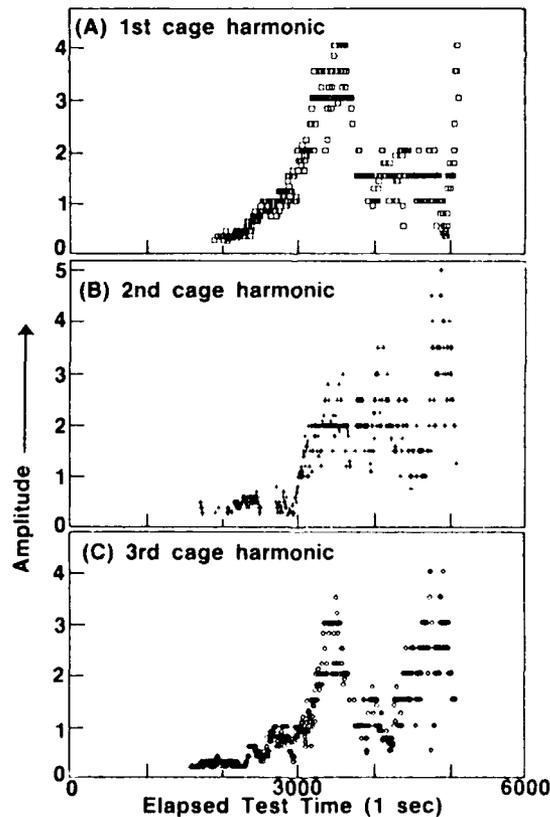
Fig. 12. Cage Harmonic Amplitudes vs Time
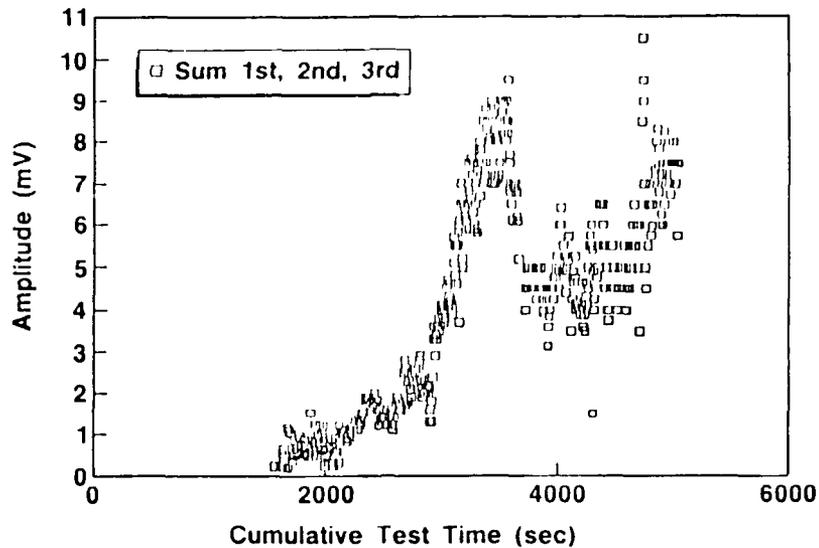
Fig. 13. HPOTP 0307 Ball Cage Harmonics
(Isolator Strain Gage)

CONCLUSION

It has been shown that with little error, the absolute bearing ball wear in an operating turbopump can be measured from ball cage frequency harmonic amplitudes detected in the pump vibration signatures. This conclusion is valid provided at least one ball remains unworn or nearly so. The dominant cage harmonics in the vibration signatures have been shown to correspond to those expected from the measured circumferential ball wear pattern in a bearing ball set. In general, increasing cage harmonic amplitudes in a turbopump vibration signature are indicative of increasing bearing wear. Changes in the cage harmonic amplitudes are indicative of increased ball wear.

REFERENCE

1.   C. S. Sunnersjö, "Rolling Bearing Vibrations--The Effects of Geometrical Imperfections and Wear," J. of Sound and Vibration, Vol. 98, No. 4, pp. 455-474, 1985

SPECTRAL NORMALIZING

Mr. Bertel Lundgaard
Mr. S. Baker Stocking
DLI Engineering Corporation
253 Winslow Way West
Bainbridge Island, WA 98110

In machinery vibration analysis and fault diagnosis, spectral plots of data which have been normalized to orders of the rotational rate offer significant advantages over traditional fixed frequency spectra, particularly for the development of diagnostic computer software. This paper explains the concept of order normalization, discusses the advantages for both human and computer analysis, and finally, describes several methods used to produce normalized spectra.

INTRODUCTION

A vibration spectrum is usually plotted or displayed with frequency as the abscissa and amplitude as the ordinate. Common dimensions for frequency are Hz (cycles per second) and CPM (cycles per minute). This paper will discuss the virtues of a different spectrum presentation; the normalized (or order normalized) spectrum. A spectrum is normalized by dividing all frequencies by the frequency of a machine order, usually the first. The order normalized spectrum is then plotted as orders versus frequency. For example, if an electric motor runs at 1760 RPM, its first, fundamental, order is 29.33 Hz, its second order is 58.66 Hz and so on. The order normalized spectrum will have 1 and 2 substituted for 29.33 and 58.66. Figure 1 shows a set of order normalized low range spectra from the turbine end of a lube oil pump, as printed by portable field equipment. The superimposed average spectra also shown will be discussed on page 4. Note that the speed of the machine decreased slightly between measurements without affecting peak alignment.

ADVANTAGES OF NORMALIZING

The major factor contributing to the value of normalizing is that it reduces the number of variables in a typical spectrum from two to one. While the ordinate showing the vibration amplitudes will continue to be variable, the abscissa, when expressed as orders, does not vary with machine speed.

The normalizing technique is particularly valuable when vibration analysis is used to detect faults in rotating or reciprocating machinery. In the case of a single shaft machine, major exciting components will generate integer order peaks in the spectrum. If the system contains a speed changer, the order of the secondary shaft will correspond to the gear ratio.
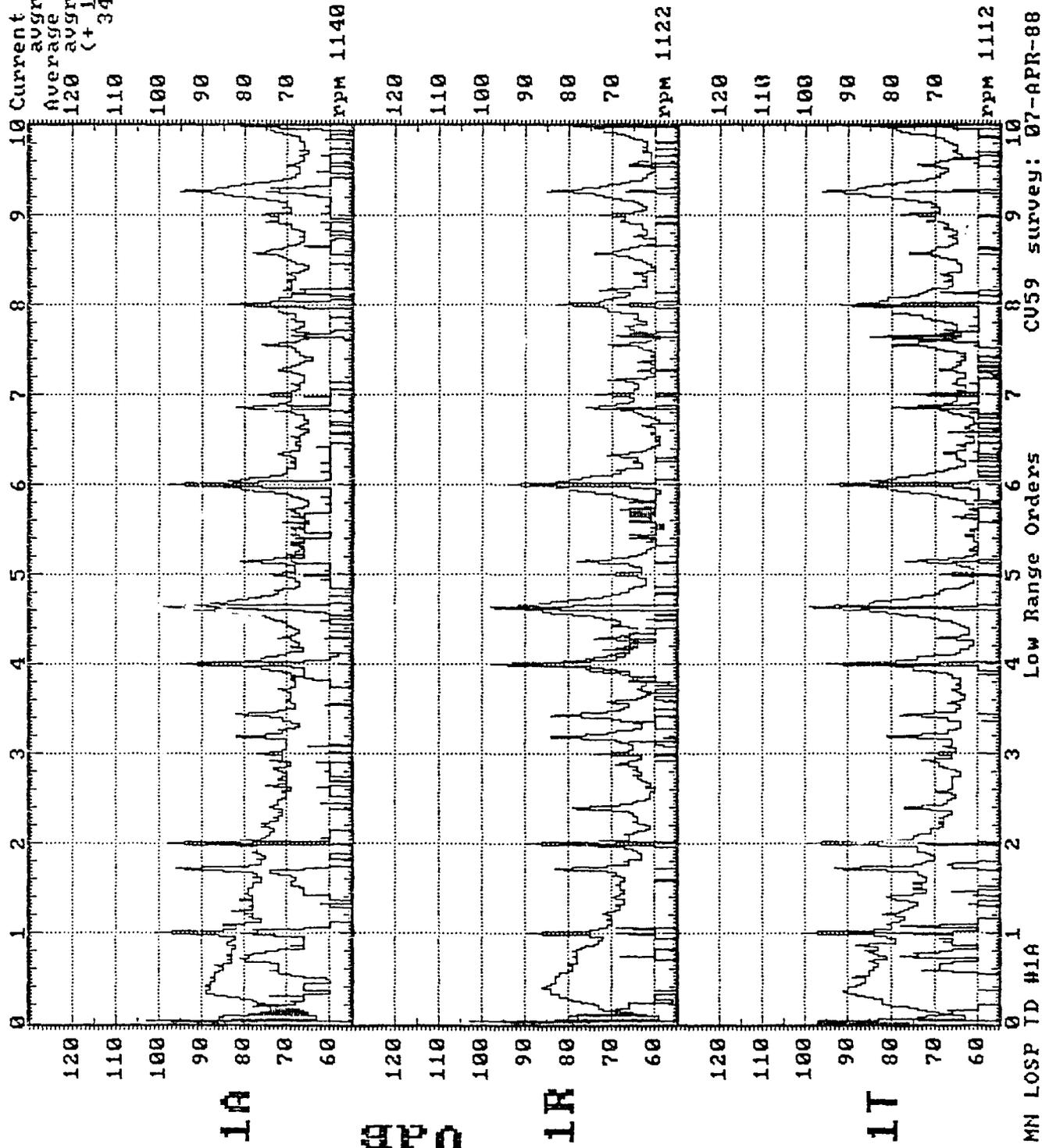
FIGURE 1 - NORMALIZED SPECTRA, CURRENT VS. AVERAGE

58

The following advantages of normalizing will be discussed in some detail:

o Diagnostic guidelines are almost always given in terms of "orders" rather than "frequency".

o Once the order being excited by a machine component has been established, it will remain constant regardless of machine speed.

o Significant peaks in normalized spectra from identical machines will line up exactly, permitting superimposition of spectra and mathematical manipulation of vibration amplitudes.

o Order normalizing permits the creation of reference spectra of typical good machines. This facilitates diagnosis through the amplitude deviation generated by faulty machine components.

o Tabulation of spectral peaks excited by machine components will correspond to peaks plotted on a graph and will not change with machine speed.

o The design of expert systems is simplified.

When an engineer takes the first halting steps toward learning to use the vibration analysis as a tool to diagnose machine problems, he is immediately made aware of the concept of rotational orders. Imbalance generates a first order peak; misalignment generates a second order peak, while an outer race fault in a given ball bearing will generate a peak whose order may be calculated from the bearing geometry. When a spectrum is plotted as frequency in Hz versus amplitude, the order can easily be found by calculating

$$ORDER = f/N \qquad\qquad (1)$$

where f is frequency in CPM and N is machine RPM.

Note that for non-normalized spectra, this calculation must be repeated each time it is desired to find the order of a vibration peak.

The deviation concept is important in vibration analysis. The absolute amplitude of a vibration peak is usually less important than its deviation from some norm, such as a new machine baseline spectrum or the spectrum from the previous survey on the same machine. With normalizing, the current spectrum may be superimposed on the reference spectrum, and significant peaks will line up exactly. Other mathematical manipulations may be easily performed; spectral amplitudes may be subtracted or divided and the difference or ratio plotted, or spectra from a number of surveys on identical machines may be averaged. Averaging is a particularly powerful to 1, since it generates a high confidence reference spectrum from which deviations may be evaluated.

Figure 2 shows in detail the average spectrum, from a 34 machine sample, used at the top of Figure 1. The lower, heavier line is the statistical average of the amplitudes, while the upper, lighter, line shows a plot of the average plus one standard deviation. Since only healthy machines were included in the sample, the "plus one standard deviation" line has proved to be a valuable quality control tool; the spectrum of overhauled machines must fall below that line, as is essentially the case in Figure 1.

Order normalizing further simplifies the diagnostic work, since it permits tabulation of exciting frequencies in terms of orders and the tabulated orders can be pre-programmed to be labelled on the graph. Tables of exciting orders are shown on Figure 4 and the graph annotation is shown on Figure 2.

A current trend in diagnostic vibration analysis is toward the use of computer programs to perform part or all of the diagnostic work, so called "expert systems". These systems may be divided into two main categories: screening systems. which distinguish good machines from machines needing attention, but leave the definition of the problem to the engineer, and true diagnostic systems. which give specific repair recommendations. The success of an expert diagnostic system depends on two major sources of information: the availability of a "good machine" reference spectrum and the ability of the computer program to identify spectral peaks. It appears obvious that for variable speed machines and for complex machines with many exciting components, the success of a diagnostic system is dubious without the support of normalized spectra.

The use of normalized spectra is not widespread in vibration analysis. That is due to the difficulty and cost in accurate tracking of machine speed. The following sections of this paper will address those difficulties.
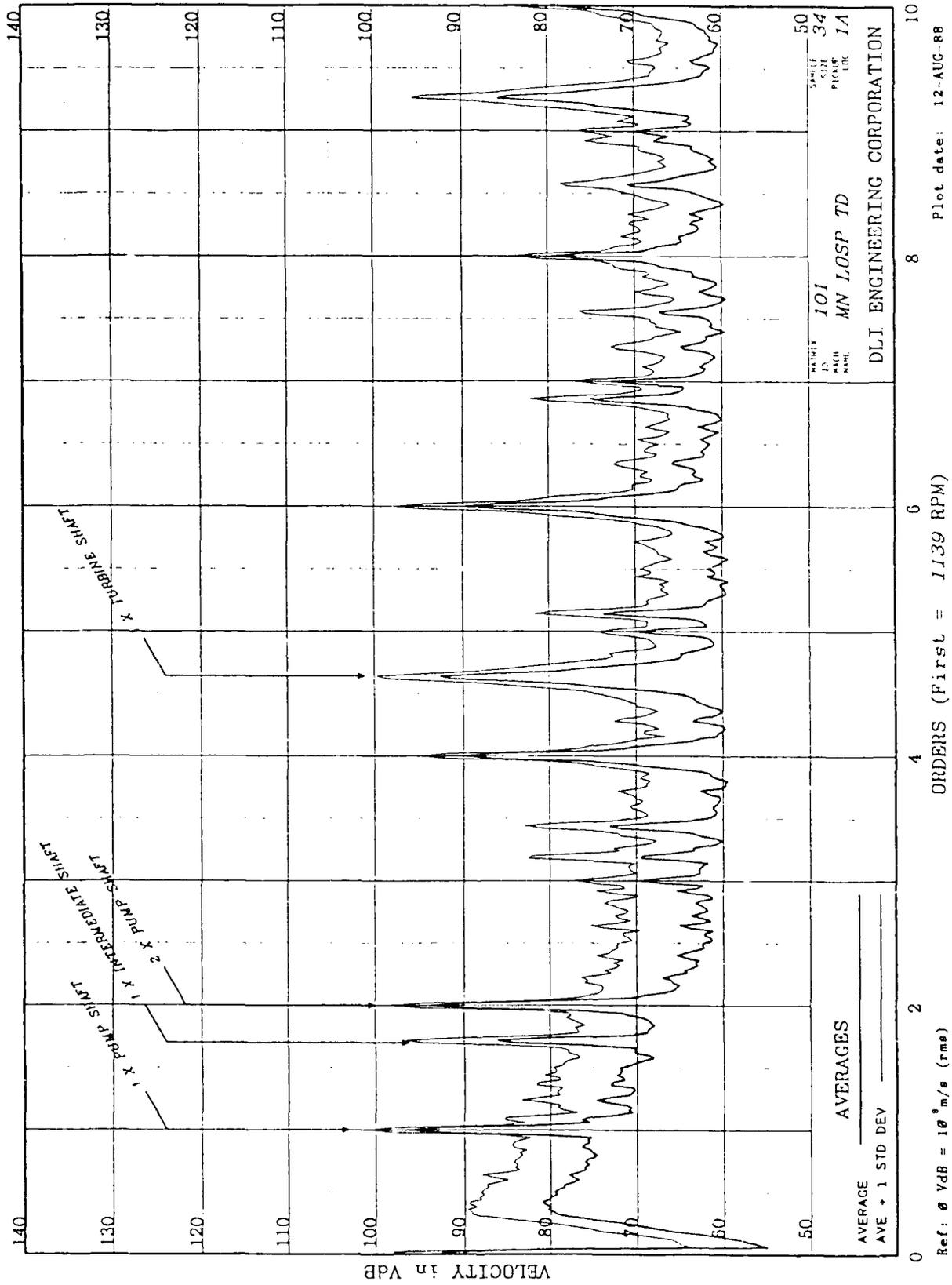
FIGURE 2 - ANNOTATED AVERAGE SPECTRUM

MACHINE: MAIN LUBE OIL SERVICE PUMP (TD)		SWAB: 262-4 MID: 101
SHIP APPLICABILITY: 59,60,61,62,63,64		DATE: FEBRUARY 1988
CV64 UNITS: 1,2,3,4		

DRIVER	INTERMEDIATE	DRIVEN

CID#: 057150141
TECH MANUAL: 347-2336
MFR: DELAVAL
HP: 41
STEAM CONDITIONS:
  Chest: 510 PSIG
  Exhaust: 15 PSIG
RPM: 6000
TYPE: RADIAL FLOW,
  VELOCITY COMPOUNDED,
  IMPULSE
	CID#: 057150141
	TECH MANUAL: 347-2336
	MFR: DELAVAL
	RATIO: 4.63 TO 1
	RPM (INPUT/OUTPUT):
	  6000/1300
	TYPE: SINGLE HELICAL,
	  SPIRAL BEVEL, DOUBLE
	  REDUCTION
		CID#: 016160255
		TECH MANUAL: 347-2336
		MFR: DELAVAL
		OUTPUT: 750 GPM @ 55 PSIG
		RPM: 1300
		TYPE: THREE SCREW, HIGH
		  PITCH, IMO

TEST RPMs AND OPERATING CONDITIONS	ANALYSIS RANGES
TURBINE: 5325 PUMP:1150	REF. RPM: 1 X PUMP ORDERS: 10, 200 FREQ HZ: 200, 5K WM RANGES: 2, 6

MAIN LUBE OIL SERVICE PUMP (TD)	262-4 - 101

FIGURE 3 - VIBRATION TEST AND ANALYSIS GUIDE

PAGE 1

VIBRATION SOURCE COMPONENTS

DRIVER				INTERMEDIATE OR AUXILIARY SHAFTS				DRIVEN			
ITEM	DESCRIPTION	ELEM	ORDER	ITEM	DESCRIPTION	ELEM	ORDER	ITEM	DESCRIPTION	ELEM	ORDER
t	**Turbine Shaft**		4.63p	i	**Intermediate Shaft**		1.71p	p	**Pump Shaft (Ref)**		1.99p
Z1	Nozzles	47	217.76p	G2	1st Reduction Gear	100	171.43p	G4	Driven Bevel Gear	36	36.00p
T1A	1st Row Turbine Blading	90	416.99p	G3	Bevel Pinion	21	36.00p	Pi	Pump Rotor	2	2.00p
S1	Stator Blading							P2	Pump Idler	2	2.00p
	3.88 Degree Spacing		429.96p	e	Oil Pump Shaft		1.82p	P3	Pump Idler	2	2.00p
T1B	2nd Row Turbine Blading	75	347.49p					G5	Oil Pump Drive Gear	61	61.00p
G1	1st Reduction Pinion	37	171.43p	G6	Oil Pump Driven Pinion	60	61.00p				
				OP	Oil Pump						

	BEARING	FUNCTION			BEARING	FUNCTION			BEARING	FUNCTION	
								G	ND 3308	R-p	
A	Journal	R-t		D	ND H20309	R,T-i		H	ND H20311	R,T-p	
B	Journal	R-t		E	ND H20309	R,T-i		J	ND H20311	R,T-p	
C	Journal	T-t		F	ND 5309	R-i		K	Journal	R,T-p	
								L	Journal	R-p	

VIBRATION SOURCE DIAGRAM

MAIN LUBE OIL SERVICE PUMP (TD)   262-4 - 101

FIGURE 4 – VIBRATION TEST AND ANALYSIS GUIDE
PAGE 2

METHODS OF SPECTRAL ORDER NORMALIZING

HARDWARE NORMALIZING USING A TACHOMETER SIGNAL

Spectral order-normalizing in digital FFT systems is most commonly performed during the very first step of digital data acquisition, the sampling of analog data by the analog to digital converter. The desired normalizing is simply a result of an appropriate adjustment of the sampling rate

These systems take advantage of the fact that the frequency range of the desired spectrum is always directly proportional to the sampling rate. Thus if the sampling rate is adjusted to cause the effective frequency range to be an exact multiple (call it N) of the tachometer rate, the resulting spectrum will have as its full scale frequency a value exactly equal to N orders of the fundamental represented by the tachometer signal, regardless of machine speed. The true frequency becomes a function of the tachometer reading, not the sampling rate.

The actual sampling frequency will always be something greater than twice the desired full scale frequency, in order to avoid aliasing; this multiplier may vary among analyzers, but is a constant for a given device. Likewise, the tachometer signal may actually be some multiple of the fundamental rotational frequency. As long as these factors become part of the equation, a suitable arithmetic relationship can be established between tach signal and sampling rate to cause any desired multiple ("Nth" order) of the rotational rate to become the full scale frequency of the final spectrum (i.e., making it an "N order" spectrum). The only limits are those imposed by the frequency limitations of the sampling and (anti-alias) filtering hardware.

In the ideal world, this method is the best choice; the results should always be accurate. The rotational rate is not in question unless the tachometer signal is poor, and the spectrum is the simple result of a direct Fourier transform on the time domain data samples, with no alteration of the data either before or after the transform.

HARDWARE NORMALIZING WITHOUT A TACHOMETER SIGNAL

In the real world, a tachometer signal is often a luxury. A channel must be provided for it by the analyzer, and considerable extra hardware and setup time may be required to provide the signal itself.

When DLI set out in the late seventies to automate the processing of large quantities of analog machinery vibration data recorded aboard aircraft carriers, one goal was the ability to order normalize most of the data without a tachometer signal. This called for a means of identifying, and isolating by means of a tracking filter, a suitable signal within the vibration data itself upon which the sampling rate could be based. All the analog tape records were acquired via triaxial accelerometers, using either a 4-channel or a 7-channel FM tape recorder. Thus, the tapes had either 3 or 6 channels of simultaneously recorded vibration data, with a spare channel reserved for the tachometer signal when needed.

In this environment the chances of finding and filtering a suitable stable signal were high, since each tape record offered either 3 or 6 different data channels as candidates to provide that signal. During the recording of the data aboard ship, the operator would observe the data on a real time analyzer during, and sometimes after, its recording. From this observation he was required to determine the machine speed and then locate and identify a spectral "peak" that represented a suitable tracking frequency on a specific data channel.

This information became part of the logged data used by the in house computer driven spectrum analyzer to process the data after the survey. For every tape record, the tracking filter was switched to the specified channel and centered on the frequency represented by the operator's RPM entry (and order, if the frequency to be tracked represented something other than the fundamental). In this manner the actual machine speed could be calculated and the sampling rate of the analyzer established accordingly. All 6 (or 3) data channels from one tape record would then be processed using this same time domain "driver" for the sampling rate base. By making two runs through each tape record and applying different multipliers to this base rate, both low range spectra (typically 10 orders) and high range spectra (up to 200 orders) were produced for each channel.

NEW SURVEY METHODS AND EFFECT ON APPROACH TO NORMALIZING

The hardware normalizing approaches just discussed are best suited to situations in which the process may be repeated if the results are not correct. The two methods we have presented both make their adjustments in the time domain--quite literally by playing with the clock, warping the sampling timer by a factor proportional to the speed of the machine. The first product in the frequency domain is the finished product--a spectrum of orders, normalized, perhaps incorrectly, to some appointed first order frequency. Correction, if needed, requires either the ability to return to the machine, or to tapes of analog data recorded from it. Current vibration survey methods often preclude, or at least discourage, either possibility.

The instrumentation market has changed significantly in the past few years with the introduction of highly portable, relatively low cost spectrum analyzers, easily interfaced with equally portable yet powerful new computers. These relatively new arrivals have tantalized both vibration engineers and their customers with the promise of nearly immediate results from a field vibration survey. Carrying tape recorded analog data home to a minicomputer-based spectrum analyzer for processing may already be an obsolete, albeit convenient, engineering luxury. The availability of spectral transforms in the field has presented new opportunities to obtain normalized spectra quickly, but not without associated difficulties.

SOFTWARE ORDER NORMALIZING IN THE FREQUENCY DOMAIN

DLI has recently been using such portable analyzers and computers to perform very large surveys of the type previously done with analog tape recorders and in-house processing. The data acquisition and FFT's are all done at high resolution using fixed frequency ranges carefully chosen from a very wide range of options. Order normalizing is performed (minutes to hours) later on the portable computer entirely by software, and strictly in the frequency domain. This software synthesizes new, normalized spectra (usually 500-line), using as input the oversized (800-line) fixed frequency spectra uploaded from the portable analyzers.

The decision not to attempt hardware normalizing at the time of the actual data acquisition has virtually guaranteed that the original spectra will be valid. Consequently, if the results of software normalizing are obviously incorrect, the fixed frequency originals may be sent back to the software for correction, repeatedly if desired.

CONCEPTUAL APPROACH AND EFFECT ON DATA ACQUISITION REQUIREMENTS

Creation of an order normalized spectrum from a fixed frequency spectrum first calls for identification of one or more specific peaks in the latter by defining the ratio of its frequency to that of the machine speed, the fundamental rotational frequency; once this has been done, every remaining peak in the spectrum can be described in terms of its own ratio, i.e. as an "x"th (integer or fractional) order peak.

The frequency domain normalizing process can thus be seen as an effort to identify that location in the fixed frequency spectral array--the "bin number" (most likely a real number representing a point somewhere between two bins)--which represents the full scale order of the desired normalized spectrum. Data from the fixed frequency spectrum up through that specified bin number only, can then be converted into a standard 400 (or 500) line order normalized spectrum. In this final product the first order in a 10 order spectrum, as an example, will always be found in the 40th (or 50th) "bin" or spectral array element.

In order to maintain the level of resolution achieved by the hardware normalizing process, the software version needs input data fixed frequency spectra covering the frequency range of interest--of a resolution greater than or equal to that of the standard end product. In the aircraft carrier machinery vibration program the standard spectral size, since computerization began 10 years ago, has been 500 lines. Even if the normalized spectrum were to be only 400 lines, an input spectrum larger than 400 lines (a common standard) would normally be needed to maintain full 400 line resolution. This is because even a large choice of fixed frequency analysis ranges would be unlikely to provide placement of the desired full scale order close enough to bin number 400 to make the difference negligible. If the full scale frequency fell much below bin 400, resolution would suffer; if above bin 400, the high end data simply would not appear.

Hence the input spectra for DLI's software normalizing program needed to be greater than the 400 lines output by the most standard portable analyzers. The next step up for a standard FFT is 800 lines, and this has become the standard input spectrum size for software normalizing.[1]

The 300-bin surplus has provided a distinct advantage when working with turbine driven machinery whose test speeds may vary substantially from the nominal or ideal test RPM. In fact, data acquisition sampling rates are chosen to place the expected full scale frequency (full scale orders times nominal test RPM) as close to bin number 650 as possible, to allow a -/- 23% (150/650 optimal) variability in machine speed, without loss of resolution or high end data in the 500-line end product. In practice, a limited number of analysis ranges, i.e. sampling rates, are available This means that most of the fixed frequency spectra will display the frequency corresponding to the desired full scale order in a spectral bin numbered somewhat lower or higher than the optimal value of 650. Again, the extra 300 bins allow a margin of safety for this limitation.

1. Standard FFT operations yield spectra of resolutions that are powers of two. Standard vibration spectra typically truncate the high end to avoid roll-off from the anti-aliasing filters used in data sampling. For example, Watchman 400-line spectra are the product of 512-point FFT's. PERA(CV)'s 500-line spectra produced from analog tape data by DLI's AVDP system are actually from 1024-point FFT's.

SOFTWARE NORMALIZING METHOD

The two main steps in software normalizing are:

1. Determining the machine speed at the time of data acquisition, and thereby calculating the effective "full scale bin number" in the fixed frequency spectrum.

2. Synthesis of the normalized spectrum using the results of Step 1.

MACHINE SPEED DETERMINATION

The first step above represents the major portion of the work, and the major challenge. DLI's approach breaks down this process of machine speed determination into several sub-processes:

a. Gathering maximum available reference data.

b. Reducing amount of information to minimum needed for processing.

c. Trial order calculations, testing for pattern matches with reference data.

d. Assessment of trials and decision for each single spectrum.

e. Review of results after first pass on whole machine.

f. "Auto-correction" of selected spectra, if required.

During a run of the normalizing program, the synthesis of normalized spectra (which we are calling the second major step) actually occurs after each of the two sub-processes labelled d and f above. An additional step is available to the user as needed; he or she may, on an individual spectrum basis, specify by keyboard entry the RPM to be used as first order for the re synthesis of spectra not correctly normalized during the automated run.

MACHINE SPEED DETERMINATION (cont'd)

Let's look at each of these subprocesses in more detail:

a. Gathering maximum available reference data.

The reference data employed by DLI's order normalizing software consists of the nominal machine speed for vibration testing, the maximum anticipated deviation from that nominal test speed, and a list of orders at which peaks may be expected to be seen. Of these, only the nominal test speed is required; all the rest will take on default values if no more specific information is available.

Separate default values for machine speed deviation, also known as an "RPM search window", exist for motor driven and turbine driven machinery. These global defaults may be altered by the user at run time. The user may also create, edit or add to an optional list of RPM search window values for specific machine types. Consultation of this list, normally enabled, may be disabled by the operator when starting up the program.

The list of orders at which peaks might be expected currently comes from two sources: averaged spectra (if they exist) for the particular machine type, and screening criteria test orders (orders at which the diagnostic/ screening program checks vibration levels). The averaged spectra, it should be noted, provide separate data for each analysis range at each transducer.

Many machines typically have clean spectra with strong harmonics of the fundamental; for these the first few integer orders would suffice as reference data. A number of others, however, have notoriously noisy signatures with weak showings of first order peaks and their harmonics. Normalization of data from such machines is greatly assisted by having information about specific peaks seen in past examples from the real world. Both screening criteria and average spectra provide this information.

The heart of DLI's software normalizing technique lies in the next two steps, b and c. The first provides the data to be tested by the second.

b. Reducing amount of information to minimum needed for processing.

Rather than looking at an entire array of spectral data, we extract only that information we expect to need for normalizing, namely the location of significant peaks. This extraction process, which we have nicknamed "feature filtering", is applied to average spectra in advance, and to current spectra as they are encountered. It is a process which could be greatly sophisticated to better warrant its nickname. For the purpose of normalizing, however, the current version seems to be providing us with all the information we need.

Amplitudes are essentially ignored. The filtering process simply provides a list of orders (in the case of average spectra) or "pseudo-orders" (in the case of current data) at which spectral peaks have been found. There are strict definitions of what qualifies as a peak, and several different thresholds determining when we have collected enough of them; the maximum is currently 16 peaks per spectrum. These definitions and thresholds are under the control of a number of parameters which DLI continues to tune, both in testing and in field use of the prototype software.

c. Trial order calculations, testing for pattern matches with reference data.

The actual process of determining machine speed we call "order alignment". The word "pseudo-orders" just mentioned provides a good key to understanding the process. Our reference array may contain up to 24 actual orders that either have been seen or might be expected in spectra similar to the one we want to normalize; sixteen may actually have been extracted from an average spectrum.

Our current data array contains up to sixteen "pseudo-orders". These are real numbers, each representing the location of a peak found in the current data in the form of **the order value it would have if the full scale order were located at a pre-assigned bin number.** They have been calculated during the "feature filtering" process by choosing a bin number in the fixed frequency spectrum where the desired full scale order would be expected to be found if the machine were running exactly at its nominal RPM.

Accordingly we call this bin number, our first attempt at locating the full scale order, the "nominal full scale bin number". There should be a bin number close to this one, if the vibration testing has been done in accordance with standards, which contains the actual Nth order vibration amplitude for our N-order spectrum. It is even more likely that the true spectral peak has its energy divided between two adjacent bins of the fixed-frequency spectrum.

The machine speed searching algorithm then becomes quite simply a series of re-calculations of pseudo-order values, using a changing "test full scale bin number" which is incremented over the range within which we have decided the real one must fall. This range is defined by the [nominal full scale bin number], plus or minus [itself times the RPM deviation factor allowed for this machine type]. During this looping process, we keep track of the number of pseudo-orders that come out very close to our real reference orders for each value of the "test full scale bin number". As one might surmise, "very close" indicates the existence of another adjustable parameter. If the difference between a calculated pseudo-order and any one of the reference orders is small enough we call it a "hit", and record the actual deviation. We keep running totals of these hits, and totals of both relative (sign-sensitive) and absolute (sign-insensitive) deviations for each trial.

d. Assessment of trials and decision for each single spectrum.

The trial process usually results in a small group of "finalists"--those test runs with the greatest number of hits. The final RPM determination is then accomplished by identifying the trial with the smallest total absolute deviations. The final full scale bin number (a real number which we call the "fractional full scale bin number", or FFSB) is calculated by adjusting the test full scale bin number from the winning trial by a factor proportional to the total relative deviations. We call this a "virtual bin" due to its likelihood of falling between two integer bin numbers.

The machine speed is then simply that frequency represented in our original fixed frequency spectrum by the virtual bin

$$VIRTBIN = (1/N)*FFSB \qquad\qquad (2)$$

where N is our desired full scale order number.

If we have been successful in recording a minimum number of "hits", a normal run of the normalizing program will, at this point, synthesize a 500-line normalized spectrum from bins 1 through FFSB of the original fixed frequency spectrum. This process, which will be discussed later in more detail, essentially involves the mapping of 500 "virtual bins" over the top of our chosen portion of the original fixed frequency spectrum.

e. Review of results after first pass on whole machine.

When the normalizing program has finished attempting to normalize all of the spectra from a single machine, it commences a review and evaluation process. Some spectra may not have been normalized at all; others may be declared to be incorrect on the basis of the standard deviation of the RPM calculations. The program creates a list of these spectra and the machine speed to which they should be normalized.

f. "Auto-correction" of selected spectra, if required.

If the current machine has any listed spectra requiring correction, that list is sent directly to the spectral synthesis part of the program for the creation of new 500 line normalized spectra. This function, which we have called "forced" re-normalizing due to the overruling of the RPM determination part of the program, is also available as a separate menu option allowing the user to make corrections via keyboard entries.

SYNTHESIS OF NORMALIZED SPECTRA

The actual synthesis of 500-line normalized spectra from the designated portion of the fixed frequency spectra is accomplished by one of two methods, depending upon whether we are expanding or contracting the spectrum. We use the term "contracting" for those cases where the input spectrum has more bins than the output spectrum, the preferred situation. In the inverse case, that of "expansion", we create a spectrum with more bins than we start with, giving the appearance of added resolution.

The methods used were chosen from several options explored and tested by DLI; although among the least complex, they were found to be the most "empirically effective". The accuracy of the methods may be open to some debate. DLI has found them to be effective within the anticipated range of error of the initial measurements (+/- approximately 2 VdB). This evaluation is based on comparisons of results with the results of hardware normalizing of the same tape-recorded analog vibration data from a small but varied sample of machinery. At the time of the writing of this paper, DLI is initiating some work to refine this portion of the normalizing software.

The general approach for both methods can be understood by visualizing the desired output spectrum as a series of adjacent bands, not spectral lines, laid like a template over the chosen portion of the input spectrum. We are interested in the contents of each of these bands or "virtual bins", which in all normal cases will be either 0, 1, or 2 of the spectral lines from the input spectrum. Except when the desired output spectrum calls for frequencies higher than the range of the input spectrum (which occasionally happens), the zero condition will only be found in cases where we are expanding the spectrum-- synthesizing more bins that we have in our input spectral segment.

To explain the method used to contract a spectrum, let's take for our example the first 650 lines or bins of a fixed frequency 800-line spectrum. Now, measuring from the two end points of the horizontal (frequency) axis, we re divide the space into 500 equal-sized virtual bands; this could be visualized as drawing 499 vertical dotted lines to separate the bands. All those virtual bands containing only one input bin result in a corresponding output bin equal in amplitude to the input bin. For the rest, which contain two or more input bins, the value of the output bin is calculated as the root mean square (via linear velocity units) of all fixed frequency peaks found within the virtual band.

The only additional adjustment we have made to date is to define a window with rather steep "skirts" for each of these virtual bins, designed to attenuate slightly any fixed frequency spectral lines lying very close to the edge of a virtual band. The use of windowing is to be explored further in the refinement work currently underway.

In expanding a spectrum, we are faced with two types of virtual bands: those containing one bin from the input spectrum and those containing none. As in the case of contraction, those containing one input bin result in a direct porting of the input bin amplitude to the corresponding output bin. The "empty" virtual bands are given values determined by a simple interpolation process using the nearest neighboring input bins on either side.

SUMMARY AND CONCLUSION

In the analysis of machinery vibration spectra for fault diagnosis, precise identification of spectral peaks as a function of rotational rate is essential. As long as machine speed can vary even slightly from one measurement to the next, the exact location in a fixed frequency spectrum of a peak associated with a particular machine component cannot be predicted in advance. The purpose of using order normalized spectra is to ensure that each spectral peak with a fixed relationship to the machine speed will be found in one well defined location on any plot of the same scale. One of the greatest benefits of the technique is the ability to average like spectra from healthy machines of a given type for use as a baseline in vibration diagnostics.

The success of spectral averaging and direct peak-to-peak comparison of normalized spectra (both with one another and with their averaged counterparts) is completely dependent upon the accuracy of the chosen normalizing process. The only techniques that can virtually guarantee accurate normalizing are those which use a tachometer signal; the classic example works in the time domain, using the tach signal to drive the sampling rate of the A/D converter at the time of data acquistion. Because a tachometer signal is often impractical, methods of normalizing without it have received considerable attention.

The availability of highly portable real time analyzers and computers has encouraged the development of techniques for obtaining nearly immediate diagnostic results during vibration surveys of large numbers of machines. For this application, a software technique has been developed for normalizing fixed frequency spectra. Although the success rate of the software is continually being improved, its effectiveness depends upon the inclusion of methods for verifying the accuracy of the normalizing process and correcting the results when needed. This effort to produce normalized spectra in the field appears to be opening a gate to successful onboard automated diagnostics in at least one major Navy machinery vibration program.

KINEMATICS OF A FLEXIBLE LENGTH
REDUNDANT ROBOTIC ARM

Alamgir Choudhury, Graduate Student

Joseph Genin, Professor

Department of Mechanical Engineering
New Mexico State University
Las Cruces, NM 88003

ABSTRACT

A kinematical model is presented for n degree of freedom manipulator systems with link lengths that vary with the translation of the link joints. A critical step in the development is the formulation of *modified Eulerian angles,* allowing finite rotations to be treated vectorially. Also using the modified Eulerian angle method the kinematics of a system can be solved by multiplying fewer transformation matrices than is required by existing methods, thus reducing the computation time in controlling the motion of a robotic system. The inverse kinematics problem is solved by minimizing an objective function that quantifies the joint displacements. A 12 degree of freedom redundant system is presented as an illustrative problem.

INTRODUCTION

Many robotic systems have arms that are free to translation as the link joints are displaced (see Figure 1). In this paper we present an approach in the kinematical modeling of such robotic systems and the solution to the inverse kinematic problem. In doing so we address the problem of how to provide more than one rotational degree of freedom to an arm while maintaining the mathematical property of the the commutativity of finite rotational motions.

A method developed by Denavit and Hartenberg [1] is most widely used in the kinematical modeling of robotic systems. Similar methods were developed by Whitney and Lozinski [2] and Stone [3]. In each of the models [1-3] the author prescribes one degree of freedom to each kinematic link, either rotary or translatory. As a consequence, in subsequent computations, it is required that one multiply n transformation matrices to solve the kinematics of an n degree of freedom system.

Without loss of generality, we orient each set of moving coordinates such that one axis is aligned along successive link joins (see Figure 2). Hence, each kinematical link may be described by four independent parameters. Each parameter represents a degree of freedom when it is a variable. Thus each link may have a maximum of four degrees of freedom, three rotational and one translational. If a parameter defining such a motion

is a constant, then the associated degree of freedom is constrained. Thus, an n degree of freedom system can be defined by a maximum of $4n$ and minimum of n parameters. Since each kinematical link is described by four parameters, it follows that for every four parameters we need one transformation matrix. Therefore, for an n degree of freedom system we may need as few as $n/4$ transformation matrices. This compares quite well to the n matrices required using existing methods. It follows that the foregoing will result in a significant reduction in computation time.

KINEMATIC MODEL

The procedure presented here is valid for both nonredundant and redundant n degree of freedom manipulator systems. Modified precession, nutation and spin angles of each link are used as independent joint angles. A position vector relative to a fixed inertial frame, locates the position of the system's end-effector. This position vector, along with the *Modified Eulerian angles* of the final link with respect to the inertial reference frame, are the only geometric constraints required to fully determine the orientation and dynamic path of each point in the system. Intermediate geometric constraints can also be accounted for in the inverse kinematic problem by defining the upper and lower bounds of the variables.

Each link is defined by four independent parameters, the link length L_i and the modified Eulerian angles θ_i, ϕ_i, and ψ_i. The link length L_i is measured from ith joint to $(i+1)$th joint relative to the ith reference frame fixed with the ith link. The other three independent parameters are θ_i, ϕ_i and ψ_i (nutation, precession and spin angles) of the ith reference frame with respect to the $(i-1)$th reference frame, each of which are fixed to the respective links. At $\theta_i = \phi_i = \psi_i = 0$ the ith reference frame coincides with the $(i-1)$th reference frame. The axis z_i is always along the vector L_i.

Mathematically, the unit vector $\bar{e}_i$ corresponding to the ith reference frame may be related to that of the $(i-1)$th reference frame by

$$\bar{e}_i = \mathbf{T}_i \bar{e}_{i-1} \tag{1}$$

where the elements of the transformation matrix $\mathbf{T}_i$ are found to be

$$T_i(1,1) = Cos\,\theta_i\,Cos\,\phi_i\,Cos\,(\phi_i - \psi_i) + Sin\,\phi_i\,Sin\,(\phi_i - \psi_i)$$

$$T_i(1,2) = Cos\,\theta_i\,Sin\,\phi_i\,Cos\,(\phi_i - \psi_i) - Cos\,\phi_i\,Sin\,(\phi_i - \psi_i)$$

$$T_i(1,3) = -\,Sin\,\theta_i\,Cos\,(\phi_i - \psi_i)$$

$$T_i(2,1) = Cos\,\theta_i\,Cos\,\phi_i\,Sin\,(\phi_i - \psi_i) - Sin\,\phi_i\,Cos\,(\phi_i - \psi_i)$$

$$T_i(2,2) = Cos\,\theta_i\,Sin\,\phi_i\,Sin\,(\phi_i - \psi_i) + Cos\,\phi_i\,Cos\,(\phi_i - \psi_i)$$

$$T_i(2,3) = -\,Sin\,\theta_i\,Sin\,(\phi_i - \psi_i)$$

$$T_i(3,1) = Sin\,\theta_i\,Cos\,\phi_i$$

$$T_i(3,2) = Sin\,\theta_i\,Sin\,\phi_i$$

$$T_i(3,3) = Cos\,\theta_i$$
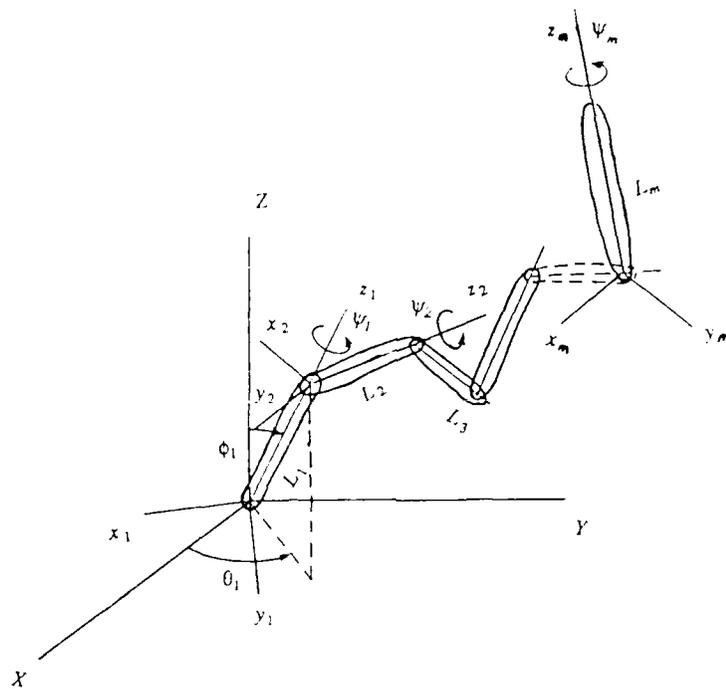
Figure 1. n Bar Linkage System
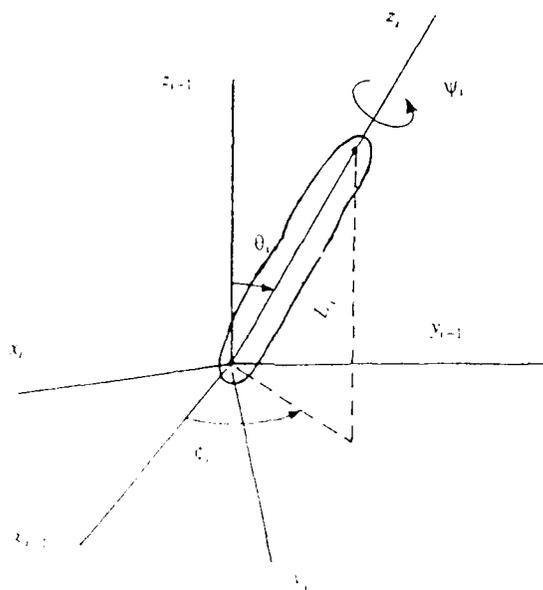
Figure 2. The Reference frames

Incorporating the chain rule one may express the vector $\bar{e}_i$ in terms of the vector $\bar{e}_0$ with respect to the *fixed inertial reference frame XYZ* shown in Figure 1.a, as follows

$$\bar{e}_i = \prod_{j=i,1} T_j \bar{e}_0$$

Using the orthogonality of the transformation matrices T_j, we have

$$\bar{e}_0 = \prod_{j=1,i} T_j^T \bar{e}_i \tag{2}$$

Defining the matrix

$$A_i = \prod_{j=1,i} T_j^T = T_1^T T_2^T \cdots T_{i-1}^T T_i^T \tag{3}$$

the position of the ith joint with respect to the fixed inertial frame XYZ may now be written as

$$[X_i \ Y_i \ Z_i]^T = \sum_{j=1}^{i} A_j [0 \ 0 \ L_j]^T$$

Therefore, we may write

$$X_i - \sum_{j=1}^{i} L_j A_j (1,3) \tag{4}$$

$$Y_i - \sum_{j=1}^{i} L_j A_j (2,3) \tag{5}$$

$$Z_i - \sum_{j=1}^{i} L_j A_j (3,3) \tag{6}$$

Now the orientation of the ith link can be defined by the nutation θ_i, precession ϕ_i and spin ψ_i angles of the ith reference frame with respect to the fixed inertial reference frame XYZ. Doing this we obtain

$$\theta_i = Arctan \left[(A_i(1,3)^2 + A_i(2,3)^2)^{1/2} / A_i(3,3) \right] \tag{7}$$

$$\psi_i = Arctan \left[A_i(3,2)/A_i(3,1) \right] - Arctan \left[A_i(2,3)/A_i(1,3) \right] \tag{8}$$

$$\phi_i = Arctan \left[A_i(3,2)/A_i(3,1) \right] \tag{9}$$

If $\theta_i = 0$ or π, then equation (9) degenerates and the foregoing reduces to

$$\theta_i = 0,\pi \tag{7.a}$$

$$\psi_i = Arctan \left[A_i(1,2)/A_i(1,1) \right] \tag{8.a}$$

Equations (7, 8, 9) are what we term the *modified Eulerian angles*.

Using subscripts 1 and 2 for the initial and final positions and orientation of the end-effector, we relate the motion of the ith link from its starting position to a desired location by noting the required changes q_i in its independent parameters. They are given by,

$$\theta_{i2} = \theta_{i1} + q_{4(i-1)+1} \ , \ \phi_{i2} = \phi_{i1} + q_{4(i-1)+2} \ , \ \psi_{i2} = \psi_{i1} + q_{4(i-1)+3} \ , \ L_{i2} = L_{i1} + q_{4(i-1)+4} \tag{10}$$

For a system with n degrees of freedom the inverse kinematics problem now reduces to finding the q_i ($i = 1,2,...,n$), subject to the constraints imposed on the system. Typically the constraints involve the position and orientation of the system's end-effector (*goal*

state). They are

$$X_{m2} - \sum_{j=1}^{m} L_{j2} A_{j2}(1,3) = H_1(q_1,q_2,...,q_n) = 0 \tag{11}$$

$$Y_{m2} - \sum_{j=1}^{n} L_{j2} A_{j2}(2,3) = H_2(q_1,q_2,...,q_n) = 0 \tag{12}$$

$$Z_{m2} - \sum_{j=1}^{m} L_{j2} A_{j2}(3,3) = H_3(q_1,q_2,...,q_n) = 0 \tag{13}$$

$$\theta_{m2} - Arctan\left[(A_{m2}(1,3)^2 + A_{m2}(2,3)^2)^{1/2}/A_{m2}(3,3)\right] = H_4(q_1,q_2,...,q_n) = 0 \tag{14}$$

$$\phi_{m2} - Arctan\left[A_{m2}(3,2)/A_{m2}(3,1)\right] + Arctan\left[A_{m2}(2,3)/A_{m2}(1,3)\right] = H_5(q_1,q_2,...,q_n) = 0 \tag{15}$$

$$\psi_{m2} - Arctan\left[A_{m2}(3,2)/A_{m2}(3,1)\right] = H_6(q_1,q_2,...,q_n) = 0 \tag{16}$$

where m is the number of links present in the system. Also setting the upper and lower bounds for the link lengths L_i's, we establish the intermediate constraints as

$$L_{imin} < L_i < L_{imax}, \quad i=1,2,....,m$$

For *nonredundant* systems, the six nonlinear algebraic equations (11) through (16) can be solved for the six unknown parameters.

For *redundant* systems the number of degrees of freedom n is greater than the number of constraints to be maintained and the uniqueness of solution becomes a problem. We address this problem by optimizing a known objective function $g(q_1,q_2,\cdots,q_n)$ subject to the constraints (11) through (16). In what follows, as an objective function we chose the weighted sum of all the joint displacements and the change in the joint variables. That is,

$$f(q_1,q_2,\cdots,q_n) = \sum_{i=1}^{n} w_i \Delta S_i + \sum_{i=1}^{n} v_i q_i \tag{17}$$

where

   w_i = weighting factor for the ith joint displacement ΔS_i with respect to the fixed inertial frame,

and

   v_i = weighting factor for the change in the ith joint variables.

The joint displacements ΔS_i are obtained from the kinematics of each manipulator link as a function of the q_i's. Using subscripts 1 and 2 for the initial and goal states respectively, in equations (4) through (6), we may write

$$\Delta S_i = \Delta X_i + \Delta Y_i + \Delta Z_i = (X_{i2} - X_{i1}) + (Y_{i2} - Y_{i1}) + (Z_{i2} - Z_{i1})$$

Therefore,

$$\Delta S_i = \left[(X_{i2} - X_{i1})^2 + (Y_{i2} - Y_{i1})^2 + (Z_{i2} - Z_{i1})^2\right]^{1/2} \tag{18}$$

$$= \sum_{j=1}^{m}\left\{\left[L_{j2}A_{j2}(1,3) - L_{j1}A_{j1}(1,3)\right]^2 + \left[L_{j2}A_{j2}(2,3) - L_{j1}A_{j1}(2,3)\right]^2\right.$$

$$\left. + \left[L_{j2}A_{j2}(3,3) - L_{j1}A_{j1}(3,3)\right]^2\right\}^{1/2}$$

$$= \Delta S_i(q_1,q_2,\cdots,q_n)$$

The weighting factors w_i and v_i are furnished as necessary. Therefore, for a redundant system the inverse kinematics problem reduces to the minimization of equation (17) subject to the constraint conditions (11) through (16).

NUMERICAL TECHNIQUE

In general, to obtain a unique solution for a redundant system one must use an optimization technique. In this paper, as an optimization procedure we chose to *minimize the weighted sum of the joint displacements and absolute changes in joint variables* between the state at $t=t_1$ and $t=t_2$. To accomplish this we modified a nonlinear programming algorithm by LaFrance, et al [4]. LaFrance's algorithm utilizes a generalized reduced gradient concept (Abadie and Carpenter [5]) to handle constraints. It also incorporates the unconstrained optimization method of Davidon, et al (presented in [6]). Our new algorithm can handle constraints in both equality and inequality forms. We have also set upper and lower bounds on some of the variables, *thus accounting for intermediate geometric constraints,*

In using the algorithm the general strategy is to divide the variables into independent and dependent sets. The unconstrained optimization method is applied to the independent variable set and the dependent variable set is adjusted in order to maintain feasibility of the constraints. The starting point for the computations is simply

$$q_i = 0 \quad i=1,2,....,n \tag{19}$$

In general, this violates the constraint conditions, rendering the starting point infeasible. To remedy this, we require that additional slack variables q_{n+j}, $j=1,2,....,6$ be subtracted from the equality constraints to reduce them to zero. That is, equations (11) through (16) reduce to

$$H_1(q_1,q_2,....,q_n) - q_{n+1} = 0 \tag{20}$$

$$H_2(q_1,q_2,....,q_n) - q_{n+2} = 0 \tag{21}$$

$$H_3(q_1,q_2,....,q_n) - q_{n+3} = 0 \tag{22}$$

$$H_4(q_1,q_2,....,q_n) - q_{n+4} = 0 \tag{23}$$

$$H_5(q_1,q_2,....,q_n) - q_{n+5} = 0 \tag{24}$$

$$H_6(q_1,q_2,....,q_n) - q_{n+6} = 0 \tag{25}$$

The objective function $f(q)$ can now be changed by adding a penalty function to it. This gives

$$F(q_1,q_2,....,q_n) = f(q_1,q_2,....,q_n) + 10^5 [\sum_{j=1}^{6} q_{n+j}^2]^{1/2} \tag{26}$$

The starting point for computations now becomes

$$q_i = 0, \quad i=1,2,....,n \tag{27}$$

$$q_{n+i} = H_i(q_1,q_2,....,q_n) , i=1,2,....,n$$

Computationally, the algorithm searches for the zero of the objective function with respect to the independent variables. The search direction is found by using the downhill criterion found in [6]. Then a line search is performed in the downhill

direction to find the absolute minimum of the objective function. Finally the additional slack variables reduce to zero, thus providing the minimization of the original objective function $f(q)$ in equation (17) and satisfying the constraint conditions (11) through (16).

The algorithm was used to solve a variety of problems with a focus directed toward the accuracy of the solution when considering motions that swept through all the octants of three dimensional space. In particular we used the algorithm to solve the kinematics of the following systems.

(a) A two link, 5 degree of freedom system with the three constraint conditions (11), (12) and (13). Here the parameters θ_1, ϕ_1, ψ_1, θ_2 and ϕ_2 are variables and the parameters ψ_2, L_1 and L_2 are constants.

(b) A three link, 9 degree of freedom system with the six constraint conditions (11) through (16). Here the parameters θ_1, ϕ_1, ψ_1, θ_2, ϕ_2, ψ_2, θ_3, ϕ_3 and ψ_3 are variables and the parameters L_1, L_2 and L_3 are constants.

(c) A three link 12 degree of freedom system with the six constraint conditions (11) through (16). Here all the parameters θ_1, ϕ_1, ψ_1, θ_2, ϕ_2, ψ_2, θ_3, ϕ_3, ψ_3, L_1, L_2 and L_3 are variables. The motions are due to translation as well as rotation of the joints.

We experimented with several objective functions by changing the weighting factors w_i and v_i. Given an initial state, solutions were obtained to achieve a prescribed final position and orientation of the end-effector. In all cases the closure error was less than 0.001%.

For brevity, in this paper we shall present the results obtained when studying the system consisting of 3 links and 12 degrees of freedom. The initial configuration we considered was given by $\theta_1=\pi/3$., $\phi_1=\pi/4$., $\psi_1=-\pi/3$., $\theta_2=-\pi/6$., $\phi_2=-\pi/7$., $\psi_2=\pi/4$., $\theta_3=\pi/9$., $\phi_3=\pi/8$., $\psi_3=-\pi/4$., $L_1=1.5$, $L_2=2.4$ and $L_3=1.0$. The variable bounds were $1.0 < L_1 < 2.0$, $2.0 < L_2 < 3.0$ and $0.8 < L_3 < 1.2$. The position and orientation of the system's end-effector at several goal states is tabulated in Table I. In all, ten positions along its trajectory are presented. Computationally, the algorithm proceeds stepwise, computing the necessary changes in the joint angles to achieve each succeeding goal state. The goal states for the end-effector of the twelve degrees of freedom system are shown in Table I. In Table II we show the associated joint variables at each of the goal states. Figure 3 is a visual representation of the trajectory of the system.

Current state of the end-effector at the start

Instant	X	Y	Z	Nutation	Precession	Spin	% Error
	2.4179	3.9106	1.0145	-84.4422	-67.7061	-121.1397	

Subsequent goal state of the end-effector

Instant	X	Y	Z	Nutation	Precession	Spin	% Error
1	2.1058	3.4052	0.7581	-77.1758	-60.7052	-114.4044	0.0002
2	1.7201	2.7649	0.4779	-71.1073	-55.1424	-109.3460	0.0000
3	1.3114	2.0847	0.2083	-65.9895	-50.7198	-105.6188	0.0000
4	0.9243	1.4476	-0.0274	-61.4820	-47.0296	-102.7460	0.0000
5	0.5857	0.9015	-0.2224	-57.1848	-43.5919	-100.1677	0.0000
6	0.3021	0.4558	-0.3844	-52.6773	-39.9018	-97.2949	0.0003
7	0.0655	0.0931	-0.5284	-47.5591	-35.4794	-93.5674	0.0000
8	-0.1403	-0.2162	-0.6725	-41.4905	-29.9160	-88.5092	0.0000
9	-0.3338	-0.5048	-0.8351	-34.2240	-22.9151	-81.7739	0.0000
10	-0.5338	-0.8048	-1.0351	-25.6296	-14.3208	-73.1796	0.0001

Table I

Joint variables at the start

θ_1	ϕ_1	ψ_1	θ_2	ϕ_2	ψ_2	θ_3	ϕ_3	ψ_3	L_1	L_2	L_3
60.00	45.00	-60.00	-30.00	25.71	45.00	20.00	22.50	-45.00	1.50	2.40	1.00

Required joint variable to achieve the subsequent goal states

θ_1	ϕ_1	ψ_1	θ_2	ϕ_2	ψ_2	θ_3	ϕ_3	ψ_3	L_1	L_2	L_3
54.68	39.91	-63.88	-39.65	-28.03	46.24	23.56	29.65	-50.28	1.27	2.23	0.86
42.82	22.43	-68.58	-63.23	-31.79	43.80	9	29.43	-52.48	1.00	2.00	0.80
28.51	-46.98	-75.15	-115.99	-39.76	-	1.44	18.29	-48.64	1.17	2.00	0.80
48.74	-74.49	-75.43	-149.15	-44.17	33.70	27.67	7.54	-53.83	1.44	2.00	0.82
58.70	-85.11	-72.43	-167.82	-45.73	34.29	31.56	7.09	-52.87	1.82	2.00	0.82
128.59	-100.41	-40.87	-176.13	-48.63	68.20	82.46	56.33	-66.71	2.00	2.00	0.80
149.24	-102.80	-35.06	-157.96	-49.76	75.71	124.89	58.85	-74.12	2.00	2.00	1.14
150.81	-103.51	-33.69	-148.77	-51.25	77.59	141.26	60.25	-75.66	2.00	2.00	1.20
152.94	-104.84	-32.98	-142.39	-53.59	80.99	156.28	62.69	-74.12	2.00	2.00	1.20
56.09	-113.75	-57.85	-136.41	-66.25	87.21	172.95	62.57	-66.90	2.00	2.00	1.20

Table II

82
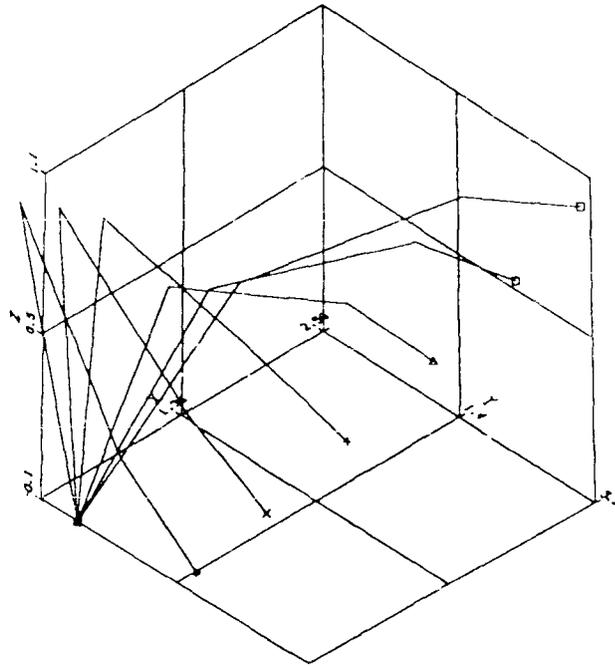
Figure 3. Six Positions of a Three Bar Linkage System.

CONCLUDING REMARK

In this paper we have developed a general formulation for the kinematics of an n degree of freedom flexible length redundant robotic arm system. By proper identification of the system parameters one can reduce the complexity of both the forward and inverse kinematical problem significantly. It is computationally faster than existing algorithms, and possibly more accurate. Our algorithm should also prove effective in designing systems that require optimization of given kinematical goals.

References

1. Denavit, J. and Hartenberg, R. S., *A Kinematic Notation for Lower-Pair Mechanisms Based on Matrices.* **Journal of Applied Mechanics.** 77(2):215-221, June, 1955.

2. Whitney, D. E. and Lozinski, C. A., *Industrial Robot Calibration Methods and Results,* **Proceedings of the International Computers in Engineering Conference,** Page 92-100. ASME, New York, August, 1984.

3. Stone, Henry W., **Kinematic modeling identification, and control of robotic manipulators.** Kluwer Academic Publishers, Norwell, MA, 1987.

4. LaFrance, L., Hamilton, J., and Ragsdell, K., *On the Performance of Combined Generalized Reduced Gradient and Davidon-Fletcher-Powell Algorithm: GRGDFF,* **Eng. Optimization,** vol. 2, 1977.

5. Abadie, J., and Carpentier, J., *Generalized Reduced Gradient Method to the Case of Nonlinear Constraints,* **Optimization,** edited by Fletcher, R., Academic Press Inc., London, 1969.

6. Fletcher, R., and Powell, M., *A Rapidly Convergent Descent Method for Minimization,* **Comp. Journal,** vol. 6, no. 2, 1963.

VIBRATION CONTROL

OPTIMIZATION OF A FIVE-PARAMETER NONLINEAR SHOCK MOUNT

Nicolas A. Roy and Vernon H. Neubert
The Pennsylvania State University
Department of Engineering Science and Mechanics
227 Hammond Building
University Park, PA 16802

The design parameters of a nonlinear mechanical shock absorber or shock mount are optimized to minimize the peak absolute transmitted acceleration, while keeping the relative displacement within set bounds, during a prescribed transient base shock. The shock absorber is located between a rigid mass and a moving support. The mass simulates equipment which is to be protected from severe accelerations of the support. The absorber consists of a linear spring and dashpot, along with two plastically deforming snubbers which prevent large relative displacements between the mass and the support. The snubber design parameters consist of an elastic stiffness, yield force, and plastic stiffness in addition to an unloading stiffness which is not necessarily equal to the elastic stiffness.

After a preliminary examination of a simple linear shock absorber without snubbers, two analyses are performed using the nonlinear absorber. First the base shock is applied directly to the support of the absorber; second, the absorber is placed on an intervening elastic structure, represented by a spring-mass system, and the shock is applied to the base of the structure. In order to perform the numerical optimization, a modification of Rosen's Projected Gradient Method is implemented. The efficiency of the algorithm is demonstrated by a direct comparison with other methods.

List of Symbols

a = initial gap between snubber and mass
$f(\underline{b})$ = a_{max} = cost function = maximum absolute acceleration of mass
$\underline{b}$ = vector of design parameters
c = viscous damping constant of dashpot
d = constraint = $(x_r)_{max}$
$f_n = \sqrt{(k/m)}/2\pi$ = undamped frequency of mass on sound mount
g = acceleration due to gravity
k = stiffness of spring for sound mount
k_e = initial elastic stiffness of snubber
k_p = plastic stiffness of snubber
k_u = unloading stiffness of snubber
m = mass of rigid body

Background

Shock absorbers are used to protect equipment from severe dynamic loads. A shock absorber may be located on the bumper of a car, to reduce the acceleration levels of the car during a front-end crash. In a shock problem where the excitation is a severe motion of the base which supports some sensitive equipment or personnel to be protected, then the shock absorber is placed between the base and the sensitive equipment and the shock absorber then is usually called a shock mount. Thus a shock mount is a particular form of shock absorber, and both terms are used herein. Often, the design of a particular absorber is attained by achieving a desired performance goal, which may be to minimize the maximum transmitted force or acceleration. In many circumstances, certain constraints might be imposed, such as weight or displacement constraints. In the present problem, the transmitted acceleration decreases as the relative displacement increases. Since it is desirable to keep both small, a trade-off is usually required between maximum relative displacement and maximum transmitted acceleration.

One of the earliest analyses involving the design optimization of a simple shock absorber was by Schmit and Fox [1] in 1964. They examined the response of linear mass-spring-dashpot oscillator subjected to a base acceleration in the form of a rectangular shock pulse. If the mass is designated by m, the problem is to determine the spring stiffness k and the dashpot damping value c such that optimal performance is achieved. Two optimization programs were considered. The first was to minimize the peak absolute acceleration of the mass with a constraint that the relative displacement between the mass and support does not achieve a certain specified value or "rattle space". The second is to minimize the relative displacement with a constraint that the maximum acceleration of the mass is not to exceed a known "fragility level".

By dividing the equation of motion by m, the value of the mass, the system is completely defined once values for k/m, c/m and the input base shock are known. Since the applied base acceleration is of a simple form, the equation of motion can be solved analytically, and most of the numerical analysis pertains to the optimization process. Schmit and Fox used a steepest descent-alternate step method. The direction of steepest descent is simply the opposite of the gradient of the objective function which is to be minimized. This vector is computed numerically by a first order finite difference representation. The alternate step is by a first order finite difference representation. The alternate step is taken when a move in the direction of steepest descent violates the constraint, the alternate step being taken in a direction tanget to the surface defined by the objective function in hopes of reaching an unconstrained point.

Bryson and Denham [2] developed a steepest-ascent numerical procedure for optimal programs with terminal constraints. A program consisting of a nonlinear objective function and a set of nonlinear equality constraints is considered initially, where the variables are divided among state variables and control variables. A vector of algebraic, or state, equations relate the state and control variables. By taking first order perturbations of both the state and control variables and solving a set of linear equations for adjoint variables (Lagrange multipliers), a direction of steepest ascent in the control space can be determined. Next they consider a program where the state and control variables are related by a set of differential rather than algebraic equations. The objective function along with the equality constraint functions are now functions of the terminal point. The adjoint variables are obtained by integrating a set of differential equations with boundary conditions given at the terminus. As the gradient approaches zero, the optimal solution is obtained. An advantage of this procedure is that the

gradients can be expressed analytically by a set of equations involving the adjoint variables. Thus the only approximation to the gradient is from the manner in which these equations are solved numerically. Examples are presented for minimum time-to-climb and maximum altitude paths for a supersonic interceptor and maximum-range paths for an orbital glider.

Sevin and Pilkey [3] described both an Indirect Method of Synthesis and a Direct Method. The direct method is basically the conventional approach of defining an explicitly objective function (perhaps peak acceleration) along with constraints, shock input, and initial design vector. A numerical algorithm is then implemented to proceed step-by-step toward the optimal solution, which works fairly well for systems with few degrees of freedom. The Indirect Method consists of two separate phases: Time Optimal Synthesis and System Identification. For a shock isolator consisting of a given number of degrees of freedom, the Time Optimal Synthesis is concerned only with determining the optimal forces acting on each mass. These force-time histories are obtained by breaking up the optimization problem into a set of n time intervals. Once the optimal isolator forces are calculated, the System Identification phase is used to come up with values for the springs and dashpots which will produce forces similar to the optimal ones, using a least-square algorithm. The Indirect Synthesis approach has the advantage that the system dynamics need be solved only once. Also, nonlinearity of the objective and constraint functions poses no problem since a "time grid" is placed over the system, thus converting it to a linear program. One concern is that time discretization of a large system with many constraints may yield a program which, although linear, is difficult to solve.

Karnopp and Trikha [4] consider shock isolation of a single mass from a rigid base given an initial velocity, which is equivalent to an acceleration impulse. They consider first an objective function which combines both peak transmitted force and the maximum relative displacement between the mass and base, with a weighting function in front of the displacement term. The resulting optimal time histories for the transmitted force and relative displacement are shown to be not unique. A disadvantage of the formulation is that the objective function is concerned only with the peak value occurring occurring during the transients, which typically occur early in the transient, and thus leave a large part of the time history undetermined. In order to incorporate a requirement that the motion die down quickly, the objective function is reformulated such that the peak terms are replaced by terms representing the area under the square of the force and displacement curves. For this specific quadratic form the resulting optimal feedback force can be determined exactly by use of a passive linear spring and dashpot.

Bartel and Krauter [5] considered a design problem of a shock absorber system which is to minimize the transmitted force resulting from the impact of a mass sliding into a linear spring and dashpot affixed to a second mass, which is grounded to a wall by second linear spring. This model is to represent a low speed collision between a fixed and moving automobile. Relative displacement constraints are imposed on both springs. A constrained steepest descent approach with state equations is used to obtain the optimal design variables.

An optimal shock absorber design in terms of the number of design elements is examined by Wilmert and Fox [6]. They analyze isolation of a mass in a single direction from a shock pulse of finite duration, with the goal minimizing the peak acceleration of the mass while satisfying a relative displacement criterion. Adding an additional degree of freedom will always results in either no change, or an improvement in the optimal solution. Rather than solve the two-degree-of-freedom system, they used a simpler approximation approach which holds fixed the optimal peak acceleration of the one-degree-of-freedom system yet

incorporates quadratic terms describing the relative displacmeents of the two-degree-of-freedom system. Upon solving this "displacement violation function," one can obtain an estimate of the improvement or decrease in peak acceleration by the additional degree of freedom, and then converge on the exact improvement. If the improvement is desirable, then the process can be repeated starting from the optimal two-degree-of-freedom system.

A shock absorber design with nonlinear stiffness and damping is considered by Afimiwaᵢa and Mayne [7]. The usual goals are considered and then an additional constraint is applied limiting the rebound displacement magnitude to no greater than 25 percent of the peak displacement. To solve the first problem, an exterior penalty function method is implemented using Powell's conjugate direction method with a quadratic one-dimensional search technique. The second problem is solved using the Method of Feasible Directions. The authors also use the method of Sevin and Pilkey [3] and the optimal stiffness and damping values determined to approximate the ideal force history in a root-mean-square sense.

Hsiao, Haug, and Arora [8] develop and apply a state space method and reformulate the problem such that the max-value functions are replaced by equivalent integral constraints. With the program now in integral form, first order variations of the constraints can be readily performed with respect to the state and design variables. With the introduction of adjoint variables, the dependence of the state variables can be eliminated. The effectiveness is demonstrated by optimizing a simple shock absorber with nonlinear stiffness and damping values. A time-saving of a factor of 10 is achieved when the method is compared to the traditional nonlinear programming techniques which involve placing a time grid over the interval.

Kasraie and Neubert [9,10] used the method of [8] to determine the op mum design for a nonlinear shock mount. The system consists of a mass supported from a base with a linear spring and dashpot plus a nonlinear snubber. The snubber is allowed to deform plastically, thus requiring the addition of two design variables pertaining to its elastic and plastic stiffness. Results show that the method is more efficient than the Steepest-Descent Alternate Step Method of Schmit and Fox [1]. A disadvantage of converting the max-value functions to integral form is that an additional "dummy" design variable is introduced along with a second nonlinear constraint.

Modified Steepest Descent Optimization Algorithm

The optimization algorithm developed in the present study is a modified steepest descent algorithm modeled after Rosen's Gradient Projection Method discussed by Bazaraa [12]. The optimal solution is approached by moving along the direction of steepest descent when such a move does not violate any of the constraints. Otherwise, a new direction is calculated by projecting the negative of the gradient of the objective function onto a hyperplane defined by the gradients of the first order approximation, moves in this direction will not violate feasibility nor cause and increase in the objective function.

Since the algorithm is to be applied to a program which has a nonlinear constraint, modifications must be introduced, since moves along the nonlinear boundary will eventually leave the boundary be entering into the interior of the infeasible region. If a move is made into the infeasible region, then a correction step must be executed in order to return to the boundary.

Thus two modifications were made to Rosen's Method. The first involves searching along curved constraint boundaries rather than straight boundaries. The second concerns the sequence of steps used in a unidirectional search. These modifications are described in detail in Ref. [15] and summarized here.

The goal for the optimization problem is to determine values of the design variables such that the resulting peak acceleration is minimized in addition to satisfying a maximum relative displacement constraint. With d defined as the maximum allowable relative displacement, the mathematical statement of the optimization problem is:

$$\text{minimize } \max_t | \ddot{x}(\underline{b},t) |$$

such that:
$$\max_t | x_r(\underline{b},t) | < d \tag{1}$$

$$\underline{b} \geq 0$$

where: $\underline{b}$ = vector of design variables

If we now define the functions:

$$f(\underline{b}) = \max_t | \ddot{x}(b,t) | = a_{max} \tag{2}$$

$$g(\underline{b}) = \max \left(|x_r(\underline{b},t)| - d \right) \tag{3}$$

then the program of Equation (5) can be written in standard form as:

$$\min f(\underline{b})$$

such that
$$g(\underline{b}) \geq 0 \tag{4}$$

with
$$-\underline{b} \geq 0$$

The details of the solution to this problem are given in [15], but the overall steps to the solution are as follows:

1) Start with an initial design vector $\underline{b}$.
2) Compute a search direction, $\underline{s}$,

$$\text{where } \underline{s} = \begin{cases} -\nabla f, & \text{(for an interior point)} \\ -P \nabla f + (\lambda/2R)\nabla g & \text{(for a point on a constraint boundary)} \end{cases} \tag{5}$$

λ = step size
P = the projection matrix
R = the radius of curvature of g at $\underline{b}$

3) Perform a unidirectional search
$$\min f(\underline{b} + \lambda \underline{s})$$
λ^* = optimal solution
4) Update design vector
$$\underline{b} \leftarrow \underline{b} + \lambda^* \underline{s}$$
5) If $\underline{b}$ is infeasible, move in the direction $-\nabla g$ to the boundary of the feasible region.
6) If $\underline{b}$ is optimal, STOP. Otherwise go to step 2.

The two modifications are imbedded in this standard algorithm in step 3 where a unidirectional search is performed. First the step is described before addressing the modifications.

A unidirectional, univariate, or line search is an optimization program embedded in the main algorithm. Its purpose is to find a minimum value of the

91

objective function by starting from a given point and searching along a fixed direction. The quantity λ, which scales the magnitude of the search direction, is the only variable in the problem. The variable λ is optimal when $f(\underline{b}+\lambda\underline{s})$ is minimum for fixed values of $\underline{b}$ and $\underline{s}$.

There are two basic components of a unidirectional search: determining an interval of uncertainty, and searching within this interval for the optimal value of λ, with as few function calculations as possible. The search algorithm used in the present analysis is a Golden Section Search. It is simple to progr   nd very efficient. The first modification is to occasionally omit the Gol   Section Search after determining the uncertainty interval. If the present design ector is not yet close to the optimal solution, then there is no reason to "home in" on λ^* since the next iteration will promptly take us away from this point in the design space. Therefore, rather than computing λ^*, one can use λ_1 and save a lot of computation time. To determine what is "close" and what is not, is based on the number of accelerated steps required to initially determine the uncertainty interval. If the interval is located after only two steps, then this is considered close and the search is performed. If more than two steps are used, the search is omitted. Obviously, this decision is sensitive to the choice of initial step size. If the initial step size is too small, then t.   search will be performed unnecessarily too often. The idea is to choose the initial step size as large as possible without encountering numerical difficulties associated with taking large steps in the infeasible region.

The second modification made to the unidirectional search involves the case when the nonlinear constraint is active. Normally, a search would be along a direction tangent to the surfaces of the active constraints. However, for convex constraints (those whose boundaries bulge out from the feasible region), any step in this tangent direction will enter the feasible region. Thus a modification is made which makes an attempt to maintain closeness to the boundary while performing the unidirectional search. This is accomplished by performing a "curve" search rather than a line search. At the starting point on the boundary, a small step is made. If this step leaves the boundary, then a corresponding small correction step is made. With these two step izes, the curvature of the boundary at the starting point can be determined. The unidirectional search now proceeds as usual except that finding both the uncertainty interval and λ^* is done along a curve rather than a straight line. This does not guarantee staying on the boundary because the curvature could very well change. However, it has been found that, if there are no drastic changes in the curvature of the active constraint, using a curve search will always result in smaller corrective steps out of the infeasible region, if not eliminating them completely.

Introductory Example, Linear Shock Absorber without Snubbers

In the present study a special case was done initially for the system of Fig. 1 which has a linear spring and dashpot and no snubbers. The base motion input acceleration was taken as a box-car shaped pulse of very short duration, resulting in an initial relative velocity V with only the free vibration period considered. The equation of motion is, with $x(t)$ the absolute displacement and x_b the input base motion,

$$m\ddot{x} + c\dot{x} + k(x-x_b) = 0. \tag{6}$$

Letting the relative displacement $x_r = x-x_b$ and dividing by m, the equation is

$$\ddot{x}_r + (c/m)\dot{x}_r + k/m\, x_r = -\ddot{x}_b \tag{7}$$

Now if it is assumed that the period of excitation is over and the base acceleration $\ddot{x}_b = 0$, the equation of motion of free vibration is

$$\ddot{x}_r + (c/m)\,\dot{x}_r + k/m\,x_r = 0. \tag{8}$$

This simple equation is solved subject to the initial conditions

$$x_r(0) = 0 \text{ and } \dot{x}_r(0) = -V. \tag{9}$$

Further, define $\omega_n^2 = k/m$ and the damping ratio $\zeta = c/(2m\omega_n)$.
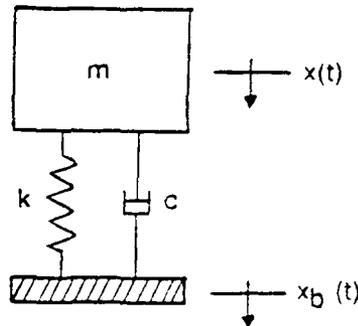
Figure 1 Linear Shock Absorber

The reason for presenting this simple case is to emphasize the fact that the damping may be helpful or detrimental with regard to its effect on the transmitted acceleration. In Figs. 2(a) and 2(b) curves are presented for $x_r\omega_n/V$ and $\ddot{x}_r/\omega_n V$ versus $\omega_n t$ for various ζ. Note that if $\ddot{x}_b = 0$ then the relative acceleration of the mass equals its absolute acceleration, that is $\ddot{x}_r = \ddot{x}$ when $\ddot{x}_b = 0$. The curves show that the character of the $\ddot{x}_r(t)$ curve changes as ζ increases, the peak value gradually shifting to earlier times, because the dashpot acts as a force transmitter as well as an energy dissipator.

For this simple example, the following summary statements are made:

1. $(x_r)_{max}$ decreases monotonically as ζ increases, given V and ω_n.

2. $(\ddot{x}_r)_{max}$ has a global minimum at $\zeta = 0.265$, given V and ω_n.

3. $(x_r)_{max}$ is proportional to V/ω_n, given ζ.

4. $(\ddot{x}_r)_{max}$ is proportional to $V\omega_n$, given ζ.

Specific Example of Optimization Process for Two Parameters

The system without the snubber involves only two parameters and the design space may be displayed graphically, so we return to that example. The design variables are k/m and c/m so the vector b is

$$\underline{b} = [k/m \; c/m]$$

With the values $V = 150$ in/sec and $d = 2.25$ inches, the initial guesses of the design variables are

$$c/m^{(0)} = 16.0 \text{ sec}^{-1} \qquad k/m^{(0)} = 6400.0 \text{ sec}^{-2}$$

93
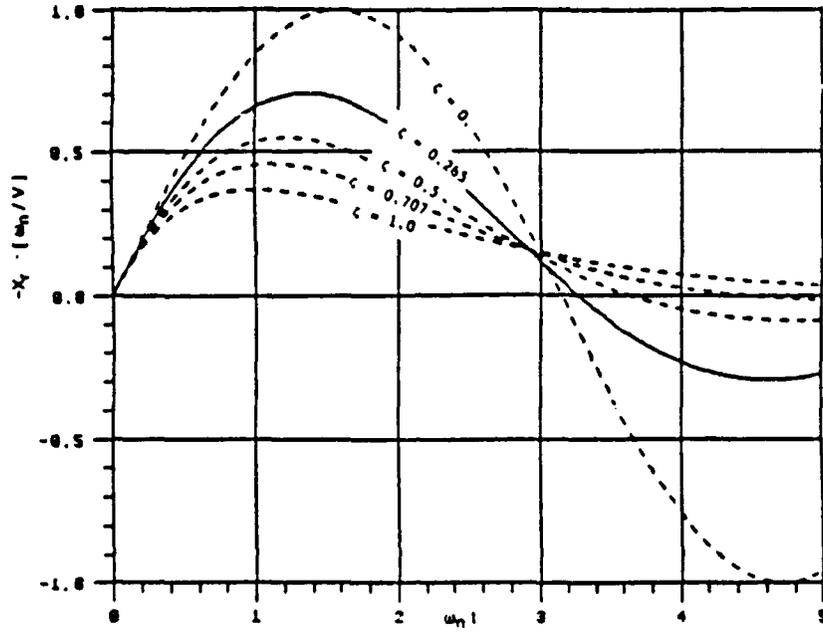
Figure 2(a) Displacement Response of Linear Shock
Absorber
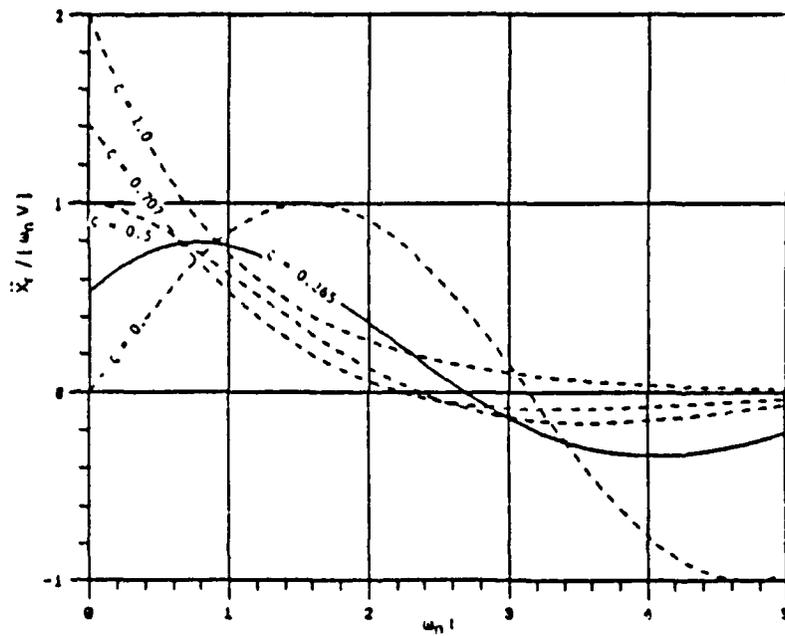
Figure 2(b) Acceleration Response of Linear Shock
Absorber

A plot of the path of optimization in the design space appear in Fig. 3. The dotted lines represent curves of constant f or peak acceleration divided by initial velocity. The solid curve represents the relative displacement constraint divided by V. The feasible region is the area above and to the right of the displacement constraint. The optimal solution can be immediately identified as the point of tangency between the smallest objective function contour and the feasible region, but the goal is to use the algorithm to find this point in a computer run.

From the initial guess, the algorithm first performs an unconstrained steepest descent search in the direction $-\Delta f(k/m^{(0)}, c/m^{(0)})$. For this particular unidirectional search, after finding the interval of uncertainty, the optimal step size, λ^* is set to λ_1. That is, no Golden section Search is performed because of being too far from the optimal solution. Note that the first line search is in a direction perpendicular to the acceleration contour, but the angle is distorted
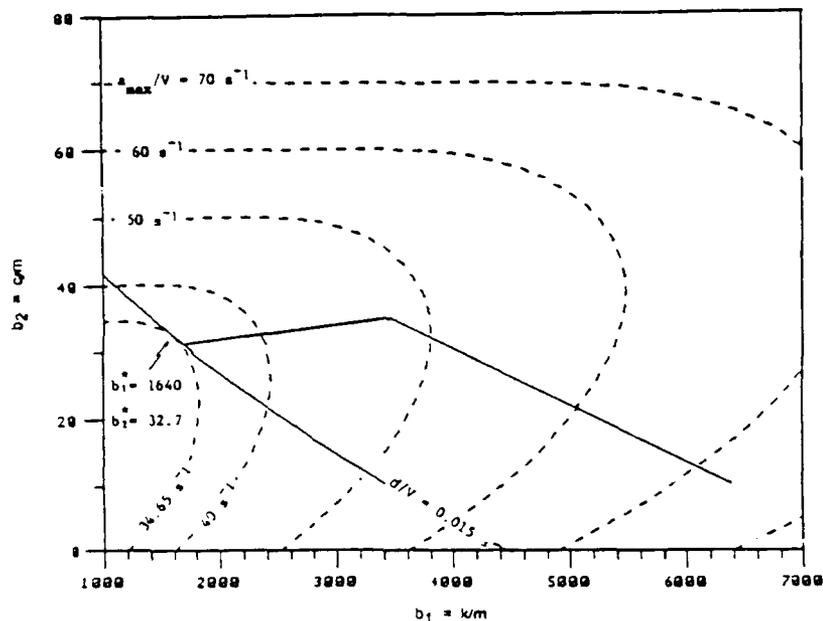
Figure 3 Optimization Path in $c/m - k/m$ Design Space

because of the graphical scales used. The first line search crosses a local minimum and the search direction is changed. As can be seen in the figure, the second line search reaches the boundary defined by the relative displacement constraint. Once on the boundary, a single search including the Golden Section Search is performed to converge to the optimal solution. Thus in only three uni-directional searches, the optimal solution is obtained with the optimal values being:

$$f(k/m^*, c/m^*) = 5200.0 \ in/sec^2$$

$$with \ k/m^* = 1640.0 \ sec^{-2}$$

$$c/m^* = 32.7 \ sec^{-1}$$

which correspond to:

$$\omega_n^* = 40.5 \text{ rad/sec and } \zeta^* = 0.404.$$

Because of its relatively simple form, the exact solution can be written in terms of V and d as:

$$f(\omega_n^*, \zeta^*) = 0.6005 \ V^2/d$$

where: $\omega_n^* = 0.6005 \ V/d$ and $\zeta^* = 0.4040$

which compare exactly with those obtained from the modified constrained steepest descent method.

This concludes the simple example, and the general problem of the absorber with snubbers will now be discussed.

General Shock Absorber System Description and Problem Approach

For the general situation with the nonlinear snubbers, two system were dealt with. The first is shown in Fig. 4(a), consisting of a single-degree-of-freedom with a mass m supported from a rigid base with the linear spring of stiffness k and viscous dashpot with damping constant c. In the practical system, these elements would operate as antivibration, or sound, mounts for the day-to-day excitations which exist. In order to limit the relative displacement during a severe base motion, which occurs infrequently, the nonlinear snubbers are provided above and below the mass, with initial clearance "a" between the snubbers and the mass. The assumed load-displacement relationship for the snubber is shown in Fig. 4(b). The essential parameters are the initial clearance a, the yield force F_y, and the stiffnesses k_e, k_p and k_u which are, respectively, the elastic, the plastic, and the unloading stiffnesses of the snubber. The curve is typical of some practical annealed, side-loaded tubes as reported by Neubert [16] where the unloading stiffness k_u is not necessarily equal to the loading stiffness k_e. Since the snubbers are not attached, each snubber acts in compression only. Thus after the load reaches zero during unloading the mass moves in the space between snubbers, supported only by the linear spring and dashpot, until the mass again impacts one of the snubbers. Because of permanent set of an impacted snubber, the clearance "a" and the yield force are both increased on each impact unless the snubber happens to stay in the elastic range during a particular impact. The logic itself becomes quite involved. It is especially important to locate the corners on the load deflection curve accurately, and the times that they occur.

The second system is the same, but mounted on another mass-spring-dahspot system, as shown in Figure 5, where the mass, spring and dashpot constants are designated capital M,K and C. This additional system might be a simple representation of some intervening support, such as a floor or a deck. The base excitation is $x_s(t)$ located as shown.

The base excitation is taken as that of [9,10], namely a triangular velocity versus time curve as shown in the inset of Figure 6. The peak input velocity is -120 in/s and occurs at t = 0.00075 seconds; the zero occurs at t = 0.050s. Thus the acceleration consists of the shaded area in Fig. 6; an initial narrow boxcar of -414g and 0.00075s duration, followed by a positive boxcar of 6.3g, terminated at t = 0.050s.

In the present work, the math program is kept in its original form, and questions associated with increased dimensionality and a second nonlinear

96
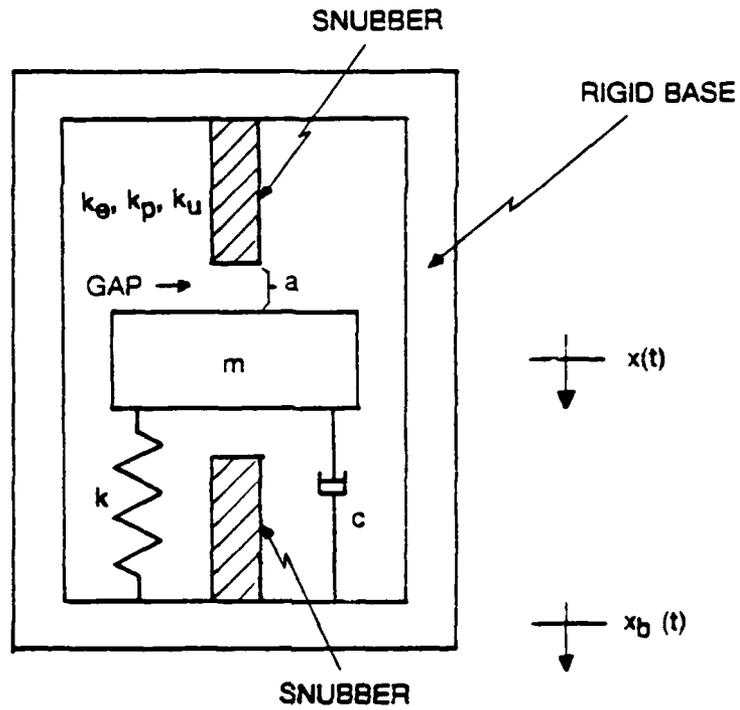
Figure 4(a) Mechanical Shock Absorber with Snubbers
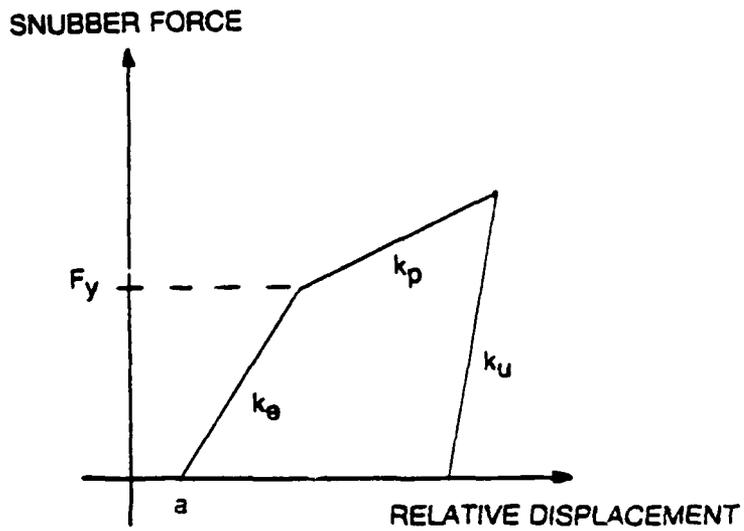
Figure 4(b) Snubber Force-Displacement Relationship

constraint are avoided. However, the ability to compute the adjoint variables is lost. To compensate, these gradients are computed numerically using a second order forward difference scheme. With these gradients, a nonlinear gradient algorithm can be implemented.

The modified constrained steepest descent algorithm described above is used to solve the problem. Modifications include performing curve searches rather than line searches on an active nonlinear constraint. This reduces the risk of taking large steps into the infeasible region. Rather than solve the equations of motion numerically by means of an integrator such as Runge-Kutta or Wilson-0, an "exact" solution based on a linear interpolation of the base acceleration. Since the input acceleration is made up of straight lines, the solution is exact. In addition, if the time step is constant, a large time savings can be achieved by not having to recalculate certain coefficients at each time interval. The details of this solution procedure are given in Ref. [5] for the three possible situations for damping levels: under-damped, overdamped, and critically damped. Craig [11] had given the solution for underdamping.
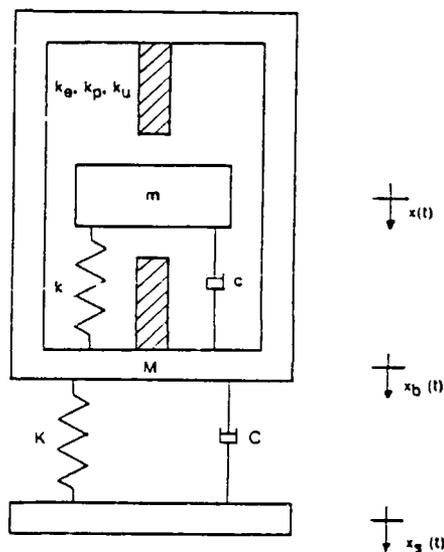
Figure 5 Nonlinear Shock Absorber Mounted on an Elastic Support

Analysis of Shock Absorber with Elastic Snubber

The effect of the various snubber gaps on the peak acceleration using elastic snubbers is shown in Fig. 7 by the use of a surface plot. The peak acceleration in g's is plotted as a function of the top and bottom snubber gaps. As expected, and as had been shown by Neubert [16], the large the snubber gap, the greater the acceleration. This can be reasoned as follows. For a larger gap, the distance between the snubber end and the constraint boundary is less, so the snubber must operate in a shorter distance and the optimal stiffness of the snubber must be greater, resulting in a greater transmitted acceleration.

Optimization of the Parameters of the Nonlinear Shock Absorber

In the optimization of the nonlinear shock mount, it is assumed that, for a given optimization run, the sound mount stiffness k, the dashpot constant c, the top and bottom gaps a_t and a_b, and the maximum allowed relative displacement d, are specified. Here the snubber gaps are taken equal, so $a_t = a_b = a$.
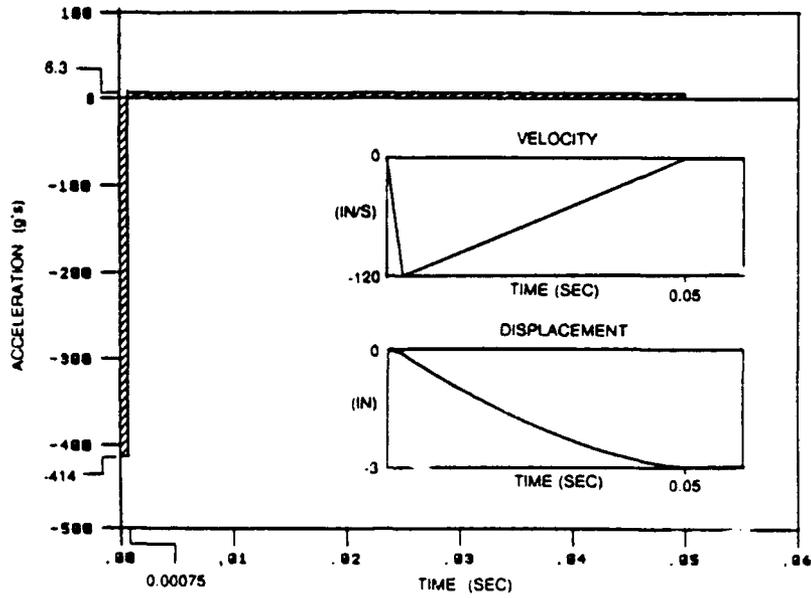
Figure 6 Applied Base Shock
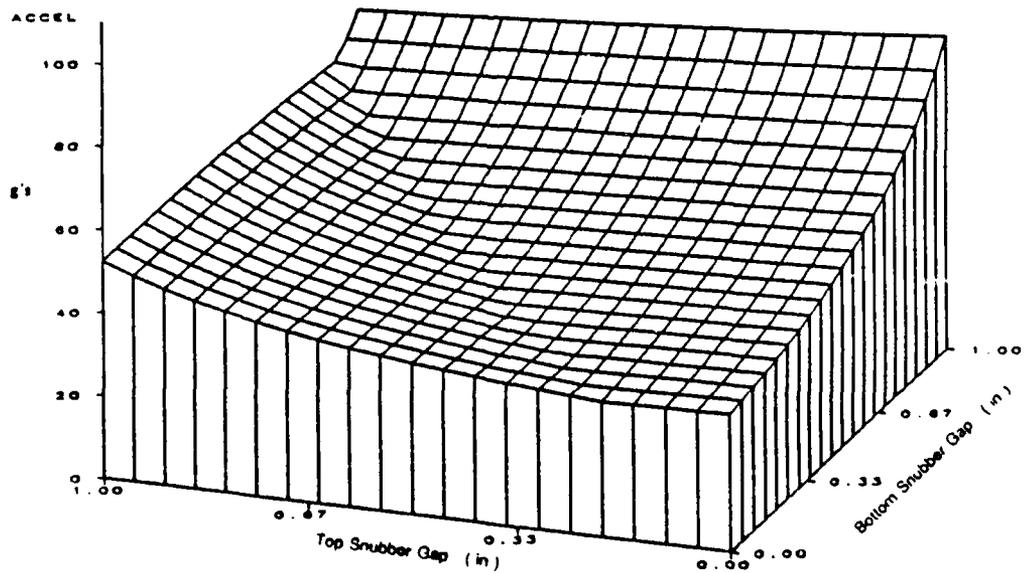
Figure 7 Peak Acceleration of Absorber as a Function
of Snubber Gaps

Inspecting Fig. 4, we see that the motion of the system can be specified within four regions: first where the relative displacement is less than the size of both gaps, with only the sound mount acting. The equation of motion is

$$\ddot{x}_r + [c/m]\,\dot{x}_r + [k/m]\,x_r = -\ddot{x}_b \tag{10}$$

When the relative displacement exceeds the gap, contact will occur between one snubber and mass. The snubber will initially deform elastically. The resulting equation of motion is

$$\ddot{x}_r + [c/m]\,\dot{x}_r + [(k+k_e)/m]\,x_r = -\ddot{x}_b + [k_e/m]a \tag{11}$$

The third region occurs during plastic deformation of the snubber. Assuming that the plastic stiffness varies linearly, the equation is

$$\ddot{x}_r + [c/m]\,\dot{x}_r + [(k+k_p)/m]\,x_r = -\ddot{x}_b - F_y/m + [k_p/m]\,a \tag{12}$$

$$\text{with } x_y = F_y/k_e + a$$

Plastic deformation of the snubber continues until the relative velocity becomes zero. At this point, the fourth region occurs as the snubber unloads with a linear stiffness k_u. The equation of motion corresponding can be used to describe the system during unloading by making four changes, which correspond to a shift in original on the load-deformation curve. The symbol "$\wedge$" indicates the updated value.

$$\hat{F}_y \leftarrow F_y + k_p(x_r - x_y) \quad \text{at } x_r = 0$$

$$\hat{x}_y \leftarrow x_r \tag{13}$$

$$\hat{a} \leftarrow x_r - F_y/k_u$$

$$\hat{k}_e \leftarrow k_u$$

Kasraie and Neubert [10] performed an optimization on a similar shock absorber system except that, rather than having top and bottom snubbers with gaps, they used a single snubber which was attached to the mass at all times. The relative displacement at which yielding initially occurs was fixed, and was not a design variable. Another slight difference from the present solution is that the static force mg was kept as part of the load. In addition, the unloading stiffness k_u was assumed to be the same as the elastic stiffness k_e, which resulted in unrealistic load-deflection curves when the optimum k_p was found to be greater than k_e as shown in Fig. 8.

Cases 1-5 in Table 1 are reported in reference [10] and should have yielded identical optimal solutions, because only the mass m was varied. The variation in k_e/m is primarily due to the fact that k_e has little effect on the maximum acceleration. Case 6 in Table 1 was done with the present program, and the optimal solutions agree quite well with those in [10].

The cases for the present nonlinear absorber are given in Table 2. Case 7 is an entirely elastic case, with d_{max} specified as 1.5in and each gap set at 0.5 in. The Cases 8-10 involve three combinations of the initial gap, using either 0.5 in or 1.0 in and the maximum relative displacement d = 1.0 or 1.5 in. The Cases 11 and 12 are the same as Case 8 except the damping value ζ is increased to 0.10 for Case 11 and the sound mount frequency is increased to $f_n = 15.0$Hz for Case 12.

The resulting optimal designs for Case 7-12 are summarized in Table 3. For Case 7, since the three stiffnesses were constrained to be equal, the values of k_e^*/m, k_p^*, and k_u^*/m, and k_u^*/m are identical. The constraint d_{max} is active and the optimum solution for a_{max} occurs on the constraint boundary, but of course
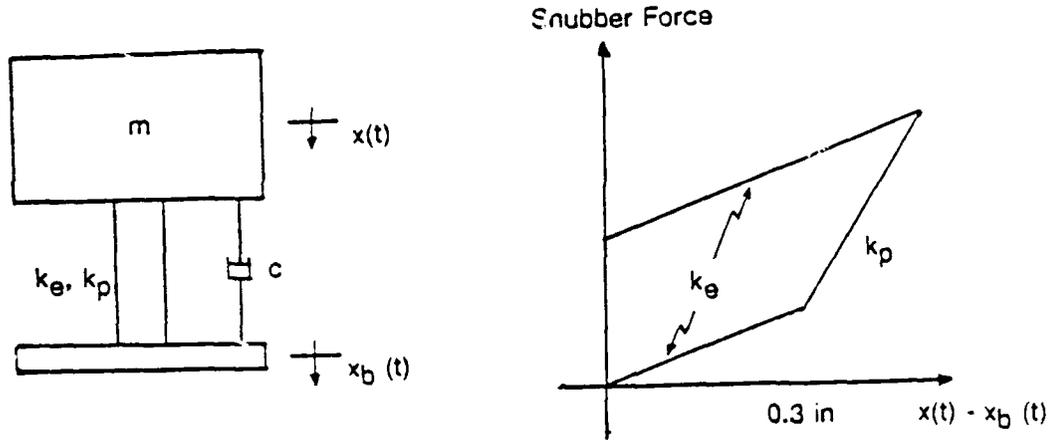
Figure 8 Shock Absorber Model used by Kasraie and Neubert

Table 1 Comparison of Optimal Solutions with Kasraie's Model

Case No.	mg (lb)	c^*/m (1/sec)	k_e^*/m (1/sec²)	k_p^*/m (1/sec²)	d_{max} (in)	a_{max} (g)
1	100.0	15.59	635.7	732.6	2.000	4.461
2	200.0	16.13	431.4	750.8	2.000	4.456
3	300.0	16.31	359.6	757.8	2.000	4.454
4	1,000.0	16.56	262.5	767.4	2.000	4.450
5	10,000.0	16.66	225.7	770.7	2.000	4.470
6	-	15.70	343.7	723.0	2.000	4.186

the two occur for the same set of design parameters, but not at the same instant of time during the timewise solution of the differential equations. The value of a_{max} = 42.10g is the smallest that can be obtained with linear shock absorbers, with the fixed parameters as specified in Table 2.

Table 2 Design Cases for Nonlinear Shock Absorber System

Case No.	Sound Mount f_n (Hz)	ζ	d (in)	Gap (in)	Snubber Restrictions
7	8.0	0.05	1.5	0.5	$k_e = k_p = k_u$
8	8.0	0.05	1.5	0.5	none
9	8.0	0.05	1.5	1.0	none
10	8.0	0.05	1.0	0.5	none
11	8.0	0.10	1.5	0.5	none
12	15.0	0.05	1.0	0.5	none

Table 3 Optimal Design for Nonlinear Shock Absorber System

Case No.	F_y^*/m (g)	k_e^*/m (g/in)	k_p^*/m (g/in)	k_u^*/m (g/in)	d_{max} (in)	a_{max} (g)
7	-	32.24	32.24	32.24	1.5000	42.10
8	8.70	∞	0.	∞	1.5000	18.61
9	23.21	∞	0.	∞	1.5000	33.20
10	21.26	∞	0.	∞	1.0000	27.91
11	5.44	∞	0.	∞	1.5000	15.57
12	9.82	∞	0.	∞	1.0000	32.96
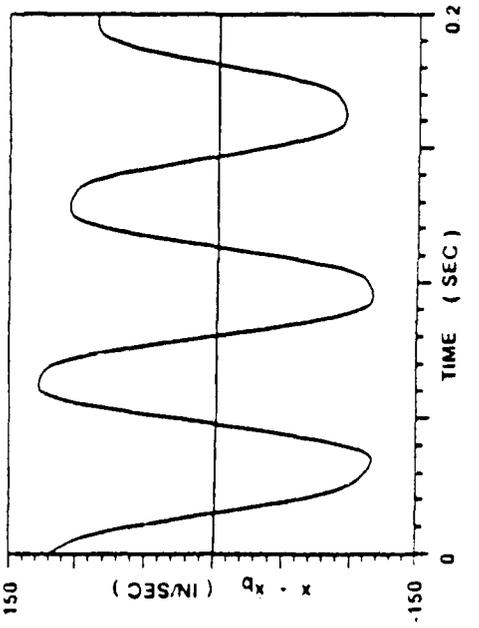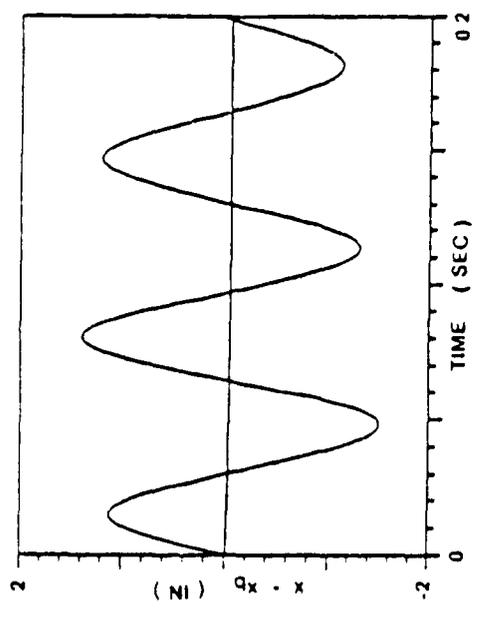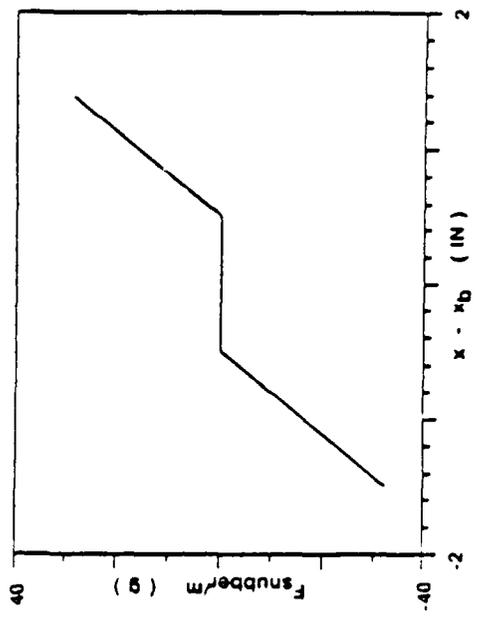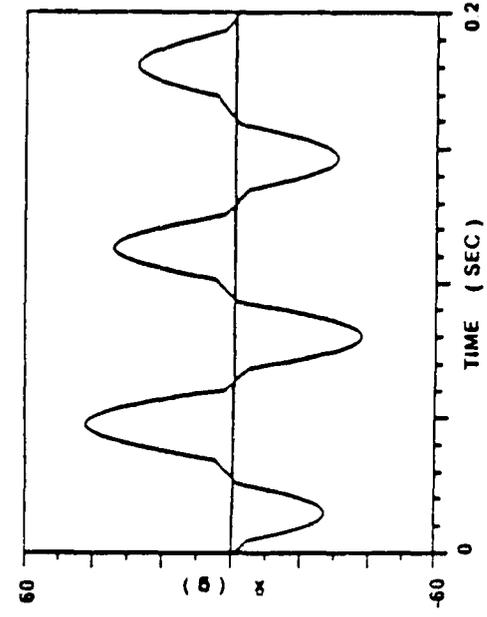
Figure 9 Optimal Shock Absorber Response for Case No. 7
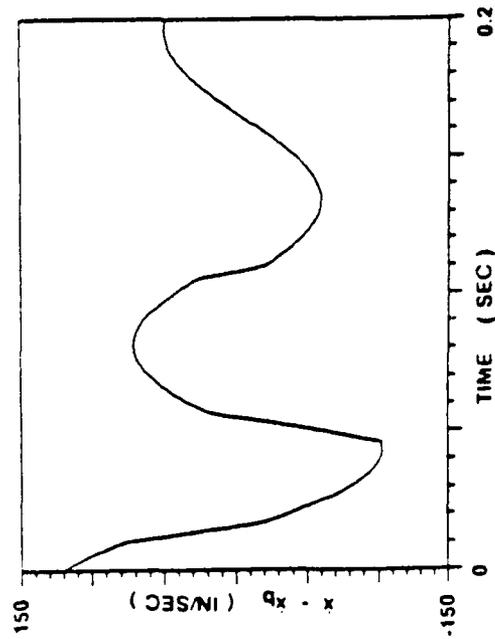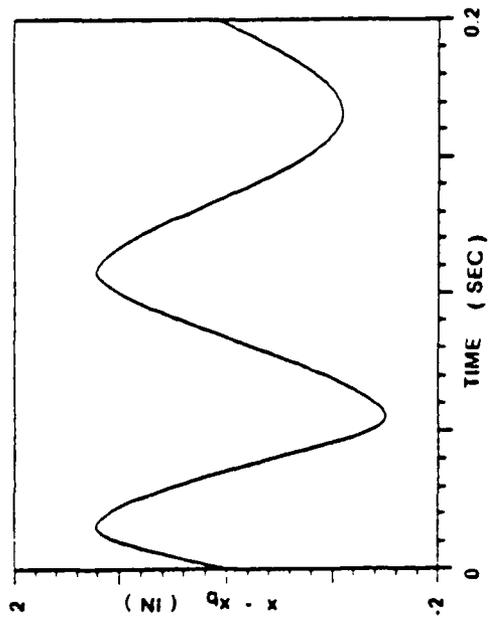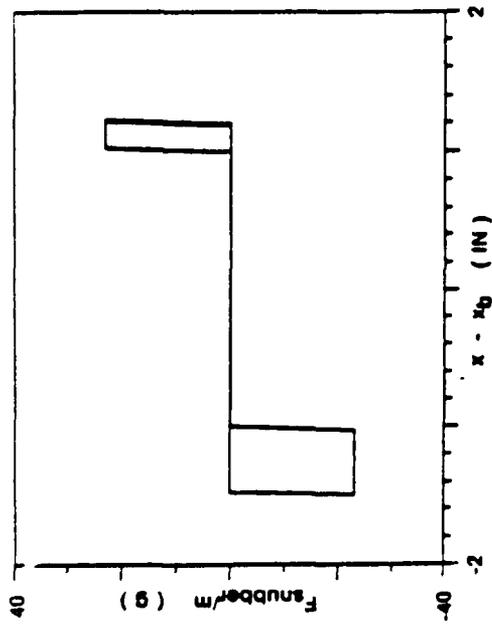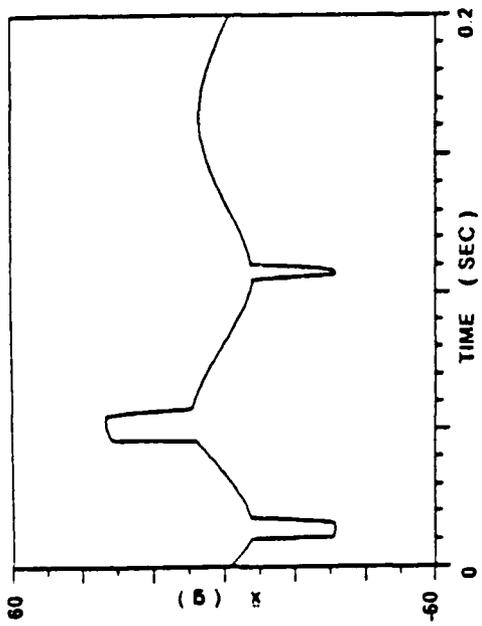
Figure 10 Optimal Shock Absorber Response for Case No. 9

For Cases 8-12 the optimal values of k_e and k_u are both infinity and the optimal value of k_p was determined to be zero. The snubber is rigid-perfectly plastic. This was intuitively expected, but did not occur in Kasraie's work because he used a prescribed value for the yield displacement rather than considering a design variable. The only positive finite design variable is F_y/m.

As expected, an increase in gap size (Cases 8 and 9), results in a larger peak acceleration. An increase in peak acceleration also occurs when the allowed maximum relative displacement is reduced (Cases 8 and 10). These higher accelerations are a direct result of the increased yield force. The effect of an increase in damping is illustrated by Case 11. By increasing the sound mount damping ratio from 5% to 10%, the peak acceleration is decreased by over 16%. This agrees with the trend for the linear shock absorber where the optimum value of damping was 40% of critical damping. Finally, comparing Cases 10 and 12, an increase in the undamped natural frequency of the sound mount increases the stiffness and results in increased peak acceleration.

The time histories and the snubber force-displacement curves for Cases 7 and 9 are shown in Figures 9 and 10. For both cases the maximum relative displacement occurs at the second peak, which is the first negative peak. The absolute acceleration, $\ddot{x}$ versus time, is not a smooth curve because of impacts on the snubbers. The acceleration is low when the mass is in the gap between snubbers, and then is discontinuous each time a snubber is impacted. The snubber force-displacement curves confirm that the snubber force is zero when the mass is in the gap between snubbers. The perfectly plastic force-displacement curve for Case 9 is apparent and the fact that one snubber is impacted twice can be seen as a cycle of unloading and reloading of that snubber. The snubber impacts can be seen clearly on the acceleration-time curves for Case 9 and it can be seen that the last impact is of shortest duration.

Absorber Mounted on a Support

In the solutions discussed thus far, the shock input was applied directly to the base of the absorber. In many situations there may be an intervening structure which possesses stiffness, mass, and damping. A simple one-directional model is shown in Fig. 5. The intervening structure is represented by the rigid mass M, dashpot C, and spring K. The mass M is shown as a rigid box, with absolute displacement $x_b(t)$, supporting the mass m which is to be protected by the sound mount and snubbers. The shock input is applied as $x_s(t)$. Two situations were compared:

(1) absorber and support uncoupled as in Fig. 11.
(2) absorber and support coupled as in Fig. 5 and

The uncoupled situation was considered because it arises in practise, where the support motions are know before the equipment and shock mount are installed. The procedures for applying inputs were, for the two situations, as follows.

(1) uncoupled system: apply the input as $\ddot{x}_s(t)$ to the one-degree-of-freedom system consisting of M, K and C, and solve for the response $x_b(t)$. Then use $\ddot{x}_b(t)$ as the input to the shock absorber base.

(2) coupled system: apply the input as $\ddot{x}_s(t)$ and solve for the response of the coupled two-degree-of-freedom system.
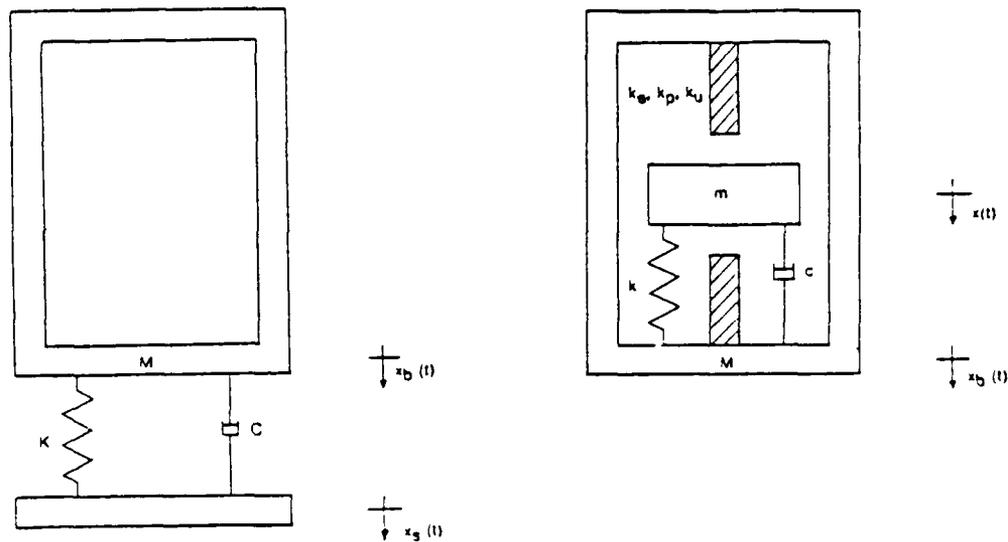
11(a) Uncoupled Support   11(b) Shock Absorber

Figure 11 Uncoupled Support and Shock Absorber

Uncoupled Support and Shock Absorber

For the uncoupled support, values of K/M and C/M must be specified in order to compute the support motion due to the input $x_s(t)$. Both a 10 Hz and a 20 Hz support natural frequency are considered in this analysis, with damping set at 5% of critical. The cases considered are listed in Table 4 as Cases 13-18. For all cases the sound mount natural frequency was 8 Hz and the damping ration 0.05. The support natural frequency was 10.0 Hz for Cases 13-15 and 20.0 Hz for Cases 16-18. The snubber stiffnesses were restricted so they were elastic in Cases 13 and 16. For 14 and 17 the unloading stiffness was set equal to the elastic stiffness. For 15 and 18 there were no restrictions on the snubber stiffnesses.

The base acceleration input to the shock absorber when the 10 Hz support was used is shown in Fig. 12. Because the duration of the shock input is only 0.05 seconds, the motion is a damped sinusoid after that time. Notice that the peak acceleration is 20 g's compared to 414 g's for the shock input.

The optimal design for the linear shock absorber (Case 13) represents a solution in which the displacement constraint is not active, that is, $d_{max}<d$, as shown in Table 5. The optimal solution lies within the interior of the feasible region. By comparison, the optimal design when the shock was applied directly to the absorber always resulted in an active constraint, $d_{max} = d$. This is explained by examining the time history responses in Fig. 13. The relative displacement curve contains a 10 Hz component from the applied acceleration as well as an 8 Hz component due to the natural frequency of the sound mount. When the relative displacement exceeds 0.5 inches, the effective shock absorber stiffness becomes $k+k_e$ resulting in a frequency component of approximately 30 Hz. As the value of the snubber stiffness changes, these three frequency components will combine to produce a different value for the peak relative displacement. Thus a decrease in snubber stiffness might produce a decrease rather than an expected increase in peak relative displacement simply because the frequency components happen to combine favorably.

106
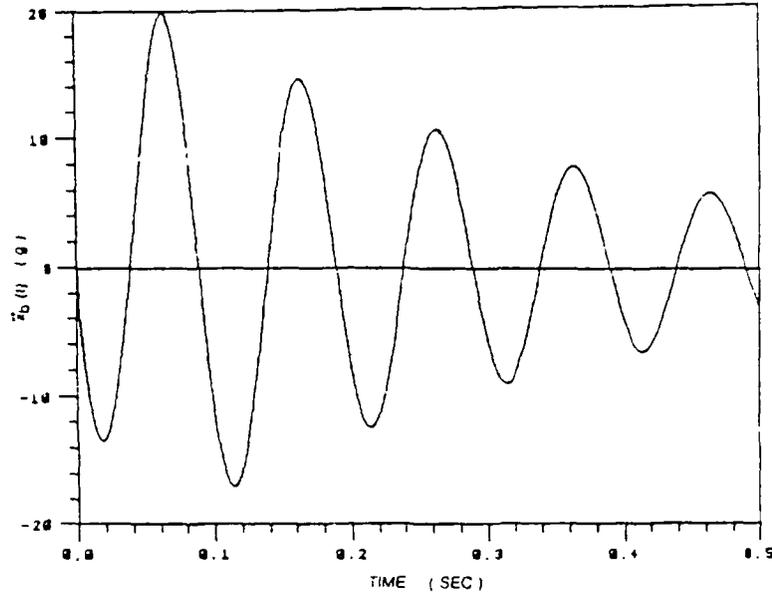
Figure 12 Acceleration Response $\ddot{x}_b(t)$ of a 10 Hz Support

Case 14 allows plastic deformation on the snubber while restricting the unloading stiffness to be equal to the elastic stiffness. This results in a decrease of peak acceleration from 63.8 to 44.79 g's. The optimal plastic stiffness of the snubber is zero although the optimal elastic stiffness is not zero, as was the case for the unsupported absorber system.

With no restrictions on the snubber design variables (Case 15), the peak acceleration drops to 34.3 g's, and the relative displacement constraint is inactive. The elastic stiffness goes to infinity while the unloading stiffness is finite. The associated time histories and the snubber load-deformation curves are shown in Fig. 14. This solution might be physically unreasonable since it represents an increase in the snubber length after compressive plastic deformation.

The optimal solutions for cases involving the 10 Hz support, cases 16-18, show similar trends. As restrictions are lifted on the snubber parameters, the optimal acceleration decreases. The magnitude of the acceleration values are greater due to the increase in the natural frequency of the support. For cases 15 and 18, which have no restrictions on the snubber design, the displacement constraint is not active.

Coupled Support and Shock Absorber

For the coupled supported and absorber system, the input is applied as $x_s(t)$ and the responses $x_b(t)$ and $x(t)$ are calculated directly. This involves a different set of differential equations for the two-mass system. To aid in writing the equations of motion, the relative displacements are defined as

$$w_1(t) = x_b(t) - x_s(t) \qquad w_2(t) = x(t) - x_s(t).$$

The resulting equations of motion for each of the three regions for the snubber are shown in Figure 15.

Table 4 Design Cases for Uncoupled Support and Absorber
System

Case No.	Support f_n (Hz)	ζ	Sound Mount f_n (Hz)	ζ	d (in)	Gap (in)	Snubber Restrictions
13	10.0	0.05	8.0	0.05	1.5	0.5	$k_e = k_p = k_u$
14	10.0	0.05	8.0	0.05	1.5	0.5	$k_u = k_e$
15	10.0	0.05	8.0	0.05	1.5	0.5	none
16	20.0	0.05	8.0	0.05	1.5	0.5	$k_e = k_p = k_u$
17	20.0	0.05	8.0	0.05	1.5	0.5	$k_u = k_e$
18	20.0	0.05	8.0	0.05	1.5	0.5	none

Table 5 Optimal Design for Uncoupled Support and
Absorber System

| Case No.	F_y^*/m (g)	k_e^*/m (g/in)	k_p^*/m (g/in)	k_u^*/m (g/in)	d_{max} (in)	a_{max} (g)
13	-	102.39	102.39	102.39	1.056	63.80
14	34.82	82.27	0.	82.27	1.500	44.79
15	25.96	∞	0.	39.00	1.265	34.30
16	-	160.02	160.02	160.02	1.500	170.05
17	102.15	232.60	0.	232.60	1.500	112.34
18	76.40	∞	0.	105.41	1.496	86.45

Figure 14 Optimum $\ddot{x}$ and Snubber Load–Deformation
for Case 15
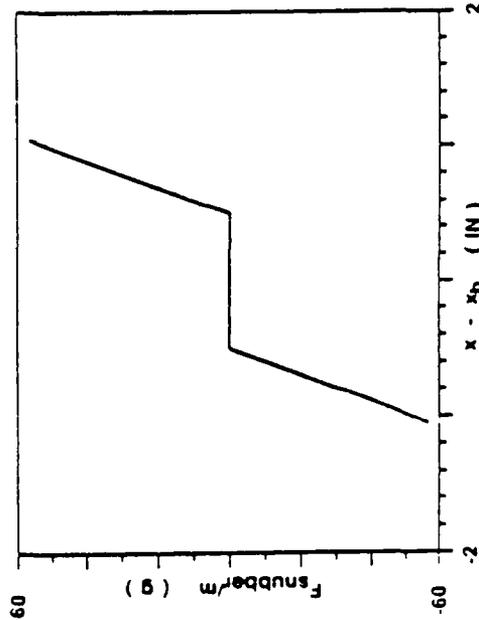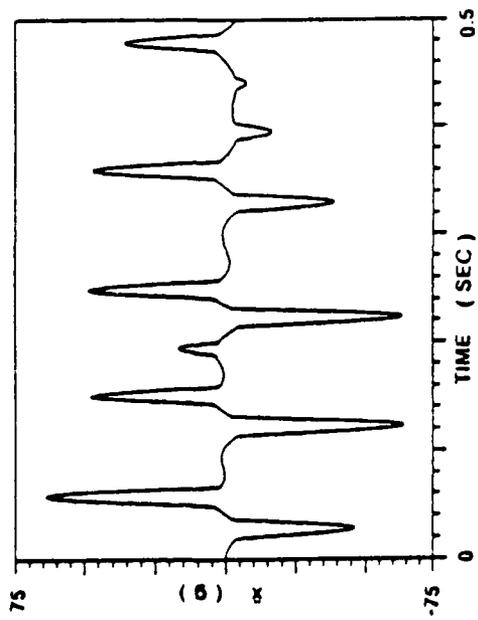
Figure 13 Optimum $\ddot{x}$ and Snubber Load–Deformation
for Case 13

$$\begin{bmatrix} M & 0 \\ 0 & m \end{bmatrix}\begin{bmatrix} \ddot{w}_1 \\ \ddot{w}_2 \end{bmatrix} + \begin{bmatrix} C+c & -c \\ -c & c \end{bmatrix}\begin{bmatrix} \dot{w}_1 \\ \dot{w}_2 \end{bmatrix} + \begin{bmatrix} (K+k) & -k \\ -k & k \end{bmatrix}\begin{bmatrix} w_1 \\ w_2 \end{bmatrix} = \begin{bmatrix} -M\ddot{x}_s \\ -m\ddot{x}_s \end{bmatrix}$$

ELASTIC SNUBBER REGION :

$$\begin{bmatrix} M & 0 \\ 0 & m \end{bmatrix}\begin{bmatrix} \ddot{w}_1 \\ \ddot{w}_2 \end{bmatrix} + \begin{bmatrix} C+c & -c \\ -c & c \end{bmatrix}\begin{bmatrix} \dot{w}_1 \\ \dot{w}_2 \end{bmatrix} + \begin{bmatrix} (K+k+k_e) & -(k+k_e) \\ -(k+k_e) & (k+k_e) \end{bmatrix}\begin{bmatrix} w_1 \\ w_2 \end{bmatrix} = \begin{bmatrix} -M\ddot{x}_s - a\,k_e \\ -m\ddot{x}_s + a\,k_e \end{bmatrix}$$

PLASTIC SNUBBER REGION :

$$\begin{bmatrix} M & 0 \\ 0 & m \end{bmatrix}\begin{bmatrix} \ddot{w}_1 \\ \ddot{w}_2 \end{bmatrix} + \begin{bmatrix} C+c & -c \\ -c & c \end{bmatrix}\begin{bmatrix} \dot{w}_1 \\ \dot{w}_2 \end{bmatrix} + \begin{bmatrix} (K+k+k_p) & -(k+k_p) \\ -(k+k_p) & (k+k_p) \end{bmatrix}\begin{bmatrix} w_1 \\ w_2 \end{bmatrix} = \begin{bmatrix} -M\ddot{x}_s + F_y[\,1 - k_p/k_e\,] - a\,k_p \\ -m\ddot{x}_s - F_y[\,1 - k_p/k_e\,] + a\,k_p \end{bmatrix}$$

Figure 15 Equations of Motion for Coupled Support and Shock Absorber

To have the same variables F_y/m, k_e/m, k_p/m and k_u/m, we divide the equations by m and M, which produces a new term M/m. The ratios k/m and c/m and K/M and C/M are used to define the natural frequencies and damping ratios for the sound mount and the support, respectively.

The design cases for the coupled system are listed in Table 6. The uncoupled support and shock absorber natural frequencies of 10 and 8 Hz respectively are identical with the values used in Case 13, 14 and 15 for the uncoupled system. For Cases 19-21 the ratio M/m = 10 and for Cases 22-24 the M/m = 5.

The only change to the analytical procedure is with respect to solving the differential equations of motion. Instead of using an exact method as before, the equations are solved accurately using a numerical approach. Since only the maximum values are used in the optimization procedure, that procedure is unchanged.

Comparing the optimum designs in Table 7 for Cases 19-21 with those for Cases 13-15 listed in Table 5 shows fairly good agreement. For the linear snubber of Case 19, the optimal solution is in the interior of the feasible region, with d_{max} - 1.154 inches. Trends for Case 20 are similar to those for Case 14, that is, the optimal plastic stiffness is zero and the elastic stiffness is finite and slightly less than that obtained for the uncoupled system. With no design parameter restrictions on the snubber, the optimal plastic stiffness becomes infinite while the unloading stiffness remains finite.

When the mass ratio is reduced to M/m = 5, the coupling effect becomes more important and the agreement between Cases 22-24 and 13-15 becomes eotdr. Although certain trends remain, large discrepancies between optimal design values occur. For example, the linear elastic snubber of Case 22 has an optimal stiffness which is just 17% of the stiffness of the uncoupled case. The corresponding peak acceleration is 27.6 g's compared to 63.8 g's. The comparison between the two-degree-of-freedom model and the uncoupled model improves for Case 23 and 24, although the peak acceleration values are approximately 50% lower.

Graphs of optimum shock absorber response are shown in Figs. 16 and 17 for Cases 19 and 21. For the elastic snubber, Fig. 16, the acceleration time curves show that there are sometimes two successive impacts on one snubber which can be related to the relative displacement peaks. For Case 21, with no restrictions on snubber stiffnesses, the load-displacement curve for the snubber shows the infinite k_u and finite k_e.

The snubbers are elastic for Case 22. The acceleration $\ddot{x}_b(t)$ is included in Fig. 18 to show how the acceleration at the base of the snubber is modified by the coupling. This should be compared to $\ddot{x}_b(t)$ in Fig. 12 for the uncoupled systems.

Table 6 Design Cases for Coupled Support and Absorber System

Case No.	M/m	Support f_n (Hz)	ζ	Sound Mount f_n (Hz)	ζ	d (in)	Gap (in)	Snubber Restrictions
19	10	10.0	0.05	8.0	0.05	1.5	0.5	$k_e = k_p = k_u$
20	10	10.0	0.05	8.0	0.05	1.5	0.5	$k_u = k_e$
21	10	10.0	0.05	8.0	0.05	1.5	0.5	none
22	5	10.0	0.05	8.0	0.05	1.5	0.5	$k_e = k_p = k_u$
23	5	10.0	0.05	8.0	0.05	1.5	0.5	$k_u = k_e$
24	5	10.0	0.05	8.0	0.05	1.5	0.5	none

Table 7 Optimal Design for Coupled SUpport and Absorber System

| Case No.	F_y^*/m (g)	k_e^*/m (g/in)	k_p^*/m (g/in)	k_u^*/m (g/in)	d_{max} (in)	a_{max} (g)
19	-	68.90	68.90	68.90	1.154	52.57
20	27.48	72.06	0.	72.06	1.500	37.43
21	19.47	∞	0.	24.12	1.500	29.34
22	-	17.75	17.75	17.75	1.500	27.60
23	10.90	83.10	0.	83.10	1.500	20.82
24	8.96	∞	0.	13.78	1.500	18.84
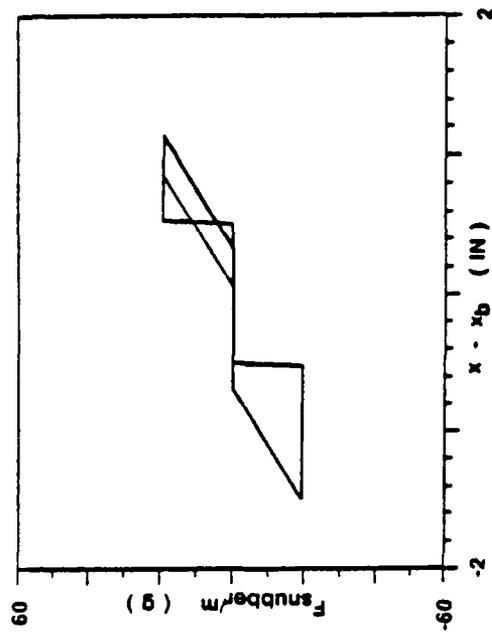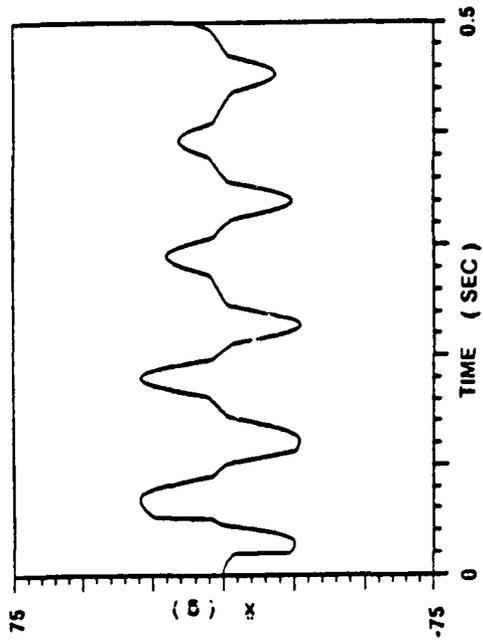
Figure 17 Optimal $\ddot{x}$ and Snubber Load-Deformation
for Case 21
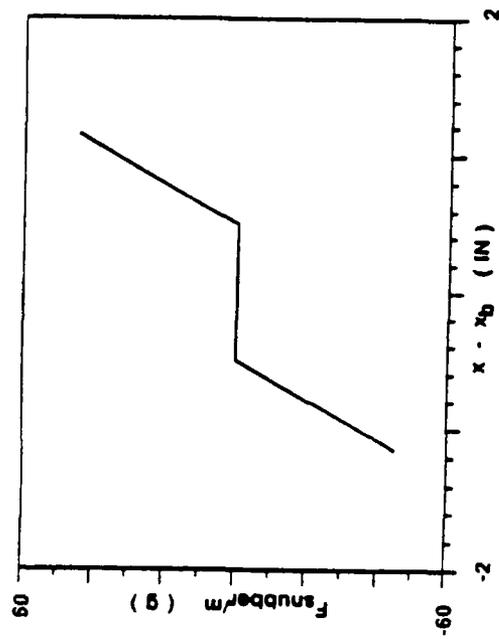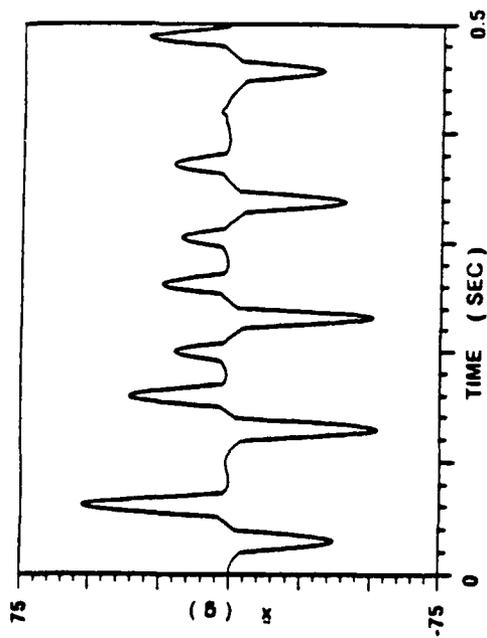
Figure 16 Optimal $\ddot{x}$ and Snubber Load-Deformation
for Case 19
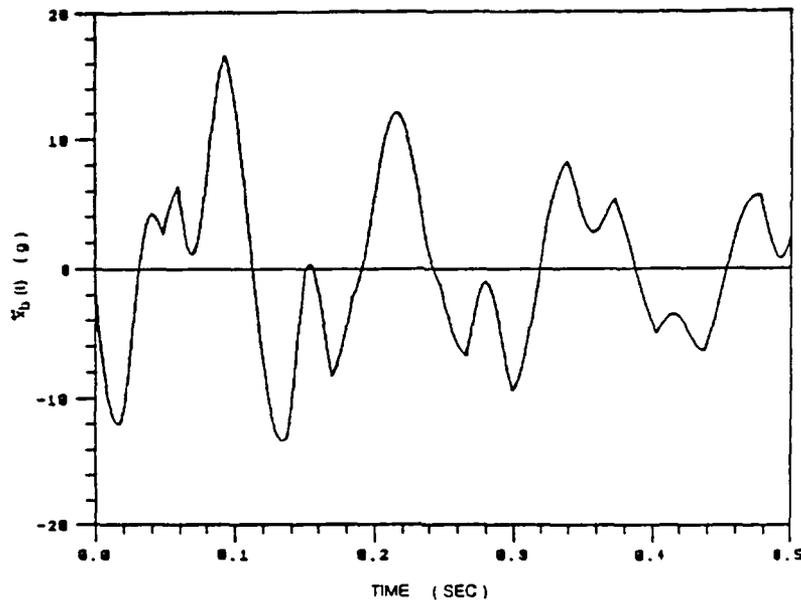
Figure 18 Acceleration Response of Support for Case No. 22

Examination of Fig. 18 shows a support acceleration response which is quite different timewise from the support acceleration response from the uncoupled system of Fig. 11. This accounts for the differences in optimal designs when the mass ratio is reduced to M/m=5.

Comparison of Algorithms

The modified constrained steepest descent algorithm relies on knowing the gradients of the objective and constraint functions. For the particular application of the nonlinear shock absorber, these gradients must be calculated numerically by a forward difference technique and objective function must be computed a number of times. This involves solving the equations of motion and picking off the maximum acceleration and relative displacement values. It might be argued that a more efficient approach would be to chose an algorithm which does not require knowledge of the gradients. Therefore two of these "direct" methods were chosen to compare to the modified constrained steepest descent algori-hm.

One of the methods chosen was the Simplex Method developed byNelder and Mead [13]. This method is not to be confused with the Simplex Method asociated with linear programming. The method operates by defining a geometric figure within the design space consisting of n + 1 vertices, where n is the dimension of the space. By successive moves of these vertices depending upon the value of the objective function at the vertices, the optimal design point is approached. The method is quite stable and very simple to program. Although the method works best for unconstrained minimization, only a slight modification is required to adjust it to a program with constraints.

The second algorithm chosen was the Hooke-Jeeves Method described in detail by Rao [14]. This method is based on a combination of exploratory as well as pattern search moves. It is very easy to implement for unconstrained problems. To use the method of Hooke-Jeeves on a constrained optimization problem, one must first convert the math program to an unconstrained form. For this comparison, the conversion was accomplished by using an exterior penalty function. That is, tne

constraint function is added to the objective function forming an unconstrained program of the form:

$$\min F(\underline{b}) = f(\underline{b}) + r[\max(0..g(\underline{b})]^2$$

where r is the penalty coefficient. As r approaches infinity, the solution becomes optimal to the original program from the infeasible direction.

These two method were compared to the modified constrained steepest descent algorithm by running four different test cases involving the optimalization of a linear oscillator. Two different initial designs and forcing functions were considered in finding the optimal stiffness and damping values to minimize the peak acceleration of the mass subject to a relative displacement constraint. Care was taken to insure that initial step sizes and convergence criteria were equivalent between the methods.

Table 8 lists the results of the comparison between the modified constrained steepest descent, the Simplex, and the Hooke-Jeeves method. total number of function evaluations as well as CPU seconds on a VAX 11/730 are shown. The results show that the modified constrained steepest descent algorithm performs well and is on the order of 2 to 3 times faster than the other algorithms.

Table 8 Comparison of Optimization Algorithms

Test Case	No. of Function Evaluations			CPU seconds		
	MCSD	SIMPLEX	H-J	MCSD	SIMPLEX	H-J
1	45	142	199	23.7	46.3	60.3
2	65	137	198	36.7	44.9	60.6
3	64	145	254	32.4	43.7	69.6
4	44	166	268	30.0	48.8	73.0

Conclusions

1. The modifed gradient projection method developed herein is more efficient than the Simplex and Hooke-Jeeves Methods.

2. The use of curve searches rather than straight line searches on the nonlinear constraint boundary improves the efficiency.

3. The optimization of k/m and c/m for the simple linear absorber provides an opportunity to see the optimization process in two dimensions. The results have not been presented previously in this form.

4. For the nonlinear shock snubber, the optimum elastic stiffness k_e was found to be infinity and the optimum plastic stiffness k_p was zero. The optimum unloading stiffness k_u in general is not equal to the optimum elastic stiffness k_e.

REFERENCES

1. Schmit, Lucien A., Jr., and Fox, Richard L., "Synthesis of a Simple Shock Absorber," NASA Contractor Report, NASA CR-55, June 1964.

2. Bryson, A. E., and Denham, W. F., "A Steepest-Ascent Method for Solving Optimal Programming Problems," Journal of Applied Mechanics, Trans. ASME, Vol. 29, June 1962, pp. 247-257.

3. Sevin, Eugene, and Pilkey, Walter D., "Optimization of Shock Isolation System," Society of Automotive Engineers, Oct. 1968, pp. 2900-2909.

4. Karnopp, D. C., and Trikha, A. K., "Comparative Study of Optimization Techniques for Shock and Vibration Isolation," Journal of Engineering for Industry, Trans. ASME, Vol. 91, Nov. 1969, pp. 1128-1132.

5. Bartel, Donald L., and Krauter, Allan I., "Time Domain Optimization of a Vibration Absorber," Journal of Engineering for Industry, Trans. ASME, Vol 93, August 1971, pp. 799-803.

6. Wilmert, K. D., and Fox, R. L., "Optimum Design of a Linear Multi-Degree-of-Freedom Shock Isolation System," Journal of Engineering for Industry, Trans. ASME, Vol 94, May 1972, pp. 465-471.

7. Afimiwala, K. A., and Mayne R. W., "Optimum Design of an Impact Absorber," J. of Engr for Industry, Vol. 96, Feb. 1974, pp. 124-130.

8. Hsiao, M. H., Haug, E. J., Jr., and Arora, J. S., "A State Space Method for Optimal Design of Vibration Isolators," Journal of Mechanical Design, Trans. ASME, Vol. 101, April 1979, pp. 309-314.

9. Kasraie, K., "State Space Method for Optimal Design of Shock Absorbers with Floating Boundaries," Ph.D. Thesis, The Pennsylvania State University, University Park, PA, 1983.

10. Kasraie, K., and Neubert, V. H., "Optimum Design for Nonlinear Shock Mounts for Transient Inputs," The Shock and Vibration Bulletin, 54, Part 2, June 1984, pp. 13-28.

11. Craig, Roy R., Jr., Structural Dynamics, John Wiley, 1981, pp. 139-142.

12. Bazaraa, Mokhtar S. and Shetty, C. M., Nonlinear Programming, John Wiley, 1979, pp. 389-399.

13. Nelder, J. A. and Mead, R., "A Simplex Method for Function Minimization," Computer Journal, Vol. 7, 1965, pp. 308-313.

14. Rao, S. S., Optimization: Theory and Applications, John Wiley, 1984, pp. 271-273.

15. Roy, Nicolas A., "Numerical Optimization of a Mechanical Shock Absorber," Doctoral Thesis, The Pennsylvania State University, 1986.

16. Neubert, Vernon H., "Analysis of Energy-Absorbing Shock Mounts," Shock and Vibration Bulletin, No. 51, 1981.

ACTIVE DAMPING DESIGN OF FLEXIBLE STRUCTURES BASED ON NON COLLOCATED SENSOR-ACTUATOR VELOCITY FEEDBACK

Q. Zhang, S. Shelley, X. N. Lou, and R. J. Allemang

Structural Dynamics Research Laboratory
Department of Mechanical and Industrial Engineering
University of Cincinnati
Cincinnati, OH 45221

The active damping design technique based on single input velocity feedback is presented in this paper. The necessary and sufficient stability conditions for SISO and SIMO velocity feedback is first stated and mathematically proved. Based on these stability conditions, two active damping design algorithms, 1) Constrained Least Squares Feedback Gain Computation, and 2) Optimal Feedback Gain Computation With Flexible Damping Factors, are proposed. The first algorithm is a straightforward way to find the feedback vector for the given damping factors and the modal frequencies. The second algorithm is based on optimization process using the flexibility in chosing the desired damping factors. The problem of locating the actuator and sensors is also discussed in this paper. The stability theory and active damping design technique are verified by an experimental example.

1 INTRODUCTION

Vibration cancellation in flexible structures is always a challenging subject for mechanical and control engineers. During the last decade, active control has become widely accepted by structural system designer as an alternative to traditional passive damping, and as an effi⌣ent tool to suppress undesired vibration and to maintain the stability of systems.

Among many different strategies of active damping design for flexible structures, pole placement is

one of the most commonly used methods. A review of the previous work on pole placement can make a long list [1-12]. For the early work in this field, the primary interest is to find the necessary and sufficient conditions for the existence of the feedback matrix which yields a set of given eigenvalues. Recently the flexibility in chosing the eigenvectors of the closed-loop system is used to increase the robustness of the control system to model uncertainty, and pole placement is also combined with other control algorithms such as LQR. It is important to note that for output feedback, pole placement methods can not guarantee overall stability of the control system.

Another commonly used method for active damping is velocity feedback with positive definite feedback gain matrix. The principle of velocity feedback is to absorb energy from the structure like viscous damper, so the stability of the control system is automatically guaranteed. Note such a stable velocity feedback implies the velocity sensors are collocated with the actuators. However, in many practical cases, the actuators can be mounted only in certain specified locations. The sensor-actuator collocation requirement hence will be a severe constraint for some applications. It is well known that the positive definite velocity feedback matrix is the sufficient condition for stability, but not "necessary". Thus a stable velocity feedback control system with non colocated sensors and actuators may exist.

In this paper, the necessary and sufficient stability condition for the single input multiple outputs velocity feedback is given. Based on this stability condition, several active damping design algorithms, which can guarantee the overall stability of the control system but without the sensor-actuator collocation requirement, are proposed. The stability theory and the active damping design algorithms are illustrated by a simple experimental example.

2. PROBLEM STATEMENT

A linear time invariant structural system with output feedback control can be described by following equations

$$\{\dot{x}(t)\} = [A]\{x(t)\} + [B]\{u(t)\}$$

$$\{y(t)\} = [D]\{x(t)\} \tag{1}$$

$$\{u(t)\} = [F]\{y(t)\}$$

where $\{x\}$, $\{y\}$, and $\{u\}$ are the state, output, and control vectors, $[A]$, $[B]$, $[D]$, and $[F]$ are the constant matrices of appropriate dimensions.

The problem to be resolved in this paper is to add viscous damping to an undamped structural system by feeding back velocity. This problem can be stated in a more straightforward way than equation (1)

$$[M]\{\ddot{z}(t)\} + [K]\{z(t)\} = \{u(t)\} \tag{2}$$

$$\{u(t)\} = -[C]\{\dot{z}(t)\}$$

where $\{\ddot{z}(t)\}$, $\{\dot{z}(t)\}$, and $\{z(t)\} \in R^N$ are the acceleration, velocity, and displacement vectors, and [M], [K], and [C] $\in R^{N,N}$ are the mass, stiffness and feedback matrices respectively.

This paper is restricted to single input control configuration, so the feedback matrix [C] can be written as

$$[C] = \{e_i\}\{c\}^T \tag{3}$$

where $\{e_i\}$ is the ith column of the identity matrix, and $\{c\}$ is the vector containing feedback gains. Note that only n (n < N) elements of $\{c\}$ are non zero, which correspond to the sensors involved in the control system.

For the purpose of the analysis, we also introduce the modal model of the undamped system : $[\Phi]$, $[\Lambda] \in R^{N,N}$ and that of the closed-loop system : $[\hat{\Phi}]$, $[\hat{\Lambda}] \in C^{N,N}$ defined from equations

$$[K - \lambda_l M]\{\phi_l\} = 0 , \quad \{\phi_j\}^T[M]\{\phi_i\} = \delta_{ij} \tag{4}$$

$$with \quad [\Phi] = [\,..\,\phi_l\,..\,] , \quad [\Lambda] = diag\{\omega_l^2\}$$

$$[\hat{\lambda}_l^2 M + \hat{\lambda}_l C + K]\{\hat{\phi}_l\} = 0 \tag{5}$$

$$with \quad [\hat{\Phi}] = [\,..\,\hat{\phi}_l\,..\,] , \quad [\hat{\Lambda}] = diag\{\hat{\lambda}_l\} , \quad \hat{\lambda}_l = -o_l + j\hat{\omega}_l$$

where δ_{ij} is the Kronecker-delta : $\delta_{ij} = \begin{cases} 1, & \text{for } i = j \\ 0, & \text{for } i \neq j \end{cases}$.

Since modal vectors span the N-dimensional space, the vector $\{\hat{\phi}_l\}$ can be written as a linear combination of the eigenvectors of the undamped system

$$\{\hat{\phi}_l\} = [\Phi]\{q_l\} \tag{6}$$

For structural systems, [M] is a positive definite matrix and [K] is a positive or semi-positive definite matrix. If the feedback matrix [C] is also positive definite, the system (2) is a stable system. If [C] is not positive definite, the system (2) may be stable or unstable, because a positive definite velocity feedback matrix is a sufficient, but not necessary condition for stabile damped system. In this paper, the necessary and sufficient stability condition for single input velocity feedback will be proved.

For stable control operation, the eigenvalues of the closed-loop system must be in the left half complex plane. This well known result will be the guide line for deriving the stability condition for velocity feedback.

3 STABILITY CONDITION

3.1 SISO Velocity Feedback

We begin by considering single input single output (SISO) velocity feedback, for which the feedback matrix has the form

$$[C] = c\{e_i\}\{e_j\}^T \tag{7}$$

where "i" and "j" indicate respectively the locations of the actuator and the sensor.

The necessary and sufficient stability condition for SISO velocity feedback can be stated then as follows

Theorem 1

The undamped real positive linear system (1) is stabilizable by a SISO velocity feedback, if and only if for all the modes $l = 1, \ldots, N$

$$\beta_l = \sum_{k=1}^{N} \frac{c\phi_{ik}\phi_{jk}}{\Delta_{kl}^2} > 0 \, , \tag{8}$$

with $\quad \Delta_{kl}^2 = (\sigma_l^2 + \omega_k^2 - \hat{\omega}_l^2)^2 + (2\sigma_l\hat{\omega}_l)^2$

where c is the feedback gain. ϕ_{ik} and ϕ_{jk} are the ith and jth elements of the kth eigenvector of the undamped system, and the "j" and "i" indicate the locations of the sensor and the actuator respectively.

Theorem 1 can be proved by algebraical manipulations of Equations (4) to (7).

Substituting (6) and (7) into (5) and premultiplying by $[\Phi]^T$ yields

$$[\hat{\lambda}_l^2 I + \hat{\lambda}_l c\{\Phi^T e_i\}\{e_j^T\Phi\} + \Omega^2]\{q_l\} = 0 \, , \quad \text{with} \quad \Omega^2 = diag\{\omega_i^2\} \tag{9}$$

Premultipling (9) again by a row vector $\{e_j^T\Phi\}$, it can be arranged as

$$(1 + \hat{\lambda}_l c\{e_j^T\Phi\}[\hat{\lambda}_l^2 I + \Omega^2]^{-1}\{\Phi^T e_i\})\{e_j^T\Phi\}\{q_l\} = 0 \tag{10}$$

(10) is a scaler function of $\hat{\lambda}_l$. Assume $\{e_j^T\Phi\}\{q_l\}$ is different from zero, the first term of the left hand side of (10) must be zero

$$1 + \hat{\lambda}_l c\{e_j^T\Phi\}[\hat{\lambda}_l^2 I + \Omega^2]^{-1}\{\Phi^T e_i\} = 0$$

or

$$-1 = c\sum_{k=1}^{N} \frac{\hat{\lambda}_l \phi_{ik}\phi_{jk}}{\hat{\lambda}_l^2 + \omega_k^2} \tag{11}$$

Considering

$$\frac{1}{\hat{\lambda}_l^2 + \omega_k^2} = \frac{1}{\sigma_l^2 - \hat{\omega}_l^2 - 2j\sigma_l\hat{\omega}_l + \omega_k^2} = \frac{\sigma_l^2 - \hat{\omega}_l^2 + 2j\sigma_l\hat{\omega}_l + \omega_k^2}{(\sigma_l^2 - \hat{\omega}_l^2 + \omega_k^2)^2 + (2\sigma_l\omega_l)_2}$$

Equation (11) can be written as

$$-1 = c\sum_{k=1}^{N}\frac{\phi_{ik}\phi_{jk}(-\sigma_l + j\hat{\omega}_l)(\sigma_l^2 - \hat{\omega}_l^2 + 2j\sigma_l\hat{\omega}_l + \omega_k^2)}{(\sigma_l^2 - \hat{\omega}_l^2 + \omega_k^2)^2 + (2\sigma_l\omega_l)^2} \tag{12}$$

Writing separately the real part and the imaginary part of (12), it results in the following two equalities

$$0 = j\left(\sum_{k=1}^{N}\frac{c\phi_{ik}\phi_{jk}}{\Delta_{kl}^2}(\omega_k^2 - \hat{\omega}_l^2 - \sigma_l^2)\right)\hat{\omega}_l \tag{13}$$

$$-1 = \left(\sum_{k=1}^{N}\frac{c\phi_{ik}\phi_{jk}}{\Delta_{kl}^2}(-\omega_k^2 - \hat{\omega}_l^2 - \sigma_l^2)\right)\sigma_l \tag{14}$$

From the first equality (13), it can be derived

$$\sum_{k=1}^{N}\frac{\phi_{ik}\phi_{jk}\omega_k^2}{\Delta_{kl}^2} = \left(\sum_{k=1}^{N}\frac{\phi_{ik}\phi_{jk}}{\Delta_{kl}^2}\right)(\hat{\omega}_l^2 + \sigma_l^2) \tag{15}$$

Substituting (15) into the second equality (14) yields

$$1 = 2\left(\sum_{k=1}^{N}\frac{c\phi_{ik}\phi_{jk}}{\Delta_{kl}^2}\right)(\hat{\omega}_l^2 + \sigma_l^2)\sigma_l$$

or

$$1 = 2\beta_l(\hat{\omega}_l^2 + \sigma_l^2)\sigma_l \tag{16}$$

Obviously, σ_l is positive, if and only if β_l is positive.

Theorem 1 is valid for both collocated or non collocated sensor-actuator velocity feedback. In the collocated sensor-actuator case (j=i), the stability indicator β_l becomes

$$\beta_l = \left(\sum_{k=1}^{N}\frac{c\phi_{ik}^2}{\Delta_{kl}^2}\right)$$

β_l is positive for any positive feedback gain c and the control system is stable. This well known result is verified by Theorem 1.

Theorem 1 can easily be extended to single input multiple output velocity feedback.

3.2 SIMO velocity feedback

For single input multiple outputs (SIMO) velocity feedback, the feedback matrix has the general form

$$[C] = \{e_i\}\{c\}^T$$

and the necessary and sufficient stability condition becomes

Theorem 2

The undamped real positive linear system (1) is stabilizable by a SIMO velocity feedback, if and only if for all the modes $l = 1, \ldots, N$

$$\beta_l = \sum_{k=1}^{N} \frac{(c_1\phi_{j1k} + c_2\phi_{j2k} + \ldots + c_n\phi_{jnk})\phi_{ik}}{\Delta_{kl}^2} > 0 , \tag{17}$$

with $\quad \Delta_{kl}^2 = (\sigma_l^2 + \omega_k^2 - \hat{\omega}_l^2)^2 + (2\sigma_l\hat{\omega}_l)^2$

where $c_1, \ldots, c_n$ are the feedback gains. $\phi_{j1k}, \ldots, \phi_{jnk}$ are the j1th, $\ldots$, jnth elements of the kth eigenvector of the undamped system, and the "j1" to "jn" indicate the locations of the sensors.

The proof of Theorem 2 proceeds in the same manner as that of Theorem 1 with $(c_1\{e_{j1}^T\Phi\} + c_2\{e_{j2}^T\Phi\} + \ldots + c_n\{e_{jn}^T\Phi\})$ replacing $c\{e_j^T\}\Phi$ in Equations (9) to (11).

As the stability condition stated in Theorem 2 is the necessary and sufficient condition, for a given feedback gain vector $\{c\}$, the stability of the control can be determined. On other hand, if the gain vector $\{c\}$ is calculated based on Equation (17), the stability of the control system will be strictly guaranteed.

For SIMO velocity feedback, Equation (16) becomes

$$1 = 2(\sum_{k=1}^{N} \frac{\phi_{ik}(c_1\phi_{j1k} + c_2\phi_{j2k} + \ldots + c_n\phi_{jnk})\phi_{ik}}{\Delta_{kl}^2})(\hat{\omega}_l^2 + \sigma_l^2)\sigma_l \tag{18}$$

(18) is one of the fundamental equations for active damping design. If it is satisfied, the stability condition will also be satisfied.

The previous analysis gives the necessary and sufficient stability conditions for SISO and SIMO velocity feedback. Based on these conditions, two active damping design algorithms are developed in this section

1. Constrained Least Squares Feedback Gain Computation
2. Optimal Feedback Gain Computation With Flexible Damping Factors

The goal of these algorithms is to find the feedback gain vector $\{c\}$ to achieve the given damping factors as close as possible without destabilizing the system.

4.1 Constrained Least Squares Feedback Gain Computation

Assume that n sensors are involved in the control system and that without loss of generality the first n elements of $\{c\}$ are non zero. For simplying the presentation, we redefine $\{c\}$ as a n-dimensional vector containing non zero feedback gains. Equation (18) can be rewritten in the form of the dot product of two vectors

$$\frac{1}{2(\hat{\omega}_l^2 + \sigma_l^2)\sigma_l} = \sum_{j=1}^{n} (\sum_{k=1}^{N} \frac{\phi_{ik}\phi_{jk}}{\Delta_{kl}^2})c_j = \{p_l\}^T\{c\} , \quad l = 1, \ldots, N \tag{19}$$

where $\{p_l\} \in R^n$ is a known vector whose general element p_j is $\sum_{k=1}^{N} \frac{\phi_{ik}\phi_{jk}}{\Delta_{kl}^2}$, and $\{c\} \in R^n$ is the feedback gain vector to be determined.

Assemblying all N equations, we obtain a linear matrix equation form

$$\{e\} = [P]\{c\} \tag{20}$$

where $\{e\} \in R^N$ is a known vector whose general element e_l is $\frac{1}{2(\hat{\omega}_l^2 + \sigma_l^2)\sigma_l}$, and [P] is a N × n known matrix whose lth row is $\{p_l\}^T$ defined in Equation (19).

Three different configurations about "n" are treated as follows.

4.1.1 n > N Equation (20) is under determined, and the solution vector $\{c\}$ is not unique. Regarding the physical limitations of the controller, it is always desirable to have a minimized feedback gain configuration. Hence we choose the solution vector $\{c\}$ with minimum norm. This minimum norm solution is defined as

$$\{c\} = [P]^\dagger\{e\} \quad \textit{with} \quad [P]^\dagger = [P]^T([P][P]^T)^{-1} \tag{21}$$

4.1.2 n = N   In this case, if the matrix [P] is singular, and (20) remains under determined. A singular value decomposition of [P] gives

$$[P] = [U_1 \ \ U_2]\begin{bmatrix} \Sigma_1 & 0 \\ 0 & 0 \end{bmatrix}\begin{bmatrix} V_1^T \\ V_2^T \end{bmatrix}$$

where the diagonal matrix Σ_1 contains non zero singular values of [P], $[U_1]$ and $[V_1]$ contain respectively the corresponding columns of the orthogonal matrices [U] and [V].

The minimum norm solution of $\{c\}$ is then defined as

$$\{c\} = [V_1][\Sigma_1]^{-1}[U_1]^T\{e\} \tag{22}$$

If [P] is a regular matrix, there is the unique solution

$$\{c\} = [P]^{-1}\{e\} \tag{23}$$

4.1.3 n < N   In the real world, flexible structures are mostly high-order linear dynamical systems, but the number of sensors is quite small due to physical limitations on the controller and other practical considerations. This is the case most often encountered in practical applications. In this case, Equation (20) is over determined and a least squares solution is appropriate. A standard least squares procedure can be used to find $\{c\}$ by minimizing : $J = \| [P]\{c\} - \{e\}\|$. It must be noted that the least squares solution is an approximate solution. Although this is the "best" solution in a least squares error sense, it may violate the stability condition, especially in the case where n << N. Due to these stability considerations, Least Distance Programming (LDP)[13] is suggested as a solution technique. LDP is in general used to find the solution of an over determined linear system by minimizing $\|x\|$ subject to $[P]\{x\} > \{h\}$. For the present problem, the stability condition (17) is directly used to establish a system of linear inequality equations matching the LDP form. (17) can be written as

$$\{p_l\}^T\{c\} > h_l \ , \quad l = 1, \ \ldots \ , \ N \tag{24}$$

where h_l is a positive real number chosen by the designer. It represents the stable design margin.

Assembling all N equations, we obtain the matrix inequality form required by LDP

$$[P]\{c\} > \{h\} \tag{25}$$

The detailed description of LDP and a Fortran routine can be found in Reference [13].

Several comments are in order for the case n < N

1. Although the given damping factors σ_l are involved in the computation of $\{c\}$ (see Equations (17), (20), and (24)), the expected control performance may not be achieved by a such feedback gain vector, for neither the objective function (Min $\|c\|$) nor the constraint functions ([P]$\{c\}$ > $\{h\}$) include explicitly the control performance.

2. The previous analysis does not give the existence condition of the feedback gain vector $\{c\}$ to satisfy the stability condition stated by Theorem 2 for the case n < N, (In the case n ≥ N, Equation (20) has an exact solution. This implies stability condition (17) is satisfied.) but LDP can automatically examine whether such a feedback gain vector exists by checking the constraints : $\{p_l\}^T\{c\} > h_l$. If LDP proceeds without violation of the constraints until the solution $\{c\}$ is achieved, this solution will be an optimal and stable feedback gain vector. In addition, for most practical cases, only a limited number of modes respond to the inputs of the system and the other modes are not excited. If it can be predicted which modes will not be excited, the corresponding constraints can be eliminated from LDP. If the number of excited modes is close to number of sensors, it is more likely the optimal and stable feedback gain vector can be achieved.

3. When the undamped system has N distinct eigenvalues, the controllability for proposed control law can be examined in a straightforward way. In fact, it can be easily proved that if $\phi_{ik} = 0$, the kth mode is uncontrollable.

4.2 Actuator and Sensor Location

The selection of the position of the actuator and the sensors is important for the controller design. In the previous analysis, it is assumed that the locations of the actuator "i" and the sensors "j1" to "jn" are are randomly chosen. As, in practice, the control system designers have some freedom to choose the locations of the actuator and, in particular of the sensors, some guide lines will be given for locating the actuator and sensors.

According to the comment 3 above, the controllability of the kth mode depends on the modal coefficient ϕ_{ik} , which correspond to the location of the actuator. Hence the controllability can be improved by moving the actuator. In particular, when the modes having the most important contribution to the response of the system can be predicted, the actuator's location "i" must be carefully selected, if it is possible, such that the corresponding modal coefficients ϕ_{ik} are not zero.

The selection of the sensors' location can not influence the controllability of the actual problem,

but it may influence the achievability of the desired damping factors. If the vector $\{e\}$ is in the subspace spanned by the columns of the matrix [P] (See Equation (20)), the desired damping factors can be exactly achieved. Note that each column of [P] is related to a sensor position. Assuming N positions on the structure are available for mounting the sensors, a square matrix of order N $[P_N]$ is formed in the same manner as [P] with N replacing n in Equation (19). For a set of given damping factors and a fixed number of sensors n, n columns of the matrix $[P_N]$ are selected to constitute a basis of n-dimensional subspace [P] such that the error, $\{\varepsilon\} = \{e\} - [P]\{c\}$ in approximating $\{e\}$ in this subspace, is minimal. This subspace is called the best approximating subspace for $\{e\}$. Hence the sensors' locations related to this subspace can be considered as the "best" locations in the sense of achieving the desired damping factors.

Two approaches are proposed as follows to constitute the best approximating subspace

1. Growing Dimension Subspace Construction

2. Global Orthogonal Basis Projection

4.2.1 Growing Dimension Subspace Construction

This approach starts by constructing the 1-dimensional best approximating subspace $\{p_{j1}\}$ such that $\|\varepsilon_{j1}\| < \|\varepsilon_r\|$ where

$$\{\varepsilon_{j1}\} = \{e\} - \{p_{j1}\}c_{j1}$$

$$\{\varepsilon_r\} = \{e\} - \{p_r\}c_r , \quad r \leq N \text{ and } r \neq j1$$

Then the 2-dimensional best approximating subspace is formed by searching for the second basis vector $\{p_{j2}\}$ among the rest $N - 1$ columns of $[P_N]$ such that $\|\varepsilon_{j2}\| < \|\varepsilon_r\|$ where

$$\{\varepsilon_{j2}\} = \{e\} - \{p_{j1}\}c_{j1} - \{p_{j2}\}c_{j2}$$

$$\{\varepsilon_r\} = \{e\} - \{p_{j1}\}c_{j1} - \{p_r\}c_r , \quad r \leq N \text{ and } r \neq j1, j2$$

This process is repeated until the n-dimensional best approximating subspace is found.

4.2.2 Global Orthogonal Basis Projection

The singular value decomposition can be used to create a N-dimensional orthogonal basis $[U] \in R^{N,N}$ where

$$[P_N] = [U][\Sigma][V]^T$$

The coordinates of each column of $[P_N]$, $\{p_r\}$ in this orthogonal basis form a vector $\{b_r\}$. Obviously,

$$\{b_r\} = [\Sigma]\{v_r\}$$

where $\{v_r\}$ is the rth column of $[V]^T$.

By projecting the vector $\{e\}$ onto the orthogonal basis, its coordinates vector $\{g\}$ is defined as

$$\{g\} = [U]^T\{e\}$$

According to the n largest elements of $\{g\}$, a n-dimensional orthogonal subspace can be found. By examining the projection of each column of $[P_N]$ in this n-dimensional orthogonal subspace, the n columns of $[P_N]$, which have the n largest elements corresponding to the n-dimensional subspace, are then selected. The n columns of $[P_N]$ thus selected constitute the best approximating subspace for $\{e\}$.

4.3 Optimal Feedback Gain Computation With Flexible Damping Factors

For vibration suppression in flexible structures, the control system is generally required to provide specified damping for certain modes of interest and need only maintain the stability of the other modes of the system. In fact, most damping factors σ_l and the modal frequencies $\hat{\omega}_l$ used for feedback gain computation by the algorithms presented in 4.1 are randomly chosen. The "optimal solution" for a given set of σ_l and $\hat{\omega}_l$ may not be optimal for another set of given σ_l and $\hat{\omega}_l$. In this section, an optimal procedure is developed by taking advantage of the flexibility in chosing non specified damping factors and modal frequencies of the closed-loop system. In this optimal process, the optimal variables are the feedback gains c_j, $j = 1, \ldots, n$, the non specified damping factors σ_l, $l = N_s + 1, \ldots, N$ and non specified modal frequencies $\hat{\omega}_l$, $l = N_s + 1, \ldots, N$. Denote the number of specified damping factors and modal frequencies by N_s, and assume they are arranged as 1 to N_s. The objective function is

$$Min\ J = \sum_{k=1}^{N_s} (e_i - \{p_k\}^T\{c\})^2 + w\{c\}^T\{c\}$$

subject to constraints

$$h_j < \{p_j\}^T\{c\} \quad , \quad j = 1, \ldots, N$$

$$\omega_{jl} < \hat{\omega}_j < \omega_{ju} \quad , \quad j = N_s + 1, \ldots, N$$

$$c_{jl} < c_j < c_{ju} \quad , \quad j = 1, \ldots, n$$

127

The subscript "l" denotes lower bound and the subscript "u" denotes upper bound in the constraint functions above. These constraints represent the stability condition for all modes and the physical limitations on the controller. As the velocity feedback has a weak influence on modal frequencies, the lower and upper bounds of $\hat{\omega}_j$ are set close to the corresponding undamped modal frequency ω_j. Note that for proportional damping case, $\hat{\omega}_j = \sqrt{\omega_j^2 - \sigma_j^2}$. However, for the present problem the damping provided by the control force is not proportional to the mass matrix nor to the stiffness matrix, so $\hat{\omega}_j$ is not fixed by σ_j, and it can be chosen as a variable in the optimal process.

After resolving this optimal problem, we obtain not only the optimal feedback gains, but also a set of "optimal" σ_l and $\hat{\omega}_l$. As this method does not need to specify all the damping factors and the modal frequencies of the the closed-loop system, the techniques described in section 4.2 can not be used to select the "optimal" sensors' locations before the optimization procedure, so the sensors' locations are "randomly" selected in this optimization process. However, after obtaining the "optimal" σ_l and $\hat{\omega}_l$, we can verify if the locations of the sensors are correctly selected. If it is necessary, the sensors' locations can be changed and the optimization process repeated.

5 ILLUSTRATIVE EXAMPLE

The stability condition for single input velocity feedback described above is demonstrated by a simple experimental example. The test structure is a light steel beam mounted, at the middle, on an electrodynamic shaker, as shown in Fig. 1. Considering the armature axial suspension stiffness and the damping due to Back-EMF (Electro-Motive Force) of the shaker coil, the shaker dynamics is modeled as a flexible support with viscous damping. A velocity feedback control loop is designed based on the necessary and sufficient condition (Theorem 2) to stabilize the vibration of the test structure due to the given initial conditions. For this experimental study, the initial condition is an initial displacement of one free end of the beam (Point A). Fig. 2-a is time response measured at point A. The decay of the amplitude is basically due to the damping provided by the shaker dynamics. Fig. 2-b is the spectrum of the time response of Fig. 1-a. There are three peaks in the spectrum. The biggest peak is at 6.5 Hz and two others at 60 Hz and 76 Hz respectively. The first peak corresponds to the fundamental resonant frequency of the system. The second peak (at 60 Hz) is due to 60 cycle noise in the electrical circuit and the third one may correspond to one of the higher modes of the system. As the last peaks are much smaller than the first one (-20 db), It can be concluded that only one mode responds to the given initial condition. For this particular case, the stability condition (see Equation (17)) can be simplified as

$$\beta_1 = \frac{(c_1 \phi_{j11} + \ldots + c_n \phi_{jn1})\phi_{i1}}{\Delta_{11}^2} > 0$$

Three different control configurations are discussed as follows.
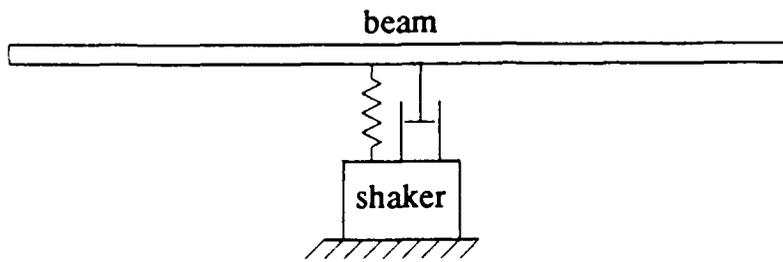
Figure 1. Test Structure

CASE 1   Sensor Mounted at Point A

The control loop scheme, as shown in Fig. 3, consists of

- An accelerometer mounted at Point A

- An analog integrator for integrating the acceleration from the sensor in order to provide velocity required by the control algorithm

- An amplifier with adjustable gain to set the feedback gain

- An electrodynamic shaker as an actuator.

The viscous damping due to the shaker back-EMF can be considered as an equivalent collocated sensor-actuator velocity feedback loop. The necessary and sufficient stability condition for this control configuration thus is

$$\beta_1 = \frac{c\phi_{A1}\phi_{O1} + c_O\phi_{O1}\phi_{O1}}{\Delta_{11}^2} > 0$$

where ϕ_{A1} and ϕ_{O1} are the modal coefficients of the first mode at the points A and O. c is the feedback gain of the control loop and c_O is the equivalent damping factor (real positive) of the shaker.

According to the stability condition, if $c\phi_{A1}$ has the same sign as ϕ_{O1}, the control system will be stable. Based on the mode shape of the first mode obtained by a finite element model, as shown in Fig. 4, ϕ_{A1} and ϕ_{O1} are both negative (or both positive, as the signs of eigenvectors are undetermined), so a positive feedback gain "c" is needed to guarantee the stability of the control

system. The time response at the point A and its spectrum are shown in Fig. 5. The first mode is significantly damped (-15 db) by applying the control force.

CASE 2   Sensor Mounted at Point B

The accelerometer is moved to point B and mounted on the other side of the beam, so the analog signal provided by the sensor is $-\ddot{x}$ This is equivalent to setting a negative feedback gain in the control loop, and if this gain is big enough such that $c\phi_{B1}\phi_{O1} > c_O\phi_{O1}\phi_{O1}$, the control system will become unstable. An unstable case is shown in Fig 8, where the first mode is destabilized.

CASE 3   Sensor Mounted at Point A and Point B

Without removing the accelerometer at point B, another accelerometer was added at point A, but mounted on the other side of the beam in order to provide a "positive" acceleration. The control scheme is shown in Fig. 7. The stability condition, in this case, can be written as

$$\beta_1 = \frac{c(\phi_{A1}\phi_{O1} - \phi_{B1}\phi_{O1}) + c_O\phi_{O1}\phi_{O1}}{\Delta_{11}^2} > 0$$

Since ϕ_{A1} and ϕ_{B1} have the same sign as ϕ_{O1} and $|\phi_{A1}| > |\phi_{B1}|$, the stability condition is satisfied. Fig. 9 shows the time response and its spectrum.

These three different control configurations implemented on the simple test structure present stable and unstable control cases. All the experimental results verify the stability condition presented in this paper.

It is interesting to note that analysts often worry about the stability and controllability of the higher modes when the control system is designed. However, in most practical cases, only few modes respond to the excitation or the inputs of the system, as shown by this simple experimental example. Thus it is very important to predict which modes will be excited by the input of the system for a given practical problem.

6   CONCLUDING REMARKS

The basic contribution of this paper is to give the necessary and sufficient stability condition for single input velocity feedback. This theory is based on the modal description of an undamped linear system. For a given feedback gain vector, it determines the stability of each mode, which is adequate for practical active damping design.

The existence condition of the feedback gain vector is not given in this paper for the case n < N.

However, it is shown that in practice, if the number of sensors is greater than the number of excited modes, such a gain vector can always be found to achieve the given damping factors and guarantee the stability of the control system.

Two active damping design algorithms, Constrained Least Squares Feedback Gain Computation and Optimal Feedback Gain Computation with Flexible Damping Factors, are described in Section 4. The first algorithm represents a direct way to find the feedback gains for the given damping factors and the modal frequencies. The second algorithm is based on an optimization process using the flexibility in chosing the damping factors and modal frequencies of the closed loop system. The objective of the optimization process is to minimize the control effort (the norm of the feedback gain vector) and to achieve designed damping factors as closely as possible. It must be noted that this is a "near optimal" solution, since the optimization package used actually can only give a local optimal solution, which depends on the given initial conditions.

The discussion in Section 4.2 gives an insight into the problem of locating the actuator and sensors. In general, a suitable location of the actuator can improve the mode controllability, and the locations of the sensors have the influence on the achievability of the given damping factors. Two approaches are proposed to systematically select the sensors' locations.

REFERENCE

[1] W. M. Wanhan , "On pole assignment in multi-input controllable linear systems", IEEE Trans. Autom. Cont. AC-12, 1967

[2] A. Jameson , "Design of a single input system for specified roots using output feedback", IEEE Trans. Autom. Cont., AC-15, 1970, pp 345-348

[3] E. J. Davison and R. Chatterjee , "A note on pole assignment in linear system with incomplete state feedback", IEEE Trans. Autom. Cont. AC-16, 1971, pp 98-99

[4] O. A. Solhein , "Design of optimal control system with prescribed eigenvalues", Int. J. Contr. 15 (1), 1972

[5] N. Munro and A. Vardulakis , "Pole shifting using output feedback", Int. J. Contr., 18 (6), 1973, pp 1267-1273

[6] H. Kimura , "Pole assignment by gain output feedback", IEEE Tras. Autom. Cont. AC-20, 1975, pp 509-516

[7] B. C. Moore , "On the flexibility offered by state feedback in multivariables systems beyond closed loop eigenvalue assignment", IEEE Trans. Autom. Cont. AC-21, 1976 pp 689-692

[8] S. Srinathkumar , "Eigenvalue/eigenvector assignment using output feedback", IEEE Trans. Autom. Cont. AC-23, 1978, pp 79-81

[9] M. M. Fahmy and J. O'Reilly , "On eigenstructure assignment in linear multivariable systems", IEEE Trans. Autom. Cont. AC-27, 1982, pp 690-693

[10] J. N. Juang, K. B. Lim, and J. K. Junkins , "Robust eigensystem assignment for flexible structures", Proc. of 1987 Guidance, Navigation and Control Conference, Monterey, CA, 1987

[11] R. E. Fennell , "An application of eigenspace methods to symmetric flutter suppression", ICASE Report No. 88-9, 1988

[12] G. A. Becus and G. Sonmez , "Eigenstructure assignment in LQR design of multivariable control system", Presented at SIAM 35th Anniversary Meeting, Oct. 1987

[13] C. L. Lawson and R. J. Handon , "Solving least square problems", Prentice-Hall Inc., Englewood Cliffs, N.J., 1974

[14] B. Porter and R. Crossley , "Modal control theory and applications", Taylor & Francis LTD, London, 1972
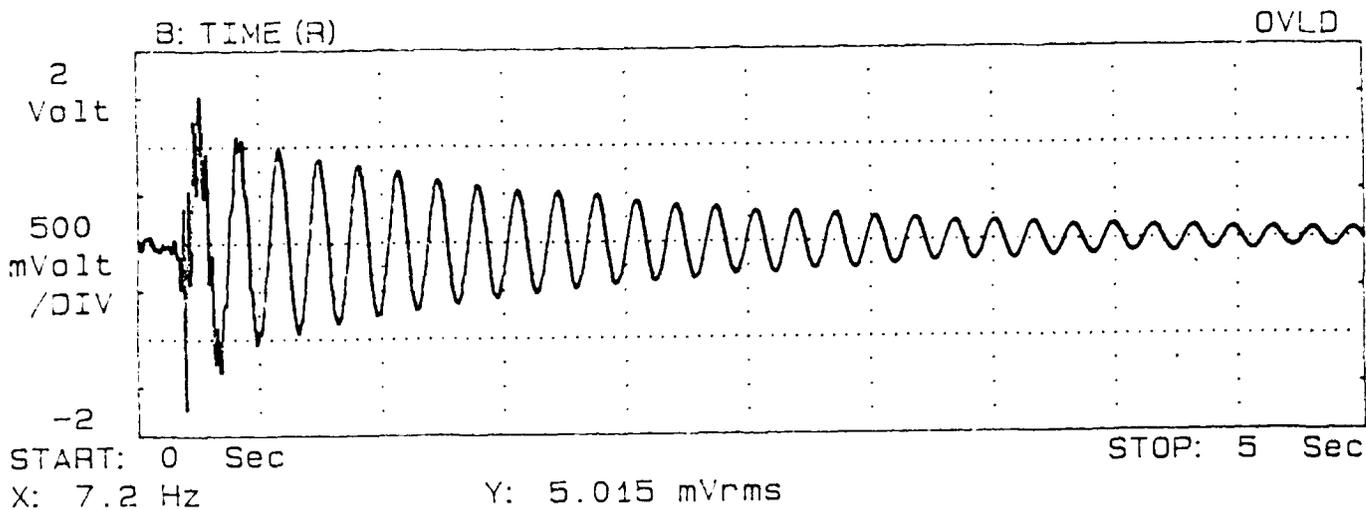
a) Time Response
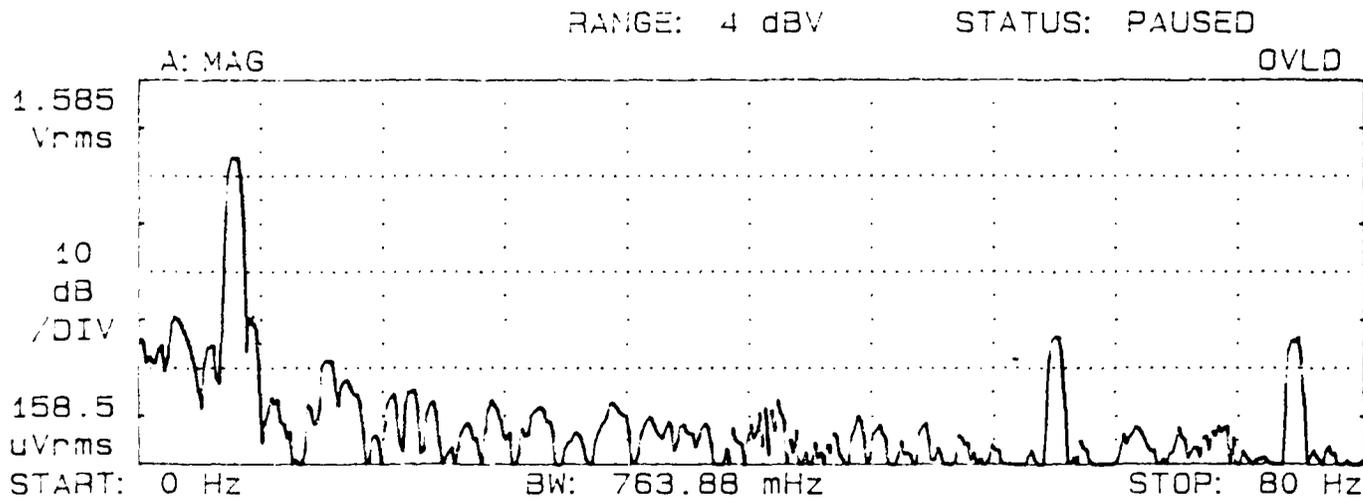
b) Spectrum

**Figure 2.** Time Response and Its Spectrum Without Control
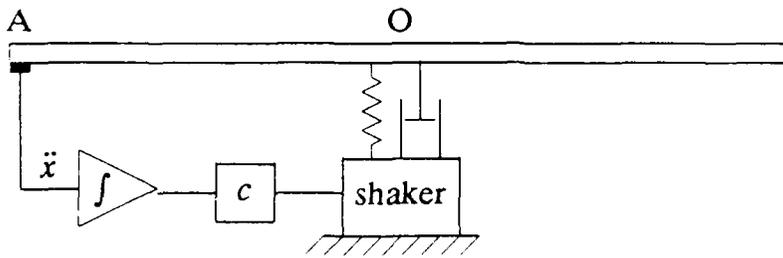
Figure 3. Control Configuration 1
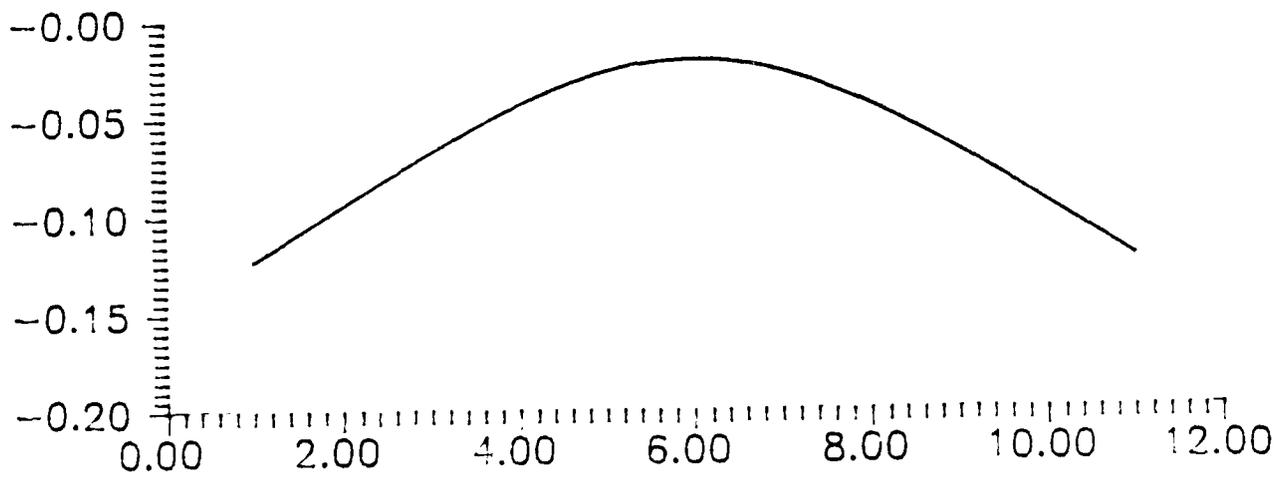

Figure 4. Mode Shape of The First Mode Based On A FEM.
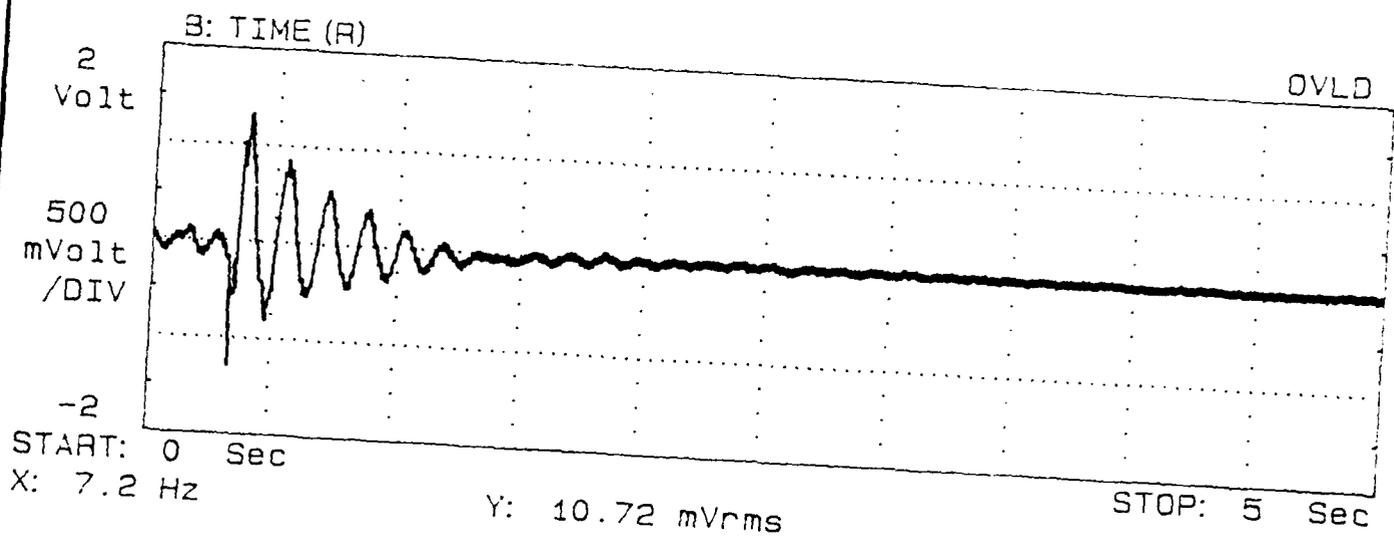
a) Time Response
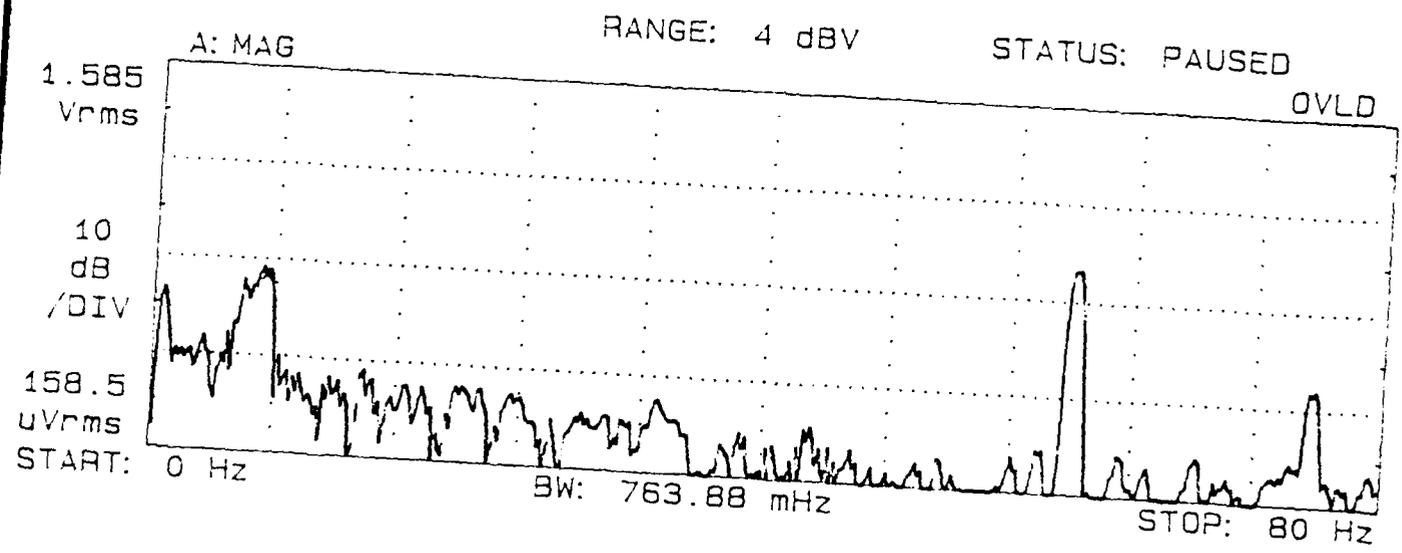
b) Spectrum

Figure 5. Time Response and Its Spectrum With Control Configuration 1
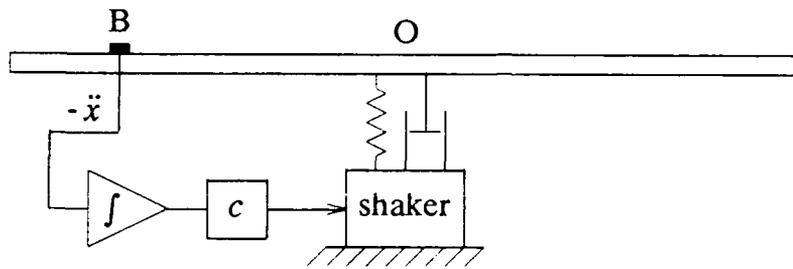
Figure 6. Control Configuration 2
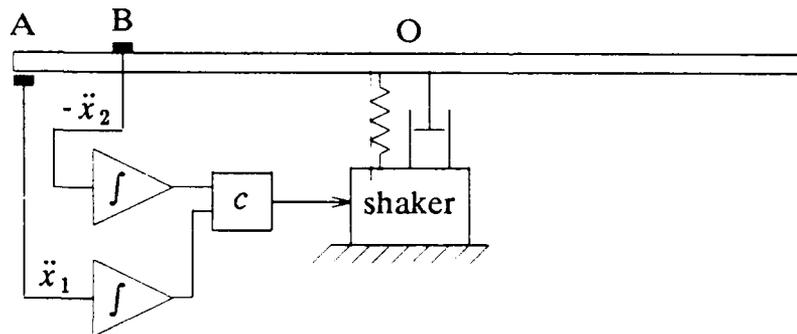
Figure 7. Control Configuration 3
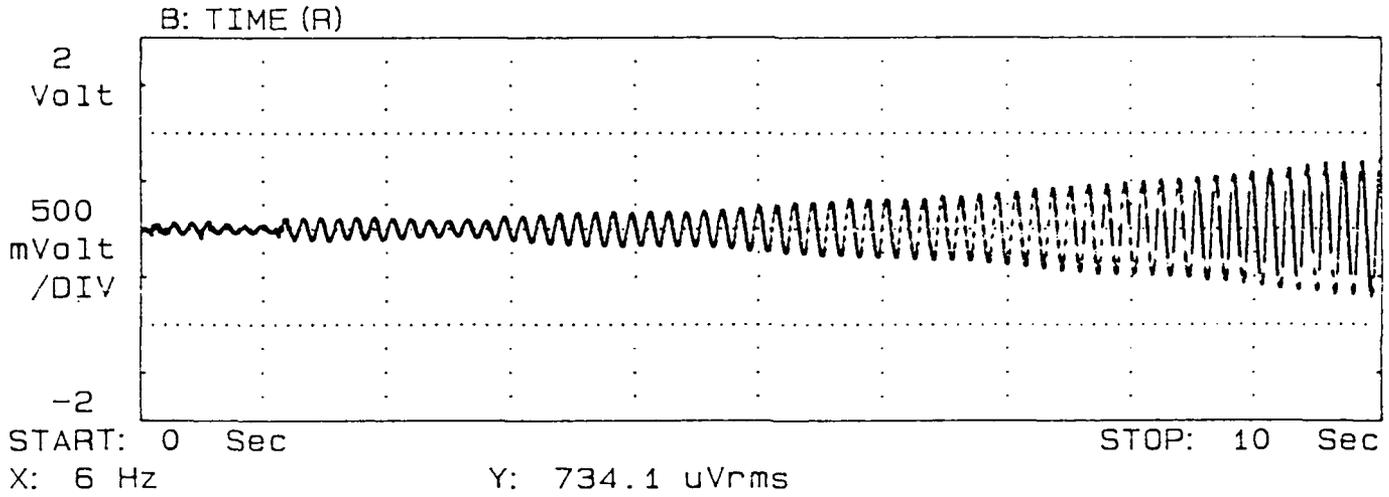
a) **Time Response**
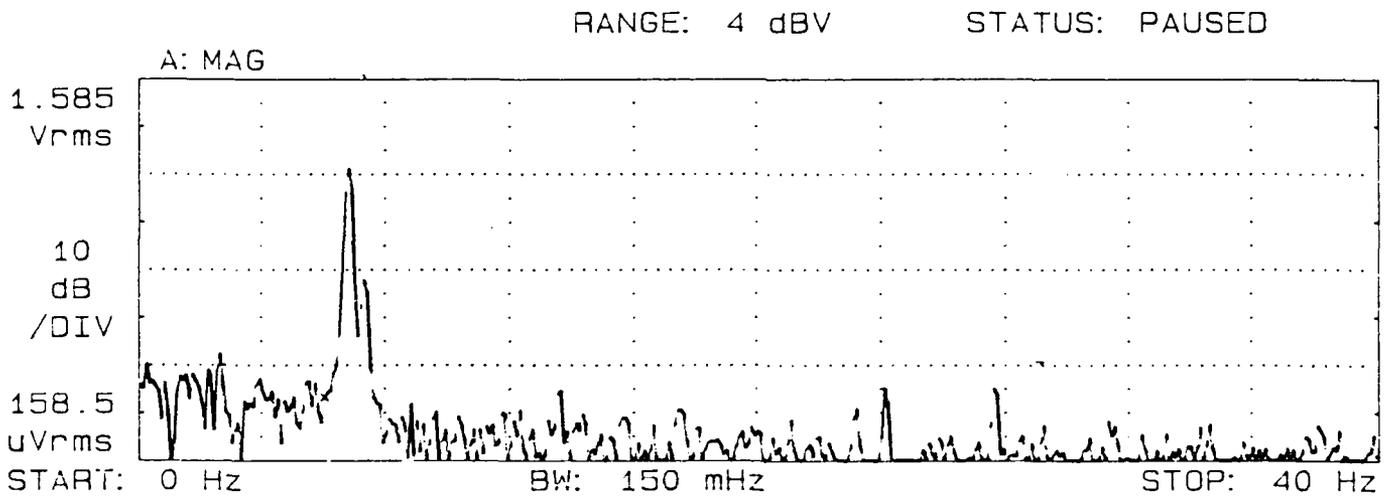
b) **Spectrum**

Figure 8. Time Response and Its Spectrum With Control Configuration 2
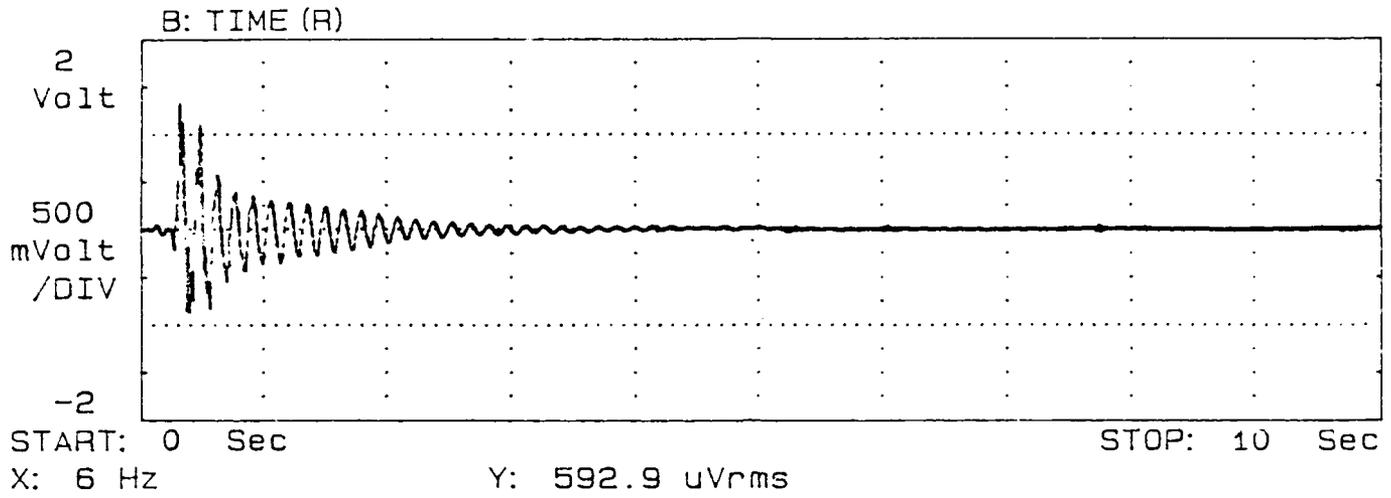
a) Time Response
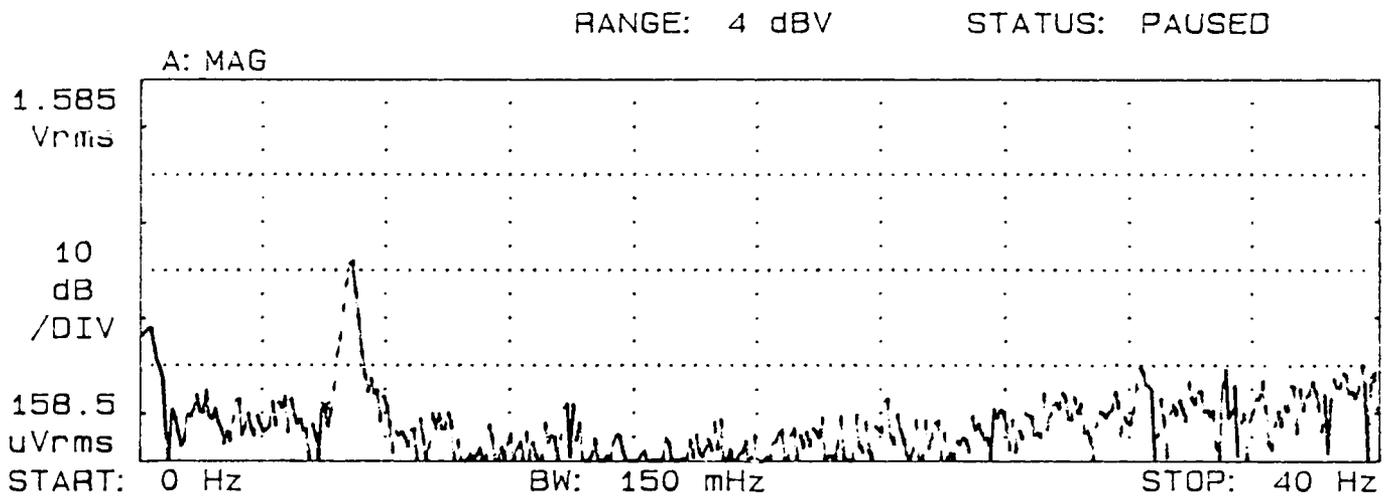
b) Spectrum

**Figure 9.** Time Response and Its Spectrum With Control Configuration 3

RELATING MATERIAL PROPERTIES AND WAVE EFFECTS IN VIBRATION ISOLATORS

M. C. Reid, S. O. Oyadiji, and G. R. Tomlinson
Department of Mechanical Engineering
Heriot-Watt University
Edinburgh, Scotland

Wave effects occurring in vibration isolators are predicted using the Love theory. It is shown that reliable complex modulus data for the viscoelastic material is required if the wave frequency predictions are to be accurate. A novel technique is described which allows the prediction of the loss factor directly from measurement of the magnitude of the complex dynamic stiffness. For a theoretical isolator model a sensitivity analysis is described, which employs the loss factor predictions to show how variations in the dynamic stiffness and damping relate to the dynamic characteristics of the isolator.

INTRODUCTION

The existence of shear and compressional waves in vibration isolators does not usually pose any serious problems with regard to the structure-borne sound transmission paths. However, in situations where the mass to be supported is large, the appropriate isolators can exhibit significant wave effects at frequencies below 300Hz [1].

Theoretical analysis of these wave effects has to date been restricted to applications of the classical theories for waves occuring in long rods. These theories have been used to predict transmissibility functions for reinforced viscoelastic pipes which show excellent correlation with experimentally obtained responses [2]. The basis for these predictions was the availability of accurate complex modulus data for the pipes, covering a wide frequency range.

The measurement of viscoelastic material properties can be achieved using a number of methods, the non-resonance dynamic stiffness technique being favoured in this case to generate modulus data over a limited frequency range, at a number of temperatures. By applying the method of reduced variables the data can be extended to cover a number of frequency decades, for a specified reference temperature.

In conjunction with this, and to overcome the problem of scatter which often affects measurements of loss factor, a technique has been developed to predict the loss factor curve directly from the measured dynamic stiffness [3, 4]. This method has successfully been applied to numerous sets of experimental data.

This paper will describe this technique for determining the loss factor and will apply it to determine the complex moduli to allow the dynamic characteristics of both a viscoelastic pipe and large vibration isolator to be

predicted. The quality assurance procedures employed by isolator manufacturers will obviously influence the dynamic properties of a particular isolator selected from a batch. The variations in isolator performance resulting from typical variations in the dynamic material properties are also investigated, in terms of a theoretical isolator model.

THEORETICAL ANALYSIS OF COMPRESSIONAL WAVES

For simple prismatic elements, the classical rod theories have been applied to predict wave effects [5]. In the first instance the Long-rod theory was used [6] but where it became necessary to account for radial effects, as in the case of vibration isolators, the Love theory was used [7].

For the viscoelastic element shown in Fig.1, expressions can be developed using the Love theory for both the point inertance and force transmissibility;
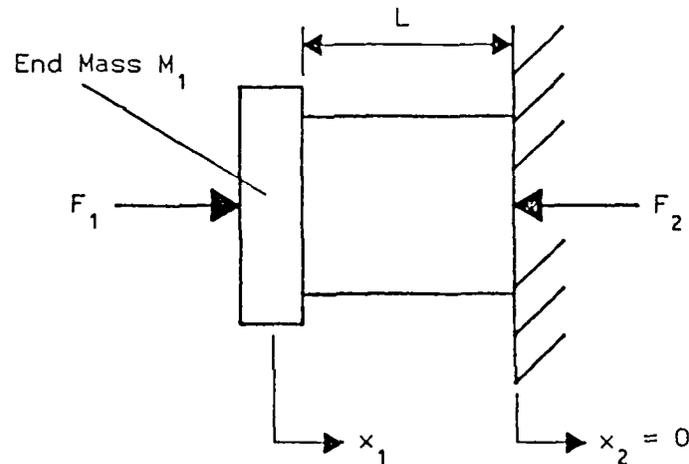
Figure 1: Axial vibration of viscoelastic element

$$IN = \frac{\ddot{x}_1}{F_1} = \frac{- M_m \sin(N^* L)}{(N^* L)[\cos(N^* L) - \gamma(N^* L)\sin(N^* L)]} \tag{1}$$

$$FT = \frac{F_2}{F_1} = \frac{1}{\cos(N^* L) - \gamma(N^* L)\sin(N^* L)} \tag{2}$$

where the governing dimensionless parameter $N^* L$ is given by

$$N^* L = \frac{(n^* L)}{[1 - (n^*)^2 \nu^2 k^2]^{1/2}} \tag{3}$$

and the complex wave number n^* is given by

$$n^* = \omega \left(\frac{\rho}{E^*} \right)^{1/2} \tag{4}$$

In equations (1) and (2), γ is the mass loading ratio M_1/M_m. For a list of other symbols refer to the Appendix. If the output end was free rather than blocked, i.e. $F_2 = 0$, then the corresponding expression for the acceleration transmissibility $\ddot{x}_2/\ddot{x}_1$ would be identical to equation (2) except that $\gamma = M_2/M_m$, with M_2 being the mass loading of the output end.

In the case of a vibration isolator, the Love theory is being used in a situation where the dimensions of the viscoelastic element are far removed from those of a long rod. It has been found that the predictions are influenced by the ratio of the isolator length to the cross section radius of gyration, L/k. Experience with the analysis of wave effects in isolators where L/k is small has indicated that the transmissibility and inertance estimates are comparable with experimental data in terms of frequency but that the predicted amplitudes are significantly in error.

For prismatic elements it is possible to quantify the magnitude of these amplitude errors. For a particular set of viscoelastic material properties and mass loading ratio, Love theory analyses can be conducted for various L/k ratios ranging from a thin rod to a squat isolator. In each case the predicted amplitudes at the wave frequencies would be recorded. As the mass loading in constant, the frequency separation between the waves and the mass/spring resonance will also be constant. Thus, in terms of transmissibility, the vibration amplitudes at the wave frequencies should also be invariant.

As an example, for the parameters listed below, transmissibility estimates were calculated for values of L/k in the range 1 to 10. The variation in the predicted amplitudes at the first two wave frequencies are shown in Fig.2.

$$E^* = 7.0E6(1 + 0.07j) \ N/m^2 \ ; \ \rho = 1000 \ kg/m^3 \ ; \ \gamma = 4$$
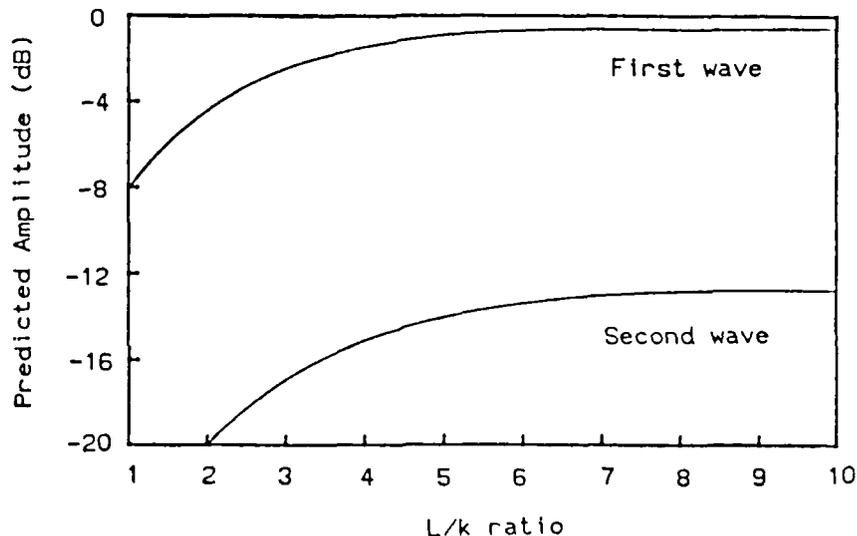
Figure 2: Variation in predicted amplitudes at wave frequencies using the Love theory

From Fig. 2 it can be clearly seen that for both waves the predicted amplitudes drop sharply as L/k becomes small. In the case of the first wave, significant errors occur for L/k < 5, such that at L/k = 2 the error is 4 dB. At the second wave the errors are significant for L/k < 8 and in some situations the Love theory does not predict the second wave as the denominator

of equation (2) tends to zero. However, this calculation demonstrates that when using the Love theory to predict wave effects for isolators, the amplitude errors due to small L/k ratios can be quantified.

In order that the frequency predictions are accurate, it is imperative that the complex modulus for the material is known over a wide frequency range. In many cases the analysis is conducted assuming E^* invariant with frequency and this results in significant errors in terms of both frequency and amplitude (as the ratio of the wave frequency to mass/spring frequency is incorrect) of the predicted wave effects.

For example,. the viscoelastic pipe and vibration isolator shown in Fig.3 have been analysed using the Love theory with constant E^* values. The predicted dynamic behaviour of these elements is compared to experimental data in Figs.4 and 5 and clearly the errors in the prediction of the wave frequencies are significant, as high as 15%. This emphasises the need to measure reliable complex modulus data.
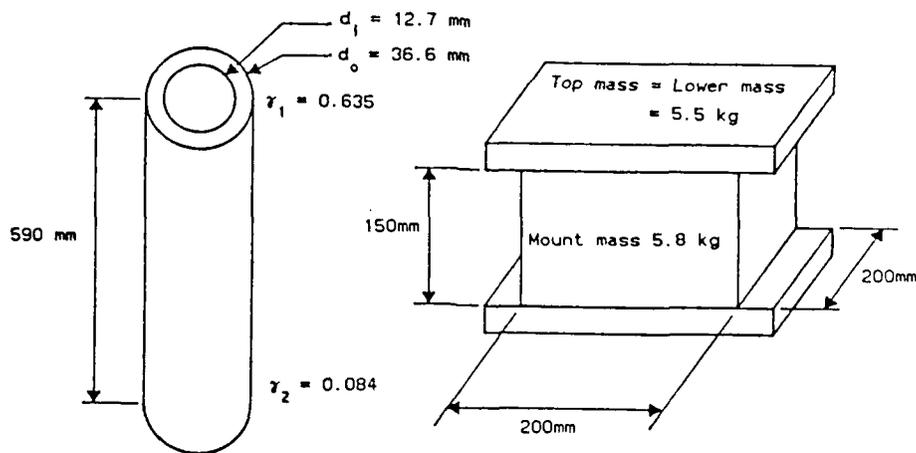

Figure 3: Viscoelastic components for analysis
(i) Reinforced pipe (ii) Isolator

Figure 5

Comparison of inertance prediction
for the isolator assuming constant
complex modulus with experimental
data

Figure 4

Comparison of transmissibility
prediction for the reinforced pipe
assuming constant complex modulus
with experimental data

143

The test method chosen in this case to generate the basic dynamic stiffness data is a non-resonance technique, as shown in Fig.6. In this method it is assumed that the frequency range of excitation is well below any resonances associated with the material sample or the test rig. The output end of the sample is rigidly mounted, with a harmonic excitation signal applied at the unconstrained end. The ratio of the output force to the input displacement gives the complex dynamic stiffness, K^*.
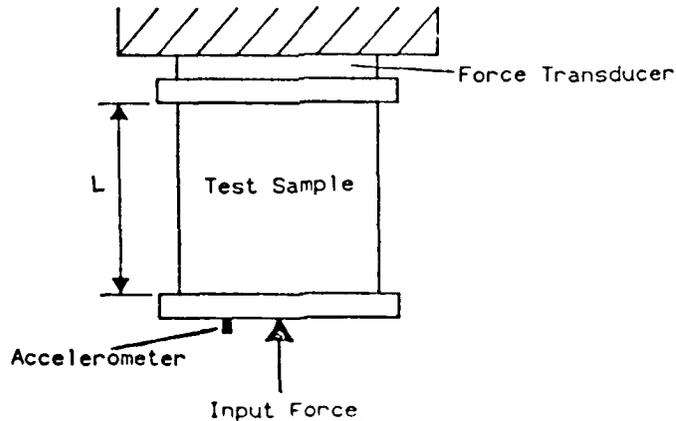
Figure 6: Measurement of dynamic stiffness using non-resonance technique

The dynamic stiffness can then be related to E^* by

$$E^* = \frac{K^* L}{C}$$
(5)

where C characterizes the shape of the test sample cross-section.

The above test is conducted over a fixed frequency range (say 20 to 80Hz) and repeated at a number of different temperatures. The method of reduced variables is then employed to generate a material master curve for the magnitude of E^* over a wide frequency range [8]. A polynomial equation is then fitted to the master curve to provide a compact representation of the modulus data. An idealised curve for a viscoelastic material is shown in Fig.7 which indicates three distinct regions; rubbery, transition and glassy. This modulus data is then used to predict the loss factor behaviour.
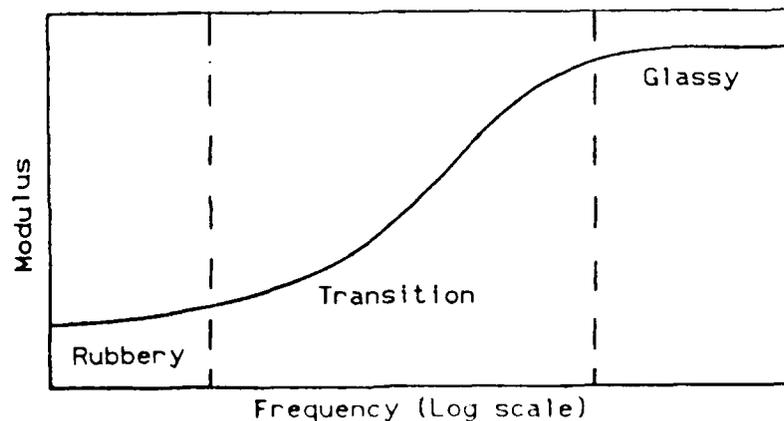
Figure 7: Complex modulus of ideal viscoelastic material

PREDICTION OF LOSS FACTOR

It has often been found that experimental measurements of loss factor are subject to large uncertainties, resulting mainly from the difficulties of measuring very small phase differences. In order to overcome this problem a technique first postulated by Vinh [9] was developed to relate the magnitude of the complex modulus to the loss factor [3,4]. This method utilises the fact that the real and imaginary parts (i.e. magnitude and phase) of the response of an analytic system are uniquely related and hence knowing the real part, the imaginary part can be determined [10]. The method is briefly described below.

The frequency response of a system $F^*(j\omega)$ due to an impulse is given by

$$F^*(j\omega) = A_1 \int_0^\infty e^{-j\omega t} f(t) dt \tag{6}$$

where $f(t)$ is the system impulse response. As $F^*(j\omega)$ will be a continuous function it can also be expressed in terms of the zeroes and poles (z_i and q_i) as the ratio of two polynomials,

$$F^*(j\omega) = A_2 \frac{\sum_{i=1}^{n} (z_i + j\omega)}{\sum_{i=1}^{m} (q_i + j\omega)} \tag{7}$$

Where $F^*(j\omega)$ is a function such as the modulus of a viscoelastic material, m and n are equal positive integers and the zeroes and poles form an alternating series of increasing magnitude [11],

$$z_1 < q_1 < z_2 < q_2 < \ldots \ldots < z_n < q_n \tag{8}$$

Equation (7) can be converted to logarithmic form, resulting in expressions for the modulus and loss angle of $F^*(j\omega)$ in terms of the zeroes and poles,

$$F = |F^*(j\omega)| = \sum_{i=1}^{n} \log \left[z_i^2 + \omega^2\right]^{1/2} - \sum_{i=1}^{n} \log \left[q_i^2 + \omega^2\right]^{1/2} + \log A_2 \tag{9}$$

$$\delta = \sum_{i=1}^{n} \arctan \left[\frac{\omega}{z_i}\right] - \sum_{i=1}^{n} \arctan \left[\frac{\omega}{q_i}\right] \tag{10}$$

Thus in order to determine the loss angle (and hence the loss factor as $\eta = \tan \delta$) it is necessary to establish the zeroes and poles of $F^*(j\omega)$ from the modulus data. This is achieved via a graphical representation of the modulus.

If one considers the following function,

$$B^*(j\omega) = \frac{1 + jT_1\omega}{1 + jT_2\omega}$$ (11)

then in terms of logarithmic coordinates the modulus is given by

$$B = \log|B^*(j\omega)| = \log\left[1 + T_1^2\omega^2\right]^{1/2} - \log\left[1 + T_2^2\omega^2\right]^{1/2}$$ (12)

and this can graphically be approximated by two horizontal lines, joined by a line of gradient 1, intersecting at $\omega = \frac{1}{T_1}$ and $\omega = \frac{1}{T_2}$, i.e. intersecting at the zero and pole of $B^*(j\omega)$.

Returning to $F^*(j\omega)$ and applying the same concept it can be seen that if one were to calculate $\log|F^*(j\omega)|$ and approximate it by a series of alternating horizontal lines and lines of gradient 1, then the zeroes and poles of $F^*(j\omega)$ would be given by the frequencies of the points where these lines intersect. Having determined the zeroes and poles, equation (10) can be applied to calculate the loss factor.

As the experimental modulus data will probably cover a frequency range which does not include the low and high frequency horizontal asymptotes, which occur for the modulus of a viscoelastic material as shown in Fig.7, errors will occur in the calculated loss factor. However, if the loss factor is calculated over a frequency range which has lower and upper bounds at least one decade above and below those of the measured data, the maximum error in the loss factor will be 10%.

In order to validate this technique, numerous sets of published modulus data were analysed with the predicted loss factor being compared to the published values [12]. The results indicated excellent correlation for a wide range of viscoelastic materials as shown in Figs. 8 and 9 for perspex and poly-iso-butylene.

At present, in order to approximate the modulus curve, many zeroes and poles may have to be calculated, resulting in a time-consuming computation. It may be possible to develop a suitable expression for the modulus curve in terms of fractional derivatives such that the number of steps required for the modulus approximation may be drastically reduced [13, 14] This possibility is currently being investigated.
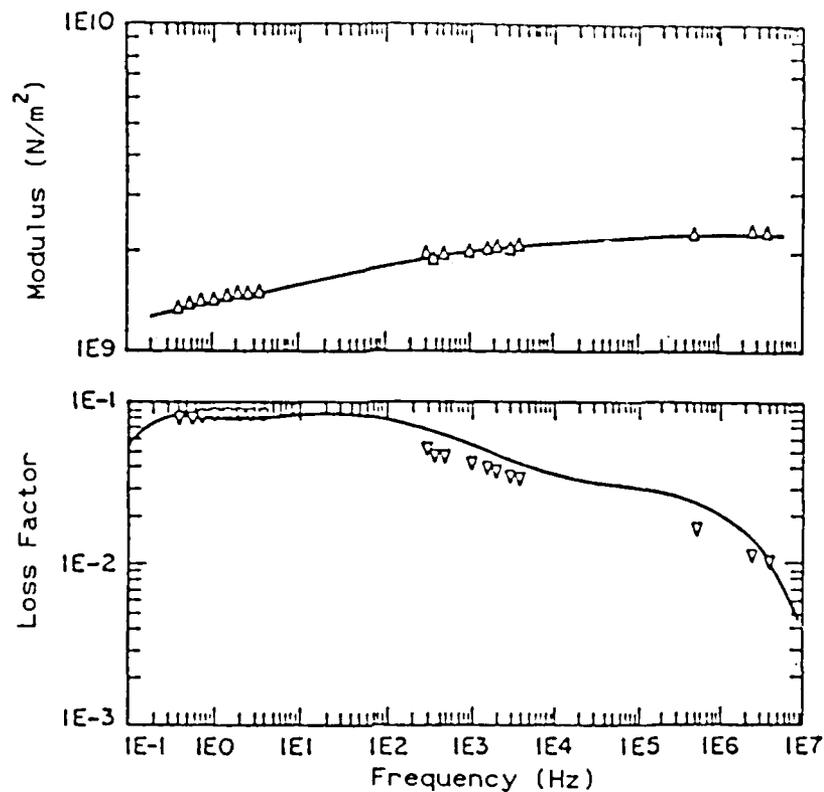
Figure 8: Master curves of shear modulus and loss factor for perspex at 21°C
Δ, measured modulus data; ∇, measured loss factor data
——, approximation to modulus data and predicted loss factor data
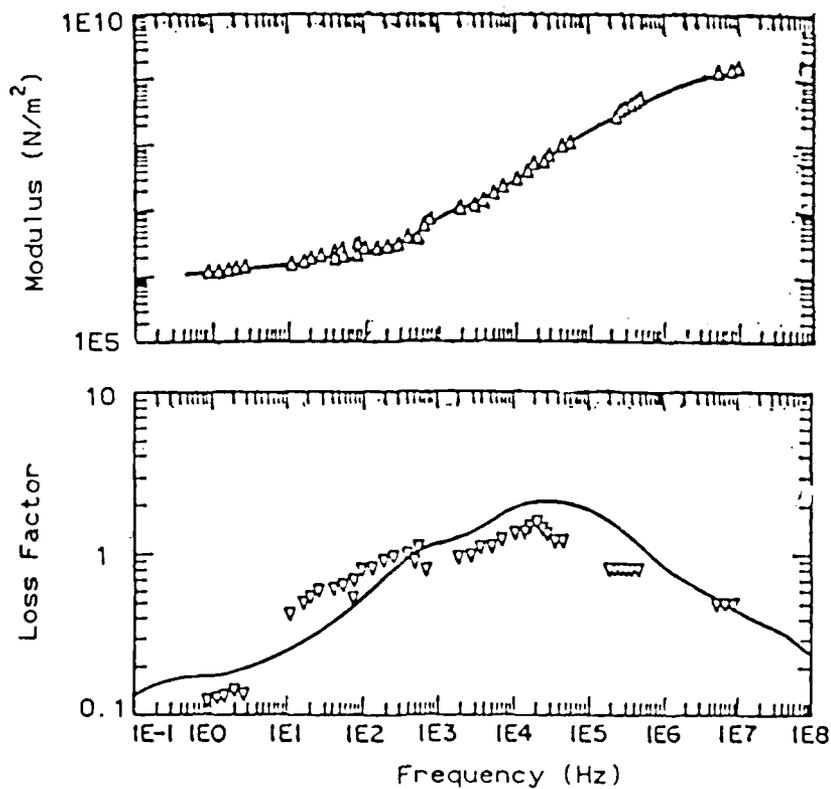
Figure 9: Master curves of shear modulus and loss factor for P-I-B at 21°C
Δ, measured modulus data; ∇, measured loss factor data
——, approximation to modulus data and predicted loss factor data

For the reinforced pipe shown in Fig.3, tests were conducted to measure the dynamic stiffness and hence to determine the modulus master curve [8]. The loss factor was then predicted as shown in Fig.10. The axial dynamic stiffness characteristics of the isolator have not yet been measured. However, shear modulus data for a similar type of compound was available. In order to demonstrate the effect of analysing the isolator using a variable modulus, the shear data was factored assuming $E = 3G$ and the loss factor predicted. The resulting modulus curves are shown in Fig.11, where it can be seen that the loss factor is predicted over two frequency decades less than the measured modulus data.

Love theory predictions of the dynamic behaviour of both components were obtained using the generated material properties and are compared to experimental results in Figs.12 and 13. It is clear that the frequencies of the predicted wave effects are now comparable with those obtained from experimental tests on the components. For the reinforced pipe the analysis has accurately predicted the amplitudes at the wave frequencies, whereas for the isolator these are in error. This is attributable to the Love theory errors discussed previously and to the material properties being inaccurate.
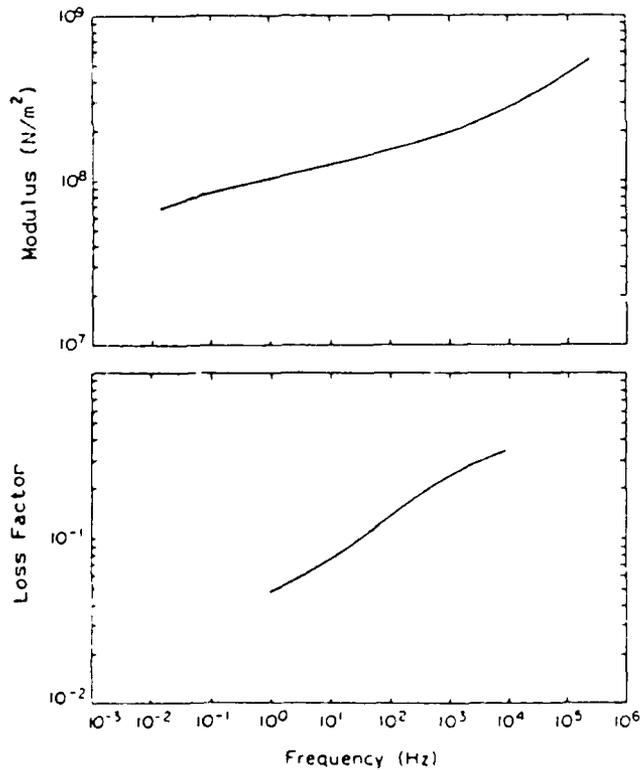
Figure 10
Complex modulus master curves for the reinforced pipe
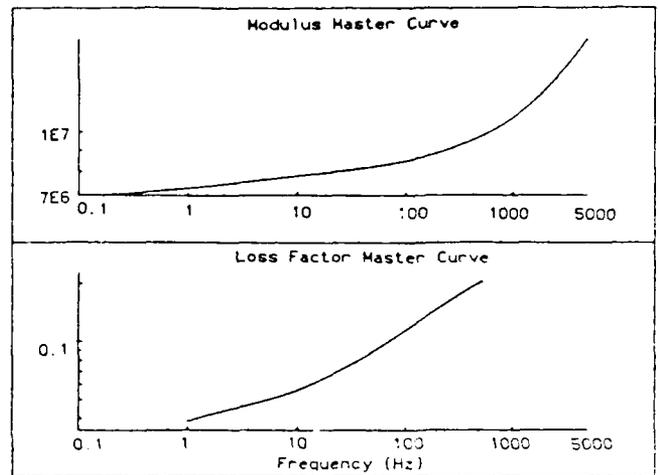
Figure 11
Complex modulus master curves for the isolator
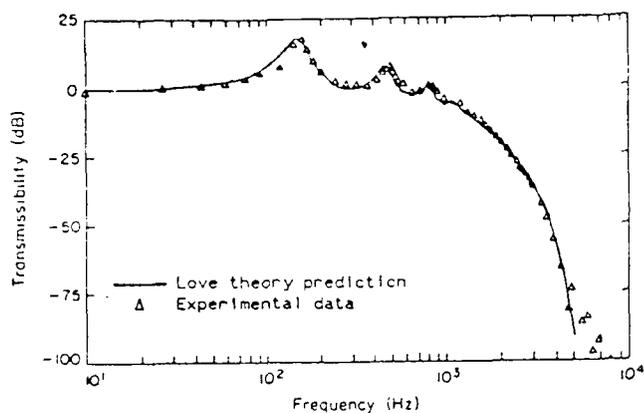
Figure 12
Comparison of transmissibility
prediction for the reinforced pipe
using variable complex modulus
with experimental data
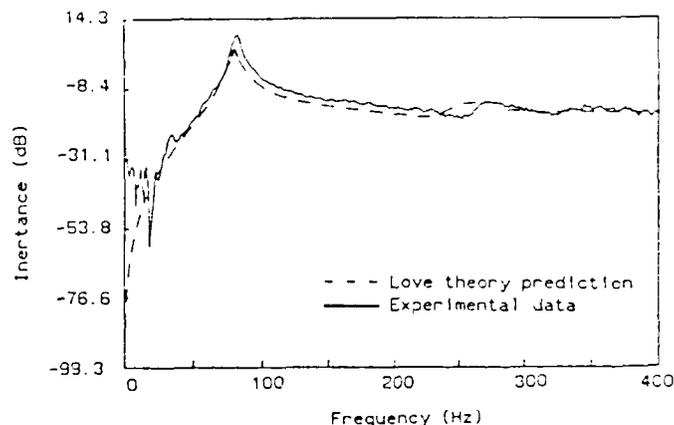
Figure 13
Comparison of inertance prediction
for the isolator using variable
complex modulus with experimental
data

EFFECT OF MATERIAL PROPERTY VARIATION ON ISOLATOR PERFORMANCE

In order to assess how variations in the material properties of a
particular isolator, resulting from variations in the composition of the
viscoelastic material which will be controlled by the quality assurance system
operated by the manufacturer, might effect the dynamic performance of the
isolator a theoretical analysis was conducted on the isolator shown in Fig.14.
The output end is assumed rigidly blocked, the L/k ratio is 2.4 and $\gamma = 1.6$.
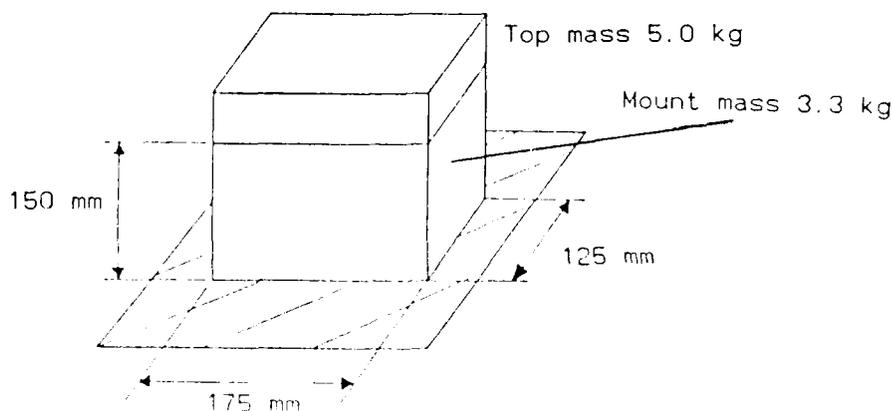
Figure 14: Theoretical isolator for sensitivity analysis

A complex modulus function similar to that obtained for the large isolator in Fig.3 was generated to represent the properties of the isolator. The resulting modulus master curves and the corresponding Love theory prediction of force transmissibility are shown in Figs.15 and 16 respectively. The transmissibility curve clearly indicates a mass/spring resonance at 52 Hz with wave effects at 213 and 336 Hz.
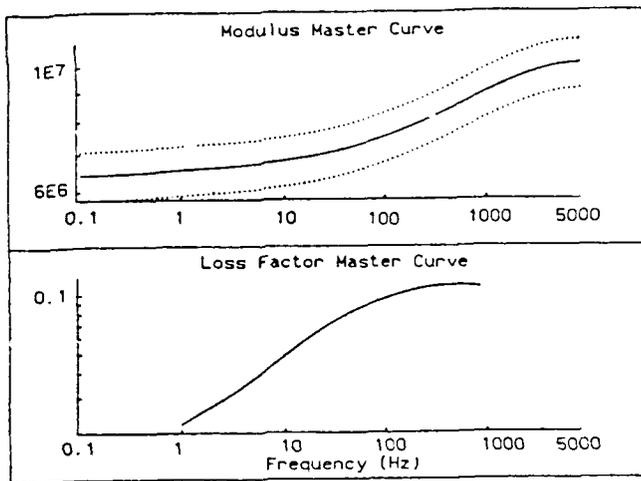
Figure 15
Assumed complex modulus master curves
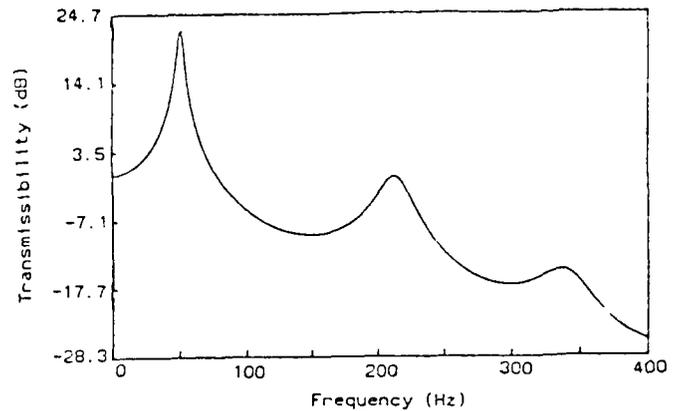
Figure 16
Force transmissibility prediction for isolator using the Love theory

Manufacturers have stated that between different batches of a particular isolator the stiffness variation, and hence the modulus variation, may be of the order of ±10%. For the modulus curve in Fig.15 the reference value was taken to be the modulus value at 100 Hz. The dotted lines indicate 10% of this reference value being added to and subtracted from the original modulus curve. Within the resulting envelope different types of modulus variation were investigated;

(1) It was assumed that the modulus curve moved to the upper dotted line on Fig.15 i.e. that the modulus was increased by a constant value. As the shape of the modulus curve was unchanged, the predicted loss factor curve was also unchanged, in terms of shape and magnitude. Likewise when it was assumed that the modulus curve was decreased by a constant value, i.e. moving to the lower dotted line on Fig.15, the loss factor curve was again unchanged.
Thus, modulus curves which are of the same shape share the same loss factor curve. The predicted transmissibility functions for these two cases are shown in Figs.17 and 18. Comparing these to Fig.16 it can be seen that the frequencies of the predicted wave effects have changed significantly. These frequency changes were approximately proportional to the square of the change in modulus, as would be expected. However, as the loss factor curve was unchanged and as the ratios between the wave frequencies and mass/spring frequency was maintained, the amplitudes of the wave resonances were also unchanged.
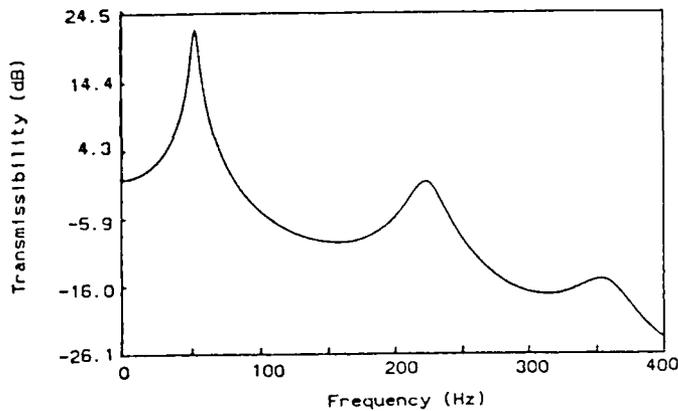
Figure 17
Force transmissibility prediction for
the isolator using the master curves
for the modulus increased by 10%
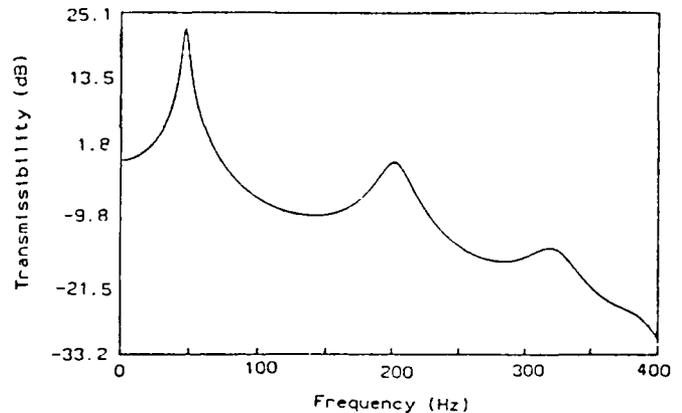
Figure 18
Force transmissibility prediction for
the isolator using the master curves
for the modulus decreased by 10%

(2)   Changes to the shape of the modulus curve were investigated.   The
       reference modulus value at 100 Hz was held constant. In the first
       instance the modulus value at 0.1 Hz was increased by 10% with the value
       at 10^4 Hz being decreased by 10%.   This was then repeated with the modulus
       variations reversed i.e. the value at 0.1 Hz was decreased by 10% and the
       value at 10^4 Hz was increased by 10%.   The loss factor curves were
       predicted in each case as shown in Figs.19 and 20 respectively.
       In the first case, the slope of the modulus curve has been reduced
       resulting in a decrease in the predicted loss factor values whereas in
       the second situation the slope is increased, in general increasing the
       damping levels.

       For both these situations, predictions of the force transmissibility were
       made and these are shown in Figs.21 and 22.   Compared to the initial
       prediction in Fig.16, the resonance frequencies have varied by only ±2 Hz
       whereas the amplitudes have changed dramatically by up to 5dB.   Obviously
       different results would have been obtained by fixing a different
       reference point on the original modulus curve, but this is only an
       illustration of the variations in dynamic performance of the isolator
       which might occur.
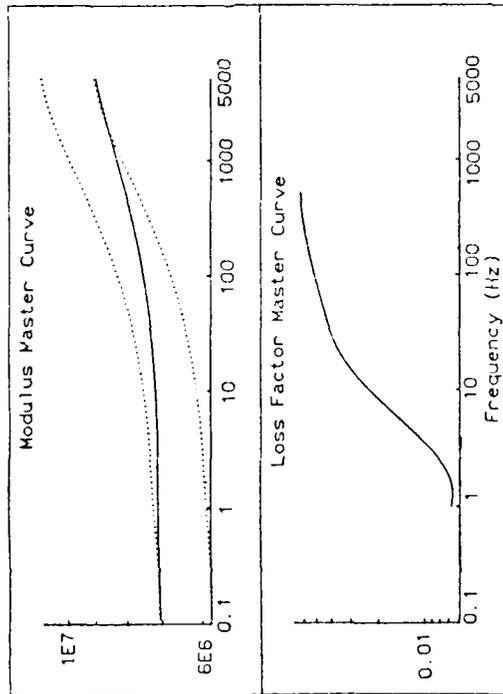
Figure 19
Modulus master curves resulting in
the lowest damping levels
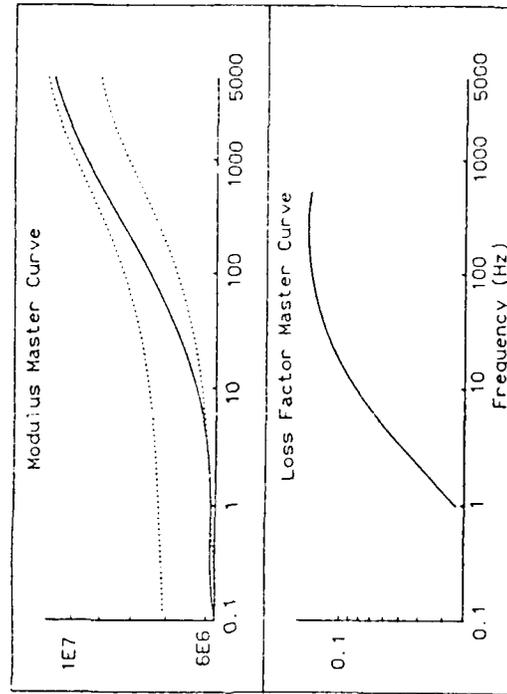
Figure 20
Modulus master curves resulting in
the highest damping levels
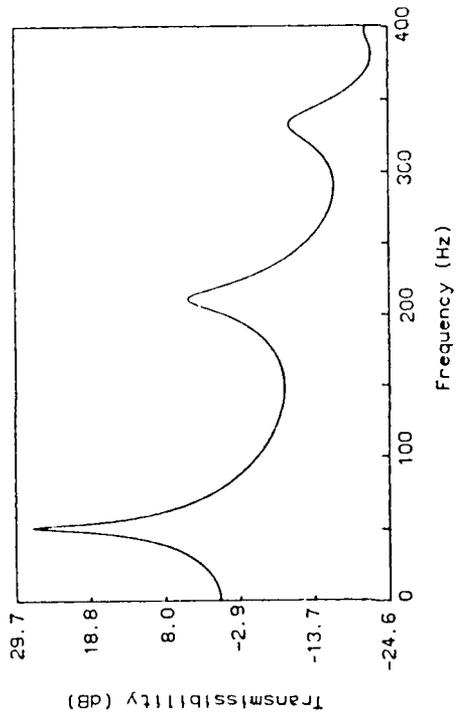
Figure 21
Force transmissibility prediction for
the isolator using the lower damping
modulus master curves in Fig.19
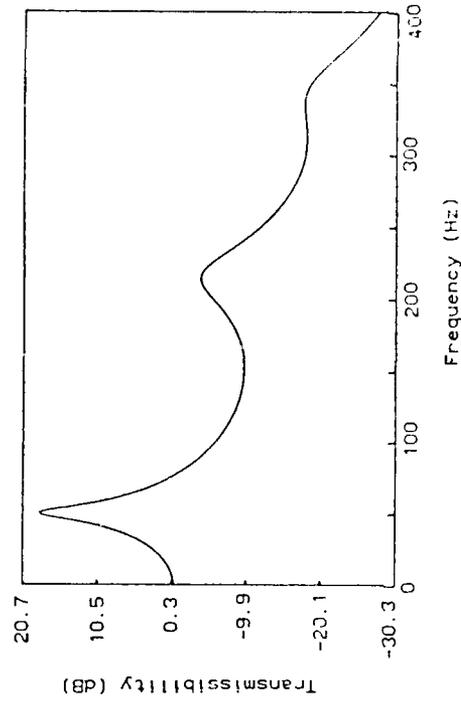
Figure 22
Force transmissibility prediction for
the isolator using the higher damping
modulus master curves in Fig.20

CONCLUSIONS

It has been shown that the Love theory can be applied to predict compressional wave effects in vibration isolators. In terms of transmissibility functions, any amplitude errors resulting from the small L/k ratios of the isolators can be quantified. However, the most important factor with regard to the prediction of both frequencies and amplitudes is the availability of reliable complex modulus data.

A method has been described which allows one to predict damping data for a viscoelastic component or material directly from a measured modulus master curve, avoiding 'the problems associated with phase measurement. This technique has been successfully applied to predict damping curves for a wide range of viscelastic materials.

The variations in isolator dynamic performance which might result from variations in material properties have been discussed. From a sensitivity analysis conducted for a theoretical isolator it has been shown that the complex modulus variations can significantly affect both frequencies and amplitudes of the predicted wave effects. This emphasises the need for stricter quality assurance techniques to be employed by isolator manufacturers.

REFERENCES

1   Tomlinson, G.R. and Milas, P.
    Impulse testing techniques applied to large vibration isolators
    3rd Inter.Conf. on Recent Advances in Structural Dynamics,
    Southampton 1988

2   Oyadiji, S.O.
    Vibration Transmissibility Characteristics of Reinforced Flexible Pipes
    PhD Thesis, University of Manchester, 1983

3   Kennedy, I.
    Vibration Transmissibility Characteristics of Fibre and Steel Reinforced
    Flexible Pipes
    PhD Thesis, University of Manchester, 1987

4   Kennedy, I. and Tomlinson, G.R.
    Torsional Vibration Transmissibility Characteristics of Reinforced
    Viscoelastic Flexible Pipes
    Journal of Sound and Vibration (1988), Vol.122(1), pp149-169

5   Snowdon, J.C.
    Vibration and Shock in Damped Mechanical Systems
    John Wiley & Sons Inc., 1968

6   Harrison, M., Sykes, A.O. and Martin, M.
    Wave Effects in Isolation Mounts
    Journal of Acoustical Society of America, (1962), Vol.24, pp62-71

7   Love, A.E.H.
    A Treatise on the Mathematical Theory of Elasticity, Vols.1 and 2
    Cambridge University Press, (1928)

8   Oyadiji, S.O. and Tomlinson, G.R.
    Determination of the complex moduli of viscoelastic structural elements by
    resonance and non-resonance methods
    Journal of Sound and Vibration (1985), Vol.101, pp277-298

9   Vinh Tuong, N.P.
    Sur le passage du regime harmonique au regime transitoire viscoelastique
    Memorial de l'Artillerie Française (1967)

10 Guillemin, E.A.
    Synthesis of Passive Networks
    John Wiley & Sons (New York), 1965

11 Bland, D.
    The Theory of Linear Viscoelasticity
    Pergamon Press, Oxford (1960)

12 Nashif, A.D., Jones, D.I.G. and Henderson, J.P.
    Vibration Damping
    John Wiley & Sons, New York (1985)

13 Bagley, R.L.
    A Theoretical Basis for the Application of Fractional Calculus to
    Viscoelasticity
    Journal of Rheology (1983), Vol.27, pp201-210

14 Torvik, P.J. and Bagley, R.L.
    Fractional Derivatives in the Description of Damping Materials and
    Phenomena
    American Society of Mechanical Engineers: The Role of Damping in Vibration
    and Noise Control - DE-Vol.5

APPENDIX - LIST OF SYMBOLS

Symbol	Description
A_1, A_2	arbitrary constants
B^*	arbitrary complex function
C	cross-section shape factor
E^*	complex dynamic modulus
F^*	frequency response function
F_1, F_2	forces
K^*	complex dynamic stiffness
L	length of viscoelastic element
M_m	mass of viscoelastic element
M_1, M_2	end masses
T_1, T_2	time constants
e	exponential constant
f	frequency
J	$(-1)^{1/2}$

k	radius of gyration
n^*	complex wave number
q_i	pole of function
t	time
x_1, x_2	displacements
z_i	zero of function
ω	radian frequency
δ	loss angle
γ	mass ratio
ρ	mass density
η	loss factor
ν	poisson ratio

COMPENSATION FOR ACTUATOR DYNAMIC EFFECTS
USING MODEL FOLLOWING ADAPTIVE CONTROL

Q. Zhang, S. Shelley, and D. L. Brown
Structural Dynamics Research Laboratory

G. L. Slater
Department of Aerospace Engineering and Engineering Mechanics

University of Cincinnati
Cincinnati, OH 45221

This paper focuses on using force feedback to compensation for loss in amplitude and phase shift of the force applied to a structure by an electrodynamic shaker. A mathematical model of an electrodynamic shaker is given and two compensators are described. The first compensator uses direct force deviation feedback. This compensator is easy to implement, but its application is restricted to a low frequency bandwidth. The second compensator is based on model reference adaptive control theory. It assumes the shaker-amplifier system is a non-linear, time varying system, and for compensator design only knowledge of the boundary values of the shaker parameters is required. Numerical and experimental results are shown to valid of the proposed methods.

1 INTRODUCTION

The force applied to a structure by an actuator system may deviate significantly from the desired force due to actuator dynamics and structure-actuator interaction. This is sometimes a concern in modal analysis and is always of importance in active vibration control, particularly when dealing with flexible structures. Therefore the actuator dynamics problem has increasingly drawn the attention of mechanical and control engineers.

Some analytical and experimental studies have been done for modeling and understanding actuator dynamics and structure-actuator interaction. Inman et al.[1] modeled an electromechanical actuator as a second order linear system and pointed out that the actuator dynamics become important if the first natural frequency of the structure falls below the break

frequency of the actuator. Olsen[2] investigated experimentally the dynamics of electrodynamic shakers and discussed the influence on the quality of the resulting frequency response measurements in modal analysis. Juang et al.[3] presented the results of a successful slewing control of a solar panel based on a combined actuator-structure model. However, in the case where no information on the structure is available before the structure is excited by the actuator, it is impossible to either study analytically the interaction between the actuator and the structure or build up a combined model. The purpose of the present paper is to design a simple control loop to compensate for actuator dynamics such that the force applied to the structure is equal (or close) to the desired force.

The actuator system studied in this paper is a voltage amplifyer - electrodynamic shaker system which is commonly used in modal analysis and other vibration tests. The results obtained for the electrodynamic shaker can easily be extended to other type of actuator systems. The shaker dynamics compensator is designed by using the following two control strategies : 1) Direct Force Deviation Feedback (DFDF); 2) Model Reference Adaptive Control(MRAC).

For the first algorithm, the difference between the desired force and the force measured by a load cell on the structure is directly fed back to the input of the actuator. It is assumed the inductance of the electrical circuit of the actuator is neglectable. This assumption is valid for a sufficiently low frequency range. The analysis shows that the corruption of the available force of the shaker due to the interaction with the structure can be significantly reduced by using DFDF. The stability criterion and the limitation of this method are also discussed in this paper. Considering the modeling uncertainty of the actuator system and its parameter variation due to temperature change and other exterior disturbances, the second compensator : adaptive compensator based on Lyapounov's stability theorem is proposed. Assume the desired force is represented by a first order linear time invariant differential equation. The control loop parameters are chosen such that the "error model", whose variable is the deviation of the available force of the shaker from the desired force, is asymptotically stable. This implies that the force applied to the structure follows the desired force. The advantage of this method is that it only requires knowledge of the lower and higher boundaries of the characteristics of the actuator system and it disregards the nonlinearity of the interaction between the structure and the actuator.

The proposed methods are appled to an electrodynamic exciter : MB Modal 50 combined with a light cantilever beam. The simulation and experimental results will be presented to demonstrate and compare the effectiveness of these two compensators.

2 MATHEMATICAL MODEL OF ELECTRODYNAMIC SHAKER

For the purpose of analysis, the electrodynamic shaker is represented by electrical components and mechanical components. The circuit of the electrical components, which consist of a voltage

amplifyer and the coil of the shaker, is shown in Fig.1. By using Kirchoff's loop law, the relation between the input voltage v_a and the current i_a is established

$$v_a = R_a\, i_a + L_a\, \frac{d\, i_a}{dt} + \beta_a\, \dot{x}_a \tag{1}$$

where R_a is the sum of internal resistance of the amplifyer and that of the shaker coil, L_a is the inductance, β_a is the back-EMF (electro-motive-force) constant, and $\dot{x}_a$ is the velocity of motion of the armature.

It is well known by Faraday's law that the terminal voltage of a circuit v is equal to the time derivative of the flux linkage Φ : $v = \dfrac{d\Phi}{dt}$. Φ is a function of the current "i" in the circuit and the displacement of the mechanical movable part in the circuit "x". Thus the terminal voltage of the circuit can be written as[4]

$$v = \frac{\partial\Phi}{\partial i}\cdot\frac{di}{dt} + \frac{\partial\Phi}{\partial x}\cdot\frac{dx}{dt}$$

If we restrict the model to be an electrically linear system whose flux linkage is a linear function of "i" and "x", the partial derivative $\dfrac{\partial\Phi}{\partial i}$ and $\dfrac{\partial\Phi}{\partial x}$ become constants, i.e. the inductance L_a and the back-EMF β_a in Equation (1).

The force generated by the shaker, f_a is proportional to the current in the shaker circuit, i_a

$$f_a = \alpha\, i_a \tag{2}$$

and it can be related to input voltage v_a by combining (1) and (2)

$$v_a = \frac{R_a}{\alpha}\, f_a + \frac{L_a}{\alpha}\, \dot{f}_a + \beta_a\, \dot{x}_a \tag{3}$$

If the inductance of the shaker circuit L_a is neglectable, i.e., the shaker works in the low frequency range, the force f_a is a linear function of the input voltage v_a . Otherwise f_a is the solution of the first order linear differential equation (3). It will be convenient to write Equation (3) in a standard state equation form

$$\dot{f}_a = -\frac{R_a}{L_a}\, f_a + \frac{\alpha}{L_a}\, v_a - \frac{\alpha\beta}{L_a}\, \dot{x}_a \tag{4}$$

The mechanical component of the shaker can be modeled as a single degree of freedom dynamic system (as shown in Fig. 2) having the equation of motion

$$f_a - f_s = m_a \ddot{x}_a + c_a \dot{x}_a + k_a x_a \tag{5}$$

where m_a is the shaker armature mass, k_a and c_a are respectively the equivalent stiffness and viscous damping constants of the shaker suspension. $\ddot{x}_a$, $\dot{x}_a$, and x_a are respectively the acceleration, velocity and displacement measured at the driven point on the structure. f_s is the available force for the structure. Differentiating both side of (5)

$$\dot{f}_s = \dot{f}_a - (m_a \dddot{x}_a + c_a \ddot{x}_a + k_a \dot{x}_a) \tag{6}$$

and substituting (4) into (6) yields

$$\dot{f}_s = -\frac{R_a}{L_a} f_a + \frac{\alpha}{L_a} v_a - \{ m_a \dddot{x}_a + c_a \ddot{x}_a + (k_a + \frac{\alpha\beta}{L_a}) \dot{x}_a \} \tag{7}$$

Equation (7) involves both $\dot{f}_s$ and f_a. In order to unify the variable we replace f_a by Equation (5). Equation (7) can be then written as

$$\dot{f}_s = -g_a f_s + b_a v_a - a \tag{8}$$

$$with \quad g_a = \frac{R_a}{L_a} , \quad b_a = \frac{\alpha}{L_a}$$

$$a = m_a \dddot{x}_a + (g_a m_a + c_a) \ddot{x}_a + (g_a c_a + k_a + b_a \beta) \dot{x}_a + g_a k_a x_a$$

"a" represents the shaker-structure interaction. Equation (8) is the fundamental equation which relates the force applied to the structure f_s and the input voltage of the shaker v_a. Fig. 3 illustrates Equation (8). From this scheme, it is obvious that the shaker-structure combined system is a closed-loop system, where the outputs of the structure at the driven point are fed back into the input of the shaker. This causes the resulting loss in force capability of the shaker and the phase shift (especially at the resonant frequencies of the structure), which is undesirable for both vibration tests and active control. In the rest of the paper, we are interested in finding control algorithms to compensate for the force loss and phase shift due to the shaker-structure interaction represented by term "a" in Equation (8).

3   DIRECT FORCE DEVIATION FEEDBACK

An explicit way to eliminate "-a" from Equation (8) is to create a control force equal to "+a". This

requires first an accurate estimate of both the mechanical and electrical characteristics of the shaker and second the capability to measure x_a, $\dot{x}_a$, $\ddot{x}_a$, and $\dddot{x}_a$. In the real world, these requirements can not be easily full filled. For this reason, compensators based on feeding back the force deviation are investigated.

In this section, we restrict the model to the case where the shaker works in the low frequency range, thus the inductance in the coil circuit is neglectable. From (3) and (5), the available force for the structure f_a can then be written as a linear function of the input voltage v_a

$$f_a = \frac{\alpha}{R_a} v_a - \hat{a} \tag{9}$$

where $\hat{a} = m_a \ddot{x}_a + (c_a + \frac{\alpha\beta}{R_a})\dot{x}_a + k_a x_a$

Denote the nominal input by $\hat{v}$, which may be the active control signal or some particular function such as a harmonic function for step-sine excitation modal testing, and the desired force by $\hat{f}$

$$\hat{f} = \frac{\alpha}{R_a} \hat{v} \tag{10}$$

If v_a is replaced by $\hat{v}$ in Equation (9), the deviation between the desired force $\hat{f}$ and the available force for the structure f_a is $\hat{a}$. In order to compensate for the term $\hat{a}$, we propose a closed-loop control scheme as shown in Fig. 4. In this loop, Equation (10) represents a reference model, and the input of the controlled plant (shaker) v_a is the sum of the nominal input $\hat{v}$ and the deviation between $\hat{f}$ and f_a

$$v_a = \hat{v} - \theta(f_a - \hat{f}) \tag{11}$$

where θ is a real positive number. Substituting (9) and (10) into (11) yields

$$v_a = \hat{v} + \frac{\theta \hat{a}}{1 + \theta \dfrac{\alpha}{R_a}} \tag{12}$$

The force f_a is then related to the nominal input $\hat{v}$ by the equation below

$$f_a = \frac{\alpha}{R_a} (\hat{v} + \frac{\theta \hat{a}}{1 + \theta \dfrac{\alpha}{R_a}}) - \hat{a}$$

$$= \frac{\alpha}{R_a} \hat{v} - \frac{1}{1 + \theta \dfrac{\alpha}{R_a}} \hat{a} = \hat{f} - \theta_a \hat{a} \tag{13}$$

The multiplying factor of $\hat{a}$ $\theta_a = \dfrac{1}{1 + \theta \dfrac{\alpha}{R_a}}$ is always less than 1, and if the feedback gain θ is big enough, the force applied to the structure f_s will be in the infinitely small neighborhood of the desired force $\hat{f}$. This is a simple control loop in which the only parameter to be determined is the feedback gain θ. To achieve an optimal control performance, the feedback gain θ must be as large as possible. However, its selection must be subject to the stability criterion.

Since Equation (9) is a simplified model, for stability analysis Equation (8) must be used. Substituting (11) into (8), the transfer function between f_s and $\hat{v}$ ($f_s = T(s)\,\hat{v}$) can be written as

$$T(s) = \frac{(\dfrac{\theta\alpha}{R_a} + 1)\, b_a}{s + g_a + \theta\, b_a + \dfrac{G(s)N(s)}{D(s)}} \tag{14}$$

where $a = G(s)x_a(s)$, $\tilde{\upsilon}(s) = s^3 m_a + s^2(g_a\, m_a + c_a) + s(g_a\, c_a + k_a + \beta_a\, b_a) + g_a\, k_a$ and $x_a(s) = \dfrac{N(s)}{D(s)}\, f_s(s)$

$\dfrac{N(s)}{D(s)} = \dfrac{(s - z_1)\, \ldots\, (s - z_m)}{(s - \lambda_1)\, \ldots\, (s - \lambda_n)}$ is the transfer function of the structure at the driven point. $z_1 \ldots z_m$ and $\lambda_1 \ldots \lambda_n$ are respectively the zeros and the poles of the structure. Assuming the structure is a dissipative system, the poles $\lambda_1 \ldots \lambda_n$ do not lie in the right-half complex plane.

For stable operation of the control system of Fig. 4, all roots of the characteristic equation

$$(s + g_a + \theta\, b_a)D(s) + G(s)N(s) = 0 \tag{15}$$

must be negative real numbers or complex numbers with negative real parts[5].

DFDF is very easy to implement. Only two parameters of the shaker-amplifyer system, R_a and α need to be estimated, and the the force applied to the structure f_s need to be measured. However, it must be noted that this method restricts itself to a low frequency bandwidth, and in addition, it can not compensate for the phase shift caused by the system itself.(The coefficient α is in general a complex number.) In the next section, a more sophisticated control algorithm is proposed for the general case.

4 MODEL REFERENCE ADAPTIVE COMPENSATOR

In the previous analysis, it is assumed the shaker-amplifyer system is a perfect linear system and its parameters being accurately estimated. However, in the real world, these assumptions are not strictly valid. In addition, the characteristics of the electrical components, generally, are time varying subject to environment changes such as temperature humidity and other exterior disturbances. Considering these practical factors, a robust control algorithm is needed to accommodate the modeling uncertainty of the system and exterior disturbances. In this section, we extend and apply the model following control scheme proposed by Ambrosino[6] to the present problem. The advantage of this control algorithm is that it can deal with nonlinear time varying plants.

Assume the desired force $\hat{f}$ is described by a linear, time invariant, first order differential equation

$$\overset{\lambda}{f} = -g\,\hat{f} + b\,\hat{v} \tag{16}$$

where $\hat{v}$ is the nominal input to the shaker. g and b are real positive constants. They may be equal to estimated values of g_a and b_a, or assigned by the control designer subject to the given problem and/or other practical considerations.

(16) along with (8) form an "error equation"

$$\dot{f_s} - \overset{\lambda}{f} = \dot{e} = -g_a\,f_s + g\,\hat{f} + b_a\,v_a - b\,\hat{v} - a$$

or

$$\dot{e} = -g\,e + w \tag{17}$$

where $e = f_s - \hat{f}$ is the state variable of the error equation, and
$$w = (g - g_a)\,f_s + b_a\,v_a - b\,\hat{v} - a$$

A control scheme is proposed, as shown in Fig. 5, such as the "error equation" (17) is asymptotically stable. In this scheme, the input voltage to the shaker v_a is

$$v_a = K_f\,f_s + K_v\,\hat{v} - h_1(e,f_s) - h_2(e,\hat{v}) - h_3(e) \tag{18}$$

with

$$h_1 = h_f\frac{u}{|u|+\delta}|f_s| \tag{19}$$

$$h_2 = h_v\frac{u}{|u|+\delta}|\hat{v}| \tag{20}$$

$$h_3 = h_0\frac{u}{|u|+\delta} \tag{21}$$

$$u = p\,e \ , \quad -2gp = -q \tag{22}$$

where K_f and K_v are real constants, h_f, h_v and h_0 are feedback gains which will be discussed later. p and q are real positive numbers.

It can be proved that if the feedback gains satisfy the following conditions

$$h_f > |K_f + \frac{g - g_a}{b_a}|(1+\frac{\delta}{\gamma}) \tag{23}$$

$$h_v > |K_v - \frac{b}{b_a}|(1+\frac{\delta}{\gamma}) \tag{24}$$

$$h_0 > |\frac{a}{b_a}|(1+\frac{\delta}{\gamma}) \tag{25}$$

the γ-neighborhood $S_\gamma = \{ e : |u| \le \gamma \}$ is asymptotically attractive everywhere.

Let a real positive function

$$V(e) = e^2 p \tag{26}$$

be take as Lyapunov function. Along with Equation (17), the time derivative of the Lyapunov function is

$$\dot{V}(e) = 2e\dot{e}p = 2e(-ge + w)p = -e^2 q + 2uw \tag{27}$$

If (23) to (25) are satisfied, it results in

$$uw = u\{(g - g_a)f_s + b_a (K_f f_s + K_v \hat{v} - h_f \frac{u}{|u| + \delta}|f_s| - h_v \frac{u}{|u| + \delta}|\hat{v}| - h_0 \frac{u}{|u| + \delta}) - b\,\hat{v} - a\} < 0 \tag{28}$$

for any $|u| \ge \gamma$

$V(e)$ is positive and its time derivative $\dot{V}(e)$ is negative. According to the theorem of Lyapunov, Equation (16) is asymptotically stable. In consequence, the deviation between the desired force $\hat{f}$ and the available force for the structure f_s will be bounded in the γ-neighborhood.

REMARKS

1. The key to this control scheme is to find feedback gains h_f, h_v, and h_0 satisfying (23) to (25). Note that Equations (23) to (25) are inequality equations, so they will be tolerant of

the estimation errors of the characteristics of the shaker. In fact, the present control law remains valid, even if g_a and b_a are bounded linear or non-linear functions of time or other physical variables with known (or estimated) lower and upper boundaries. In this case, the "dangerous" (lower or upper) boundary values of g_a and b_a are used to determine h_f, h_v, and h_0 in Equations (23) to (25).

2. An appropriate choice of constants K_f and K_v in Equation (18) can reduce the magnitude of the feedback gains. A natural way to choose these constants is K_f equal (or close) to $g_a \cdot g$ and K_v equal (or close) to $\dfrac{b}{b_a}$.

3. If $\delta = 0$ in (19) to (21), the control system becomes a variable structure system, discontinuous on the line $u = 0$. Ambrosino[6] discussed the disadvantages of the discontinuous control law $(\delta = 0)$ by comparing with the continuous control law $(\delta \neq 0)$. An illustrative example for a pendulum tracking control showed the discontinuous control law causing undesired chattering of the control signal. By our experience, this chattering can very easily destabilize the control system in practical implementation due to unmodeled higher modes of the shaker and hardware limitations of the control loop. It is advisable to take δ equal to $(0.4 - 0.6)p$ ($u = pe$ Equation (22)).

5 NUMERICAL AND EXPERIMENTAL VALIDATION

The proposed methods are applied to compensate for the dynamic effects of an electrodynamic shaker which is used to excite a flexible structure. The numerical and experimental process is described as follows.

5.1 ACTUATOR The actuator studied is an electrodynamic exciter type : MB Modal 50, which can provide 50 lb. peak dynamic force with 1" stroke. Mechanical parameters specified by the manufacturer are : armature mass < 0.4 lb. and armature axial suspension stiffness < 15 lb/in. All parameters of the shaker-amplifyer system required by this study are experimentally determined. This parameters are listed in Table 1.

TABLE 1. Characteristics of Electrodynamic Exciter

Electrodynamic Exciter : MB Modal 50		
Characteristics	Measured Values	
	English Units	Metric Units
Armature mass (m_a)	0.54 lb	0.24 kg
Armature axial suspension stiffness (k_a)	12.9 lb/in	2235 N/m
Armature axial suspension damping (c_a)	0.035 lb/in/sec	6.1 N/m/sec
Resistance of Amplifyer and Shaker (R_a)	2 Ω	2 Ω
Inductance of Shaker coil (L_a)	0.00183 H	0.00183 H
Back-EMF constant (β_a)	0.52 volt/in/sec	20.5 volt/m/sec
Current-force coefficient (α)	4.25 lb/amp	18.87 N/amp

In addition, the frequency response function between the force input to the armature and armature response (for "zero output impedance"), as shown in Fig. 6, provides a very useful value : the fundamental resonant frequency of the shaker which is around 15 Hz. This value is very important to understand the shaker-structure interaction.

5.2 STRUCTURE The structure to which the shaker is attached is a cantilever beam. The geometrical and physical parameters of this structure can be found in Table 2.

TABLE 2. Parameters of Cantilever Beam

Cantilever Steel Beam		
Characteristics	Measured Values	
	English Units	Metric Units
Length	42.6 in	1.08 m
Width	2.75 in	70 mm
Thickness	0.125 in	3.2 mm
Module of elasticity	0.303×10^8 lb/in^2	$2.08\times10^{11} N/m^2$
Unit weight	0.282 lb/ in^3	7800 kg/ m^3
Poisson's ratio	0.3	0.3
Uniformly distributed lumped masses	6×0.069 lb	6×0.0315 kg

The first four modes of the beam were experimentally identified. Both frequencies and mode shapes match those calculated from a Finite Element Model with 12 elements. Since this structure

is to be used for the active vibration control research, there are 6 sensors uniformly distributed on the beam. The mass of the sensors is taken into account in the FEM. The shaker is connected with the beam at point 6 (see Fig. 7).

5.3 NUMERICAL SIMULATION SYSTEM
A numerical simulation system is built up for the purpose of

- Investigation of the actuator-structure interaction
- Validation of the measured physical parameters of the shaker
- Prediction of the performance of the controller design.

This numerical simulation system consists of an actuator-structure combined model

$$
\begin{bmatrix}
C + c_a & M + m_a & 0 \\
M + m_a & 0 & 0 \\
0 & 0 & L_a
\end{bmatrix}
\begin{Bmatrix}
\dot{x} \\
\ddot{x} \\
\frac{di}{dt}
\end{Bmatrix}
=
\begin{bmatrix}
-K - k_a & 0 & \alpha \\
0 & M + m_a & 0 \\
0 & \beta_a & R_a
\end{bmatrix}
\begin{Bmatrix}
x \\
\dot{x} \\
i
\end{Bmatrix}
+
\begin{Bmatrix}
0 \\
0 \\
V_a
\end{Bmatrix}
$$

where $[M]$, $[C]$, and $[K]$ are the mass matrix, damping matrix, and stiffness matrix of the structure respectively.

The first five eigenvalues of the structure alone and those of the actuator-structure combined system are listed in Table 3.

TABLE 3. Eigenvalues of Structure and Actuator-Structure Combined System

Structure		Actuator-Structure System	
Damping	Freq.	Damping	Freq.
0.0%	2.13 Hz	-31.38%	5.08 Hz
0.0%	13.30 Hz	-23.87	0.0
		-165.14	0.0
0.0%	37.17 Hz	-0.09%	37.13 Hz
0.0%	72.67 Hz	-10.08%	63.27 Hz
0.0%	119.66 Hz	-0.04%	119.58 Hz

Note that the fundamental resonant frequency of the shaker (15 Hz) is close to the natural frequency of the second mode of the structure. Coincidently, the second eigenvalue of the actuator-structure combined system becomes a negative real number (its complex conjugate too). Through a series of tests by changing the connection point of the shaker with the structure, it has been observed that the perturbation due to the presence of the shaker on the second mode is always much larger than the perturbation on the other modes, and the further the modes from the resonant frequency of the shaker, the smaller the effect of the shaker dynamics on them.

In order to verify the measured physical parameters of the shaker, we simulate the force f_s generated by a sinusoidal input at 5 Hz and compare it with the force measured by a load cell mounted on the structure. Fig. 8 (a) and (b) illustrate the simulated and measured forces. The desired force, which is proportional to the input signal v_a, is drawn in these figures as a reference. The phase shift and loss in amplitude of the measured force f_s with respect to the desired force match the simulation results quite well. In this way, the measured physical parameters of the shaker are verified.

5.4 EXPERIMENTAL SETUP The experimental set up is shown in Fig. 9. First the analog signals from the signal generator G and the load cell L enter the control bloc C. After on line computation in the control bloc, the resulting signal v_a is then sent out to the voltage amplifyer A. The control bloc consists of an EAI-1000 analog computer containing integrators, summers, multipliers and analog switches, which enables the realization of the control laws described in Section 3 and Section 4. The only sensor involved in this control loop is a load cell type PCB Model 208A02 with sensitivity 55 mv/lb.

5.5 DISCUSSION OF RESULTS The numerical simulation results and the experimental results are shown in Fig. 9 and in Fig. 10 respectively. It is understandable that the numerical results are very good, since the simulation operates on an exact mathematical model. The analysis in Section 4 reveals for MRAC the deviation between f_s and f_a will be kept in the γ-neighborhood. If $|u| < \gamma$, the stability condition may be violated and $|u|$ will increases until $|u| > \gamma$. This phenomenon can be observed clearly in Fig. 9-b.

In the previous analysis, the phase shift caused by the shaker system itself is not taken into account. However, for the experimental implementation the phase shift due to the filter, analog computer, and amplifier (the phase lag due to amplifier implies that α is a complex number) will influence the control performance. Fig. 10 shows that the loss of the force f_s in amplitude is almost fully compensated, but the phase shift is only partially compensated.

6 CONCLUDING REMARKS

The mathematical model of an electrodynamic shaker is given in this paper. The force applied to the structure is related to the input voltage of the power amplifier by a first order differential equation, which reveals also the shaker-structure interaction. It must be noted that this model is based on the assumption of the flux linkage Φ being a linear function of the current "i" and the position of the armature "x", which leads to L_a and β_a constant. However, the experimental study[7] shows that both L_a and β_a are not constant : L_a varys with the frequency of the input signal and β_a is in function of the position of the armature. The advantage of the proposed compensation methods is their robustness to the variation of the shaker parameters.

The first compensator restricts itself to a low frequency bandwidth, so the inductance of the coil L_a is negligible. Effects due to back-EMF of shaker dynamics are accounted by the variable $\hat{a}$. thus the force deviation feedback deals with the error in global manner rather than handling each shaker parameter separately.

The second compensator only requires the boundary values of g_a and b_a and it disregards whether shaker parameters are linear or non-linear functions of time or other physical variables.

The proposed methods are verified numerically and experimentally.

Further research on will be oriented in the following directions

- Compensating for the phase shift due to the shaker-amplifier-compensator system itself

- Updating the proposed compensation algorithms to other types of actuator system.

REFERENCES

[1] D. J. Inman , R. W. Mayne and D. C. Zimmerman , "Comments on electromechanical actuators for controlling flexible structures" , Proc. of 5th AFOSR Forum on Space Structures, Aug. 1987 , Monterey CA

[2] N. L. Olsen , "Using and understanding electrodynamic shakers in modal applications", Proc. of 4th IMAC, Los Angeles, CA, pp. 1160-1167, 1986

[3] J. N. Juang , L. G. Horta , H. H. Robertshaw , "A slewing control experiment for flexible structures", J. Guidance Control & Dynamics, Vol.9, No.5, pp. 599-607, 1986

[4] H. H. Woodson and J. R. Melcher , "Electromechanical dynamics Part I : Discrete System", John Wiley & Sons Inc., New York, 1968

[5] H. L. Harrison and J. G. Bollinger , "Introduction to automatic control", International Textbook Company, New York, 1969

[6] G. Ambrosino , G. Celentano and F. Garofalo , "Robust model tracking control for a class of nonlinear plants", IEEE Trans. Auto. Contr., AC-30 pp 275-279, 1985

[7] S. Shelley , Q. Zhang , X. N. Luo , R. J. Allemang and D. L. Brown , "Experimental study of compensation for shaker dynamic effects", Proc. of 13th Int. Seminar on Modal Analysis, Belgium, Sep. 1988
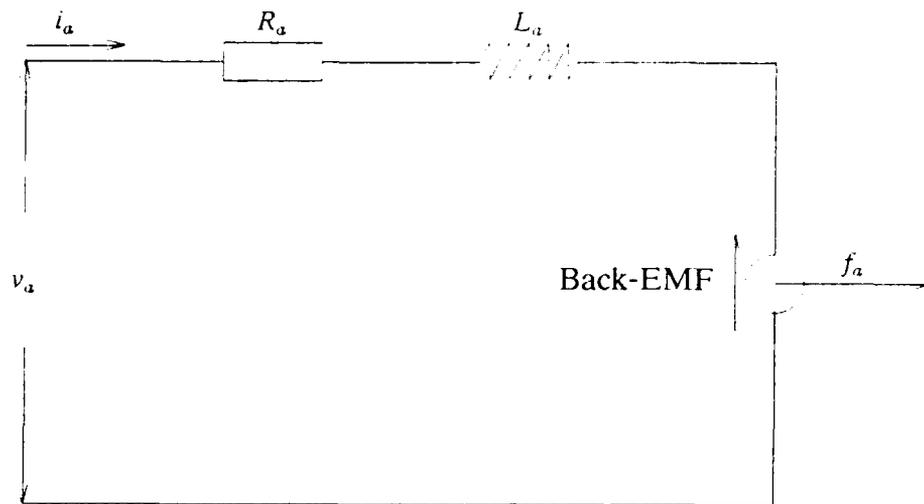
**Figure 1.** Electronical Component Circuit of Shaker
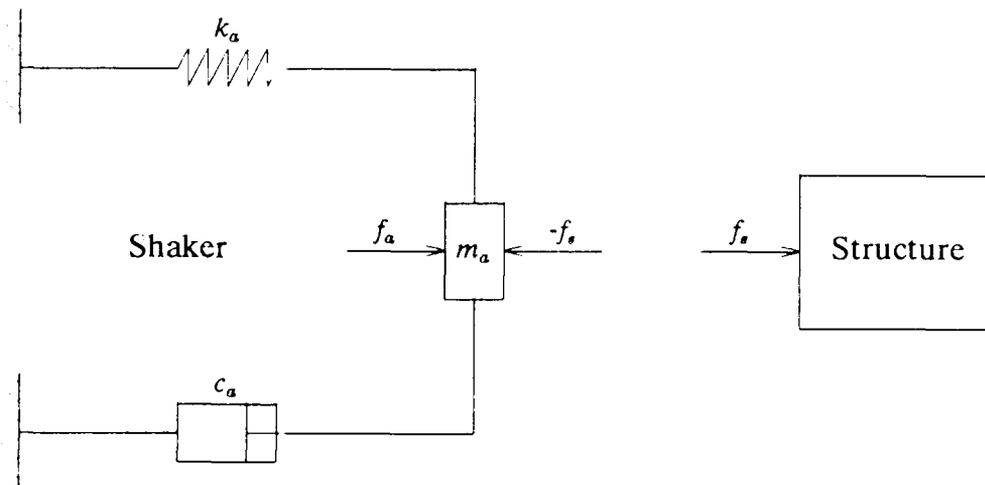

Figure 2. Mechanical Model of Shaker
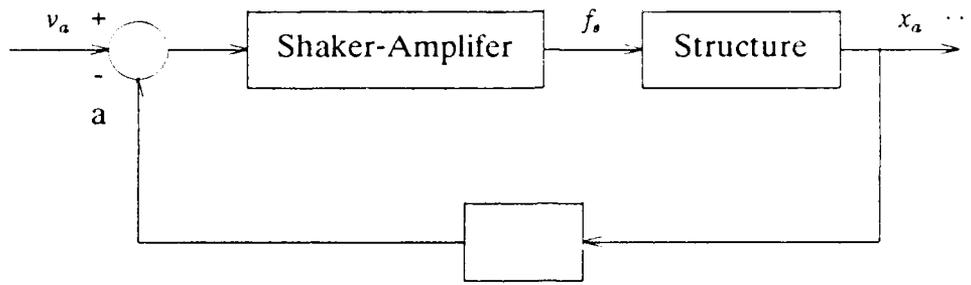
Figure 3. Bloc-Diagram of Equation (8)
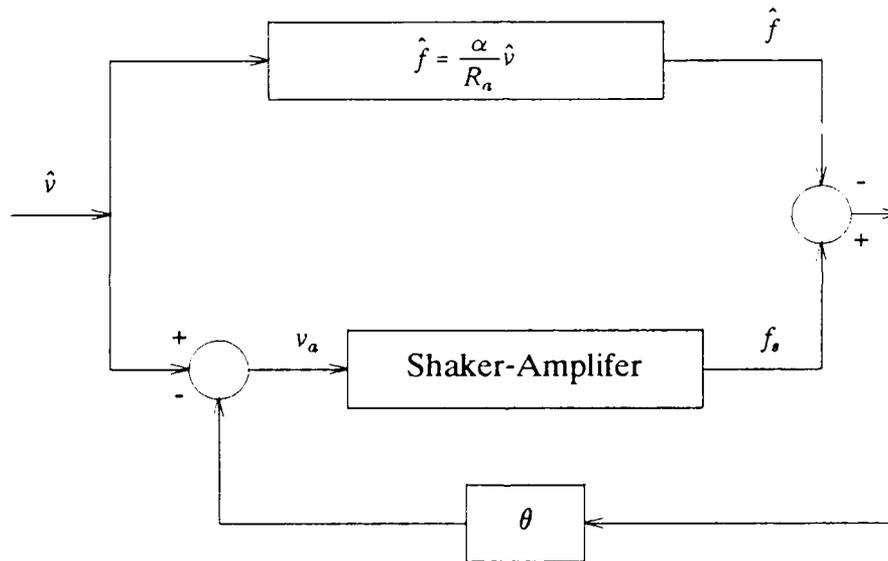
Figure 4. Bloc-diagram of Direct Force Deviation Feedback

$$\dot{\hat{f}} = -g\hat{f} + b\hat{v}$$
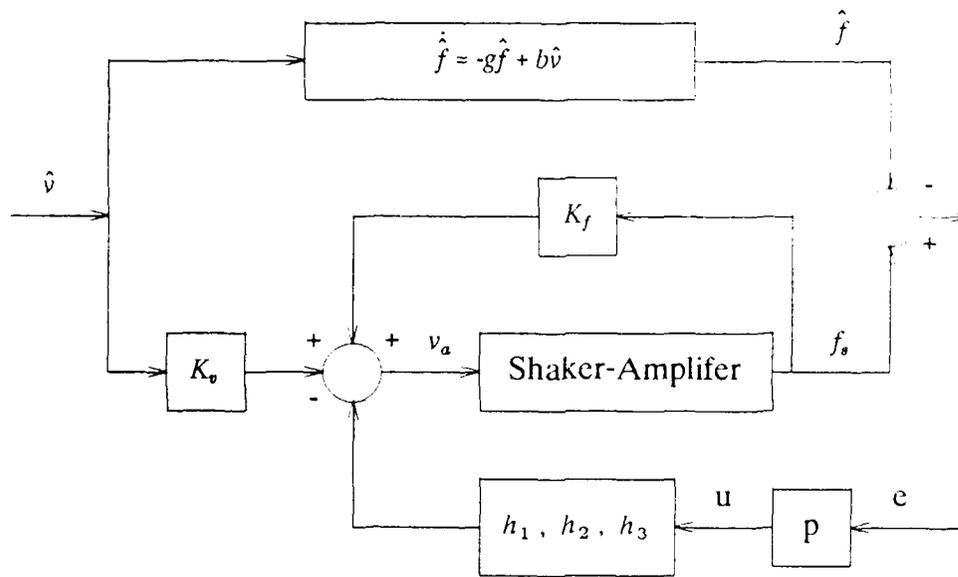
Figure 5. Bloc-Diagram of Model Reference Adaptive Compensator

MAG

0 0

0.0   HZ   100.00
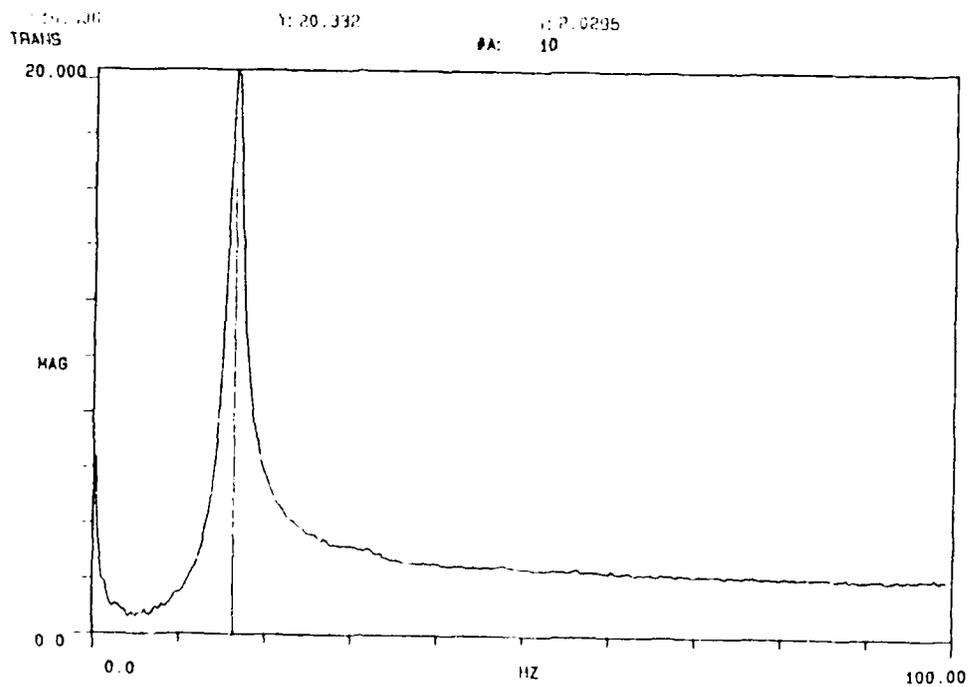
Figure 6. FRF Between Force Input And Response Of Armature
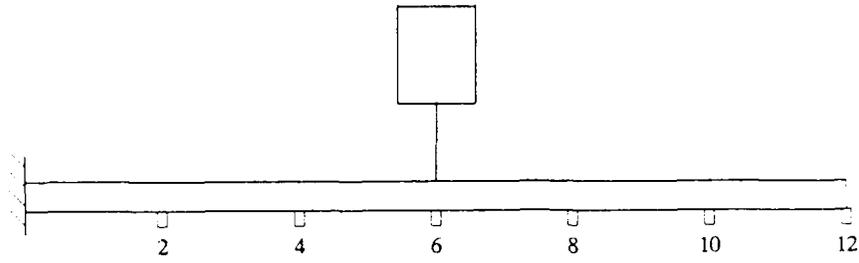
Figure 7. Actuator-Structure Combined System
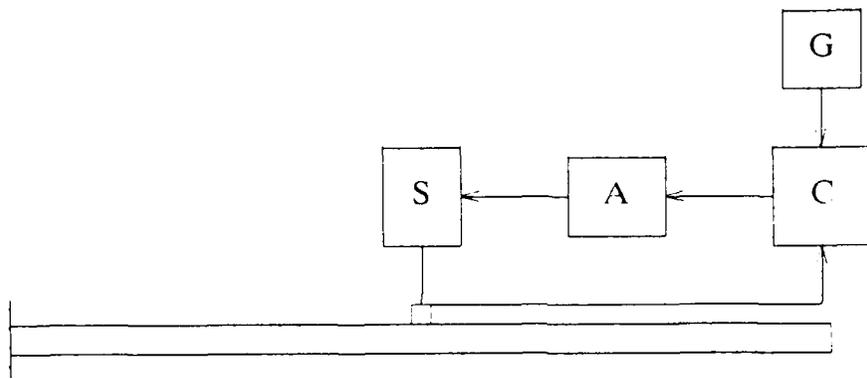
Figure 8. Experiment Setup Scheme

SETUP   **GRP TIME**   **LOWR**   **VW 40DB**   **CH AB**   **FR 400HZ**

03: 07: 19   TIME B   INP   OG X5   WTG H   A .5V   B .5V
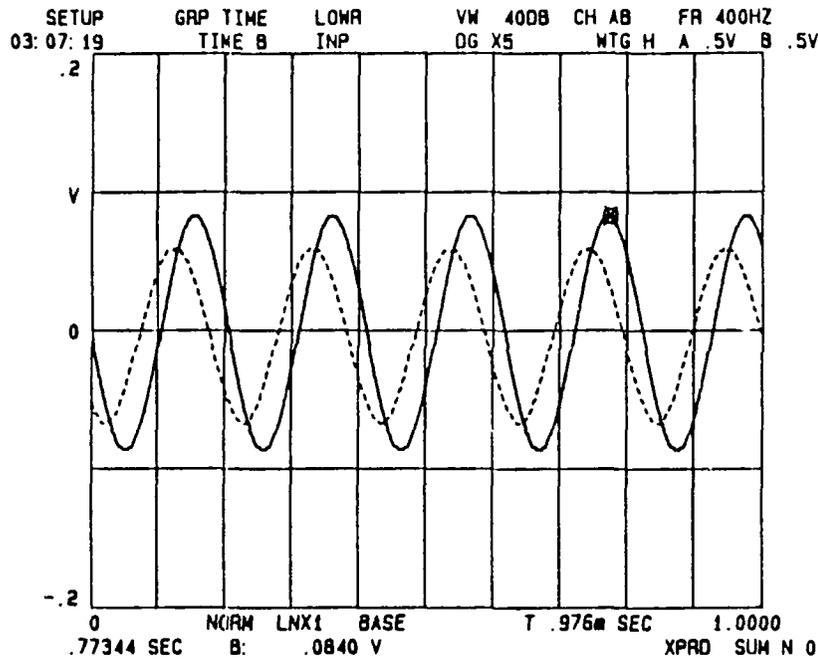
a) Experimental Result

SIMULATION RESULTS
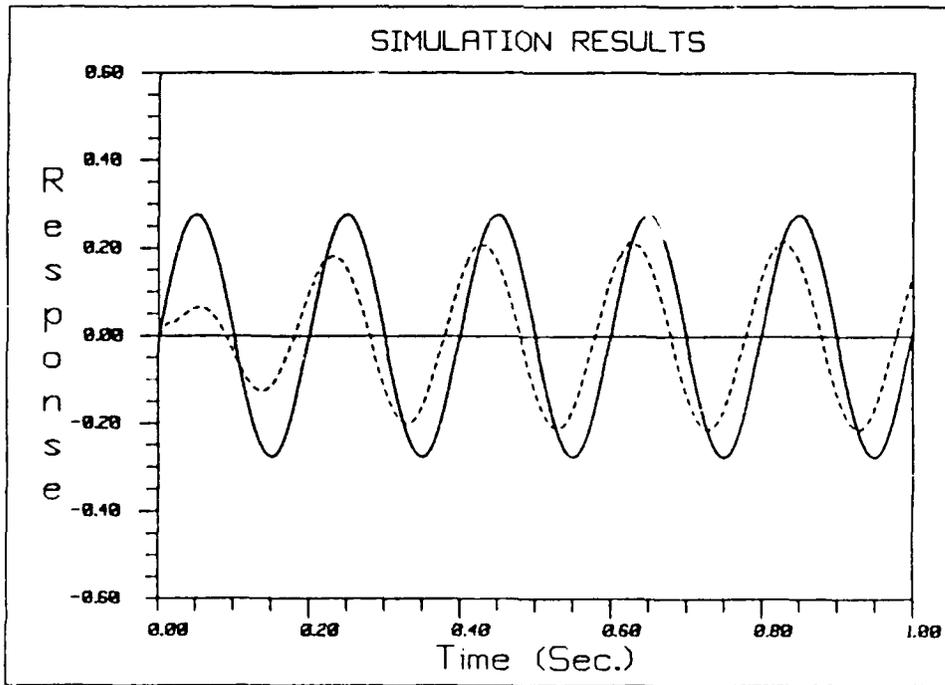
Figure 9. Force Applied To The Structure & Desired Force

"Dashed line" : Force Applied To The Structure
"Solid line" : Desired Force
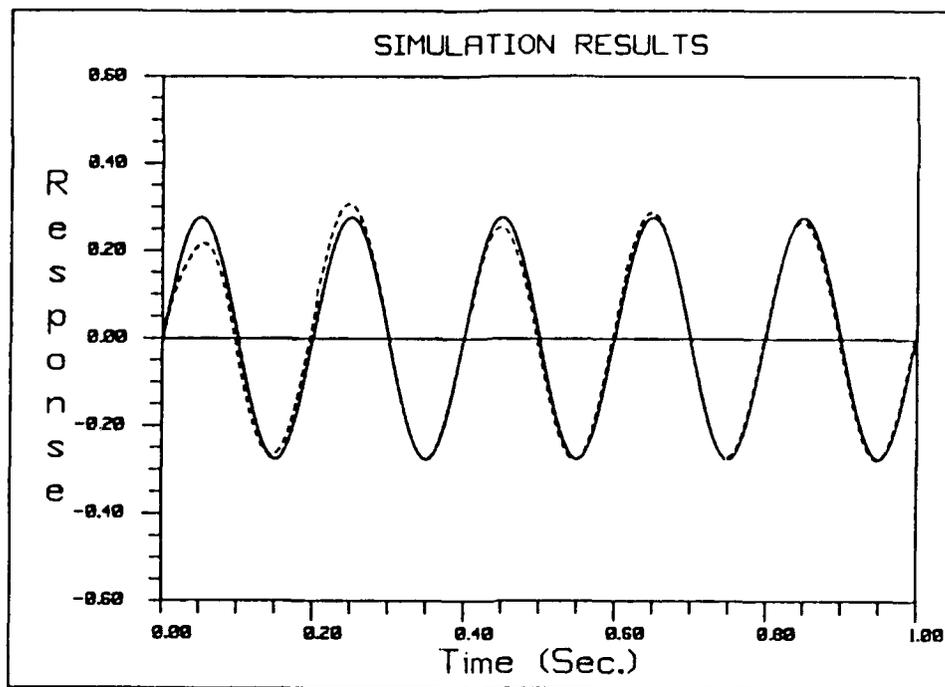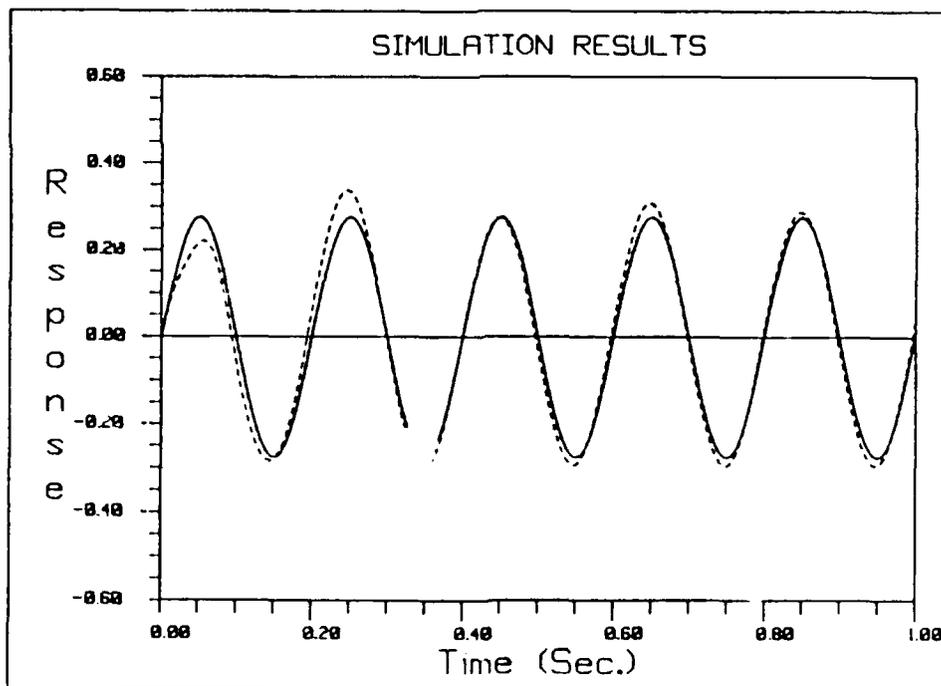
a) **Result Of DFDF**

b) **Result Of MRAC**

**Figure 10. Force Applied To The Structure With Compensation
(Simulation Results)**

"Dashed line" : Force Applied To The Structure
"Solid line" : Desired Force
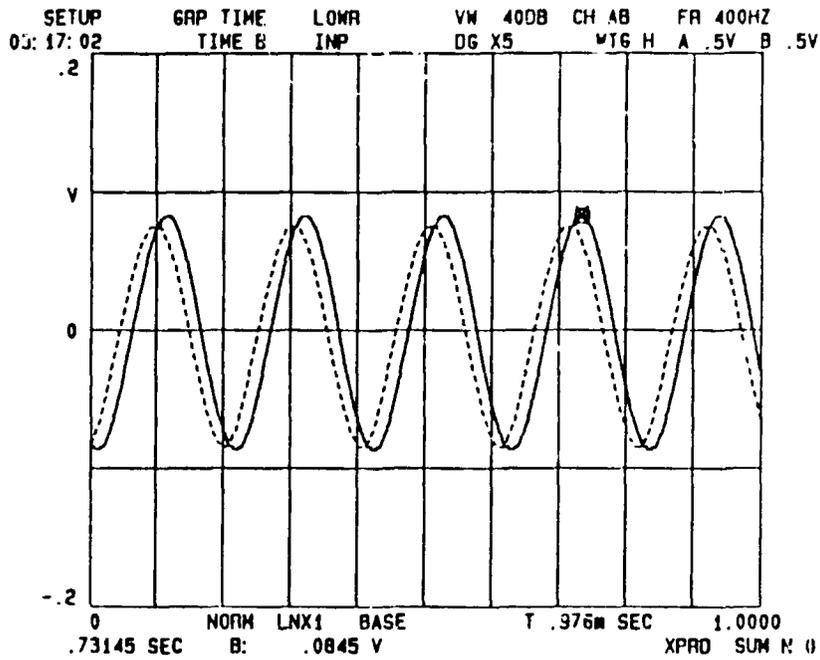
a) **Result Of DFDF**
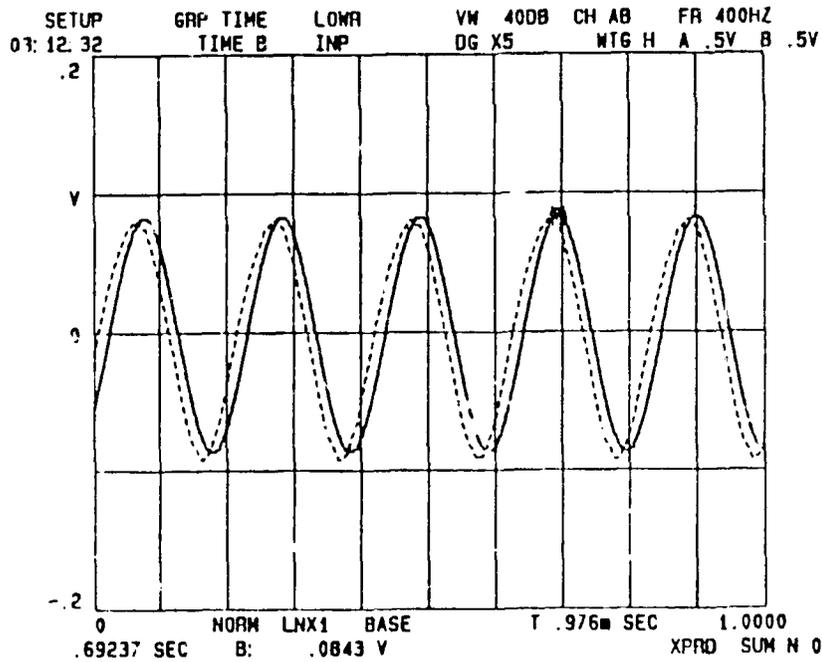
b) **Result Of MRAC**

Figure 11. Force Applied To The Structure With Compensation (Experimental Results)

"Dashed line" : Force Applied To The Structure
"Solid line" : Desired Force

# DAMPING AND VIBRATION CONTROL OF UNIDIRECTIONAL COMPOSITE BEAMS USING ADD-ON VISCOELASTIC MATERIALS[1]

C. T. Sun, B. V. Sankar, and V. S. Rao

Department of Aerospace Engineering,
Mechanics and Engineering Science
University of Florida
Gainesville, FL 32611

In this paper a methodology for vibration control of composite beams is introduced. A constrained viscoelastic layer treatment is applied to the surface of the beam. Analytical results of structural damping, frequencies of vibration, and maximum displacement are obtained by using a finite element numerical program. Some analytical results are also compared with experimental data which are obtained by using the Fast Fourier Transform based impulse technique. Numerical results of structural damping and displacement ratios are plotted as functions of the length of the viscoelastic material and some other geometrical parameters.

Introduction

Most composite structural elements are used in severe dynamic environments which may produce a considerable amount of displacement, thus, vibration control to reduce resonance displacement and noise level is extremely necessary. Excessive displacements cannot be controlled by simply increasing the stiffness of the structural elements, since increasing the stiffness is equivalent to increasing the natural frequencies of free vibration, excessive displacements are still possible at resonance.

To the authors' knowledge, one of the best ways in vibration control is to introduce additional damping to the composite structural elements. With sufficient damping in the structure, excessive displacements will be drastically reduced at resonance. However, up to now, most of the vibration control research has been

limited to metal structures only.

The objective of this paper is to develop some methodologies in vibration control and to improve the performance of composite structural elements under dynamic load environments.

The method under consideration is using add-on viscoelastic material on the surface of the beam to increase the structural damping (loss factor). This method has been used extensively for metallic structural elements by Nashif, Jones and Henderson [1]. In the beginning, we limit our attention to vibration control of unidirectional composite beams only.

It is generally well-known that viscoelastic materials will dissipate considerable energy through shear deformation. In order to utilize this phenomenon, the viscoelastic material is constrained with a constraining layer with rigidity comparable to that of the composite beam. The viscoelastic material will be forced to deform in shear due to the high mismatch in rigidities between the constraining layer, viscoelastic material and the composite beam structure. In order to reduce the total weight of the structure we try to use discontinuous add-on material as shown in Fig. 1. Since the beam thickness is discontinuous, it is convenient to use a finite element method as our analytical tool. This method will generate numerical values of material damping, natural frequencies, and displacements at some critical points. In future applications, this method will also be able to accommodate continuous variation of cross-section and pre-stress due to centrifugal forces, and initial twisting, such as in helicopter blades. Development of the finite element program will be discussed in detail in the next section.
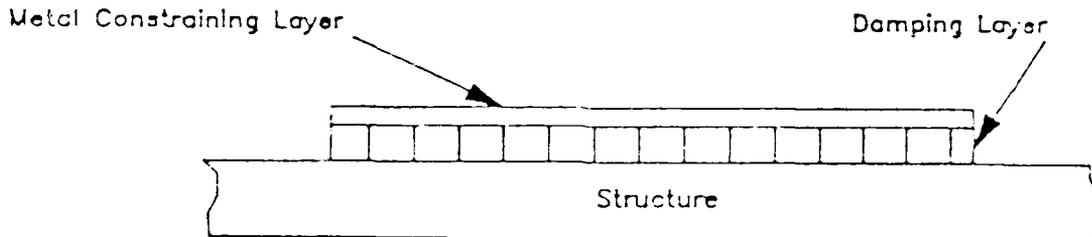
Figure - 1 CONSTRAINED LAYER DAMPING TREATMENT

This research is also carried out experimentally. A brief description of the experimental set-up and experimental proceaures are presented in this subsequent section. Some numerical results are compared with experimental data. Reasonable agreement between analytical and experimental results are observed.

Finite Element Analysis

The finite element method was used to evaluate damping in the structure for different lengths of treatment of the constrained viscoelastic layer. Figure 2 shows the arrangement used for

modeling of the three layer sandwich. The base structure and the constraining layer were modeled using a specially developed three-node, seven-degree-of-freedom, offset beam element. A key feature of this element is its ability to account for coupling between stretching and bending deformations. This allows for the beam nodes to be offset to one surface of the beam, coincident with the nodes of the adjoining element. The viscoelastic core is modeled using rectangular plane stress elements with two translational degrees of freedom per node.
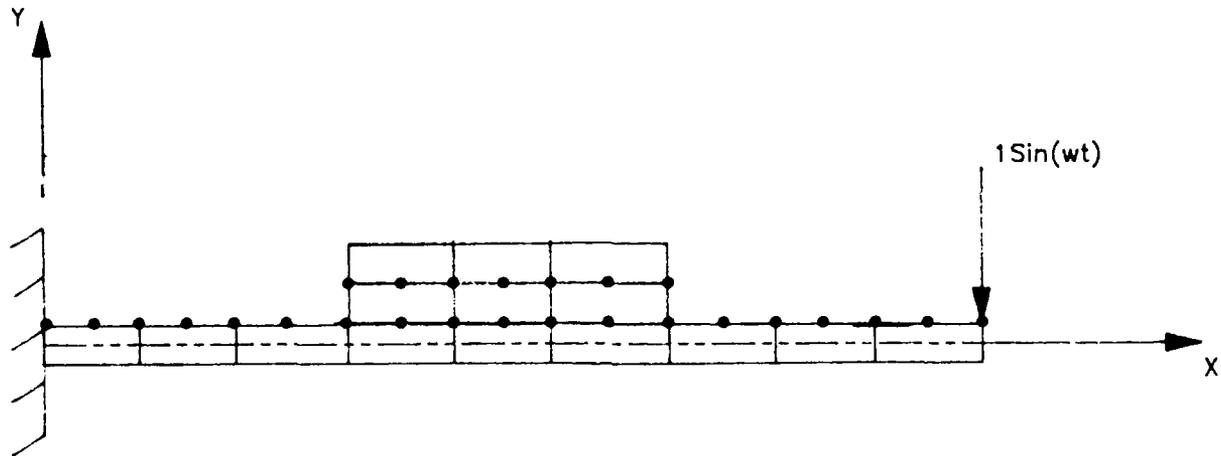
Figure — 2   TYPICAL FINITE ELEMENT MESH

Offset Beam Element

The element matrix for the offset beam element shown in Fig. 3 is formulated as follows. The different displacement components are given by,

$$
\left.
\begin{aligned}
u(x,y) &= u_o(x) + (z - \tfrac{h}{2})\psi(x) \\
w(x,y) &= w(x) \\
\psi(x,y) &= \psi(x)
\end{aligned}
\right\}
\tag{1}
$$

u_o and ψ are defined using linear interpolation functions.

$$
\left.
\begin{aligned}
u_o(x) &= [\, (1-{}^X/_{L_e}) \quad {}^X/_I \,]\ [u_1^e \ u_2^e\ ]^T \\
\psi(x) &= [\, (1-{}^X/_{L_e}) \quad {}^X/_{L_e} \,]\ [\psi_1^e \ \psi_2^e\ ]^T
\end{aligned}
\right\}
\tag{2a}
$$

where, u_1^e, u_2^e, ψ_1^e and ψ_2^e are corresponding nodal displacements. w is defined using quadratic interpolation functions.

$$w = \begin{bmatrix} (1-{}^{3x}/L_e + \dfrac{2x^2}{L_e^2}) \\[12pt] 4(\dfrac{x}{L_e} - \dfrac{x^2}{L_e^2}) \\[12pt] (\dfrac{-x}{L_e} + \dfrac{2x^2}{L_e^2}) \end{bmatrix}^T \begin{Bmatrix} w_1^e \\[12pt] w_2^e \\[12pt] w_3^e \end{Bmatrix} \qquad (2b)$$

where w_1^e, w_2^e and w_3^e are nodal displacements.

Strains are derived from the displacement using the kinematic strain-displacement relations of linear elasticity.

$$\left. \begin{aligned} \epsilon_x &= \frac{\partial u}{\partial x} = \frac{\partial u_o}{\partial x} + z\frac{\partial \psi}{\partial x} \\[12pt] \gamma_{zx} &= \frac{\partial u}{\partial z} + \frac{\partial w}{\partial x} = \psi + \frac{\partial w}{\partial x} \end{aligned} \right\} \qquad (3)$$

The strain energy density for the system is given by

$$U_o = \frac{1}{2} C_{11} \epsilon_{xx}^2 + \frac{1}{2} k^2 C_{55} \gamma_{xz}^2 \qquad (4)$$

C_{11} and C_{55} are constants from the constitutive equations. The total strain energy for the system is given by

$$U = \int_V U_o\, dv = b \int_0^{L_e} \int_{-h/2}^{h/2} U_o\, dv \qquad (5)$$

Using equations (2), (3), (4) and (5), the strain energy of the system is reduced to,

$$U = \frac{1}{2} \{d_e\}^T [K_e] \{d_e\}$$

where,

$\{d_e\}$ = vector of elemental D.O.F.

$[K_e]$ = element stiffness matrix

The calculations involved are lengthy, but straight forward and are not presented here. The distributed mass matrix is evaluated similarly from the kinetic energy of the system.
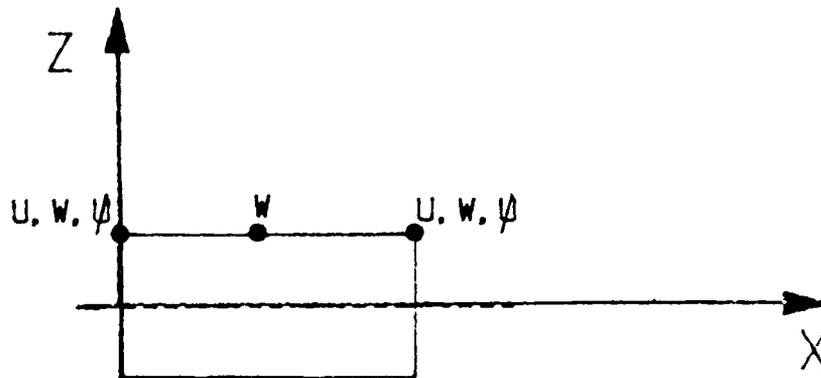
$$U(x, z) = U0(x) + (z - h/2) * \psi$$

$$W(x, z) = W(x)$$

$$\psi(x, z) = \psi(x)$$

Figure 3 OFFSET BEAM ELEMENT

Modeling and Solution Technique

As mentioned before the base structure was modeled using the three-node shear-deformable beam element. Typically, ten elements are used to model the beam. Very large aspect ratios are common for elements used to model the viscoelastic core. Values as high as 5000 to 1 have been used successfully [2], and are sometimes even necessary, since the viscoelastic core is only two mils thick. Aspect ratios up to 200 to 1 were used in the present study. To validate this formulation, several calculations were made to determine natural frequencies and tip displacement of simple systems, closed form solutions to which are easily derived.

The loss factor was evaluated using the direct frequency response technique. In this method, a forced vibration at a known frequency is considered. System displacements are obtained by solving a system of complex-valued linear equations. The frequency response spectrum is obtained by plotting amplitudes over a range of frequencies. The loss factor, a measure of damping, is obtained as shown in Fig. 4. This technique, though not the most efficient, was used for two reasons, simplicity and the relative small size of the problem in question.

The modeling method used is reasonably efficient. A three layer structure is modeled using only two layers of nodes. This technique can be easily extended to two-dimensional problems.

However, alternative methods for determining system loss factor will have to be used as the problem size increases.
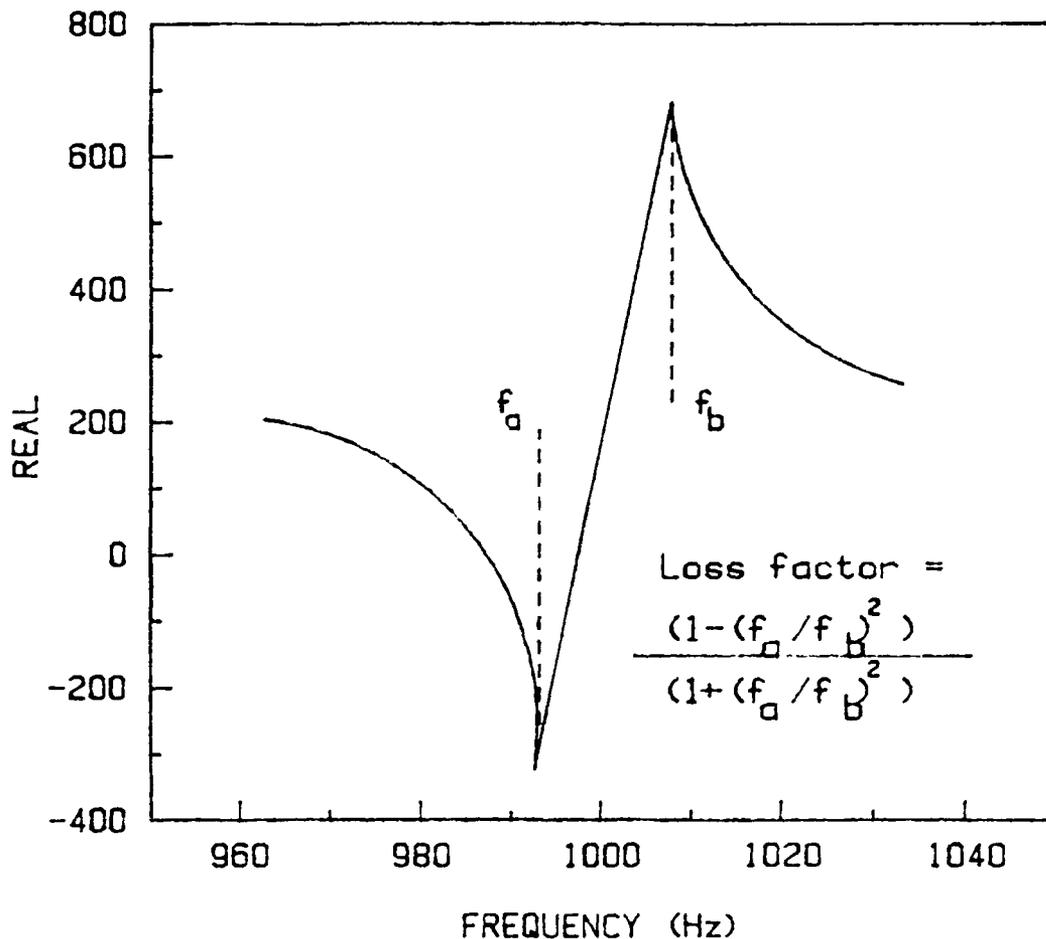
Figure - 4   TYPICAL REAL PART OF THE
             TRANSFER FUNCTION

The figure shows a plot with y-axis labeled REAL (from -400 to 800) and x-axis labeled FREQUENCY (Hz) (from 960 to 1040), with vertical dashed lines at f_a and f_b, and the equation:

$$\text{Loss factor} = \frac{(1-(f_a/f_b)^2)}{(1+(f_a/f_b)^2)}$$

Experimental investigation

In this investigation, the impulse technique was used for measurement of material damping. A schematic drawing of the experimental set-up is presented in Fig. 5. A detailed description of this technique can be found in Ref. [3]. We have used this technique to measure material damping of various composite materials with great success.
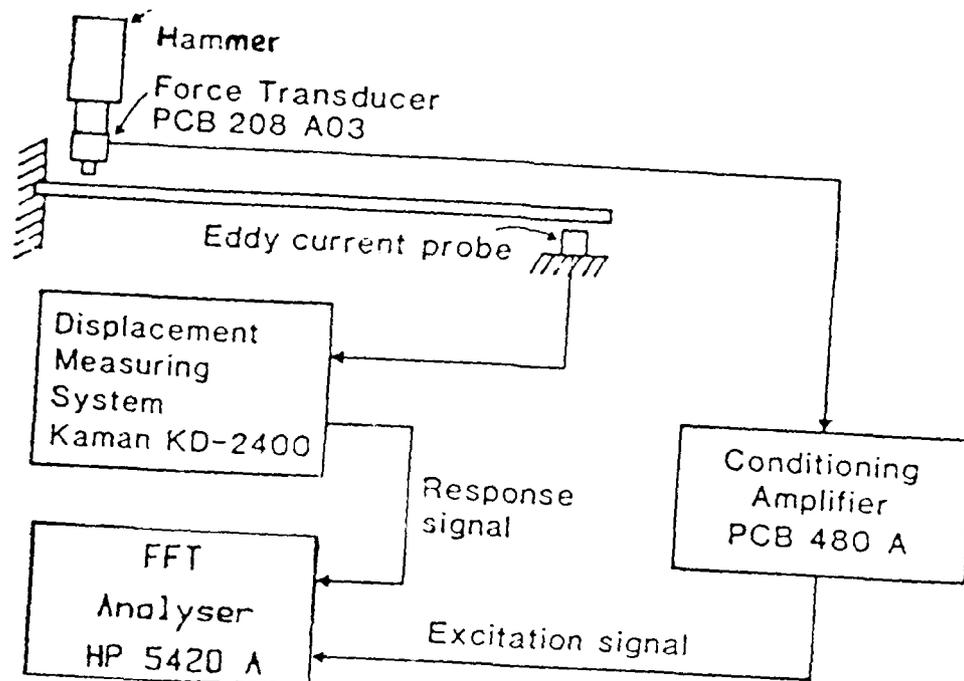
Figure - 5   FLEXURAL VIBRATION TESTING APPARATUS

Numerical Results and Discussion.

The material properties such as moduli, Poisson's ratio, loss factor (damping) for each material i.e., constraining layer, visco-elastic material and the glass-epoxy composite beam are tabulated in Table 1.

Material Properties

			Glass-epoxy composites (0°)				
V_f	ρ g/cm^3	E_L GPa	E_T GPa	G_{LT} GPa	ν_{LT}	η_L	η_T
0.50	1.90	38	8.80	3.0	0 28	0.0033	0.01

3M ISD-110 (ST-2052X visco-elastic material)				
ρ $g/_{cm^3}$	E GPa	Poisson's ratio	G GPa	η
1.10	0.03	0.50	0.01	1

Soft Aluminum (constraining layer)				
ρ $g/_{cm^3}$	E GPa	Poisson's ratio	G GPa	η
2.75	52	0.32	19.7	0.28

Two important quantities, structural damping and the maximum tip deflection with and without add-on visco-elastic tape are evaluated numerically using the finite element program discussed previously. The important parameters which will affect the structural damping and the maximum deflection are the location and length of the add-on material, the condition whether the add-on material is fixed to the fixed end of the composite beam or not, and the ratio between the frequency of the forced vibration to one of the natural frequencies of free vibration. In addition to the above parameters the loss factor of the soft aluminum (constraining layer) may also play an important role to affect the structural damping and the tip deflection of the composite beam. Since there are so many parameters to be considered, we cannot include all the effects in this paper. In this paper we limit attention to vibration in the neighborhood of the fundamental frequency of the system. Results corresponding to higher frequencies will be published in separate papers. Also, the data corresponding to zero loss factor of the constraining layer (η aluminum =0) is called data set one, and corresponding to η aluminum =0.28 as data set two. Data set one represents the case of a stiff but elastic constraining layer with no damping and data set two represents a stiff and high damping material such as soft aluminum. In order to see the effects of the loss factor of the base structure (composite beam) we evaluate the damping and tip displacement ratio as a function of $^a/_L$ (η aluminum=0.28) using η composite as a parameter. This is designated as data set three.

Figure 6 shows the real and imaginary parts of the tip deflection as a function of the frequency of the forced vibration with four lengths of the viscoelastic material and the corresponding structural loss factor evaluated from the finite element program. The amplitude of the tip deflection is also obtained from the response of the real and imaginary parts. At resonance the tip deflection is about seventy times the amplitude of the forcing function when $^b/_L$=0.1 (b=length of the viscoelastic tape) at frequency 1020 rad/se; to forty-five times the amplitude of the forcing functions when $^b/_L$=0.4 at frequency 1100 rad/sec. The value of the fundamental frequency of the system changes slightly because of the influence of the length of the viscoelastic tape. In order to see the effects of the length of the viscoelastic material to the
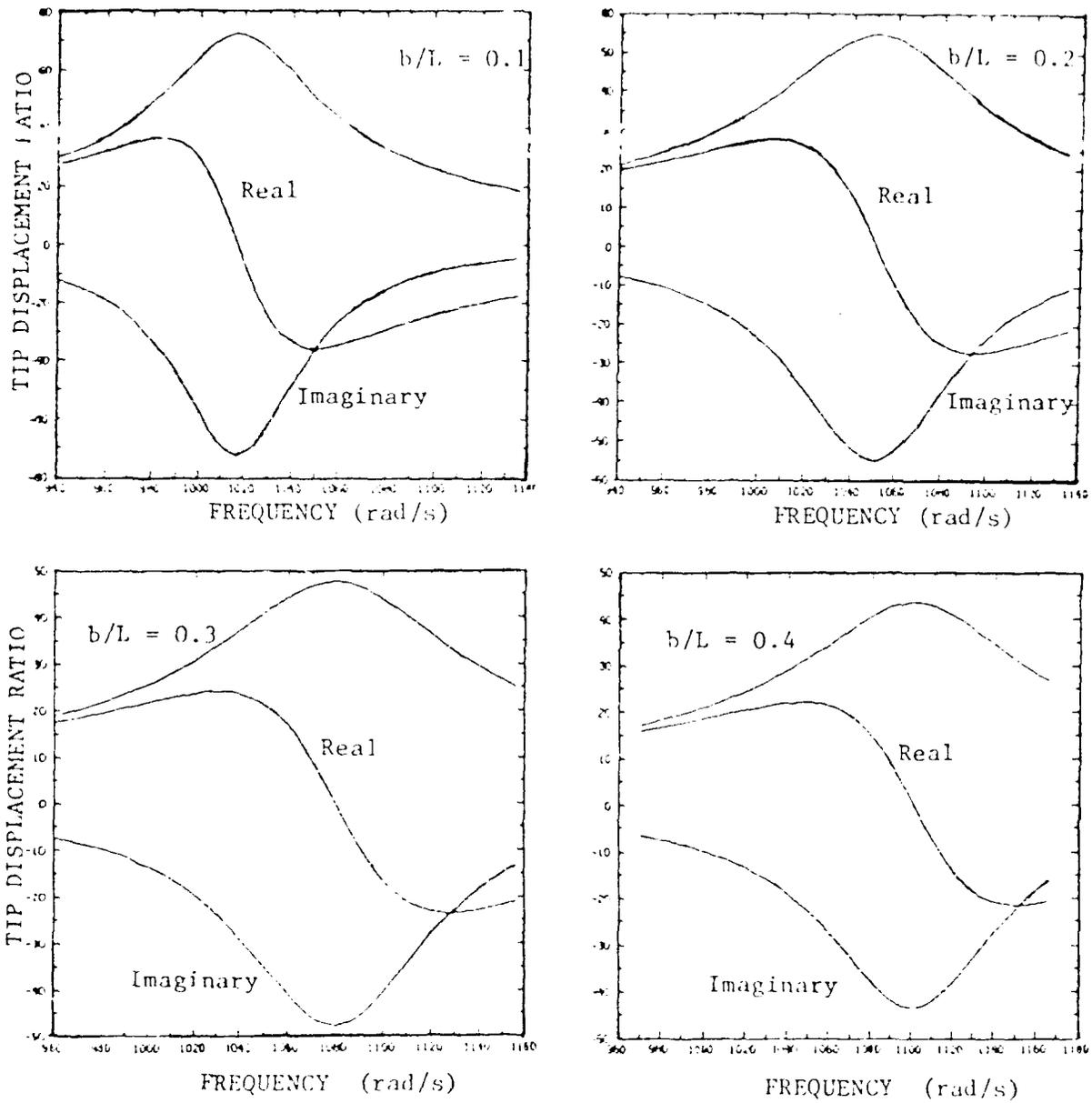
Figure – 6   REAL AND IMAGINARY PARTS OF RESPONSE SPECTRUM (ANALYTICAL
              RESULTS FOR DATA SET 2 WITH a/L = 0.0)

loss factor of the taped and untaped beam we plot the loss factor ratio as a function of the nondimensional tape length in Fig. 7 for two different locations of the tape; one starts from the fixed end of the beam and another starts from 0.1L (L=length of the beam) from the fixed end. It is observed that the loss factor ratio increases as b/L increases and at $b/L \approx 0.4$ the maximum value is reached. The maximum ratio is about 11 for $a/L = 0$ and 7.5 for $a/L = 0.1$. After the peak value is reached, the loss factor ratio suffers a small drop and then maintains this value up to $b/L = 1.0$ for the case $a/L = 0$, and up to $b/L = 0.9$ for the case $a/L = 0.1$. Similar observation is also true for a similar plot of data set two (i.e. η aluminum=0.28) as shown in Fig. 8. The maximum loss factor ratio is 19 for $a/L = 0$ and about 12 for $a/L = 0.1$. The existence of an optimized length of the visco-elastic material at which the structural damping is maximum is significant. This phenomenon was also observed by Plunckett and Lee [4], for metallic materials. This result confirms our previous assumption that the primary mechanism for introducing damping through the viscoelastic material is through shear deformation of the material. At the optimized length the shear deformation reaches a maximum value. For lengths greater than the optimized value (say close to the beam length) the deformation of the viscoelastic material is controlled by extensional deformation of the surface of the beam.
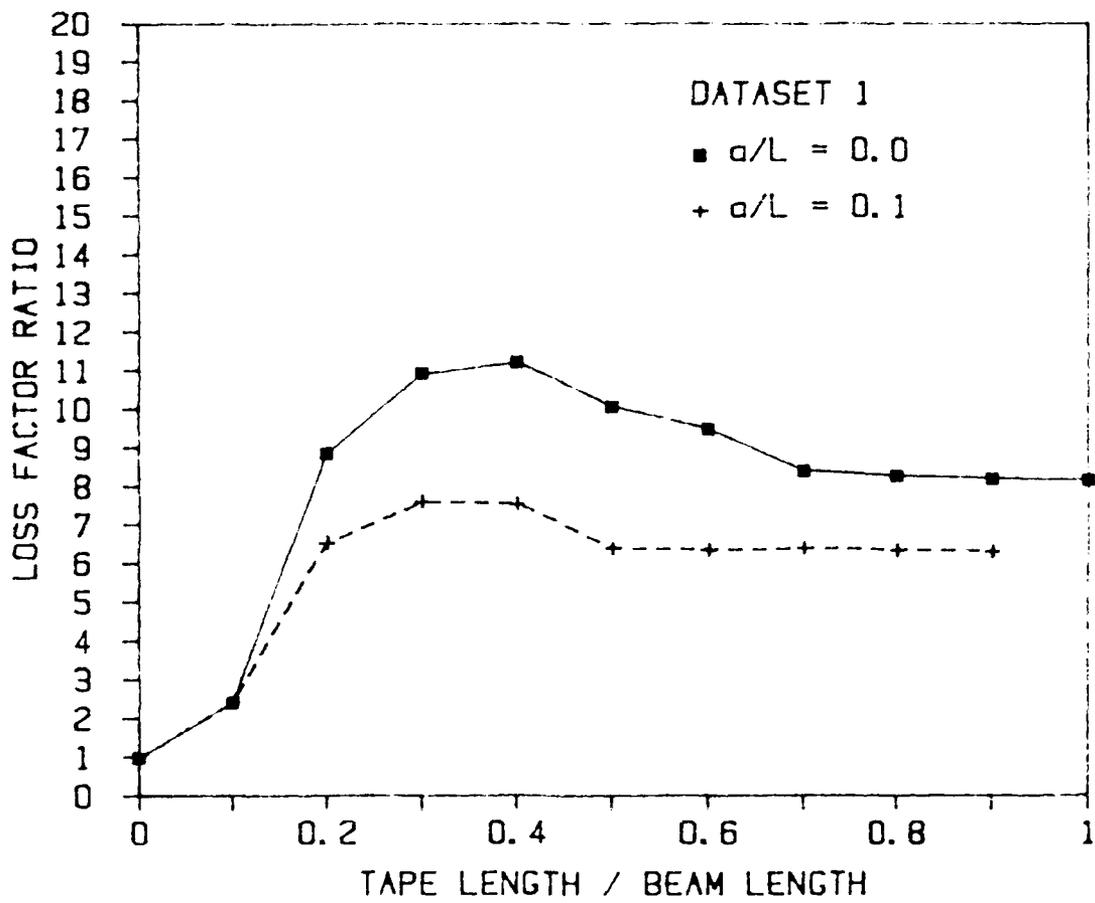
Figure - 7   VARIATION OF LOSS FACTOR WITH
              TAPE LENGTH FOR DATASET 1
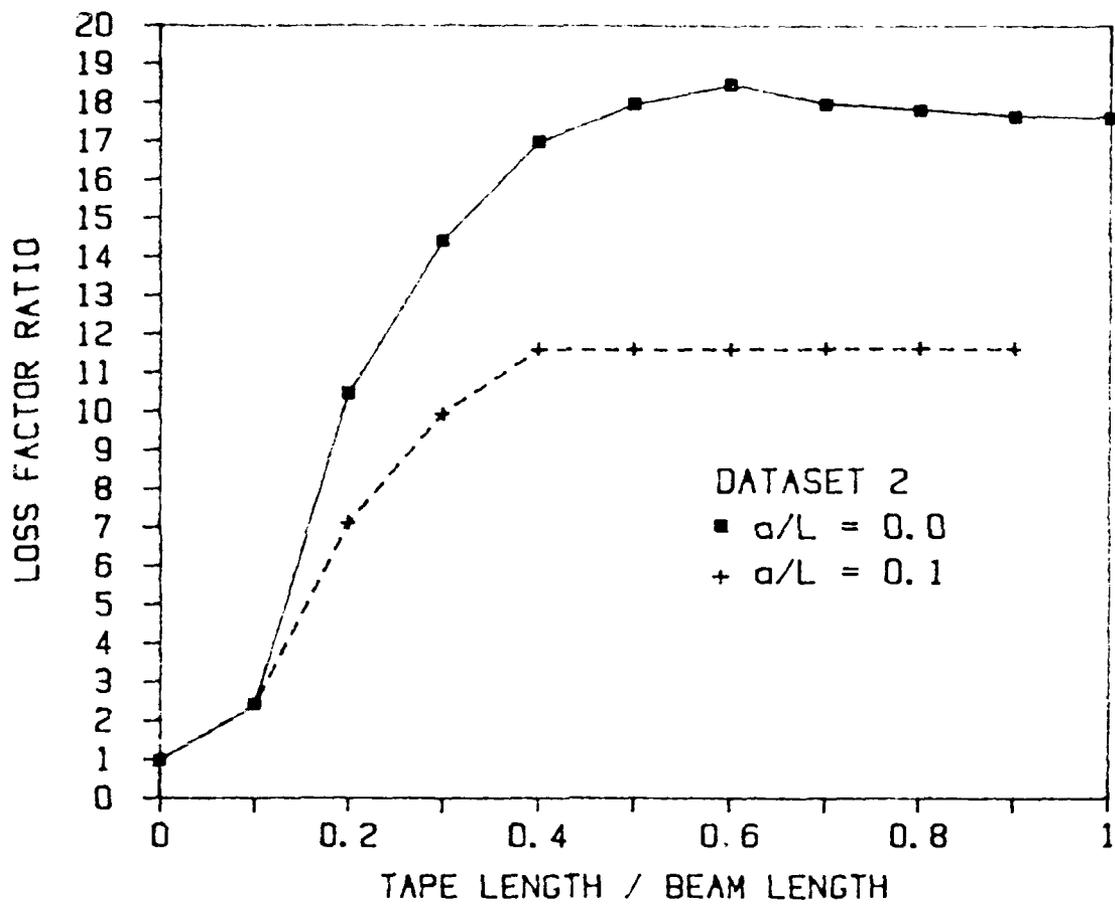
Figure - 8   VARIATION OF LOSS FACTOR WITH
TAPE LENGTH FOR DATASET 2

Figure 9 shows the variation of loss factor ratio with the tape length for data set 3. This helps to examine the influence of the loss factors of the base structure on system damping. Comparisons between figures 8 and 9 reveal that percentage increase in loss factor is greater for the base structure with lower loss modulus. System damping, however, is greater for data set 3. Experimental calculations for loss factor were made only for data set 3, and are plotted in Fig. 9 along with the analytical curve. Reasonable agreement between analytical and experimental data was observed. The trend observed from the analytical calculations was reproduced by experimental measurements.
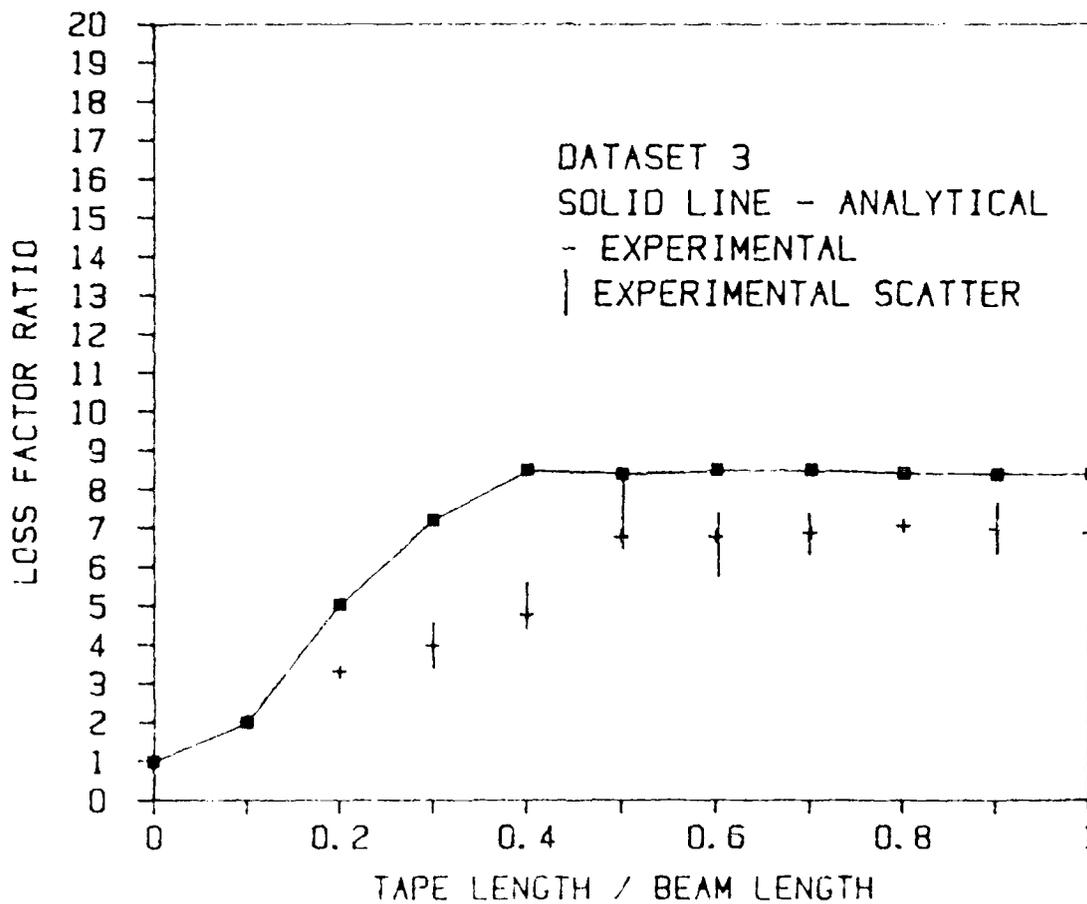
Figure - 9   VARIATION OF LOSS FACTOR WITH
             TAPE LENGTH FOR DATASET 3

In Fig. 10 we plot the ratio of the amplitude of the tip deflection ratio with and without the viscoelastic tape for the case $^a/_L=0$ and $^a/_L=0.1$ for data set one. In Figures 11 and 12 a similar plot is presented for data set two and data set 3. We observed that tip deflection at resonance is reduced more than 35% for the case of $a/_L=0$ and η aluminum=0.28 and for $^a/_L=0$ η composite=0.0075, and is reduced to 95% for the case of $^a/_L=0$ and η aluminum=0.
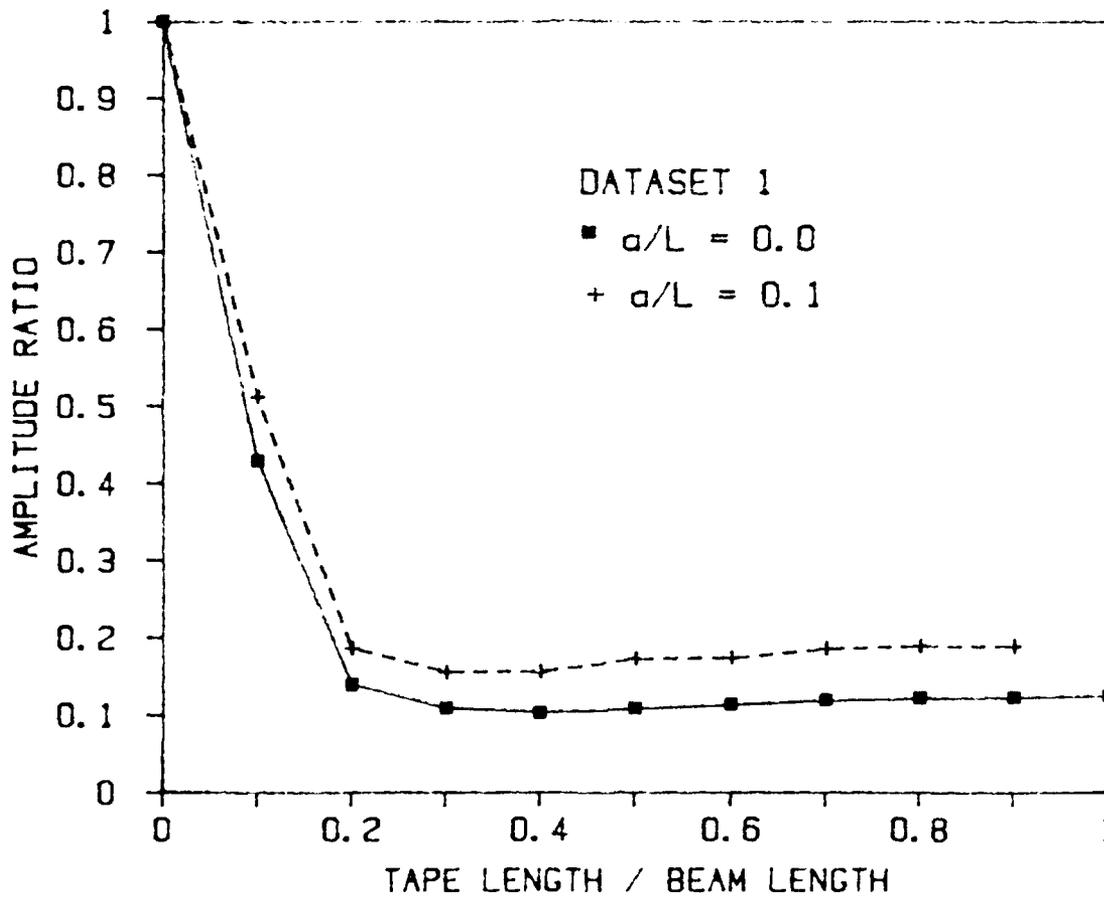
Figure 10   VARIATION OF AMPLITUDE RATIO
WITH TAPE LENGTH FOR DATASET 1
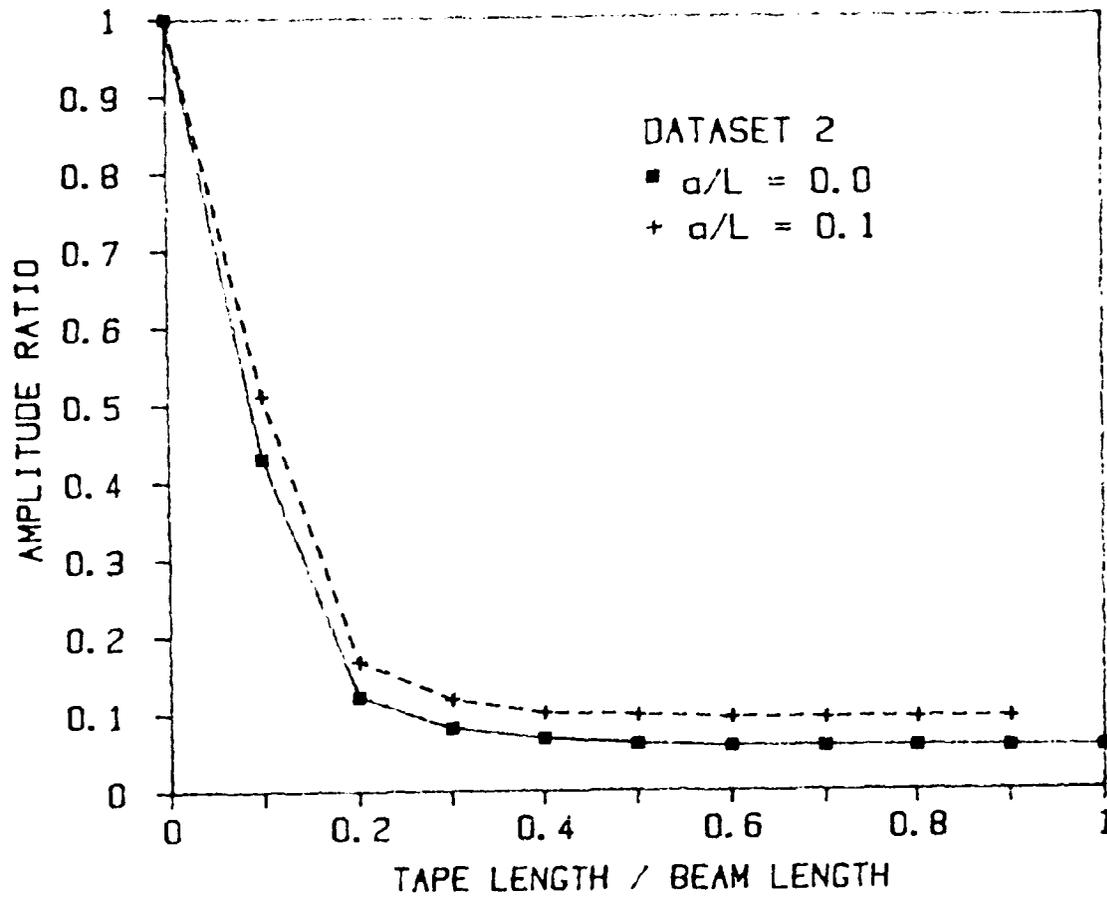
Figure - 11   VARIATION OF AMPLITUDE RATIO
                WITH TAPE LENGTH FOR DATASET 2
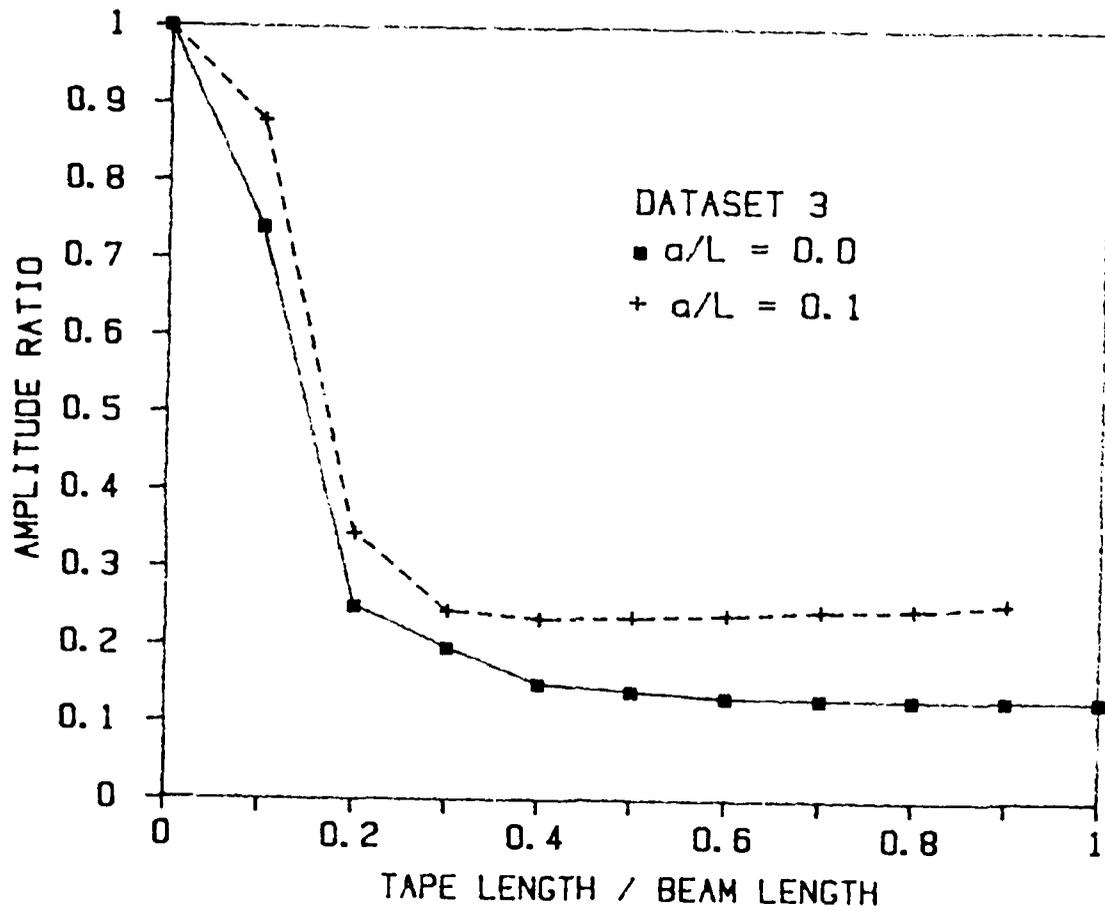
Figure - 12   VARIATION OF AMPLITUDE RATIO
               WITH TAPE LENGTH FOR DATASET 3

In Fig. 13 we plot the loss factor ratio as a function of b/L corresponding to two cases: In one case the viscoelastic tape is fixed at the fixed end of the beam and in the other case it is free at the fixed end the beam. We find out from Fig.13 that the loss factor for the case of free at the fixed end is slightly higher. The greatest difference between these two cases is at the optimized length of the viscoelastic material $b/L=0.4$. In Fig. 14 a similar plot for the amplitude ratio as a function of b/L is presented. Again, the amplitude ratio for the case of free viscoelastic tape at the fixed end of the beam is slightly smaller than the corresponding case of fixed viscoelastic tape at the fixed end of the beam.
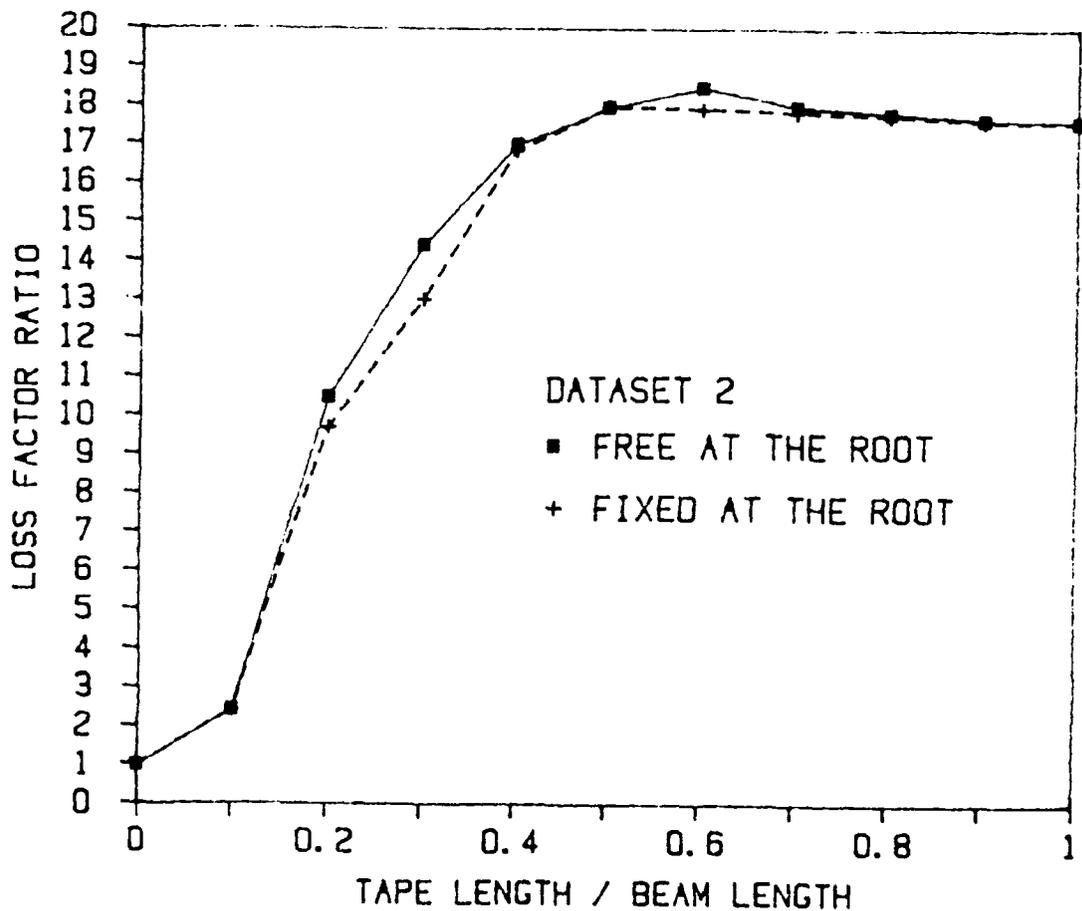
Figure - 13   VARIATION OF LOSS FACTOR WITH
               TAPE LENGTH FOR DIFFERENT B.C.
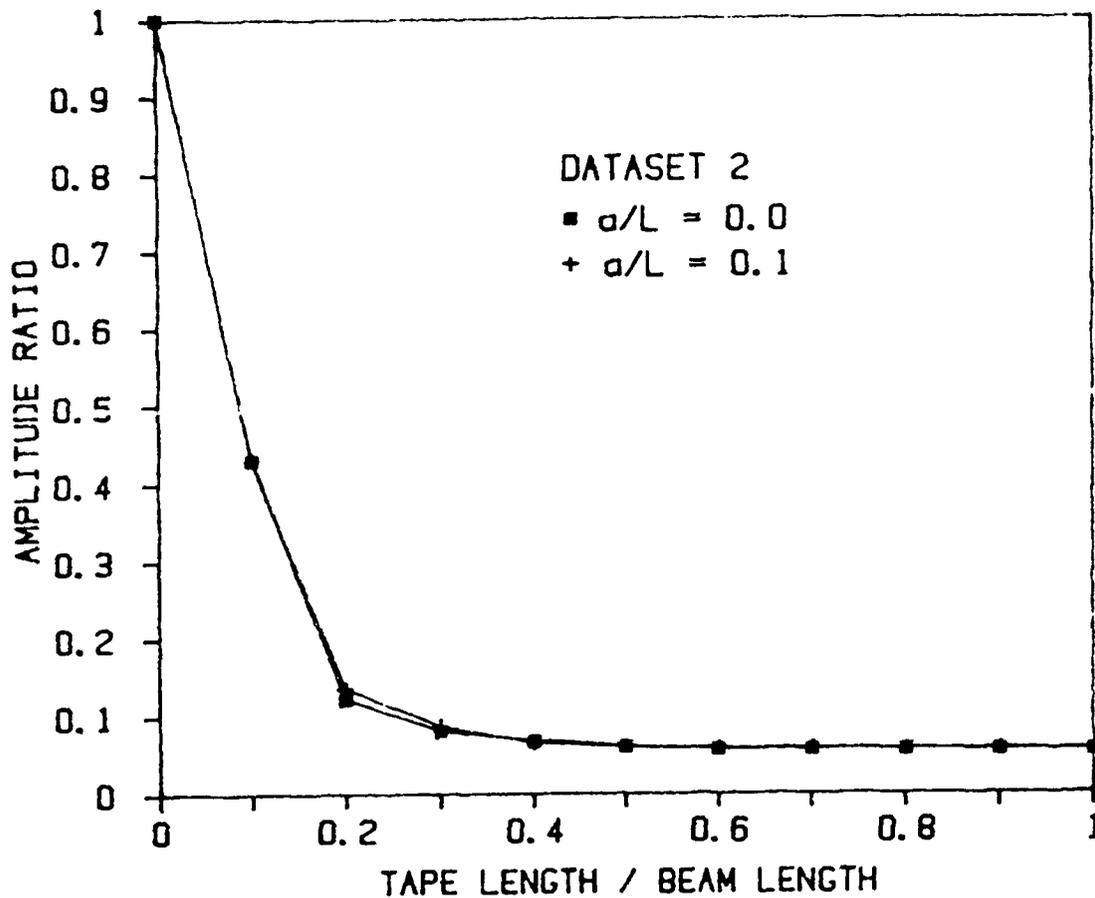
Figure - 14   VARIATION OF AMPLITUDE RATIO
WITH TAPE LENGTH FOR
DIFFERENT B.C.

Concluding Remarks

Based upon the numerical results we have found that for glass-epoxy unidirectional composite beams there exists an optimized length of the add-on viscoelastic material at which the structural damping becomes a maximum. By using commercially available viscoelastic material (3M ISD-110 SJ-2052X tape) with soft aluminum constraining layer [5] the structural damping is increased from 2 to 20 times and the maximum tip deflection can be reduced to about 40%-90% of the value for the composite beam without add-on viscoelastic tape.

In conclusion, the methodology of using add-on viscoelastic tape with a constraining layer to composite structural element seems very useful in vibration control under dynamic load environments. It is very useful to helicopter rotor blades design. Further research for other composite materials such as graphite epoxy, boron-epoxy, etc., should be done. Also, the effects of the initial stress due to centrifugal forces should be taken into consideration in the future research.

References

[1] Nashif, A. D., Jones, D. I. G. and Henderson J. P., "Vibration Damping," John Wiley and Sons, 1985.

[2] Johnson, C. D., Kienholz, D. A., Austin, E. M. and Schneider, N. E., "Finite Element Design of Viscoelastically Damped Structures," Proceedings of Vibration Damping Workshop, February 27-29, 1984 Workshop.

[3] Halvorsen, W. G., and Brown, D. L., "Impulse Technique for Structural Frequency Response Testing," Sound and Vibration p. 8, November 1977.

[4] Plunkett, R. and Lee, C. T., "Length Optimization for Constrained Viscoelastic Layer Damping." Journal of Acoustical Society of America, Vol. 48, p. 151, 1970.

[5] Manufactured by Structural Products Department, 3M Center, St. Paul, Minnesota 55166, Contact Mr. R. A. Frigstad, manager of the department.

CREEP AND LOAD-DEFLECTION CHARACTERISTICS
OF RUBBER ELEMENTS FOR VIBRATION
CONTROL DEVICES

Eugene I. Rivin, Professor
Byoung-Sun Lee, Graduate Student
Department of Mechanical Engineering
Wayne State University
Detroit, MI 48202

This paper describes an experimental study of
load-deflection (or natural frequency-load) characteristics and
creep characteristics of cylindrical rubber components. An
accelerated test procedure was developed for comparative
creep evaluation.

INTRODUCTION

Rubber components loaded in compression play an important role in design of vibration/shock/noise control, as well as power transmission components. This is due to much higher effective elastic modulus and allowable stresses in compressed rubber parts as compared with parts loaded in shear. Accordingly, vibration isolators, couplings, etc.. using rubber in compression can be made smaller and lighter [1,2]. In order to achieve reliable performance characteristic of the compressed parts, rubber elements are bonded between metal plates. Bonding is associated with high processing costs, stress concentration is usually induced in bonded rubber-metal connections under compression [3]. As a result, much smaller relative deformation is allowed for bonded rubber elements loaded in compression (usually 10-20%) as compared with rubber in shear devices (50-100%). As a result, axial dimensions of rubber parts loaded in compression are significantly larger than those of rubber-in-shear parts for required rated axial deflection in the payload direction. Both loaded (bonded) and free surface areas of the bonded components are constant during loading process, thus resulting in the constant shape factor and largely linear load-deflection characteristic. However, a hardening nonlinear characteristic is more beneficial for vibration control devices [1,2].

Rubber blocks without bonding would introduce slippage in the rubber-metal interface. It causes accelerated wear as well as indeterminacy of load-deflection characteristics due to unstable and unpredictable friction characteristics at the interface [4]. In cases where unbonded rubber blocks are compressed (such as spider couplings) onset of slippage is considered as an indication of overloading [5].

One way of avoiding these problems is to use unbonded rubber elements with curvilinear surfaces, whose contact area with flat or shallow curved loading plates would be gradually increasing with the increasing compression force, thus eliminating or alleviating friction-related effects, as well as reducing stress concentration. Intuitively, the best shapes for such elements are classical streamlined bodies such as spheres, toruses, ellipsoids, and cylindrical cords. The concept of using such rubber elements for vibration control devices has a long history. Use of a car suspension with spherical rubber elements was proposed in 1872 [6].

Test results in [7] showed excellent fatigue resistance of spherical rubber parts, even at cyclical compression with the relative deformation alternating between $\epsilon_{min} = 0$ and $\epsilon_{max} = 0.5D$ (D is diameter of the sphere). Intuitively, this is due to reduced stress concentrations in streamlined components. One can make an a priori conclusion that such component would demonstrate also a superior creep behavior. Sometimes, creep phenomenon is called "*static fatigue*". In addition to the advantageous stress distribution, streamlined rubber elements are characterized by continuously changing shape factor with changing load and, thus, by a desirable hardening nonlinearity [10].

This paper will describe some results of experimental study of load-deflection and creep characteristics of cylindrical rubber components.

COMPARATIVE STUDY OF CREEP AS INFLUENCED BY PART SHAPE

Creep can be of critical importance for vibration control devices. Creep differential between individual vibration isolators causes loss of leveling and distortions in machine frames. Creep in vehicle engine mounts, which is naturally enhanced by elevated temperatures in engine compartments and large initial deflections of the mounts, calls for larger clearances between the units in the engine compartments. Creep in power transmission couplings could lead to increasing clearances.

Studies of creep phenomena in rubber are not as extensive as for metals, partly due to a very long time required for conventional creep testing procedures and a need for multiple test rigs in order to simultaneously conduct protracted tests of *several samples. Due to* insufficient available data on creep properties as well as poor communication between mechanical engineers and rubber technologists, there is a widespread belief that a positive correlation exists between relative energy dissipation in a particular rubber blend and its rate of creep. This notion precludes the use of high-damping rubber blends for machinery and engine mounts due to, in part, their allegedly high rates of creep. However, a feasibility of selecting rubber compounds combining high damping and low creep has been demonstrated [1,8].

Creep rate is determined not only by material properties, but also by maximum stresses as well as by the spacial stress distribution in the loaded component. Accordingly, it is reasonable to expect that the creep rate can be modified by judicious shape changes of the element. This issue is addressed below. To exclude influence of compounding/vulcanization, test samples were fabricated from the same rubber stock for a given test group. These samples were tested under various loads and deformations to study influence of part shape. Standard creep tests require a long time($10^3 - 10^4$ min., i.e., 17 h - 7 days). Such prolonged individual tests preclude use of state-of-the-art servo-hydraulic test systems for creep evaluation due to cost considerations. To improve feasibility of creep studies, an accelerated creep testing technique has been developed.

It is generally agreed that creep in rubber elements is a combination of primary (or physical) creep and secondary (or chemical) creep [8]. Primary creep, which dominates at short duration tests, is related to the displacement or slippage of cross links in rubber under loading. Secondary creep dominates at prolonged tests and is mainly associated with chemical degradation of the rubber due to attack by atmospheric constituents such as oxygen and ozone. Overall creep intensity can be characterized by the percentage relative creep.

$$C_\epsilon = \frac{y_t - y_i}{y_i} \times 100\% \qquad (1)$$

where y_t is deformation of the sample after t minutes of loading; and y_1 is its deformation of the sample after 1 minute of loading. The deformation y_1, practically, fully recovers upon removal of the initial load.

The primary creep rate usually slows with time, with the creep deformation being approximately proportional to the logarithm of time. Thus its magnitude can be expressed per a decade of time, by dividing (1) by log t (min.). Beginning as a straight line, the creep plot then passes through a transition region (at 10^3 or 10^4 min.) due to the effect of the secondary creep.

In this report, the primary creep which is more dependent on stresses and strains in rubber elements is studied for a comparative evaluation of how creep rate is influenced by the shape of rubber parts.

An accelerated creep testing procedure was first described in [9]. It was shown that a cyclical loading of a rubber specimen (application and removal of deadweights with a 20 sec period) creates continuous increase in deformation. A *"creep rate per decade of cycles"* characteristic was introduced, and has shown a remarkable correlation with the standard *"creep rate per decade of time"* while being numerically higher about 8 times for the employed loading sequences. In our work, cyclic creep tests were performed using two different sinusoidal loading waveforms (double amplitude sinusoidal waves and single amplitude, or haver sine, sinusoidal waves), for which percentage relative creep deformation is defined, respectively, as

$$C_{cd} = \frac{y_n - y_1}{y_0} \times 100\% \quad ; \quad C_{cs} = \frac{y_n - y_1}{y_1} \times 100\% \tag{2}$$

where y_1, y_n is deformation after the first, n-th cycle; y_0 is initial static deformation.

Dividing C_{cd} and C_{cs} by log n results in cyclic creep rates per decade for the respective waveforms.

GEOMETRY OF TEST SPECIMENS AND TEST PROCEDURE.

The test specimens were solid cylinders (durometer 60 Shore A) made from neoprene rubber. To assure consistency of rubber parameters, the cylinders were fabricated by a precision cutting of a required length from a long extruded cylindrical cord. Three samples were tested for each test condition. All the tested specimens were not subjected to loading before the actual test. The tests were performed on Instron servo-hydraulic testing machines (models 1350 and 1331). Nicolet digital oscilloscope (model 4094) was used for recording and storing output signals and also for monitoring feedback signals generated by load and stroke controllers of the testing machines. Stored output waveforms in Nicolet digital oscilloscope were transferred into PC via RS 232 interface and Waveform BASIC developed by Blue Feather Software Co. (Figure 1). Ambient temperature and relative humidity were in the general range of 70°F – 85°F and 40% – 70%, respectively.

Load-deflection Characteristics. Each cylindrical specimen was gradually deformed in the radial direction at 0.4 inch/min. (ISO standard speed) without interruption up to 55% relative deflection. The compression was repeated for three consecutive cycles.

Several surface conditions had been tested: (a) Petroleum-jelly on polished flat metal platens to eliminate friction; (b) Sandpaper (grit 400) attached to the platens to resist lateral slippage; (c) Polished flat metal platens without sandpaper or lubrication; (d) Specimens were embedded in flexible silicon foam molded around them.

As shown in [1], the "constant natural frequency" characteristic is of special importance for vibration isolators. Accordingly, instead of load-deflection characteristics, load-natural frequency characteristics, were studied. Natural frequency was calculated as $f_z = 1 / 2\pi\sqrt{K_z g / P}$ where $Kz = \Delta P/\Delta x$ is vertical stiffness; g is acceleration of gravity; and P is applied load, considered as a weight load.

Rubber elements, radially compressed between the platens with restriction on sliding (with sandpaper) have the highest stiffness, and those embedded in foam – the lowest stiffness. It is clearly indicated in Figure 2. For the "constant natural frequency" range, which is defined as loaded range in which f_z variation is within ± 5%, f_z=9.3; 9.1; 8.7; 8.3 Hz for surface with sandpaper; cleaned without lubrication; lubricated; for samples embedded in foam, respectively.

Static creep test. To establish reference database for accelerated creep tests, static (constant load) tests were performed for several specimens using "load control" mode at 15% and 30% deformations. The specimen deflection was automatically sampled every minute for the first decade of time (1 – 10 min.) and every 10 min. for the second decade of time (10 – 100 min.) using programmed computer data acquisition system. Figure 3 compares static creep data for samples d=1.0", L/d=1.0" for deformations 15, 30, and 45% for axial and radial loading.

Cyclic creep test. Cyclic creep tests were performed using the same static load levels as before (corresponding to 15% and 30% deflections). The specified initial static load was applied quickly in case of double amplitude sine waveform test and then the cyclic test was initiated (see Figure 4a). The initial preload is not necessary for a haver sine waveform, Figure 4b. Peak values of deflection were sampled every cycle for the first decade (1 – 10 cycle) and every 10 cycles for the second decade (10 – 100 cycle) using the data acquisition system. Due to specifics of the LVDT sensors of the testing machines, it was difficult to obtain consistent accurate reading of the minimum deformations. Thus, only the maximum peak values of deflection had been monitored. Due to nonlinearity of samples, significant nonlinear distortions of the load feedback signal were even at 0.1 Hz observed on the model 1350.

Accordingly, both amplitudes and frequencies had been limited. During this study, since only basic creep characteristics as influenced by shapes of rubber components were studied, the test length was usually limited to 100 cycles (two decades). Figure 5 shows cyclic creep rate of cylindrical specimens d=1.0", L/d=1 for 30% of radial and axial compression 0.1 Hz and 0.4 Hz tested with haver sine waveforms.

DISCUSSION

Nonlinearity of load-deflection characteristics of cylindrical rubber elements results in their load-natural frequency characteristics having wide "constant natural frequency" segments with ratio of maximum and minimum loads for these segments $P_{max} : P_{min}$. = 4:1 – 10:1. This is a very beneficial feature for vibration control applications. Use of the elements embedded in foam allows to achieve the lowest natural frequencies together with high consistency of the characteristics.

It can be seen from Figures 3, 5 that both static and cyclic creep at the same relative compression is 30-40% less for specimens loaded in the radial direction with absolute values being lower for static tests. For the same other conditions, creep values are increasing with increasing frequency; this effect is more pronounced for axial loading (Figure 5). Another interesting effect is reduction in relative creep with increasing relative compression as can be seen in Figure 3. Use of the developed accelerated creep testing technique allowed to perform a two decade test at 0.1Hz in less than 20 min. thus allowing to use state-of-the-art test systems.

ACKNOWLEDGMENT

REFERENCES

1. Rivin, E.I., "Principles and criteria of vibration isolation," ASME J. Mechanical Design, Vol. 101, pp. 682-691, 1979

2. Rivin, E.I., "Design and application criteria for connecting couplings," ASME J. of Mechanisms, Transmissions, and Automation in Design, Vol. 108, pp. 96-105, 1986

3. Stevenson, A., "Fatigue life determinations of rubber springs." Polymer Testing, No. 4, pp. 289-305, 1984

4. Holowuia, B.P., "Stiffness of rubber blocks in contact with different surfaces," Plastics and Rubber processing and Applications, Vol. 3, pp. 9-12, 1983

5. Mikhailov, Yu.K., Lazarev, S.O., "Durability of a rubber spider coupling," Izvestiya VUSOV "Mashinostroeaie", No.10, pp. 34-38, 1983 (in Russian)

6. King, A.H., "Improvement in car springs," U.S. Patent 123.999, Feb. 27, 1872

7. Kerr, M.L. and Schmitt, R.V., "A new elastomeric suspension spring," SAE paper 710058, 1971

8. Meier, J.F., Rudd, G.E., Siemon, J.T. and Kelly, C., "Development of creep resistant elastomeric mounts," Elastomeric, March, pp. 23-27, 1986

9. Thomas, A.G. and Derham, C.J., "Creep of rubber under repeated stressing," Rubb. Chem. Technol., Vol. 50, pp. 397-402, 1977

10. Rivin, E.I., "Applications of Nonlinear Mechanical Systems for advanced Machine Elements," in The Theory of Machines and Mechanisms, Proc. of the 7th World Congress, Vol. 3, Pergamon Press, Oxford, pp. 1613-1618, 1987
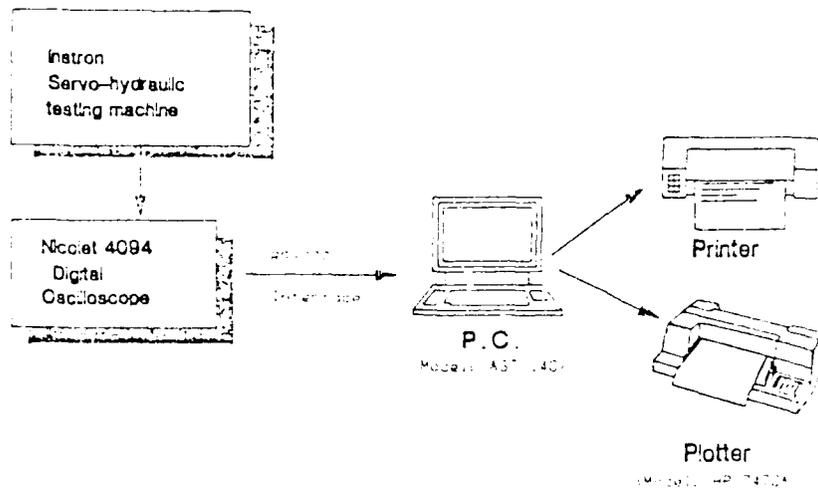
Figure 1. Schematic representation of the Instron servo-hydraulic system and data acquisition system.
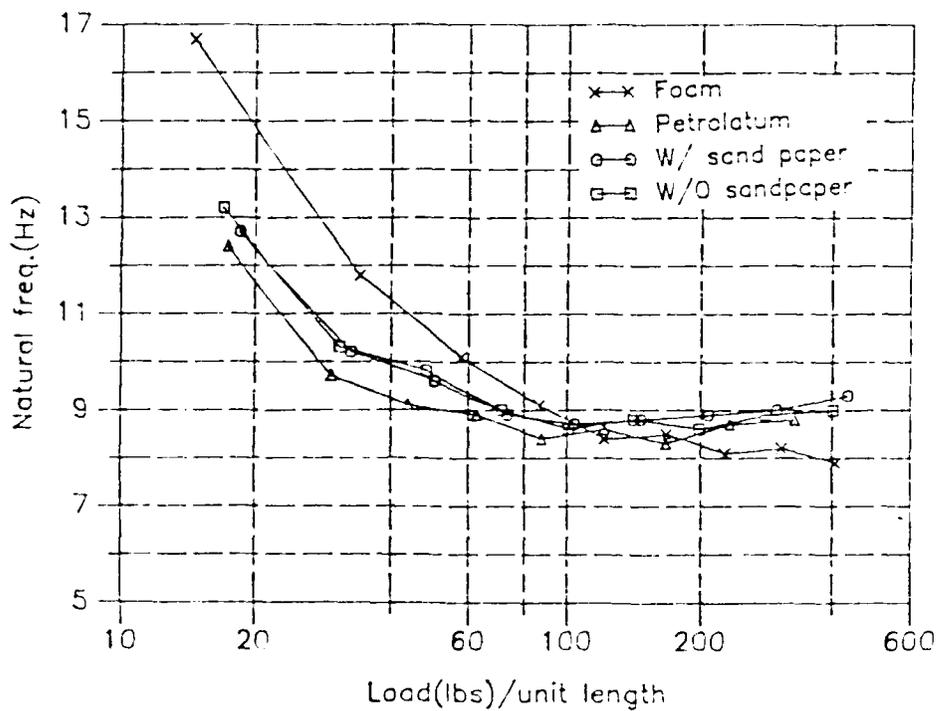
Figure 2. Load-natural frequency characteristics radially compressed for cylindrical specimens d=0.87", L/d=1.15.
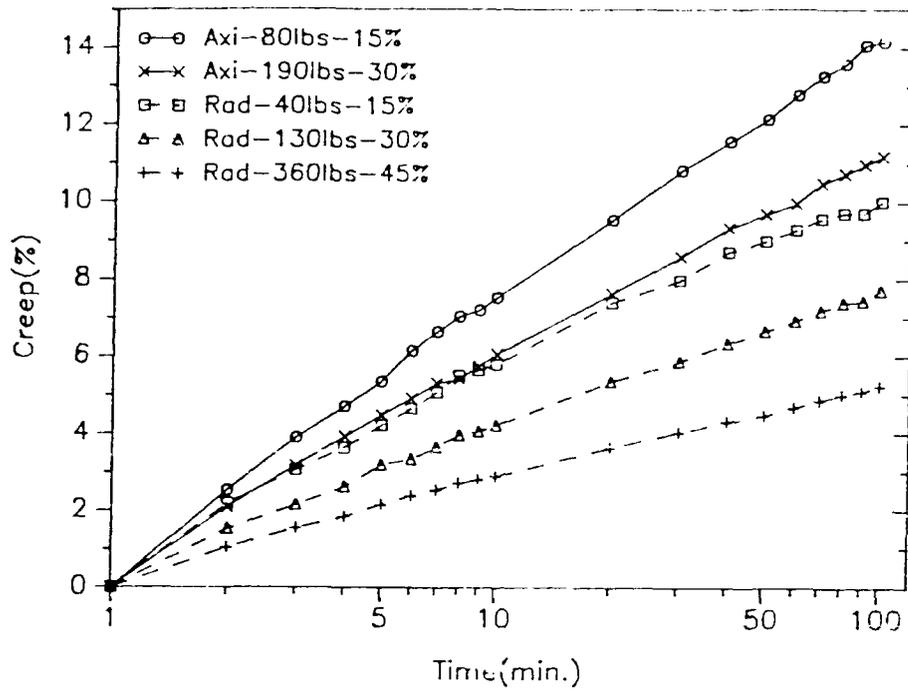
Figure 3. Static creep rate of specimens d=1.0", L/d=1.0 at 15, 30 and 45% deformations for axial (solid lines) and radial (broken lines) compression (platens with sandpaper).
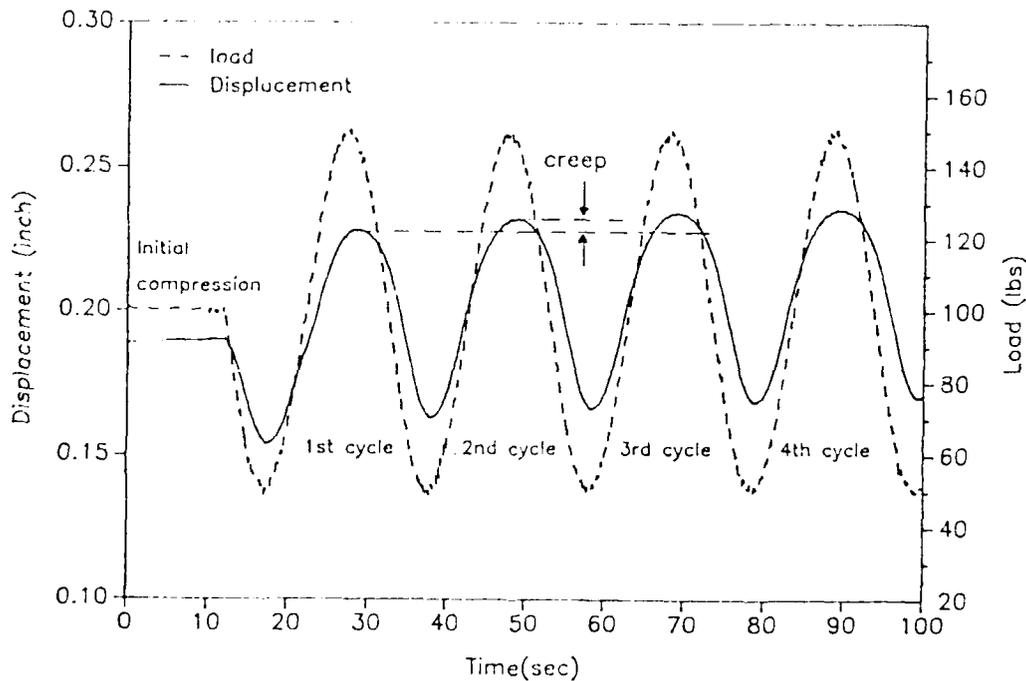
Figure 4a. Cyclic creep test using double amplitude sinusoidal waves.
* Sample size; D=0.87", L=1.0" (putting two samples on the plates)
* Given load; radial compression, 100 ± 50 lbs f_0=0.05 Hz.
* Surface condition; with sandpaper.
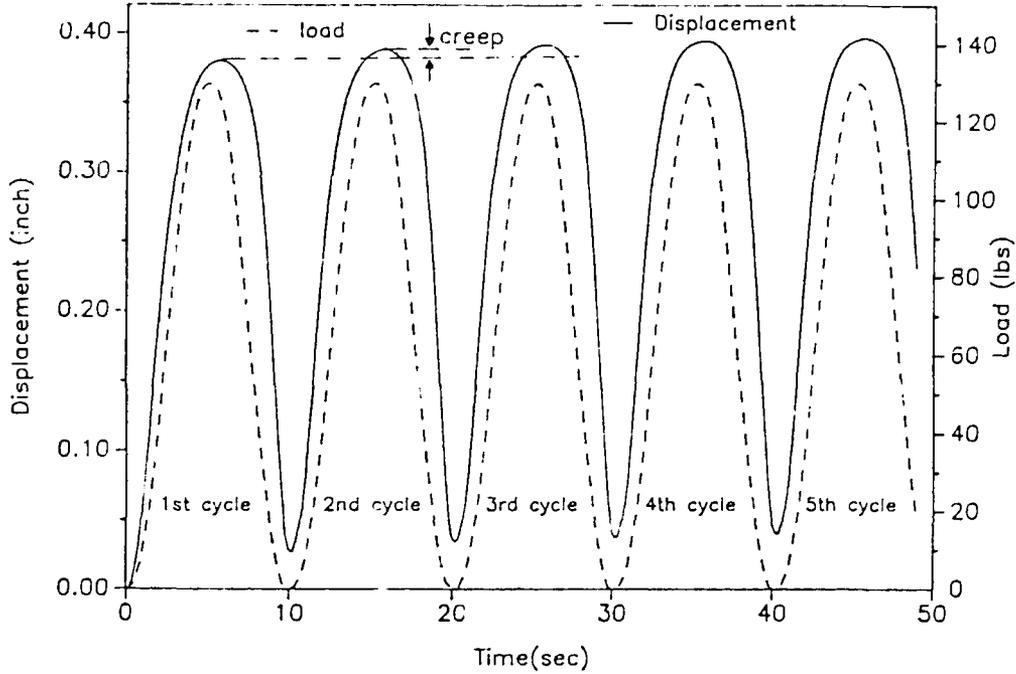
Figure 4b. Cyclic creep test using single amplitude sinusoidal waves.
* Sample size; d=1.0", L=1.0"
* Given load; radial compression. max.=130 lbs, min.=0 lbs
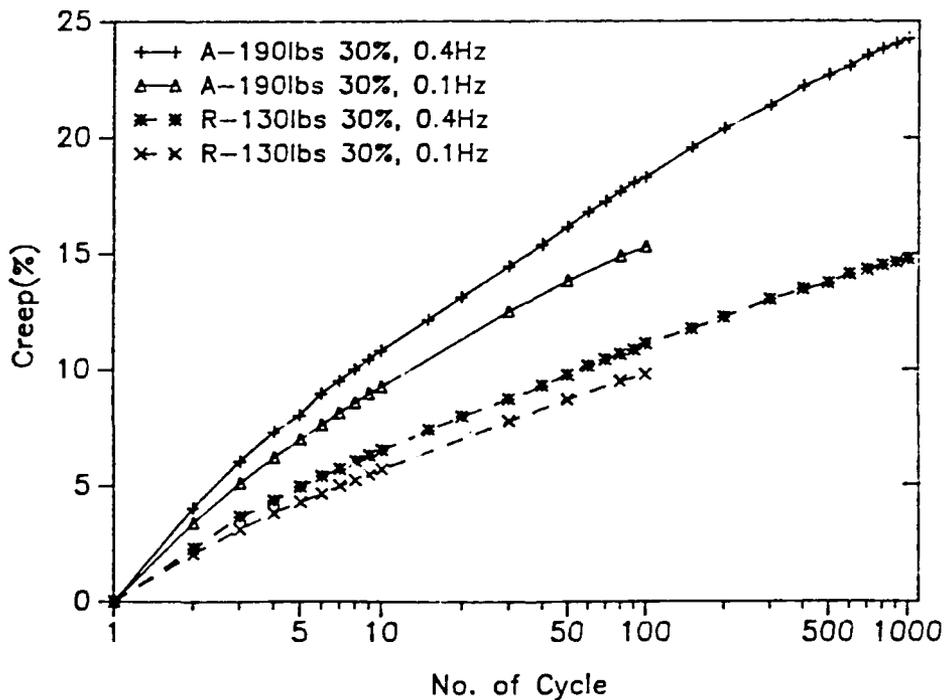
Figure 5. Cyclic creep rate of specimens d=1.0", L/d=1.0 for axial (solid lines) and radial (broken lines) compression at 0.1Hz, 0.4Hz Haver-sine loading (platens with sandpaper).

AIRBLAST

ENVELOPE MODELS FOR FINDING THE RESPONSE
OF STRUCTURES IN BLAST WAVES

Stuart J. C. Dyne and Joseph K. Hammond
Institute of Sound and Vibration Research
University of Southampton
Southampton, England

Many techniques exist for the prediction of response time histories for structures subject to convecting pressure fields. Often the full detail of these time histories is not required and approximate methods that yield their main features of interest are sought. Indeed it is usually possible to predict only the main features with confidence since experimental results inevitably deviate from precise theoretical expectations. One aspect of a response curve is its envelope – a concept which is useful as a measure of peak values and decay rates and which finds application in damage assessment criteria. This paper presents an economical method for the prediction of an *upper bound for* the envelope of the response curve of a structure subject to a distributed loading and hence an upper bound for the structural response.

INTRODUCTION

Detailed models of structural systems are often inappropriate: Model parameters such as elasticity modulii or structural dimensions may not be known with precision and material assumptions such as isotropic properties or frictionless couplings may be invalid. Nominally identical physical structures inevitably exhibit subtly different characteristics and the same structure produces different results as its environment changes or as it ages. Further, there may be a requirement for only limited information from response curves such as peak response levels in a given frequency band or vibration decay rates.

Davies [1] has shown how an envelope/Hilbert transform technique could be used to find an upper bound for the envelope of the response of a general linear bandlimited single input system. The key results of this analysis are given below together with an example. The system response envelope satisfies an inequality involving the envelopes of the input and the system *impulse* response and hence produces an upper bound for the system response. This technique is extended to consider systems with distributed loading which cannot be reduced to single

input systems, and is used predict the response of simple structures to convecting pressure waves.

SINGLE INPUT SYSTEMS

A useful definition of the envelope of a signal is given by Dugundji [2] and follows from the theory of analytic functions: For a given time history $x(t)$, the analytic function evaluated on the real axis of which $x(t)$ is the real part is denoted $\sigma_x(t)$ and is formed from $x(t)$ and its Hilbert transform $\hat{x}(t)$. That is

$$\sigma_x(t) = x(t) + j\hat{x}(t) \tag{1}$$

where j is the root of -1 and where the Hilbert transform is defined as

$$\hat{x}(t) = x(t) * \frac{1}{\pi t} \tag{2}$$

where $*$ denotes time domain convolution. Now the analytic function $\sigma_x(t)$ may also be expressed in modulus/phase form as

$$\sigma_x(t) = A_x(t)e^{j\phi x(t)} \tag{3}$$

where, from equation (1), the real functions $A_x(t)$ and $\phi_x(t)$ are

$$A_x(t) = \sqrt{x^2(t) + \hat{x}^2(t)} \tag{4}$$

and

$$\phi_x(t) = tan^{-1}\left(\frac{\hat{x}(t)}{x(t)}\right) \tag{5}$$

$A_x(t)$ is defined as the envelope of $x(t)$ and $\phi_x(t)$ is defined as the phase of $x(t)$. It should be noted that the Hilbert transform defined in equation (2) is acausal - the function $\hat{x}(t)$ may be non-zero prior to the first non-zero portion of $x(t)$. As a consequence, the envelope is generally also acausal and this will be a feature of some of the figures below. While the topic receives no further treatment here, it is worth noting that the instantaneous frequency of a signal may be obtained by differentiating the expression for phase (equation (5)) with respect to t.

Approximations to the Hilbert transform in discrete form [3] exist and form the basis of algorithms to calculate envelopes numerically for sampled data. One such algorithm has been employed to compute the envelope of the signal shown in Figure 1. We note that the envelope always exceeds the signal values and follows the signal amplitude as anticipated. In this particular case there is a ripple effect in the

208

envelope which is due to the finite length (128 points) of the Hilbert transform filter and the sine wave frequency/data sample rate ratio.
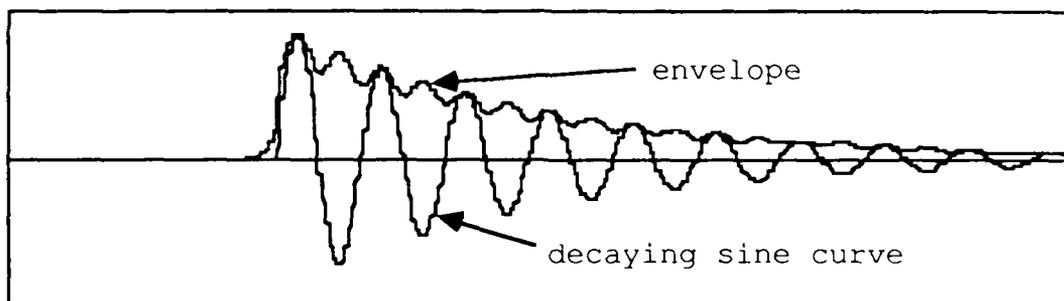

Figure 1: Exponentially decaying sine curve and envelope.

Consider now the general bandlimited time invarient system sketched schematically in Figure 2. The system response $y(t)$ to an input $x(t)$ is given by the convolution of the input and the system impulse response function $h(t)$ [4 etc.]. That is

$$y(t) = \int_{-\infty}^{\infty} x(\tau) h(t-\tau) d\tau \tag{6}$$

with dummy variable τ, or, more consisely,

$$y(t) = x(t) * h(t) \tag{7}$$
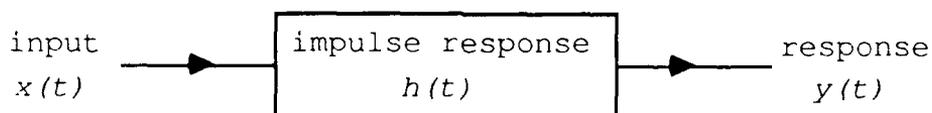
Figure 2: Linear single input system.

It can be shown [1 and 5] that the envelopes of the input $A_x(t)$ and output $A_y(t)$ are related by an inequality:

$$A_y(t) \leq \frac{1}{\cdot} A_x(t) * A_h(t) \tag{8}$$

The convolution on the right hand side thus provides an upper bound for the envelope of the response of the system; hence an upper bound for the response of a system can be predicted from a knowledge of only the envelope of the input and the envelope of the impulse response function. The example below illustrates these ideas.

SINGLE INPUT SYSTEM EXAMPLE
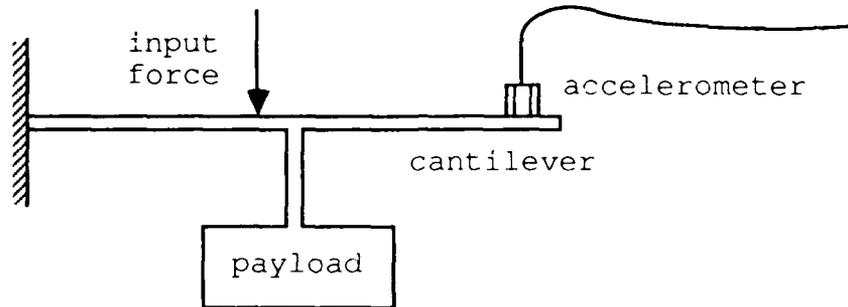
Figure 3: Cantilever beam with attached payload
subject to impact force input.

We show an application of inequality (8) to produce an upper bound for the tip response of a cantilever beam with attached payload and subject to a hammer blow (Figure 3).

The beam response is recorded using an accelerometer mounted on the free end of the cantilever. The force input is recorded using a force transducer attached to the impact device. A Fourier approach is then used to find the impulse response function $h(t)$, of the beam. The experiment is repeated giving a new response function $y(t)$, for which an upper bound is to be found using only a recording of the new force input $x(t)$ and $h(t)$. The envelopes of $x(t)$ and $h(t)$ are calculated applying the analysis above and from these the convolution on the right hand side of inequality (8) is found. This is shown in Figure 4 as the upper bound for $A_y(t)$ together with the envelope $A_y(t)$ obtained directly from $y(t)$. It can be seen that the upper bound always exceeds the response envelope.
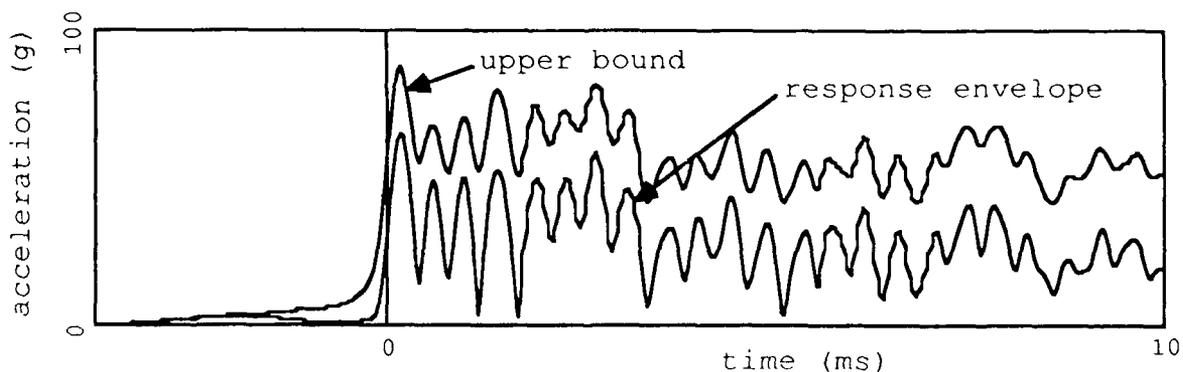

Figure 4: Cantilever tip acceleration envelope and upper bound.

Thus we have been able to predict an upper bound for the response of a structure with a single input using only the envelope of the system input and the envelope of the impulse response of the system.

DISTRIBUTED INPUT SYSTEMS

It is a simple matter to extend the analysis above for systems with multiple discrete inputs. Linearity has been assumed and so superposition may be applied to combine the effects of each input. Note however that the phase information is not retained in the signal to envelope transformation so that whereas the sum of two signals of near equal amplitude but opposite phase (from two sources say) results in a small signal, the addition of their *envelopes* produces a yet larger envelope.

A blast environment however is still more complicated. The input (blast wave) to the distributed system (structure) is continuous and may vary over one or more spatial variables in addition to time dependence. The pressure on a plate mounted in a shock tube for example may vary with location on the plate (specified by two position vectors) and time. The envelope analysis above may be extended to consider distributed loading although linearity must again be assumed.

input:
$x(t,\boldsymbol{s})$

response:
$y(t,\boldsymbol{r})$

system: $h(t,\boldsymbol{r},\boldsymbol{s})$
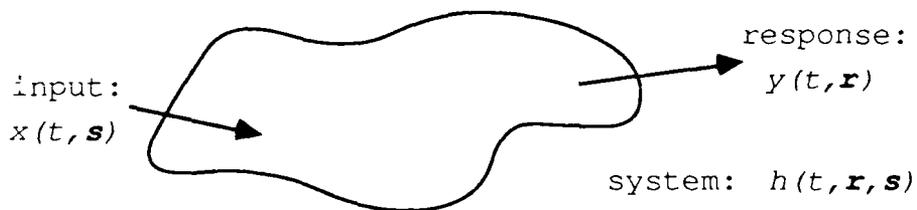
Figure 5: Distributed system.

Consider the general distributed system sketched schematically in Figure 5. The response at a point with position vector $\boldsymbol{r}$ is denoted $y(t,\boldsymbol{r})$ when the system is subject to input $x(t,\boldsymbol{s})$ over the domain of points with position vector $\boldsymbol{s}$. The transfer function relating the output to the input is denoted $h(t,\boldsymbol{r},\boldsymbol{s})$. Thus

$$y(t,\boldsymbol{r}) = \int_{S} x(t,\boldsymbol{s})*h(t,\boldsymbol{r},\boldsymbol{s})\,ds \qquad (9)$$

where S denotes the range for $\boldsymbol{s}$ and the * again denotes convolution in the time domain. The Hilbert transform of this equation is taken to give

$$\hat{y}(t,\boldsymbol{r}) = \int_{S} \hat{x}(t,\boldsymbol{s})*h(t,\boldsymbol{r},\boldsymbol{s})\,ds \qquad (10)$$

Equations (9) and (10) are combined to give

$$y(t, \boldsymbol{r}) + j\hat{y}(t, \boldsymbol{r}) = \int_S \big(x(t, \boldsymbol{s}) + j\hat{x}(t, \boldsymbol{s}) \big) * h(t, \boldsymbol{r}, \boldsymbol{s}) \, ds \qquad (11)$$

This can be expressed more consisely using the notation of equation (1)

$$\sigma_y(t, \boldsymbol{r}) = \int_S \sigma_x(t, \boldsymbol{s}) * h(t, \boldsymbol{r}, \boldsymbol{s}) \, ds \qquad (12)$$

It can be shown [6] that the Hilbert transform of an already transformed signal restores the original signal but with a change of sign. The transform of equation (12) therefore yields

$$\hat{y}(t, \boldsymbol{r}) - jy(t, \boldsymbol{r}) = \int_S \sigma_x(t, \boldsymbol{s}) * \hat{h}(t, \boldsymbol{r}, \boldsymbol{s}) \, ds \qquad (13)$$

Multiplying this by j and adding to equation (11) gives

$$2\sigma_y(t, \boldsymbol{r}) = \int_S \sigma_x(t, \boldsymbol{s}) * \sigma_h(t, \boldsymbol{r}, \boldsymbol{s}) \, ds \qquad (14)$$

From the theory of complex variables [9] it can be shown that

$$\left| \int_a^b f(z) \, dz \right| \leq \int_a^b |f(z) \, dz| \qquad (15)$$

Thus

$$2 |\sigma_y(t, \boldsymbol{r})| \leq \int_S |\sigma_x(t, \boldsymbol{s}) * \sigma_h(t, \boldsymbol{r}, \boldsymbol{s})| \, ds \qquad (16)$$

This may be expanded by expressing each analytic function in modulus/phase form as in equation (3). Hence

$$2 \left| A_y(t, \boldsymbol{r}) e^{j\phi_y(t, \boldsymbol{r})} \right| \leq \int_S \left| A_x(t, \boldsymbol{s}) e^{j\phi_x(t, \boldsymbol{s})} * A_h(t, \boldsymbol{r}, \boldsymbol{s}) e^{j\phi_h(t, \boldsymbol{r}, \boldsymbol{s})} \right| ds$$

$$(17)$$

Eliminating the phase components of each function

$$A_y(t,\mathbf{r}) \le \frac{1}{2} \int_S A_x(t,\mathbf{s}) \,{}^\star A_h(t,\mathbf{r},\mathbf{s})\,ds \tag{18}$$

That is, the response envelope $A_y(t,\mathbf{r})$ is bounded by a function obtained from the envelope of the input $A_x(t,\mathbf{s})$ and the envelope of the impulse response function $A_h(t,\mathbf{r},\mathbf{s})$ integrated over the domain of influence of the input. Again, an example provides clarification of the final result.

DISTRIBUTED SYSTEM EXAMPLE
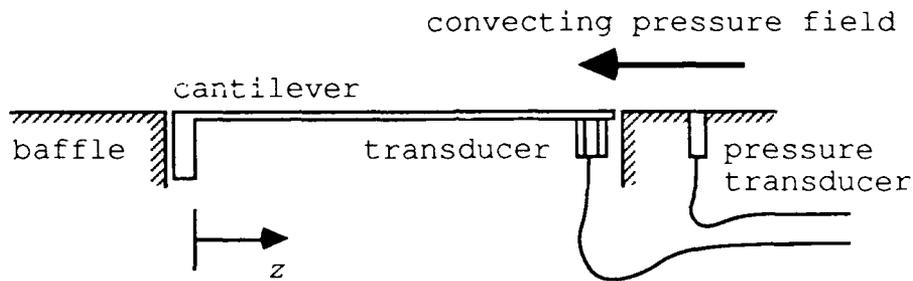
Figure 6: Schematic cantilever subject to grazing incidence blast wave.

We show how the result above may be used to provide an upper bound for the peak displacement response at the tip of a uniform cantilever subject to a convecting pressure field at grazing incidence. The geometry of the simulation is illustrated in Figure 6. A cantilever beam of rigidity modulus EI, damping coefficient γ, mass m, and length l is subject to the pressure field specified by the time history $p(t)$ shown in Figure 7 on its upper surface. We assume that a baffle protects the lower surface from the blast wave which convects across the upper surface without changing shape. The given pressure field was recorded in a shock tube travelling at Mach 2.4.

We first identify the co-ordinates for the beam system with those of relation (18). We wish to find the response only at one location – the cantilever tip – and so eliminating the response position vector $\mathbf{r}$, equation (18) reduces to

$$A_y(t) \le \frac{1}{2} \int_S A_x(t,\mathbf{s}) \,{}^\star A_h(t,\mathbf{s})\,ds \tag{19}$$

In our example the spatial dependence of the input and impulse response refers only to the distance from the cantilever root, reducing

213

the vector **s** to the scalar distance z, the domain of influence of the input $x(t,z)$ being the beam length. That is

$$A_y(t) \le \frac{1}{2} \int_0^l A_x(t,z) *A_h(t,z)\,dz \qquad (20)$$
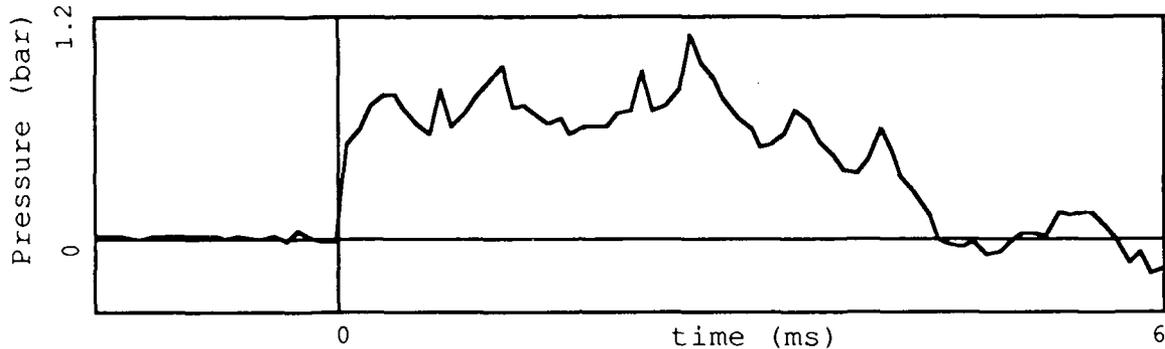
Figure 7: Recorded pressure time history.

The system input, or pressure distribution deduced from our recorded time history $p(t)$, travels along the beam at a constant velocity c and may therefore be expressed in the form

$$x(t,z) = p(t-z/c) \qquad (21)$$

An Euler-Bernoulli beam model [7] may be assumed with governing equation

$$\left\{ \frac{m}{l}\frac{\partial^2 y}{\partial t^2} + \frac{\partial^2}{\partial z^2}\left\{ EI\left[\frac{\partial^2 y}{\partial z^2} + \gamma\frac{\partial^3 y}{\partial z^2 \partial t} \right]\right\}\right\} = x(t-z/c) \qquad (22)$$

For this problem modal methods may be employed both to determine the tip response $y(t)$ in discrete form and the impulse response $h(t,z)$ explicitly. The envelope $A_h(t,z)$ can then be found using the Hilbert transform algorithms mentioned above. The time convolution in inequality (20) can then be performed using Fourier methods and the integration along the beam length can be achieved using a trapezoidal integration algorithm, giving an upper bound for the response envelope $A_y(t)$. Figure 8 shows the envelope of the simulation displacement response together with the upper bound from the right hand side of inequality (20).

For this simulation the upper bound (which is again acausal) has a maximum which exceeds the peak response level by a factor of 1.6. This factor is attributable to the coarseness of inequality (15) which is itself due to the phase component of the integrand before the modulus is taken. For our application the integrand comprises the convolution of the input and impulse response analytic functions and so it is the

phase components of these functions, or the bandwidth under consideration, which governs the coarseness of the upper bound.
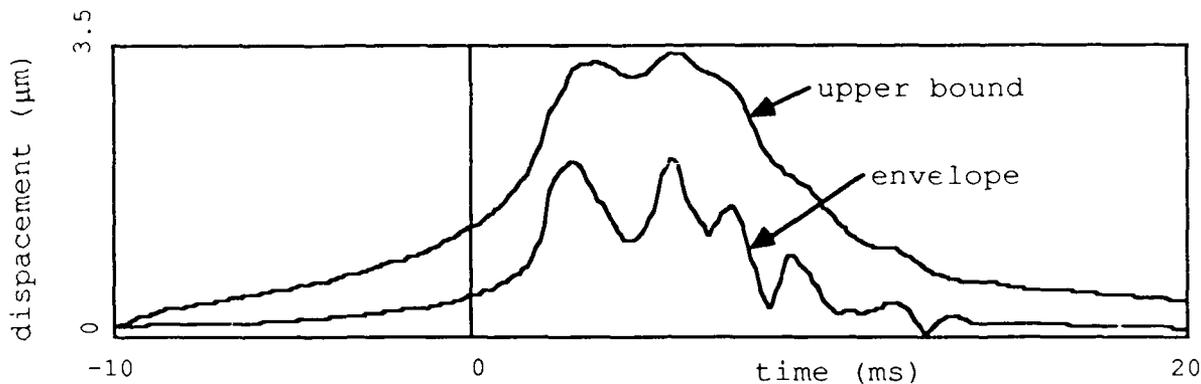

Figure 8: Blast excited cantilever tip displacement envelope and upper bound.

CONCLUSIONS

The method presented can be applied to any linear system with distributed loading where the convolution and integration in the envelope relation (inequality (18)) can be performed. The coarseness of the upper bound generated is due to the bandwidth of the system and excitation, and the upper bound will approach the actual envelope as the bandwidth is reduced. The system impulse response function may not be available in analytical form as in the example above and may need to be determined experimentally. In this context we note from experimental observations that whilst detailed response curves show large variations as a force input location traverses the surface of a structure, the *envelopes* of these response curves show less variation and so impulse response envelopes across the input domain may be deduced by interpoloation of a limited number of impulse response functions. These envelopes may then be combined with the envelope of a measured or predicted input to produce an upper bound for the envelope of the response of the system.

ACKNOWLEDGEMENTS

REFERENCES

1.   P. Davies, "The Analysis of Vibration (and Acoustic) Data Using Time Domain Methods," PhD Thesis, University of Southampton, 1985.

2.   J. Dugundji, "Envelopes and Pre-envelopes of Real Waveforms," IRE
      Trans. on Info. Theory, Vol. 4, 1958.

3.   L.R. Rabiner and R.W. Schafer, "On the Behaviour of Minimax FIR
      Digital Hilbert Transformers," Bell Systems Tech. J., Vol. 53,
      No. 2, 1974.

4.   A. Papoulis, Signal Analysis, McGraw-Hill, 1985.

5.   J.K. Hammond, and P. Davies, "Envelope Models for the
      Characterisation of Coupled Systems," Proc. of the 5th
      International Modal Analysis Conference, Vol. I, 1987.

6.   Bendat and Piersol, Random Data, Wiley, 1986.

7.   G.B. Warburton, The Dynamical Behaviour of Structures, Pergamon,
      1976.

DYNAMIC NONLINEAR FRAME ANALYSIS
FOR BLAST AND SHOCK

Larry M. Bryant and Scott D. Campbell
JAYCOR, Structures Division
2734 Washington Street
Vicksburg, MS 39180

Dale Nebuda
U.S. Army Engineer District, Omaha
215 North 17th Street
Omaha, NE 68102-4978

This paper documents the formulation and computer implementation for dynamic analysis of nonlinear two-dimensional frames subjected to blast-induced pressure loading and ground shock motions. The theories, methodologies, and equations implemented in the computer code STABLE (Structure Analysis for Blast Loading Effects) are described. The computer program includes numerous facilities to allow a generally complete description of the structure, its support and loading environment, element and structure response, and considerable flexibility in selection of printed and plotted results.

INTRODUCTION

The analysis of structures subjected to blast pressure loading and ground shock displacements and velocities is not easily accomplished by most available computer codes. A computer program has been developed, STABLE (Structure Analysis for Blast Loading Effects), which represents a significant enhancement of a previous program, DYNFA [1]. Numerous enhancements to the existing code were added to allow better and more complete description of the structure, its support and loading environment, element and structure response, and more flexibility in printed and plotted results. In addition to added capability of the code, the general approach and methods of equation solution were completely rewritten to increase the computational efficiency of the program. As a result of these significant modifications, very little of the original DYNFA computer code remains in STABLE. The computer implementation, input guide, and supporting information are presented in a Documentation Report [2]. A companion Validation Report [3] documents 12 problems used to demonstrate and validate the capabilities of STABLE.

FORMULATION

The computer program STABLE retains the previous capabilities of DYNFA [1] and adds several capabilities which improve its usefulness for dynamic nonlinear analysis of frames subject to blast loading effects. These added capabilities are described below in terms of general capabilities, element description, support conditions, and blast loading.

General Capabilities

The general approach in STABLE is based on the direct stiffness method and utilizes direct integration of the equations of motion assuming linear acceleration over any time step. The input and output units of the program are pound, inch,

millisecond, and angular degrees. Enhancements to other general capabilities are described in the following paragraphs.

Initial Conditions. The computer code is capable of determining the initial conditions for the dynamic analysis by static analysis of the structure for the input static loads. This analysis is a linear analysis of the structure for the applied static loads. The computed displacements from the static analysis are taken as the initial displacements in the incremental dynamic solution.

Structure Mass. Structure mass may be described in the model by input of discrete nodal weights in either or both translational degrees of freedom (DOF) at any node. These discrete weights are internally converted to mass by dividing by the acceleration of gravity. In addition to input of discrete nodal masses, the code allows the option of computing nodal masses automatically from the input gravity loads. For input concentrated loads, the translational masses are computed as:

$$m_i = F_i/g \qquad (1)$$

where:

m_i = Translational mass at node "i."
F_i = Concentrated load input at node "i."
g = Acceleration due to gravity.

For uniform load w_i on an element with nodes "j" and "k" and length "L," the nodal masses are computed similarly and distributed to the nodes by tributary length, i.e.:

$$m_j = m_k = w_i L/(2g) \qquad (2)$$

where the load direction (X or Y) of the input load indicates to which DOF the generated masses correspond.

In addition to specification of translational masses, the program allows input of nodal mass moments of inertia (rotary mass) in a manner similar to the lumped nodal translational masses. The rotary mass is input and added directly to the total diagonal mass matrix.

Secondary Bending (P-delta) Effects. Second-order effects of axial load, commonly called P-delta effects, are approximated in the solution by inclusion of a pair of equivalent shears at both ends of the element. This procedure is illustrated in Figure 1. As shown in the figure, the second-order moment caused by axial load in the deflected element is:

$$M = P \cdot \Delta \qquad (3)$$

This second-order moment is modeled by inclusion of the shown equivalent shear pair which creates the couple:

$$M_e = V_e \cdot L \qquad (4)$$

Equivalence of the moments leads to the magnitude of the equivalent shear:

$$V_e = P \cdot \Delta/L \qquad (5)$$

The equivalent shears are computed and added to the dynamic loads at each time step.
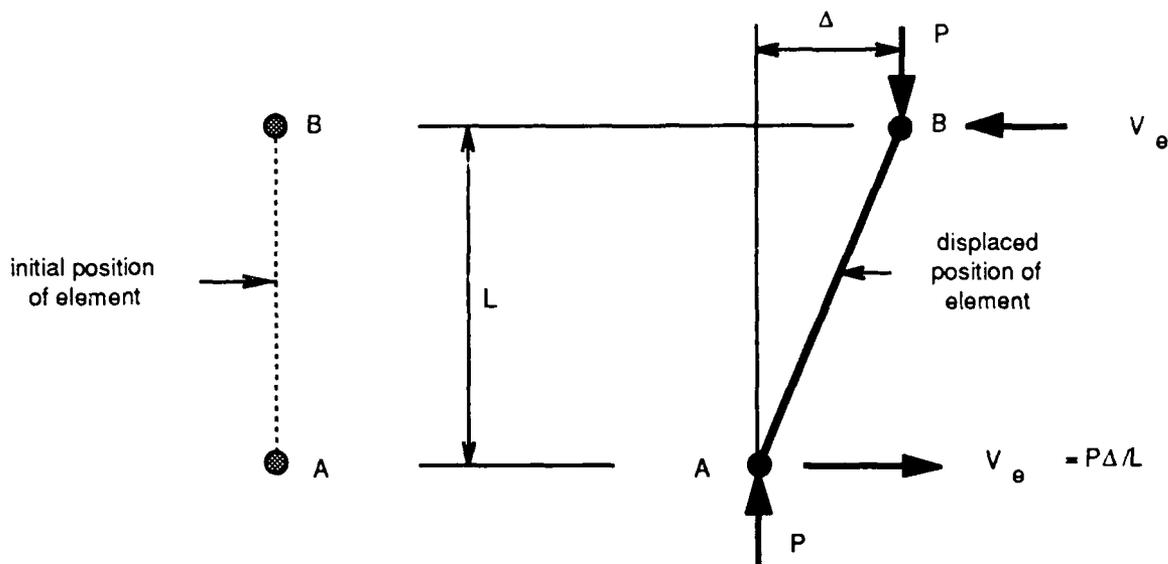
Figure 1. Model of P-delta effects in STABLE.

Equilibrium Correction. The step-by-step time integration of the equations of motion introduces some error at each time step. This error is introduced by the assumption of linear acceleration over each time step, coupled with nonlinear behavior of elements and supports. To efficiently minimize this effect, the code utilizes a noniterative approach recommended by Wilson [4] and Bryant [5]. This procedure involves calculation of the load imbalance at the end of any time step directly from the equation of motion. The equation of motion at time "t" is expressed as:

$$M\ddot{y} + C\dot{y} + Ky = P(t) + e(t) \qquad (6)$$

where:

M   = Structure mass matrix.
C   = Structure damping matrix.
K   = Structure stiffess matrix.
P(t) = Applied loading vector.
e(t) = Load imbalance vector.

Note: $\ddot{y}$, $\dot{y}$, and y are the acceleration, velocity, and displacement vectors respectively, at time "t".

The load imbalance, e(t) , is computed directly from Equation 6, i.e.:

$$e(t) = M\ddot{y} + C\dot{y} + Ky - P(t) \qquad (7)$$

The load imbalance is computed and applied in the opposite direction with other applied loads at the following time step. This procedure was previously demonstrated to work well for highly nonlinear problems [5].

Element Description

Material Models. Beam elements in the model are one-dimensional and prismatic, with constant cross-sectional area, moment of inertia, and plastic moment capacity. Element properties may be modeled in one of three ways in the program. A general element model permits general input of elastic properties, plastic moment capacity, and compressive and tensile axial load capacities. Steel shapes described in the AISC Manual of Steel Construction [6] may be specified in the input, with the appropriate elastic and plastic properties automatically computed. Structural shapes, including "W", "M", "S", "HP", structural tees cut from "W", "M", "S", "HP" shapes, double angles, pipe, and tubing, may be simply selected by section name in the input. In each element model, the material is assumed to behave in a bilinear, elasto-plastic manner, as illustrated in Figure 2. As shown in this figure, unloading and reloading follows the original elastic stiffness between positive and negative plastic levels.
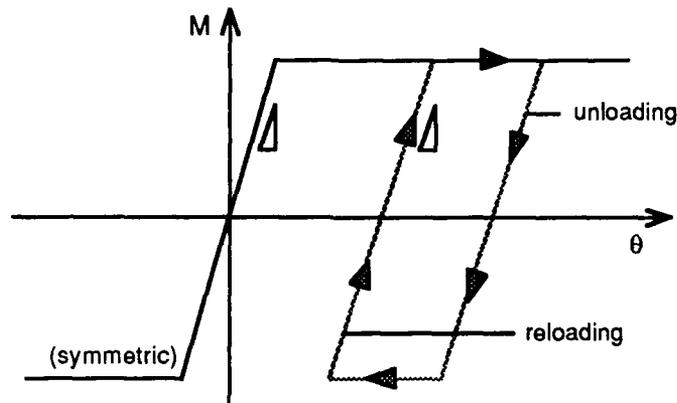

Figure 2.   Elasto-plastic behavior of steel material models.

A reinforced concrete element model may be specified in the input which permits a moment-rotation curve illustrated in Figure 3.
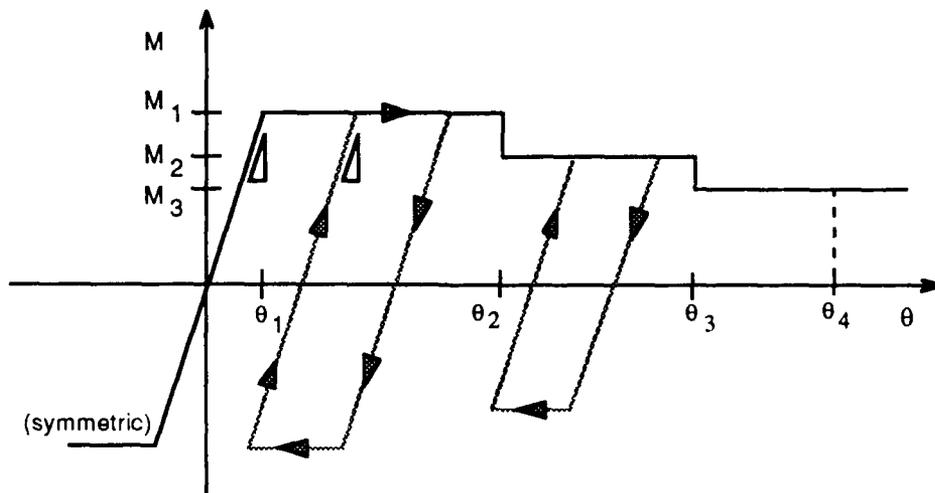

Figure 3.   Moment-rotation curve for STABLE reinforced concrete model.

In this model, the moment-rotation response permits reduction in moment capacity, corresponding to two levels of cracking, above user-defined levels of rotation. In the concrete model, the behavior is also elasto-plastic, with reduced plastic levels beyond the limiting rotations. For any loading cycle in which a

220

limiting rotation is exceeded, a compensating moment, M_C , is applied to reduce the internal moment to the reduced capacity. Until unloading, this compensating moment is determined as the difference between capacity and computed internal moment. After unloading commences, the capacity is permanently reduced to the proper level and the compensating moment vanishes. Beyond an input level of maximum rotation, θ_4, a warning is issued but the solution continues.

Axial Load and Bending Interaction. As part of the model of nonlinear member response, members in compression are checked for Euler-type, in-plane member buckling. Axial capacities are input for the general and concrete models, and unbraced lengths are input for the steel shape element model. If a member is determined to have buckled, the element stiffness is considered nil until it unloads. The interaction of bending and axial load is considered utilizing the equation previously implemented by Stea et al. [1], i.e. yielding or buckling is assumed to have occurred when:

$$|P/P_C| + |M/M_m| > 1 \tag{8}$$

where:

P = internal axial load.
M = internal bending moment.
P_C = Axial load capacity (yield or buckling).
M_m = Moment capacity.

Capacities P_C and M_m are computed automatically for properties in the AISC structural steel shape library.

Member End Conditions. A basic assumption in the formulation is that structural continuity exists at all nodal points in the model, except at support nodes. Provision is made, however, to model nonrigid structural connections by allowing pins to be placed at either end of an element. This provision permits modeling of elements as pinned at one end and continuous at the other as well as the standard conditions of continuous at both ends or continuous at one end and free at the other. Pins are introduced in the solution at the element level by formation of the element stiffness for a fixed-pinned element.

Support Conditions

Support conditions for the frame analysis include structural restraints, such as fixed or spring-supported DOF, and damping restraints, such as viscous or Coulomb dampers.

Structural restraint, such as foundation connections, may be modeled by specifying any combination of fixed or free DOF at support nodes. Of the three DOF at a support node (two translational and one rotational), any one, two, or all three may be declared either fixed or free. Fixed DOF are deleted from the equations of motion before the solution commences.

General Nonlinear Spring. A more general representation of structural restraint may be modeled in the analysis using general nonlinear elastic springs at any DOF in the model. These springs may be specified by an input piecewise linear force-displacement relation, as illustrated in Figure 4. The input springs are defined by force and displacement pairs and may be applied to any translational or rotational DOF. At each time step, the code checks the computed displacement component at the specified spring support to determine the appropriate tangent stiffness and intercept force. This spring stiffness is added to the conventional stiffness matrix for this time step. This spring is nonlinear, but elastic, i.e. unloading

and reloading occur along the original input curve. Linear support restraints may be modeled by specifying a single branch curve (two force-displacement pairs) in the general spring table.
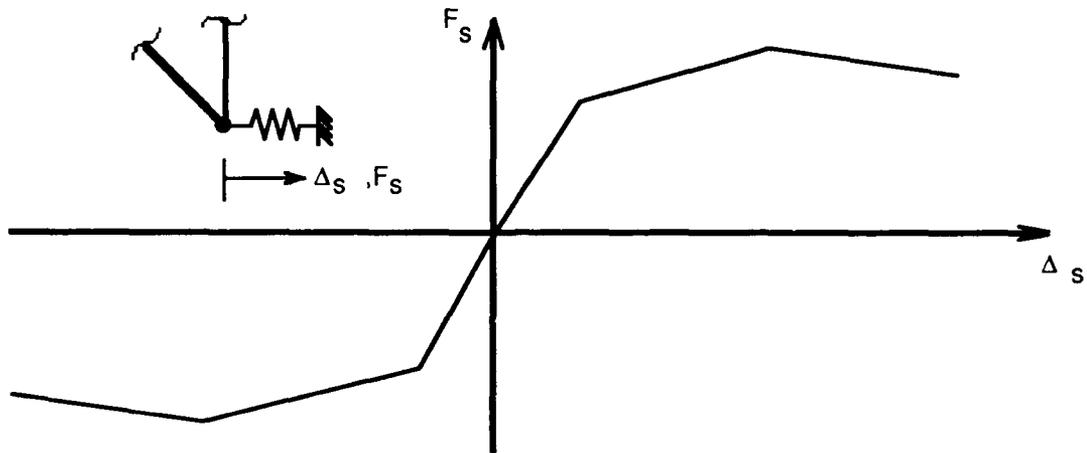

Figure 4. General nonlinear support restraint spring.

One-Way Soil Spring. A more specialized form of structural restraint is available using the elasto-plastic, one-way soil spring depicted in Figure 5. This spring may be applicable for foundation restraint where resistance occurs only in one direction. The restraint responds as elasto-plastic in the compression range, but allows no restraint for tension. At each time step, the code performs a check similar to the general spring and adjusts the stiffness and load accordingly.
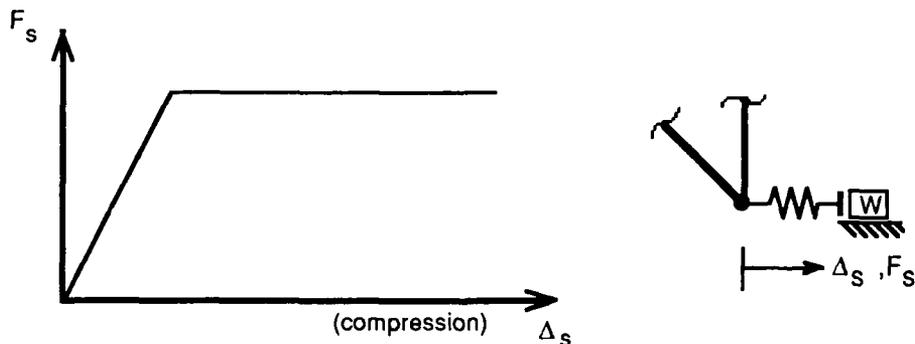
Figure 5. Elasto-plastic one-way soil support spring.

Viscous Damping. Velocity-dependent damping restraint may be modeled by specifying a viscous damper at any DOF in the model. At each time step, the opposing damping force at this DOF, F_v , is computed as:

$$F_v = -C_v \cdot \text{(velocity)} \tag{9}$$

where C_v is the viscous damping constant. As evident from Equation 9, the computed damping force opposes the direction of velocity, and is added to the dynamic load vector.

222

Coulomb Damping. Support damping restraint may also be modeled with an axial Coulomb damper at any DOF. At each time step, the opposing damping force at this DOF, F_c, is computed as:

$$F_c = -C_c \cdot F_a \cdot \text{(sign of velocity)} \tag{10}$$

where:

C_c = Coulomb damping constant.
F_a = Element axial force.

The computed damping force, F_c, opposes the direction of velocity, and is added to the dynamic load vector.

Dynamic Loading

Blast Pressure Loading. Blast loading on a frame may be modeled in STABLE by specification of pressure versus time waveforms and tributary areas at any DOF. Piecewise linear pressure-time waveforms (histories) are specified independent of specific nodal DOF and are defined by pairs of pressure and time values. Loading may be applied to individual DOF by specification of pressure-catching areas, pressure waveform number, and arrival time of the pressure pulse. The effects of multiple blast loadings at a DOF are accumulated by algebraic summation of the individual loading components.

Ground Shock Displacement. Ground motions due to blast (or other source) may be specified by user-defined piecewise linear ground shock displacement-time waveforms. The support motions are integrated in the general equations of motion by typical transformation to equivalent applied loading. This transformation is simply demonstrated by review of equations of motion for a system with support motion:

$$M\ddot{y} + C\{\dot{y} - \dot{y}_s\} + K\{y - y_s\} = P(t) \tag{11}$$

where:

$\dot{y}_s$ = Support velocities = $\dot{y}_s(t)$.
y_s = Support displacements = $y_s(t)$.

The equation of motion can be rewritten as:

$$M\ddot{y} + C\dot{y} + Ky = P(t) + C\dot{y}_s + Ky_s \tag{12}$$

therefore, the standard solution for forced vibration is applicable by computing the equivalent forcing function on the right side of equation 12.

For the case where displacement $y_s(t)$ is specified, $\dot{y}_s(t)$ is evaluated by numerical differentiation of $y_s(t)$, i.e.:

$$\dot{y}_s(t) = d(y_s(t))/dt \tag{13}$$

For a piecewise linear support displacement function, the numerical differentiation is accomplished as illustrated in Figure 6a. Over any linear region of $y_s(t)$, the velocity is constant and equal to the slope over that region, i.e.:

$$\dot{y}_s(t) = (y_{sk} - y_{sj})/(t_k - t_j) \quad , \quad t_j \leq t < t_k \tag{14}$$

where y_{sk} and y_{sj} are support displacements at times t_k and t_j, respectively. The resulting velocity function is a summation of step functions, as illustrated in Figure 6b.
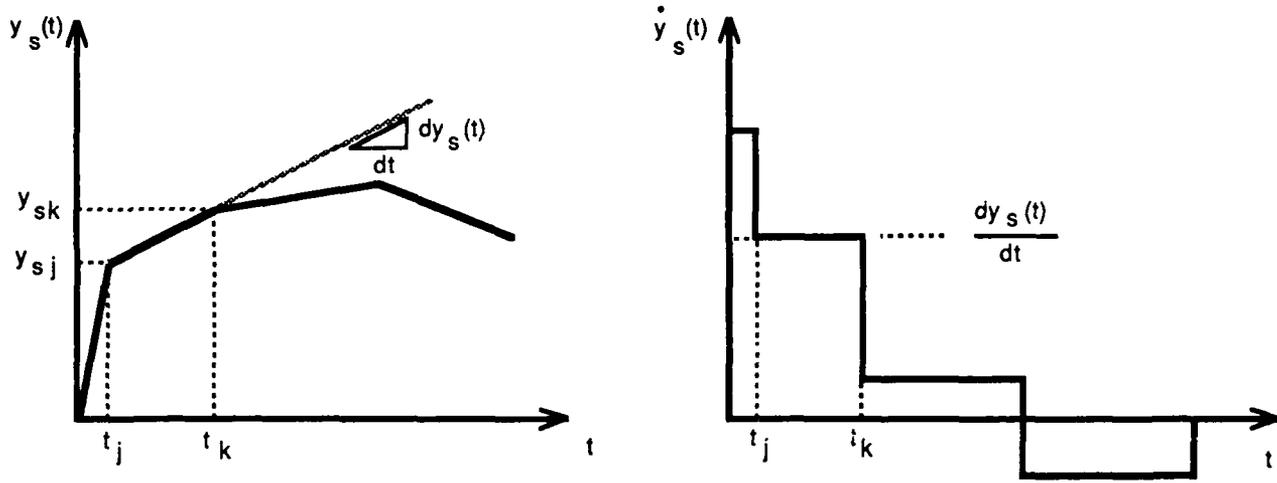
a. Support motion displacement function   b. Derived support motion velocity function.

Figure 6. Numerical differentiation of support motion displacements.

Ground Shock Velocities. Support velocity waveforms are input to the analysis in the same manner as support displacements, i.e. by ordered pairs of support velocities and times. The incorporation of support velocities in the solution utilizes a transformation to support displacement, i.e. the input support velocities are numerically integrated to compute support displacement waveforms:

$$y_s{}^*(t) = \int \dot{y}_s(t)\, dt \tag{15}$$

This numerical integration of $\dot{y}_s(t)$ is illustrated in Figure 7. Support displacement, $y_s{}^*$, is evaluated at every time step using the trapezoidal rule. As shown in the figure, for an increment of time Δt, the incremental displacement Δy^*, is the area under $\dot{y}_s(t)$ from time t to Δt, i.e.:

$$\Delta y^*{}_{t+\Delta t} = 0.5(\dot{y}_t + \dot{y}_{t+\Delta t})\Delta t \tag{16}$$

and thus:

$$y^*{}_{t+\Delta t} = y^*{}_t + \Delta y^*{}_{t+\Delta t} \tag{17}$$

The resulting support displacement function is piecewise quadratic over each linear region of support velocity. The solution utilizes the input support velocity and derived $y_s{}^*(t)$ in Equation 12. Note from Equation 12 that support displacements or velocities may be applied in conjunction with pressure loadings.
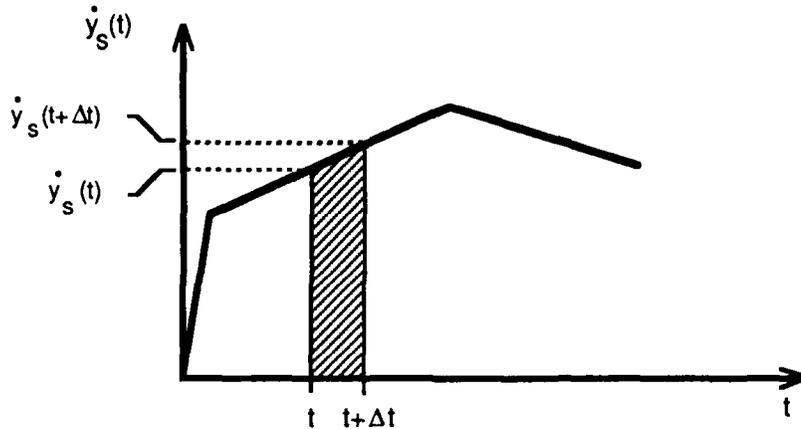
Figure 7. Numerical integration of support motion velocities.

COMPUTER IMPLEMENTATION

Hardware and Software Requirements

The computer program is written in 1977 ANSI Standard FORTRAN, and has been implemented on a VAX minicomputer and IBM PC-AT and Macintosh personal computers. The code is written using only standard FORTRAN, permitting simple implementation on most computers. Input and output are accomplished through standard file operations. Plot calls are implemented by the use of the Graphics Compatibility System (GCS) available throughout the US Army Corps of Engineers [7]. Therefore, plotted output is available on a variety of graphic devices including all graphic terminals and plotters supported by GCS.

Program Flow and Description

The program is implemented in modular subroutine form, with each routine generally performing a single defined task or step in the solution. The source listing of each routine, major variable names and information regarding required array dimensions are presented in the Documentation Report [2]. Each routine is well documented internally by comment cards for each calculation, loop, or function. In addition to internal documentation, the data is examined for possible errors which are reported during the input stage.

Printed Output

Printed output for STABLE includes four general types of output. The first output from any problem is a card image listing, or echo print, of the input data. It is in this table that detectable errors are also reported to assist in debugging the input data file. Following the echo print of the data, the problem data is printed in structured tables with appropriate headings to confirm validity of the input. Results of the analysis are presented in two forms – tables of specific results for each time step and maximum and minimum results over the range of the analysis. Numerical results may be selectively output as time histories of nodal response, element forces, or support reactions. Peak response tables are also selectable for nodal response, element forces, or support reactions. In each case, the user specifies the node, element, or support number for which output is desired.

225

Plotted Output

Plotted output for STABLE includes four general types of plots, two of which are useful in verifying input data and two which graphically display selected results. First, the overall frame layout with all nodes, elements, and supports shown can be plotted in a configuration geometry plot. This plot is useful in verifying accuracy of the input frame data and integrity of the model. Second, the user can choose to plot any input pressure or ground shock motion time history (waveform). At any times selected by the user, the deflected shape of the frame can be plotted to indicate overall frame behavior. Finally, time histories of nodal response, element forces, and support reactions may be selectively plotted in the same manner as for printed output. The selected output for plotting does not, however, have to be the same as for the printed output.

ILLUSTRATIVE EXAMPLES

Two example problems are presented here to illustrate a few of the capabilities of the STABLE computer code and compare the results with accepted solutions. These examples are but two of the twelve validation problems presented in the STABLE Validation Report [3].

Two-bay Frame with Blast Loading and Linear and Nonlinear Support Springs

This structure is a single-story, two-bay frame with linear and nonlinear support, subject to a suddenly applied constant lateral load. The STABLE structure model is shown in Figure 8 with the springs and loading indicated in Figure 9.
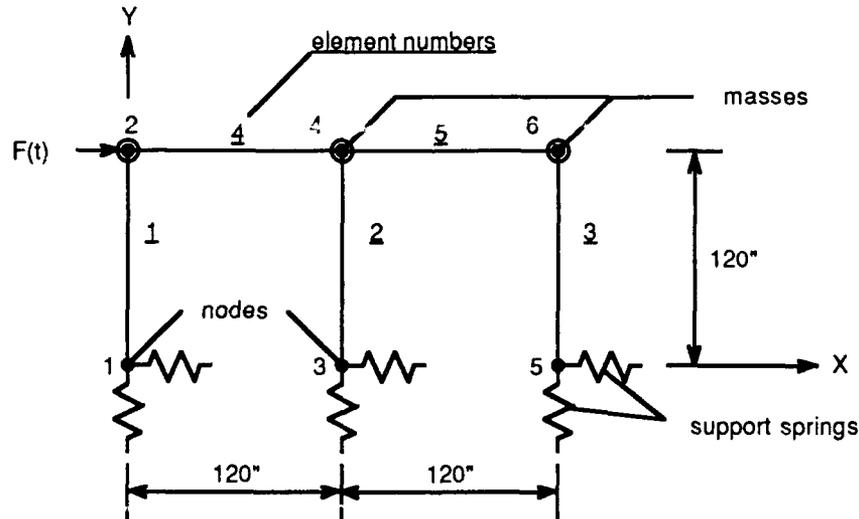

Figure 8. STABLE model including nonlinear support springs

For comparative purposes, the structure was also analyzed using ADINA [8]. In both models the beam and column elements were considered as linear elastic beam elements. In the ADINA model the support springs were modeled as linear and nonlinear truss elements with specified stress-strain curves to provide the behavior depicted in Figure 9.

a. Soil spring resistance.   b. Dynamic loading.
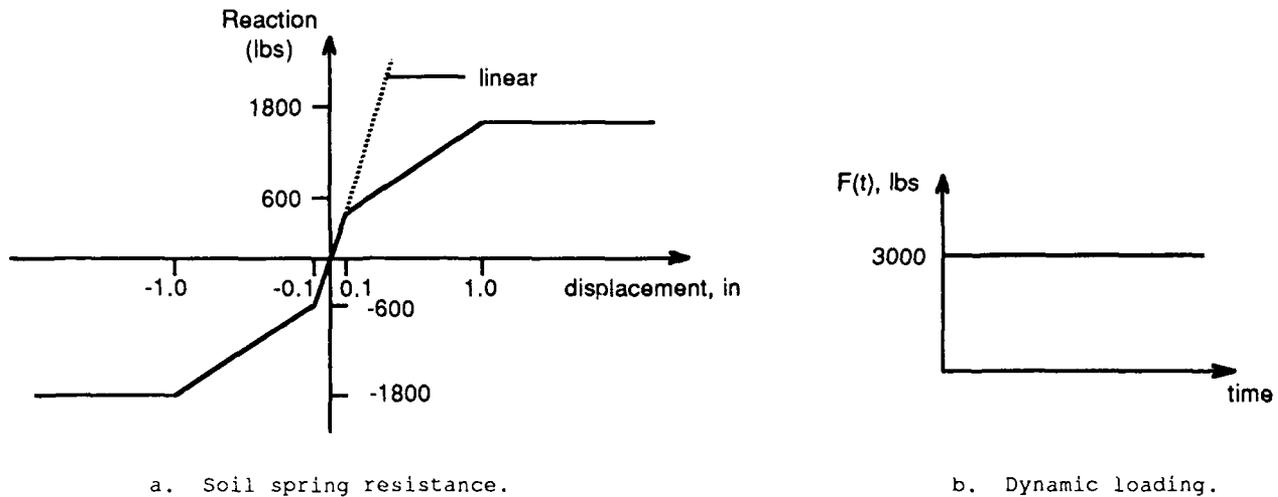
Figure 9. Spring resistance and dynamic loading.

The results of the analyses are compared in Figure 10, which plots the computed lateral displacements at nodes 1, 2, and 3. As seen in this comparison, the results from STABLE are almost identical to those from ADINA. It should be noted that the ADINA analysis was conducted using full Newton iteration with line search (iterative equilibrium correction) to achieve satisfactory results. Without equilibrium correction, the ADINA results were not satisfactory.
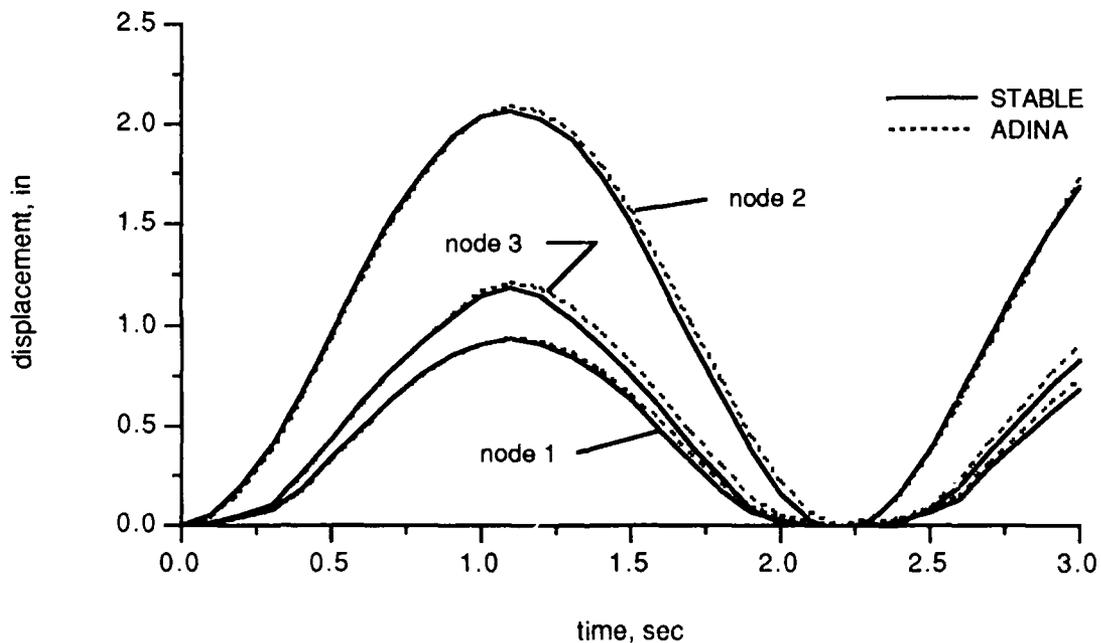

Figure 10. Lateral displacements of frame with nonlinear springs

Two-story Frame with Sinusoidal Support Motions

This problem was presented by Biggs [9] to illustrate support motion analysis. The structure, depicted in Figure 11, is a one-bay, two-story frame composed of two different column sizes and two different beam sizes. Mass is lumped at the two floor levels. The ground motion is assumed to be sinusoidal with an amplitude of

0.5 in. and a period of 500 msec. Biggs solved this problem as a two DOF system assuming rigid girders. The structure was analyzed by assigning large moments of inertia to the girders and applying ground motions at the base of both columns.
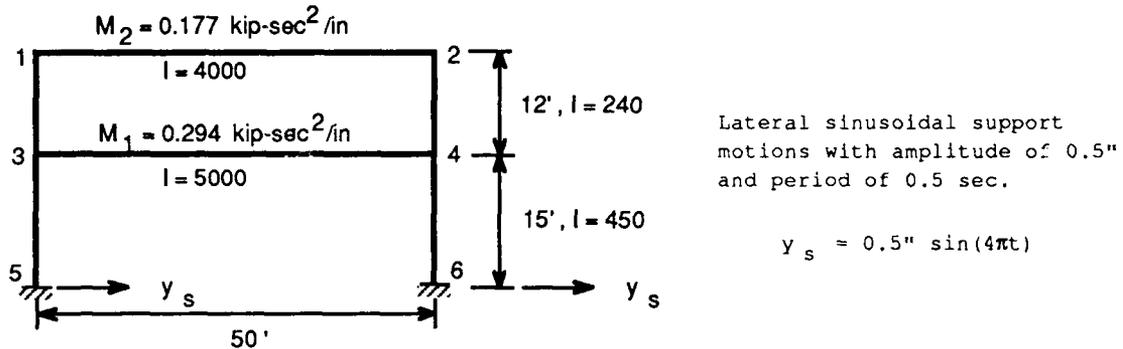

Figure 11. Frame with support motion.

The results of the STABLE analysis are compared with Biggs' results in Figure 12 which plots the lateral displacements at the two levels for elastic response. As seen in this plot, the STABLE results compare favorably with Biggs' two DOF model.
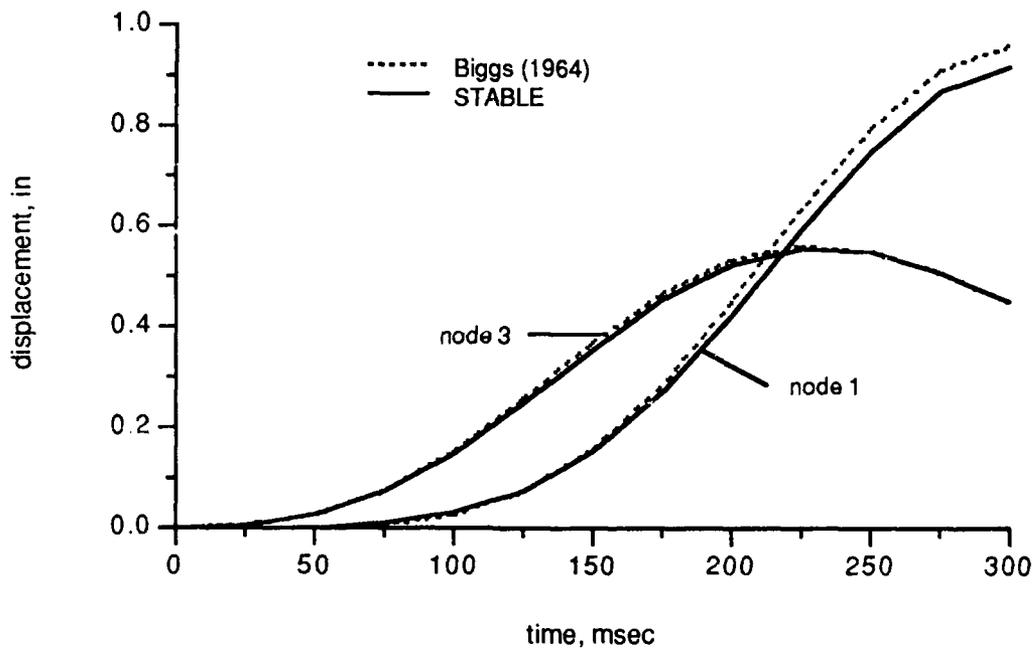

Figure 12. Lateral displacements of frame with support motion.

CONCLUSIONS

The computer code developed for dynamic analysis of nonlinear two-dimensional frames subjected to blast pressure loading and ground shock motions, STABLE represents the current state-of-practice for analysis of blast-loaded frame structures. The code has been validated by application to twelve problems which exercise most of its capabilities [3]. Several enhancements to the existing code are envisioned which would improve its usefulness. These enhancements to the computer program generally

include improvements in representation of the structure, loading and support conditions, and improvements in actual application of the program (ease of use). Pre- and post-processing modules are envisioned to simplify input data preparation and output results extraction.

ACKNOWLEDGEMENTS

REFERENCES

1. W. Stea, et al., "Nonlinear Analysis of Frame Structures Subjected to Blast Overpressures," Contractor Report ARLCD-CR-77008, US Army Armament Research and Development Command, Dover, NY, May 1977.

2. L. M. Bryant and Scott D. Campbell, "Structure Analysis for Blast Loading Effects, STABLE Computer Program, Final Documentation Report", JAYCOR Report No. J650-88-006/1411, prepared for US Army Engineer District, Omaha, August 1988.

3. L. M. Bryant and Scott D. Campbell, "Structure Analysis for Blast Loading Effects, STABLE Computer Program, Final Validation Report", JAYCOR Report No. J650-88-006/1411, prepared for US Army Engineer District, Omaha, August 1988.

4. E. L. Wilson, "A Computer Program for the Dynamic Stress Analysis of Underground Structures," Structures and Materials Research Report No. 68-1, University of California, Berkeley, 1968.

5. L. M. Bryant, "Static and Dynamic Response of Geometrically Nonlinear Plane Frames," MS Thesis, The University of Texas at Austin, Austin, TX, August 1971.

6. American Institute of Steel Construction, Inc., Manual of Steel Construction, 8th ed., Chicago, IL, 1980.

7. ...., "Primer on Computer Graphics Programming", Instruction Report K-82-3, Automatic Data Processing Center, US Army Waterways Experiment Station, Vicksburg, MS, April 1982.

8. ADINA Engineering, Inc., "Automatic Dynamic Incremental Nonlinear Analysis Users Manual", Report AE 84-1, Watertown, MA, December 1984.

9. J. M. Biggs, Introduction to Structural Dynamics, McGraw-Hill Company, New York, NY, 1964.

BEHAVIOR OF A REINFORCED CONCRETE BLAST SHELTER IN AN OVERLOAD ENVIRONMENT

T. R. Slawson and J. L. Davis
Structures Laboratory
U.S. Army Engineer Waterwa, s Experiment Station
Vicksburg, MS 39180-0631

The ultimate capacities of most structures are not well defined due to the limitations of existing computational procedures and the lack of data on large deformation response. To better understand the large deformation behavior of a shallow-buried, reinforced concrete structure, a dynamic test was conducted in a blast environment designed to severely damage the structure.

This paper summarizes the test results and presents data analyses.

INTRODUCTION

An extensive program to develop an... experimentally evaluate a family of blast shelters was conducted for the Federal Emergency Management Agency (FEMA). One design investigated was a 100-man reinforced concrete shelter as shown in Figure 1. The design specifications require the shelter to resist the airblast and radiation effects of a 1-Mt nuclear surface detonation at the 50-psi peak overpressure level. The airblast loading from this threat can be represented as an initial peak overpressure with an exponential decay and a long positive phase duration. Soil covered shelters were determined to be the most cost effective designs to provide adequate radiation and blast protection. The original design was based on conventional design guides that neglect soil structure interaction effects on the behavior of shallow-buried structures.

The design of the 100-man blast shelter has evolved from the original overly conservative design to its present form based on experimental and analytical investigations performed by the US Army Engineer Waterways Experiment Station (WES) and the US Army Engineer Division, Huntsville (HND). Reductions in construction costs as the result of labor and material savings and less stringent backfill specifications were made without adversely affecting the structural performance. Design modifications were validated using small-scale static and dynamic tests during the design process. The constructibility and overall performance of the design were also investigated by the construction of several prototype shelters. The resulting structural design consists of a three bay reinforced concrete shelter with one-way roof and floor slab construction. The span-to-thickness (L/t) ratio of the roof slab was 12.8, and principal steel reinforcement ratios were 0.01 and 0.0034 in the tension and compression zones, respectively. The structure was buried to a depth equal to 36 percent of the clear span (4-ft) in compacted sand backfill. Roof principal reinforcement had a mean yield strength in tension of 61.6 ksi, and the mean compressive strength of the roof concrete was 3300-psi. More complete details of the shelter and its construction are given by Woodson and Slawson [1] and Slawson [2].

PLAN VIEW

ELEVATION
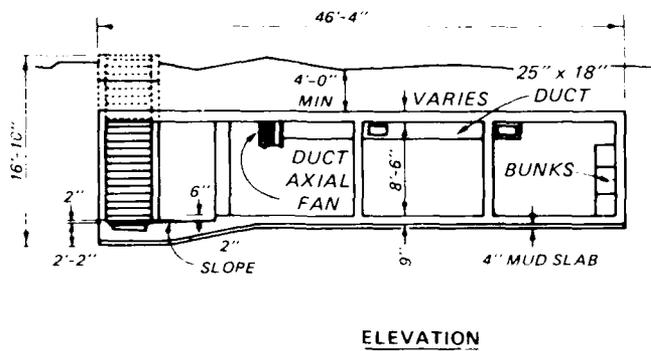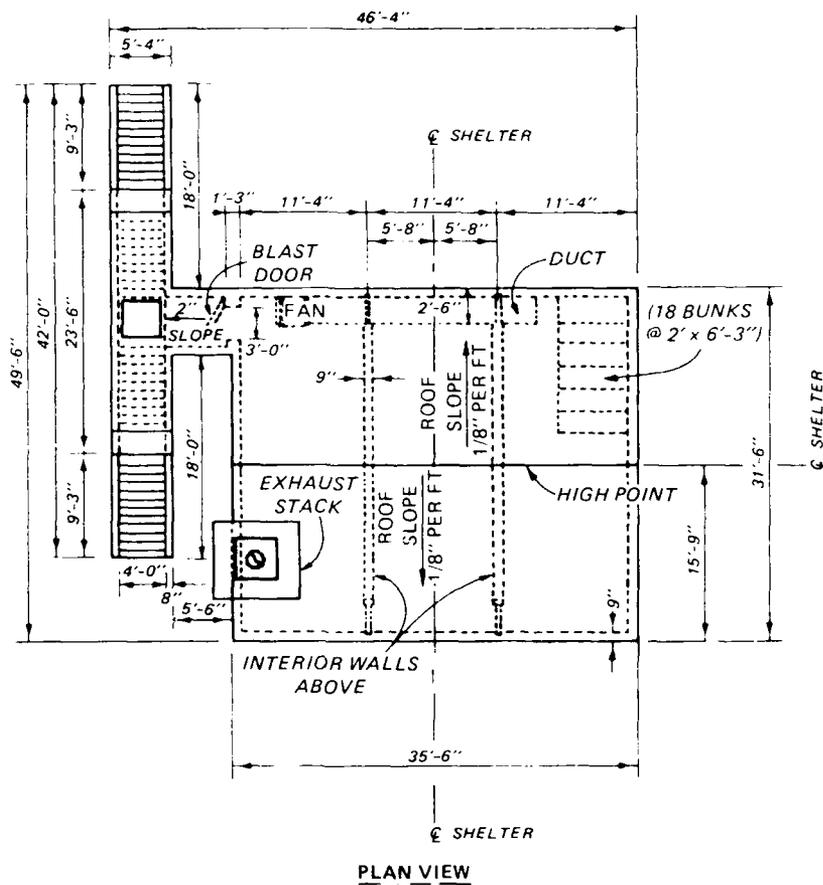
Figure 1.   The 100-man shelter.

A prototype demonstration test of the shelter was conducted in a high explosive (HE) simulation [1]. The shelter survived at the predicted 75-psi peak overpressure level (measured pressures were approximately 60-psi) with minor damage (1/8-inch permanent midspan roof deformation).

The results of the scale model testing [3,4] indicate that the shelter will withstand up to 160-psi peak overpressure from a 1-Mt detonation under ideal backfill conditions. However, this large factor of safety (160/50) is required to account for uncertainties in typical site conditions and backfill placement control. A retest of the shelter at a severe damage level was required to investigate the shelter's large deformation behavior. Also, since the function of a blast shelter is to ensure the survival of its occupants, the in-structure shock environment during this overload test is of utmost importance.

This paper describes the retest of the prototype shelter using the HEST to evaluate the shelter's large deformation behavior and to investigate equipment and occupant survivability.

TEST PROCEDURE

The HEST was originally developed by the Air Force Weapons Laboratory [5] to reproduce the peak overpressure, the rate of pressure decay, and duration of a given nuclear yield at a given peak overpressure or range. Two types of HEST configurations have been used by WES for nuclear weapon simulators during the last ten years: the Foam and Air HEST's. Use of a Foam HEST in a series of tests at WES is discussed by Kiger [6]. The HEST discussed herein is more specifically described as an Air HEST since the charge cavity volume is predominantly air rather than the low density plastic foam used in the Foam HEST tests. The Air HEST construction sequence consists of (a) constructing a framing support system on the ground surface above the test bed, (b) uniformly distributing high explosives throughout the charge cavity, (c) covering the charge cavity with plywood, (d) covering the charge cavity with soil overburden to momentarily confine the blast pressure, and (e) detonating the high explosive. The detonation of the high explosive generates a blast pressure within the charge cavity that decays as the volume of the charge cavity expands. The rate of pressure decay determines the simulated nuclear yield for the given peak overpressure. In addition, blast wave reflections from the cavity boundaries and thermodynamic effects play important roles in the shape of the blast pressure-time history generated during a HEST test. The test configuration is shown in Figure 2, and the charge cavity under construction is shown in Figure 3.

Recorded electronic data include: (1) airblast pressure at the ground surface; (2) roof and wall interface pressure; (3) soil stress; (4) free-field, structure and mannequin accelerations; and (5) structure deflections.

In addition to the recorded electronic data, the responses of the mannequins (Figure 4) were monitored by high-speed photography, and the survivability of equipment was investigated by the inclusion of a generator, an air circulation system, and lighting in the shelter.

TEST RESULTS

Structural damage during the HEST retest of the shelter was significant as shown in Figure 5. The maximum permanent roof deflection was approximately 17 inches for bay 1, 8 inches for bay 2, and 13 inches for bay 3. The exterior bays (1 and 3) received more damage than the interior bay as expected. The roof
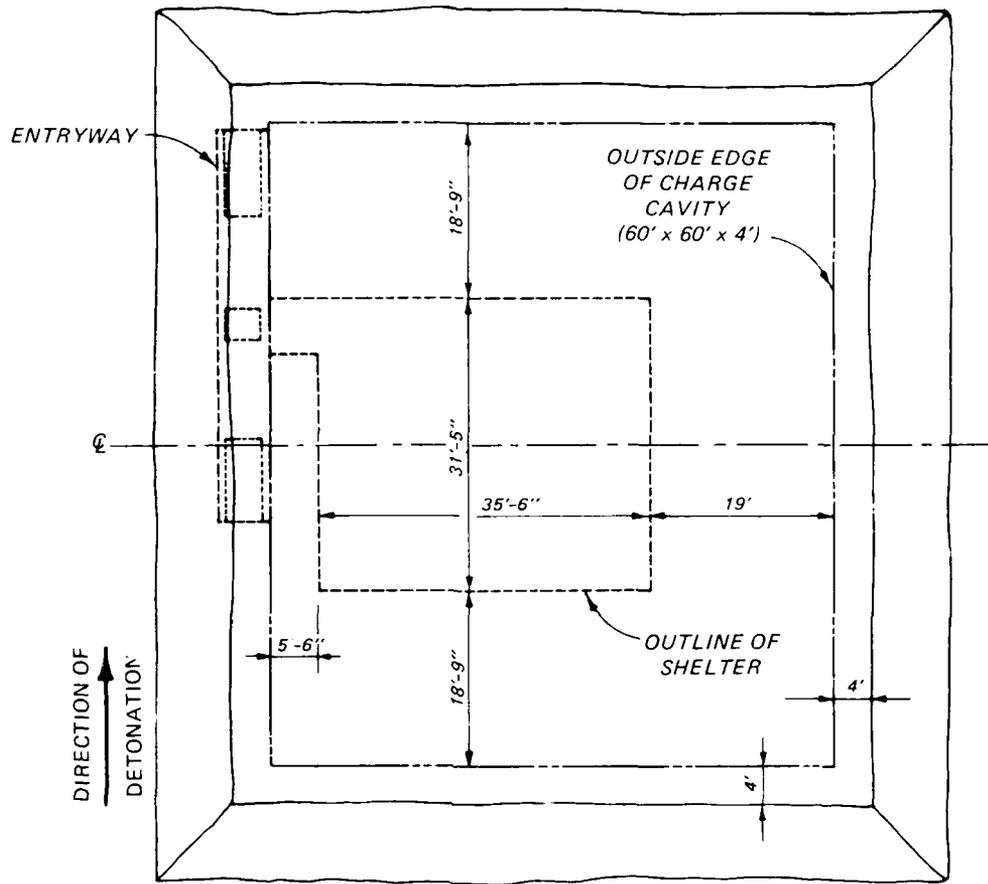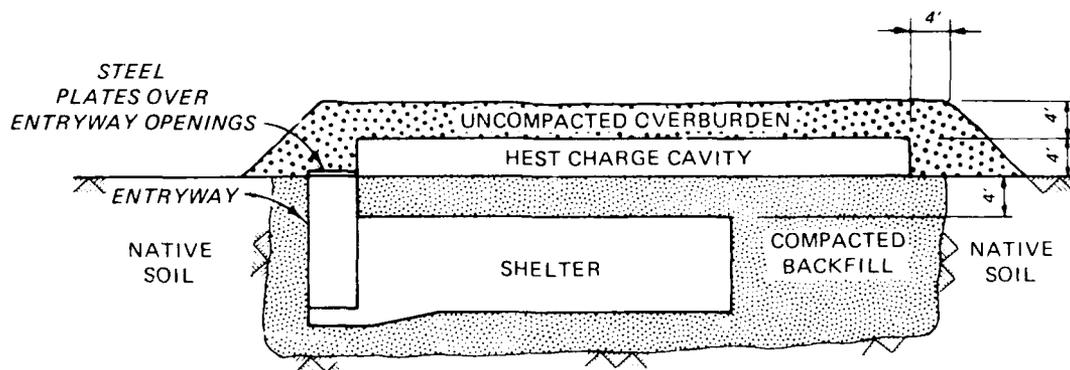
Figure 2. HEST test configuration.

Figure 3. Construction of the HEST charge cavity.

Figure 4. Interior view of the shelter showing the mannequins
and high speed camera setup.

response mode for each bay was a combination of shear and flexure. No roof steel appeared to be broken in the exposed areas.

The shear deformations at the roof slab-to-wall connections were surprisingly large, ranging from 44 to 62 percent of the total deformation of the roof spans. This resulted in the failure of the roof decking-to-wall connection. The decking was used as forms to support the shelter roof during casting and to protect shelter occupants from falling concrete. Some crushed concrete was allowed to fall to the shelter floor near the walls and at the entryway due to this failure.

The walls and floor slabs survived with only minor cracking. The entryway was severely damaged during this test, as shown in Figure 6. However, the test configuration did not load the entryway in the same manner as the HE test [1]. The tops of the entryway shafts were covered with steel plates to support the soil overburden covering the HEST cavity. The HEST cavity did not cover the entryway openings but did extend to the edge of the entryway. Therefore, only the sides of the entryway closest to the shelter were loaded. In an HE event, all sides and the interior of the entryway would be loaded. The entryway was still usable after the test except that it was filled with debris (soil overburden) from the HEST cavity. The HEST test did not retest the blast door.

All mechanical equipment (generator, air intake, and exhaust fans) and related hardware (air ductwork, valves) survived the test in operable condition. Roof-mounted electrical conduits and fluorescent light fixtures failed during the test as the result of excessive roof deflection (Figure 7).

The final positions of the mannequins were essentially unchanged from pretest locations as shown in Figure 7.

GROUND SURFACE AND ROOF LOADING

The airblast overpressure-time history was recorded at eight locations during the test. To describe the ground surface loading the airblast data were fit using exponential functions with polynomial coefficients of the following form:

$$p = e^{(a + bt + ct^2 + dt^3)} \tag{1}$$

where:
p = blast pressure, psi
t = time, msec
a,b,c,d = fit parameters

The fits were performed using the principle of least squares on an average of all the data records. The best-fit peak overpressure determined by this method was 226 psi. Since the HEST test was designed to simulate a 160-psi peak overpressure from the design threat, another fit was performed with the peak overpressure fixed at 160 psi. These fits are summarized in Table 1, and comparisons of the fits with data are presented in Figure 8.

Table 1. Fit parameters for the airblast data.

CURVE	a	b	c	d
BEST FIT	5.42	-0.0470	0.00054	-0.00000221
BEST 160-psi FIT	5.08	-0.0136	0	0

Figure 5. Overview of the shelter after the test.
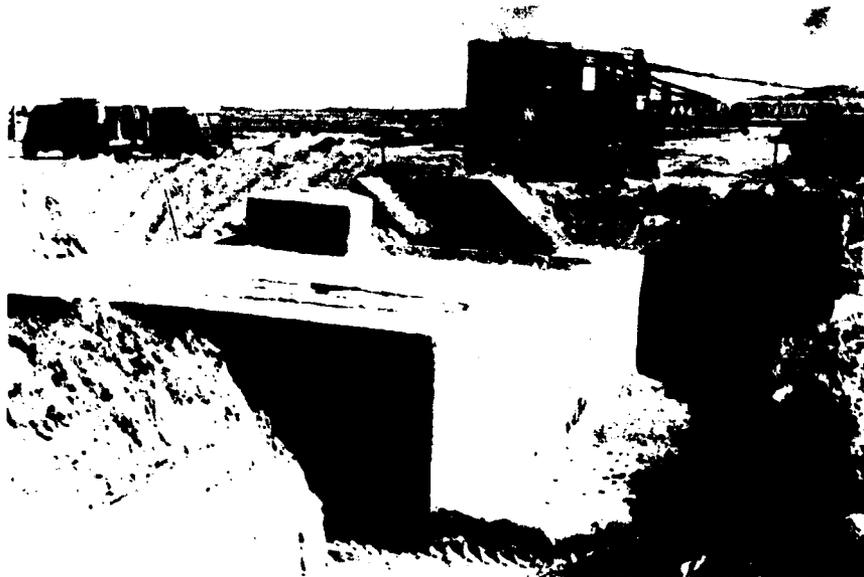
Figure 6. Exterior view of structure showing damage to entryway.

Figure 7.   Interior view of bay 1 showing roof damage and mannequins.
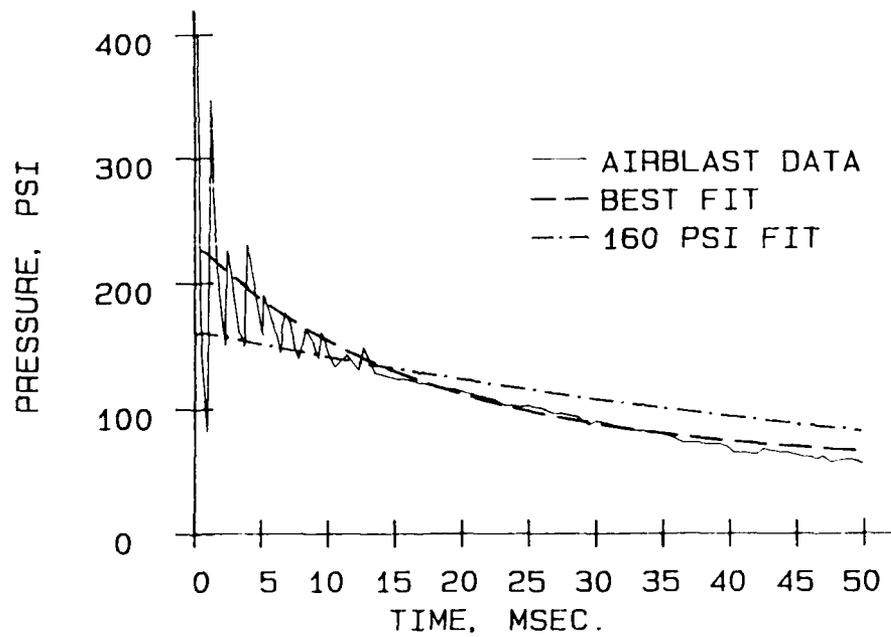
Figure 8.   Comparison of airblast data with exponential pressure fits.

The static and dynamic tests performed at WES in support of this blast shelter program have clearly demonstrated the load mitigating effects of soil arching on the roof loading distribution. Soil arching acts to transfer load from the midspan of the roof as it deforms to the roof supports reducing the induced bending moments in the roof for a given total load. The effective roof loading was reduced from its original uniform distribution to parabolic distributions at later times as shown in Figure 9.
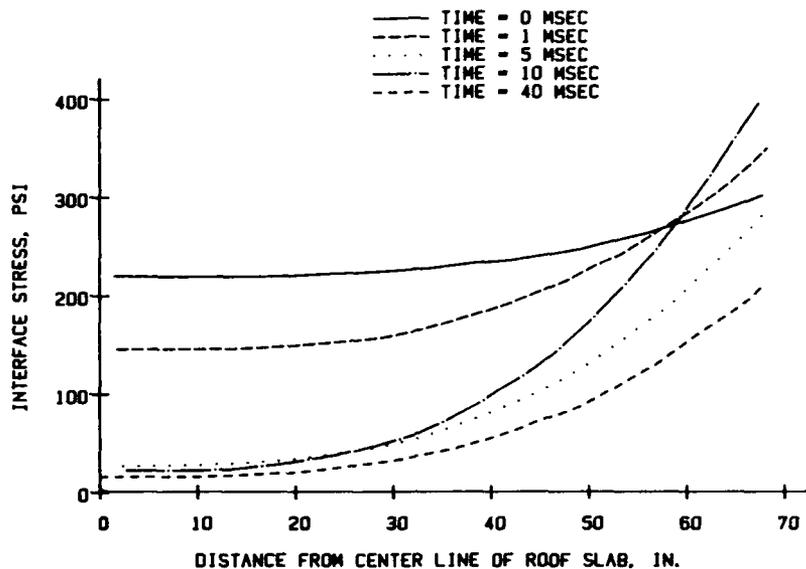

Figure 9. Roof loading distributions at selected times.

IN-STRUCTURE SHOCK AND SURVIVABILITY

In-structure shock is typically represented in terms of shock spectra. Shock spectra are plots of the maximum responses, usually of relative displacement, pseudovelocity, and/or acceleration of all possible linear oscillators with a specified amount of damping to a given input base acceleration-time history. Vertical shock spectra were calculated using the recovered floor acceleration data as input to a computer program developed at WES. The shock spectra were generated for damping ratios of 0, 5, and 10 percent of critical damping. Figure 10 compares the experimentally determined vertical shock spectra (smoothed by hand with damping of 10 percent) for the shelter floor with fragility curves for typical floor-mounted equipment [7]. Based on the comparison of the shock spectra and fragility curves, generators and communication equipment should be shock isolated to ensure their survivability. However, the diesel generator (mounted on top of its fuel tank) in the shelter was undamaged during the test. The test results indicate that the generator will survive the design overpressure of 50 psi and has survived one overload test of 160 psi.

Crawford, et al, [8] presents a summary of human shock tolerance and recommends a design maximum acceleration of 10 g for a standing man at or below the frequency of 10 Hz (resonant frequency). The experimental shock spectra show that a man in the standing position (most vulnerable) would not suffer compressive fractures; however. impact injuries can occur at much lower shock
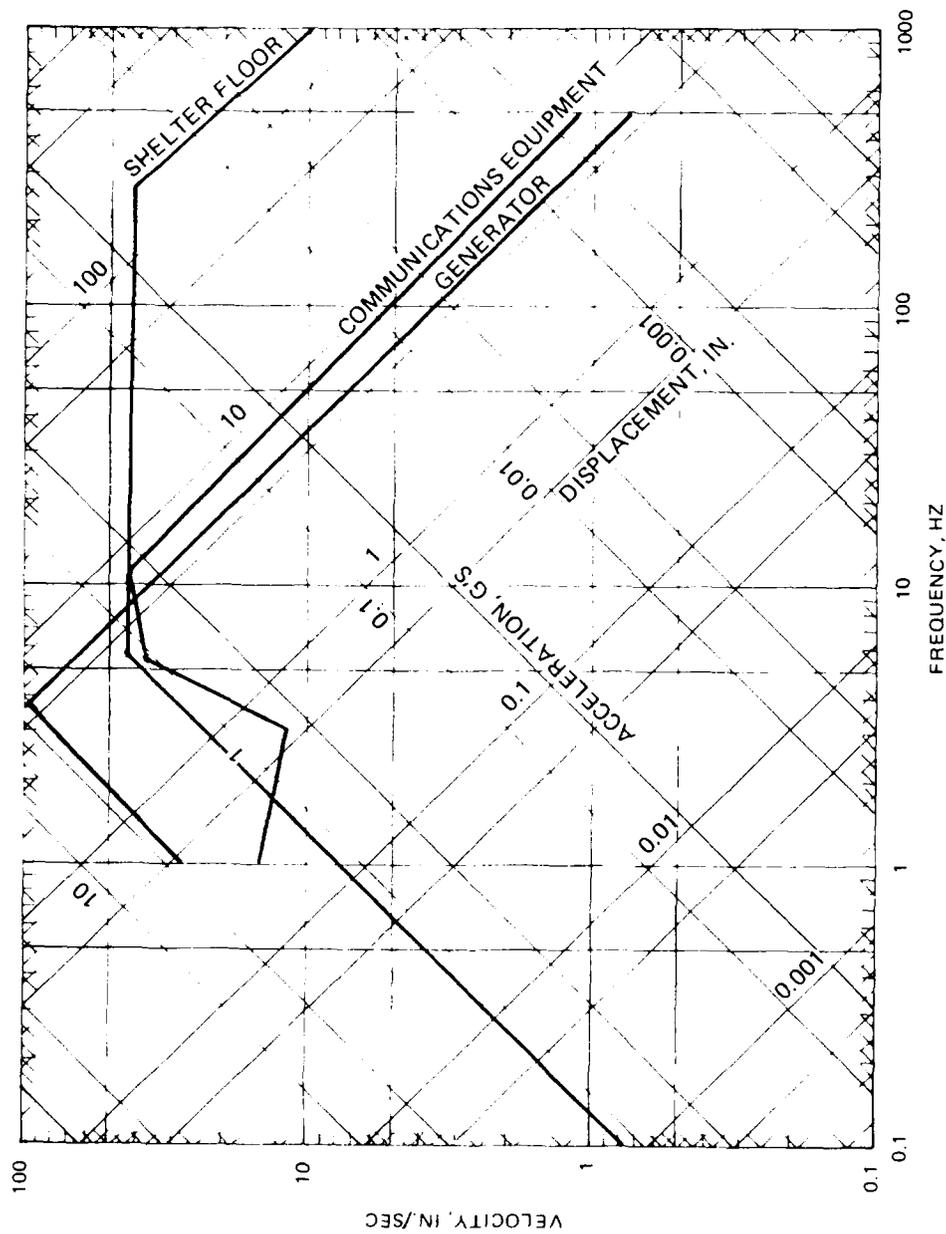
Figure 10. Comparison of the vertical shock spectra for the shelter floor with fragility curves for typical shelter equipment.

levels as a result of loss of balance and falling. The high-speed movies of the mannequin motion showed that impact injury was not probable. Plots of mannequin movement are presented in Figure 11.

RELATIVE MANNEQUIN MOTION
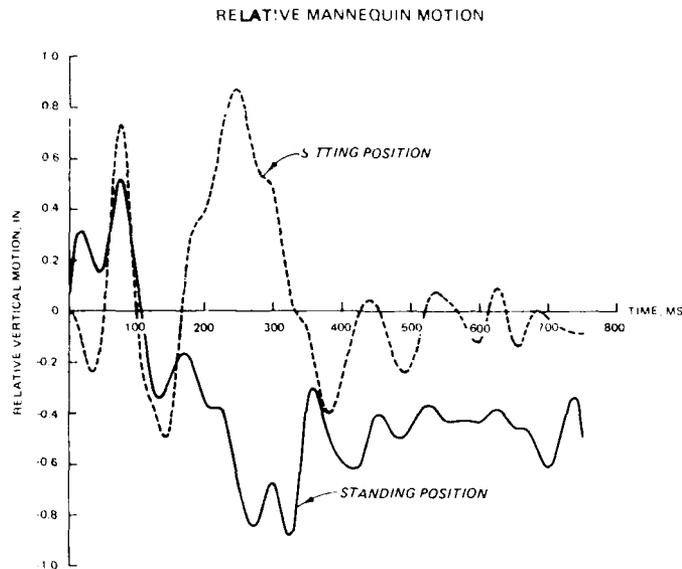
Figure 11. Plots of mannequin relative (to the floor) vertical displacement.

CONCLUSIONS AND RECOMMENDATIONS

The HEST test of the prototype Keyworker blast shelter demonstrated that the shelter has reserve capacity to resist overloads of up to three times the design peak overpressure of 50 psi without catastrophic failure. The series of tests performed on this shelter design indicates that it has adequate reserve capacity to resist the design load under less than ideal backfill conditions.

Even though the shear response of the roof slab was significant, the failure mode was very ductile. The roof decking prevented most of the crushed concrete from falling to the floor except near the walls and doorway. Use of the roof decking adequately protects the shelter occupants from projectile injuries caused by spalled concrete when the roof is significantly damaged. The connection of the roof decking and embedded angle to the exterior shelter walls needs revision to prevent the embedded angle from pulling out at large roof deformations. However, this detail is adequate for the minor damage incurred at the design overpressure level.

The entryway design proved adequate at the design overpressure but was severely damaged during the HEST test. Since this test did not realistically retest the entryway, no design modifications are suggested.

The mechanical equipment and their mounting details were adequate for the design loading and for the overload environment. During the HEST test, the lighting fixtures were detached from the roof slab, and the exhaust stack connection to the roof slab was damaged (but not failed). These details were adequate at small roof deformations, but the lighting fixtures should be hardened to withstand large roof deformations for a balanced shelter design. Some shock

isolation may be required for communication equipment, but this was not investigated by the test. Occupant survivability is probable even at the 160-psi level.

The results of this test and the scale model test programs conducted by WES validate the 100-man Keyworker blast shelter design. The minor revisions suggested make the shelter perform better at large deformations resulting from overload conditions. The experimental and analytical programs conducted by WES have resulted in a balanced shelter design that can be used without a redesign for site-specific conditions in most cases. In addition, the data base for the response of shallow buried structures was significantly expanded.

ACKNOWLEDGMENTS

REFERENCES

1. Woodson, S. C. and Slawson, T. R. (1986), "Demonstration Test of the Keyworker Blast Shelter: Minor Scale," Technical Report SL-86-40, Dec 1986, US Army Engineer Waterways Experiment Station, Vicksburg, Miss.

2. Slawson, T. R., (1987), "Vulnerability Evaluation of the Keyworker Blast Shelter," Technical Report SL-87-10, April 1987, US Army Engineer Waterways Experiment Station, Vicksburg, Miss.

3. Slawson T. R., et al, (1985), "Structural Element Tests in Support of the Keyworker Blast Shelter Program," Technical Report SL-85-8, Oct. 1985, US Army Engineer Waterways Experiment Station, Vicksburg, Miss.

4. Slawson, T. R., Garner, S. B., and Woodson, S. C., (1986), "Yield Effects on the Response of a Buried Blast Shelter," Technical Report SL-86-5, April 1986, US Army Engineer Waterways Experiment Station, Vicksburg, Miss.

5. Wampler, et al. (1978), "A Status and Capability Report on Nuclear Airblast Simulation Using HEST," Proceedings of the Nuclear Blast and Shock Simulation Symposium, 28-30 November 1978, Vol 1, General Electric-TEMPO, Santa Barbara, Calif.

6. Kiger, S. A., (1981), "Use of a Foam HEST to Simulate Low Yield Nuclear Overpressures," Miscellaneous Paper SL-81-12, July 1981, US Army Engineer Waterways Experiment Station, Vicksburg, Miss.

7. Headquarters, Department of the Army, (1987), Fundamentals of Protective Design for Conventional Weapons, Technical Manual 5-855-1, Washington, DC.

8. Crawford, R. E., et al, (1974), The Air Force Design Manual for Design and Analysis of Hardened Structures, Air Force Weapons Laboratory, Kirtland Air Force Base, New Mex.

SHELTER RESPONSE IN A SIMULATED
8-KT NUCLEAR BLAST ENVIRONMENT

R. L. Holmes, S. C. Woodson, and T. R. Slawson
U.S. Army Engineer Waterways Experiment Station
Vicksburg, MS

ABSTRACT

An 18-man blast shelter was tested dynamically on May
14, 1987 in the Defense Nuclear Agency (DNA) sponsored
33.5-TJ (8-kt) High Explosive Event, MISTY PICTURE, at
White Sands Missile Range (WSMR), NM. The shelter was
located at a distance of 150 m (490 ft.) from the high
explosive charge at the predicted 1.4-MPa (200-psi)
peak overpressure level. The main section of the
shelter was 2.7 m (9 ft) in diameter, 8.4 m (27.5 ft)
long, and fabricated from 10-gage, galvanized,
corrugated steel. The shelter included a vertical
entryway with a blast closure, light-weight endwalls, a
ventilation system, and an emergency exit. Results
indicate that the shelter has the reserve capacity to
resist overpressures as high as 1 MPa (148 psi) from a
33.5-TJ (8-kt) nuclear detonation without catastrophic
failures, provided the emergency exit is redesigned.
Acceleration data recorded during the test were used to
generate shock spectra at damping values equal to 0, 5,
and 10 percent of critical. The shock spectra indicate
that occupant survivability is highly probable with
little or no injuries, and that the survivability of
generators, and communication equipment can be achieved
by shock isolation.

INTRODUCTION

The Federal Emergency Management Agency (FEMA) tasked the US Army Engineer
Division, Huntsville (HND) to develop keyworker blast shelter designs. The US
Army Engineer Waterways Experiment Station (WES) assisted HND in the testing
and the analyses of the shelter designs, including an 18-man blast shelter
which was constructed by a private contractor and furnished to WES by HND.
The design criteria required that the 18-man shelter survive a peak
overpressure of 0.34 MPa (50 psi) from a 4200-TJ (1-MT) nuclear weapon. This
requirement and the levels of initial and residual radiation associated with
the threat weapon resulted in the design of an earth-covered shelter with a
depth of burial of 1.2 m (4 ft).

The original design of the 18-man blast shelter was validated at the
design load conditions by Woodson, Slawson, and Holmes [1]. The design was
found to be conservative, and some constructibility problems were

identified with the entryway-to-shelter connection. Design changes were proposed based on the test results and consultation with Messrs. Conrad Chester and Greg Zimmerman of the Oak Ridge National Laboratory. Primary modifications of the shelter design consisted of: replacing the stiffened endwalls with lighter-weight unstiffened plates, connecting the entryway to an endwall rather than to the main section of the shelter, and the inclusion of an emergency exit.

The study investigated the response of the modified 18-man blast shelter in an overload (relative to the design loading) environment. This paper discusses the dynamic test and the shock environment within the shelter. A more detailed description of the test procedure and results is presented by Holmes, Slawson, and Harris [2].

TEST DESCRIPTION AND RESULTS

The 18-man blast shelter, shown in Figure 1, was tested in the Defense Nuclear Agency (DNA) sponsored 33.5-TJ (8-kt) High Explosive Event, MISTY PICTURE. The shelter was located 150 m (490 ft.) from the high explosive charge at the predicted 1.4-MPa (200-psi) peak overpressure level. The high explosive charge consisted of approximately 4250 Mg (4,685 tons) of an Ammonium Nitrate and Fuel Oil (ANFO) mixture contained in a 26.8-m (88-ft.) diameter hemispherical fiberglas shell. The test bed, shown in Figure 2, was approximately 15.2 m (50 ft.) long, 11 m (36 ft.) wide, and 4.3 m (14 ft.) deep. The backfill material used during this test was a locally available material referred to as blow sand. A 0.31-m (1-ft.) layer of blow sand was placed in the test bed prior to placement of the main section of the shelter. Based on experience and the backfill densities obtained using blow sand during similar tests at the WSMR, the backfill was placed in the test b l in compacted layers approximately 10.2 cm (4 in.) thick.

The shelter and the free field were instrumented with a total of 18 channels to monitor structural and ground motions and airblast overpressures. Fifteen Endevco accelerometers were used to monitor the structural and free field accelerations. Thirteen accelerometers were installed at mid-length of the shelter along the interior surface to measure structural accelerations. Two accelerometers were located in the free field to measure vertical and horizontal acceleration. The surface of the test bed was leveled, and three Kulite Model XT-190 airblast pressure gages were installed to monitor the airblast overpressure. These gages were positioned along the center line of the shelter at the ground surface as shown in Figure 3.

Figure 4 is a posttest view of the 18-man shelter. The damage sustained by the main section of the shelter, the entryway, and the ventilation system was minor. Figure 5 shows that the predominant structural response and rigid-body motion occurred during the first 75-msec after the blast wave arrived at the shelter. Overall, the permanent structural deformations were small and major structural components remained structurally sound. The failure of the emergency exit cover plate, Figure 6, was the only failure of the test. The bolts used to connect the emergency exit cover plate to the shelter were spot welded to the inside surface of the shelter. Three of the fifteen bolts failed in shear during the backfilling operation. During the test, three bolts pulled through the cover plate and nine bolts failed in shear.

Figure 1. 18-man blast shelter.

PLAN VIEW

END VIEW
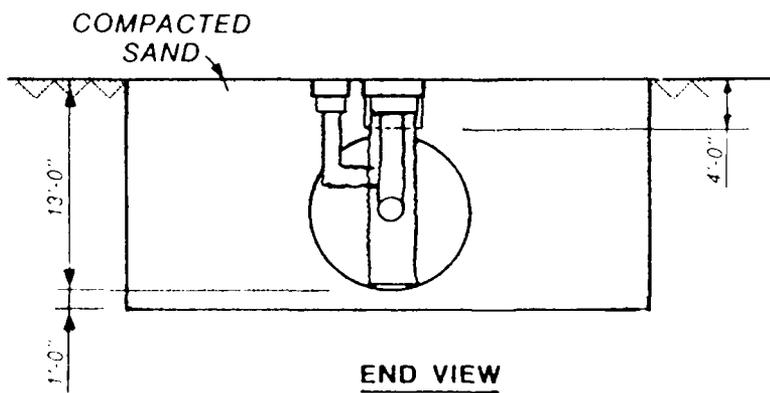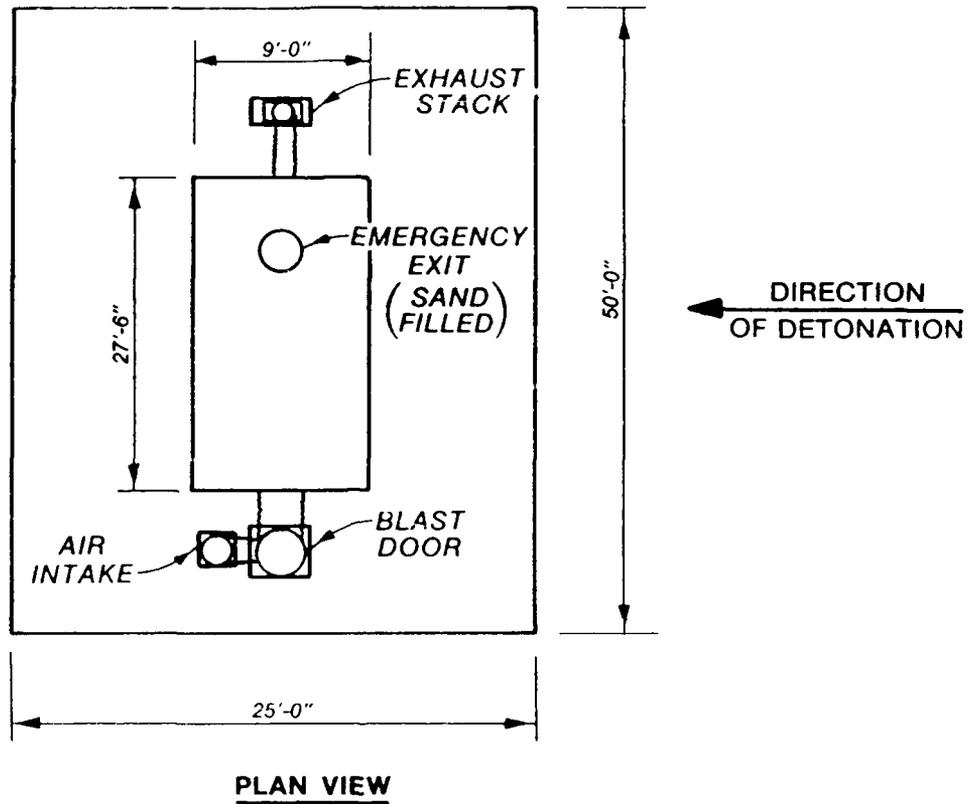
Figure 2. Test bed layout.

246
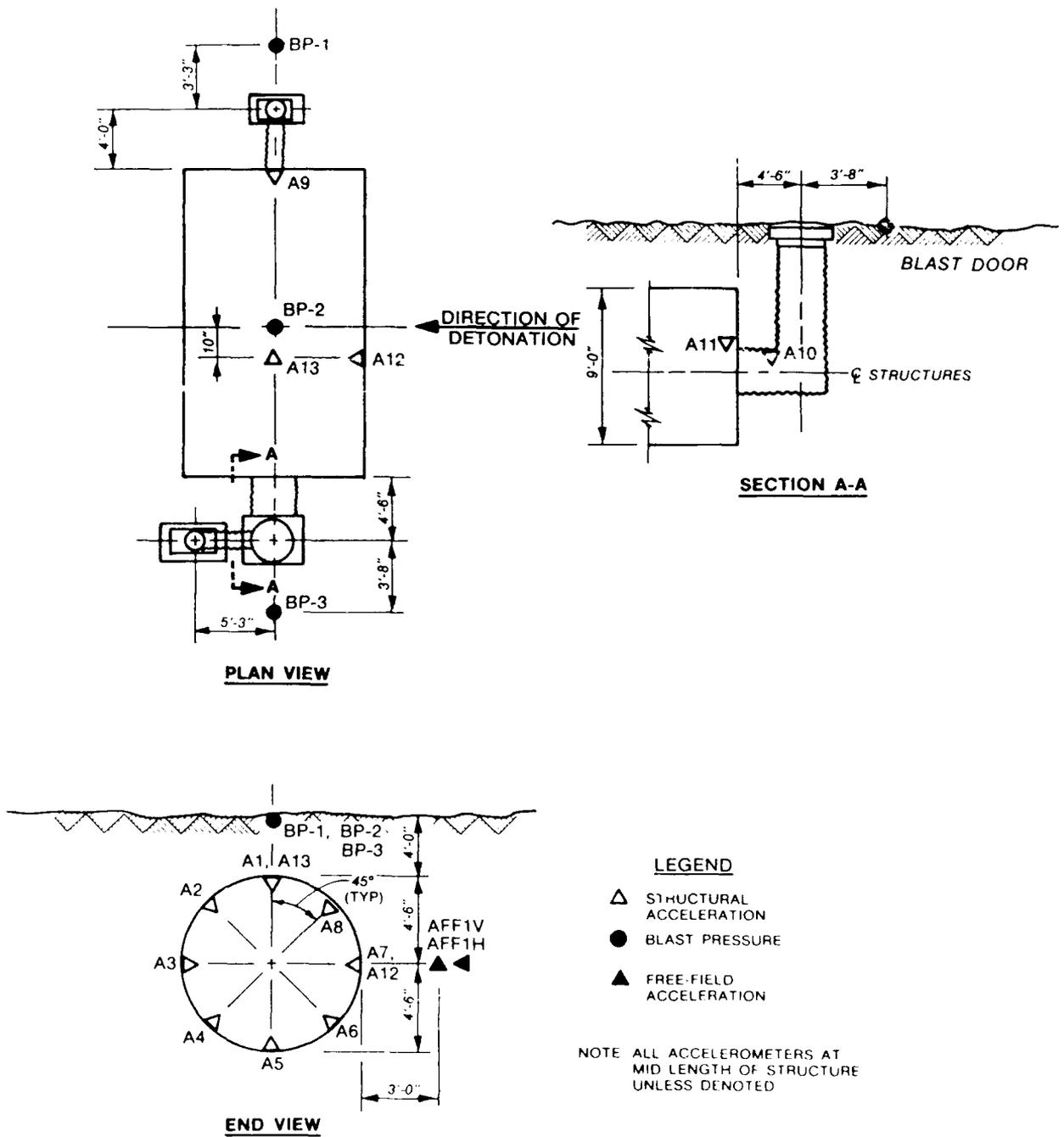
Figure 3. Instrumentation layout.

Figure 4. Posttest view of partially excavated shelter.
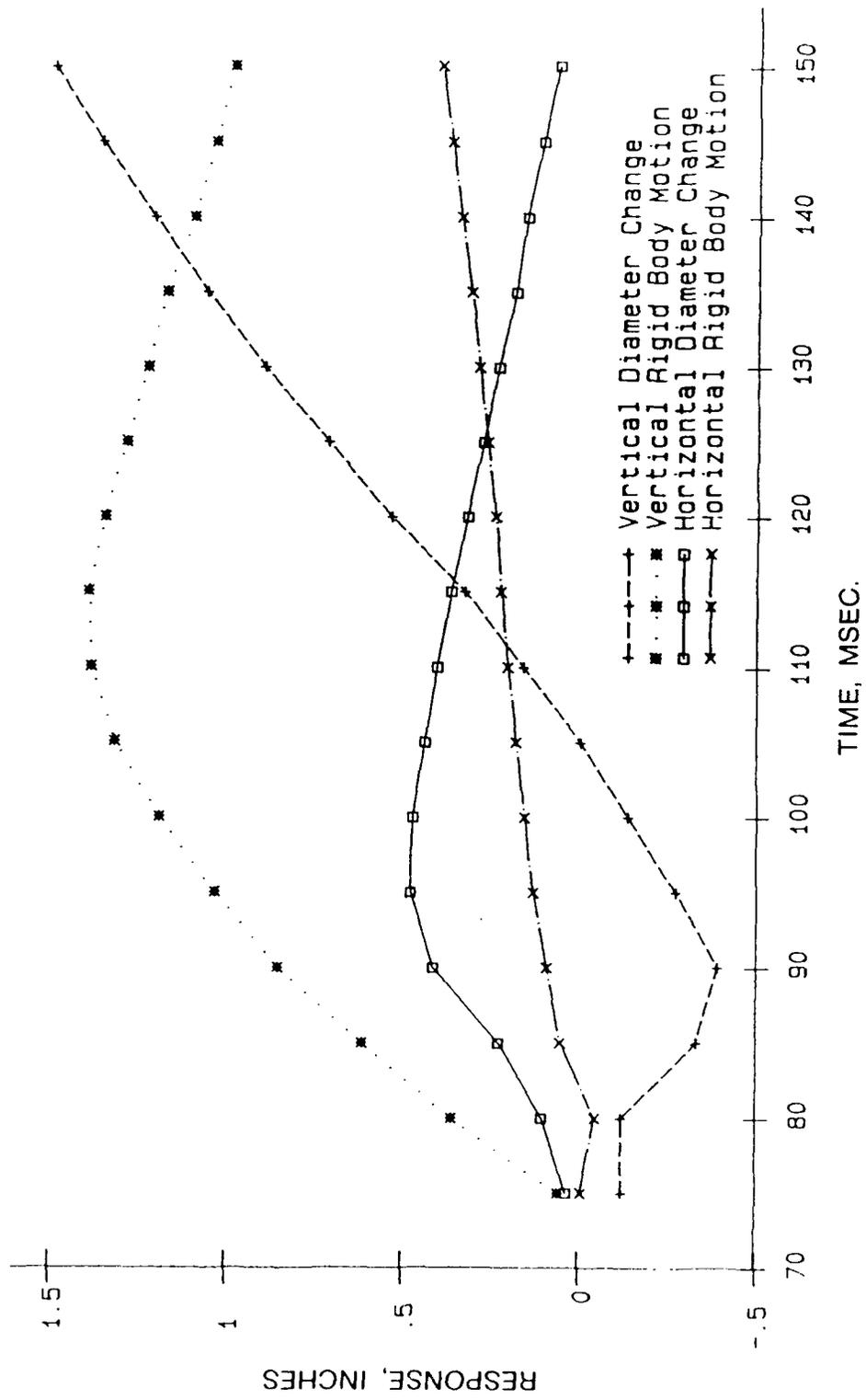
Figure 5. Structural response.

Legend:
+ Vertical Diameter Change
* Vertical Rigid Body Motion
□ Horizontal Diameter Change
× Horizontal Rigid Body Motion

TIME, MSEC.

RESPONSE, INCHES

Figure 6. Failure of emergency exit cover plate.

DATA ANALYSIS

Estimates of the surface-burst nuclear weapon yield and overpressure which best correspond to the airblast data records are required to define the loading function at the ground surface. Weapon simulations were determined by fitting, in a least squared sense, 50 msec of airblast impulse data to nuclear weapon impulse-time curves as defined by Speicher and Brode [3]. The airblast records were fit individually and collectively using the procedure developed by Mlakar and Walker [4] and modified by Mr. James Baylot of WES. The peak overpressure for the average 33.5-TJ (8-kt) yield weapon fit airblast record was 1.0 MPa (148 psi), and the average best fit was a 10.0 TJ (2.4 kt) weapon yield at a peak overpressure of 1.4 MPa (198 psi).

IN-STRUCTURE SHOCK

In-structure shock is typically represented in terms of shock spectra. Shock spectra are plots of maximum responses (usually of relative displacement, pseudo-velocity and/or absolute acceleration) of all possible linear oscillators with a specified amount of damping to a given input base acceleration-time history. Shock spectra were generated using acceleration data obtained during the dynamic test as input data for a computer code developed at WES. The shock spectra were constructed using damping values of 0, 5, and 10 percent of critical damping. The shock spectra developed from the data of accelerometers A5 and A7 are shown in Figures 7 and 8. Figure 9 compares the experimentally determined vertical shock spectra (smoothed by hand and using a damping ratio of 10 percent of critical) for the shelter floor with the fragility curve for typical floor-mounted equipment found in Reference 5. Floor-mounted equipment includes items such as generators and communication devices. This comparison indicates that typical floor mounted equipment would not have survived at the overpressure level of this test. The experimental shock spectra were generated from data recovered from gages located on the shelter and not attached to any floor surface. Typical equipment would be mounted to a plywood floor in an actual shelter. The floor tends to reduce the amplitudes observed in the shock spectra and increases the chances of survival of equipment and occupants.

Based on the results found in References 1, 6, and 7 of similar experiments with the equipment installed, the fragility curves for typical floor-mounted equipment [5] are design conservative (ie, the equipment survived at shock levels exceeding their fragility curves). Figure 9 indicates that any floor-mounted equipment should be shock isolated to ensure survivability.
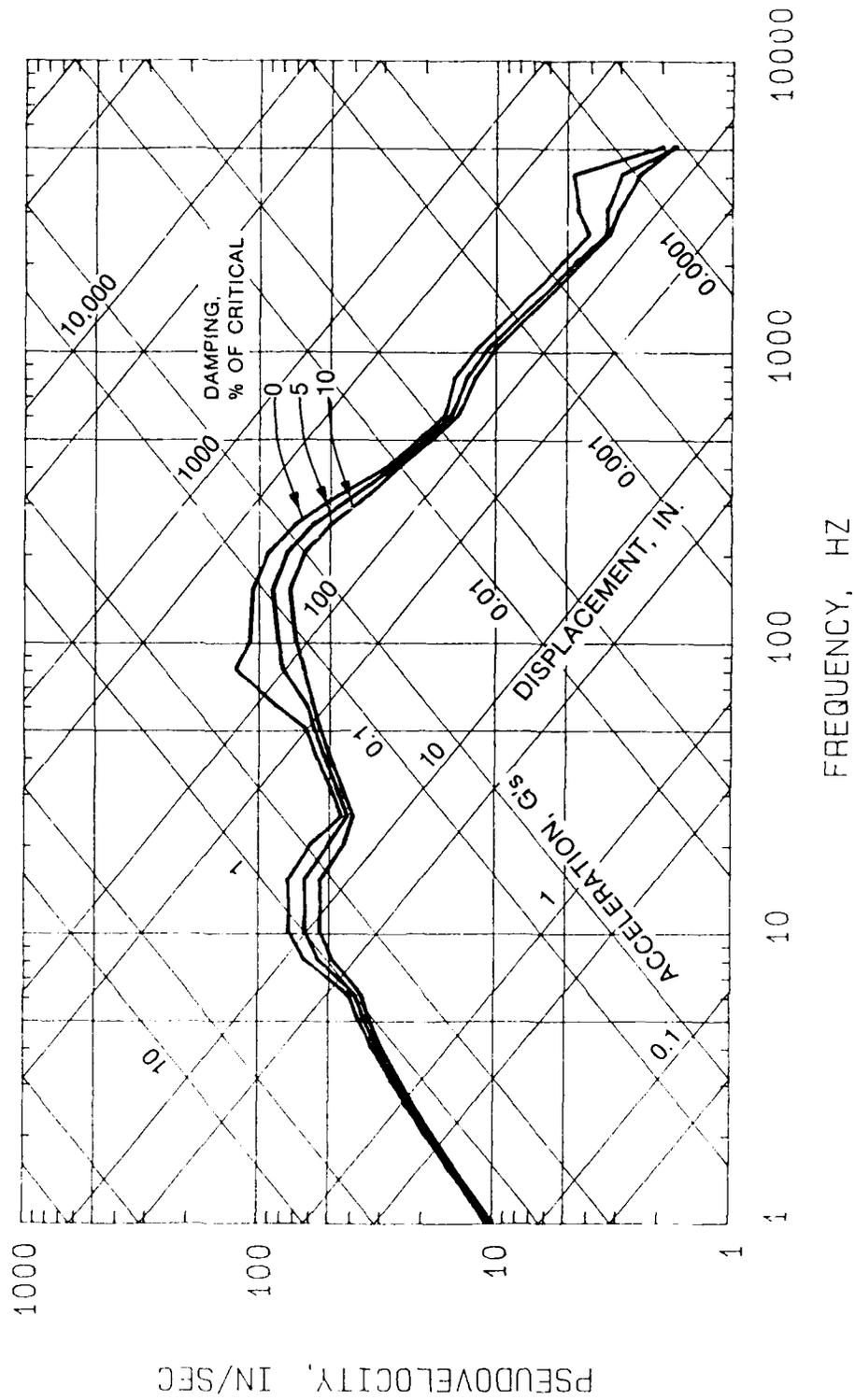
Figure 7. Shock spectra for accelerometer A5.
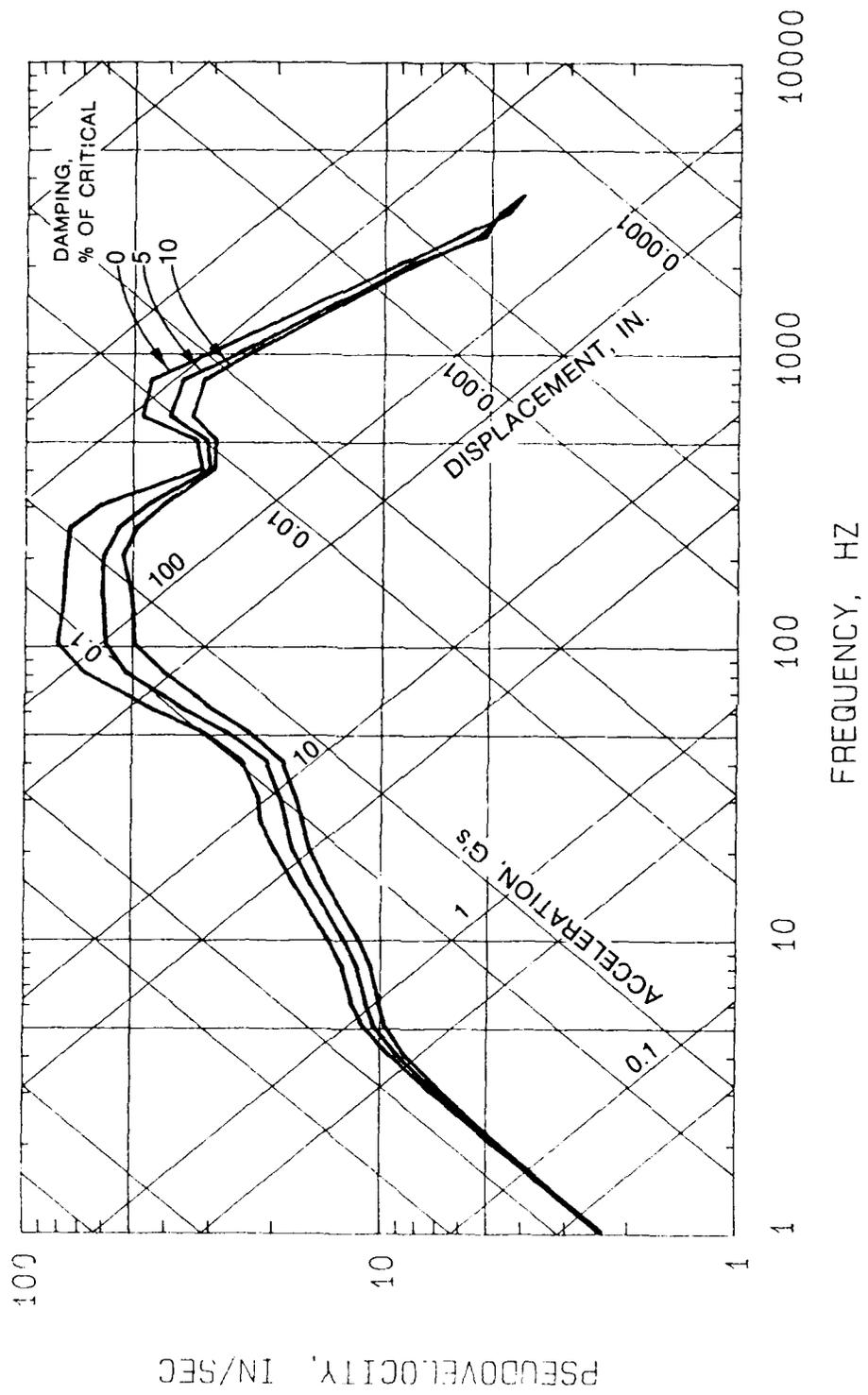
Figure 8. Shock Spectra for accelerometer A7.
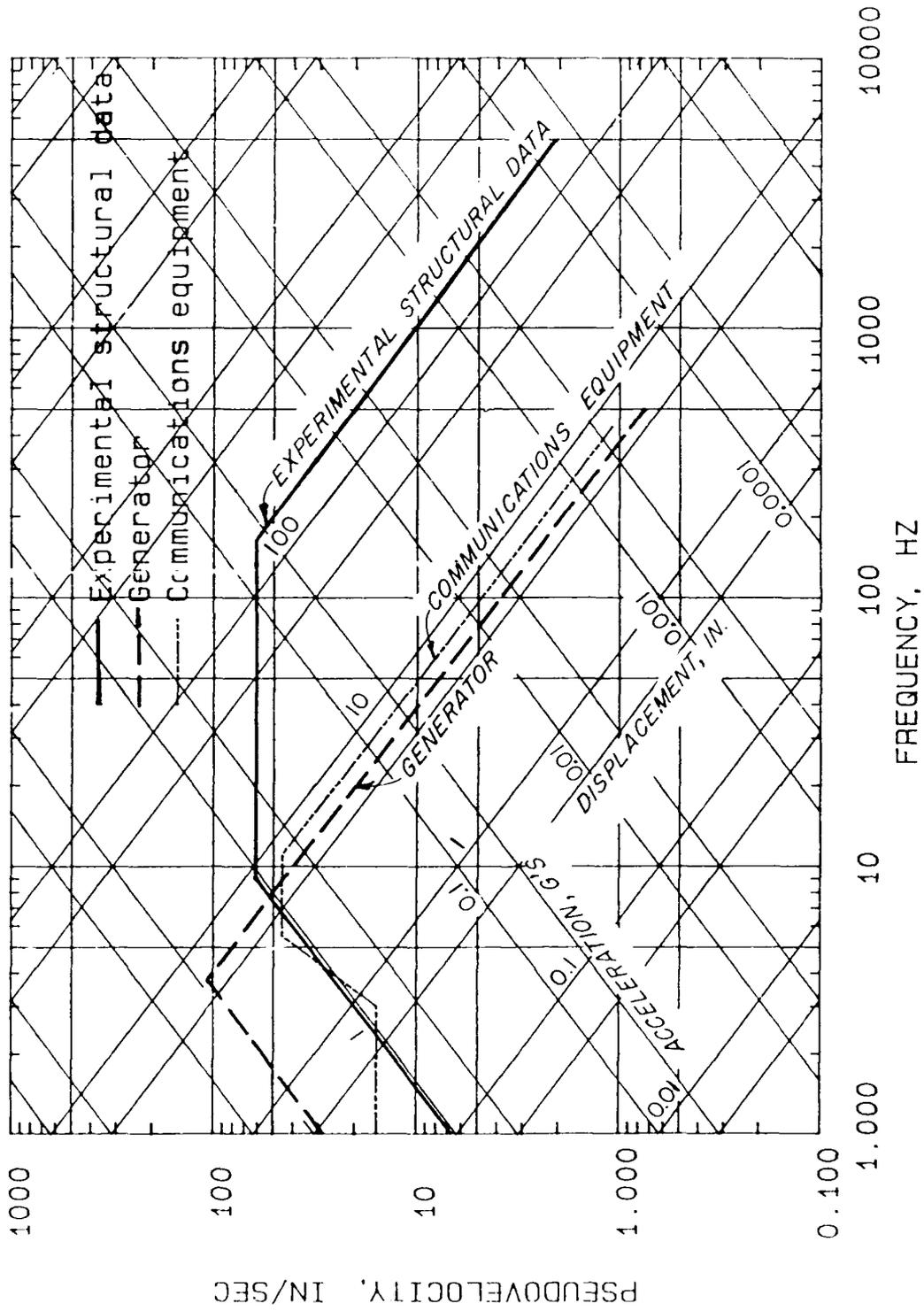
Figure 9. Comparison of experimental shock spectra with
response spectra for typical floor-mounted equipment.

OCCUPANT SURVIVABILITY

Crawford [8] discusses human shock tolerance. The effects of shock on personnel inside the shelter depend on the position of the individual and the magnitude, duration, frequency, and direction of the motion. It is recommended that a maximum design acceleration of 10 g's at frequencies at or below a man's resonant frequency in the standing position (10 Hz) be used. Figure 7 shows that the floor acceleration measured on the inside bottom shelter surface was at or slightly less than 10 g's at a frequency of 10 Hz. Also, the use of a plywood floor will decrease the effective shock amplitudes received by the occupants. Since human shock tolerance is higher in the seated and supine positions than in the standing position, the probability of

injury decreases for these positions.

Impact injuries occur at much lower accelerations than compressive bone fractures. Generally, impact injuries may occur at acceleration of 0.5 to 1 g for an unrestrained man in the standing or seated positions. These injuries are the results of one falling and hitting the floor or other objects. Impact injuries may be reduced by the use of padded surfaces and/or restraints to prevent movement. No simulated occupants were used during this test; however, the results presented by Slawson [7] of tests conducted under similar conditions show relatively small occupant motions that did not result in the occupants falling down or falling off of bunks.

STRUCTURAL RESPONSE

The failure of the emergency exit cover plate allowed blast pressure to fill the shelter. Since internal pressure reduces the effective external structural loading, it was necessary to determine if enough pressure entered the shelter to affect its structural response. The Chamber computer program [9] was used to perform these calculations. The magnitude and the rate-of-fill of the entering pressure were considered in the analysis. Although the shelter filled with pressure at a fast enough rate to affect the shelter's structural response, the magnitude of the fill-pressure was relatively low in comparison with the overpressures measured at the ground surface. Therefore, the pressure inside the shelter did not significantly affect the structural response of the shelter. From a structural response point of view, it is concluded that the failure of the emergency exit did not adversely affect the results of the test.

CONCLUSIONS AND RECOMMENDATIONS

The 18-man blast shelter test in the MISTY PICTURE Event was a partially successful validation of the modified structural design. Although the entryway (with blast closure), the ventilation system, and the modified endwalls were damaged during the test, their designs proved to be adequate. The failure of the emergency exit cover plate was the only structural failure.

In-structure shock levels were survivable by equipment and personnel. Shock isolation of shelter equipment is suggested to ensure equipment survivability. Padding of sharp corners, possible impact surfaces and/or restraint of shelter occupants is recommended as a precautionary measure to prevent impact injuries.

The modifications to the structural design investigated in this test should be incorporated in the final shelter design except for the emergency exit cover plate detail. The connection of this plate to the shelter barrel should be modified to prevent shearing of the bolts.

ACKNOWLEDGMENT

REFERENCES

1. Woodson, S. C., Slawson, T. R., and Holmes, R. L., "Dynamic Test of A Corrugated Steel Keyworker Blast Shelter," Technical Report SL-86-6, May 1986, US Army Engineer Waterways Experiment Station, Vicksburg, Mississippi.

2. Holmes, R. L., Slawson, T. R., and Harris, A. L., "Dynamic Test of A Corrugated Steel Keyworker Blast Shelter: Misty Picture," Technical Report SL-87-31, November 1987, US Army Engineer Waterways Experiment Station, Vicksburg, Mississippi.

3. Speicher, S. J., and Brode, H. L. "Airblast Overpressure Analytic Expression for Burst Height, Range and Time Over an Ideal Surface," PSR Note 385, November 1981 (with updates through November 1982), Pacific-Sierra Research Corporation, Santa Monica, California.

4. Mlakar, P. F., and Walker, R. E., "Statistical Estimation of Simulated Yield and Overpressure," Shock and Vibration Bulletin, Bulletin 50, Part 2, September 1980, The Shock and Vibration Information Center, Naval Research Laboratory, Washington, DC.

5. Headquarters, Department of the Army, "Fundamentals of Protective Design for Conventional Weapons," Technical Manual 5-855-1, 1987, Washington, DC.

6. Woodson, S. C. and Slawson, T.R., "Demonstration Test of the Keyworker Blast Shelter: Minor Scale," Technical Report SL-86-49, December 1986, US Army Engineer Waterways Experiment Station, Vicksburg, Mississippi.

7. Slawson, T. R., "Vulnerability Evaluation of the Keyworker Blast Shelter," Technical Report SL-87-10, April 1987, US Army Engineer Waterways Experiment Station, Vicksburg, Mississippi.

8. Crawford, R. E., et al., "The Air Force Design Manual for Design and Analysis of Hardened Structures," 1974, Air force Weapons Laboratory, Kirtland Air Force Base, N. Mexico.

9. Britt, J. R. and Drake, J. L., "Chamberm User's Manual," 1986, Applied Research Associates, Inc., Vicksburg, Mississippi.

BLAST INDUCED LIQUEFACTION
FIELD EXPLOSIVE TESTS

H. A. Hassen and W. A. Charlie
Department of Civil Engineering
Colorado State University
Fort Collins, CO 80523

Abstract

This paper discusses liquefaction of water saturated sands under planar blast waves and describes our experimental field testing program that we conducted at the Liquefaction Field Testing Site at Colorado State University. The facility is capable of testing soil sample tens of tons in size and uses actual explosives to produce ground strains to any level desired. Reported here are the results from a series of tests that were performed on a subangular riverbed sand by subjecting it to planar compressive stress waves generated from a grid formed from detonating cords. The response of the saturated soil during and after the passage of the stress wave was recorded and some results are presented and discussed.

INTRODUCTION

Loose cohesionless soils tend to decrease in volume and may suffer severe loss of shear strength when subjected to dynamic or monotonic static loadings. This phenomenon is termed soil liquefaction and is associated primarily with saturated cohesionless soils. Liquefaction can be triggered by a large number of inputs; natural or artificial. Liquefaction induced by shock waves and the resulting rapid and large release of energy is potentially a more serious threat than that caused by other inputs. Shock waves generated by explosions or by blast loads lie in this category. Regardless of the causing mechanism, effects that occur during and after liquefaction are similar and can be catastrophic. These effects may take many forms. Flow failures of natural slopes or earthdams, tipping of buildings and collapse of bridges are some

disastrous effects. Liquefaction can also produce sinking or flooding or tilting of military structures above or under ground. An explosion, detonated above or in saturated sandy soils usually results in a damage disproportionate to the energy released. These effects clearly indicate that the potential for liquefaction whether by explosions or by other inputs, poses serious questions to the design civil and military engineers. The vast and serious damage caused the liquefaction during the Niigata and Alaska earthquakes in 1964, initiated a considerable amount of research on earthquake-induced liquefaction. Now the related parameters are known and determined and the causing mechanism is well understood. In the case of explosive induced liquefaction, however, similar efforts have only recently started (International Workshop on Blast-Induced Liquefaction, 1978; Blouin and Shinn, 1983). More research is still needed to understand the mechanism causing it and to develop the technology necessary for designing engineering structures and for mitigating potential hazards.

Our paper reviews shock-induced soil liquefaction and describes an experimental testing program that we are conducting at the Liquefaction Testing Site at Colorado State University under a grant from the Air Force Office of Scientific Research (AFOSR). Laboratory and field testing and theoretical investigations are being conducted under this research program. A theoretical finite element model that treats saturated sands as a coupled two-phase system is currently being developed, and the laboratory testing phase has been completed (Charlie, et al. 1987a). As part of the field testing program saturated sand response to planar shock waves was tested. Some results are reported here. These tests were carried out to simulate loading of saturated soil elements near the explosive . Intense compressive loadings having less than a millisecond rise times occur in this region, (Figure 1).
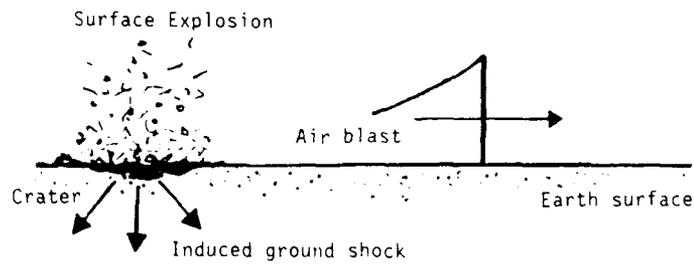
Figure 1. Surface Explosion Effects in Soils
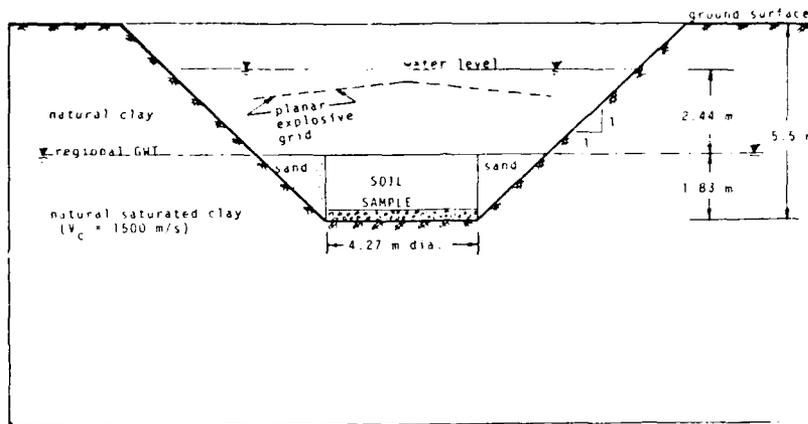
Figure 2. Cross-section of Explosive Test Pit and Soil Sample
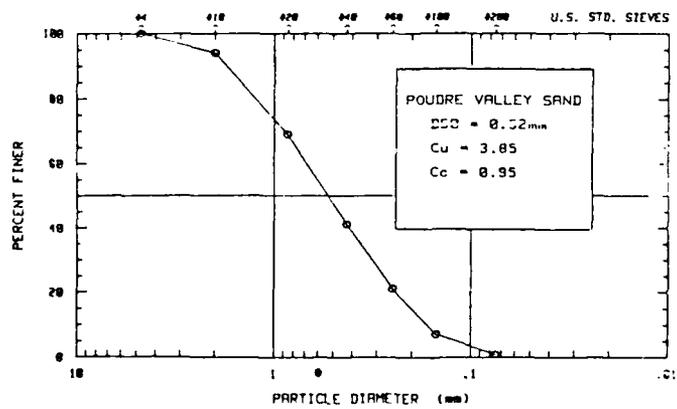
Figure 3. Poudre Valley Sand Gradation Curve

SHOCK-INDUCED LIQUEFACTION

Liquefaction, as the term will be used in our paper, describes a state of saturated sands in which the shear strength of the soil is greatly reduced. Physically, this can be viewed as the loss of grain to grain contact between the sand grains. The material thus acquires the properties and behaves like a dense fluid or mixture of water and sand grains. When a saturated sand is subjected to compression from a shock loading, most of the external volumetric stress is carried by the water phase because its stiffness is much higher than that of the skeleton phase. Upon unloading, the removal of this volumetric stress is accompanied by an elastic stress relief of the induced porewater pressure. If the loading strains were large enough to plastically compress the soil skeleton, residual porewater pressures greater than the hydrostatic value will be induced. Large compressive stresses can produce a pore pressure rise upon unloading equal to the initial effective stress carried by the soil skelton resulting in a state of complete liquefaction.

The tendency for a saturated sand deposit to liquefy under shock loading is dependent on many parameters that can be grouped into: 1) soil media related parameters and 2) explosives related parameters. However, here only a summary of the explosive related parameters will be given. Soil media related parameters have been given in detail by others (Rischbieter, 1977; Hassen, 1988).

- Magnitude of applied stresses. Larger stress intensities are needed to trigger liquefaction with increasing effective soil stresses. Also, a series of small delayed explosions have proven to be more effective than single large ones. (Damitio, 1978; Ivanov, 1967).

- Depth of burial. A contained explosion creates a larger zone of liquefaction than does a surface explosion.

- Charge weight. Ground strains decrease and ground shock frequencies increase with decreasing charge weight.

- Charge Shape. Spherical charges, for example, can cause more liquefaction than a planar one of similar mass because the soil will be strained both radially and in the tangential direction.

Stress waves are usually attenuated as they travel away from the detonation point. This geometrical attenuation is a function of the charge shape. Planar stress waves are not subjected to geometrical attenuation but are material damped. The amount of attenuation generally changes with increasing distance from the charge point.

FIELD EXPERIMENTAL FACILITIES

Large scale field tests and actual explosives have been suggested by many researchers as the best way of modeling free field conditions in a sizeable volume of sand (Blouin and Shinn, 1983; Ivanou, 1967; Veyera, 1985). We conducted a series of six planar field tests on very large samples of placed Poudre Valley sand. Our tests were designed to evaluate explosive induced pore water pressure increases and liquefaction of water saturated cohesionless soil subjected to explosive induced planar compressive stress waves, having submillisecond rise time to peak. These tests were performed at the explosive test site located at the Colorado State University Engineering Research Center. As shown in Figure 2, the test facility is located below the regional groundwater table. Locating the sample below the water table minimized potential stress wave reflections from the sample's boundaries. We instrumented the sand at three different levels with porewater pressure transducers, accelerometers and stress gages to record the transient pore pressure, acceleration and total stress response respectively as a function of distance and charge intensity. Piezometers were utilized to obtain late time or residual porewater pressure reponse, digital transient data recorders were utilized to record the response of the embedded instruments and strain gages were used to determine the charges in soil density. Full account of this state-of-the-art instrumentation program is given in Charlie, et al. 1987b.

SAND USED AND TEST PROCEDURES:

Our tests were conducted on Poudre Valley sand, a sand commercially produced by crushing gravel obtained from the Poudre River in Northern Colorado. This sand has an angular grain shape, a mean grain size of 0.52 mm, a specific gravity of 2.68 and

a USCS classification of SP. The gradation curve of this sand is given in Figure 3. The sample size was 4.4 m in diameter by 1.7m high. The soil volume was 26 m^3 and the dry mass of thesample was approximately 45,000 kg. Once the sand was placed and saturated, 1.8m of water was added above the top of the samples and explosives were detonated in the water 1.2m above sand. After each shot, the settlement of the sample was measured and checked against that recorded by the strain gages. After the tests were completed, the water was pumped out and the final location of the gages were recorded. The explosives were obtained from Buckley Power Company of Englewood, Colorado. Detonating cord (Prima Cord manufactured by the Ensign-Bickford Company) was woven in to a grid to produce the required planar stress wave.

RESULTS

Tests were performed on the saturated Poudre Valley sand that was placed at average relative density of about 90 percent. To produce a planar compressive stress wave, a 7m diameter grid of the detonating cord was placed in the water 1.2m above the sand's surface. Because of the burn speed of detonating cord is approximately 6,700 m/sec, the center of the grid was lifted about 65cm to ensure a true planar wave. The grid was centered detonated with an instantaneous electric blasting cap. Grid spacings used were 0.3m or 0.6m, depending on the detonating cord explosive rating and explosive density required to produce the required peak stresses. Total explosive mass for the six grids detonated ranged from 0.531 to 2.55 kg giving a charge intensity , Wi, ranging from 0.15 to 0.73 gm/m^2. Table 1 shows the measured porewater pressure ratios for all tests. The best fit equations for the measured peak porewater pressure u_{pk} and the pore pressure ratio , PPR, respectively as a function of scaled distance, (R/Wi) are:

$$u_{pk} = 30073 \left(\frac{R}{Wi} \right)^{-0.442}$$

Eq. 1

$$PPR = 1.11 \left(\frac{R}{Wi} \right)^{0.084}$$

Eq. 2

where u_{pk} is in kPa, PPR ranges from 0 to 1, R is distance from charge in m and wi the charge intensity in gm/m^2. A porewater pressure ratio of 0 indicates no residual increase in porewater pressure and a PPR of 1 indicates liquefaction.

Combining Equations 1 and 2 and solving for peak strain, ϵ_{pk}, from

$$\epsilon_{pk} = \frac{(V_p)_{pk}}{V_c} \qquad\qquad \text{Eq. 3}$$

where V_p is the particle velocity in m/sec and V_c is the compressive stress wave propogation velocity through the saturated sand in m/sec., the porewater pressure ratio can be presented in terms of peak strain as given in Figure 4. The best fit equation for this is

$$PPR = 1.48 \ (\epsilon_{pk})^{0.29} \qquad\qquad \text{Eq. 4}$$

The above equations can be used to estimate the transient porewater pressure and porewater pressure ratio as a function of charge intensity.

CONCLUSIONS

Our new field explosive testing facility can be used to test near surface saturated soils under 1-D compressive blast loadings. The test conditions created allow for use of very large soil samples to eliminate boundary problems commonly associated with laboratory and small scale field testing. This technique also has the advantage of being capable of using actual explosives to produce high stresses to any desired level. Experimental results have shown that it is possible to induce liquefaction in saturated sand under one dimensional compressive explosive loadings. An empirical relationship between the porewater pressure ratio (PPR) and the scaled distance was found. However, because of the small number of tests carried, its use should be limited to range of stress used in the experiment.

Table 1. Residual Pore Pressure and Charge Intensities for Planar Stress Waves

Test No.	Total Charge Wt (kg)	Average Charge Weight per Area (kg/m²)	Peak Rise of Water in Piezometer (m)	PPR	Explosive used
Dense (relative density approximately 89 percent)					
P1	0.53	0.15	1.37	0.86	Primacord[R] 3.8 g/m (61x61 cm grid)
P2	0.74	0.21	1.55	0.97	Primacord[R] 5.3 g/m (61x61 cm grid)
P3	1.46	0.42	1.68	1.05	Primacord[R] 10.7 g/m (61x61 cm grid)
P4	1.46	0.42	1.39	0.87	Primacord[R] 10.7 g/m (61x61 cm grid)
P5	2.55	0.73	-	-	Primacord[R] 10.7 g/m (30x30 cm grid)
P6	1.28	0.26	-	-	Primacord[R] 5.3 g/m (30x30 cm grid)

Charge Location In water 1.22 m above tank and 0.61 m below water surface.

Piezometer is located at a depth of 1.67 m below soil surface and at a distance, R, from the charge grid of 2.89 m. The rise of water required for PPR = 1 is 1.6 m.


PORE PRESSURE RATIO VS. PEAK STRAIN %
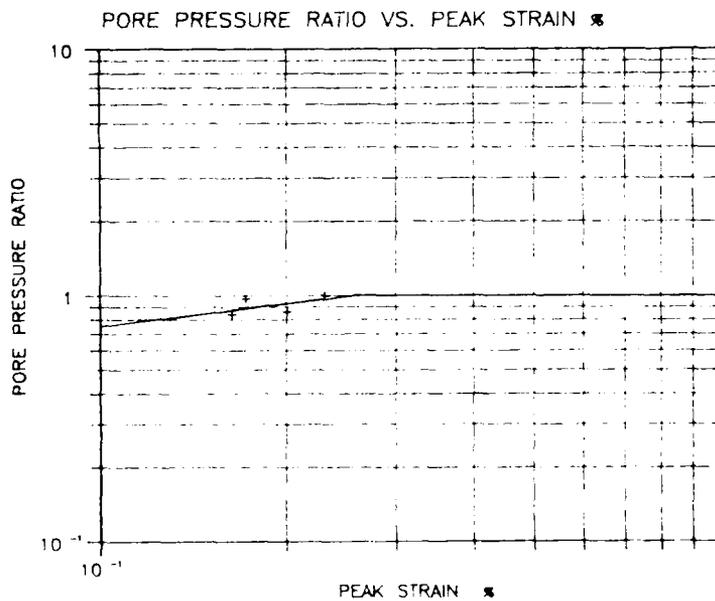
Figure 4. Porewater Pressure Ratio versus Peak Strain

REFERENCES

1.   Blouin, S. E. and Shinn, K. J., (1983), "Explosion Induced Liquefaction", U.S. Air Force Office of Scientific Research (ASOFR) Contract: F49620-81-C-0014, Applied Research Associates, Inc., New England Division, South Royalton, Vermont, September, 227 pp.

2.   Charlie, W. A., Veyera, G. E., Bretz, T. E. and Allard, D. J., (1987a) "Shock Induced Porewater Pressure Increases in Water Saturated Soils", Shock and Vibration Bulletin, No. 57, Part 2, January, pp. 161-166.

3.   Charlie, W. A., Hassen, H. A., Doehring, D. O. and Hubert, M. E., (1987b), "Microcomputers in Shock Testing of Water Saturated Sands," Shock and Vibration Bulletin, No. 57, Part 2, January pp. 157-160.

4.   Damitio, C., (1978), "Field Experience on Blast-Induced Liquefaction:, Transcripts of the International Workshop on Blast-Induced Liquefaction, Dames and Moore, AFOSR, Maidenhead, U.K., September, pp. 137-148.

5.   Hassen, H. A., (1988), "Saturated Sand Response Under Planar Blast Loadings", Doctoral Dissertation, Department of Civil Engineering, Colorado State University, Fort Collins, Colorado, expected in Fall.

6.   Ivanov, P.L., (1967), "Compaction of Noncohesive Soils by Explosions", Izdatel'stvu Literatury Po Stroitel'stru, Leningrad, U.S.S.R., Translated by the Indian National Scientific Documentation Center, New Delhi, India; Published for the U.S. Department of the Interior Bureau of Reclamation and National Science Foundation, Washington, D.C., 211 pp.

7.   International Workshop on Blast-Induced Liquefaction, (1978), Dames and Moore, AFOSR, Maidenhead, U.K., September, pp. 137-148.

8.   Rischbieter, F., (1977), "Soil Liquefaction - A Survey of Research", Proc. 5th International Symposium on Military Application of Blast Simulation, Stockholm, Sweden, May, pp. 7:1:1-7:1:24.

9.   Veyera, G. E., (1985), "Transient Porewater Pressure Response and Liquefaction in a Saturated Sand", Doctoral Dissertation, Department of Civil Engineering, Colorado State University, Fort Collins, Colorado, Fall, 198 pp.

GUNS AND PROJECTILES

WAVE COUPLING AND RESONANCE IN GUN TUBES

T. E. Simkins
U.S. Army Armament Research, Development, and Engineering Center
Close Combat Armaments Center
Benet Laboratories
Watervliet, NY 12189-4050

Uncommonly large dynamic strains observed during the firing
of a 120-mm gun tube have been found to be due to a projec-
tile velocity which causes resonant type behavior of a par-
ticular axisymmetric wave. The theory explaining this
phenomenon is reviewed and extended to show the potential
for excitation of non-axially symmetric waves through
coupling when the tube has an eccentric bore. These non-
axially symmetric waves, one of which resonates at a projec-
tile velocity extremely close to that which causes
axisymmetric resonance, cause a beamlike motion of the gun
tube which can affect accuracy at the target.

INTRODUCTION

The work presented herein was motivated by a collection of unusual strain data
acquired during a series of test firings of a 120-mm gun tube during the latter part
of 1985. During these tests, circumferential strains exceeding three times those
predicted by the customary Lamé [1] were recorded from the outer surface of this
tube a few feet from the muzzle. Subsequent inspection of the strain data showed
that these strains increased dramatically with projectile velocity and possessed an
oscillatory waveform with a frequency approaching 15 kHz.

It was soon discovered that the extremely large strains were caused by a pro-
jectile velocity which was very close to critical. The existence of such a critical
velocity had been predicted in the literature at least thirty years ago [2-4], but
to the best of our knowledge, no observations such as these have been reported in
the literature. In the following, the essence of the 'critical velocity' theory of
axisymmetric vibrations of a circular cylinder is reviewed and the theory is
extended to include the case of non-axially symmetric vibrations which can be
excited through coupling.

CRITICAL VELOCITY THEORY

This theory predicts a limit as to how fast the tube deformation--in the imme-
diate vicinity of the projectile--can be made to travel before some sort of wave
develops. An exaggerated view of this deformation when the projectile velocity is
low is shown in Fig. 1. Under these 'quasi-static' conditions, the deviation from
the Lamé-predicted deformation is less than 3 percent. However, as the projectile
velocity approaches a certain critical value, the tube deformation in the neighbor-
hood of the base of the projectile--that is, at the front of the moving pressure--
grows dramatically. As with classical resonance, the deformation is theoretically

unbounded when the critical velocity is reached unless damping is present.
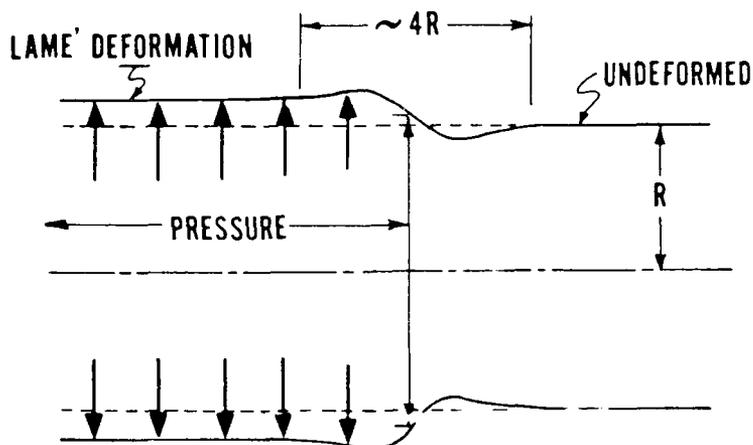
DEFORMATION OF BORE SURFACE
(STATIC)

Fig. 1

The simplest equation containing the essential physics of the situation is [2]

$$D \frac{\partial^4 w}{\partial x^4} + \frac{Eh}{R^2} w + m \frac{\partial^2 w}{\partial t^2} = Q(1-H(x-vt)) \tag{1}$$

where Q is a constant and represents the magnitude of the pressure which is assumed to be moving at constant velocity v. H is the heaviside step function:

$$H(x-vt) = 0 \quad x < vt$$
$$= 1 \quad x > vt$$

In this equation, w is the radial displacement of a point on the median surface of a cylindrical shell located at a distance x along, and R from, the central axis; h is the shell thickness and is assumed to be small compared to R; $m = \rho h$ where ρ is the mass density of the shell material; $D = Eh/12(1-\nu^2)$; E is Young's modulus of elasticity; ν is Poisson's ratio; and v is the velocity of the moving pressure, assumed to be finite and constant.

Conventionally, steady-state solutions to Eq. (1) are sought under the conditions that the displacement remain bounded at $x = \pm \infty$ and that the stresses and displacements be continuous at the location of the pressure front x = vt. Usually, a change of variable from x to ξ is made where ξ = x-vt. Then the moving pressure front (the projectile) is always at ξ = 0 and the partial differential equation (Eq. (1)) becomes an ordinary differential equation which is easily solved. In particular, these solutions have the form $w = Ae^{\pm ik\xi}$ and are steady when seen by an observer moving with the pressure front at ξ = 0. k is the wave number and, in general, is complex. Only when k is real does the assumed form of the solution represent a wave. To find what waves can exist naturally in the cylinder, one sets Q = 0, and substitutes the assumed solution into Eq. (1). It is seen that real waves are possible for those values of k which are the real roots of the equation

$$v(k) = k\sqrt{\frac{D}{m}\left(1+\left(\frac{\gamma}{k}\right)^4\right)}$$

(2)

where $\gamma^4 = \frac{Eh}{R^2D}$ and v is the phase velocity (real). A plot of these wave numbers

versus phase velocity is called a dispersion curve and is shown in Fig. 2 ($C_c = \sqrt{E/\rho}$). This plot shows that waves with low wave number (long waves) travel with phase velocities which decrease with wave number, while those with high wave number (short waves) have phase velocities which increase with wave number. This happens because of two competing restoring forces in Eq. (1). The tube can deform as a cylindrical membrane in which case the second term of Eq. (1) dominates the behavior, or the tube wall can undergo axisymmetric flexure in which case the first term dominates. The fact that these two restoring forces compete to produce a minimum in the dispersion curve of Fig. 2 is the important part of the critical velocity theory.
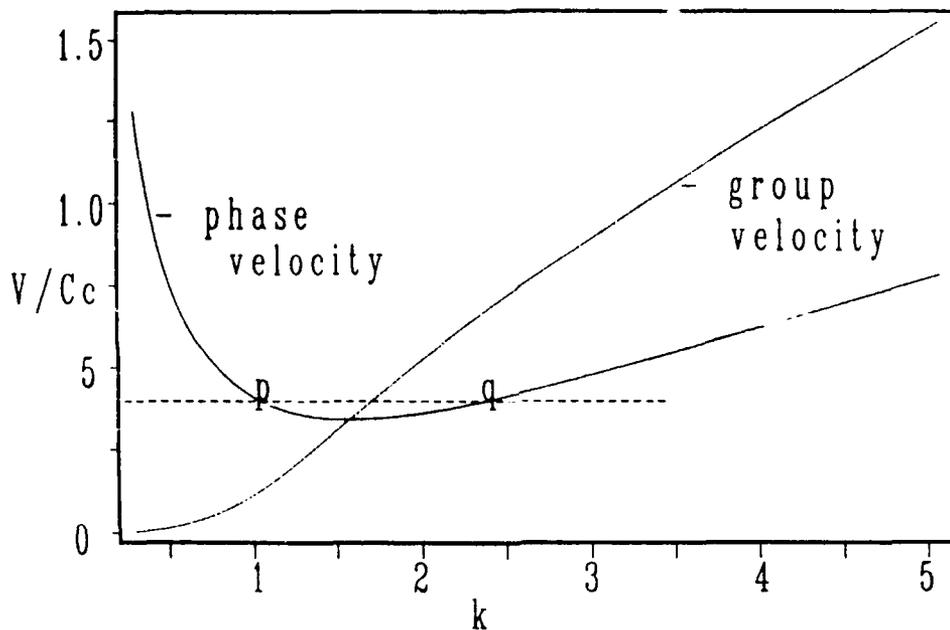

Fig. 2 Phase and group velocities--thin shell theory.

For the purpose of discussion, it can be considered axiomatic that if waves are generated by a moving axisymmetric pressure Q, the phase velocity of these waves will be the velocity of this moving pressure. That is, the load must be in phase with the wave(s) it creates. With this in mind, Fig. 2 shows that such waves are possible provided the load velocity equals or exceeds the minimum possible value. Let us assume for the moment that the load velocity (the projectile velocity) somewhat exceeds this minimum. According to Fig. 2, there are two waves with this phase velocity. Now, physically we know that the energy contained in these two waves must radiate away, not toward, the source of the disturbance, namely the moving pressure front. Further, it is known that energy travels not at the phase velocity, but at another velocity called the 'group velocity,' related to the phase velocity as follows:

$$V_g(k) = k \frac{dv(k)}{dk} + v(k) \tag{3}$$

where $v(k)$ is the phase velocity (dispersion curve) from Fig. 2. A plot of group velocity versus wave number is also shown in Fig. 2 and provides a criterion for deciding whether a given wave belongs in the region $\xi > 0$ or $\xi < 0$. For example, the wave corresponding to the point p has a group velocity which is smaller than its phase velocity. Since the wave energy must flow away, not toward, the pressure front at $\xi = 0$, this wave belongs in the region $\xi < 0$ only, i.e., it is a 'trailing wave.' Conversely, the wave corresponding to the point q is a 'head wave,' belonging to the region $\xi > 0$. Assigning the two waves to their appropriate regions results in the following solution for the midwall displacement $w(x,t)$ when the load velocity v is greater than the minimum phase velocity of Fig. 2

$$\frac{w^{(1)}}{C} = \frac{-b^2}{b^2 - a^2} \cos a\xi + 1 \quad ; \quad \xi \leqslant 0$$
$$\frac{w^{(2)}}{C} = \frac{-a^2}{b^2 - a^2} \cos b\xi \quad \quad ; \quad \xi \geqslant 0 \tag{4}$$

where

$$a,b = \sqrt{\frac{1 + \lambda}{2}} \mp \sqrt{\frac{\lambda - 1}{2}} \quad ; \quad \lambda = \frac{mv^2}{2} \sqrt{\frac{R^2}{EhD}}$$

and $C = QR^2/Eh$ approximates the Lamé displacement. Note that for $\lambda \gg 1$, the solution for $x \leqslant vt$ approaches $2C$, twice the Lamé displacement.

It can easily be seen from Eq. (3) that should dv/dk ever vanish, the group velocity and the phase velocity would be equal and energy could not radiate away from the pressure front, but would continually build the deformation in the neighborhood of the front as time progressed, i.e., resonance would result. Thus, the minimum phase velocity of Fig. 2 is indeed a 'critical velocity' and it is the near attainment of this velocity which caused the high strains in the 120-mm gun tube.

Finally, if the velocity of the moving pressure is less than the minimum possible for wave formation, the wave number k is complex and the solution to Eq. (1) has the form of a damped harmonic

$$\frac{w^{(1)}}{C} = \frac{e^{d\xi}}{2} (-\cos c\xi + \frac{d^2 - c^2}{2cd} \sin c\xi) + 1 \quad ; \quad \xi \leqslant 0$$

$$\frac{w^{(2)}}{C} = \frac{e^{-d\xi}}{2} (\cos c\xi + \frac{d^2 - c^2}{2cd} \sin c\xi) \quad \quad ; \quad \xi \leqslant 0 \tag{5}$$

where

$$c = \sqrt{\frac{\lambda + 1}{2}} \quad \text{and} \quad d = \sqrt{\frac{1 - \lambda}{2}}$$

A REFINED MODEL FOR THE 120-MM GUN TUBE

From the standpoint of gun tube design, it is important to be able to predict critical velocities as accurately as possible and to be able to predict the steady-state deformation at any velocity of the pressure front. Thus, it is necessary to use a model which is not restricted to cylinders with thin walls. Equations of motion for thick-walled cylinders have been derived by Mirsky and Herrmann [5] and are considerably more complicated than Eq. (1). They are used to obtain the results which follow in much the same way as discussed previously. These equations and the details leading to their solution have been reported by the author [6].

Although transient effects, boundary reflections, non-uniformity of wall thickness, and variable pressure (projectile) velocity are ignored, steady-state calculations for thick-walled cylinders nevertheless produce results in remarkable agreement with measured values when the projectile velocity is close to critical. (The assumption of constant projectile velocity is justified in the forward regions of many gun tubes where the projectile velocity/travel curve is relatively flat.) Figures 3 and 4 compare predicted and measured values of circumferential strain. Figure 3 shows the tube deformation in the neighborhood of the projectile and Fig. 4 shows the maximum strain as a function of projectile velocity. The strains have been normalized with respect to the static values predicted by the Lamé formula. The disagreement between the measured and predicted strains at low velocities is thought to be due to the non-uniform outside dimensions of the real tube as opposed to the uniform length assumed in the model.
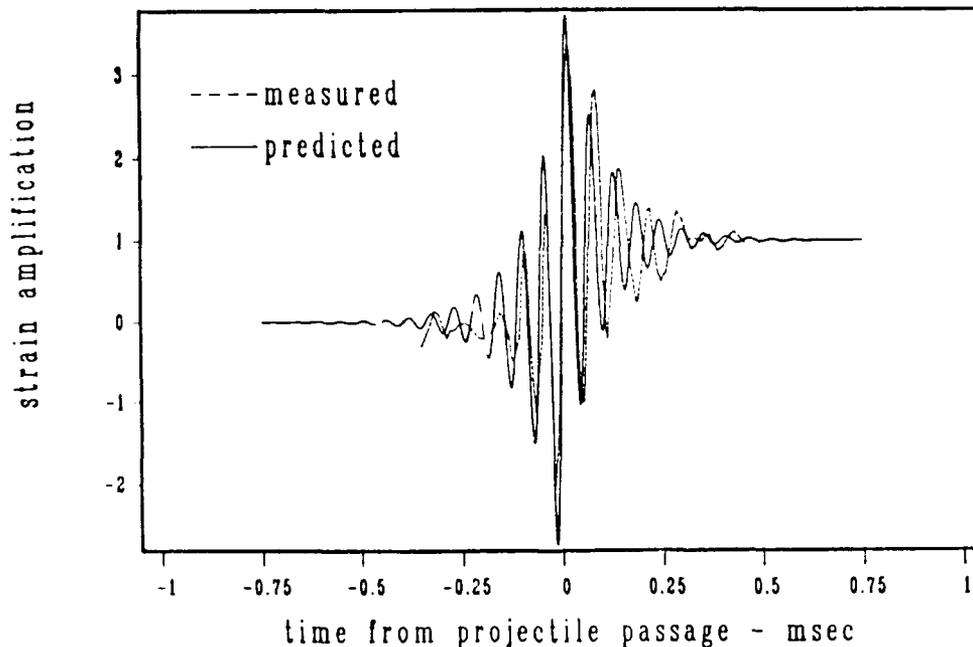

Fig. 3 Comparison of measured and predicted circumferential strains located at the pressure front.
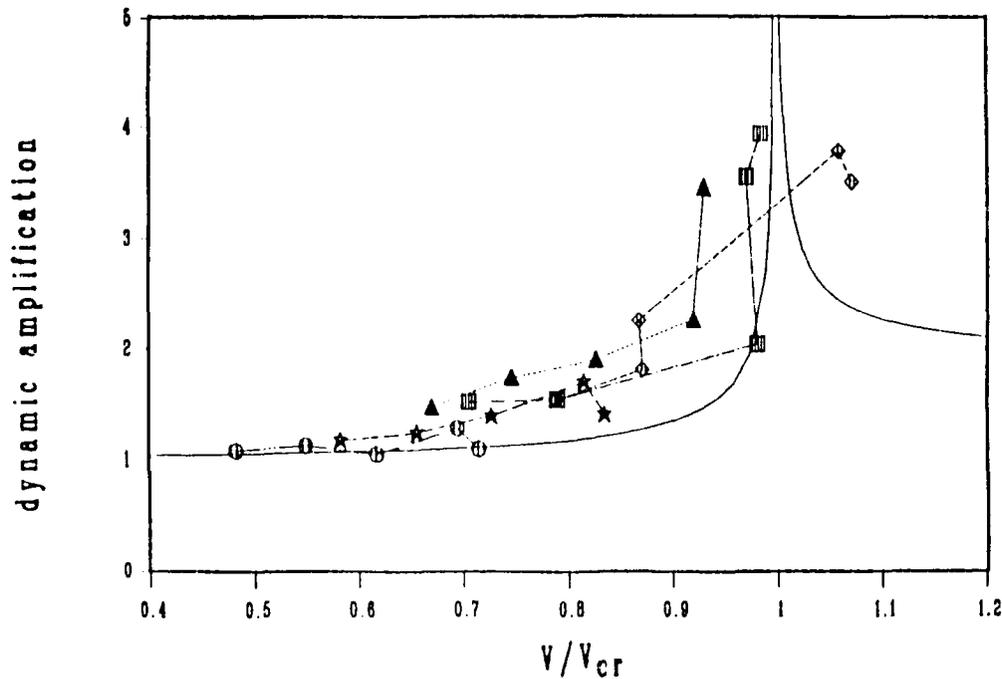
Fig. 4   Comparison of measured and predicted strains located at
the pressure front.

AXISYMMETRIC AND NON-AXIALLY SYMMETRIC WAVE COUPLING

Mirsky and Herrmann [7] have also derived a set of five equations governing
both axisymmetric and non-axially symmetric motions of a uniform hollow cylinder.
Gazis [8] has gone a step further, accomplishing the same using the more accurate
three-dimensional equations of elasticity. These investigators have computed the
dispersion curves for several of these modes. Viewed in the context of critical
velocity theory, it is interesting that the dispersion curves of the first non-
axially symmetric mode and the previously considered axisymmetric mode have minimum
values in close proximity to one another. This is shown in Figure 5. Both curves
were constructed using the equations of Mirsky and Herrmann. The ordinate values
have been normalized with respect to the velocity of shear waves in the material, C_s
= $\sqrt{G/\rho}$, where G is the shear modulus of the material. The abscissa is the non-
dimensional wave number h/L, where L is the wave length. The non-axially symmetric
mode referred to in the figure corresponds to a beamlike deformation of the axis of
the cylinder. Since the moving pressure is perfectly axisymmetric, the only means
for exciting real waves of this type, in particular the resonance indicated by the
minimum, is by some sort of coupling whereby energy can be exchanged between the
axisymmetric and non-axially symmetric modes.
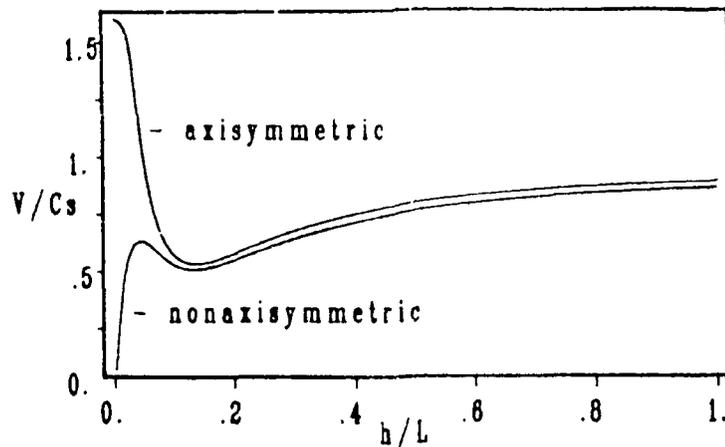
Fig. 5 Uncoupled dispersion curves ($\epsilon = 0$)--Mirsky and Herrmann, thick-wall shell theory.

One source of modal coupling which is of importance in gun tube design is the non-uniformity of the thickness of the tube wall. Intuitively, it is clear that when a tube having an eccentric wall thickness is dynamically pressurized, the bore centerline tends to move as well as the tube wall. In effect, the eccentricity of the wall thickness creates a non-axially symmetric wall stiffness and inertia. A good indication of what may be expected has been obtained by neglecting the asymmetric stiffness and including only the eccentric inertia coupling. This is the work reported herein.

Basically, it is assumed that we are dealing with a cylinder which has a sinusoidal distribution of mass around its circumference and that this distribution is uniform along the direction of the bore axis. Thus

$$\rho = \rho_0(1 + \epsilon \cos \theta) \tag{6}$$

represents the mass distribution of the cylinder with ϵ serving as the eccentricity parameter. ρ_0 is the mass density of the material. The coupling effect sought does not require the use of sophisticated thick-wall cylinder equations such as those used by Mirsky and Herrmann or those employed by Gazis, and considering the idealism reflected in neglecting asymmetric stiffness effects and the assumed mass distribution of Eq. (6) above, the use of such equations is not required. However, the essential character of the dispersion curves--especially near the dual minimums and throughout the long wave regions--must be contained in whatever equations are chosen. It is surprising that the Donnell-Mushtari equations [9] do not suffice for this purpose, failing to provide a dispersion curve for the beamlike vibration which passes through the origin. Consequently, the equations of Flugge were chosen. Though more complicated than those of Donnell-Mushtari, these equations provide the necessary features in the dispersion curves and are considerably simpler than those of Mirsky and Herrmann.

The Flugge equations of motion are as follows [9]:

$$\left\{ \begin{bmatrix} \begin{bmatrix} \dfrac{\partial^2}{\partial s^2} + \dfrac{(1-\nu)}{2}\dfrac{\partial^2}{\partial\theta^2} \\[2mm] -\rho\dfrac{(1-\nu^2)R^2}{E}\dfrac{\partial^2}{\partial t^2} \end{bmatrix} & \dfrac{(1+\nu)}{2}\dfrac{\partial^2}{\partial s\partial\theta} & \nu\dfrac{\partial}{\partial s} \\[10mm] \dfrac{(1+\nu)}{2}\dfrac{\partial^2}{\partial s\partial\theta} & \begin{bmatrix} \dfrac{(1-\nu)}{2}\dfrac{\partial^2}{\partial s^2} + \dfrac{\partial^2}{\partial\theta^2} \\[2mm] -\rho\dfrac{(1-\nu^2)R^2}{E}\dfrac{\partial^2}{\partial t^2} \end{bmatrix} & \dfrac{\partial}{\partial\theta} \\[10mm] \nu\dfrac{\partial}{\partial s} & \dfrac{\partial}{\partial\theta} & 1+k\nabla^4+\rho\dfrac{(1-\nu^2)R^2}{E}\dfrac{\partial^2}{\partial t^2} \end{bmatrix} \right.$$

$$\left. + k\begin{bmatrix} \dfrac{(1-\nu)}{2}\dfrac{\partial^2}{\partial\theta^2} & 0 & -\dfrac{\partial^3}{\partial s^3}+\dfrac{(1-\nu)}{2}\dfrac{\partial^3}{\partial s\partial\theta^2} \\[6mm] 0 & \dfrac{3(1-\nu)}{2}\dfrac{\partial^2}{\partial s^2} & -\dfrac{(3-\nu)}{2}\dfrac{\partial^3}{\partial s^2\partial\theta} \\[6mm] -\dfrac{\partial^3}{\partial s^3}+\dfrac{(1-\nu)}{2}\dfrac{\partial^3}{\partial s\partial\theta^2} & -\dfrac{(3-\nu)}{2}\dfrac{\partial^3}{\partial s^2\partial\theta} & 1+2\dfrac{\partial^2}{\partial\theta^2} \end{bmatrix} \right\}\begin{bmatrix} u \\ v \\ w \end{bmatrix} = \begin{bmatrix} 0 \\ 0 \\ Q \end{bmatrix}$$

$$\tag{7}$$

where $k = h^2/12R^2$, $s = x/R$, and θ is measured tangentially. u, v, and w are the displacement components in the x, θ, and R directions, respectively. $Q = pR^2(1-\nu^2)/Eh$ is the applied load due to the pressure p.

Solutions to Eq. (7) are assumed in the form of a linear superposition of axisymmetric motion (u_o,w_o) and motion from the first non-axially symmetric mode (u_1,v_1,w_1). (v_o can be omitted because it produces an equation for torsional motion which is uncoupled from the non-axially symmetric variables.) Thus,

$$u(s,\theta,t) = u_o(x,t) + u_1(x,t)\cos\theta$$
$$v(s,\theta,t) = v_1(x,t)\sin\theta$$
$$w(s,\theta,t) = w_o(x,t) + w_1(x,t)\cos\theta \tag{8}$$

Equations (8) can be considered as approximation functions for use with the Galerkin method [10]. The variations $\delta u = \delta u_o + \delta u_1\cos\theta$, $\delta v = \delta v_1\sin\theta$, and $\delta w = \delta w_o + \delta w_1\cos\theta$ multiply the first, second, and third of Eqs. (8), respectively.

The resulting expressions and Eq. (6) for $\rho(\theta)$ are substituted in Eq. (7) followed by an integration between the limits $\theta = 0$ and 2π. This results in the five equations:

$$- k \frac{\partial^3 w_0}{\partial s^3} + \nu \frac{\partial w_0}{\partial s} - \frac{\epsilon}{2} \frac{\partial^2 u_1}{\partial t^2} - \frac{\partial^2 u_0}{\partial t^2} + \frac{\partial^2 u_0}{\partial s^2} = 0$$

$$- k \frac{\partial^3 w_1}{\partial s^3} + \nu \frac{\partial w_1}{\partial s} - \frac{k}{2} (1 + \nu) \frac{\partial w_1}{\partial s} + \frac{(\nu+1)}{2} \frac{\partial v_1}{\partial s} - \frac{\partial^2 u_1}{\partial t^2} + \frac{\partial^2 u_1}{\partial s^2}$$

$$- k \frac{(1-\nu)}{2} u_1 - \frac{(1-\nu)}{2} u_1 - \epsilon \frac{\partial^2 u_0}{\partial t^2} = 0$$

$$\frac{k}{2} (3-\nu) \frac{\partial^2 w_1}{\partial s^2} - w_1 - \frac{\partial^2 v_1}{\partial t^2} + \frac{3k(1-\nu)}{2} \frac{\partial^2 v_1}{\partial s^2} + \frac{(1-\nu)}{2} \frac{\partial^2 v_1}{\partial s^2} - v_1 - \frac{(\nu+1)}{2} \frac{\partial u_1}{\partial s} = 0$$

$$\frac{\epsilon}{2} \frac{\partial^2 w_1}{\partial t^2} + \frac{\partial^2 w_0}{\partial t^2} + k \frac{\partial^4 w_0}{\partial s^4} + k w_0 + w_0 - k \frac{\partial^3 u_0}{\partial s^3} + \nu \frac{\partial u_0}{\partial s} = Q$$

$$\frac{\partial^2 w_0}{\partial t^2} + k \frac{\partial^4 w_1}{\partial s^4} - 2k \frac{\partial^2 w_1}{\partial s^2} + w_1 + \epsilon \frac{\partial^2 w_0}{\partial t^2} - k \frac{(3-\nu)}{2} \frac{\partial^2 v_1}{\partial s^2} + v_1$$

$$- k \frac{\partial^3 u_1}{\partial s^3} + \nu \frac{\partial u_1}{\partial s} - \frac{k(1-\nu)}{2} \frac{\partial u_1}{\partial s} = 0 \tag{9}$$

Steady-state solutions to Eqs. (9) can be obtained in exactly the same way as the steady-state solution to Eq. (1). Under the substitution $\xi = \smallfrown - v\tau$ (where $\tau = [E/\rho_0 R^2(1-\nu^2)]^{\frac{1}{2}}t$), Eqs. (9) become five ordinary differential equations with ξ as the independent variable.

$$-kw_0''' + \nu w_0' - \frac{\epsilon v^2}{2} u_1'' + (1-v^2)u_0'' = 0$$

$$-2kw_1''' + [\nu(k+2) - k]w_1' (1+\nu)v_1' + 2(1-v^2)u_1'' - 2\epsilon v^2 u_0''$$

$$+ [(k+1)(\nu-1)]u_1 = 0$$

$$k(3-\nu)w_1'' - 2w_1 - [2v^2 + (3k+1)(\nu-1)]v_1'' - 2v_1 - (1+\nu)u_1' = 0$$

$$\frac{\epsilon v^2}{2} w_1'' + kw_0'''' + v^2 w_0'' + (k+1)w_0 - ku_0''' + \nu u_0' = Q$$

$$kw_1'''' + (v^2-2k)w_1'' + w_1 + \epsilon v^2 w_0'' + \frac{k}{2}(\nu-3)v_1'' + v_1 - ku_1'''$$

$$+ [\frac{k}{2}(\nu-1) + \nu]u_1' = 0 \tag{10}$$

The complementary solutions of Eqs. (10) are obtained by substituting solutions of the form $A_j e^{-i\alpha\xi}$ for each of the variables u_0, u_1, v_1, w_0, and w_1, where A_j is a different arbitrary constant in each substitution and α is the wave number. The result is a set of five linear equations which only have non-trivial solutions if the determinant of the coefficients of the A_j vanishes, i.e.,

$\alpha^2(v^2-1)$	$\dfrac{\alpha^2\epsilon v^2}{2}$	0	$-i\alpha(v+\alpha^2 k)$	0
$\alpha^2\epsilon v^2$	$\alpha^2(v^2-1)+\dfrac{v}{2}(k+1)-\dfrac{1}{2}(k+1)$	$-\dfrac{i\alpha}{2}(1+v)$	0	$-i\alpha(\dfrac{kv}{2}+v+\alpha^2 k -\dfrac{k}{2})$
0	$\dfrac{i\alpha}{2}(1+v)$	$\dfrac{\alpha^2}{2}[2v^2+v(3k+1)-3k-1]-1$	0	$\dfrac{\alpha^2 k}{2}(v-3)-1$
$-i\alpha(v+\alpha^2 k)$	0	0	$-\alpha^2(v^2-\alpha^2 k)+k+1$	$-\dfrac{\alpha^2\epsilon v^2}{2}$
0	$-i\alpha(\dfrac{kv}{2}+v+\alpha^2 k -\dfrac{k}{2})$	$\dfrac{\alpha^2 k}{2}(3-v)+1$	$-\alpha^2\epsilon v^2$	$-\alpha^2(v^2-\alpha^2 k-2k)+1$

$$(11)$$

Setting this determinant to zero results in the dispersion relation. The first two branches are shown in Fig. 6 for the value $\epsilon = 0.1$. The similarity to those of Mirsky and Herrmann (Fig. 5) is evident.
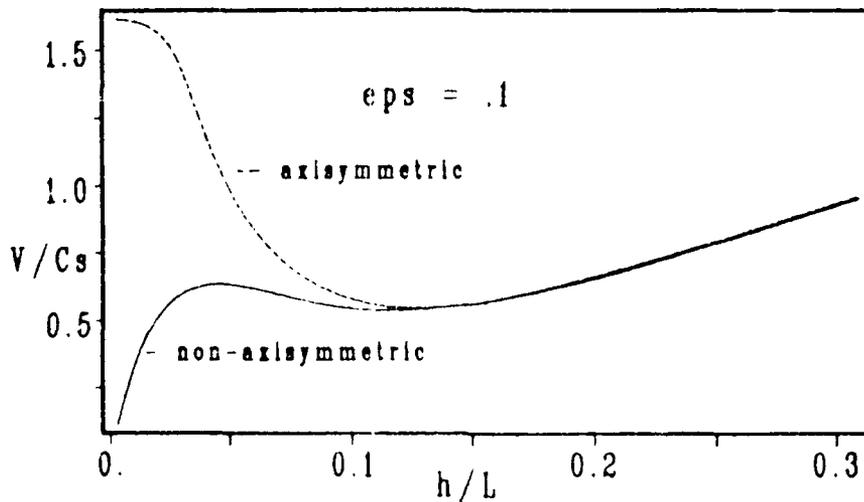

Fig. 6

The dispersion curves of Fig. 6 represent the natural (unforced) waves of the cylinder which are the complimentary solutions to Eq. (10). As was the case in dealing with Eq. (1), the stresses and displacements are required to be continuous

at the location of the pressure front. In terms of the variables defined in Eqs. (8), the following quantities must be continuous at $\xi = 0$ [11]:

$$\frac{h^2}{4R^2}\,(w_1'' + v_1'') + v_1' - u_1 \quad ,$$

$$\nu(w_1+v_1) + u_1' - w_1'' \quad ,$$

$$w_0'' - u_0' \quad ,$$

$$(\frac{\nu-1}{2})u_1 + (\nu-2)w_1' + \frac{(\nu-3)}{2}\,v_1' + w_1''' - u_1'' \quad ,$$

$$w_0''' - u_0'' \quad ,$$

and $\quad v_1, w_0, w_1', w_0', w_1$

The continuity relations plus the boundedness criteria at infinity and/or the group velocity argument are sufficient to uniquely determine the displacements once the particular solutions have been determined. The particular solutions corresponding to the load terms on the right-hand side of Eqs. (9) may be found by eliminating all but one of the dependent variables through the use of Cramer's rule and the commutativity of the differential operators [12]. This procedure is much simpler than inverting Fourier transforms--a common solution technique used in connection with these problems (cf. [3]).

From the previous discussion in connection with Eq. (1), several load velocities are of interest. For example, from the dispersion curves of Fig. 6, it is clear that a real wave will be excited regardless of how small the projectile velocity might be. As a typical value, $v = 0.382\,C_s$ has been chosen and the corresponding mid-wall radial displacement at the top of the cylinder ($\theta = 0$) is shown in Fig. 7 using the value $\epsilon = 0.1$ (10 percent mass eccentricity). The ordinate in Figs. 7 through 10 is the ratio of the dynamic displacement in the radial direction (w) to the static axisymmetric radial displacement as approximated by the particular solution for w_0.
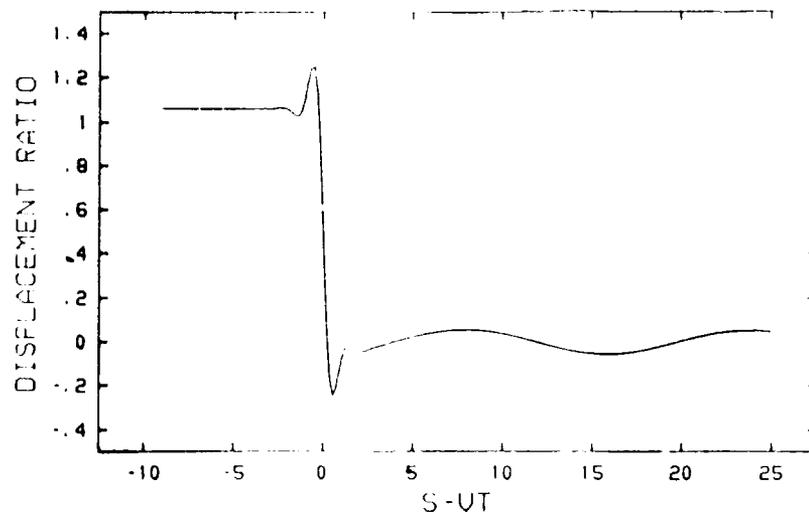

Fig. 7 Radial displacement from coupled Flugge equations, $v/C_s = 0.382$, $\epsilon = 0.1$.

This radial displacement is essentially quasi-static except for the existence
of a wave which, from the group velocity argument, exists in front of the pressure
only. The presence of any 'head wave' will be felt at the gun muzzle prior to the
arrival of the projectile and therefore constitutes a possible cause of round inac-
curacy at the target.

Another load velocity of interest is $v = 0.515 \, C_S$ which is just below the
lowest critical value. Again, $\epsilon = 0.1$ and the radial displacement at the top of the
cylinder is shown in Fig. 8a. The head wave of Fig. 7 is evident. The axisymmetric
portion of this displacement is shown in Fig. 8b, so that the difference between the
two figures is the contribution of the beamlike motion at this velocity and is
substantial.
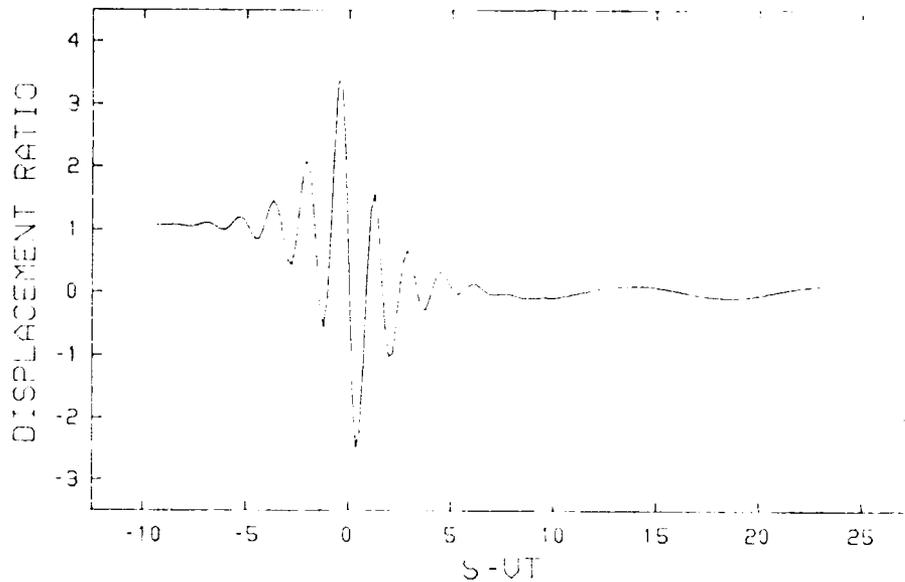
Fig. 8a Radial displacement, $\theta = 0$, $v/C_S = 0.515$, $\epsilon = 0.1$.
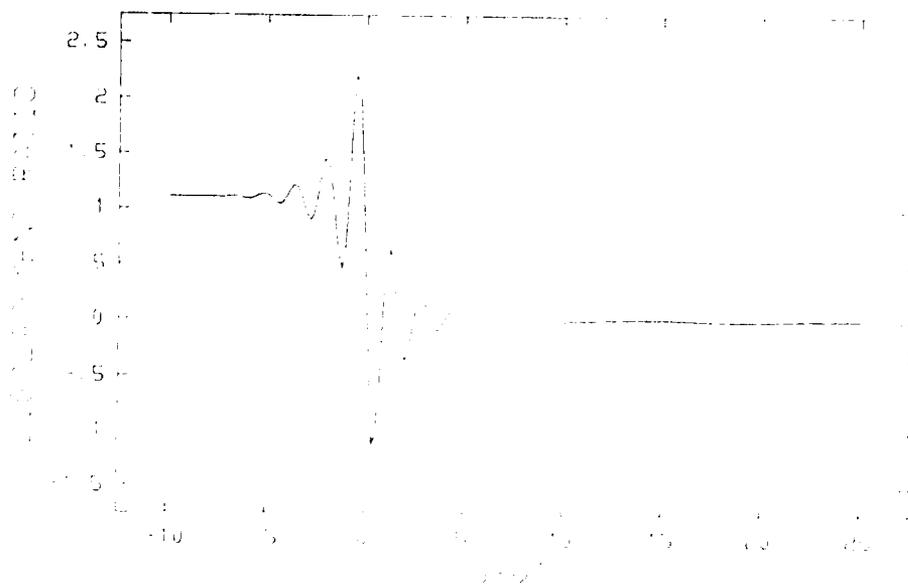

Fig. 8b Non-axially symmetric (beamlike) component of Fig. 8a.

The presence of a maximum value in the long wavelength region of the lower dispersion curve is also cause for interest. It is known, however, that the dispersion curve for the next non-axially symmetric mode (in which the tube distorts more or less into an elliptical shape) passes through this region and has a minimum value there. This mode is not included in the present analysis and therefore the model is considered to be inaccurate in this region.

Probably the most interesting load velocity is that which falls between the minimums (v_{cr1}, v_{cr2}) of the two curves of Fig. 6. For a load velocity exactly halfway between these minimums, i.e.,

$$v = \frac{v_{cr1} + v_{cr2}}{2}$$

Fig. 9 shows that the axisymmetric and beamlike motions are nearly equal in magnitude for values of ϵ as small as 0.01. This is apparently due to the fact that the minimums (critical velocities) of the two branches of Fig. 6 approach each other as ϵ diminishes. Consequently, a load velocity halfway between them is closer to both critical values when ϵ is smaller. This is shown in Fig. 10--a blowup of Fig. 6 in the vicinity of the minimums in the neighborhood of the critical velocities for two values of ϵ. From one point of view, the non-axially symmetric wave acts as a vibration absorber for the axisymmetric motion. This is not likely to reduce the maximum stress in the cylinder however, since the wall will then be subjected to biaxial stresses of comparable magnitudes.
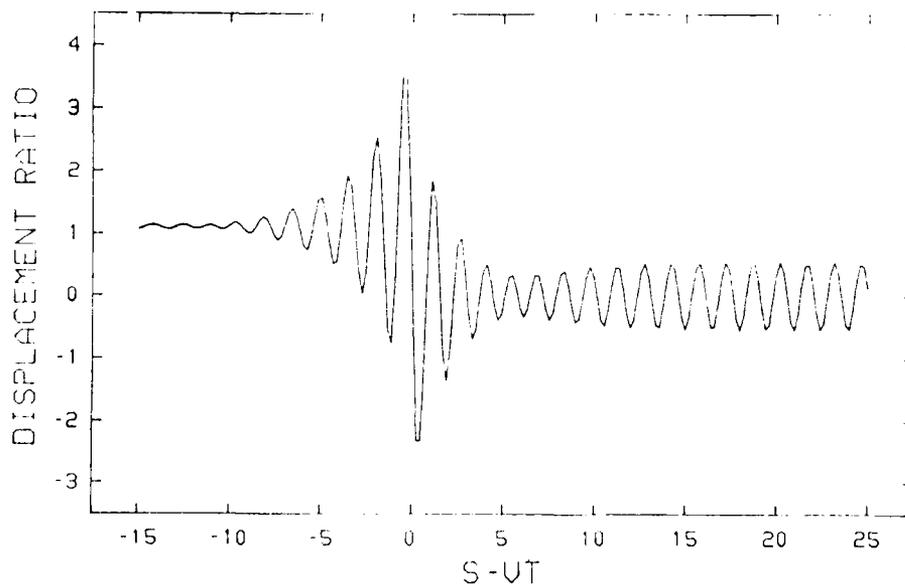

Fig. 9a   Axisymmetric component of radial displacement, $\theta = 0$,

$$v = \frac{v_{cr1} + v_{cr2}}{2} = 0.541, \; \epsilon = 0.01.$$
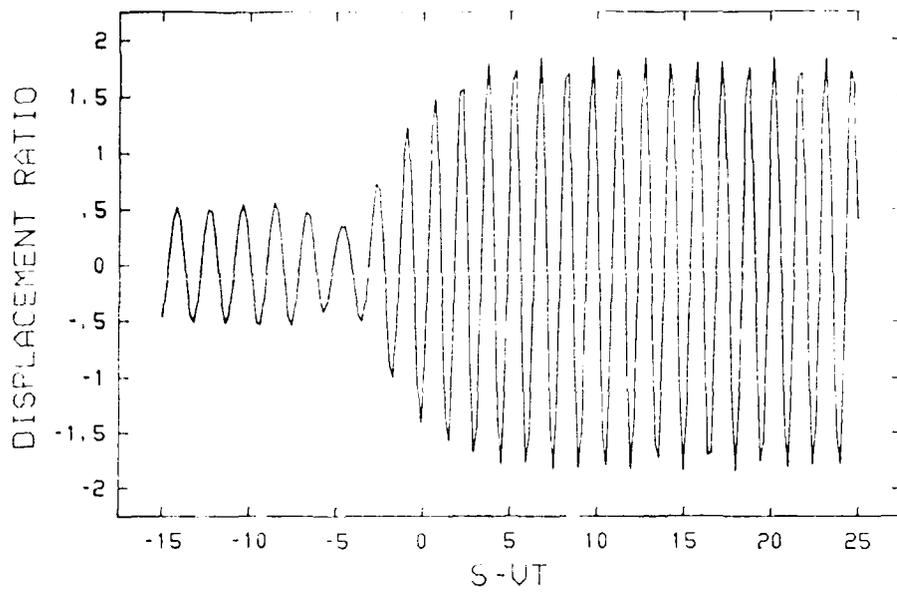
Fig. 9b   Non-axially symmetric (beamlike) component of radial displacement, θ = 0.

$$V = \frac{V_{cr1} + V_{cr2}}{2} = 0.541, \quad \varepsilon = 0.01.$$
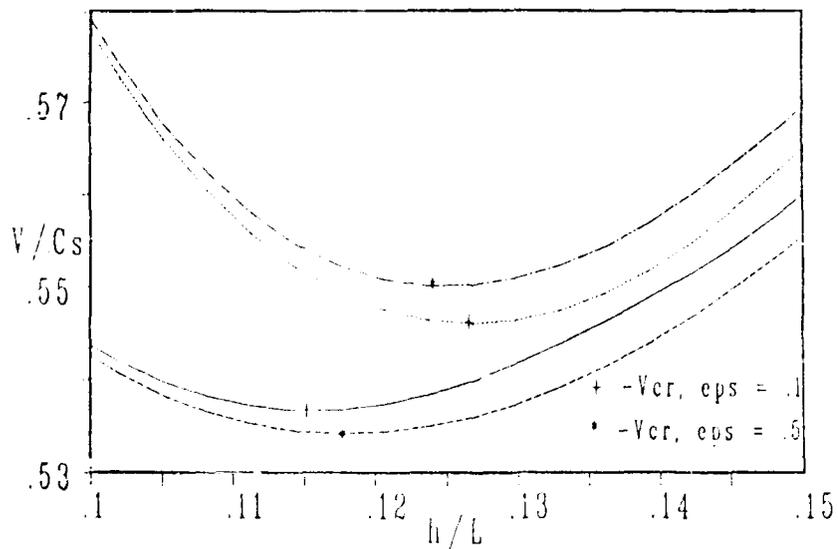
Fig. 10   Dispersion curves near their minimum valves, $\epsilon = 0.1$ and $c = 0.5$.

REFERENCES

1. S. P. Timoshenko and J. N. Goodier, Theory of Elasticity, Third Edition, pp. 68-71, McGraw-Hill, 1970.

2. H. Reismann, "Response of a Prestressed Cylindrical Shell to Moving Pressure Load, Developments in Mechanics," Solid Mechanics - Proceedings of the Eighth Mechanics Conference, Part II, Vol. 2, pp. 349-363, Pergamon Press, 1965.

3. S. Tang, "Dynamic Response of a Tube Under Moving Pressure," Journal of the Engineering Mechanics Division, Proceedings of the ASCE, Part 1, Vol. 91, pp. 97-122, Oct. 1965.

4. J. P. Jones and P. G. Bhuta, "Response of Cylindrical Shells to Moving Loads," Journal of Applied Mechanics, Vol. 31, pp. 105-111, Mar. 1964.

5. I. Mirsky and G. Herrmann, "Axially Symmetric Motions of Thick Cylindrical Shells," Journal of Applied Mechanics, Vol. 25, pp. 97-102, Mar. 1958.

6. T. E. Simkins, "Resonance of Flexural Waves in Gun Tubes," Technical Report ARCCB-TR-87008, Benet Weapons Laboratory, Watervliet, NY, July 1987.

7. I. Mirsky and G. Herrmann, "Nonaxially Symmetric Motions of Cylindrical Shells," Journal of the Acoustical Society of America, Vol. 29, No. 10, pp. 1116-1123, Oct. 1957.

8. D. C. Gazis, "Three-Dimensional Investigation of the Propagation of Waves in Hollow Cylinders: I. Analytical Foundation, II. Numerical Results," Journal of the Acoustical Society of America, Vol. 31, No. 5, pp. 569-578, May 1959.

9. A. W. Leissa, "Vibration of Shells," NASA SP-288, Washington, D.C., pp. 32-34.

10. L. V. Kantorovich and V. I. Krylov, Approximate Methods of Higher Analysis, p. 258, Interscience Pubishers, New York, 1964.

11. A. W. Leissa, "Vibration of Shells," NASA SP-288, Washington, D.C., p. 29, 1973.

12. F. B. Hildebrand, Advanced Calculus for Engineers, Ninth Edition, pp. 21-22, Prentice-Hall, 1960.

THE BLAST FIELD PRODUCED BY A CANNON HAVING A PERFORATED MUZZLE BRAKE

G. C. Carofano
U.S. Army Armament Research, Development, and Engineering Center
Close Combat Armaments Center
Benet Laboratories
Watervliet, NY 12189-4050

In a study of perforated muzzle brakes, Nagamatsu, Choi, Duffy, and Carofano calculated the three-dimensional steady flow through one vent hole and used the results to predict overall brake performance. In the present study, the analysis is extended to the calculation of the blast field. The results compare favorably with previously unpublished shadowgraphs obtained by Dillon in his experimental program.

INTRODUCTION

A perforated muzzle brake consists simply of a set of vents drilled through the wall of a cannon near the muzzle (see Fig. 1). Compared with conventional baffle brakes, they are lighter and simpler to manufacture and, as shown in a series of reports by Dillon and Nagamatsu [1-5], they can be designed to provide significant levels of recoil reduction. Also, because the vented area can be located symmetrically around the tube, a more favorable flow environment is provided for finned projectiles. Asymmetrical venting can lead to bending and even breakage of the fins.
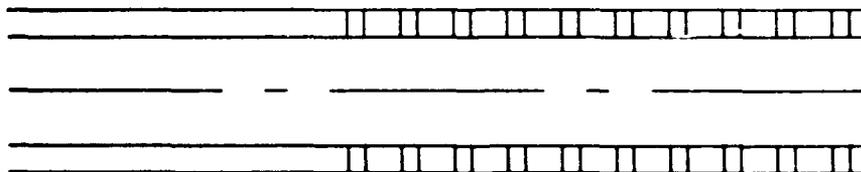

Fig. 1 Schematic drawing of a perforated muzzle brake.

Nagamatsu, Duffy, Choi, and Carofano [6] calculated the steady three-dimensional flow through a single vent in the wall of a shock tube. The predicted pressure distribution on the vent wall compared favorably with the experimental measurements of Nagamatsu, Duffy, and Choi [7]. It was also shown that these results could be combined with a one-dimensional model of the transient flow in a cannon to predict the impulse reduction produced by a perforated muzzle brake. The predictions agreed well with the experimental measurements of Dillon [1] for a 20-mm cannon. A more comprehensive comparison of the theory with these experiments, including a discussion of brake efficiency and scaling, was made by Carofano [8].

The transient development of the three-dimensional flow through a conventional baffle brake is discussed by Wang, Widhopf, and Chen [9].

In the present study, the analysis is extended to the calculation of the blast field. The complex transient three-dimensional problem is reduced to a one-dimensional flow inside the tube coupled to an axisymmetric model outside. The three-dimensional character of the flow through the tube wall is retained, however, by treating it as quasi-steady. The results are compared with previously unpublished shadowgraphs obtained by Dillon in his experimental program.

THE VENT FLOW FIELD

When the propellant gas expands through the brake, an asymmetric pressure distribution develops in each hole with the highest pressures acting on the downstream surface. The vector and pressure contour plots of Figs. 2 and 3 show typical flow patterns in the symmetry plane of one hole and the portion of the tube associated with it. The flow variables in the tube are uniform across the entrance plane. The solid lines in the vector plot indicate where the local Mach number is unity.

In Fig. 2, the flow enters at Mach one and accelerates to supersonic velocities as a portion of the gas expands and turns into the hole. The shock at the downstream lip of the hole turns the expanded flow parallel to the solid surfaces and reduces the velocities to subsonic levels. The pressure on the lip is nearly twice the static pressure of the incoming stream. The flow accelerates away from this region and leaves the tube and hole at supersonic velocities. There is a large subsonic region in the upstream portion of the hole. A more complete description of the flow and a comparison with shock tube data are given in [6].

To calculate the blast field, the flow through each vent is required at each instant of time during tube blowdown. Because the flow is three-dimensional, it is not practical to obtain the complete solution with a transient calculation. Fortunately, the flow contains many features which permit a vigorous simplification of the problem.

First, because of the large volume of the gun tube, the blowdown process takes on the order of tens of milliseconds, while the three-dimensional calculations indicate that the flow in a hole is established in a fraction of a millisecond. Therefore, the latter can be treated as quasi-steady and only the flow inside and outside of the tube must be considered as time-dependent.

Secondly, in the applications of interest, the flow is either sonic or supersonic as it enters the brake and, due to the venting, expands to higher Mach numbers as it travels downstream. Also, because of the high tube pressures, the gas exits each hole at near sonic or supersonic velocities over most of the exit plane area (see Figs. 2 and 3). Experience has shown that the flow is rather insensitive to the outflow boundary condition over the remaining subsonic portion. Thus, the flow at a particular hole location is not influenced by events occurring farther downstream or outside of the tube. It depends solely on the conditions in the tube upstream of the hole.
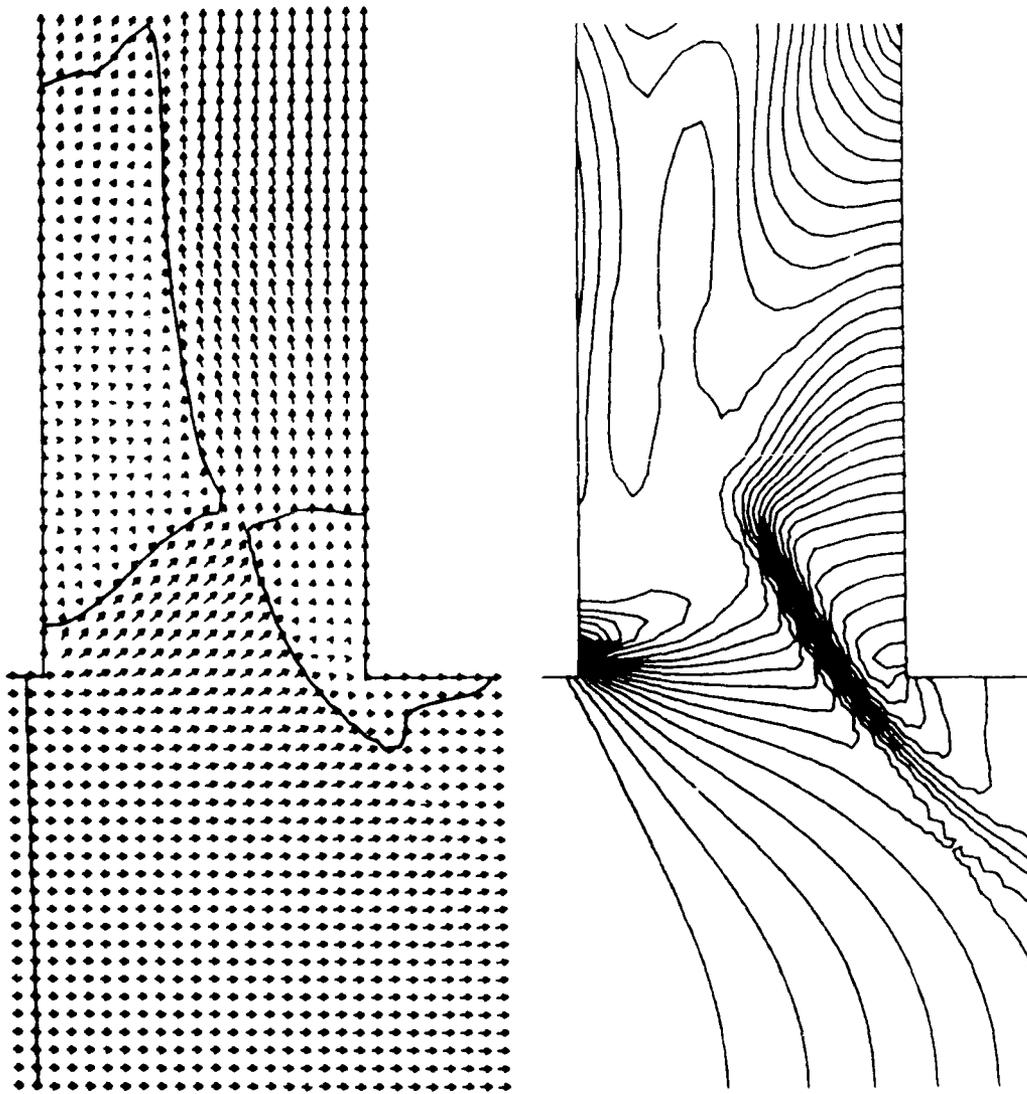
Fig. 2 Velocity vector and pressure contour plots for a vent flow with a
Mach number of unity at the entrance plane.
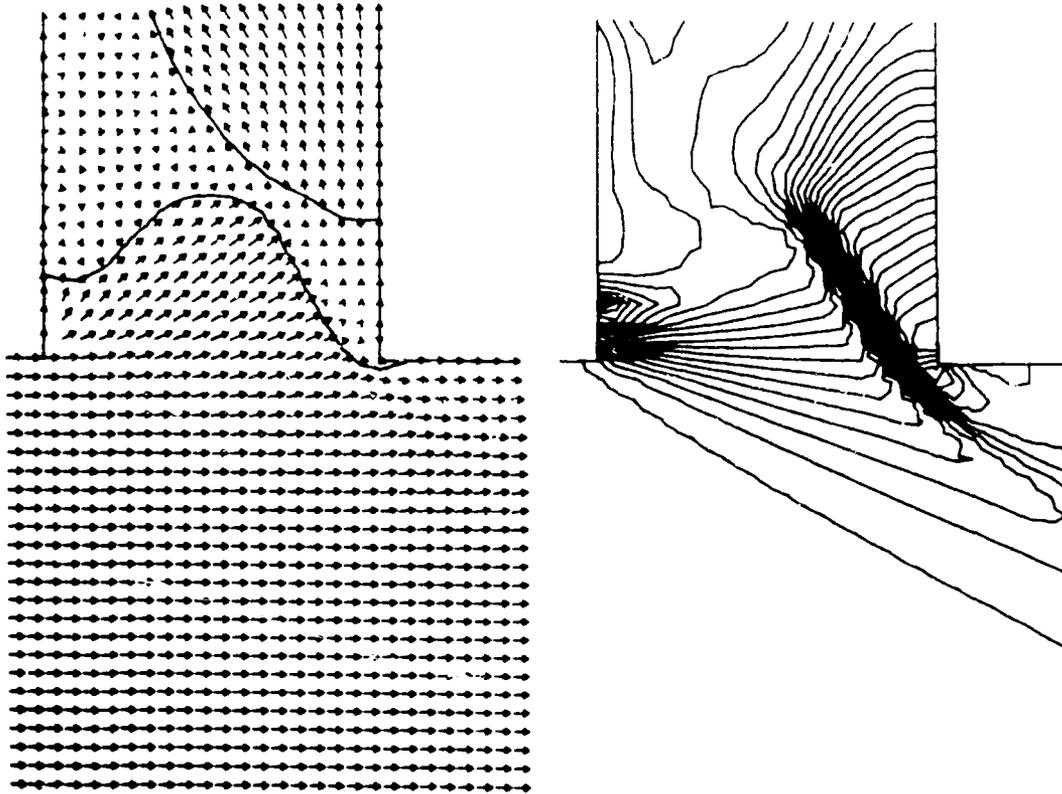
Fig. 3   Velocity vector and pressure contour plots for a vent flow with a
Mach number of two at the entrance plane.

The Euler equations may be written in conservative form as

$$\frac{\partial Q}{\partial t} + \frac{\partial F}{\partial x} + \frac{\partial G}{\partial y} + \frac{\partial H}{\partial z} = 0 \tag{1}$$

where

$$Q = \begin{bmatrix} \rho \\ m \\ n \\ \ell \\ E \end{bmatrix}, \quad F = \begin{bmatrix} m \\ m^2/\rho+P \\ mn/\rho \\ m\ell/\rho \\ (E+P)m/\rho \end{bmatrix}, \quad G = \begin{bmatrix} n \\ nm/\rho \\ n^2/\rho+P \\ n\ell/\rho \\ (E+P)n/\rho \end{bmatrix}, \quad H = \begin{bmatrix} \ell \\ \ell m/\rho \\ \ell n/\rho \\ \ell^2/\rho+P \\ (E+P)\ell/\rho \end{bmatrix}$$

ρ is the density; $m = \rho u$, $n = \rho v$, and $\ell = \rho w$ are the momentum components in the x, y, and z directions, respectively; u, v, and w are the corresponding velocity components. P is the pressure and E is the total energy per unit volume defined as

$$E = \rho e + (m^2+n^2+\ell^2)/2\rho \tag{2}$$

where e is the specific internal energy. Both the propellant gas and the air are taken to be perfect gases, so the pressure is related to the state variables ρ and e by the expression

$$P = (\gamma-1)\rho e \tag{3}$$

where γ is the specific heat ratio.

Consider the result of nondimensionalizing the Euler equations in the following way:

$$\rho' = \rho/\rho_2 \quad , \quad m' = m/\sqrt{P_2\rho_2} \quad , \quad n' = n/\sqrt{P_2\rho_2} \quad , \quad \ell' = \ell/\sqrt{P_2\rho_2}$$

$$P' = P/P_2 \quad , \quad E' = E/P_2 \quad , \quad e' = e\rho_2/P_2 \quad , \quad c' = c\sqrt{\rho_2/P_2}$$

$$x' = x/D \quad , \quad y' = y/D \quad , \quad z' = z/D \quad , \quad t' = t\sqrt{P_2/\rho_2}/D$$

where ρ_2 and P_2 are the density and pressure of the uniform flow at the upstream plane of the tube and D is the vent diameter. The form of the Euler and state equations remains unchanged, while the inflow boundary conditions become

$$\rho' = 1 \tag{4}$$

$$m' = \sqrt{\gamma}M_2 \tag{5}$$

$$n' = \ell' = 0 \tag{6}$$

$$E' = 1/(\gamma-1) + \gamma M_2^2/2 \tag{7}$$

Since the flow depends only on the inflow boundary conditions, which are completely described by the upstream Mach number, M_2, the specific heat ratio, γ, and the hole geometry, one solution with these parameters specified is valid for all upstream pressures and densities. This observation is central to the success of the analysis because, while a wide range of physical states are encountered during blowdown only a few three-dimensional solutions are required to describe them.

Data from the three-dimensional solution are used to obtain average values of the density, ρ_H, pressure P_H, the mass flux, $\rho_H v_H$, and the axial component of the radial momentum flux, ... $_H u_H$, in the exit plane of the vent using the following expressions:

$$\rho_H = (1/A_H) \int_{A_H} \rho' dA \tag{8}$$

$$P_H = (1/A_H) \int_{A_H} P' dA \tag{9}$$

$$\rho_H v_H = (1/A_H) \int_{A_H} \rho' v' dA \tag{10}$$

$$\rho_H v_H u_H = (1/AH) \int_{A_H} \rho' v' u' dA \tag{11}$$

where u is the velocity component parallel to the tube axis and v is the component parallel to the vent axis. The integration is carried out over the vent exit area, A_H. The fluxes are calculated rather than the velocities because they are used directly to compute the local vent rate in the interior solution and the weapon impulse [8]. The averages are dimensionless and are functions of the parameters that appear in the three-dimensional solution. Their use will be described below.

The gas venting through the brake will either be the air ahead of the projectile--the precursor flow--or propellant gas. Experience has shown that the three-dimensional solutions are not particularly sensitive to the value of γ, therefore the numerical results obtained in [8] for $\gamma = 1.22$ were used in this study. The interior and exterior flows are computed using the appropriate specific heat ratios, however.

The averaged functions are shown in Fig. 4. The hole geometry is characterized by the ratio of its height, L_H, to its diameter, D_H. The height is equal to the tube wall thickness. Note that the momentum flux is negative for both vent heights, especially the shorter one. This is consistent with the velocity vector plots of Figs. 2 and 3--the flow leaving the shorter vent is, on balance, direct   ore upstream.
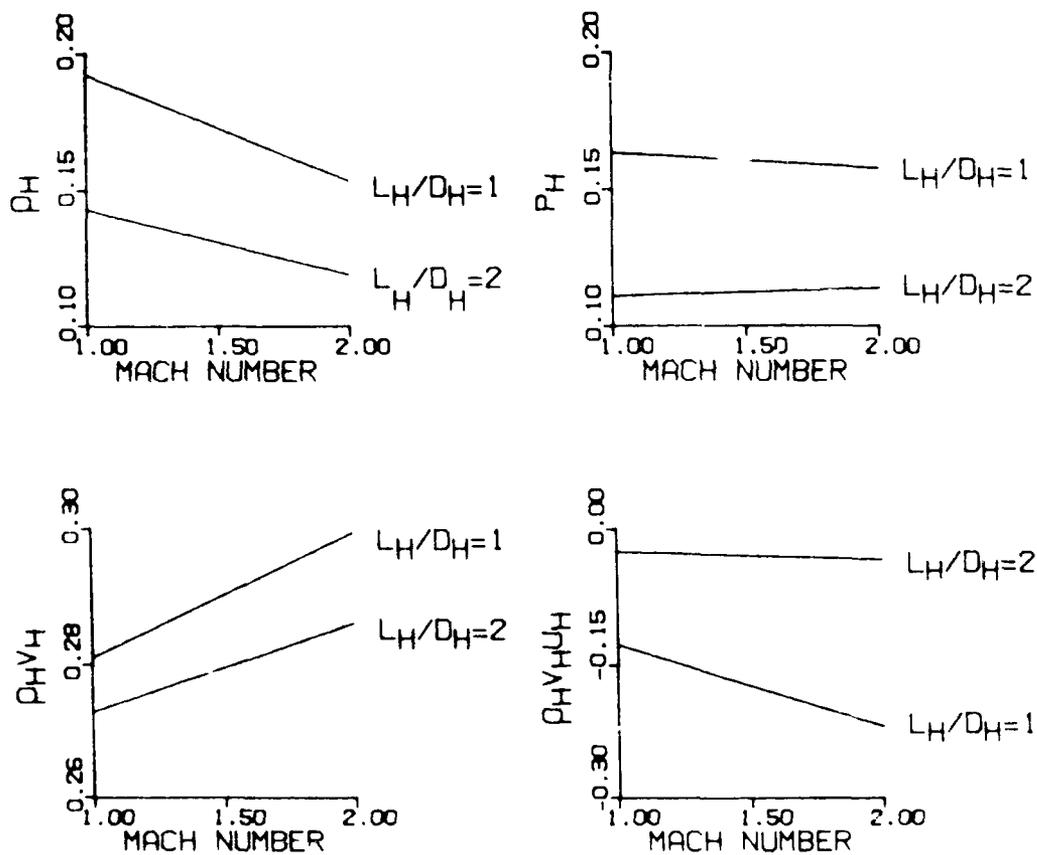

Fig.4   The averaged functions computed from the three-dimensional solutions.

292

THE INTERIOR FLOW FIELD

The flow inside the tube is calculated using the one-dimensional Euler equations with a source term included to represent the venting at the tube wall.

$$\frac{\partial \rho}{\partial t} + \frac{\partial m}{\partial x} = \frac{1}{A}\frac{d\dot{m}}{dx} \tag{12}$$

$$\frac{\partial m}{\partial t} + \frac{\partial (m^2/\rho + P)}{\partial x} = \frac{m}{\rho A}\frac{d\dot{m}}{dx} \tag{13}$$

$$\frac{\partial E}{\partial t} + \frac{\partial (m(E+P)/\rho)}{\partial x} = \frac{(E+P)}{\rho A}\frac{d\dot{m}}{dx} \tag{14}$$

The vent term $(1/A)d\dot{m}/dx$ represents the mass of fluid per unit time per unit volume leaving the tube at x. A is the bore area. The fluid is assumed to leave at the local velocity u in the momentum equation and with the local enthalpy per unit mass $(E+P)/\rho$ in the energy equation (see [10] for the derivation of these equations).

The theory will be compared with an experimental brake having holes of a single diameter and a uniform spacing, S_H, along the tube. The vent area per unit length is $\pi N_C D_H^2/4S_H$ where N_C is the number of holes per row (rows run around the circumference of the tube). The vent term can then be written in dimensional form as

$$(1/A)d\dot{m}/dx = -\rho_H v_H \sqrt{P\rho}(N_C/S_H)(D_H/D_B)^2 \tag{15}$$

where D_B is the tube diameter. P and ρ are the local values of pressure and density in the one-dimensional solution; they appear since these quantities were used to nondimensionalize the product $\rho_H v_H$ in the three-dimensional solution. The latter is also a function of the local Mach number.

THE EXTERIOR SOLUTION

The flow outside of the tube is treated as axisymmetric. The large number of vents typical of such brakes and their symmetrical placement around the tube makes this feasible. The Euler equations take the following form:

$$\frac{\partial Q}{\partial t} + \frac{\partial F}{\partial x} + \frac{\partial G}{\partial y} + W = 0 \tag{16}$$

where

$$Q = \begin{bmatrix} \rho \\ m \\ n \\ E \\ S \end{bmatrix}, \quad F = \begin{bmatrix} m \\ m^2/\rho + P \\ mn/\rho \\ (E+P)m/\rho \\ Sm/\rho \end{bmatrix}, \quad G = \begin{bmatrix} n \\ nm/\rho \\ n^2/\rho + P \\ (E+P)n/\rho \\ Sn/\rho \end{bmatrix}, \quad W = \frac{n}{y}\begin{bmatrix} 1 \\ m/\rho \\ n/\rho \\ (E+P)/\rho \\ S/\rho \end{bmatrix}$$

Since two gases are present, the state variables must be evaluated for a mixture. The details are fully explained in [11]. The last equation in this set is a species equation where S represents the mass concentration of the air at a particular location.

At the muzzle, the one-dimensional equations are solved simultaneously with the axisymmetric equations downstream. The remainder of the tube is a solid boundary except for the vented region. Since the area of each vent represents only a portion of the local tube area, the averaged variables at the vent exit have to be adjusted to provide an appropriate boundary condition for the axisymmetric equations.

The sketch in Fig. 5 represents a cross section through the vented region of the tube along a plane parallel to the tube axis. Three rows of holes are shown. The center row has an annular control volume drawn above it which extends completely around the circumference of the tube. The width of the control volume is the hole spacing, S_H, and its height is δ. If δ is allowed to approach zero, then the only relevant flux vector in Eq. (16) is $G(Q)$. The flow adjusts instantaneously from the smaller vent exit area, A_H, to the larger tube surface area $A_S = \pi(D_B + 2L_H)S_H/N_C$. Writing this balance out gives

$$\rho_H v_H A_H = \rho_S v_S A_S \tag{17}$$

$$P_a(A_S - A_H) + (\rho_H v_H^2 + P_H)A_H = (\rho_S v_S^2 + P_S)A_S \tag{18}$$

$$\rho_H v_H u_H A_H = \rho_S v_S u_S A_S \tag{19}$$

$$(E_H + P_H)v_H A_H = (E_S + P_S)v_S A_S \tag{20}$$

The species equation is not written out since the vented gas will either be air with $S_S = \rho_S$ or propellant gas with $S_S = 0$.
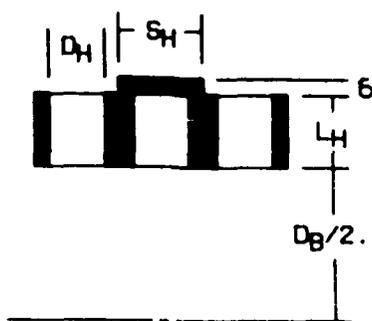

Fig. 5   Control volume used to construct the boundary conditions along the vented portion of the tube.

The first term on the left-hand side of the axial momentum equation represents some average pressure, P_a, acting on the area difference $(A_S - A_H)$. Since this pressure is not known, it will be assumed that the gas undergoes an isentropic expansion so that this equation can be replaced with the expression

$$P_S/P_H = (\rho_S/\rho_H)^\gamma \tag{21}$$

where γ is appropriate to the gas being vented. With a little algebra, the following results are obtained:

$$M_S = M_H \frac{A_H}{A_S} \left[\frac{2 + (\gamma-1)M_H^2}{2 + (\gamma-1)M_S^2}\right]^{\frac{1}{2}\frac{(\gamma+1)}{(\gamma-1)}} \tag{22}$$

$$\rho_S = \rho_H \left[\frac{M_H A_H}{M_S A_S}\right]^{2/(\gamma+1)} \tag{23}$$

$$v_S = v_H(\rho_H A_H/\rho_S A_S), \qquad u_S = u_H \tag{24}$$

where $M = u/\sqrt{\gamma P/\rho}$. After determining M_S by iteration, the conserved variables in the Euler equations can be formed. The quantities at the vent exit are related to the interior flow through the averaged functions given above. Because the vent exit flow is supersonic, the exterior boundary condition is completely determined by the local conditions in the tube.

Harten's Total Variation Diminishing scheme [12] was used in conjunction with a time-splitting algorithm to solve the Euler equations. A more thorough description of the numerical methods is given in [6] and [11].

THE STARTING SOLUTION

The first two configurations of [1] will be analyzed: the bare muzzle case and brake #1. This brake has 16 rows of holes arranged in a staggered pattern with every other row of 12 holes rotated 15 degrees with respect to the adjacent rows. The holes are drilled perpendicular to the tube axis. The brake adds 11.84 cm to the length of the cannon. A more complete description of the experimental setup, including photographs of the brakes, is given in [1]. The data in Table 1 are also taken from that source.

Table 1   Initial Data for 20-mm Cannon

P_m = 287.0 atm	U = 41.7 cm³	γ_p = 1.25
V_m = 1045.0 m/sec	C = 0.0389 kg	M_p = 22.8
T_L = 143.0 cm	W = 0.098 kg	D_H = 0.0579 cm
L_p = 7.5 cm	γ_a = 1.40	S_H = 0.0866 cm
D_B = 2.00 cm	M_a = 29.0	L_H = 0.0709 cm

P_m and V_m are the measured projectile base pressure and velocity, respectively, at the muzzle exit plane. T_L is the projectile travel length, L_p is the projectile length, D_B is the bore diameter, U is the chamber volume, C is the charge mass, and W is the projectile mass. γ is the specific heat ratio and M is the molecular weight of the gases; the subscripts "a" and "p" refer to the air and propellant gas, respectively.

The starting configurations are shown schematically in Fig. 6. The overall length of 156.3 cm in the bare muzzle case includes a uniform extension of the barrel to account for the chamber volume. The projectile velocity is kept constant throughout the calculation.
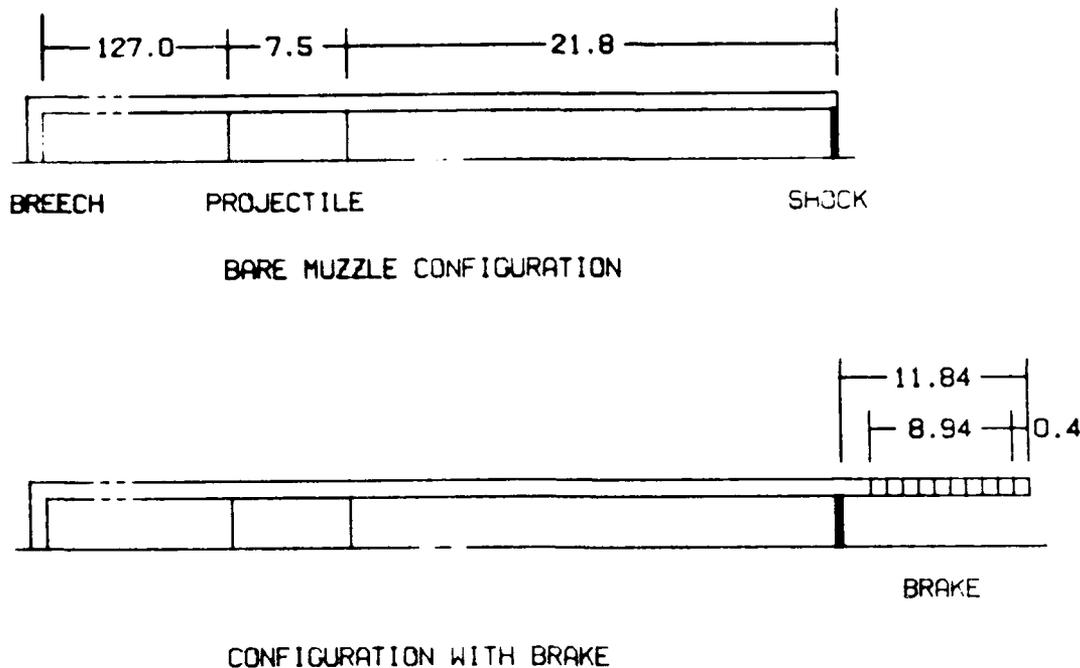
Fig. 6 The starting configurations with and without the brake.
All dimensions are in centimeters.

Initially, the projectile nose is 21.8 cm from the muzzle with the precursor shock at the muzzle exit plane. This distance places the precursor shock at the correct position in the first shadowgraph to be presented below. The state of the air ahead of the projectile corresponds to a shock Mach number based on the ratio of the projectile velocity to the acoustic speed in the stagnant environment. This method of introducing the precursor flow into the calculation underestimates the mass of air expelled from the weapon which is $(T_L-Lp)A\ \rho_e$. ρ_e is the density of the environment. In the computation, the 21.8-cm air column has a density of 4.52 ρ_e. Taking the ratio of the two masses shows that 38 percent more air is expelled by the weapon. The deficiency could be corrected by using a projectile travel-time curve from an internal ballistics code to generate the precursor flow from shot start but the computation time would also increase significantly. The effect of the precursor flow on the blast field will be explored below. Identical starting conditions were used when the brake was added, as indicated in Fig. 6.

The calculation proceeds until the projectile base reaches the position of the bare muzzle exit plane. At this instant, the state of the propellant gas behind the projectile is computed from the information in Table 1. The distributions of pressure, density, and velocity are based on the Pidduck-Kent limiting solution [13] specialized to a perfect gas. These are given by

$$\Omega = \frac{(\gamma-1)}{2\gamma}\ \frac{C}{W}\ (\frac{(\gamma-1)}{2\gamma}\ \frac{C}{W} + \int_0^1\ (\frac{1-\Omega\mu^2}{1-\Omega})^{1/(\gamma-1)}d\mu)^{-1} \tag{25}$$

$$X_s = (T_L + U/A) \tag{26}$$

$$X = x/X_s \tag{27}$$

$$P = P_m \left[\frac{1 - \Omega X^2}{1 - \Omega}\right]^{\gamma/(\gamma-1)} \tag{28}$$

$$\rho = \frac{C}{U} \frac{2\gamma}{(\gamma-1)} \frac{\Omega}{(1-\Omega)} \frac{W}{C} \left[\frac{1 - \Omega X^2}{1 - \Omega}\right]^{1/(\gamma-1)} \tag{29}$$

$$u = X V_m \tag{30}$$

Ω is obtained by solving Eq. (25) by iteration. X_s is the projectile base position which includes the uniform chamber volume extension. It remains unchanged when the brake is added.

RESULTS

A set of five shadowgraphs was obtained for each of the brakes tested by Dillon [1], but they were not included in that report. Some of these shadowgraphs are presented here--the complete sets are included in [14].

The density contour plot in Fig. 7 shows the precursor flow just after the projectile clears the muzzle. As noted earlier, the starting configuration was chosen so that the intersection of the precursor shock with the tube axis would closely match that in this shadowgraph. In all of the contour plots to be presented, the data were dumped at the instant the projectile reached its position in the corresponding shadowgraph. Thus, what is being compared between a contour plot-shadowgraph pair is the structure of the remainder of the flow field. The computed shock shape and plume size compare reasonably well with the experiment in Fig. 7.

The shadowgraph in Fig. 8 shows that the blast wave does not have the smooth appearance of the precursor shock. The pressure contour plot in the figure also has this feature. It is due to the nonuniform environment generated by the precursor flow. This can be demonstrated by starting the calculation with the projectile nose just upstream of the muzzle, thereby eliminating the precursor flow. The smooth blast wave and simpler plume structure of Fig. 9 result. Including the precursor flow increases the computation time by 60 percent, but it appears to be necessary.

The flow field development with the brake in place is depicted in Figs. 10 through 12. In the density plot of Fig. 10, the expansion of the precursor flow in the tube due to the venting through the brake is evident. It does not appear in Figs. 11 and 12 because the contour levels were chosen to emphasize the structure of the exterior flow.

Except for the region where the blast wave intersects the tube wall, the geometries of the precursor and main shocks show good agreement with those in the shadowgraphs. The weak shocks resulting from the interaction of the brake-driven and muzzle-driven portions of the flow are also captured nicely. Unfortunately, the dense propellant gas conceals the rich structure of the plumes in the shadowgraphs.
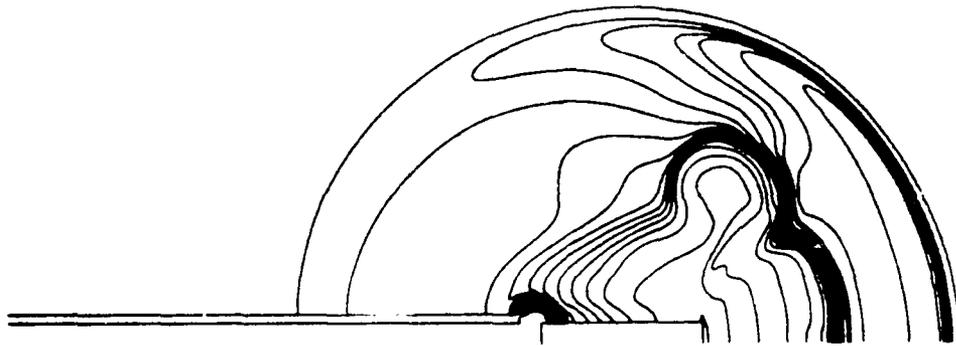
Fig. 7   Density contour plot and shadowgraph for the bare muzzle case,
t = 0.290 msec.
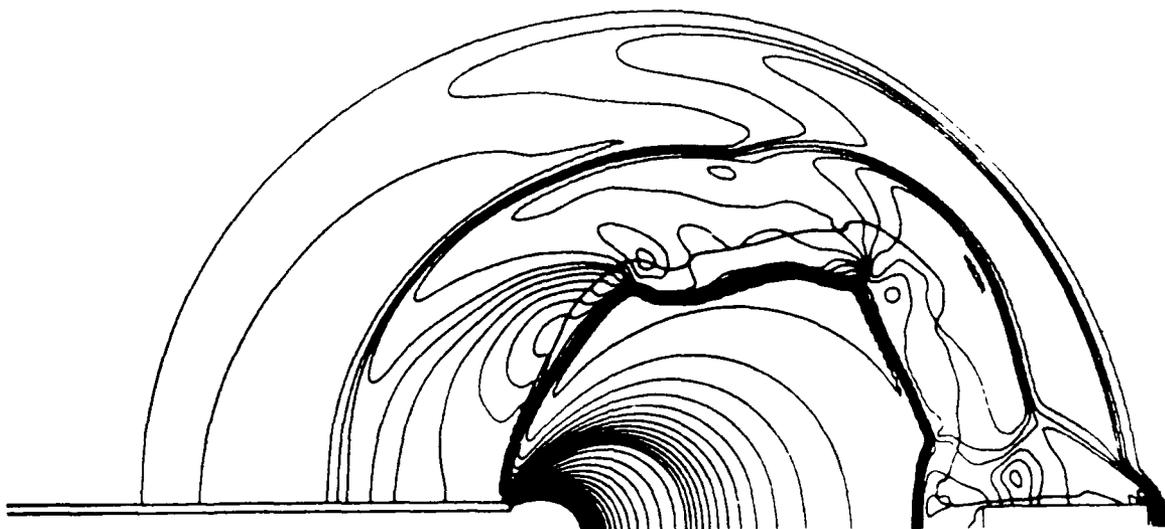
Fig. 8 Pressure contour plot and shadowgraph for the bare muzzle case, t = 0.497.
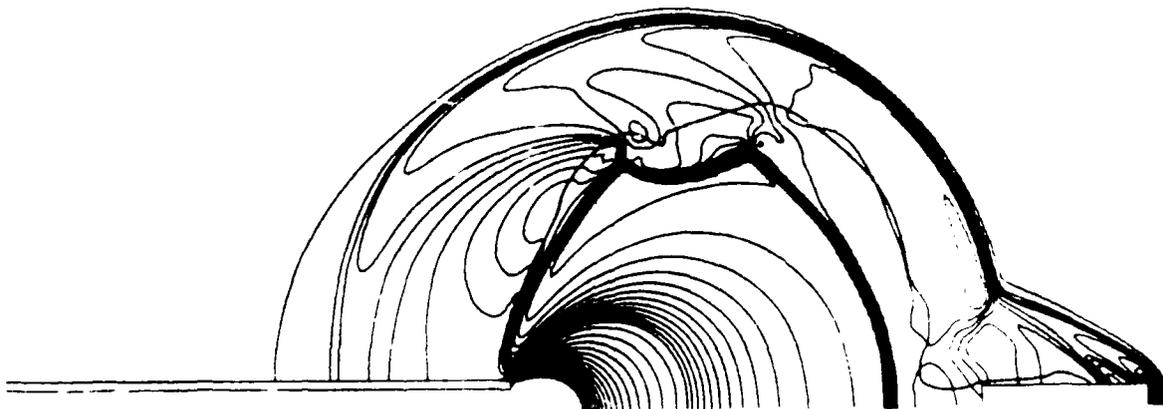
Fig. 9   Pressure contour plot for the bare muzzle case
with precursor flow eliminated.
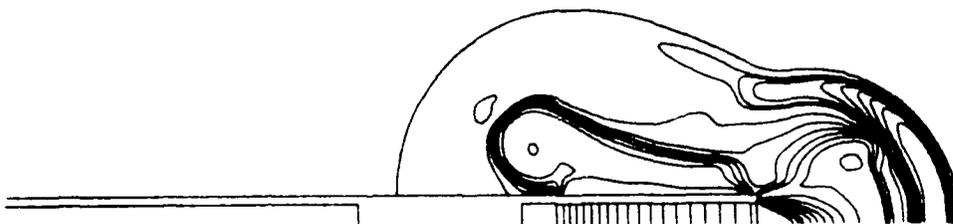
Fig. 10   Density contour plot and shadowgraph for the brake case,
t = 0.213 msec.
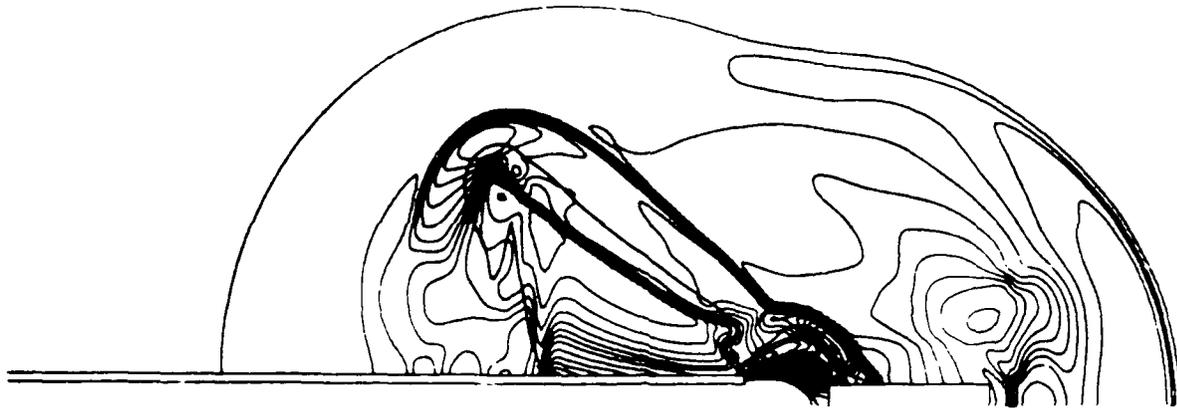
Fig. 11 Pressure contour plot and shadowgraph for the brake case,
t = 0.423 msec.

Fig. 12   Pressure contour plot and shadowgraph for the brake case,
           t = 0.546 msec.

302

Perhaps the most intriguing feature in the figures is that the primary thrust of the brake flow is directed considerably rearward even though the holes are drilled perpendicular to the tube axis. This is the result of the expansion of the propellant gas remaining in the tube as it passes the vented region. The pressure drop along the tube axis, shown in Fig. 13, is considerable. Also shown in this figure is the pressure distribution along the outside surface of the tube, that is, the boundary condition P_S in Eq. (21). P_S depends directly on the tube pressure, so its variation with distance is geometrically similar to that in the tube. It is well above atmospheric pressure at the upstream end of the brake, but only slightly above it at the downstream end. Relative to the pressure level between the plume boundary and the main blast wave, the gas at the upstream end of the brake is underexpanded, while that at the downstream is overexpanded.
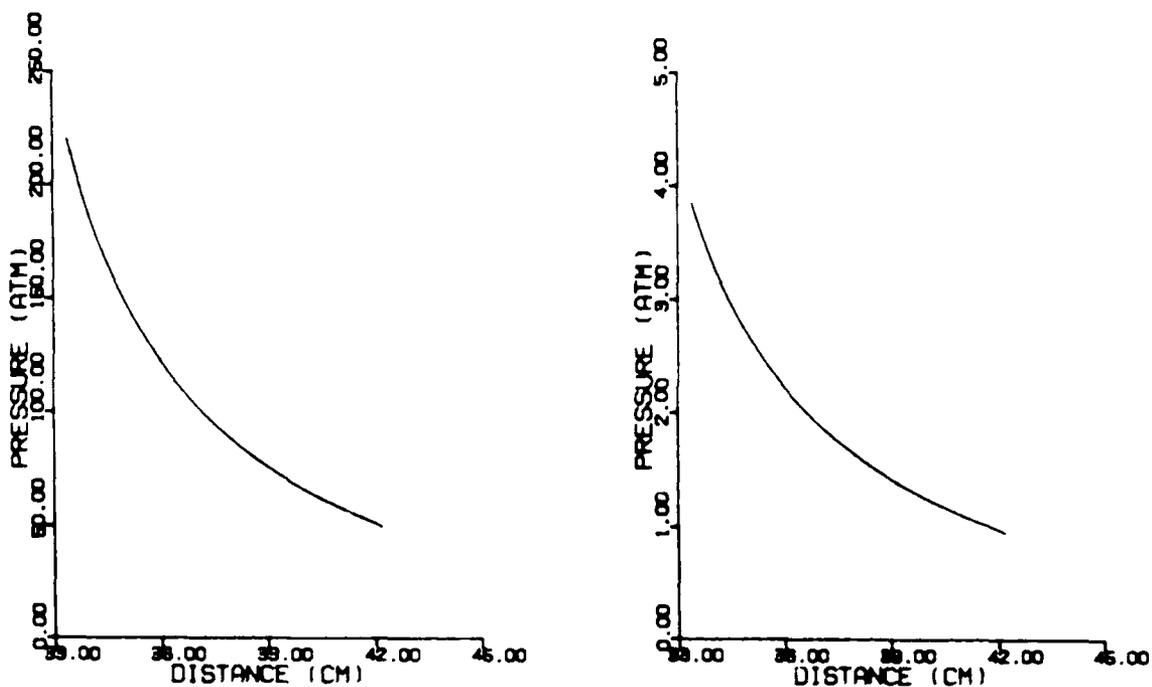

Fig. 13   Pressure distribution on the tube axis through the vented region (left) and outside of the brake (right), t = 0.546 msec.

The velocity plot in Fig. 14 shows the motion of the propellant gas within the plume. Every fourth vector is plotted to render some clarity to the figure. The plume boundaries are indicated by the solid lines which are actually a plot of the mass fraction of air with contour levels spaced closely around 0.5. They also appear in the pressure plots.
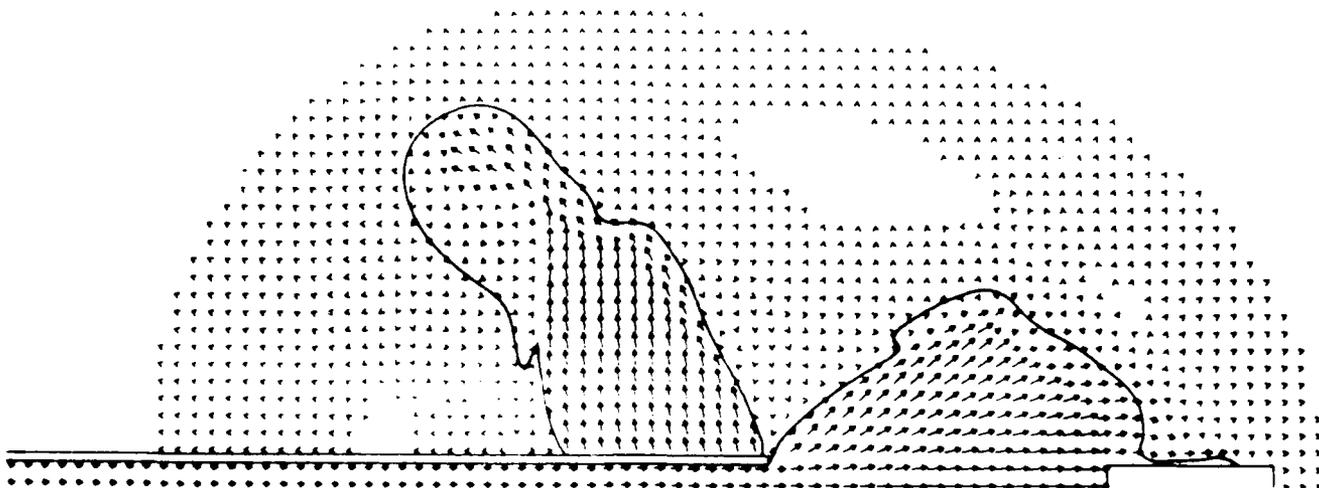
Fig. 14   Velocity vector plot for the brake case, t = 0.546 msec.

The vectors indicate that the gas leaves the brake with a slight upstream bias over most of its length.   At the upstream e d, the underexpanded flow is graduJlJy turned nearly perpendicular to the tube by a weak compression shock.   At the downstream end, the overexpanded flow is turned immediately upstream by a compression shock.   The shock system which terminates the supersonic flow in the plume also turns the flow upstream.   It then undergoes an expansion near the top of the plume where the flow is turned nearly parallel to the tube axis.   This expansion is terminated by another shock and the flow then circulates around a large vortex on the left side of the plume.   Note the absence of a vortex on the right side.

To determine the influence of the muzzle flow on the shape of the brake plume, the calculation was repeated with the muzzle moved farther downstream.   The pressure plot in Fig. 15 shows that the brake plume develops essentially as before.

Removing the precursor flow by placing the projectile nose just upstream of the brake at the start of the calculation produced the result in Fig. 16.   The plume shape is modified only slightly.   It is interesting, however, that now the upstream portion of the blast wave more closely resembles the shadowgraph.   This suggests that it may be important to include the full development of the precursor flow from shot start to obtain proper results in this region.   It should also be mentioned that failure to include the 45-degree ramp on the tube exterior just upstream of the experimental brake (see shadowgraph in Fig. 10) might contribute to the poor agreement, although the corresponding step in the bare muzzle case (see Fig. 7) does not seem to influence either the precursor or the main shock development there.

CONCLUSIONS

In general, the predicted results compare favorably with the shadowgraphs.   The coupling of the interior and exterior flows using a control volume model to make the transition appears to be practical.   Perhaps more attention should be paid to the development of the precursor flow.
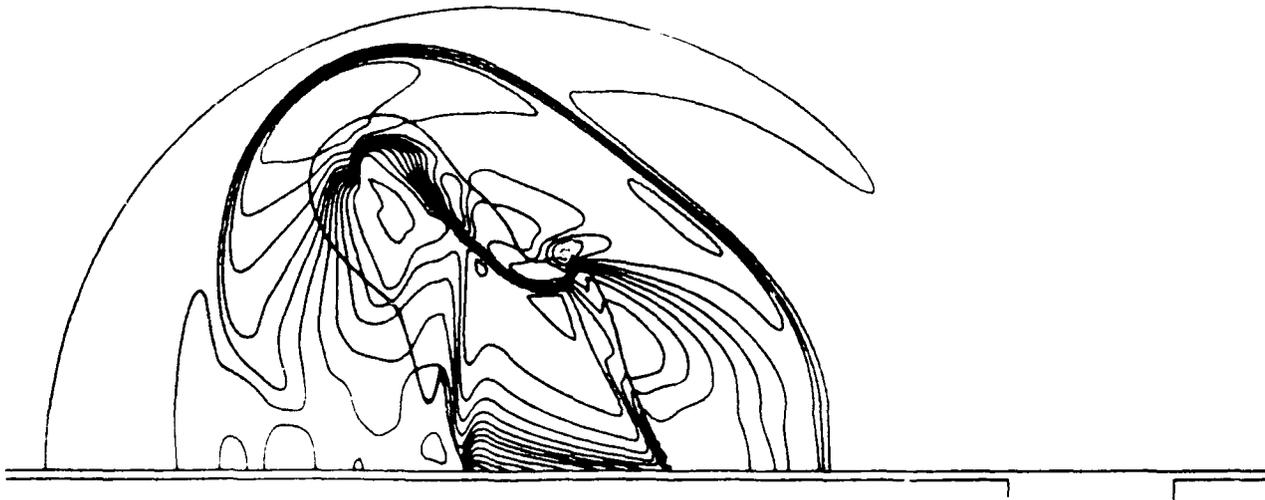
Fig. 15   Pressure contour plot for the brake case with muzzle flow removed,
t = 0.546 msec.
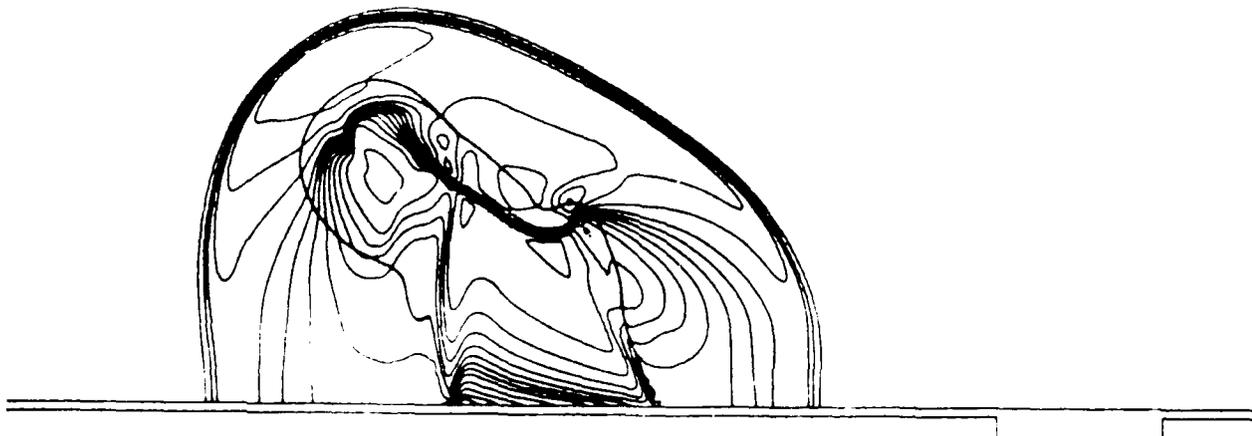
Fig. 16   Pressure contour plot for the brake case with muzzle and precursor
flows removed, t = 0.546 msec.

305

ACKNOWLEDGEMENT

REFERENCES

1. R. E. Dillon, Jr., "A Parametric Study of Perforated Muzzle Brakes," Technical Report ARLCB-TR-84015, Benet Weapons Laboratory, Watervliet, NY, May 1984.

2. R. E. Dillon, Jr. and H. T. Nagamatsu, "An Experimental Study of Perforated Muzzle Brakes," Technical Report ARLCB-TR-84004, Benet Weapons Laboratory, Watervliet, NY, February 1984.

3. R. E. Dillon, Jr. and H. T. Nagamatsu, "A Method of Analyzing Perforated Muzzle Brake Performance," Technical Report ARLCB-TR-84002, Benet Weapons Laboratory, Watervliet, NY, February 1984.

4. R. E. Dillon, Jr., "Wall Thickness and Vent Area Effects on Perforated Muzzle Brake Performance," Technical Report ARLCB-TR-84020, Benet Weapons Laboratory, Watervliet, NY, June 1984.

5. R. E. Dillon, Jr. and H. T. Nagamatsu, "An Experimental Study of Perforated Muzzle Brakes," AIAA Paper 84-1642, presented at the AIAA 17th Fluid Dynamics, Plasma Dynamics, and Lasers Conference, June 25-27, 1984, Snowmass, CO.

6. H. T. Nagamatsu, K. Y. Choi, R. E. Duffy, and G. C. Carofano, "An Experimental and Numerical Study of the Flow Through a Vent Hole in a Perforated Muzzle Brake," Technical Report ARCCB-TR-87016, Benet Weapons Laboratory, Watervliet, NY, June 1987.

7. H. T. Nagamatsu, K. Y. Choi, and R. E. Duffy, "Wall Thickness and Flow Mach Number Effects on Pressure Distribution in the Vent Hole for Perforated Muzzle Brakes," ARDEC Contractor Report ARCCB-CR-86038, Rensselaer Polytechnic Institute, Troy, NY, November 1986.

8. G. C. Carofano, "The Gasdynamics of Perforated Muzzle Brakes," Technical Report ARCCB-TR-88006, Benet Laboratories, Watervliet, NY, February 1988.

9. J. C. T. Wang, G. F. Widhopf, and S. H. Chen, "A Three-Dimensional, Finite Volume TVD Scheme for Geometrically Complex Steady and Transient Flows," AIAA Paper 88-0228, presented at the AIAA 26th Aerospace Sciences Meeting, January 11-14, 1988, Reno, NV.

10. M. J. Zucrow and J. D. Hoffman, Gas Dynamics - Volume 2: Multidimensional Flow, John Wiley and Sons, New York, 1977, Chapter 19.

11. G. C. Carofano, "Blast Computation Using Harten's Total Variation Diminishing Scheme," Technical Report ARLCB-TR-84029, Benet Weapons Laboratory, Watervliet, NY, October 1984.

12. A. Harten, "High Resolution Schemes for Hyperbolic Conservation Laws," J. Computational Physics, Vol. 49, No. 3, pp. 357-393, Mar. 1983.

13. J. Corner, Theory of the Interior Ballistics of Guns, John Wiley and Sons, New York, 1950.

14. G. C. Carofano, "The Blast Field Produced by a Cannon Having a Perforated Muzzle Brake," Benet Laboratories Technical Report, Watervliet, NY, to be published.

LAGRANGIAN MODELLING OF BLUNT
PROJECTILE IMPACTS AGAINST THICK PLATES

J. C. Schulz and O. E. R. Heimdahl
Research Department
Naval Weapons Center
China Lake, CA 93555

A technique for Lagrangian modelling of blunt projectile impacts against thick plates is presented. This technique involves inclusion in the model of a conical cap of target material ahead of the projectile and separated from the remainder of the target by an eroding interface. This technique ensures that erosion will occur, not at the interface between the projectile and the target, but at the interface between the cap and the remainder of the target. Comparison with gun firing results indicates that inclusion of a cap reduces the effective drag on the projectile and leads to results that are in significantly better agreement with experiment.

INTRODUCTION

Historically, Lagrangian codes have had limited success modelling projectile impacts against thick plate targets where significant penetration occurs. This is because material fracture and comminution, which are essential parts of the penetration process, are difficult to model with such codes. Also, the extreme element distortions associated with penetration can lead to solution stoppage.

Recently, however, the so-called "eroding interface" has been developed [1], which leads to improved results in this situation. With an eroding interface, elements along the interface boundary are allowed to fail as their effective strains exceed a critical value. The volumetric effects of failed elements are eliminated from the solution and the interface is redefined to include only non-eroded material. The masses of failed elements are retained as point masses which are constrained to lie outside the eroded interface.

Eroding interfaces are applicable to problems where material erosion is the primary mode of penetration. This requirement is approximately satified in the case of a pointed or round-fronted projectile where eroded material can flow around the side of the projectile and escape to the rear. It is not satisfied, however, for a blunt-fronted projectile where a cap of non-eroding material forms in the stagnation zone ahead of the projectile. This cap changes the effective nose shape of the projectile and forces erosion to occur between it and the remainder of the target. An ordinary eroding interface between projectile and target does not reproduce this behavior.

In this paper a new technique for modelling penetration of blunt projectiles is examined, which takes into account experimental observations regarding the formation of stagnation caps of target material on the fronts of blunt projectiles during penetration. The technique involves inclusion in the finite element model of a conical cap of target material ahead of the projectile with an eroding interface between the surface of the cap and the remainder of the target. This new technique has been used to model impacts of small steel cylinders against concrete slab targets, for which gun-firing data is available. The inclusion of a cap reduces the effective drag of the target and leads to results that are in significantly better agreement with experiment.

STAGNATION CAP FORMATION

Experimental evidence for the formation of stagnation caps during blunt projectile penetrations, since it forms the basis for the modelling technique, will be briefly reviewed in this section.

Although the notion that caps of target material might form in the stagnation zones ahead of penetrating projectiles was put forth by Newton in his Principia, it was many years before such caps were actually reported experimentally. Apparently, this was first done by Allen, et al [2], for penetrations into sand. The existence of roughly conical caps ahead of steel cylinders impacting aluminum plates was described by Backman [3]. Winter [4] has observed stagnation caps resulting from penetrations into titanium and polymethylmethacrylate.

The most extensive study of stagnation cap formation is that of Backman, et al [5]. They fired small-diameter steel cylinders into plaster of Paris and simulated concrete targets, which were fabricated with different-colored layers. The targets were cross-sectioned after test to reveal the projectile penetration paths and the stagnation caps ahead of the projectiles. A typical cap formed on a steel cylinder during penetration into simulated concrete is shown in Figure 1. Detailed examination of the layers indicated that the caps formed almost immediately and remained essentially intact, causing the projectiles to become effectively conically-fronted for the duration of the impact event.

Figure 1. Stagnation cap ahead of steel cylinder penetrating simulated concrete.

MODELLING TECHNIQUE

The basic idea behind the modelling technique described in this paper is to artificially create a stagnation cap of target material ahead of the projectile at the solution start. This is accomplished by modelling the target in two parts, a cone of material ahead of the projectile and the remainder of the target, with an eroding interface between them. The projectile impacts the base of the cone and propels it into the remainder of the target.

The main approximations in this technique involve the "pre-shearing-out" of the cone and the choice of a suitable cone angle. If the strength of the target material is relatively low, the work required to form the cone should be small. The experiments in [5] indicate that a cone angle of 45 degrees is reasonable for impacts into concrete-like materials. This value was used for all computations in this paper.

A related modelling technique involving use of a cap of target material ahead of an impacting projectile is described in [6]. In that case, however, the remainder of the target was not modelled and no eroding interface was used. Instead, an approximate pressure loading to represent effect of the remainder of the target was applied to the surface of the cap.

To test the feasibility of the present technique, the normal incidence impact of a steel cylinder against a concrete slab was modelled. The projectile diameter was 10 inches, the projectile length was 15 inches and the slab thickness was 10 inches. The impact speed was 1000 feet per second. The EPIC-2 code [7] was used. Models not including and including a target cap were constructed. Material properties for the steel and concrete were taken from the EPIC-2 library. A critical erosion strain of 1.5 was used. Deformed structure plots without and with a target cap are shown in Figures 2 and 3. The residual speeds of the projectile were 671 and 741 feet per second, respectively. Inclusion of a cap increased the residual speed by about 10 percent.

For both models, a large "bubble" of low density target material formed behind the target so that the projectile never broke through the rear surface. Physically, one would expect a cloud of highly comminuted rubble rather than this cohesive bubble. This bubble can be eliminated by introducing a critical volumetric strain into the erosion algorithm in addition to the usual critical erosion strain.

Deformed structure plots for computer runs for models not including and including a target cap, and with a critical volumetric strain of 1.0, are shown in Figures 4 and 5. The residual speeds of the projectile were 689 and 750 feet per second. In both cases, a cloud of point masses has been produced and the projectile has broken out at the rear of the target. It should be emphasized that volumetric erosion has little physical justification and is included for cosmetic purposes only. It results in slightly higher residual speeds (less than 3 percent).

COMPARISON WITH EXPERIMENT

Experimental firings of small, blunt-nosed cylindrical steel projectiles against simulated reinforced concrete slabs are described in [8]. The projectiles were 0.5 inch in diameter and had an internal cavity filled with plasticine. Weight of projectile and filler was about 26.4 grams. Slab targets consisting of simulated concrete (concrete patching compound) reinforced with layers of
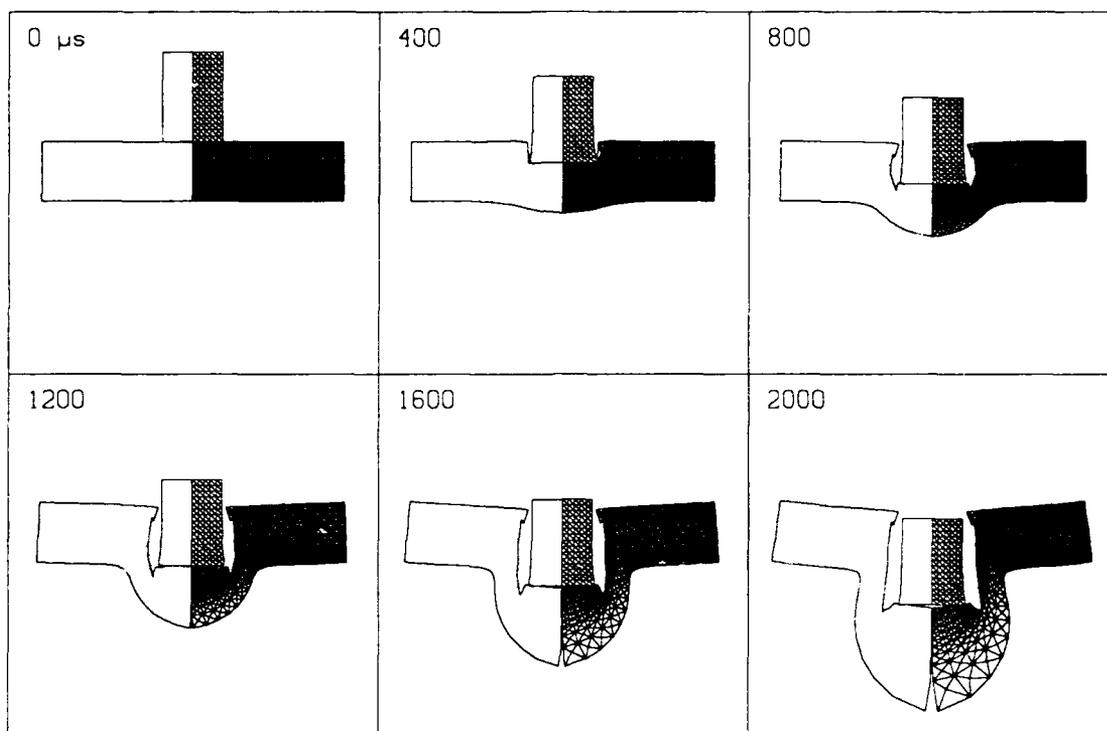
Figure 2. Steel cylinder impacting concrete slab, no target cap, erosion strain = 1.5.
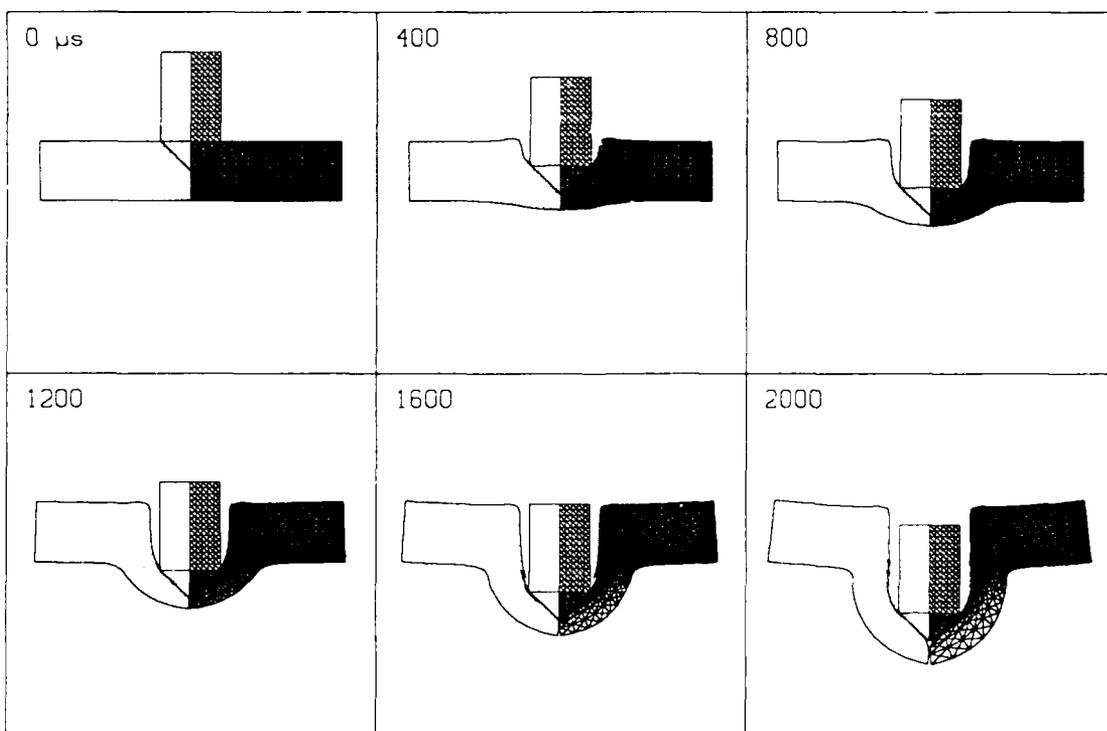

Figure 3. Steel cylinder impacting concrete slab, target cap, erosion strain = 1.5.
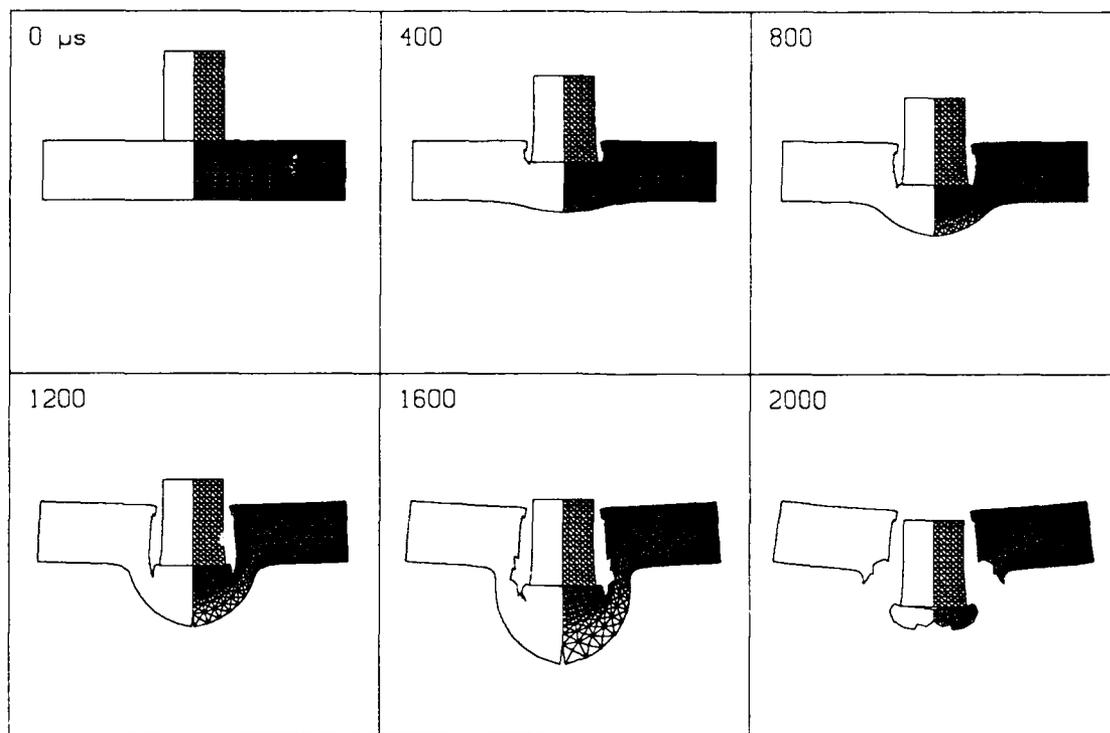
Figure 4. Steel cylinder impacting concrete slab, no target cap, erosion
strain = 1.5, volumetric strain = 1.0.
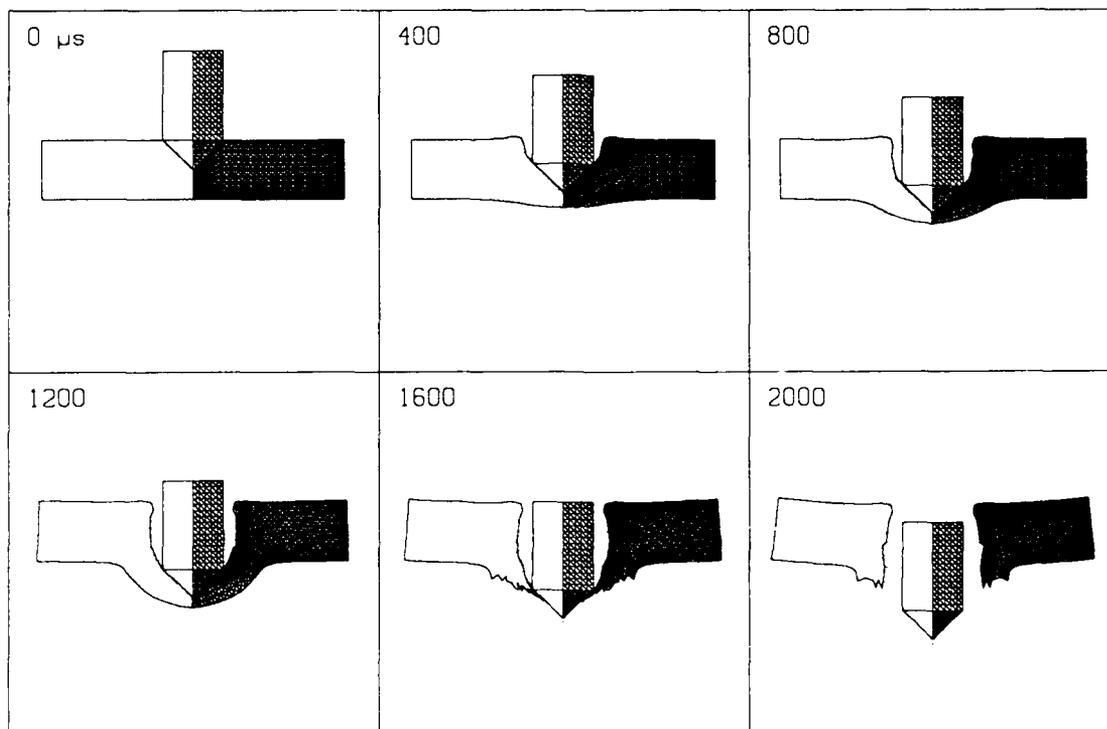
Figure 5. Steel cylinder impacting concrete slab, target cap, erosion strain
= 1.5, volumetric strain = 1.0.

hardware cloth were constructed in four thicknesses (0.5, 1.0, 2.5 and 5.0 inches). Firings were made at normal incidence at an impact speed of 1800 feet per second.

Computer code modelling runs without and with target caps were made for these conditions. A solid steel projectile with length adjusted so as to give the same mass as a filled projectile was modelled. Critical values of 1.0 for both the critical erosion and volumetric strains were used. (The lower erosion strain value produced better agreement with test results.) The EPIC-2 material model for concrete was modified to account for the lower compressive strength and lower density of the concrete patching compound.

Deformed structure plots for computer runs without and with caps against the four slab thicknesses are given in Figures 6-13. Residual speeds or penetration depths are summarized in Table 1. It is apparent that the presence of a target cap significantly reduces the effective drag of the target material and leads to results that are in considerably better agreement with gun firing results.

Table 1. Comparison of computer results with experiment.

Slab thickness, in.	0.5	1.0	2.5	5.0
Residual speed, ft/s (gun firing results)	1615	1420	1020	155
Residual speed, ft/s (model without cap)	1515	1268	482	—
Residual speed, ft/s (model with cap)	1585	1397	881	—
Penetration depth, in. (model without cap)	—	—	—	2.53
Penetration depth, in. (model with cap)	—	—	—	3.85

CONCLUSION

A technique for Lagrangian modelling of blunt projectile impacts against thick plates has been described. This technique involves inclusion in the model of a conical cap of target material ahead of the projectile and separated from the remainder of the target by an eroding interface. In addition to forcing creation of a stagnation cap, this procedure ensures that erosion will occur, not at the interface between the projectile and the target, but at the interface between the stagnation cap and the remainder of target. The following closing comments can be made regarding this technique:

1. Inclusion of the cap significantly reduces drag on the projectile and produces results that are in better agreement with experiment. Its use where stagnation caps are known to occur appears warranted.

2. Volumetric erosion was introduced to eliminate the low-density bubble of target material formed at the rear of the target. It would be desirable to incorporate a more physically justifiable failure mechanism for this purpose.
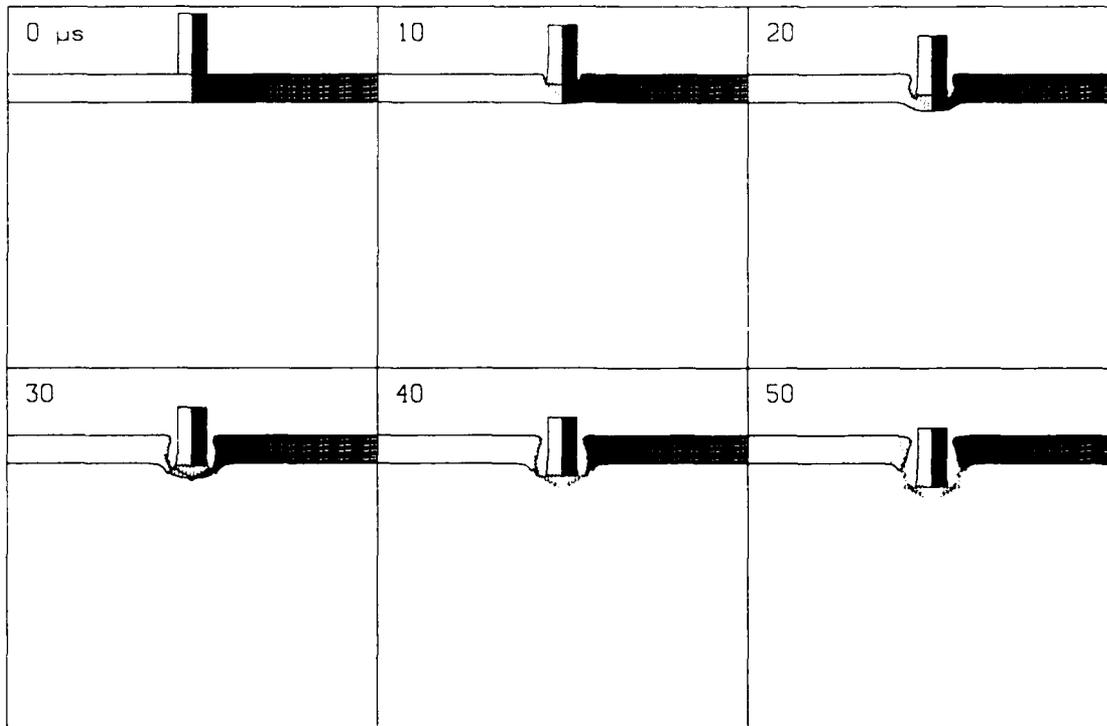
Figure 6. Steel cylinder impacting 0.5 inch simulated concrete slab, no target cap.
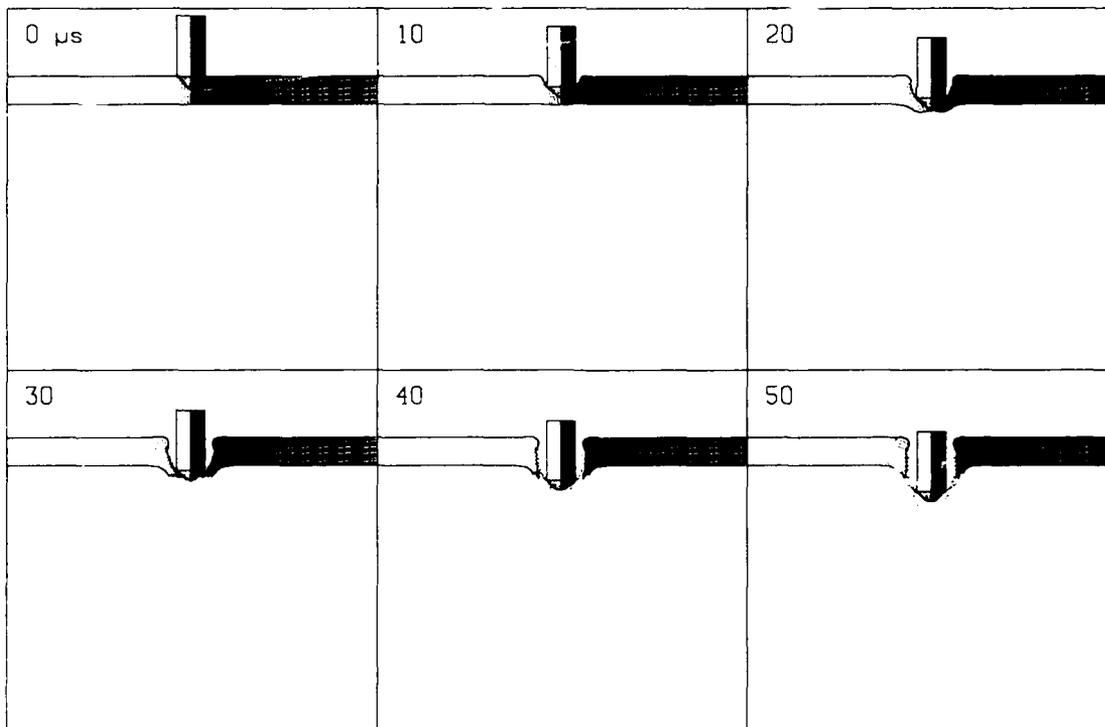
Figure 7. Steel cylinder impacting 0.5 inch simulated concrete slab, target cap.
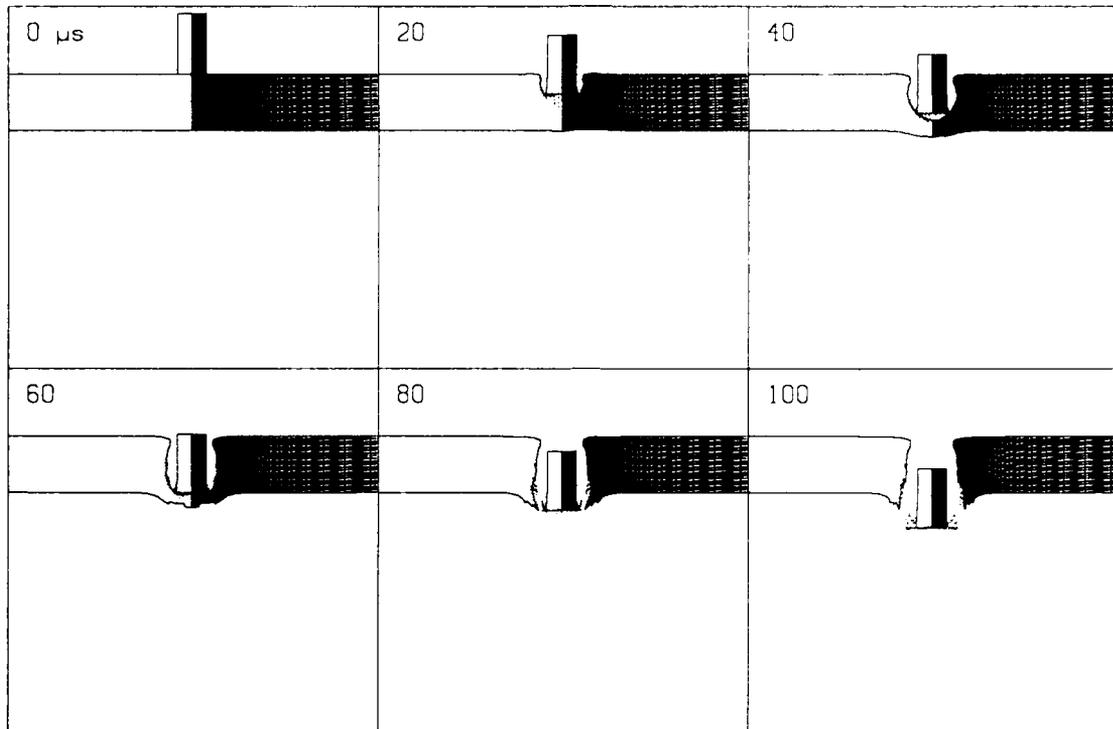
Figure 8. Steel cylinder impacting 1.0 inch simulated concrete slab, no target cap.
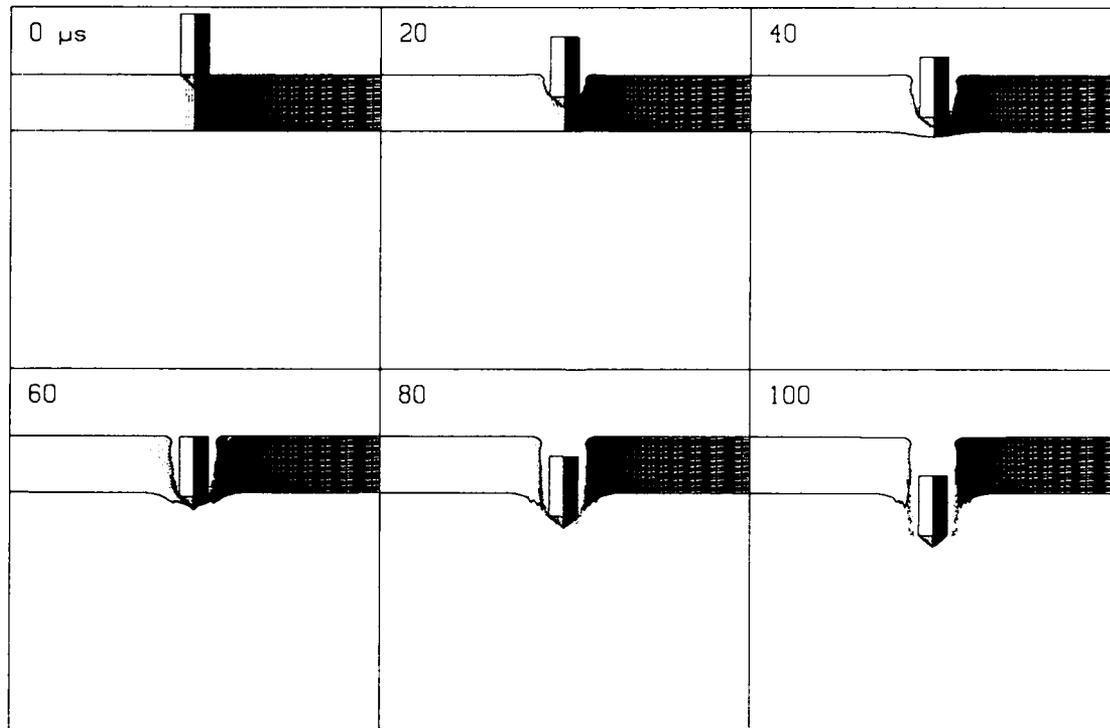
Figure 9. Steel cylinder impacting 1.0 inch simulated concrete slab, target cap.
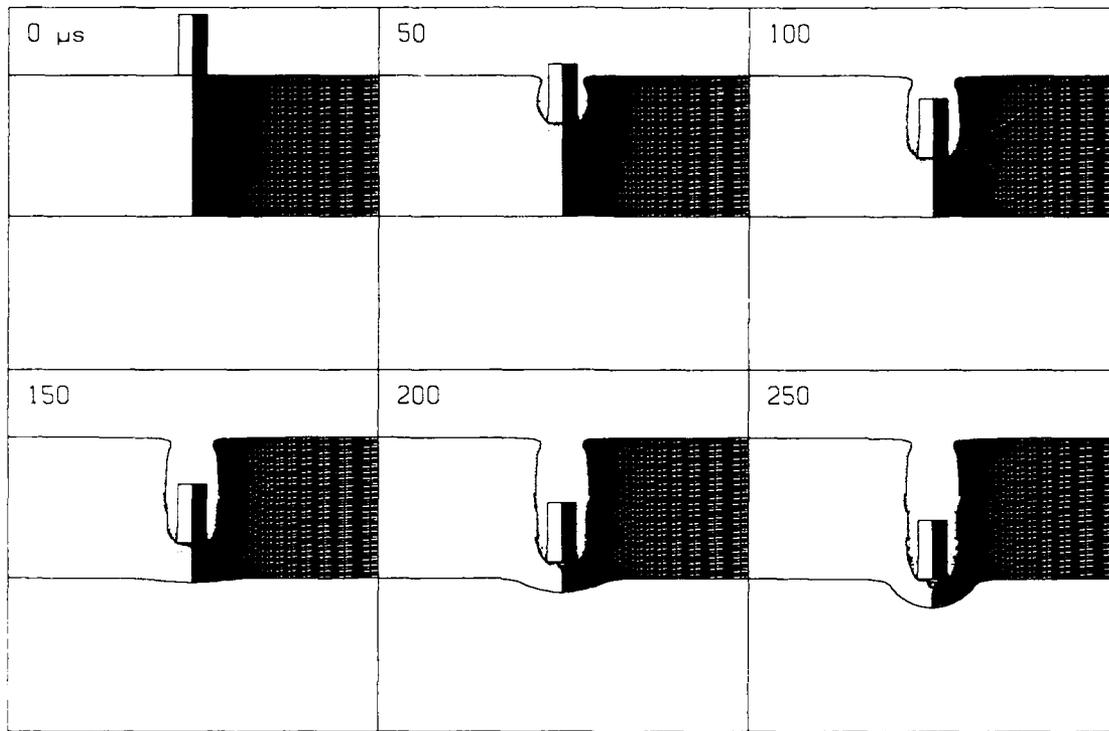
Figure 10. Steel cylinder impacting 2.5 inch simulated concrete slab, no target cap.
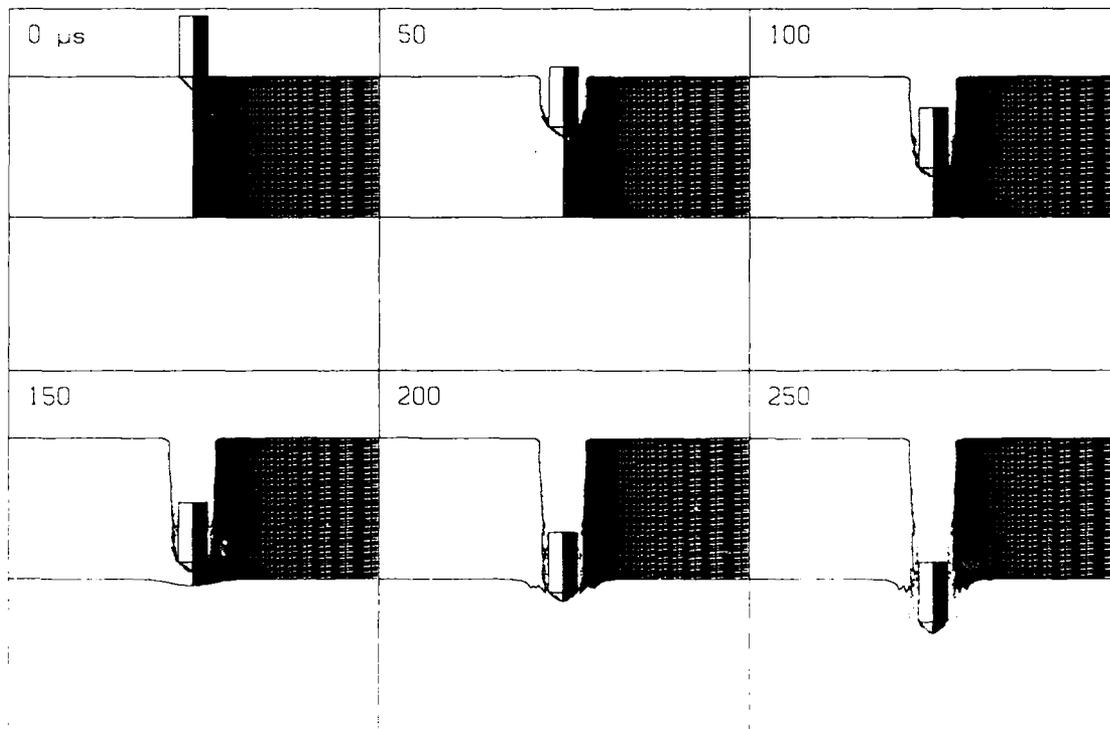
Figure 11. Steel cylinder impacting 2.5 inch simulated concrete slab, target cap.
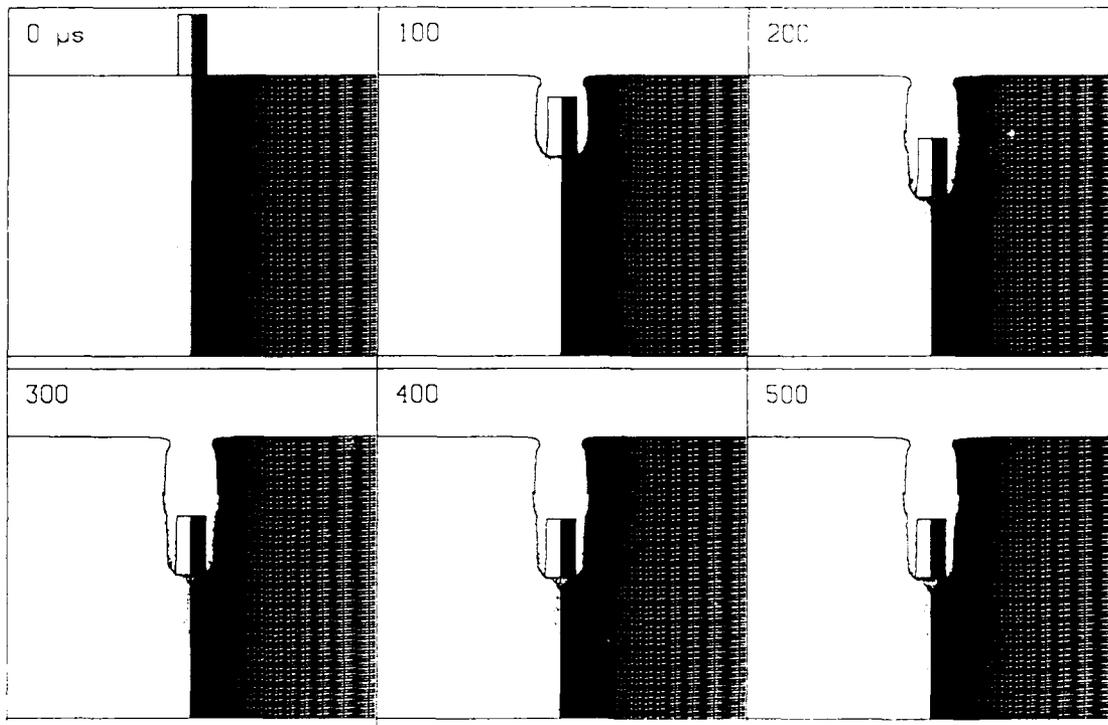
Figure 12. Steel cylinder impacting 5.0 inch simulated concrete slab, no target cap.
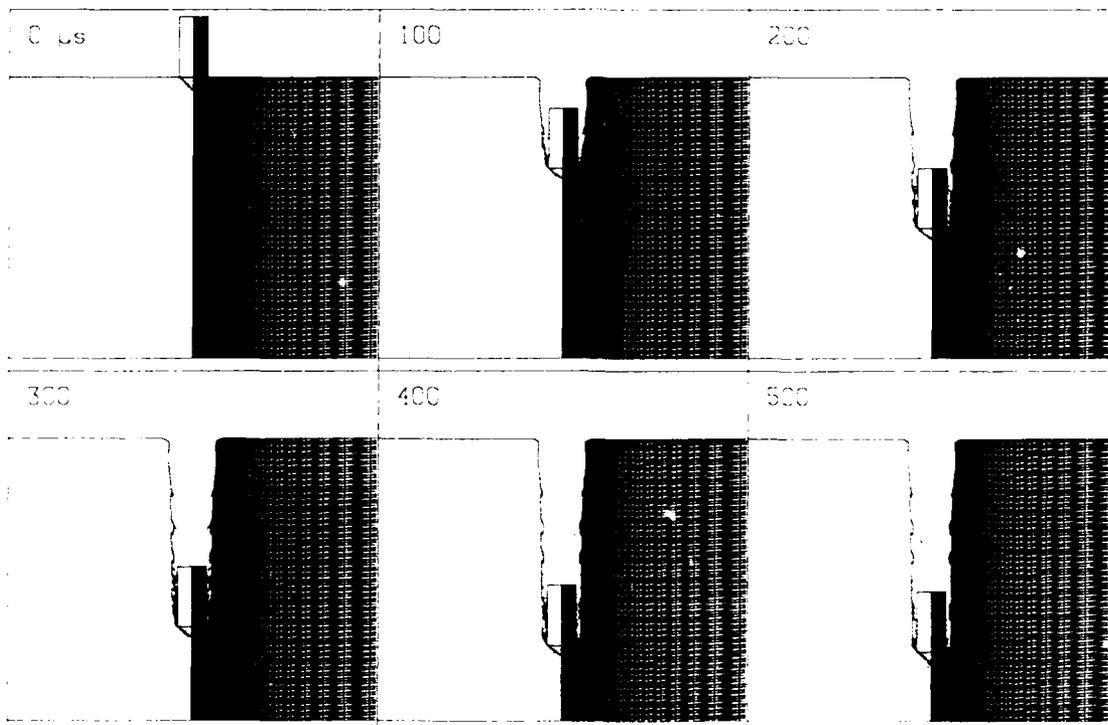
Figure 13. Steel cylinder impacting 5.0 inch simulated concrete slab, target cap.

3. The effect of cone angle on penetration should be examined. It appears likely that this effect may be small over a reasonable range of cone angles, but this has not been determined.

4. The results in [5] show that stagnation caps also form during oblique incidence impacts. It should be possible to extend this technique to such impacts utilizing a distorted cone as described in [6]. In this case, a line of contact would sweep across the base of the distorted cone as the projectile moved forward into the target. Some difficulty generating this contact might be expected.

REFERENCES

1. F. P. Stecher and G. R. Johnson, "Lagrangian Computations for Projectile Penetration into Thick Plates," Proceedings of the 1984 International Computers in Engineering Conference and Exhibit, American Society of Mechanical Engineers, 1984.

2. W. A. Allen, E. B. Mayfield and H. L. Morrison, "Dynamics of a Projectile Penetrating Sand," J. Appl. Phys., Vol. 28, 1957.

3. M. E. Backman, "Elastic and Plastic Behavior in the Impact of Cylinders Against Plates," J. Appl. Phys., Vol. 30, 1959.

4. R. E. Winter, "Adiabatic Shear of Titanium and Polymethylmethacrylate," Phil. Mag., Vol. 31, 1975.

5. M. E. Backman, S. A. Finnegan and K. G. Whitham, "The Formation of Stagnation Zones in Stable Penetrations of Brittle Materials," Proceedings of the 6th International Symposium on Ballistics, American Defense Preparedness Association, 1981.

6. J. C. Schulz, O. E. R. Heimdahl and S. A. Finnegan, "Finite Element Modelling of Impacting Warhead Structural Response Using 'Target Plug' Approach," Proceedings of the 8th International Symposium on Ballistics, American Defense Preparedness Association, 1984.

7. G. R. Johnson and R. A. Stryk, "User Instructions for the EPIC-2 Code," AFATL-TR-86-51, Air Force Armament Laboratory, 1986.

8. J. C. Schulz, O. E. R. Heimdahl and S. Finnegan, "Small Steel Projectile Firings Against Simulated Reinforced Concrete Slabs at Normal Incidence and Obliquity," NWC TP 6501, Naval Weapons Center, 1984.

# ANALYTICAL ESTIMATE OF ARTILLERY PROJECTILE BALLOTING LOAD BASED UPON CORRELATION WITH STRAIN GAGE TEST DATA

Mr. Al Meyer
Motorola, Inc.
Government Electronics Group
8220 E. Roosevelt St. (MD-R4246)
Scottsdale, AZ 85252

The internal ballistic environment experienced by artillery projectiles due to ballotting (i.e. impact between the projectile and the gun tube) is investigated in this paper. An analysis has been performed to estimate the ballotting load by correlating with strain gage data obtained during test firings of 155 mm projectiles at Yuma Proving Ground. It involved the use of modal synthesis and included the inertial effects of spin velocity, rate of change of spin and setback acceleration of the projectile.

Introduction

The internal and external ballistic environments to which artillery projectiles are subjected, are severe and therefore of great concern in fuze design. One specific phenomenon, balloting, is addressed in this paper. Balloting, which occurs often, is the impact between the bourrelet of the projectile and the gun tube. This lateral loading applied to the projectile can cause component failures which can result in failure of the entire system. This paper describes an analytical method which has been developed to estimate the magnitude and duration of this loading and the resulting acceleration levels produced in the projectile by correlating the results of the analysis with test data from two firings.

This method was applied during the development of an artillery projectile for the 155 mm gun as part of a test program to observe the effects of wear on the interior ballistics of a gun tube at various stages of its life. This testing was conducted at Yuma Proving Ground by Harry Diamond Laboratories in the early eighties. The test data that is referenced herein, specifically strain-time history data, was obtained using an FM-FM telemetry system designed by Harry Diamond Laboratories. An instrumented beam sensor, located along the flight axis within the telemetry package as shown in Figure 1,
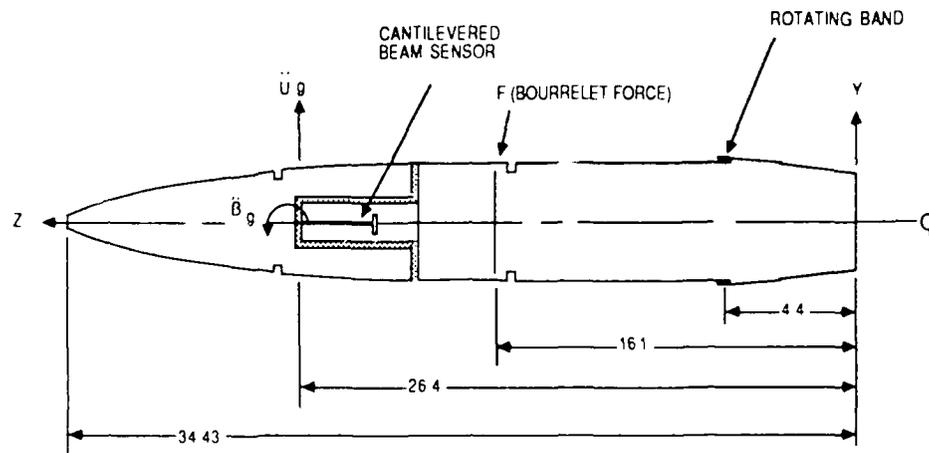
Figure 1. 155mm Projectile with Beam Sensor

was used to sense transverse loads produced inbore by excessive balloting loads. Measurements were taken for gun tubes at various stages of life. The wear on the end-life gun tube analyzed was considered atypical and characterized by severe local asymmetric erosion observed near the cannon breach. This contributed to excessive asymmetric gas blow-by past the obturating and rotating band, thereby, increasing the possibility of balloting. Consequently, the end-life case analyzed demonstrated higher than anticipated balloting loads.

Approach

The method of modal analysis was applied in this analysis. It involved the generation of two mathematical models. The first model generated was a lateral model of the entire projectile. It was modeled as a beam structure grounded by a linear spring located at the position of the rotating band of the projectile. The second model was a beam model of the beam sensor. The purpose of the projectile model was initially to produce a linear (transverse) and a rotational acceleration time history at a location in the projectile model corresponding to the position of the beam sensor for an assumed balloting load. These acceleration time histories were then applied as ground acceleration excitations to the beam sensor model to determine the strain time history of the beam for comparison with test data. If the comparison with test data was good, the estimate of the balloting load was assumed to be valid. Once this correlation was achieved, the lateral acceleration response of the projectile at any position defined by the model could be calculated as well as the shear and bending moment responses as a result of the balloting load assumed.

Analytical Method

A gun launch imposes several varied acceleration loadings on the projectile and its cargo. These loadings which include setback and angular accelerations, affect the response of the projectile. The setback acceleration applies a compressive load to the projectile and a tensile load to the beam sensor, consequently, it lowers the resonant frequencies of the projectile and increases the the resonant frequencies of the beam sensor. The spin of the projectile also has an effect on the resonant frequencies of the projectile and the beam sensor. These effects as well an those of angular acceleration and Coriolis acceleration have been included in this analysis.

It was determined for the case of the projectile model that only spinning had a noticeable effect on the modal properties. The variation of the modal properties with spin rate however was not large, consequently it was not considered necessary to allow these properties to vary in the analysis. Therefore, in this analysis it was assumed that balloting occurred when the projectile had a spin rate of 12,000 RPM and the modal properties of the projectile at that spin rate were used to determine its response to the balloting load. The mode shapes and corresponding resonances of the projectile model are displayed in Figure 2. The resonant frequencies and
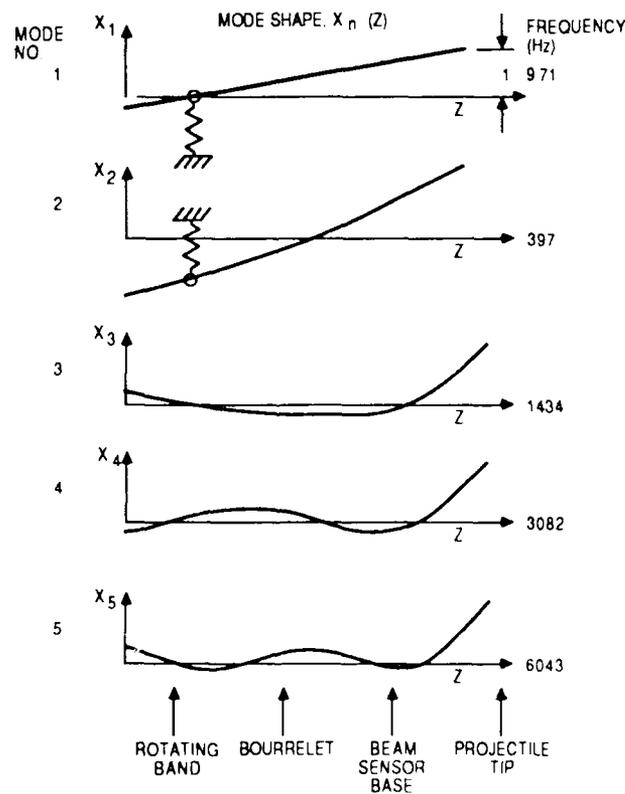

Figure 2. 155mm Projectile Mode Shapes and Frequencies

other modal properties of the projectile model are given in Table 1. These results were determined using an in-house computer code which utilizes the transfer matrix technique (References 1 and 2).

Table 1

Modal Properties of 749 Projectile Assuming Setback Acceleration is zero g's & Spin Rate is 12,000 RPM (Rotating Band Spring Rate is 1×10^6 # in.)

Mode	f_n (hz)	m_n (#-in-sec^2)	Z_{imp} (in)	Z_{beam} (in)	β_{beam} (rad)	Z_{cg} (in)
1	9.7082	.031407	.3909	.7357	-.03338	.2071
2	396.97	.13348	-.2286	.4360	-.07015	-.5490
3	1434.1	.004495	-.1329	.2110	-.08702	-.07445
4	3082.4	.003296	.02769	-.07927	-.09058	.08067
5	6043.3	.003058	.1370	-.1949	-.02582	-.03685

Z_{imp} = modal deflection at bourrelet

Z_{beam} = modal deflection at base of beam sensor

Z_{cg} = modal deflection at projectile center of gravity

β_{beam} = modal slope at base of beam sensor

The mode shapes and resonant frequencies of the beam sensor were determined using the same in-house computer code. The beam sensor and its resonant frequencies and mode shapes are shown in Figure 3 for the case in which the setback acceleration and spin rate were set equal to zero.

a.) BEAM SENSOR MODEL

0.200

0.275

1.000

3.500

b.) MODE SHAPES AND FREQUENCIES

MODE

MODE SHAPES, X_n (Z)

*FREQUENCY (Hz)

1

Z

408.2

2

Z

3227

* Ω = 0 RPM
  g = 0 g's

74341-1
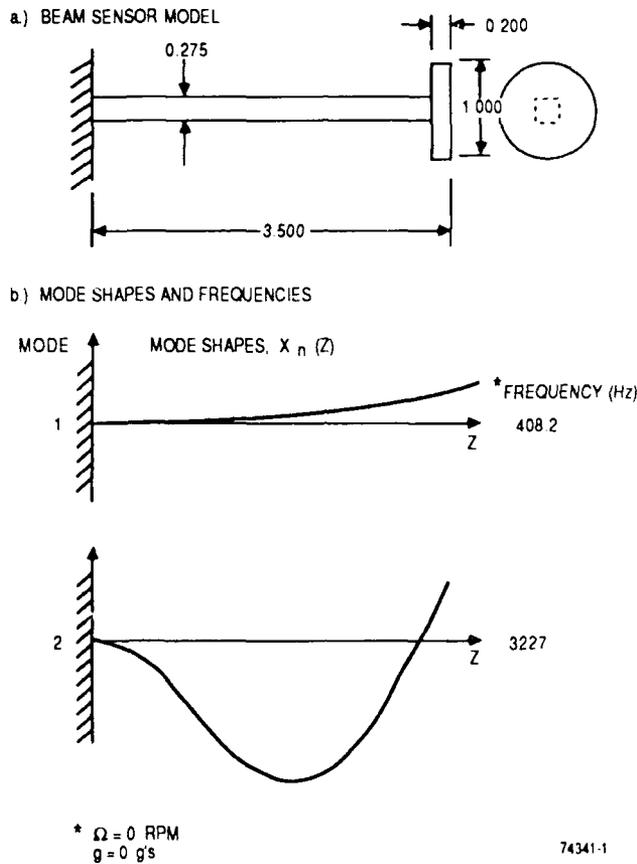
Figure 3. Beam Sensor Model Geometry and Mode Shapes

Table 2 shows the effect of setback acceleration on the modal properties of the first two modes of the beam sensor. As shown in this table, only the resonant frequencies vary significantly as a function of setback acceleration. Therefore only the resonant frequency data in this table is used by the computer code to update using linear interpolation, its value in the analysis as a function of the current setback acceleration.

Table 2

Beam Sensor Modal Properties for Various Setback Acceleration Levels

Mode	Accel. (g's)	fn (Hz)	m_n $\times 10^{-4}$ ($\#$in-sec^2)	I_n $\times 10^{-6}$ ($\#$in-sec^2)	I_{nzx} $\times 10^{-3}$ (in$\#$sec^2)	σ_{nx} $\times 10^{-4}$ ($\#$sec^2)	$^*\epsilon_n$
1	0	408.2	.8059	1.787	.2952	.9855	-.02413
	100	408.6	.8059	1.787	.2992	.9856	-.02413
	4000	425.9	.8065	1.781	.2994	.9862	-.02402
	8000	443.0	.8070	1.774	.2995	.9869	-.02391
	12000	459.4	.8076	1.768	.2996	.9876	-.02380
	16000	475.3	.8081	1.762	.2997	.9882	-.02371
2	0	3227.	2.699	117.3	-.09514	-.9078	-.06403
	100	3228.	2.698	117.3	-.09513	-.9077	.06403
	4000	3246	2.688	117.1	-.09455	-.9047	-.06403
	8000	3265	2.678	117.0	-.09398	-.9017	-.06401
	12000	3284	2.668	116.9	-.09342	-.8988	-.06399
	16000	3302	2.659	116.7	-.09287	-.8959	-.06397

*modal strain 1 inch from base

The effect on the response of the beam sensor of other acceleration loads is accounted for in the modal equations of motion. The other acceleration loads acting on the beam sensor during launch are due to spin rate, rate of change of spin rate and Coriolis acceleration. The beam sensor model deflected in the x direction of the rotating coordinate system with the inertial loads applied as a result of these accelerations is shown in Figure 4.
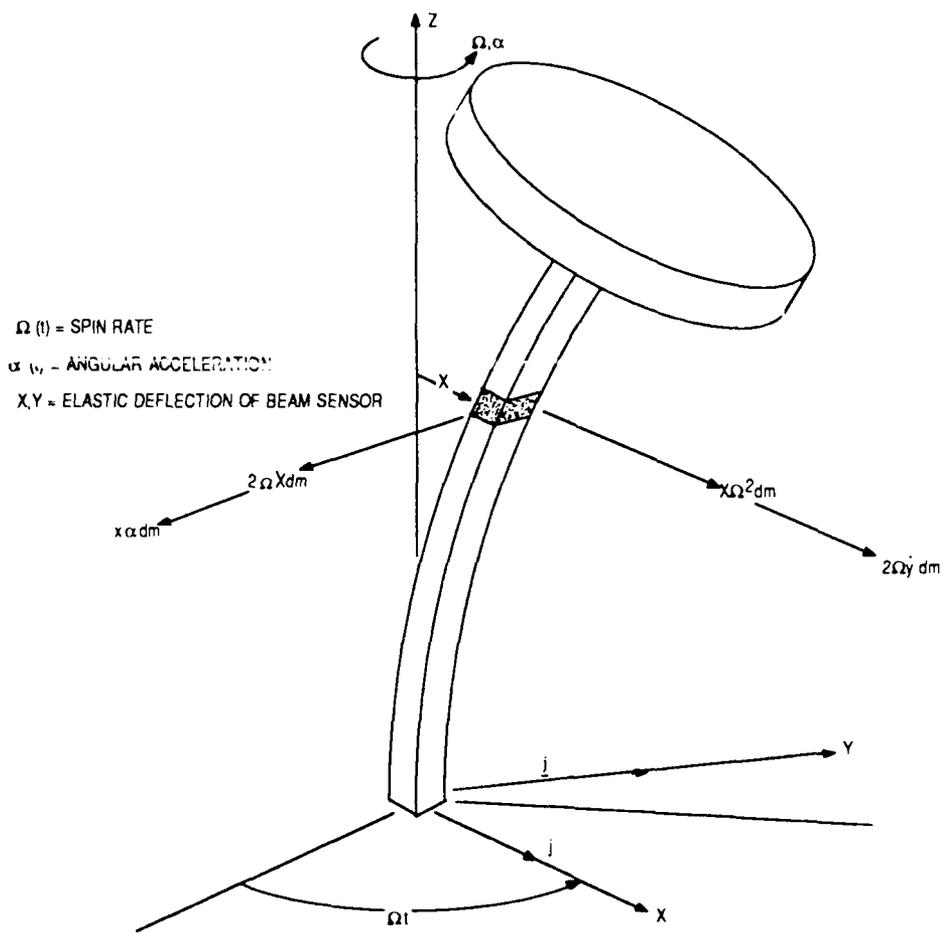
Figure 4. Beam Sensor Analytical Model

The inertial loads on an elemental mass and rotary inertia are;

$$\mathbf{F_x} = -\int_0^1 \mathbf{A_x} dm = \int_0^1 (x\Omega^2 + 2\Omega\dot{y} + y\alpha)dm \tag{1}$$

$$\mathbf{F_y} = -\int_0^1 \mathbf{A_y} dm = \int_0^1 (y\Omega^2 - 2\Omega\dot{x} - x\alpha)dm \tag{2}$$

327

$$M_x = \Omega^2 \int_0^1 \beta_x d(I_p - I_d) \tag{3}$$

$$M_y = -\Omega^2 \int_0^1 \beta_y d(I_p - I_d) \tag{4}$$

The beam sensor disk shown in Figure 4, has a polar mass moment of inertia I_p that is approximately twice the diametral mass moment of inertia I_d, therefore, the difference between the polar and diametral mass moments of inertia shown in equations 3 and 4 will be represented simply by I the diametral mass moment of inertia. The elastic motions of the beam sensor, namely, x, y, β_x and β_y are functions of both position z along the beam sensor and time t. They can be represented as the sum of the modal responses of the beam sensor, therefore,

$$x(z,t) = \sum_n x_n(z) q_{nx}(t) \tag{5}$$

$$y(z,t) = \sum_n y_n(z) q_{ny}(t) \tag{6}$$

$$\beta_x(z,t) = -\sum_n \beta_{nx}(z) q_{ny}(t) \tag{7}$$

$$\beta_y(z,t) = \sum_n \beta_{ny}(z) q_{nx}(t) \tag{8}$$

where,

- x_n and y_n are the modal deflections of the beam sensor in the x and y directions respectively, corresponding to mode n

- β_{nx} and β_{ny} are the modal slopes of the beam sensor, positive about the x and y directions respectively, corresponding to mode n

- q_{nx} and q_{ny} are the generalized coordinate responses of mode n in the x and y directions respectively

Substituting these in the inertial loading equations (5) through (8) yields,

$$F_x = \int_o^1 (\Omega^2 \sum_n x_n q_{nx} + 2\Omega \sum_n y_n \dot{q}_{ny} + \alpha \sum_n y_n q_{ny}) dm \tag{9}$$

$$F_y = \int_o^1 (\Omega^2 \sum_n y_n q_{ny} - 2\Omega \sum_n x_n \dot{q}_{nx} - \alpha \sum_n x_n q_{nx}) dm \tag{10}$$

$$M_x = - \Omega^2 \int_o^1 \sum_n \beta_{nx} q_{ny} dI \tag{11}$$

$$M_y = - \Omega^2 \int_o^1 \sum_n \beta_{ny} q_{nx} dI \tag{12}$$

The generalized forces for a particular mode m developed as a result of these inertial loadings is therefore,

$$Q_{xm} = F_x x_m + M_y \beta_{my} \tag{13}$$

$$Q_{xm} = \int_o^1 (\Omega^2 \sum_n x_n x_m q_{nx} + 2\Omega \sum_n y_n x_m \dot{q}_{ny} + \alpha \sum_n y_n x_m q_{ny}) dm - \Omega^2 \int_o^1 \sum_n \beta_{ny} \beta_{my} q_{nx} dI \tag{14}$$

The integrals for $n \neq m$ m are zero due to orthogonality of the mode shapes hence,

$$Q_{xm} = \Omega^2 (m_n - I_n) q_{nx} + 2\Omega m_n \dot{q}_{ny} + \alpha m_n q_{ny} \tag{15}$$

Similarly,

$$Q_{ym} = \Omega^2 (m_n - I_n) q_{ny} - 2\Omega m_n \dot{q}_{nx} - \alpha m_n q_{nx} \tag{16}$$

where,

$$m_n = \int_o^l x_n^2 dm = \int_o^l y_n^2 dm = \int_o^l x_n y_n dm$$

$$I_n = \int_o^l \beta_{nx}^2 dI = \int_o^l \beta_{ny}^2 dI$$

The equation of motion of mode n for a non-spinning beam sensor in the x or y directions is,

$$(m_n + I_n)\ddot{q}_n + 2\zeta_n\omega_n(m_n + I_n)\dot{q}_n + (m_n + I_n)\omega_n^2 q_n = Q_n \tag{17}$$

Substituting equations 15 and 16 for the generalized forces Q_n in equation 17 yields in matrix form,

$$\begin{bmatrix} m_n+I_n & 0 \\ 0 & m_n+I_n \end{bmatrix} \begin{Bmatrix} \ddot{q}_{nx} \\ \ddot{q}_{ny} \end{Bmatrix} + \begin{bmatrix} 2\zeta_n(m_n+I_n)\omega_n & -2\Omega m_n \\ 2\Omega m_n & 2\zeta_n(m_n+I_n)\omega_n \end{bmatrix} \begin{Bmatrix} \dot{q}_{nx} \\ \dot{q}_{ny} \end{Bmatrix} \tag{18}$$

$$+ \begin{bmatrix} (m_n+I_n)\omega_n^2-(m_n-I_n)\Omega^2 & -\alpha m_n \\ \alpha m_n & (m_n+I_n)\omega_n^2-(m_n-I_n)\Omega^2 \end{bmatrix} \begin{Bmatrix} q_{nx} \\ q_{ny} \end{Bmatrix} = \begin{Bmatrix} \overline{Q}_{nx} \\ \overline{Q}_{ny} \end{Bmatrix}$$

At this point the loads produced by the projectile accelerations at the base of the beam sensor resulting from the balloting load defined earlier can be introduced. Figure 5 shows a sketch of the beam sensor and the ground acceleration inputs $\ddot{u}_g$ and $\ddot{\beta}_g$ applied at an angle γ relative to the rotating coordinate system x, y.

$\ddot{U}_g$ APPLIED LINEAR ACCELERATION   74341-6
$\ddot{\beta}_g$ APPLIED ANGULAR ACCELERATION
γ ANGLE RELATIVE TO BEAM SENSOR OF APPLIED ACCELERATION LOADING
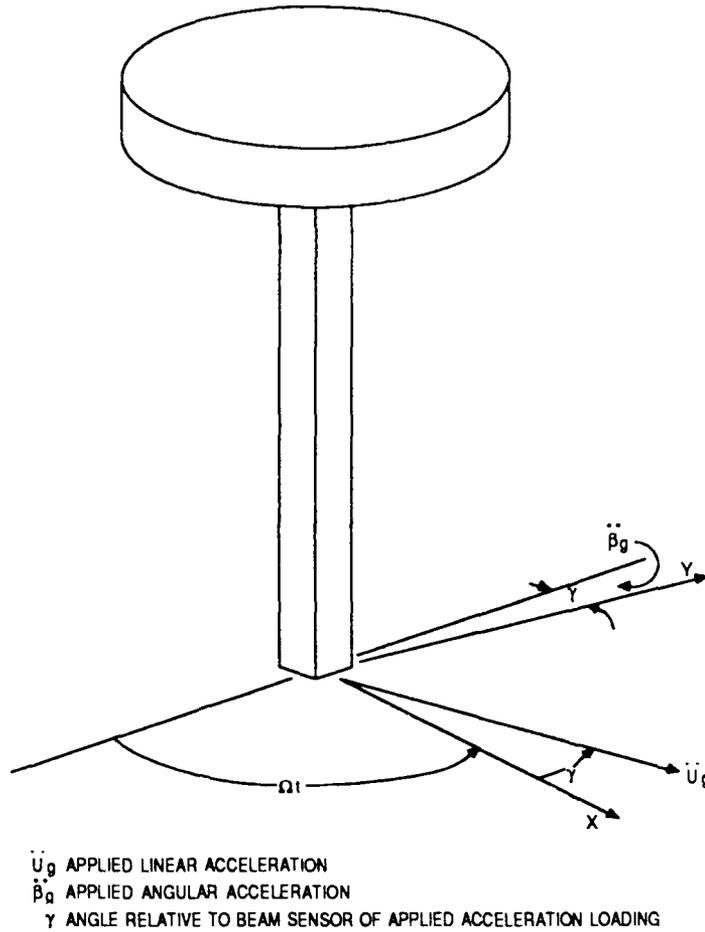
Figure 5. Ground Acceleration acting at Base of Beam Sensor

The generalized force induced by these ground accelerations to the beam sensor are,

$$\mathbf{Q}_{nx} = -\ddot{u}_g\cos(\gamma)\int_0^1 x_n dm \; - \; \ddot{\beta}_g\cos(\gamma)\int_0^1 x x_n dm \; - \; \ddot{\beta}_g\cos(\gamma)\int_0^1 \beta_{ny} dI$$

or,

$$\mathbf{Q}_{nx} = -\left(\ddot{u}_g\sigma_{nx} + \ddot{\beta}_g(I_{nxx} - \hat{\sigma}_{ny})\right)\cos(\gamma) \tag{19}$$

331

Similarly,

$$\overline{Q}_{ny} = -\ (\ddot{u}_g \sigma_{ny} + \dot{\beta}_g(I_{nsy} - \hat{\sigma}_{nx}))\ \sin(\gamma) \tag{20}$$

where,

$$\sigma_{nx} = \int_0^1 x_n dm \qquad \sigma_{ny} = \int_0^1 y_n dm$$

$$\hat{\sigma}_{nx} = \int_0^1 \beta_{nx} dI \qquad \hat{\sigma}_{ny} = \int_0^1 \beta_{ny} dI$$

$$I_{nsx} = \int_0^1 s x_n dm \qquad I_{nsy} = \int_0^1 s y_n dm$$

The modal equations of motion of the beam sensor are given in matrix form by equation 18. They include the generalized forces $\overline{Q}$ due to the ground acceleration excitations defined in equations 19 and 20. These equations were programmed to predict the bending strain time histories of each of the strain gage sets on the beam sensor by summing the modal strains. As indicated by these equations, each non-spinning mode of the beam sensor produces two equations of motion, one for each of the direction x and y, which are coupled by Coriolis acceleration in the damping matrix and angular acceleration in the stiffness matrix. The spin rate, angular acceleration and setback acceleration acting on the beam sensor during gun launch are all functions of time in the analysis. In addition, the resonant frequencies of the beam sensor modes are a function of the setback acceleration. Tables defining each of these variations are input to the computer code so that the proper value of each of them can be used for a gun launch simulation.

Correlation of Test Data with Analysis

An estimate of the magnitude and duration of the balloting load using the above analytical procedure was performed for two firings of the 155 mm parachute recovery projectile. In one firing, flight 309, occurring on June 25, 1982 the gun tube was at mid-life. The other firing, flight 405, was made on August 4, 1982. The condition of the gun tube was considered at end-life for this firing.

A sketch of the beam sensor and some of its pertinent properties are shown in Figure 6. As indicated in this figure, the beam has a square cross-section with two sets of strain gages mounted to it to obtain strain response data in the two directions corresponding to the rotating x and y axes discussed earlier.
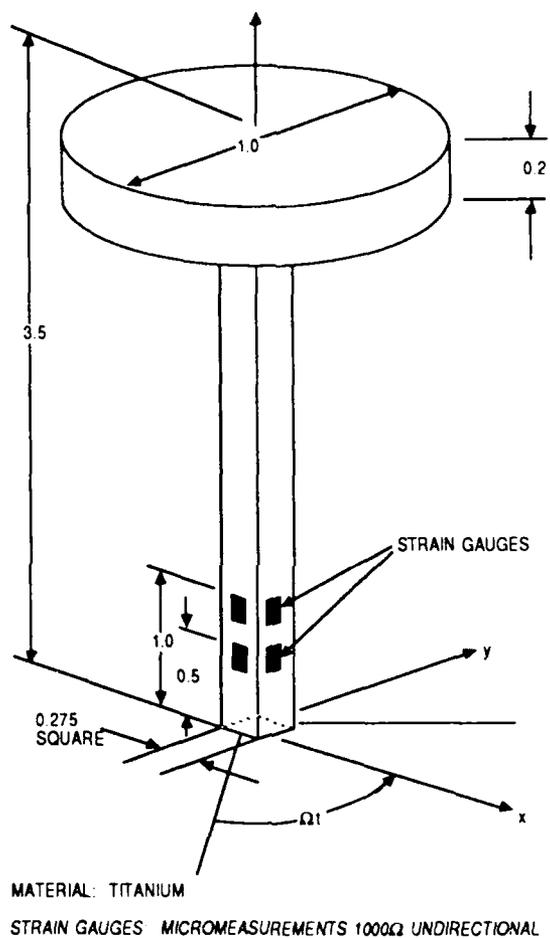
Figure 6. Beam Sensor Guage Locations

Along the axial direction, the gages are positioned at 0.5 and 1.0 inches from the base of the beam which is cantilevered from forward housing (Figure 1). This structure was analyzed and found to be stiff relative to the beam sensor, therefore, the beam sensor was considered to be rigidly mounted at its base.

The predicted time histories of the linear and angular ground accelerations acting at the base of the beam sensor for flights 309 and 405 are shown in Figures 7(a) and 7(b) respectively.
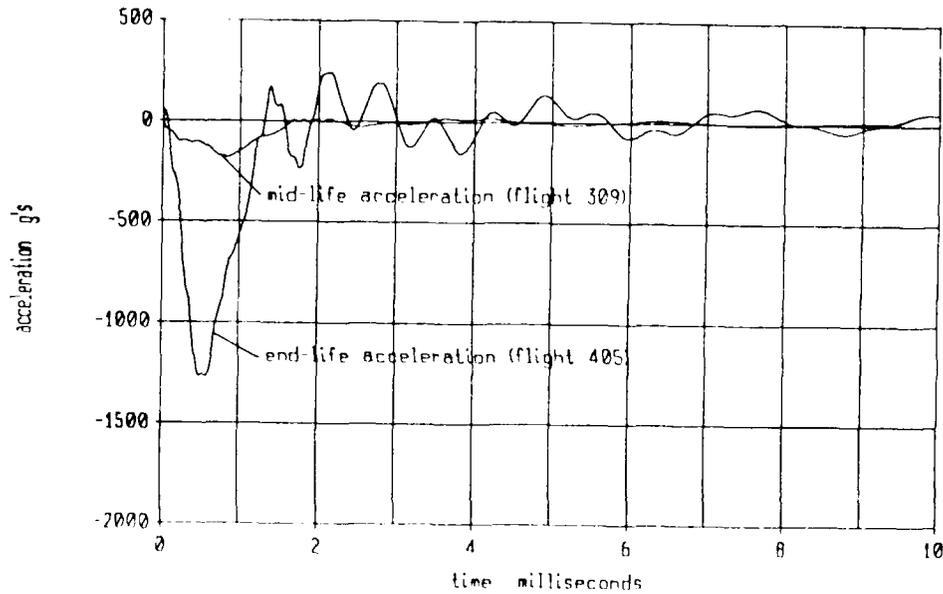

Figure 7a - Linear Acceleration vs Time at Beam Sensor Location
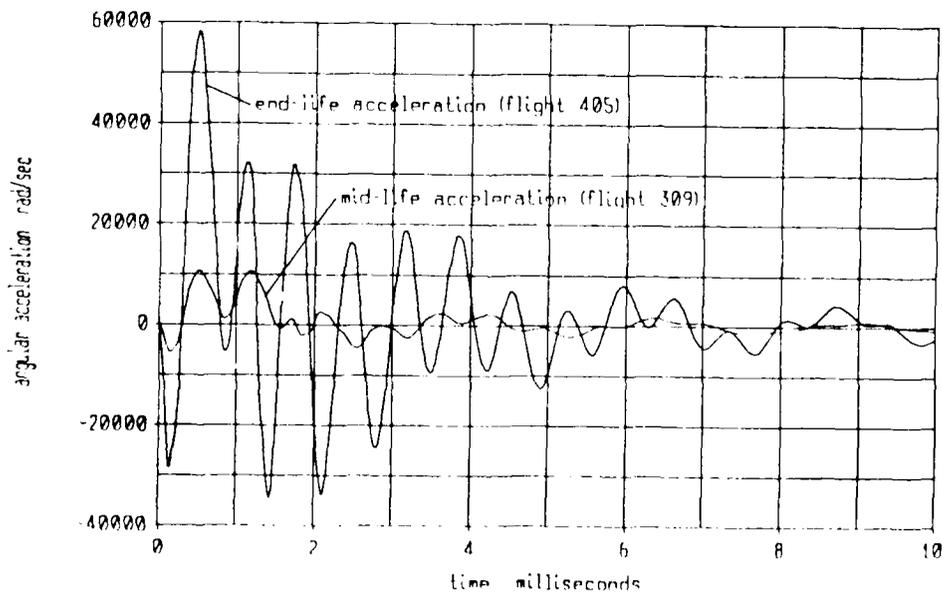

Figure 7b - Angular Acceleration vs Time at Beam Sensor Location

The actual and predicted strain response of the beam sensor at the 1.0 inch position during the flight 309 firing (mid-life gun tube) is shown in Figure 8.
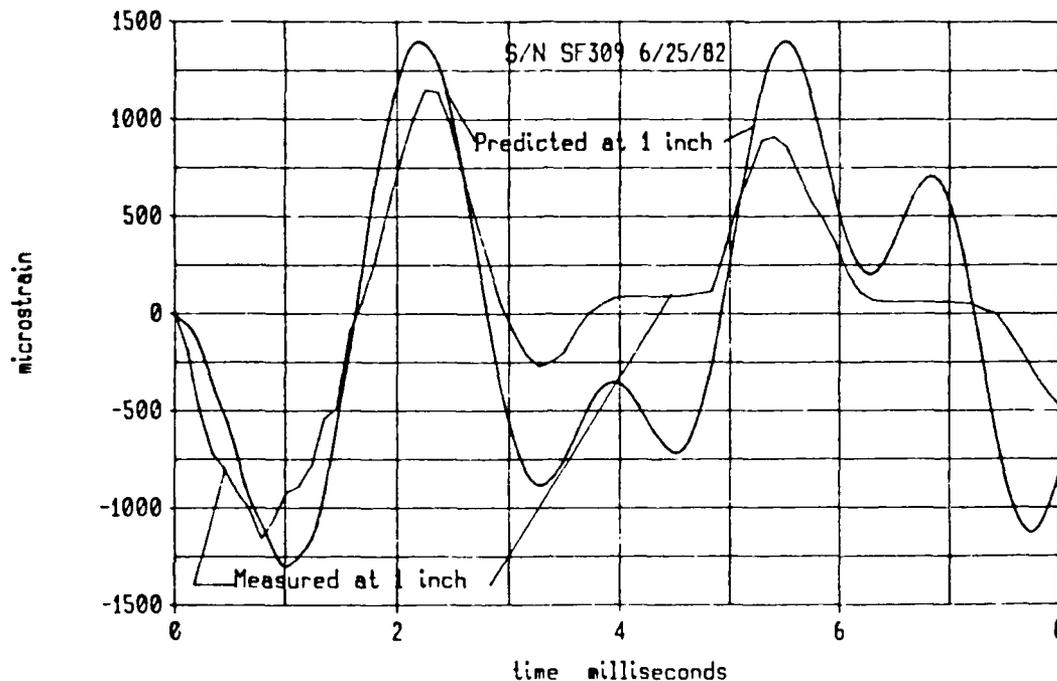

Figure 8 – Measured & Predicted Strain vs Time due to Ballotting

A comparison of the actual and predicted strain time histories shows fairly good correlation. The response frequencies are very close. At approximately 3 8 to 4.8 and 6.2 to 7.2 milliseconds, the test data is somewhat flat in its response. The cause for this is unknown. The balloting load applied to the projectile model required to obtain the correlation shown in Figure 8 was a half sine pulse having a magnitude of 12,900 pounds and a duration of 1.7 milliseconds. Since correlation with the strain gage test data was acceptable, the predicted acceleration responses from the projectile model are considered valid. The maximum predicted acceleration response at the tip of the projectile due to this balloting load was 547 g's.

In the second flight analyzed (flight 405), an end-life gun tube was used. For this case, the predicted balloting load was far more severe. The predicted balloting load required to obtain the correlation shown in Figure 9 was a half sine pulse with a magnitude of 45,000 pounds and a duration of 1.2 milliseconds.
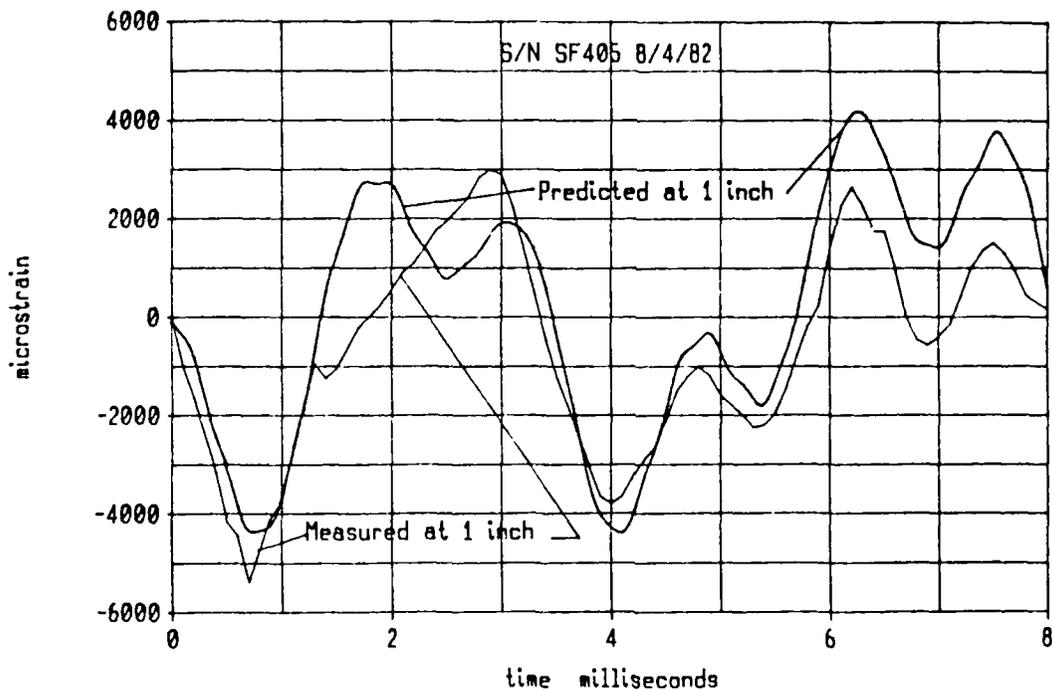
Figure 5 - Measured & Predicted Strain vs Time due to Balloting

As in flight 309 the comparison of the frequency content of the actual and predicted strain time histories is good. The magnitude of the strain levels and the phasing of the actual and predicted strain responses are also fairly close. As in the previous case, since the correlation with the strain test data was good the predicted acceleration responses from the projectile are considered to be valid. The maximum predicted acceleration response at the tip of the projectile for this flight was 2,662 g's which is far greater than the previous case due to the greater balloting load.

Table 3 shows a summary of the maximum acceleration responses of the projectile based on the predicted balloting loads for the two flights studied.

Table 3

Calculated Response Summary

| Test | Balloting Load | | Acceleration at Tip (g's) | Response at CG (g's) |
	Magnitude (#)	Duration (msec)		
mid-life (309)	12,900	1.7	547	101
end-life (405)	45,000	1.2	2,662	311

As indicated, the maximum accelerations of the projectile during the firing with the end-life gun tube (flight 405) was 2,662 g's at the tip and 311 g's at the cg. These same accelerations on the projectile when using the mid-life gun tube (flight 309) were 547 g's at the tip and 101 g's at the cg. The levels of acceleration occurring in the projectile for the firing using the mid-life gun tube were in the order of 20 to 30 percent of those using the end-life gun tube.

Summary

Telemetered strain data taken during the firing of an 155 mm test projectile on two occasions has been compared with analytically predicted strain data. The data was taken from a beam sensor designed to sense lateral loads due to balloting. The purpose for the comparison was to achieve correlation with this data and therefore conclude that the balloting load used in the analytical model was close to the actual load occurring during gun launch. Comparisons showed fairly good correlation for the two firings analyzed, one using a mid-life gun tube and the other using an end-life gun tube. The magnitude of the balloting loads for these two cases were 12,900 pounds and 45,000 pounds respectively. The pulse shape assumed in both cases was a half sine wave. For the mid-life and end-life gun tubes the simulated balloting pulse durations used in the analyses were 1.7 and 1.2 milliseconds respectively. The accelerations predicted at the tip of the projectile for the end-life gun tube simulation was 2,262 g's, approximately five times the predicted results for the mid-life gun tube result.

Acknowledgement

List of Symbols

α angular acceleration of projectile about longitudinal axis (rad/sec**2)

β slope of projectile due to bending (rad)

β_g rotational ground acceleration at base of beam sensor (rad/sec**2)

ϵ_n modal strain (nd)

ω_n resonant frequency of mode n (Hz)

Ω angular velocity of projectile about longitudinal axis (rad/sec)

σ_{nx} modal participation factor in x direction (lbf-sec**2)

σ_{ny} modal participation factor in y direction (lbf-sec**2)

I_{nsx} rotational modal participation factor in x direction (lbf-in-sec**2)

I_{nsy} rotational modal participation factor in y direction (lbf-in-sec**2)

A_x acceleration along x axis of rotating system (in/sec**2)

A_y acceleration along y axis of rotating system (in/sec**2)

F_x inertial force in x direction of rotating system (lbf)

F_y inertial force in y direction of rotating system (lbf)

M_x inertial moment about x direction of rotating system (in-lbf)

M_y inertial moment about y direction of rotating system (in-lbf)

I_p polar moment of inertia of beam sensor disk (lbf-in-sec**2)

I_d diametral moment of inertia of beam sensor disk (lbf-in-sec**2)

m_n generalized mass due to linear displacement of mass (lbf-in-sec**2)

I_n generalized mass due to bending rotation of rotary inertia (lbf-in-sec**2)

q_n generalized coordinate response of mode n (nd)

$\ddot{u}_g$ linear ground acceleration at base of beam sensor (in/sec**2)

x displacement along x axis of rotating system (inches)

y displacement along y axis of rotating system (inches)

z displacement along z axis of rotating system (inches)

Z_{imp} modal deflection at bourrelet (inches)

Z_{beam} modal deflection at beam sensor location (inches)

Z_{cg} modal deflection at projectile cg location (inches)